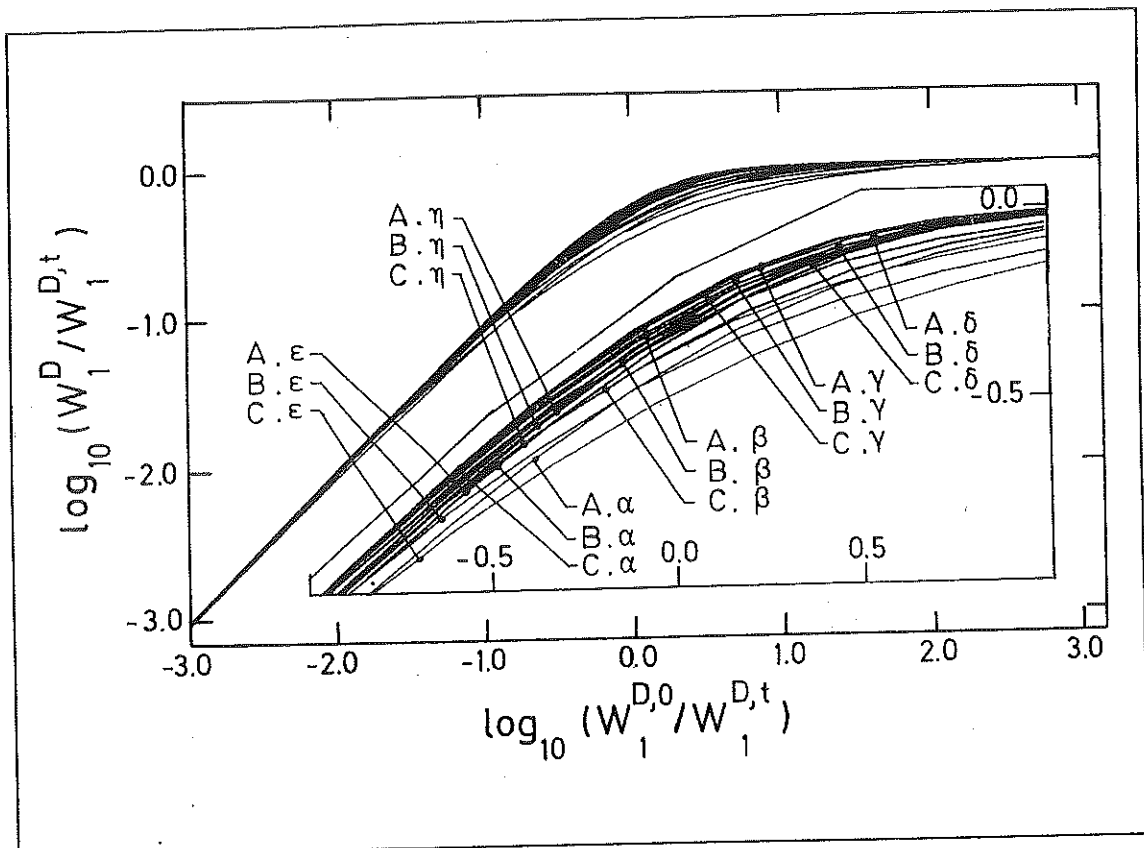


PROFILS DE RAIES DE TYPE P CYGNI: MOMENTS D'ORDRE N,  
EFFETS DE CONTAMINATION PHOTOSPHÉRIQUE ET DE  
MICRO-LENTILLE GRAVITATIONNELLE



par  
Jean SURDEJ  
Astrophysicien  
Docteur en Sciences  
Chercheur Qualifié FNRS

Dissertation présentée en vue de l'obtention  
du grade d'Agrégé de l'Enseignement Supérieur

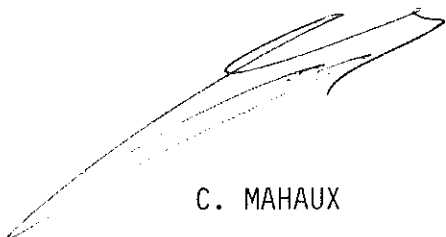


Le présent travail peut être livré à l'impression.

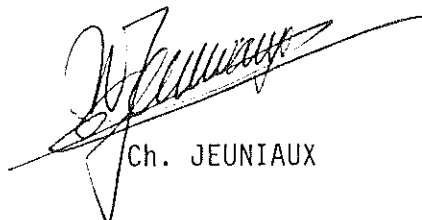
Liège, le 19 octobre 1990.

Le Secrétaire de la  
Faculté des Sciences,  
Secrétaire du Jury,

Le Doyen de la  
Faculté des Sciences,  
Président du Jury,



C. MAHAUX



Ch. JEUNIAUX

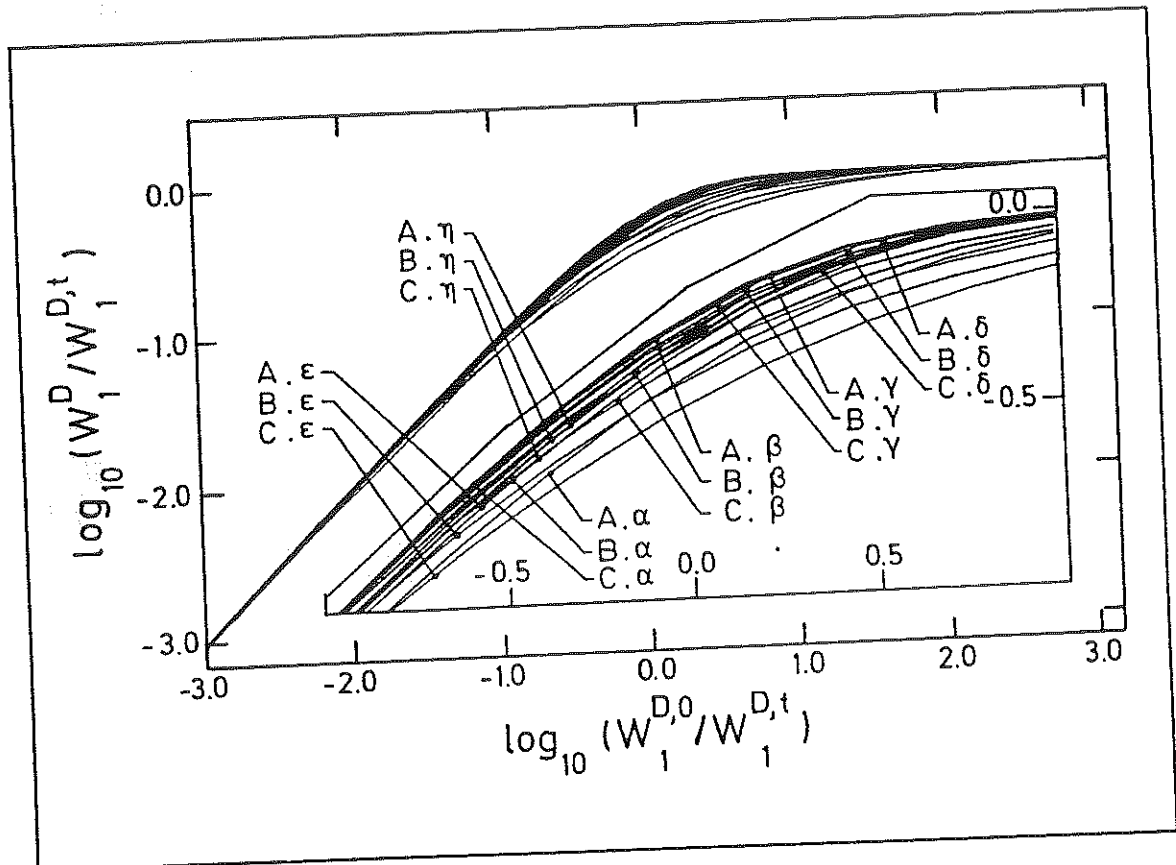
Article 6 de l'arrêté royal du 10 mars 1931 appliquant la loi du 21 mai 1929 sur la collation des grades académiques et le programme des examens universitaires :

"En aucun cas, les opinions de l'auteur ne peuvent être considérées, par le fait de l'autorisation d'impression de la dissertation, comme étant celles du Jury ou de l'Université".





PROFILS DE RAIES DE TYPE P CYGNI: MOMENTS D'ORDRE N,  
EFFETS DE CONTAMINATION PHOTOSPHERIQUE ET DE  
MICRO-LENTILLE GRAVITATIONNELLE



par  
Jean SURDEJ  
Astrophysicien  
Docteur en Sciences  
Chercheur Qualifié FNRS

Dissertation présentée en vue de l'obtention  
du grade d'Agrégé de l'Enseignement Supérieur



A mon père et à ma mère,

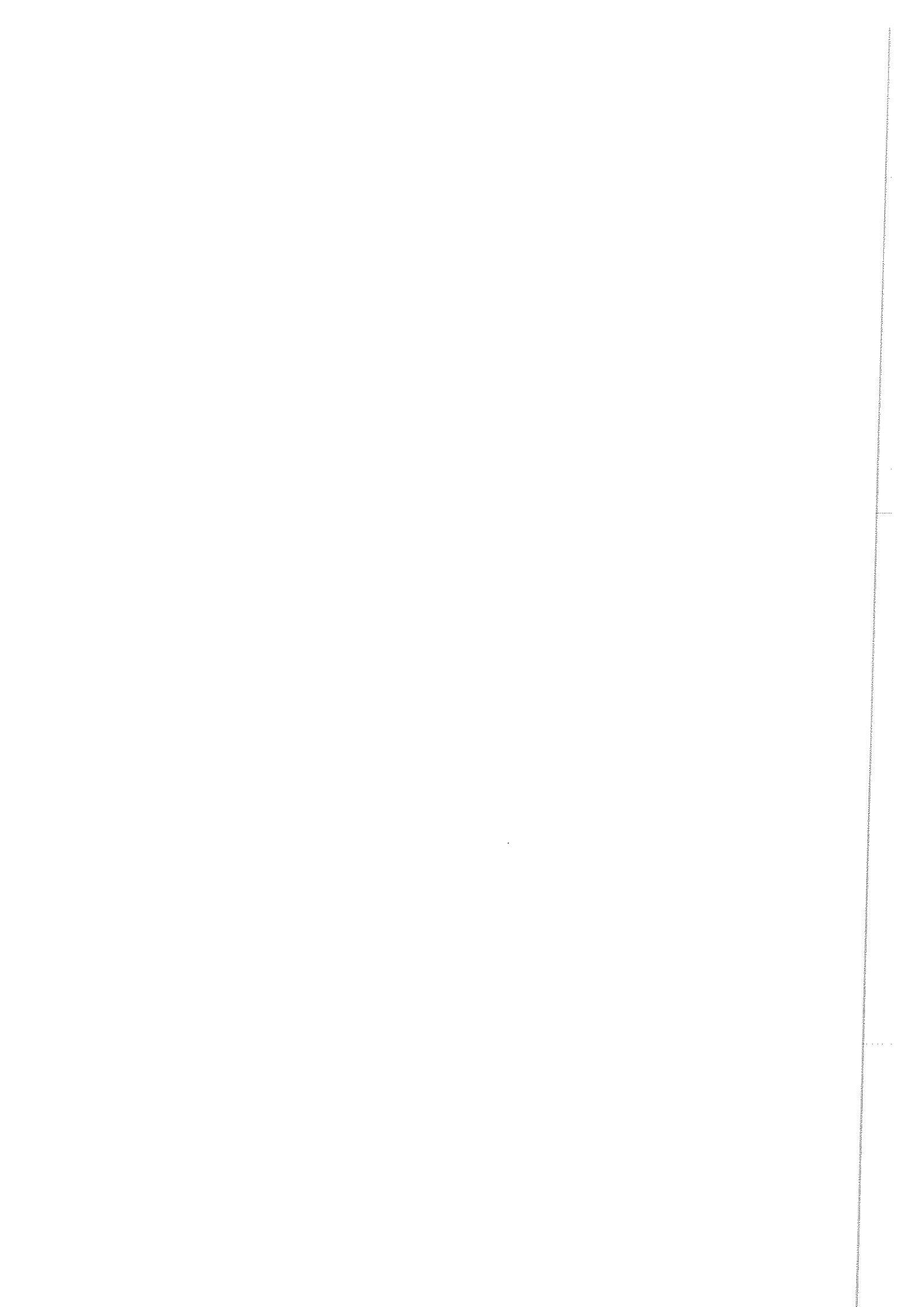


## TABLE DES MATIERES

	<u>Pages</u>
Préface et remerciements .....	i
 Chapitre 1	
INTRODUCTION .....	1
 Chapitre 2	
LES MOMENTS $W_N$ DES PROFILS DE RAIES DE TYPE P CYGNI .....	7
Article 1: The far-UV spectrum of the low-excitation planetary nebula HD138403 .....	17
Article 2: Determination of mass-loss rates from the first order moment $W_1$ of unsaturated P Cygni line profiles .....	29
Article 3: A generalized method for deriving mass-loss rates: the first order moment of unsaturated P Cygni line profiles .....	55

Article 4: Determination of mass-loss rates from early-type stars on the basis of " $\log(W_1) - \log(W_1^0)$ " diagrams .. 71

Articles 5 et 6:

A powerful method for deriving mass-loss rates from planetary nebulae and other objects: the first order moment  $W_1$  of unsaturated P Cygni line profiles

A new approach for deriving the mass-loss rates of BAL quasars: - the first order moment  $W_1$  of an unsaturated P Cygni absorption component ..... 79

Article 7: Analysis of P Cygni line profiles: generalization of the  $n^{\text{th}}$  order moment  $W_n$  ..... 89

Article 8: The  $n^{\text{th}}$  order moment  $W_n^D$  of a resonance doublet P Cygni line profile ..... 101

Article 9: Formation of P Cygni line profiles in relativistically expanding atmospheres ..... 141

Article 10: Revisited mass-loss rates for the nuclei of the planetary nebulae NGC 6210, NGC 6826 and NGC 6543: the first order moment  $W_1$  of subordinate line profiles ..... 183

Article 11: Revisited mass-loss rates for a sample of central stars of planetary nebulae ..... 193

### Chapitre 3

CONTAMINATION PHOTOSPHERIQUE DES PROFILS DE RAIES DE TYPE P CYGNI OBSERVES DANS LE SPECTRE ULTRAVIOLET DES ETOILES DE TYPE O ..... 197

Article 12: Pollution of P Cygni line profiles by FeIV and FeV photospheric absorption in the ultraviolet spectrum of O-type stars .....	201
--	-----

#### Chapitre 4

QUASARS DE TYPE BAL ET EFFETS DE MICRO-LENTILLE GRAVITATIONNELLE .....	219
--	-----

Article 13: Geometry of the mass-outflows around broad absorption line QSOs and formation of the complex Ly $\alpha$ + NV line profile .....	227
--	-----

Article 14: Observational aspects of gravitational lensing ....	239
---	-----

Article 15: A new case of gravitational lensing .....	261
---	-----

Article 16: Discovery of a quadruply lensed quasar: the 'clover leaf' H1413+117 .....	265
---	-----

Article 17: New observations and gravitational lens models of the clover leaf quasar H1413+117 .....	269
--	-----

Article 18: First spectroscopic evidence of micro-lensing on a BAL quasar?: the case of H1413+117 .....	305
---	-----

#### Chapitre 5

CONCLUSIONS GENERALES ET PERSPECTIVES .....	319
---	-----

Bibliographie .....	323
---------------------	-----





## PREFACE ET REMERCIEMENTS

L'objet de la présente dissertation trouve certainement une origine dans l'aspect quelque peu magique et mystérieux que révèlent les profils de raies de type P Cygni, observés pour la première fois dans le spectre d'une ancienne nova du XVII<sup>ème</sup> siècle. En fait, de tels profils sont détectés non seulement dans les spectres d'astres galactiques (étoiles particulières, nuages de gaz interstellaire en mouvement, etc.) mais aussi dans ceux d'objets extragalactiques beaucoup plus lumineux, tels que les quasars BAL situés jusqu'aux confins de notre Univers. De multiples questions viennent alors naturellement à l'esprit: Que régit la formation de ces profils de raies? Leur origine est-elle entièrement intrinsèque aux astres en question? Quelle(s) information(s) physique(s) peut-on déduire de l'analyse des observations? En développant la théorie des moments d'ordre  $n$ , et aussi grâce à l'étude des effets de contamination photosphérique et de micro-lentille gravitationnelle sur la formation des profils de raies de type P Cygni, nous proposons dans ce travail quelques éléments de réponse aux questions posées ci-dessus.

Je tiens à exprimer ma reconnaissance à tous les astrophysiciens liégeois qui ont partagé avec moi, de près (en collaboration) ou d'un peu plus loin (par des discussions), les plaisirs et parfois les difficultés des recherches exposées dans cet ouvrage. En essayant de respecter une certaine chronologie, ces collègues et amis sont: Jean-Pierre Swings, Damien Hutsemékers, Françoise Nemry, Pierre Magain, Marc Remy, Alain Smette, Alain Detal et Eddy Van Drom. Je forme le voeu que nous

puissions ensemble, dans un futur proche et avec nos nombreux collaborateurs étrangers, faire un bon usage du temps d'observation considérable qui nous a déjà été octroyé avec le Télescope Spatial de Hubble, les télescopes de l'Observatoire Européen Austral, etc., en vue de chercher des solutions aux nombreuses questions restées jusqu'ici sans réponse.

Je remercie aussi tous les autres membres de l'Institut d'Astrophysique (ULg) qui font de cet observatoire un lieu de travail où je me rends toujours avec grand plaisir.

Les divers séjours, longs ou courts, que j'ai effectués aux observatoires de l'ESO (Chili et République d'Allemagne Fédérale), du Mont Wilson et de Las Campanas (Californie), du NRAO (Virginie et Nouveau-Mexique), du MMT (Arizona) et du CFH (Hawaii) ont bien sûr aussi été très propices au développement des idées et travaux présentés dans cette dissertation. Je tiens à exprimer tout spécialement ma gratitude à Lo Woltjer (ESO), Ray Weymann (MWLC), Ken Kellermann et Paul Van den Bout (NRAO), et Craig Foltz et Fred Chaffee (MMT) pour leur accueil dans ces différents observatoires.

C'est grâce au soutien de l'Observatoire Européen Austral et du Fonds National de la Recherche Scientifique que j'ai pu exercer le métier de chercheur depuis 1975 et mener à bien la plupart des travaux exposés dans cet ouvrage: que ces institutions trouvent ici l'expression de ma gratitude.

Je remercie aussi Messieurs Léo Houziaux, Jean-Pierre Swings et Jean-Marie Vreux pour avoir lu une première version de cette dissertation et pour m'avoir fait part de leurs remarques et suggestions.

Merci à Jacqueline Bosseloirs, à Denise Caro et à Armand Kransvelt, pour leur gentillesse et l'aide qu'ils m'ont apportée lors de la mise en forme des figures et pour la frappe de la bibliographie apparaissant dans cette dissertation.

Mes remerciements vont également aux familles Clersy et Legast pour m'avoir soulagé lors des travaux d'impression et de reliure du présent ouvrage.

Qu'il me soit enfin permis de remercier tout particulièrement Anna, mon épouse, pour sa compréhension, son soutien, son aide et surtout sa patience dans toutes les étapes qui ont servi à réaliser cette dissertation, et dans mon travail en général.

## Chapitre 1

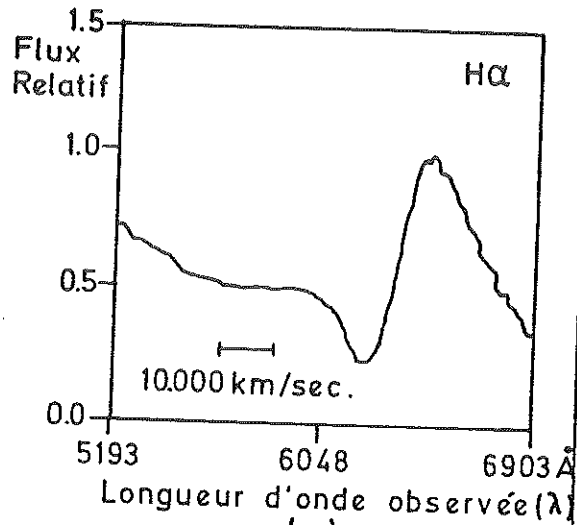
### INTRODUCTION

Un profil de raie de type P Cygni consiste en une large raie spectrale en émission dont l'aile bleue est découpée par une composante en absorption (voir Figure 1.1a). De tels profils de raies sont bien connus des astrophysiciens pour avoir été observés dans les spectres de tout une série d'astres particuliers. Nous citerons parmi ceux-ci l'étoile P Cygni (une ancienne nova qui a été visible au XVII<sup>ème</sup> siècle), les novae, les supernovae (cf. la très brillante supernova 1987a), les étoiles de types Wolf-Rayet, Of, Be, P Cygni, T Tauri, des noyaux de nébuleuses planétaires, des nuages interstellaires formés de molécules diatomiques et même les quasars de type BAL (Broad Absorption Line).

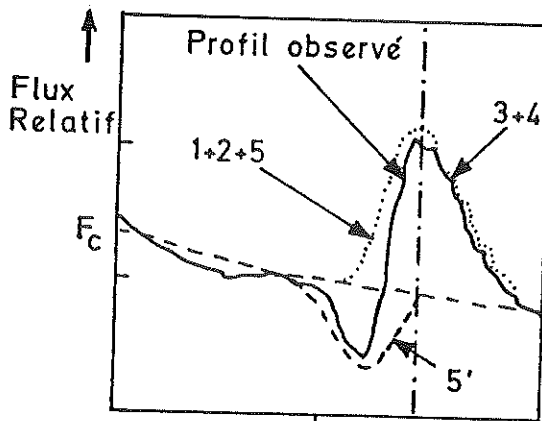
Acceptant d'interpréter en termes d'effets Doppler la séparation entre deux points d'un profil de raie de type P Cygni, Beals (1929, 1931) a été le premier à fournir l'explication intuitive de la formation de tels profils dans les spectres de novae et d'étoiles de type Wolf-Rayet (cf. Figures 1.1b et 1.1c). Ces profils sont tout simplement le reflet de phénomènes de perte de masse affectant l'évolution des astres étudiés. C'est pourquoi il est très important de pouvoir déterminer pour tous ces objets particuliers des taux de perte de masse  $\dot{M}$  aussi précis que possible et la méthode des moments d'ordre  $n$ , présentée au chapitre 2, constitue un outil très puissant d'analyse et d'interprétation de tels profils de raies de type P Cygni. Cette méthode peut être utilisée pour déduire les valeurs de paramètres physiques tels que  $\dot{M}$ , le champ de vitesse  $v(r)$  et la loi d'opacité  $\tau_{12}^r(v)$  caractérisant les atmosphères en expansion.

## OBSERVATION

Exemple de profil de raie de type P Cygni observé pour H $\alpha$  dans le spectre de SN 1987A



## INTERPRETATION



←  $\lambda_0$  →  
bleu ( $\lambda \downarrow$ )      rouge ( $\lambda \uparrow$ )  
(b)

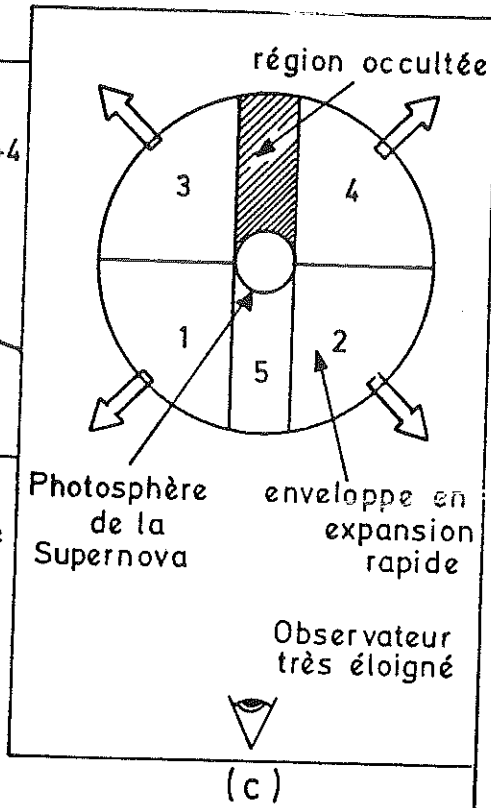


Figure 1.1: Exemple de profil de raie de type P Cygni (voir légende à la page suivante).

Figure 1.1: Exemple de profil de raie de type P Cygni.

Nous avons reproduit dans le diagramme (a) une portion du spectre de SN 1987a, observé le 27 février 1987, à l'Observatoire Européen Austral (Danziger et al. 1987). L'intervalle spectral choisi illustre le profil de raie de type P Cygni dû à la transition  $H\alpha$  de la série de Balmer de l'atome d'hydrogène. Un profil de raie de type P Cygni est généralement formé d'une composante centrale en émission (cf. les contributions 1+2+5 et 3+4 représentées en (b)), découpée sur son aile bleue par une composante en absorption (contribution 5' en (b)). La formation d'un tel profil de raie résulte essentiellement de la re-distribution en longueur d'onde ( $\lambda$ ) des photons émis dans une transition radiative entre deux niveaux atomiques discrets (cf. la longueur d'onde  $\lambda = 6563 \text{ \AA}$  pour la raie  $H\alpha$ ) à la suite d'importants effets Doppler dus aux mouvements d'expansion rapide d'une enveloppe autour d'un objet central (voir le diagramme (c)). Ainsi, les photons émis par les atomes d'hydrogène qui s'approchent d'un observateur distant (cf. les régions 1, 2 et 5 représentées en (c)) donnent lieu à la formation de la composante bleue en émission. De même, l'émission de photons par les atomes qui s'éloignent de l'observateur (cf. les régions 3 et 4 en (c)) rendent compte de la composante rouge en émission. Enfin, l'absorption du continuum  $F_c$ , émis par la photosphère de la supernova, par les atomes situés entre le disque stellaire et l'observateur (voir la région 5 en (c)) donne naturellement lieu à la formation d'une composante en absorption décalée vers les courtes longueurs d'onde. Nous avons aussi indiqué dans le diagramme (a) l'intervalle de longueurs d'onde qui correspond à des mouvements Doppler de l'enveloppe en expansion équivalent à  $10.000 \text{ km/sec}$ . En divisant par deux la largeur Doppler totale du profil observé, on peut ainsi déduire que les mouvements d'expansion de l'enveloppe autour de SN 1987a étaient supérieurs à  $18.000 \text{ km/sec}$  le 27 février 1987. Plus de détails sur l'origine, l'évolution de SN 1987a et l'interprétation des profils de raies observés dans le spectre de cet objet sont donnés dans Surdej (1987b, 1988).

L'étude théorique des moments  $W_n$ , développée tout d'abord dans le cadre de l'approximation de Sobolev<sup>1</sup> pour le transfert de la radiation spectrale (cf. les cas d'une raie simple, d'une raie issue d'un niveau excité et d'un doublet de résonance) et ensuite en tenant compte des effets de turbulence pour les faibles opacités, des effets relativistes d'expansion de l'atmosphère, etc., constitue l'objet essentiel du chapitre 2 et de la présente dissertation. Quelques applications numériques à un échantillon de noyaux de nébuleuses planétaires (NNPs) observés avec le satellite IUE (International Ultraviolet Explorer, voir Boggess et al. 1978) y sont aussi décrites.

Lorsque nous avons essayé d'appliquer la méthode des moments  $W_n$  aux profils de raies de type P Cygni observés pour les transitions de résonance de SiIV, CIV, HeII, etc. dans les spectres IUE d'étoiles de type O, nous nous sommes heurtés au problème de contamination des profils observés par des raies photosphériques sous-jacentes, la plupart de ces dernières étant inconnues jusqu'ici. Le chapitre 3 est consacré à l'identification et à l'étude de l'effet de pollution de ces raies photosphériques sur l'évaluation des taux de perte de masse  $\dot{M}$ .

La découverte récente par notre groupe de chercheurs en astrophysique extragalactique de plusieurs mirages gravitationnels au sein d'un échantillon de quasars très lumineux a motivé l'étude spectroscopique du quasar de type BAL H1413+117, aussi connu sous le nom du *trèfle à quatre feuilles*. L'observation des quatre composantes distinctes de ce mirage cosmique a révélé que des effets de micro-lentille gravitationnelle étaient responsables des différences spectroscopiques observées entre les profils de raies de type P Cygni des quatre images illusoire de cet objet. L'hypothèse que certaines composantes des profils de raies de type

---

<sup>1</sup>L'approximation de Sobolev consiste à supposer homogènes les propriétés physiques (coefficients d'absorption  $\alpha_{12}$  et d'émission  $\epsilon_{12}$ , température cinétique  $T_e$ , etc.) et cinématiques (gradient de vitesse  $\partial v_s / \partial s$ , etc.) de l'enveloppe en expansion le long de distances spatiales  $\Delta s$  à l'intérieur desquelles la vitesse macroscopique  $v_s$  varie d'une quantité  $\Delta v_s$  égale, en ordre de grandeur, à la vitesse maximale  $u_{\max}$  d'agitation thermique et/ou de turbulence des atomes.

P Cygni observés dans le spectre des quasars BAL puissent être induites par des effets de micro-lentille fait l'objet du chapitre 4. Des conclusions générales ainsi que des perspectives d'avenir sont résumées dans le dernier chapitre.

Nous avons choisi de rédiger, au début de chacun des chapitres 2-4, une petite entrée en matière et aussi d'y résumer l'essentiel de nos travaux. La liste complète des articles les plus importants sur lesquels est basée la présente dissertation est donnée dans la table des matières. Les articles déjà publiés, soit en cours de l'être, ont été rassemblés à la fin des différents chapitres.





## Chapitre 2

### LES MOMENTS $W_N$ DES PROFILS DE RAIES DE TYPE P CYGNI

Se plaçant dans le cadre de l'approximation de Sobolev (voir Sobolev, 1947, 1957, 1958; Castor, 1970 et Lucy, 1971) pour traiter le transfert de la radiation spectrale au sein d'une atmosphère en expansion rapide, Castor et Lamers (1979) ont montré combien il était simple et naturel de caractériser les profils de raies de type P Cygni observés dans les spectres d'étoiles de type O au moyen de seulement une distribution de vitesse radiale  $v(r)$  et d'une loi d'opacité fictive  $\tau_{12}^r(v)$ ; cette dernière étant définie à une constante multiplicative près fixant le taux de perte de masse  $\dot{M}$  de l'étoile centrale. Mais alors que la composante en absorption d'un profil de raie de type P Cygni montre une simple dépendance du type  $\exp(-\tau_{12}^r)$ , la composante en émission s'avère être une fonction beaucoup plus complexe des deux distributions  $v(r)$  et  $\tau_{12}^r(v)$ . Pour plus de détails, nous renvoyons le lecteur à quelques travaux antérieurs (Surdej, 1977, 1978a, 1978b, 1979a, 1979b) dans lesquels sont développés les hypothèses de base, le formalisme du transfert radiatif et l'expression générale d'un profil de raie  $E(\lambda)/E_c$  formé au sein d'une atmosphère en expansion accélérée extérieurement (abrégé dans la suite par "atmosphère A.E"). La théorie du transfert radiatif dans des enveloppes décélérées extérieurement (enveloppes D.E) a déjà fait l'objet d'études par Rybicki et Hummer (1978), Surdej (1979b) et Surdej et Swings (1981) et ne sera plus considérée dans la suite du présent travail.

En vue de déterminer les paramètres physiques des enveloppes A.E éjectées à partir d'étoiles de type O, Castor et Lamers (1979) suggèrent alors de comparer les profils de raies observés aux profils de raies théoriques qu'ils ont calculés et présentés sous forme d'un atlas. Bien que cette méthode d'analyse ait été très utilisée dans le passé pour interpréter les profils de raies de résonance observés dans le spectre ultraviolet des étoiles de type O, nous nous sommes heurtés à de sérieuses difficultés lors d'essais de détermination de  $\dot{M}$  à partir des profils de raies saturés observés pour CIV et SiIV dans le spectre IUE ( $\lambda \approx 1170-2070 \text{ \AA}$ ,  $\lambda/\Delta\lambda \approx 1,2 \cdot 10^4$ , voir Figure 2.1) du noyau de la nébuleuse planétaire à faible excitation HD138403 (Surdej et Heck, 1982, présenté comme article 1 dans la présente dissertation; voir aussi Surdej, Surdej et Swings, 1982 pour une étude cinématique de cette nébuleuse).

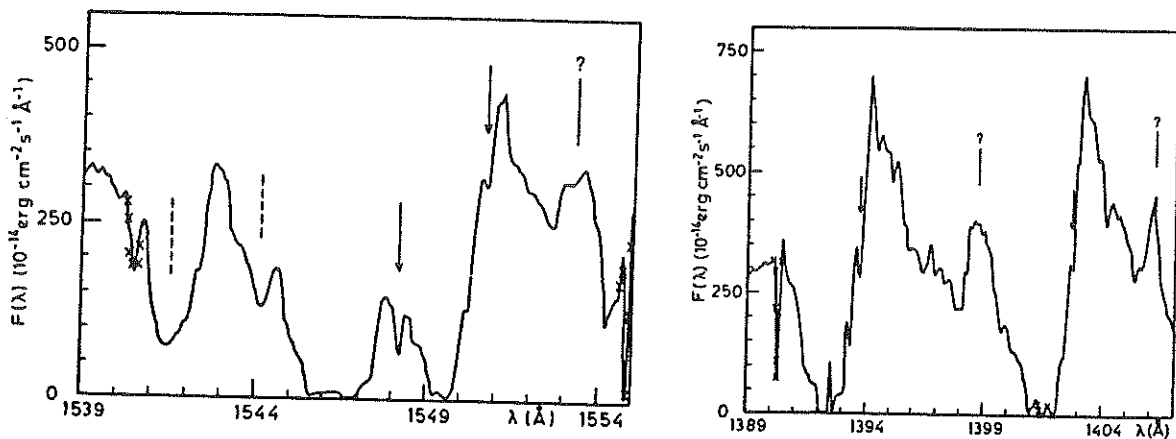


Figure 2.1: Profils de raies saturés pour CIV et SiIV dans le spectre IUE du noyau de la nébuleuse planétaire HD138403. Ces portions du spectre SWP 10855, observé pour le noyau de la nébuleuse planétaire HD138403 au moyen du satellite IUE, illustrent les profils de raies de type P Cygni pour les doublets de résonance de CIV (gauche) et SiIV (droite). Les flèches indiquent les positions au repos des transitions radiatives de CIV ( $\lambda \lambda 1548,18$  et  $1550,77 \text{ \AA}$ ) et SiIV ( $\lambda \lambda 1393,75$  et  $1402,77 \text{ \AA}$ ). Les points d'interrogation correspondent à des raies spectrales non identifiées. A cause de la saturation des profils de raies observés, la méthode qui consiste à comparer ces observations à des profils de raies théoriques ne permet pas de déduire les valeurs des paramètres physiques caractérisant les effets de perte de masse de l'étoile centrale (voir texte).

Par ailleurs, d'autres questions plus fondamentales relatives à l'utilisation de la méthode de Castor et Lamers se sont posées à nous: i) l'inversion des profils de raies observés est-elle unique en termes des distributions  $v(r)$  et  $\tau_{12}^r(v)$  et du taux de perte de masse  $\dot{M}$ ?, ii) comment évaluer les incertitudes affectant la détermination de  $\dot{M}$ ?, iii) que se passe-t-il lorsque la résolution spectrale des profils de raies étudiés n'est pas optimale (cf. les spectres IUE à faible résolution)?, et enfin iv) quels sont les profils de raies observés les mieux adaptés en vue de déterminer des taux de perte de masse  $\dot{M}$  aussi précis que possible?

Un élément de réponse à la question iii) ci-dessus est apparu lorsque Castor, Lutz et Seaton (1981) ont appliqué pour la première fois la méthode du moment d'ordre 1 d'un profil de raie en vue de déterminer la valeur de  $\dot{M}$  pour le noyau de la nébuleuse planétaire NGC 6543. Adoptant pour définition du moment d'ordre  $n$

$$W_n = \left( \frac{c}{\lambda_{12} v_{\max}} \right)^{n+1} \int (E(\lambda)/E_c - 1) (\lambda - \lambda_{12})^n d\lambda, \quad (2.1)$$

où  $E(\lambda)/E_c$  représente l'expression du profil de raie normalisé au continuum stellaire local en fonction de la longueur d'onde  $\lambda$ ,  $\lambda_{12}$  la longueur d'onde centrale de la transition radiative considérée entre les niveaux atomiques discrets 1 et 2,  $c$  la vitesse de la lumière et  $v_{\max}$  la vitesse maximale d'expansion de l'enveloppe, Castor et ses collaborateurs ont montré que les moments  $W_n$  étaient tout à fait insensibles à la dégradation de la résolution instrumentale. De plus, pour le cas des profils de raies non saturés, ces auteurs ont établi une simple relation entre le moment  $W_1$  et  $\dot{M}$ . Malheureusement, cette relation a été déterminée pour un choix bien particulier du champ de vitesse  $v(r)$  et de la loi d'opacité  $\tau_{12}^r(v)$ .

Une de nos contributions principales au développement de la théorie des moments  $W_n$  a été de montrer que la relation existant entre  $W_1$  et  $\dot{M}$  est d'application beaucoup plus générale qu'initialement suggéré, et que les moments d'ordre  $n$  constituent un outil très puissant d'analyse et d'interprétation des profils de raies observés, pour autant que ceux-ci ne soient pas optiquement saturés (i.e.  $\tau_{12}^r \leq 1$ ). Il est par exemple très simple de montrer que la relation entre  $W_1$  et  $\dot{M}$  est indépendante du choix du champ de vitesse  $v(r)$  et de la loi d'opacité  $\tau_{12}^r(v)$ . En effet, si l'atmosphère en expansion est optiquement mince à la radiation

spectrale au voisinage de la longueur d'onde  $\lambda_{12}$ , on conçoit aisément que (négligeant pour l'instant l'effet d'occultation de l'étoile centrale) la radiation émise par les régions de l'enveloppe s'approchant et s'éloignant d'un observateur très distant contribuera de façon égale au profil bleu et rouge de la composante en émission (cf. Figure 1.1c); en d'autres termes, le profil de raie en émission est une fonction symétrique par rapport au déplacement spectral  $\lambda - \lambda_{12}$ . Représentant par  $E_{\text{abs}}(\lambda)/E_c$  le profil de la composante en absorption formée suite à la diffusion des photons émis par l'objet central dans l'atmosphère en expansion, l'équation (2.1) pour  $n = 1$  se réduit à

$$W_1 = \left( \frac{c}{\lambda_{12} v_{\text{max}}} \right)^2 \int ( E_{\text{abs}}(\lambda)/E_c - 1 ) ( \lambda - \lambda_{12} ) d\lambda . \quad (2.2)$$

Etant donné que

$$E_{\text{abs}}(\lambda)/E_c = \exp(-\tau_{12}^r(\lambda)) , \quad (2.3)$$

et que l'approximation de faible opacité permet d'écrire

$$\exp(-\tau_{12}^r(\lambda)) \approx 1 - \tau_{12}^r(\lambda) , \quad (2.4)$$

l'équation (2.2) se simplifie en

$$W_1 = \left( \frac{c}{\lambda_{12} v_{\text{max}}} \right)^2 \int \tau_{12}^r(\lambda) ( \lambda - \lambda_{12} ) d\lambda . \quad (2.5)$$

Dans le cadre de l'approximation de Sobolev, l'expression de  $\tau_{12}^r$  peut être exprimée sous la forme (Surdej, 1978b)

$$\tau_{12}^r = n_1 ( \Pi e^2 / mc ) f_{12} \lambda_{12} / \frac{dv}{dr} , \quad (2.6)$$

où  $n_1$  représente la population volumique des atomes dans le niveau inférieur,  $f_{12}$  la force d'oscillateur de la transition radiative  $1 \rightarrow 2$ ,  $dv/dr$  le gradient de vitesse radial évalué à une distance  $r$  de l'objet central et,  $e$  et  $m$  respectivement la charge électrique et la masse de l'électron. En nous servant de la relation Doppler classique

$$( \lambda - \lambda_{12} ) / \lambda_{12} = v / c , \quad (2.7)$$

l'expression (2.5) de  $W_1$  peut être ré-écrite comme suit

$$W_1 = \left( \frac{\pi e^2 f_{12} \lambda_{12}}{m c v_{\max}^2} \right) \int_R^{r_{\max}} n_1 v dr, \quad (2.8)$$

$R$  et  $r_{\max}$  étant respectivement les rayons de l'objet central et de l'atmosphère en expansion contribuant à la formation du profil de raie de type P Cygni. Définissant l'abondance fractionnaire  $n(\text{level})$  de l'ion peuplant le niveau atomique inférieur 1 au moyen de la relation

$$n(\text{level}) = n_1 / N(\text{élément}), \quad (2.9)$$

où  $N(\text{élément})$  représente la densité totale de l'élément considéré ayant une abondance

$$A(\text{élément}) = N(\text{élément}) / N_{\text{tot}}, \quad (2.10)$$

$N_{\text{tot}}$  étant la densité nucléique totale évaluée à une distance  $r$ , il est aisé de combiner l'équation (2.8) ci-dessus avec l'expression du taux de perte de masse

$$\dot{M} = - 4\pi r^2 v(r) N_{\text{tot}} \bar{\mu} M_{\text{amu}}, \quad (2.11)$$

pour obtenir finalement

$$W_1 = \left( \frac{\pi e^2}{m c} \right) f_{12} \lambda_{12} A(\text{élément}) \dot{M} \bar{n}(\text{level}) \left( \frac{1}{L_{\max}} - 1 \right) / \left( 4\pi \bar{\mu} M_{\text{amu}} v_{\max}^2 R \right). \quad (2.12)$$

Dans cette dernière expression,  $\bar{\mu}$  représente le poids atomique moyen de tous les ions dans le vent stellaire,  $M_{\text{amu}}$  l'unité de masse atomique et

$$\bar{n}(\text{level}) = \int_1^{L_{\max}} n(\text{level}) d(1/L) / \int_1^{L_{\max}} d(1/L), \quad (2.13)$$

$L$  étant la distance radiale  $r$  à l'objet central, exprimée en unités du rayon  $R$

$$L = r / R. \quad (2.14)$$

Cette simple démonstration nous a conduit au résultat attendu (voir Equation (2.12)): une relation unique existe entre  $W_1$  et  $\dot{M}$ , quel que soit le choix adopté pour le champ de vitesse  $v(r)$  et/ou la loi d'opacité  $\tau_{12}^r(v)$ . Par ailleurs, si on prend en compte l'effet d'occultation par l'objet central des parties de l'atmosphère en expansion les plus éloignées de l'observateur, on trouve au moyen d'une démonstration plus rigoureuse la relation  $\dot{M} - W_1$  suivante

$$\dot{M}(-M_{\odot}/\text{an}) = -1,19 \cdot 10^{-21} \frac{v_{\text{max}}^2 (-\text{km/sec}) R(-R_{\odot}) W_1}{f_{12} \lambda_{12}(-10^3 \text{Å}) A(\text{élément}) \bar{n}(\text{level})} , \quad (2.15)$$

où

$$\bar{n}(\text{level}) = \int_1^{L_{\text{max}}} (W(L) - 1) n(\text{level}) d(1/L) / \int_1^{L_{\text{max}}} (W(L) - 1) d(1/L) , \quad (2.16)$$

$W(L)$  représentant le facteur de dilution géométrique

$$W(L) = 0,5 \left( 1 - \sqrt{1 - \frac{1}{L^2}} \right) . \quad (2.17)$$

Cette relation est vérifiée de façon tout à fait générale indépendamment:

- i) du type du champ de vitesse  $v(r)$  et/ou de la distribution de l'opacité  $\tau_{12}^r(v)$  ( voir Surdej 1982b, article 2 dans la présente dissertation; Surdej, 1983a, article 3; Surdej 1983b, article 4 et Surdej, 1982a, article 5),
- ii) de l'existence de processus d'excitation collisionnelle dans l'atmosphère en expansion rapide (cf. article 2),
- iii) d'une rotation d'ensemble de l'enveloppe dans laquelle est formé le profil de raie (cf. article 2),
- iv) de la présence d'une raie photosphérique sous-jacente en absorption ( $\Delta\dot{M}/\dot{M} \leq 20 \%$ ) (cf. article 2) et/ou en émission (voir Surdej 1983c, article 6),
- v) d'un important effet d'assombrissement centre-bord de l'objet central (voir Surdej, 1981 et article 2),

vi) de la validité de l'approximation de Sobolev utilisée pour traiter le transfert de la radiation spectrale (voir article 3 et Surdej, 1985, article 7),

vii) de la structure du multiplet des transitions de résonance considérées (voir article 2; Surdej et Hutsemékers, 1990, article 8; et Surdej, 1980 pour une étude plus détaillée de la formation des profils de raies dus à un doublet de résonance),

viii) et enfin, des effets induits par des mouvements relativistes d'une atmosphère en expansion très rapide ( $v/c \gg 0,1$ , voir Hutsemékers et Surdej, 1990, article 9).

En vue de fournir des éléments de réponse au problème de l'unicité de l'inversion d'un profil de raie de type P Cygni en termes des quantités  $\dot{M}$ ,  $v(r)$  et  $\tau_{12}^r(v)$  caractérisant les atmosphères étudiées, nous avons généralisé la définition des moments d'ordre  $n$  pour le cas d'une raie de résonance simple (article 7). Considérant des distributions réalistes pour  $v(r)$  et  $\tau_{12}^r(v)$  (cf. Castor et Lamers, 1979; Garmany et al. 1981), nous avons construit deux différents types de diagrammes ayant un intérêt astrophysique immédiat. Ceux-ci apparaissent comme étant la généralisation de la courbe de croissance utilisée pour l'étude des raies formées dans des atmosphères statiques. Ainsi, pour le cas des profils de raies non saturés, les premiers diagrammes de type " $\log(W_n) - \log(W_n^0)$ " nous ont permis d'établir que la relation  $W_n = W_n^0$  est vérifiée pour  $n = 0-3$ , indépendamment du choix de  $v(r)$  et  $\tau_{12}^r(v)$ . Pour  $n = 0, 1, 2$  et  $3$ , nous avons montré que  $W_n^0$  est une quantité liée respectivement à la densité de colonne  $N_1$ , au taux de perte de masse  $\dot{M} \bar{n}(\text{level})$ , à la colonne d'impulsion et à (deux fois) la colonne d'énergie cinétique de l'ion détecté dans le vent stellaire. Nous avons aussi décrit comment il était possible de déduire le champ de vitesse  $v(r)$  et la loi d'opacité  $\tau_{12}^r(v)$  caractérisant un profil de raie observé en reportant dans des diagrammes de type " $\log(W_n) - \log(W_0)$ " les valeurs mesurées des moments  $W_n$  ( $n = 1-3$ ).

Nous avons ensuite élargi cette étude au cas d'une transition formée par un doublet de résonance (cf. article 8). La définition des moments  $W_n^D \propto \int (E(\lambda)/E_c - 1) (\lambda - \lambda_D)^n d\lambda$  nous a ainsi permis pour  $n, n' = 0-3$  de construire des diagrammes de type " $\log(W_n^D/W_n^{D,t}) - \log(W_n^{D,0}/W_n^{D,t})$ " (cf. Figure 2.2 pour  $n = 1$ ) et " $\log(W_n^D) - \log(W_n^D)$ " (cf. Figure 2.3 pour  $n = 1$  et  $n' = 0$ ) en vue de déterminer le taux de perte de masse  $\dot{M}$ , le champ de vitesse  $v(r)$

et la loi d'opacité  $\tau_{12}^R(v)$  à partir de l'analyse de profils de raies observés pour des doublets de résonance. Nous rappelons que  $W_n^{D,t}$  représente la valeur asymptotique de  $W_n^D$  lorsque  $W_n^{D,0} \rightarrow \infty$ .

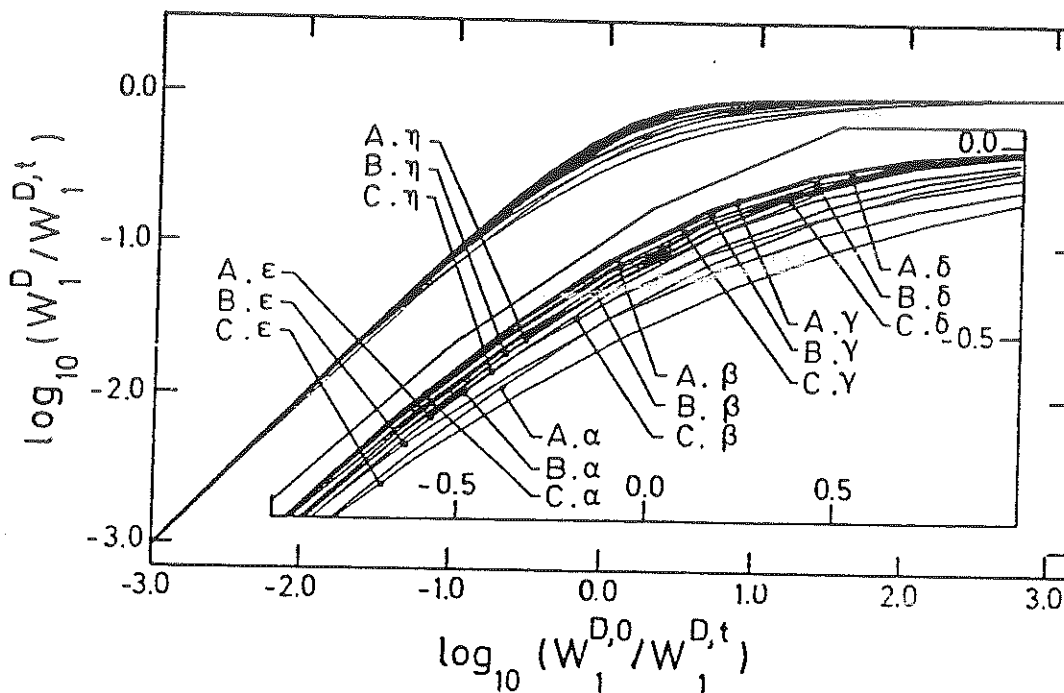


Figure 2.2: Diagramme " $\log(W_1^D/W_1^{D,t}) - \log(W_1^{D,0}/W_1^{D,t})$ ".

Ce diagramme, aussi représenté sur la page de couverture, illustre l'ensemble des courbes théoriques calculées pour 18 choix différents du champ de vitesse  $v(r)$  (modèles A-C) et de la loi d'opacité  $\tau_{12}(v)$  (modèles  $\alpha$ - $\eta$ ), pour une séparation du doublet de résonance  $\Delta v_{23}/v_{\max} = 0,5$ . Un tel diagramme est utilisé pour déterminer le taux de perte de masse  $\dot{M} \propto W_1^{D,0}$  à partir de la mesure du moment  $W_1^D$  d'un profil de raie observé (voir article 8).

Dans le cadre de l'approximation de Sobolev, nous avons adapté l'approche probabiliste du transfert de la radiation spectrale (Surdej, 1979a) au cas d'atmosphères en expansion relativiste (voir article 9). Pour un modèle d'atome à deux niveaux (transition de résonance simple), nous avons établi les expressions relativistes de la fonction source  $S_{12}$ , du profil de raie  $E(X)/E_c$  et des moments  $W_n^R$ . Nous avons montré que même dans le cadre de la relativité restreinte, le moment d'ordre 1 reste un outil très puissant pour déterminer les taux de perte de masse  $\dot{M}$  d'objets tels que les supernovae (Weiler et Sramek, 1988) et les quasars BAL (Weymann et Foltz, 1983).



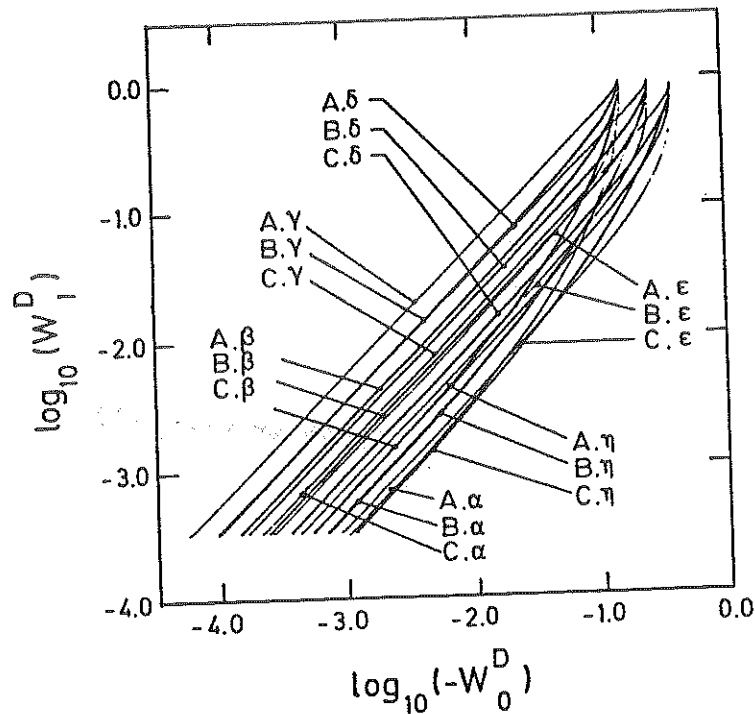


Figure 2.3: Diagramme " $\log(W_1^D) - \log(-W_0^D)$ ".

Pour les mêmes choix des distributions  $v(r)$  et  $\tau_{12}^r(v)$  que celles utilisées à la figure 2.2 lors du calcul de  $W_1^D$ , ce diagramme illustre les différentes courbes  $\log(W_1^D) - \log(-W_0^D)$  résultantes. En reportant dans un tel diagramme les valeurs mesurées pour  $W_1^D$  et  $W_0^D$ , il est possible de déterminer les caractéristiques du champ de vitesse  $v(r)$  et de la loi d'opacité  $\tau_{12}^r(v)$  qui reproduisent au mieux les profils de raies observés (cf. article 8).

Enfin, nous terminons ce chapitre par quelques exemples d'application numérique de la théorie du moment d'ordre 1 à la détermination du taux de perte de masse  $\dot{M}$ . Tout d'abord, nous avons établi une relation entre le moment  $W_1$  et  $\dot{M}$  pour une raie simple issue d'un niveau atomique excité (Hutsemékers et Surdej, 1986; 1987, article 10 et 1988a). La construction de diagrammes de type " $\log(W_1) - \log(W_1^0)$ " nous a alors permis d'évaluer les taux de perte de masse  $\dot{M}$  pour un échantillon de noyaux de nébuleuses planétaires observés spectroscopiquement au moyen du satellite IUE (Hutsemékers et Surdej, 1989b et 1989a, article 11). Ces déterminations sont basées sur la mesure du moment  $W_1$  de profils de type P Cygni observés pour les raies de OIV  $\lambda$  1342 et

OV  $\lambda$  1371. Cette étude nous a permis de calculer les écarts à la relation  $W_1^0 = W_1$  et de montrer que les évaluations précédentes des taux de perte de masse  $\dot{M}$  pour les étoiles centrales des nébuleuses planétaires NGC 6210, NGC 6826 et NGC 6543 avaient été sous-estimées par un facteur allant de 7 à 20 (cf. article 10). Par ailleurs, l'estimation de  $\dot{M}$  pour un échantillon de dix-sept noyaux de nébuleuses planétaires observés avec IUE nous a permis de confirmer le danger d'extrapoler la relation  $\dot{M} - L$  établie pour des étoiles jeunes de type OB en vue de déterminer le taux de perte de masse  $\dot{M}$  des NNPs à partir de la mesure de leur luminosité  $L$  (cf. Cerruti-Sola et Perinotto, 1985, 1989 et article 11).

## Article 1

# THE FAR-UV SPECTRUM OF THE LOW-EXCITATION PLANETARY NEBULA HD138403

Surdej, J., Heck, A.: 1982, *Astron. Astrophys.* 116, 80-88.

Nous présentons dans cet article les résultats de l'analyse de spectres ultraviolets ( $\lambda\lambda \approx 1170-2070 \text{ \AA}$ ,  $\lambda/\Delta\lambda \approx 1,2 \cdot 10^4$ ) obtenus pour le noyau de la nébuleuse planétaire à faible excitation HD138403, au moyen du satellite astronomique IUE. La détection de profils de raies de type P Cygni pour les transitions de résonance de NV, SiIV et CIV et pour la raie de HeII  $\lambda 1640$  révèle un phénomène de perte de masse importante pour l'étoile centrale de type O7(f)eq, avec une vitesse terminale de l'ordre de 800 km/sec. La difficulté d'interpréter en termes physiques les profils de raies saturés observés pour SiIV et CIV dans le spectre de cet objet a motivé notre intérêt initial pour l'étude théorique des moments d'ordre  $n$  des profils de raies de type P Cygni.

04 13 40 4

## The Far-UV Spectrum of the Low-excitation Planetary Nebula HD 138403\*

J. Surdej<sup>1,\*\*</sup>, and A. Heck<sup>2,\*\*\*</sup>

<sup>1</sup> Institut d'Astrophysique, Université de Liège, Avenue de Cointe 5, B-4200 Cointe-Ougrée, Belgium

<sup>2</sup> Astronomy Division, ESTEC, European Space Agency, Noordwijk, The Netherlands

Received May 18, accepted June 11, 1982

**Summary.** The IUE satellite was used to record the first high resolution ( $\lambda/\Delta\lambda \sim 1.2 \cdot 10^4$ ) far-ultraviolet spectra ( $\lambda \sim 1170$ – $2070 \text{ \AA}$ ) of the low-excitation planetary nebula HD 138403.

The most prominent spectral features of this object consist of a stellar continuum cut by numerous interstellar lines, on which are superimposed various types (I, VIII, IX) of P Cygni profiles. Those due to the resonance doublets of N V, C IV, Si IV, etc. and to the He II  $\lambda 1640$  line transition indicate the presence of an important mass-loss from the central object, with terminal velocities of the order of  $800 \text{ km s}^{-1}$ .

The only nebular emissions identified in the far-UV spectrum are the C III]  $\lambda 1909$  intercombination line with its associated  $2s^2 1S_0 - 2s2p^3 P_2^0$  magnetic quadrupole transition. Using the ratio of the line fluxes measured for these components, we have derived a value  $n_e = 1.1(\pm 0.4) \cdot 10^5 \text{ cm}^{-3}$  for the electron density in the main nebula.

Furthermore, a remarkable asymmetry in the red wing of the C III]  $\lambda 1908.734$  emission profile is found to be consistent with the presence of an emission satellite, shifted by  $+123 \text{ km s}^{-1}$  with respect to the central main component. These data support the hypothesis that a bipolar structure is expanding around HD 138403, via the selective radiative process of edge and/or line locking mechanism(s).

**Key words:** ultraviolet spectra – planetary nebula – HD 138403 – mass-loss

### 1. Introduction

It is well established (Heap, 1977a, b) that HD 138403  $\equiv 315$ – $13^{\circ}1 \equiv \text{He}2$ –131 is a young, very bright and compact evolving low-excitation planetary nebula whose central nucleus, classified 07(f)eq with a visual absolute magnitude  $M_v = -2.1$ , undergoes a continuous mass-loss.

Thackeray (1950) has measured a circular disk, about  $6''$  in diameter, around the central star HD 138403 and Koelbloed

(1962) has derived the physical conditions prevailing in the nebula:  $n_e = 210^4 \text{ cm}^{-3}$ ,  $T_e = 9000 \pm 1000 \text{ K}$ .

Various observers (cf. Méndez and Niemela, 1979) have reported spectral variations over time scales ranging from a few days to a few tens of years, in the strength and P Cygni profile of various line transitions of He, C, N, and Si ions. Surdej et al. (1982, referred to below as Paper I) have further discussed the variability of the visible spectrum of HD 138403 and they have reported the discovery of faint blue and red satellites, shifted by approximately  $124 \text{ km s}^{-1}$ , on each side of the Balmer and [O II] emission lines. Invoking the near coincidence ( $v_s = 122 \text{ km s}^{-1}$ ) between the wavelengths of line transitions due to  $\text{H}(n=1, 2, \dots \rightarrow n')$  and  $\text{He II}(n=2, 4, \dots \rightarrow 2n')$ , they have interpreted these spectral features in terms of the formation of a bipolar structure, nearly aligned along the line of sight, and driven away from the central star by the selective radiative processes of edge and/or line locking (Milne, 1926).

These conclusions prompted us to obtain ultraviolet observations of this interesting planetary nebula. Two UV spectra have been recorded on last December 1980 at high dispersion with the SWP camera of the IUE satellite (for detailed information about the IUE Satellite instrumentation see Boggess et al., 1978a). These observations are presented and discussed in the next sections. Let us mention that the only far-ultraviolet observations reported so far for HD 138403 have been made using the ANS satellite, in five intermediate bands about  $150 \text{ \AA}$  wide (Pottasch et al., 1978). With this same instrument, Gilra et al. (1978) have detected spectral variations of the C IV resonance doublet at  $\lambda 1550 \text{ \AA}$ , on time scales of half a year.

### 2. Observations

Two high resolution ( $\lambda/\Delta\lambda \sim 1.2 \cdot 10^4$ ) spectra of HD 138403 were obtained on 21 December, 1980 with the International Ultraviolet Explorer (IUE) at the ESA satellite tracking station at Villafranca, Spain (VILSPA). These two echelle spectra cover the same spectral range ( $\sim 1170$ – $2070 \text{ \AA}$ ) in the far-ultraviolet, with a velocity resolution of  $25 \text{ km s}^{-1}$ . The first spectrum (image SWP 10854), recorded during 180 min, is somewhat underexposed; therefore a second one (image SWP 10855) was taken during the last 200 min of our shift: this spectrum is fairly well exposed longward of  $\lambda 1300 \text{ \AA}$ . Let us directly mention that due to the absence of strong nebular emissions in the ultraviolet spectrum of HD 138403, no line was found to be saturated.

Because the nebula surrounding HD 138403 has an angular size of approximately  $6''$  and that the IUE large rectangular ( $10 \times 20''$ ) aperture was used, the recorded spectra are those of the

Send offprint requests to: J. Surdej.

\* Based on observations by the International Ultraviolet Explorer collected at the Villafranca Satellite Tracking Station of the European Space Agency

\*\* Chercheur Qualifié au Fonds National de la Recherche Scientifique (Belgium)

\*\*\* Permanent address: ESA Satellite Tracking Station, Apartado 54065, Madrid, Spain

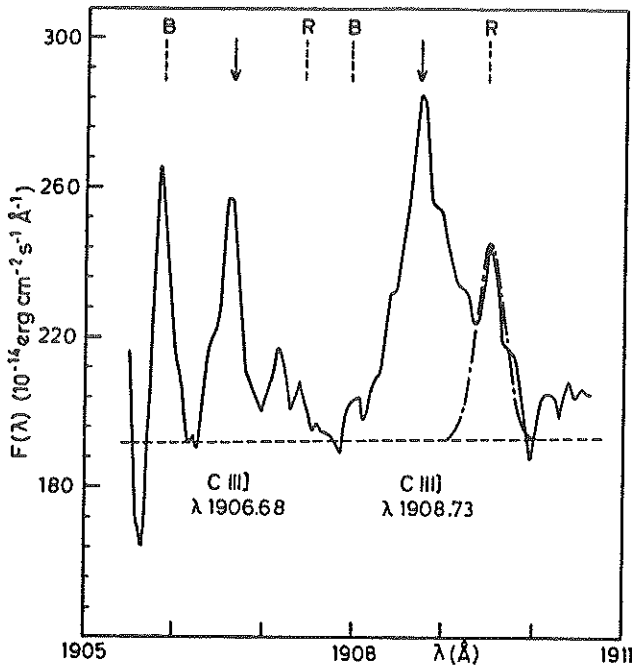


Fig. 1. The C III] line profiles resulting from the average of the two SWP 10854 and SWP 10855 images. The arrows indicate the rest positions of the two C III] components at  $\lambda\lambda$  1906.68 and 1908.73 Å. The dashed vertical bars correspond to the hypothetical positions of the red and blue emission satellites associated with these central components. The dot-dashed line represents a gaussian profile fitted to the  $\lambda$  1908.73 red emission satellite (see text). The adopted continuum level is shown by the horizontal dashed line

whole planetary nebula with its central star. These spectra were processed at VILSPA with the standard routines (see Boggess et al., 1978b and the subsequent NASA and ESA IUE Newsletters).

### 3. The Far-ultraviolet Spectrum

As a whole, the far-ultraviolet spectrum of HD 138403 may be characterized by a stellar continuum on which are superimposed a few emission lines (see Sect. 3.1) and a great variety of different types of P Cygni profiles (see Sect. 3.2). The spectrum is also marked by the presence of many interstellar absorptions (see Sect. 3.3).

The identification of line transitions was made on the basis of the two recorded spectra. Although the signal to noise ratio is generally better on the SWP 10855 image, only those lines appearing on both spectra were considered as definitely present. However, due to the difficulty for defining the continuum in certain spectral regions, for ascertaining the type (emission?, absorption?) of some complex profiles, etc. there remains a non-negligible fraction of unidentified spectral features. The most conspicuous of these are listed in a separate Table (see Sect. 3.4).

We detail and discuss here below each of the principal constituents of the far-UV spectrum of HD 138403.

#### 3.1. Emission Lines

At the short-wavelength end, the strong emission due to Ly $\alpha$  is mostly, if not all, attributable to the geocoronal Ly $\alpha$  emission

which fills in the  $10 \times 20''$  entrance aperture. As usually, this emission is superimposed on a very shallow absorption due to the interstellar Ly $\alpha$  line.

With the possible exception of the faint emission lines at  $\lambda\lambda$  1304.86, 1306.03 Å due to O I multiplet No. 2 (see Fig. 5, the third line of this multiplet at  $\lambda$  1302.17 Å being masked by a camera reseau mark located at the same position), the only nebular emission identified in the far-UV spectrum of HD 138403 is due to the C III]  $\lambda$  1908.734 intercombination line with its associated  $2s^2\ ^1S_0 - 2s2p\ ^3P_2^0$  magnetic quadrupole transition at  $\lambda$  1906.68 Å. This constitutes one more rare example of a magnetic quadrupole transition detected in the spectrum of an astronomical object.

The wavelength scales assigned to IUE spectra are derived from Pt-Ne lamp spectra taken at more or less regular intervals. The resulting zero-point uncertainties can be as great as  $20\text{--}30\text{ km s}^{-1}$  (Harvel, 1980).

In order to find the shift in the wavelength calibration of the large aperture images, we assume that the emission peaks of the C III] lines at  $\lambda\lambda$  1907, 1909 Å originate in a frame at rest with respect to the central star. Out of 33 nebular emissions in the visible spectrum, the heliocentric radial velocity of HD 138403 was determined to be  $v = 7 \pm 3\text{ km s}^{-1}$  (see Paper I). We therefore shifted in wavelength the IUE spectra in order to achieve the desired consistency in the heliocentric radial velocity of the nebula surrounding HD 138403.

We have illustrated in Fig. 1 the C III] line profiles as the result of averaging the two image spectra. The arrows which are drawn in that figure indicate the rest positions of the two C III] components at  $\lambda\lambda$  1906.68 and 1908.734 Å.

It is then remarkable to see on that tracing the presence of a strong asymmetry in the red wing of the C III]  $\lambda$  1908.734 emission. Of course, this feature is similarly well displayed on both individual spectra. Since the velocity separation between this spectral feature and the main central component amounts to  $+123 \pm 13\text{ km s}^{-1}$  and since the presence of emission satellites, red- and blue-shifted by about  $122\text{ km s}^{-1}$ , is well established for the Balmer ( $H_\alpha - H_\beta$ ) and [O II]  $\lambda\lambda$  3726, 3729 lines (see Sect. 1 and Paper I for further details), it is straightforward to identify the above feature with the red emission satellite due to the C III] dipole transition.

The dashed vertical bars represented in Fig. 1 correspond to the hypothetical positions of those red and blue emission satellites shifted by  $122\text{ km s}^{-1}$  with respect to their central components. The probable absence of the blue (resp. red) emission satellite associated with the dipole (resp. magnetic quadrupole) transition of C III] is striking but it may be simply interpreted as being caused by large differences between the emissivity, electron density, etc. prevailing in the two lobes of the bipolar structure from which, we assume (see Paper I), they arise. Despite the near coincidence between the emission feature seen at  $\lambda$  1905.9 Å and the hypothetical position of the blue satellite associated with the magnetic quadrupole transition of C III], we cannot ascertain the reality of this observation due to the poor photometric accuracy existing at the extreme edge of spectral order No. 72. Therefore, the presence of this blue satellite remains questionable and should be confirmed on better quality data.

For the case of a homogeneous optically thin gaseous nebula, Osterbrock (1970) has first mentioned the possibility of determining electron densities from the observed intensity ratio of the two C III] components. The very small sensitivity of this ratio to temperature is well illustrated by the theoretical dependence of the

**Table 1.** Electron densities derived from the ratio of the two  $^1S_0 - ^3P_{1,2}^0$  components of C III associated with the main and satellite emissions (see Nussbaumer and Schild, 1979)

Line flux $\times 10^{14}$ ( $\text{erg cm}^{-2}\text{s}^{-1}$ )	Main Component	Red Satellite	Blue Satellite
Dipole transition ( $\lambda$ 1908.73)	58.1 $\pm$ 12.7	20.2 <sup>**</sup>	< 1.3 $\pm$ 0.3
Magnetic quadrupole transition ( $\lambda$ 1906.68)	19.1 $\pm$ 1.0	< 2.5 $\pm$ 0.9	?
Electron density $n_e$ ( $\text{cm}^{-3}$ )	1.1 ( $\pm$ 0.4) $10^5$	> 3.7 $10^5$	-

<sup>\*\*</sup> Line flux of the theoretical gaussian profile  
(see text and Fig. 1)

? Uncertain photometric accuracy (see text)

emissivity ratio  $\rho(\lambda 1906.68/\lambda 1908.73)$  as a function of the electron density and temperature (see Louergue and Nussbaumer, 1976<sup>1</sup>; Nussbaumer and Schild, 1979).

Under the hypothesis that the red satellite associated with the dipole transition of C III has a gaussian profile (see the dot-dashed line in Fig. 1) with a FWHM =  $57.4 \text{ km s}^{-1}$ , we have measured the effective line flux of the central component as well as that of the other central component and satellites. The mean values of these line fluxes, based upon measurements of both IUE spectra, are summarized in Table 1. By means of the theoretical values of  $\rho$ , versus  $n_e$  and  $T_e$ , given in Nussbaumer and Schild (1979), we have also indicated in Table 1 the resulting electron densities, assuming an electron temperature  $T_e = 10,000 \text{ K}$  (Koelbloed, 1962).

The value  $n_e = 1.1 (\pm 0.4) 10^5 \text{ cm}^{-3}$  (see Table 1), inferred for the electron density in the main nebula, appears somewhat larger than the one  $n_e = 210^4 \text{ cm}^{-3}$  derived by Koelbloed (1962) on the basis of the ratio  $\rho(\lambda 3729/\lambda 3726)$  observed for the [O II] doublet<sup>2</sup>. However, within the uncertainties affecting our electron density determination and those inherent to the equivalent width measurements of strong forbidden lines on photographic emulsions (Koelbloed, 1962), the agreement between these two independent results is not so bad.

As to the value derived for the electron density in the receding lobe ( $v_r = +122 \text{ km s}^{-1}$ ) of the bipolar structure, we can only state that it is at least three times greater than the density prevailing in the main nebula (see Table 1).

### 3.2. P Cygni-type Profiles

Evidence for mass-loss from the central star of the planetary nebula 315-13<sup>o</sup>1 is well established from the analysis of its visual spectrum: P Cygni-like profiles are seen for various line transitions of He, C, N, and Si ions. A typical value for the velocity separation between the emission peak and the most blueshifted

edge of the P Cygni absorption is  $\bar{v}_{eo} = -127 \pm 38 \text{ km s}^{-1}$  (Thackeray, 1956). Despite the similarity between the values of  $\bar{v}_{eo}$  and  $v_r$ , it was concluded in Paper I that the mass-loss mechanism leading to the formation of the observed P Cygni profiles was essentially different from that responsible for the presence of the emission satellites.

Therefore, when discovering for the first time the far-UV spectrum of HD 138403 on the console screen of the data acquisition system of VILSPA, we were not surprised to see velocity shifts greater than  $500 \text{ km s}^{-1}$  in the well developed C IV and Si IV P Cygni profiles (see Figs. 2 and 3). A detailed analysis of the IUE spectra has further revealed that there was a great number of other P Cygni profiles (see Figs. 4-7) associated with line transitions of both low- and high-ion stages.

Following Beals (1951) who has classified eight different types of P Cygni profiles, we shall retain the following ones:

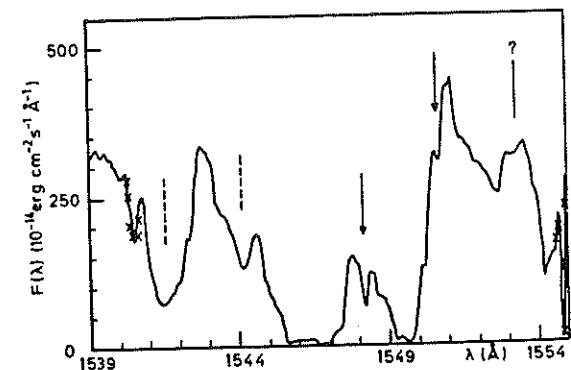


**Fig. 2.** The C IV resonance doublet P Cygni profiles (smoothing of SWP 10855 spectrum). The arrows indicate the rest positions of the two C IV components at  $\lambda\lambda 1548.185, 1550.774 \text{ \AA}$ . The dashed vertical bars correspond to the hypothetical positions of C IV absorptions blue-shifted by  $1288 \text{ km s}^{-1}$  (see text). In this and all subsequent figures, crosses refer to the presence of camera reseau marks and an interrogation mark denotes an unidentified spectral feature

- 1  $\log \rho$  should be replaced by  $\rho$  in Fig. 4 of that paper
- 2 As noted by the referee, this ratio can hardly point to values  $n_e > 2 \cdot 10^4 \text{ cm}^{-3}$  because of saturation

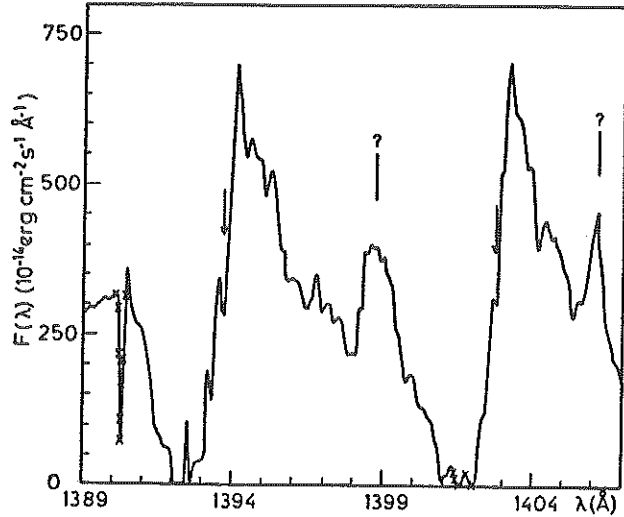


Fig. 3. The Si IV resonance doublet P Cygni profiles (smoothing of SWP 10855 spectrum). The arrows indicate the rest positions of the two Si IV components at  $\lambda\lambda$  1393.755, 1402.770 Å

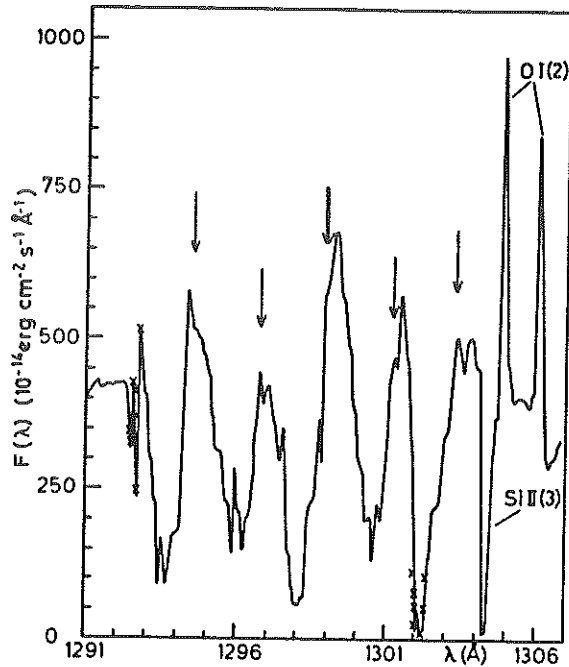


Fig. 5. P Cygni profiles for the Si III (4) line transitions (smoothing of SWP 10855 spectrum). The arrows indicate the rest positions of the six Si III (4) components (see Table 2). Also indicated are the emission lines at  $\lambda\lambda$  1304.86, 1306.03 Å due to O I (2) and the Si II  $\lambda$  1304.372 interstellar absorption

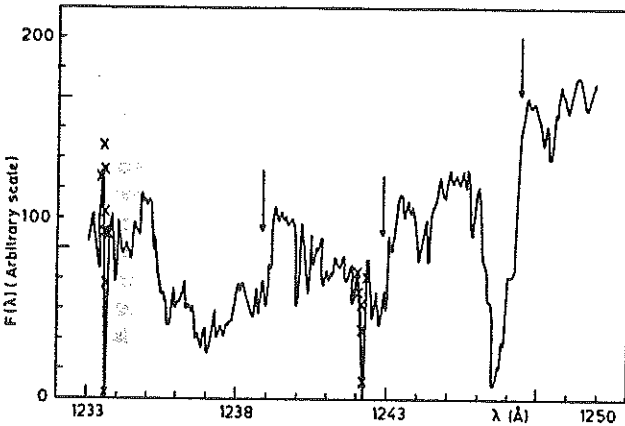


Fig. 4. Type VIII P Cygni profiles for the N V resonance doublet and the C III  $\lambda$  1247.382 line transition (smoothing of SWP 10855 spectrum). The arrows indicate the rest positions of the two N V components at  $\lambda\lambda$  1238.821, 1242.804 Å and that of C III  $\lambda$  1247.382. The flux scale is arbitrary (uncertain calibration below  $\lambda$  1250 Å)

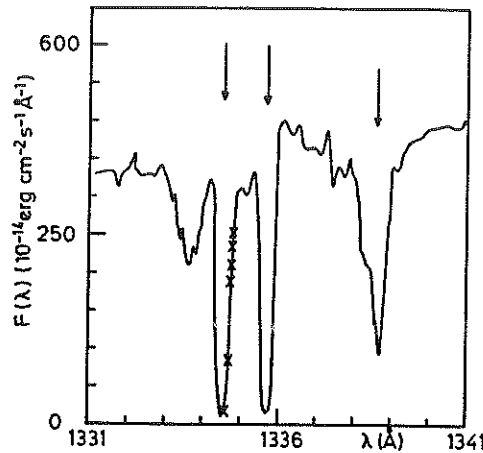


Fig. 6. Type VIII and IX P Cygni profiles for the C II  $\lambda$  1334.532 and O IV  $\lambda$  1338.612 line transitions, respectively (smoothing of SWP 10855 spectrum). The arrows indicate the rest positions of the C II  $\lambda\lambda$  1334.532, 1335.703 and O IV  $\lambda$  1338.612 components. The interstellar absorptions due to C II (1) are nearly saturated

type I: the emission is near its laboratory wavelength in the star's frame and there is an accompanying blueshifted absorption, type VIII: as type I but the emission component is absent.

We shall also consider an additional type IX (cf. Snow and Morton, 1976) consisting of an asymmetric line with an unshifted minimum and an extended wing on the short-wavelength side.

With that classification, we have reported in Table 2 the identification and type of all observed P Cygni profiles, together with the velocities (relative to the star) of the short-wavelength edge, of the line center of the absorption component and of the peak at half maximum of the emission, if present. Whenever relevant, additional remarks appear at the end of that Table.

A short look at Table 2 leads us to conclude that lines showing type I, VIII or IX P Cygni profiles have been found in the far-UV spectrum of HD 138403 for C II, III, IV; N III, IV, V; O IV, V; Si III, IV; and He II, giving this object the largest variety of ions so far observed in the wind of a nucleus of planetary nebula.

Considering only the resonance P Cygni profiles in Table 2, there appears to be a net correlation between the observed edge velocities and the total ionization potentials of the corresponding ions. The trend of this correlation is of course an increase of the maximum observed velocity with the total ionization potential. It is very probable that this relation reflects an increase of the ionization temperature with the height in the wind of the central nucleus (cf. relation 7c in Olson, 1978). Furthermore, on the basis of the striking similarities between the UV spectral characteristics



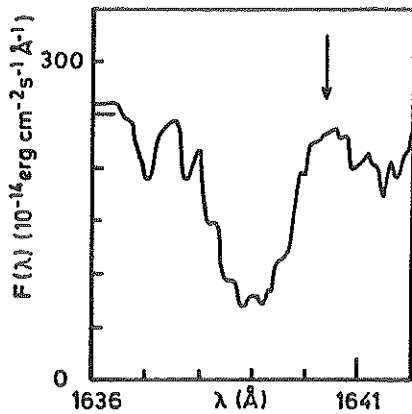


Fig. 7. Type VIII P Cygni profile for the He II(12) line transitions (smoothing of SWP 10855 spectrum). The arrow indicates the rest position of these components at  $\lambda$  1640.428 Å

of HD 138403 (see remarks in Table 2) and those found in O-type supergiants, it is not excluded that a high temperature corona may be somewhere required in the flow in order to account for the NV blueshifted absorption lines. Observations of the O VI resonance doublet at  $\lambda\lambda$  1031.928, 1037.619 Å in the spectrum of HD 138403 would be a crucial test for this hypothesis. Let us still mention that the edge velocities observed for the subordinate line transitions of a given ion [cf. Si IV  $\lambda\lambda$  4088.863, 4116.104; C II  $\lambda\lambda$  4267.02, 4267.27; etc. in Thackeray (1956) and Si III(4) in Table 2] are found systematically smaller than those associated with the corresponding resonance line transitions [cf. Si IV(1), C II(1), Si III(2) in Table 2]. This effect is well known from spectral studies of various other O-type stars for which a velocity-excitation relation has been firmly established (cf. Hutchings, 1978): as expected on theoretical grounds, the excitation temperatures decrease with increasing distance from the photosphere.

Due to the large uncertainties affecting our determinations of the edge velocity for the NV and C IV resonance doublet profiles,

Table 2. Velocities ( $\text{km s}^{-1}$ ) of the P Cygni profiles in the far-UV spectrum of HD 138403

Line transition		P Cygni	Velocities and error estimates <sup>x</sup>			Remarks
(Kelly and Palumbo, 1973)		type	Edge	Center	Em.	(Explanation below Table)
C III(4)	1174.933 } 1176.370 } Å	I	-438 $\pm$ 91	-	R	1
Si III(2)	1206.510	VIII?	-551 $\pm$ 82	R		2
N V(1)	1238.821	VIII	[-657, -822]	-391 $\pm$ 48		3, see Fig. 4
	1242.804	VIII	[-475, -716]	R		
C III(9)	1247.382	VIII	-293 $\pm$ 35	-134 $\pm$ 25		see Fig. 4
Si III(4)	1294.543	I	-336 $\pm$ 50	-223 $\pm$ 50	27 $\pm$ 50	4, see Fig. 5
	1296.726	I-VIII?	-342	-154		
	1298.891	I	-326	-194	61	
	1298.960	I				
	1301.146	I	-308	-153	61	
	1303.320	I	R	R		
C II(1)	1334.532	VIII	-344 $\pm$ 25	-198 $\pm$ 25		5, see Fig. 6
O IV	1338.612	IX	-165 $\pm$ 40	+4 $\pm$ 10 $\frac{1}{2}$		6, see Fig. 6
	1342.992	IX	-126			
	1343.512	IX				
O V(7)	1371,292	IX	-287 $\pm$ 80	-3 $\pm$ 10 $\frac{1}{2}$		7
Si IV(1)	1393.755	I	-629 $\pm$ 35	-271 $\pm$ 50	199 $\pm$ 70	8, see Fig. 3
	1402.770	I	-681 $\pm$ 70	-276	160	
C IV(1)	1548.185 } 1550.774 }	I? ) I )	<-853 $\pm$ 60?			9, see Fig. 2
				-278 $\pm$ 45	105 $\pm$ 40	
He II(12)	1640.332 } 1640.474 } 1640.490 }	VIII	-445 $\pm$ 35	-260 $\pm$ 35		10, see Fig. 7
N IV(7)	1718.551	VIII	-483 $\pm$ 45	-292 $\pm$ 45		
N III(19)	1747.86	VIII	-275 $\pm$ 45	-47 $\pm$ 45		11
	1751.24	VIII	R	R		
	1751.75	VIII	R	R		

#### Explanation of symbols

<sup>x</sup> - The error estimates represent r.m.s. values as derived from three independent measurements of the velocities on both IUE spectra. Because the velocity determinations depend on the accurate setting of the continuum level, on the exact location of the absorption edge, etc. one should be aware that the values reported in Table 2 are somewhat subjective and that the error estimates should be just considered as internal deviations of our velocity determinations.

Edge - Velocity, as measured in the star's frame, of the short-wavelength edge of the P Cygni absorption.

Center - Velocity, as measured in the star's frame, of the center of the absorption component or its minimum, if asymmetric.

- Em. - Velocity, as measured in the star's frame, of the peak at half maximum of the emission component.  
 R - Denotes the presence of a camera reseau mark at the position of the corresponding feature.  
 ? - Stands for uncertain.  
 § - The nearly zero velocity observed for the unshifted minimum of these type IX profiles if fully consistent with the zero-point correction applied to the wavelength scale of both IUE spectra (cf. Section 3.1).  
 } - Denotes a blend between two or more line transitions.

#### Additional remarks to Table 2

- 1 Multiplet No. 4 of C III consists of six line transitions in the range  $\lambda\lambda$  1174.933, 1176.370 Å. The edge velocity was therefore derived on the basis of the  $\lambda$  1174.933 transition but no center velocity could be inferred. For this six-lines multiplet, Snow and Morton (1976) report the presence of well developed P Cygni profiles in the spectrum of all supergiants, bright giants and giants with spectral types O4-O9, but none are found in the spectrum of dwarfs and subgiants.
- 2 The wide absorption due to Ly  $\alpha$  as well as the presence of an interstellar absorption due to Si III(2) prevent the detection of a possible emission near the rest position. In all supergiants ranging from O7Ia to B0.5Ia, the Si III(2) line profile displays large velocity displacements (Snow and Morton, 1976).
- 3 The N V resonance doublet profiles are ill-defined but definitely present on both IUE spectra (see Fig. 4). Although the presence of interstellar and/or circumstellar features cannot be totally excluded (cf. Section 3.3), the N V profiles appear to be mainly composed of optically thin, blueshifted absorptions. Let us further mention that P Cygni type profiles are observed for N V in all stars hotter and more luminous than B0 (Abbott, Bohlin and Savage, 1982) and that their presence in hot supergiants probably requires the existence of a high temperature stellar corona (Snow and Morton, 1976).
- 4 Fig. 5 clearly shows that for all type I P Cygni profiles due to Si III(4), the equivalent width of the emission component is much smaller than that of the shifted absorption. It is also quite possible that there is an overlap between the red wing of the emission component and the short-wavelength edge of the absorption of two consecutive profiles. Due to the presence of a TV reseau mark at  $\lambda \sim 1302$  Å and of the Si II  $\lambda$  1304.372 interstellar feature, no velocities are reported for the Si III(4)  $\lambda$  1303.320 profile. Let us finally note that for stars with spectral types later than O7, absorption lines coinciding with the line transitions of Si III(4) are evident in the Snow and Jenkins (1977)'s atlas of P Cygni spectra.
- 5 Additional cases of type VIII P Cygni profiles observed for the C II  $\lambda\lambda$  1334.5, 1335.7 transitions in the spectrum of early-type stars are reported by Snow and Morton (1976). The presence of a reseau mark at  $\lambda$  1335 and of the deep C II(1)  $\lambda\lambda$  1334.532, 1335.703 interstellar absorptions prevent the detection of a type VIII profile for the C II(1)  $\lambda$  1335.703 component (see Fig. 6).
- 6 Similar asymmetric lines are seen for O IV  $\lambda\lambda$  1338.612-1343.512 in the far-UV spectrum of  $\zeta$  Puppis,  $\rho$  Ori,  $\delta$  Ori A and  $\tau$  Ori A (Snow and Morton, 1976).
- 7 A similar profile is observed for the line transition O V(7)  $\lambda$  1371.292 in the spectrum of  $\zeta$  Puppis (Snow and Morton, 1976).
- 8 The Si IV resonance doublet P Cygni profile usually provides a good mass-loss indicator in O4-B0.5 supergiants. However, the saturation of the shifted absorptions prevents us to make such an analysis (see text).
- 9 The C IV resonance doublet profile is rather complex (see Fig. 2). As for the case of the Si IV doublet, the P Cygni absorptions are nearly ?-saturated. Furthermore, it is very likely that the two absorption features near  $\lambda$  1541.4 and  $\lambda$  1544.2 Å are also attributable to C IV in a high velocity cloud with  $v_{\text{center}} \sim -1288$  km s<sup>-1</sup>. Indeed, there is a good agreement in both the position and strength (ratio 2:1) of these absorption components. A reseau mark at  $\lambda \sim 1540.5$  Å precludes the determination of the terminal velocity of that cloud.
- 10 The reported velocities were calculated with a mean effective wavelength  $\lambda = 1640.428$  Å.
- 11 It is not excluded that Mg I  $\lambda$  1747.795 also contributes to the N III  $\lambda$  1747.86 P Cygni absorption.

we can only state that the terminal velocity of the stellar wind around HD 138403 is of the order of 800 km s<sup>-1</sup>. However, it is not excluded that matter (blobs?) - transparent to most of spectral line radiations - is also present at velocities as high as 1300 km s<sup>-1</sup> (cf. remark 9 in Table 2).<sup>3</sup>

Finally, we shall invoke arguments against any attempt of determining a mass-loss rate for HD 138403 from the analysis of its ultraviolet resonance profiles (cf. Olson, 1978; Castor and Lamers, 1979; Surdej, 1980). Indeed, the variability detected at low resolution by Gilra et al. (1978) in the strength and profile of the C IV resonance doublet at  $\lambda \sim 1550$  Å, on time scales of six months, should first of all be confirmed on the basis of an additional UV spectrum similar to those analysed here. If, as it is the case for the visible spectrum (see Paper I), spectral variations are found to affect considerably the UV line profiles, it would be a direct proof that the mass-loss around HD 138403 takes place erratically (blobs?) and that, consequently, the approximations of spherical geometry, continuous flow, steady state, etc. inherent to all classical theories of line formation are irrelevant for the present

3 Similar components have already been found in the spectra of Wolf-Rayet and other O-type stars (e.g. de Boer and Nash, 1982; Fitzpatrick et al., 1982)

case studied. One indication in favour of such an overview is that the absorption trough in the profiles of the strong C IV (see Fig. 2) and Si IV (see Fig. 3) lines is observed to be at - nearly ? - zero intensity over a small range of wavelengths. No theory of line formation built upon the approximations mentioned above can account for such a zero residual intensity.

It is therefore very plausible to assume that the envelope expanding around HD 138403 is not spherically symmetric and that material optically thick to line radiation, moving along the line-of-sight with the required velocity, causes the observed zero residual intensity.

Furthermore, one should be aware that the poor photometric accuracy and/or ill-defined character of certain line profiles (cf. N V in Fig. 4), the saturation of some P Cygni absorptions (cf. the case of C IV and Si IV discussed before), the systematic observed redshift of the peak of the emission component for type I profiles (see Table 2), the relative small range of observed velocities ( $\lesssim 800$  km s<sup>-1</sup>), etc. render very doubtful and questionable the applicability of the only practical methods of mass-loss rate determinations based upon Sobolev-type theories. In this context, we must reject the mass-loss rate estimated by Pottasch (cited as a personal communication in Nussbaumer, 1980) of  $10^{-10} M_{\odot}/\text{yr}$  for He2-131. The large variety of ions and line transitions

Table 3. Heliocentric velocity and equivalent width of interstellar absorption lines in the far-UV spectrum of HD 138403

Line transition (Kelly and Palumbo, 1973)	Heliocentric velocity (km s <sup>-1</sup> ) and error estimates*	Equivalent width (mÅ) and error estimates*	Remarks (Explanation below Table)
S III(1) 1190.170 } $\lambda$	2.6	} 382 $\pm$ 44	
Si II(5) 1190.416 }	7.4		
Si II(5) 1193.289	-3.4	674 $\pm$ 22	1
N I(1) 1199.550	8.6	239 $\pm$ 32	
N I(1) 1200.223	1.3	398 $\pm$ 22	
N I(1) 1200.710	11.8	310 $\pm$ 29	
Si III(2) 1206.510	-0.4	128 $\pm$ 3	2
N V(1) 1238.808	-4.7	227 $\pm$ 35	2, 3, see Fig. 4
N V(1) 1242.796	0.2	175 $\pm$ 17	2, 3, see Fig. 4
S II(1) 1250.586	6.9	138 $\pm$ 51	
S II(1) 1253.812	9.3	226 $\pm$ 47	
S II(1) 1259.520	10.7	183 $\pm$ 6	
Si II(4) 1260.421 }	—	} 363 $\pm$ 33	
Fe II(9) 1260.542 }	—		
Si II(4) 1264.737	-11.4?	112 $\pm$ 41	4
Si II(3) 1304.372	8.4	290 $\pm$ 5	see Fig. 5
C II(1) 1334.532	R	R	see Fig. 6
C II(1) 1335.703	9.2	196 $\pm$ 47	see Fig. 6
Si IV(1) 1393.755	0.8	—	2, see Fig. 3
Si IV(1) 1402.770	7.0	—	2, see Fig. 3
Si II(2) 1526.708	R	R	
C IV(1) 1548.188	5.9	—	2, see Fig. 2
C IV(1) 1550.762	8.0	—	2, see Fig. 2
Fe II(8) 1608.456	-1.6?	—	5
Al II(1) 1670.787	R	R	
Si II(1) 1808.012	21.5?	56 $\pm$ 31	6
Zn II(1) 2025.512	6.3	} 388 $\pm$ 7	
Mg I(2) 2025.824	15.4		
Zn II(1) 2062.016	13.4	154 $\pm$ 6	

Explanation of symbols

\* - The heliocentric velocity measurements refer to positions of the line centers at half depth. The error estimates in Table 3 represent r.m.s. values as derived from three independent measurements of the velocity and equivalent width of interstellar absorptions on both IUE spectra. Unless otherwise stated, the mean deviations affecting the determination of the heliocentric velocities and equivalent widths amount to 13 km s<sup>-1</sup> and 25 mÅ, respectively.

R - Denotes the presence of a camera reseau mark at the position of the corresponding feature.

? - Stands for uncertain.

} - Denotes a blend between two line transitions.

Additional remarks to Table 3

- 1 The absorption line is located between two spectral orders and is therefore affected by a higher noise background.
- 2 The interstellar (circumstellar ?) absorption is superimposed on the P Cygni absorption due to the same line transition (cf. Table 2).
- 3 The multi-components appearance of the N V interstellar (circumstellar ?) absorptions is very probably due to noise background. This should, however, be checked on better exposed spectra.
- 4 The profile of this absorption line is somewhat ill-defined and its identification is therefore only tentative. We have searched for the presence of other absorptions arising from an excited fine structure level of Si II but found only little evidence for the detection of the  $\lambda\lambda$  1197.394, 1309.278 line transitions.
- 5 On the blue wing of this sharp absorption, the continuum appears to be affected by the presence of another absorption line. It cannot be excluded that the observed spectral feature is entirely due to Fe II  $\lambda$  1608.456 (type II P Cygni profile ?).
- 6 This line is possibly affected by the presence of an unidentified emission feature.

Table 4. List of unidentified spectral features in the far-UV spectrum of HD 138403

Corrected wavelength	Type of profile (see below)	Remarks (Explanation below Table)
1276.9 Å	a, m, b	1
1320.5	a, m	
1321.5	a, m	
1398.7	e, m, b	see Fig. 3
1406.1	e, m	see Fig. 3
1409.2	a, m	
1430.0	a, m, vb	
1448.8	a, m	
1472.2	a, d, b	
1553.4	e, m, b	see Fig. 2
1591.0	a, m, b	
1620.5	a, m, b	
1646.1 } 1647.5 }	a, d, b } e, m, b }	2
1660.4 } 1661.5 } 1663.8 } 1666.1 }	e, m } a, m, b } e, m } e, m }	3
1680.6	a, m, b	
1687.0	a, m, b	
1764.3 } 1765.3 }	a, m, b } e, m }	2
1819.3	a, m, b	
1827.9	e, m } a, m }	2
1852.4 } 1853.9 } 1855.6 } 1858.5 }	e, m } a, m, b } e, m, b } e, m }	4, see Fig. 8
1860.9	e, m	
1862.1	a, m, b	
1863.6	e, m	

observed from the wind of HD 138403, the saturation of the C IV and Si IV P Cygni absorptions, etc. definitely point out to higher mass-loss rates from that 07(f)eq star.

### 3.3. Interstellar Absorption Lines

Although it is not our intention to analyze here the contents of the interstellar medium in front of HD 138403, we feel important to report our observations of interstellar absorption lines in the far-UV. Indeed, due to the location of 315-13°1 in the direction of the Sagittarius-Carina major arm (Georgelin et al., 1979) and because of its large distance from the sun (see Paper I,  $D = 2.8 \pm 1.0$  kpc), people interested in modeling the line-of-sight distribution of absorbing clouds, in deriving abundances from curve of growth analysis, etc. could combine our data with others in order to probe the interstellar medium in that direction.

We have reported in Table 3 the heliocentric velocity and equivalent width of all identified interstellar absorptions in the far-UV spectrum of HD 138403. Some of the observed lines are illustrated in Figs. 2-6. Our main conclusions follow:

The interstellar species detected include C II, N I, Mg I, Si II, Si III, S II, S III, Zn II and possibly Al II and Fe II.

The only absorptions arising from an excited fine structure level are found for C II  $\lambda$  1335.703 and probably for Si II  $\lambda$  1264.737.

Faint absorption features, identified with interstellar absorptions, are definitely (resp. possibly) present for the two line transitions of the N V, C IV (resp. Si IV) resonance doublets.

The mean heliocentric velocity of all (21) measurable interstellar absorptions amounts to  $6 \pm 5$  km s<sup>-1</sup>.

Because instrumental blemishes near the rest position of the Si IV, C IV, and N V lines in high resolution IUE spectra have been previously noticed (see Savage and de Boer, 1981) and/or because we are not totally sure of the real origin of the observed faint absorptions (interstellar?, circumstellar?), we shall just mention the possibility that these spectral features arise in very hot interstellar gaseous clouds, collisionally ionized ( $T \sim 2 \cdot 10^5$  K). We actually stress the importance to collect additional observations before accepting this latter interpretation.

#### Explanation of symbols used in column 2

- a : absorption line.
- e : emission line.
- m : moderate, i.e. the depth of the line center is smaller than half the continuum level.
- d : deep, i.e. the depth of the line center is greater than half the continuum level.
- b : broad, i.e. the full width of the spectral feature is greater than 200 km s<sup>-1</sup>, but smaller than 400 km s<sup>-1</sup>.
- vb : very broad, i.e. the full width of the spectral feature is greater than 400 km s<sup>-1</sup>.

#### Additional remarks to Table 4

- 1 Possible blend of interstellar absorptions due to C I  $\lambda\lambda$  1276.482, 1277.245 and 1277.513.
- 2 These absorption and emission components probably form a type I P Cygni profile.
- 3 It is very tempting to identify the emission lines at  $\lambda\lambda$  1660.4, 1666.1 Å with O III  $\lambda\lambda$  1660.803, 1666.153. The observed blueshift of the first emission component is possibly caused by the presence of the unidentified absorption at  $\lambda$  1661.5 Å.
- 4 Fig. 8 illustrates very well the ill-defined character of some unidentified spectral features. It is possible that the two sets of absorption and emission components at  $\lambda\lambda$  1853.9, 1855.6 and  $\lambda\lambda$  1862.1, 1863.6 Å are type I P Cygni profiles due to the resonance lines of Al III at  $\lambda$  1854.716 and  $\lambda$  1862.790 Å. If this is the case, the velocity of the short-wavelength edge of the P Cygni absorptions is about equal to  $-270 \pm 56$  km s<sup>-1</sup>.

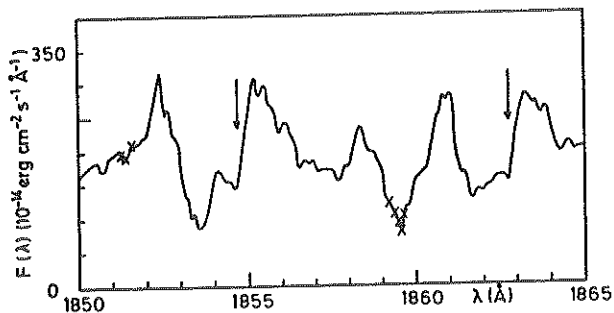


Fig. 8. Example illustrating the ill-defined character of some unidentified spectral features (smoothing of SWP 10855 spectrum). The arrows indicate the rest positions of the resonance lines of Al III  $\lambda\lambda$  1854.716, 1862.790 (see Table 4)

#### 3.4. Unidentified Spectral Features

For the sake of completeness, we present in Table 4 the list of the most conspicuous spectral features which remain unidentified in the far-UV spectrum of HD 138403. The wavelength - corrected for the heliocentric radial velocity of the star - of each spectral feature is given in that Table as well as the type of the observed line profiles. Tentative identification is proposed for some of these. Due to possible motions present in the atmosphere surrounding HD 138403, the wavelength of spectral features reported in Table 4 may not correspond any longer to the laboratory wavelength of the unidentified line transition.

#### 4. Conclusions

A description of the far-ultraviolet (1200–2000 Å) spectrum of the low-excitation planetary nebula 315–13°1 has been given in the present paper.

We have stressed the importance of the mass-loss from the central nucleus HD 138403 as revealed by the presence of numerous P Cygni profiles (types I, VIII or IX) for C II, III, IV; N III, IV, V; O IV, V; Si III, IV and He II, giving this object the greatest variety of ions so far observed in the stellar wind of a planetary nebula. Although the terminal velocities are found to be of the order of  $800 \text{ km s}^{-1}$ , it is not excluded that greater velocities ( $\sim 1300 \text{ km s}^{-1}$ ) are attained by discrete blobs of matter driven away from the central star. In this context and with the known fact that HD 138403 is a rapidly evolving object (see Paper I), it would be imperative to collect additional ultraviolet spectra in order to search for variability in the UV line profiles. Such observations would certainly also shed more light on the nature, role and mechanism of mass-loss present in most - if not all - planetary nebulae (Benvenuti and Perinotto, 1980).

Nussbaumer (1980) has mentioned that for the dynamic range attainable with IUE observations, the ratio between the line fluxes measured for the magnetic quadrupole and dipole transitions of C III] can help in density determinations for  $n_e \lesssim 5.5 \cdot 10^5 \text{ cm}^{-3}$ . This ratio has been previously measured in IC 4997 (Flower et al., 1979) as 0.06 ( $n_e \sim 5 \cdot 10^5 \text{ cm}^{-3}$ ), in NGC 7027 (Ponz cited in Nussbaumer and Schild, 1979) as 0.6 ( $n_e = 5 \cdot 10^4 \text{ cm}^{-3}$ ), in NGC 6210 and NGC 7009 (Köppen and Wehrse, 1980) as 1.2 and 1.1 ( $n_e \sim 10^4 \text{ cm}^{-3}$ ). In a similar way and for the case of 315–13°1, we have been able to derive  $n_e = 1.1 (\pm 0.4) \cdot 10^5 \text{ cm}^{-3}$  for the electron density in the main nebula. Furthermore, identifying the spectral feature seen in the red wing of the C III]  $\lambda$  1908.734 emission profile with an emission satellite due to the dipole

transition, a lower limit  $n_e \gtrsim 3.7 \cdot 10^5 \text{ cm}^{-3}$  has been inferred for the electron density prevailing in the receding lobe of a bipolar structure, assumed to be responsible for a similar splitting of the Balmer ( $H_\beta$ – $H_\gamma$ ) and [O II]  $\lambda\lambda$  3726, 3729 emission lines. These UV data also support the hypothesis that this bipolar structure is expanding around HD 138403 with a velocity  $v_e \sim 122 \text{ km s}^{-1}$ , via the selective radiative process of edge and/or line locking mechanism(s) (see Paper I).

*Acknowledgements.* One of us (J. S.) acknowledges financial support from the "Fonds National de la Recherche Scientifique" (Belgium) during the observational phase of this work. We wish also to thank the "Centre de Données Stellaires de Strasbourg", specially Agnès Acker, for providing us with an extensive bibliography of the planetary nebula HD 138403. Our thanks also go to Dr. de Boer for some helpful comments.

#### References

- Abbott, D.C., Bohlin, R.C., Savage, B.D.: 1982 (preprint)  
 Beals, C.S.: 1951, *Publ. Dominion Astrophys. Obs.* **9**, 1  
 Benvenuti, P., Perinotto, M.: 1980, Proc. Symp. The Second Year of IUE, ESA SP-157 p. 187  
 Boggess, A., et al.: 1987a, *Nature* **275**, 372  
 Boggess, A., et al.: 1978b, *Nature* **275**, 377  
 Castor, J.I., Lamers, H.J.G.L.M.: 1979, *Astrophys. J. Suppl.* **39**, 481  
 de Boer, K.S., Nash, A.G.: 1982, *Astrophys. J.* **255**, 447  
 Fitzpatrick, E.L., Savage, B.D., Sitko, M.L.: 1982, *Astrophys. J.* **256**, 578  
 Flower, D.R., Nussbaumer, H., Schild, H.: 1979, *Astron. Astrophys.* **72**, L1  
 Georgelin, Y.M., Georgelin, Y.P., Sivan J.-P.: 1979, *IAU Symp.* **84**, p. 65  
 Gilra, D.P., Pottasch, S.R., Wesselius, P.R., Van Duinen, R.J.: 1978, *Astron. Astrophys.* **63**, 297  
 Harvel, C.: 1980, *NASA IUE Newsletters* **10**, 32  
 Heap, S.R.: 1977a, *Astrophys. J.* **215**, 609  
 Heap, S.R.: 1977b, *Astrophys. J.* **215**, 864  
 Hutchings, J.B.: 1978, *Earth Extraterr. Sci.* **3**, 123  
 Kelly, R.L., Palumbo, L.: 1973, *NRL Dept. No.* 7599  
 Koelbloed, D.: 1962, *Bull. Astron. Inst. Neth.* **16**, 163  
 Köppen, J., Wehrse, R.: 1980, Proc. Symp. The Second Year of IUE, ESA SP-157, p. 191  
 Loulergue, M., Nussbaumer, H.: 1976, *Astron. Astrophys.* **51**, 163  
 Méndez, R.H., Niemela, V.S.: 1979, *Astrophys. J.* **232**, 496  
 Milne, E.A.: 1926, *Monthly Notices Roy. Astron. Soc.* **86**, 459  
 Nussbaumer, H., Schild, H.: 1979, *Astron. Astrophys.* **75**, L17  
 Nussbaumer, H.: 1980, Proc. Symp. The Second Year of IUE, ESA SP-157, p. XLIII  
 Olson, G.L.: 1978, *Astrophys. J.* **226**, 124  
 Osterbrock, D.E.: 1970, *Astrophys. J.* **160**, 25  
 Pottasch, S.R., Wesselius, P.R., Wu, C.C., Fieten, H., Van Duinen, R.J.: 1978, *Astron. Astrophys.* **62**, 95  
 Savage, B.D., de Boer, K.S.: 1981, *Astrophys. J.* **243**, 460  
 Snow, T.P., Morton, D.C.: 1976, *Astrophys. J. Suppl.* **32**, 429  
 Snow, T.P., Jenkins, E.B.: 1977, *Astrophys. J. Suppl.* **33**, 269  
 Surdej, J.: 1980, *Astrophys. Space Sci.* **73**, 101  
 Surdej, A., Surdej, J., Swings, J.P.: 1982, *Astron. Astrophys.* **105**, 242 (Paper I)  
 Thackeray, A.D.: 1950, *Monthly Notices Roy. Astron. Soc.* **110**, 524  
 Thackeray, A.D.: 1956, *Vistas in Astronomy* **2**, 1380

3. 3. 3. 3.

## Article 2

### DETERMINATION OF MASS-LOSS RATES FROM THE FIRST ORDER MOMENT $W_1$ OF UNSATURATED P CYGNI LINE PROFILES

Surdej, J.: 1982, *Astrophys. Space Sci.* 88, 31-54.

Nous montrons dans ce premier article consacré à l'étude théorique des moments d'ordre  $n$  l'intérêt et l'originalité d'utiliser le moment  $W_1$  des profils de raies de type P Cygni non saturés en vue de déterminer le taux de perte de masse  $\dot{M}$  des objets étudiés. Nous avons tout d'abord établi l'expression de  $W_n$  pour le cas d'une étoile ponctuelle en termes des paramètres physiques inhérents aux théories de type Sobolev utilisées pour le transfert de la radiation spectrale au sein d'atmosphères en expansion rapide. Nous avons alors trouvé, pour le cas des raies optiquement minces, que la relation  $W_1 - \dot{M}$  est indépendante du choix du champ de vitesse  $v(r)$  et de la loi d'opacité  $\tau_{12}^r(v)$  caractérisant l'enveloppe en mouvement. Nous avons ensuite étudié les effets des collisions ( $\epsilon \neq 0$ ) et/ou de la superposition d'un champ de vitesse  $v^{\perp}(r)$  décrivant une rotation d'ensemble de l'atmosphère et nous avons conclu que la relation  $W_1 - \dot{M}$  établie précédemment restait inchangée. Nous avons montré que négliger la présence d'une raie photosphérique sous-jacente en absorption avait pour effet de sous-estimer le taux de perte de masse  $\dot{M}$  de 20% au maximum. Nous avons par ailleurs établi l'expression des moments  $W_n$  pour des

profils de raies de type P Cygni non saturés, associés à des doublets de résonance pour lesquels la séparation  $\Delta v_{23}$  des deux niveaux atomiques supérieurs 2 et 3 est plus petite que la vitesse maximale d'expansion  $v_{\max}$  de l'atmosphère dans laquelle ils sont formés. Nous avons trouvé ici aussi que la relation  $W_1 - \dot{M}$  restait inchangée à condition d'introduire la longueur d'onde  $\lambda_D$  et la force d'oscillateur  $f_D$  effectives du doublet dans l'expression des moments  $W_n$ . Nous avons ensuite tenu compte de la dimension finie de l'objet central (effets d'inclinaison, d'occultation et d'assombrissement centre-bord) lors du calcul de  $W_n$  et ceci nous a permis d'affiner la valeur de la constante multiplicative liant  $W_1$  à  $\dot{M}$ . Tenant compte de toutes les sources possibles d'incertitude théorique et observationnelle, nous avons finalement conclu que la relation suivante

$$\dot{M}(-M_{\odot}/\text{an}) = -1,19 \cdot 10^{-21} \frac{v_{\max}^2 (-\text{km/sec}) R(-R_{\odot}) W_1}{f_{12} \lambda_{12} (-10^3 \text{ \AA}) A(\text{élément}) \bar{n}(\text{level})} ,$$

fournissait une méthode très puissante d'évaluation des taux de perte de masse  $\dot{M}$  à partir de la mesure du moment  $W_1$  de profils de raies de type P Cygni non saturés. L'erreur totale possible pouvant affecter la détermination de  $\dot{M}$  par notre méthode devrait rester inférieure à 60%.



# DETERMINATION OF MASS-LOSS RATES FROM THE FIRST ORDER MOMENT $W_1$ OF UNSATURATED P CYGNI LINE PROFILES

J. SURDEJ\*

*Institut d'Astrophysique, Université de Liège, Belgium*

(Received 24 May, 1982)

**Abstract.** The escape probability method introduced by Sobolev to treat the transfer of line photons is used in order to derive the expressions of the  $n$ th order moment  $W_n \propto \int (E(\lambda)/E_c - 1)(\lambda - \lambda_{12})^n \cdot d\lambda$  of a P Cygni profile formed in rapidly expanding envelopes around a central point-like source under various physical and geometrical conditions.

With the only assumption that there is mass-conservation of the species in the flow, we state for the case of optically thin lines that the relation between the first order moment  $W_1$  and the quantity  $\dot{M}n$  (level), first established by Castor *et al.* (1981) under more restrictive conditions, is in fact independent of the type of velocity field  $v(r)$  and a fortiori of the distribution adopted for the radial opacity  $\tau'_{12}(X')$ . These results also remain unchanged when including collisions ( $\epsilon \neq 0$ ) and/or an additional rotational velocity field  $v^\perp(r)$  in the expanding atmosphere. We investigate the presence of an underlying photospheric absorption line and conclude that for realistic cases, neglecting this boundary condition to the radiative transfer leads to an underestimate of the mass-loss rate by a factor of about 20%. By means of a three-level atom model, we demonstrate that all results derived for a single line transition equally apply for an unresolved doublet profile provided  $W_1$  and  $\dot{M}n$  (level) are calculated with the weighted wavelength  $\lambda_D$  and total oscillator strength  $f_D$  of the doublet.

Considering the occultation and inclination effects caused by the finite size of the central core, we refine the value of the multiplicative constant fixing the ratio of  $W_1$  to  $\dot{M}n$  (level). We show that this relation allows a determination of the mass-loss rate with an uncertainty less than 30%, irrespective of the size  $L_{\max}$  of the atmosphere and of the limb-darkening affecting the stellar core. Reviewing all possible sources of error, we finally conclude that this method of deriving a mass-loss rate from the analysis of an unsaturated P Cygni profile is very powerful. The total uncertainty affecting the determination of  $\dot{M}n$  (level) from the measurement of  $W_1$  should be smaller than 60%.

## 1. Introduction

Unsaturated P Cygni profiles are known to provide the best means of deriving mass-loss rates from early-type stars. In this context, Castor *et al.* (1981) have developed a theory particularly suitable for the interpretation of IUE and other low resolution spectra. In the framework of the Sobolev approximation (Sobolev, 1947, 1957, 1958; Castor, 1970; Lucy, 1971), these authors have established that for optically thin lines, the first order moment  $W_1 \propto \int (E(\lambda)/E_c - 1)(\lambda - \lambda_0) d\lambda$  is proportional to the quantity  $n$  (level).  $\dot{M}$ , where  $n$  (level) is the fractional abundance of an element in the lower atomic level associated with the given line transition, and  $\dot{M}$  is the mass-loss rate.

Whereas Castor *et al.* (1981) have discussed the negligible dependence of  $W_1$ , and consequently of  $\dot{M}$ , onto errors caused by the location of the continuum level  $E_c$  and

\* Chargé de Recherches au Fonds National de la Recherche Scientifique (Belgium).

to errors in the wavelength scale  $\lambda$ , it is not clear how much their choice of an ad hoc velocity field  $v(r)$ , fictitious radial opacity  $\tau'_{12}(X')$ , etc. may affect the mass-loss rate they derived for the central star of the planetary nebula NGC 6543.

It is our purpose to investigate in the present paper the relation between  $W_1$  and  $\dot{M}$  when taking into account various physical and geometrical effects. Because it is essentially a good approximation to assume that the size of the expanding envelope from which arise the observed P Cygni profiles is large with respect to the central stellar core, we first establish for the case of a point-like source the general expression of the  $n$ th order moment  $W_n$  in terms of the usual parameters inherent to Sobolev-type theories (see Section 2). In the subsequent sections, we show how these first results are altered when considering separately the possible effects caused by collisions and rotation (Section 3), by the presence of an underlying photospheric absorption line (Section 4), by a doublet line transition (Section 5), by the finite size of the central source and by the limb-darkening of the stellar core (Section 6). A discussion and general conclusions constitute the last section.

## 2. General Hypotheses and Expression of the Moment $W_n$ for the Case of a Point-Like Star

In the frame of a two-level atom model and using Sobolev-type approximations for the transfer of line radiation (conservative scattering) in a spherical envelope accelerated radially outward around a point-like source, the expression  $E(X)/E_c$  of a P Cygni line profile as a function of the dimensionless frequency  $X \in [-1, 1]$  is given by (see Surdej, 1979; referred to below as Paper I)

$$\frac{E(X)}{E_c} = \int_{\text{Max}(X', -X_{\min})}^1 \frac{P(X')P(X', X) dX'}{2X'} + \begin{cases} \exp(-\tau'_{12}(X)), & \text{if } X \in [-1, X_{\min}] \\ 1 & \text{if } X \in [X_{\min}, 1] \end{cases}, \quad (1)$$

with

$$X_{\min} = -v_0/v_{\max}, \quad (2)$$

$$P(X') = 1 - \exp(-\tau'_{12}(X')), \quad (3)$$

and

$$P(X', X) = \frac{(1 - \exp(-\tau_{12}(X', X)))}{\tau_{12}(X', X)} / \beta_{12}^1(X'). \quad (4)$$

We briefly recall hereafter the physical meaning of the different quantities appearing in the previous relations.  $v_0$  (resp.  $v_{\max}$ ) denotes the initial (resp. maximal) radial velocity  $v(r)$  of the flow.  $\tau_{12}(X', X)$  (resp.  $\tau'_{12}(X')$ ) represents the fictive opacity evaluated at the

distance  $L(X')$  along the direction making an angle  $\theta$  (resp.  $\theta = 0$ ) with respect to the radial direction.  $\beta_{12}^1(X')$  stands for the usual escape probability of a line photon emitted along any direction in the expanding medium. We still have the relation

$$X = X' \cos(\theta), \quad (5)$$

with

$$X' = -v(L)/v_{\max}, \quad (6)$$

where  $L(X')$  expresses the radial distance  $r$  to the central star in stellar radii  $R^*$  units.

Adopting the definition of Castor *et al.* (1981; hereafter referred to as CLS)

$$W_n = \left( \frac{c}{\lambda_{12} v_{\max}} \right)^{n+1} \int \left( \frac{E(\lambda)}{E_c} \right) - 1 (\lambda - \lambda_{12})^n d\lambda, \quad (7)$$

for the  $n$ th order moment of a line profile, and making use of relation (5) combined with the classical Doppler relation, the former expression reduces to

$$W_n = \int_{-1}^1 X^n \left( \frac{E(X)}{E_c} - 1 \right) dX. \quad (8)$$

Inserting expression (1) for the line profile function into relation (8), we easily obtain for the moments (see Appendix)

$$W_n = (1 + (-1)^n) \int_{-X_{\min}}^1 \frac{P(X') X'^n}{2\beta_{12}^1(X')} \int_0^1 \mu^n \frac{(1 - \exp(-\tau_{12}(X', \mu)))}{\tau_{12}(X', \mu)} d\mu dX' -$$

$$- (-1)^n \int_{-X_{\min}}^1 X'^n (1 - \exp(-\tau_{12}(X'))) dX', \quad (9)$$

where  $\mu = \cos(\theta)$ .

Recalling (cf. Surdej, 1977) the expression of the escape probability

$$\beta_{12}^1(X') = \int_0^1 \frac{(1 - \exp(-\tau_{12}(X', \mu)))}{\tau_{12}(X', \mu)} d\mu, \quad (11)$$

we find it straightforward to establish that

$$W_0 = 0, \quad (12)$$

and

$$W_1 = \int_{-X_{\min}}^1 X' (1 - \exp(-\tau'_{12}(X'))) dX'. \quad (13)$$

Within our assumptions of conservative scattering and of a point-like source, the first of these results simply indicates that the equivalent width of a P Cygni profile is equal to zero in accordance with the principle of energy conservation. If a given line is optically thick everywhere in the expanding medium, relation (13) becomes

$$W_1 = \int_{-X_{\min}}^1 X' dX' \sim \frac{1}{2}. \quad (14)$$

For optically thin lines (i.e.,  $\tau'_{12}(X') < 1$ ), relation (13) becomes

$$W_1 = \int_{-X_{\min}}^1 X' \tau'_{12}(X') dX', \quad (15)$$

and only in this particular case will it be possible to infer a relation between the first order moment  $W_1$  and the mass-loss rate  $\dot{M}$  of the central source. In order to do so, we shall follow CLS in defining the fractional abundance  $n$  (level) of an element in the lower atomic level 1 for the given line transition as

$$n(\text{level}) = n_1/N(\text{element}), \quad (16)$$

where  $N(\text{element})$  is the total number density for the element concerned. The abundance  $A(\text{element})$  of this same element can then be expressed by

$$A(\text{element}) = N(\text{element})/N_{\text{tot}}, \quad (17)$$

$N_{\text{tot}}$  being the total nucleon density. Combining the expression for the mass-loss rate

$$\dot{M} = -4\pi L^2 R^* v(L) N_{\text{tot}} \bar{\mu} M_{\text{amu}}, \quad (18)$$

where  $\bar{\mu}$  and  $M_{\text{amu}}$  denote, respectively, the mean atomic weight of the nuclei and the unit of atomic mass, with relation (4.7) in CLS, we derive a useful relation for the fictitious radial opacity

$$\tau'_{12}(X') = \frac{\pi e^2}{mc} f_{12} \lambda_{12} \frac{A(\text{element}) \dot{M}}{2\pi \bar{\mu} M_{\text{amu}} v_{\text{max}}^2 R^*} \frac{d(1/L)}{d(X'^2)} n(\text{level}). \quad (19)$$

The general expression for the fictitious opacity  $\tau_{12}(X', \mu)$  is similarly found to be

$$\tau_{12}(X', \mu) = \tau'_{12}(X') / \left( \mu^2 \left( 1 - \frac{d \ln L}{d \ln X'} \right) + \frac{d \ln L}{d \ln X'} \right). \quad (20)$$

Making use of the variable transformation  $L = L(X')$  and inserting relation (19) into

(15), we obtain

$$W_1 = \frac{\Pi e^2}{mc} f_{12} \lambda_{12} \frac{A(\text{element}) \dot{M}}{4 \Pi \bar{\mu} M_{\text{amu}} v_{\text{max}}^2 R^*} \int_1^{L_{\text{max}}} n(\text{level}) d(1/L). \quad (21)$$

We conclude that unless the ionization equilibrium is specified throughout the expanding atmosphere, it will not be possible to evaluate the integral factor in the previous relation. However, a very reasonable approach simply consists in assuming that the fractional abundance  $n(\text{level})$  is a constant across the medium, i.e., there is mass conservation of the species under study. This is certainly a good approximation for the resonance lines of dominant ions in the flow. In that case, relation (21) reduces to

$$W_1 = \frac{\Pi e^2}{mc} f_{12} \lambda_{12} \frac{A(\text{element}) \dot{M} n(\text{level})}{4 \Pi \bar{\mu} M_{\text{amu}} v_{\text{max}}^2 R^*} (1/L_{\text{max}} - 1), \quad (22)$$

and we note that this result is totally independent of any assumption concerning the type of velocity field, and a fortiori of any ad hoc distribution for the fictive radial opacity. Despite the fact that CLS have derived a very similar relation – only differing by a multiplicative constant – between  $W_1$  and  $\dot{M}$  (see their relations (4.15) and (4.16)), one should be aware that these authors have adopted specific relations for the velocity field and for the fictitious radial opacity.

### 3. Effects of Collisions and Rotation

Assuming as previously a central point-like source, let us first establish the expression of the  $n$ th order moment of a P Cygni profile when taking into account the effects due to collisions.

#### A. COLLISIONS

In the framework of the Sobolev approximation, the expression of the source function  $S_{12}$  for a two-level atom model is (see Castor, 1970)

$$S_{12} = \frac{(1 - \epsilon) I_c \beta_{12}^3 + \epsilon B_{\nu_{12}}(T_e)}{\epsilon + \beta_{12}^3 (1 - \epsilon)}, \quad (23)$$

where  $\epsilon$  is the probability of de-excitation of the upper atomic level by collisions,  $B_{\nu_{12}}(T_e)$  the Planck function calculated at the electron temperature  $T_e$  and  $I_c \beta_{12}^3$  the mean intensity of the stellar radiation field. Because of the collisions, it is easy to visualize that every time a 'stellar' photon is scattered in the line transition  $1 \rightleftharpoons 2$ , a fraction  $\epsilon B_{\nu_{12}}(T_e) / (1 - \epsilon) I_c \beta_{12}^3$  of 'thermal' line photons is simultaneously created at the same place. Considering these radiative processes at a distance  $L(X')$  from the stellar core, we may state that these emitted line photons will escape the expanding atmosphere along

a direction  $\theta$  after any number  $n$  ( $n = 0, 1, 2, \dots$ ) of local scatterings with a frequency  $X \in [X', -X']$  and a probability  $P(X', X)/|2X'|$ , where

$$P(X', X) = (1 - \varepsilon) \left( \frac{1 - \exp(-\tau_{12})}{\tau_{12}} \right) + (1 - \varepsilon)(1 - \beta_{12}^1) \times \\ \times (1 - \varepsilon) \left( \frac{1 - \exp(-\tau_{12})}{\tau_{12}} \right) + \dots$$

or

$$P(X', X) = (1 - \varepsilon) \left( \frac{1 - \exp(-\tau_{12})}{\tau_{12}} \right) \frac{1}{(\varepsilon + \beta_{12}^1(1 - \varepsilon))}. \quad (24)$$

If we combine all previous results, the expression (1) for the line profile function becomes

$$\frac{E(X)}{E_c} = \int_{\text{Max}(|X'|, -X_{\min})}^1 g(X') \frac{P(X')}{2X'} \left( \frac{1 - \exp(-\tau_{12})}{\tau_{12}\beta_{12}^1} \right) dX' + \\ + \begin{cases} \exp(-\tau_{12}(X)), & \text{if } X \in [-1, X_{\min}], \\ 1, & \text{if } X \in [X_{\min}, 1], \end{cases} \quad (25)$$

where

$$g(X') = \frac{((1 - \varepsilon)I_c\beta_{12}^3 + \varepsilon B_{v_{12}}(T_e))\beta_{12}^1}{I_c\beta_{12}^3(\varepsilon + \beta_{12}^1(1 - \varepsilon))} \quad (26)$$

i.e., it expresses the ratio between the source functions calculated with ( $\varepsilon \neq 0$ ) and without ( $\varepsilon = 0$ ) collisions.

If we follow a similar procedure as in the Appendix, the  $n$ th order moment  $W_n$  is now found to be

$$W_n = (1 + (-1)^n) \int_{-X_{\min}}^1 \frac{g(X')P(X')X'^n}{2\beta_{12}^1(X')} \times \\ \times \int_0^1 \mu^n \frac{(1 - \exp(-\tau_{12}(X', \mu)))}{\tau_{12}(X', \mu)} d\mu dX' - (-1)^n \times \\ \times \int_{-X_{\min}}^1 X'^n (1 - \exp(-\tau_{12}(X'))) dX'. \quad (27)$$

For  $n = 0$ , we obtain

$$W_0 = \int_{-X_{\min}}^1 (1 - \exp(-\tau_{12}^r(X'))) (g(X') - 1) dX', \quad (28)$$

with the expected results that  $W_0 \geq 0$ , if  $B_{v_2}(T_e) \geq I_c \beta_{12}^3 / \beta_{12}^1$  everywhere in the medium. Due to the symmetry of the expanding atmosphere with respect to the central core, expression (13) for the first order moment  $W_1$  remains unchanged and relation (22) between the mass-loss rate and  $W_1$  equally applies for the case of unsaturated P Cygni profiles affected by collisions.

#### B. ROTATION

If one superimposes a rotational velocity field  $v^\perp(r)$  to the outward-accelerated motion of the atmosphere, it is straightforward to demonstrate that expression (13) for  $W_1$  and relation (22) for the case of optically thin lines are still valid. Indeed, if there is rotation, the part of the line profile which accounts for the emissivity of the atmosphere remains a symmetric function of the frequency  $X \in [-1, 1]$ . Furthermore, as the expression of the velocity gradient

$$\frac{\partial v_s}{\partial s} = \frac{dr}{dr} \cos^2(\theta) + \frac{v(r)}{r} \sin^2(\theta) + \left( \frac{dv^\perp}{dr} - \frac{v^\perp}{r} \right) \sin(\theta) \cos(\theta), \quad (29)$$

evaluated along the radial direction is unaffected by the presence of a transverse velocity field, we conclude that the first order moment  $W_1$  still reduces to its expression (13).

#### 4. Underlying Photospheric Absorption Line

With some direct calculations, Castor and Lamers (1979) have shown the importance of treating rigorously the interplay between photospheric and envelope lines in the calculation of P Cygni profiles. Since the latter cannot be considered as a linear superposition of the photospheric and envelope profiles, we naturally expect the expression of  $W_1$  to be dependent on the presence of an underlying photospheric absorption line. If  $\zeta(X')$  denotes the photospheric absorption profile in the frequency interval  $X' \in [-1, 1]$ , the line profile function (see relation (1)) is easily found to be

$$\begin{aligned} \frac{E(X)}{E_c} = & \int_{\text{Max}(X', -X_{\min})}^1 \frac{\zeta(X') P(X') P(X', X)}{2X'} dX' + \\ & + \begin{cases} \zeta(X) \exp(-\tau_{12}^r(X)), & \text{if } X \in [-1, X_{\min}], \\ \zeta(X), & \text{if } X \in [X_{\min}, 1], \end{cases} \end{aligned} \quad (30)$$

assuming that  $\zeta(-X) = \zeta(X)$ .

If we combine relations (8) and (30), the expression for  $W_n$  now takes the form

$$\begin{aligned}
 W_n = & (1 + (-1)^n) \int_{-X_{\min}}^1 \frac{\zeta(X')P(X')X'^n}{2\beta_{12}^2(X')} \int_0^1 \mu^n \left( \frac{1 - \exp(-\tau_{12}(X', \mu))}{\tau_{12}(X', \mu)} \right) \times \\
 & \times d\mu dX' - (1 + (-1)^n) \int_0^1 X'^n (1 - \zeta(X')) dX' - \\
 & - (-1)^n \int_{-X_{\min}}^1 \zeta(X')X'^n (1 - \exp(-\tau_{12}(X'))) dX'. \quad (31)
 \end{aligned}$$

For  $n = 0$ ,

$$W_0 = \int_{-1}^{+1} (\zeta(X') - 1) dX', \quad (32)$$

i.e., the zero order moment gives a measure of the equivalent width of the photospheric absorption line. For  $n = 1$ , we obtain

$$W_1 = \int_{-X_{\min}}^1 \zeta(X')X'(1 - \exp(-\tau_{12}(X'))) dX', \quad (33)$$

and for the particular case of optically thin lines,

$$W_1 = \int_{-X_{\min}}^1 \zeta(X')X' \tau_{12}(X') dX'. \quad (34)$$

Inserting results (16)–(20) in (34) and assuming that there is mass conservation of the species in the flow, we derive a new relation between  $W_1$  and  $\dot{M}n$  (level): namely,

$$W_1 = \frac{\Pi e^2}{mc} f_{12} \lambda_{12} \frac{A(\text{element}) \dot{M}n(\text{level})}{4\Pi \bar{\mu} M_{\text{amu}} v_{\text{max}}^2 R^*} q, \quad (35)$$

where

$$q = \int_{-X_{\min}}^1 \zeta(X') \frac{d(1/L)}{dX'} dX'. \quad (36)$$

With these and previous results, we can now evaluate quantitatively the effect of an underlying photospheric absorption line when deriving the quantity  $\dot{M}n$  (level) from the measurement of the first order moment  $W_1$  of a P Cygni profile. By means of relations (22) and (35) we may directly infer that the relative error, expressed in %, which results between the determinations of  $\dot{M}n$  (level) when including or neglecting the presence of a photospheric line is equal to  $1 + q$ . Calculations of this last quantity



prompt us to adopt realistic functions for  $\zeta(X')$  and  $X'(L)$ . In the following, we assume  $\zeta(X')$  to have a Gaussian shape (cf. Olson and Castor, 1981) represented by

$$\zeta(X') = 1 - k \exp\left(-\frac{X'^2}{\sigma^2}\right), \quad (37)$$

where  $k$  is the line center absorption depth and  $\sigma = X(\frac{1}{2})/\sqrt{\ln 2}$  is a width chosen such that the half width at half maximum is  $X(\frac{1}{2})$ . We also adopt the velocity laws

$$\left. \begin{aligned} X' &= -X_{\min} + (1 + X_{\min})(1 - \sqrt{1/L}), & (a) \\ X' &= -X_{\min} + (1 + X_{\min})(1 - 1/L), & (b) \\ X' &= \sqrt{1 + (X_{\min}^2 - 1)/L}, & (c) \end{aligned} \right\} \quad (38)$$

which are thought to encompass most of observed velocity fields prevailing in the winds of early-type stars (Castor *et al.*, 1975; Castor and Lamers, 1979; Olson, 1981; Olson and Ebbets, 1981).

Combining relations (36) and (37) for the velocity laws (a), (b), (c) in (38), we obtain

$$\left. \begin{aligned} 1 + q &= \frac{-k\sigma^2}{(1 + X_{\min})^2} (\exp(-X_{\min}^2/\sigma^2) - \exp(-1/\sigma^2)) + \\ &+ \frac{2k\sigma}{(1 + X_{\min})^2} \int_{-X_{\min}/\sigma}^{1/\sigma} \exp(-y^2) dy, & (a) \\ 1 + q &= \frac{k\sigma}{(1 + X_{\min})} \int_{-X_{\min}/\sigma}^{1/\sigma} \exp(-y^2) dy, & (b) \end{aligned} \right\} \quad (39)$$

and

$$1 + q = \frac{k\sigma^2}{(1 - X_{\min}^2)} (\exp(-X_{\min}^2/\sigma^2) - \exp(-1/\sigma^2)). \quad (c)$$

For  $-X_{\min} \ll 1$  and  $-X_{\min} < \sigma < 1$ , the corresponding asymptotic expressions are

$$\left. \begin{aligned} 1 + q &= k\sigma(\sqrt{\pi} - \sigma), & (a) \\ 1 + q &= k\sigma\sqrt{\pi}/2, & (b) \\ 1 + q &= k\sigma^2. & (c) \end{aligned} \right\} \quad (40)$$

Considering a deep photospheric absorption line with  $k = 0.9$  such that  $X(\frac{1}{2}) = 0.05, 0.1,$  and  $0.5$ , we have summarized in Table I the values of the relative error  $1 + q$  resulting between the determinations of the quantity  $\dot{M}n$  (level) when making use of relations (22) ( $L_{\max} \gg 1$ ) and (35).

Being aware that the asymptotic expressions (40) consist in upper limits of the true value  $1 + q$  and that, for most realistic cases (see Olson and Castor, 1981),  $k < 0.9$  and  $X(\frac{1}{2}) < 0.1$ , we conclude that neglecting the presence of an underlying photospheric absorption line (see relation (22)) leads to an underestimate of the mass-loss rate never exceeding 20%. We also notice from Table I that the relative error  $1 + q$  decreases as the steepness of the velocity field near the star increases.

TABLE I  
Relative error  $1 + q$  between the values of  $\dot{M}_n$  (level)  
derived by means of Equations (35) and (22) for  
 $k = 0.9$

$1 + q$ (in %)	Velocity law		
	(a)	(b)	(c)
$X(1/2)$			
0.05	9.3	4.8	0.3
0.1	17.9	9.6	1.3
0.5	63.3	47.9	32.5

### 5. Case of a Doublet Transition

Most of P Cygni profiles observed in the ultraviolet spectrum of early-type stars are due to the scattering of line photons by a resonance doublet for which the separation of the two upper atomic levels 2 and 3, expressed in terms of the Doppler velocity  $\Delta v_{23}$ , is usually smaller than the maximal expansion velocity  $v_{\max}$  of the envelope where they are formed. For such cases, the radiative transfer in outward-accelerating envelopes is complicated by the fact that photons emitted at a point  $R$  in the transition  $3 \rightarrow 1$  can interact with atoms at distant points  $R'$ , via the line transition  $1 \rightleftharpoons 2$ . In a more general context, the formation of resonance doublet profiles which takes into account these distant interactions between atoms and line photons has been throughout investigated by Surdej (1980, hereafter referred to as Paper II).

Considering as previously a central point-like source, we recall (cf. Paper II) that in terms of the dimensionless frequency  $X$  (cf. relation (5)) chosen such that  $X = 0$  corresponds to the unshifted position of the red component  $1 \rightleftharpoons 2$  of the doublet, the resonance profile is formed in the frequency interval  $X \in [-1 - \Delta X_{23}, 1]$ , where

$$\Delta X_{23} = \frac{\Delta v_{23}}{v_{\max}}. \quad (41)$$

If we follow a similar reasoning as in Paper I, it is straightforward to derive the expression  $E(X)/E_c$  of the doublet profile. Separating the distinct contributions due to the scattering of line photons in the transitions  $1 \rightleftharpoons 2$ ,  $1 \rightleftharpoons 3$  and that due to the stellar

photons which did not suffer any scattering, we find that

$$\frac{E(X)}{E_c} = \frac{E_{12}(X)}{E_c} + \frac{E_{13}(X)}{E_c} + \frac{E_{\text{abs}}(X)}{E_c}, \quad (42)$$

with

$$\left. \begin{aligned} \frac{E_{12}(X)}{E_c} &= \int_{\text{Max}(X', -X_{\min})}^1 \frac{P_{12}(X')P_{12}(X', X)}{2X'} dX', \\ &\text{if } X \in [-1, 1], \quad (a) \\ \frac{E_{13}(X)}{E_c} &= \int_{\text{Max}(X + \Delta X_{23}, -X_{\min})}^1 \frac{P_{13}(Y')P_{13}(Y', X + \Delta X_{23})}{2Y'} \times \\ &\times \exp(-\tau_{12}(L(Y', X))) dY', \quad (b) \\ &\text{if } X \in [-1 - \Delta X_{23}, 1 - \Delta X_{23}], \end{aligned} \right\} (43)$$

and

$$\frac{E_{\text{abs}}(X)}{E_c} = \left\{ \begin{array}{ll} \exp(-\tau'_{13}(X + \Delta X_{23})), & \text{if } X \in [-1 - \Delta X_{23}, -1], \\ \exp(-\tau'_{12}(X) - \tau'_{13}(X + \Delta X_{23})), & \\ \exp(-\tau'_{12}(X)), & \text{if } X \in [X_{\min} - \Delta X_{23}, X_{\min}], \\ 1, & \text{if } X \in [X_{\min}, 1]. \end{array} \right\} (c)$$

The functions  $P_{ij}(X')$ ,  $P_{ij}(X', X)$  have their usual meaning (cf. relations (3) and (4)), and we notice in the integral of the contribution (43.b) the presence of the attenuation factor  $\exp(-\tau_{12}(L(Y', X)))$  accounting for the distant radiative interactions mentioned above (see also Paper II).

With the definition (7) for the  $n$ th order moment of a resonance doublet profile, we obtain

$$W_n = \int_{-1 - \Delta X_{23}}^1 X^n \left( \frac{E(X)}{E_c} - 1 \right) dX. \quad (44)$$

To perform this last integration is a long but not difficult task. If one takes care of integrating expression (42) along each of the frequency intervals defined in (43.c) and using, when necessary, the variable transformations  $Y = X + \Delta X_{23}$ ,  $X = X' \mu$  or  $Y = Y' \mu$  according to a similar procedure as shown in the Appendix, we easily derive the

interesting result asserting that

$$\begin{aligned}
W_n = & (1 + (-1)^n) \int_{-X_{\min}}^1 \frac{P_{12}(X') X'^n}{2\beta_{12}^1(X')} \int_0^1 \mu^n \left( \frac{1 - \exp(-\tau_{12}(X', \mu))}{\tau_{12}(X', \mu)} \right) d\mu dX' + \\
& + \int_{-X_{\min}}^1 \frac{P_{13}(Y')}{2\beta_{13}^1(Y')} \int_{-1}^1 (Y' \mu - \Delta X_{23})^n \left( \frac{1 - \exp(-\tau_{13}(Y', \mu))}{\tau_{13}(Y', \mu)} \right) \times \\
& \times \exp(-\tau_{12}(Y', \mu)) d\mu dy' - \\
& - (-1)^n \left[ \int_{-X_{\min}}^{-X_{\min} + \Delta X_{23}} X'^n (1 - \exp(-\tau'_{12}(X'))) dX' + \right. \\
& + \int_{1 + \Delta X_{23}}^1 X'^n (1 - \exp(-\tau'_{13}(X' - \Delta X_{23}))) dX' + \\
& \left. + \int_{-X_{\min} + \Delta X_{23}}^1 X'^n (1 - \exp(-\tau'_{12}(X') - \tau'_{13}(X' - \Delta X_{23}))) dX' \right]. \quad (45)
\end{aligned}$$

For the case of optically thin lines, i.e.,  $\tau_{12} < 1$ ,  $\tau_{13} < 1$ , the expression of the first order moment  $W_1$  as given by (45) reduces to

$$W_1 = \int_{-X_{\min}}^1 X' (\tau'_{12}(X') + \tau'_{13}(X')) dX', \quad (46)$$

and we conclude that the moment  $W_1$  for a doublet is the same as that for a single line transition provided that  $\lambda_{12}$  and  $f_{12}$  in Equation (22) are replaced by

$$\lambda_D = \frac{f_{12}\lambda_{12} + f_{13}\lambda_{13}}{f_{12} + f_{13}}, \quad (47)$$

and

$$f_D = f_{12} + f_{13}. \quad (48)$$

However, when including for instance the effect of collisions (cf. Section 3) in the treatment of radiative transfer, we do not recover the result (46). Instead, we obtain

$$\begin{aligned}
W_1 = & \int_{-X_{\min}}^1 X' (\tau'_{12}(X') + \tau'_{13}(X')) dX' + \\
& + \Delta X_{23} \int_{-X_{\min}}^1 \tau'_{13}(X') (1 - g(X')) dX'; \quad (49)
\end{aligned}$$

and, similarly,

$$W_0 = \int_{-X_{\min}}^1 (\tau'_{12}(X') + \tau'_{13}(X'))(g(X') - 1) dX', \quad (50)$$

with  $g(X')$ \* being defined in (26).

To remedy this situation, it is in fact necessary to redefine  $W_1$  such that in relation (7)  $\lambda_{12}$  is replaced by  $\lambda_D$ . In doing so, we find the equation

$$W_1^D = W_1 + \frac{f_{13}}{f_D} \Delta X_{23} W_0, \quad (51)$$

and when replacing  $W_1$  and  $W_0$  in this last relation by their expression given in (49) and (50), we obtain the expected result

$$W_1^D = \int_{-X_{\min}}^1 X' (\tau'_{12}(X') + \tau'_{13}(X')) dX'. \quad (52)$$

We finally conclude that relation (22) between the mass-loss rate and  $W_1$  derived for a single line transition equally applies for the case of a resonance doublet profile provided that  $\lambda_{12}$  in Equations (7) and (22) is replaced by the effective wavelength  $\lambda_D$  (see relation (47)) and  $f_{12}$  in Equation (22) is taken to be the doublet oscillator strength  $f_D$  (see relation (48)).

## 6. Finite Dimensions and Limb Darkening of the Stellar Core

In Sections 2–5, we have explicitly assumed that the size of the expanding atmosphere from which arise the observed P Cygni profiles is large with respect to the central stellar core, i.e.,  $L_{\max} \gg 1$ . In the context of deriving mass-loss rates from the analysis of unsaturated P Cygni profiles, we naturally wonder about the validity of all previous results (cf. Equation (22)) when the point-like source approximation is not exactly fulfilled. Therefore, we investigate in the present section how the transfer of line radiation is affected by the effects of occultation and inclination (cf. Paper I) due to the finite size of the central source.

### A. OCCULTATION EFFECT

At a distance  $L$  from the stellar core (see Figure 1), a certain fraction of emitted line photons, roughly proportional to the dilution factor

$$W = \frac{1}{2}(1 - \sqrt{1 - (1/L)^2}), \quad (53)$$

are back-scattered towards the star and thus remain unobservable. In the frame of an

\* Let us note that in the optically thin approximation, the function  $g(X')$  has the same form for both line transitions.

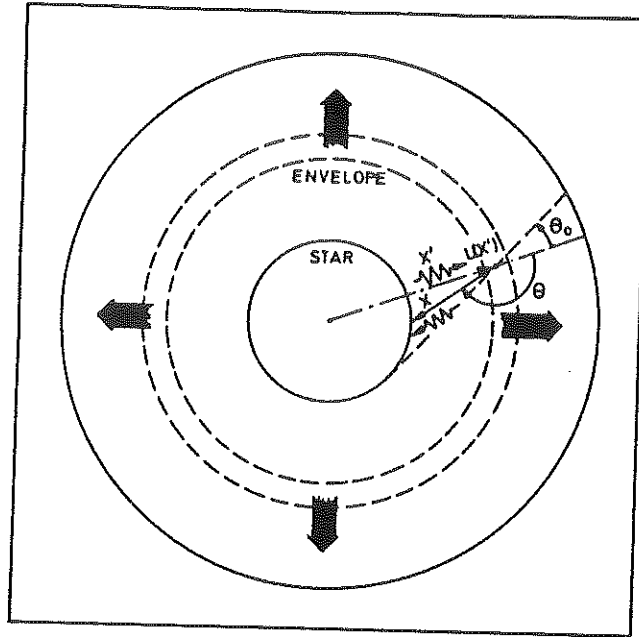


Fig. 1. Occultation by the stellar core of the line photons emitted with a frequency  $X = X'\mu$  along a direction  $\mu \leq -\mu_0$  (see text). Not to scale.

observer, these lost photons have positive frequencies  $X \in [0, 1]$  and there results a gap in the red wing of the observed line profile. This is the well-known occultation effect.

In the following, let us evaluate quantitatively this occultation effect. If a line photon is emitted locally at a distance  $L(X')$  along a direction  $\theta$  with a frequency  $X \in ]0, 1]$ , it will be seen by a fixed observer (see Figure 1) if, and only if

$$\left. \begin{array}{l} \cos(\theta) \geq -\cos(\theta_0), \\ \text{where} \\ \cos(\theta_0) = 1 - 2W(L(X')). \end{array} \right\} \quad (54)$$

By means of relation (5), Equation (54) may be rewritten as

$$X' \leq -X/(1 - 2W(L(X'))). \quad (55)$$

This last condition implies that only those stellar photons having a frequency such that  $X' \in [-1, X^N]$ , where

$$X^N(1 - 2W(L(X^N))) = -X, \quad (56)$$

will contribute to the formation of the line profile  $E(X)/E_c$  at the frequency  $X$ . Consequently, in the frequency interval  $X \in ]0, 1]$ , the lower limit of integration in Equation (1) must be replaced by  $\text{Max}(|X^N|, -X_{\min})$ . Let us still remark that in the

frequency interval  $X \in [X^0, 1]$ , where

$$X^0 = 1 - 2W(L_{\max}), \tag{57}$$

there will be no contribution at all by the scattered stellar photons to the line profile.

**B. INCLINATION EFFECT**

A second effect caused by the finite size of the stellar core arises from the fact that atoms located at a distance  $L$  interact with the stellar photons not only along the radial direction, but also along inclined directions such as  $\theta \in [0, \arcsin(1/L)]$  (see Figure 2). We shall call this the 'inclination effect'.

Considering first the contribution of scattered light to the line profile function  $E(X)/E_c$ , it is clear that in Equation (1) the factor  $P(X')$  must be replaced by a new quantity  $P^N(X')$  which accounts for the fraction of stellar photons emitted along directions  $\theta \in [0, \arcsin(1/L(X'))]$  which undergo at  $L(X')$  a first scattering. Denoting by  $\beta_{12}^3$  (resp.  $\beta_{12}^3(\infty)$ ) the escape probability for a photon emitted at  $L(X')$  to strike the stellar source (resp. the point-like source), we have the obvious relation

$$P^N(X')/P(X') = \beta_{12}^3/\beta_{12}^3(\infty). \tag{58}$$

If  $\psi(\mu^*)$  is the limb-darkening law of the stellar core such that

$$I_c(\mu^*) = I_c \psi(\mu^*) \tag{59}$$

represents the specific intensity radiated by the central source along a direction

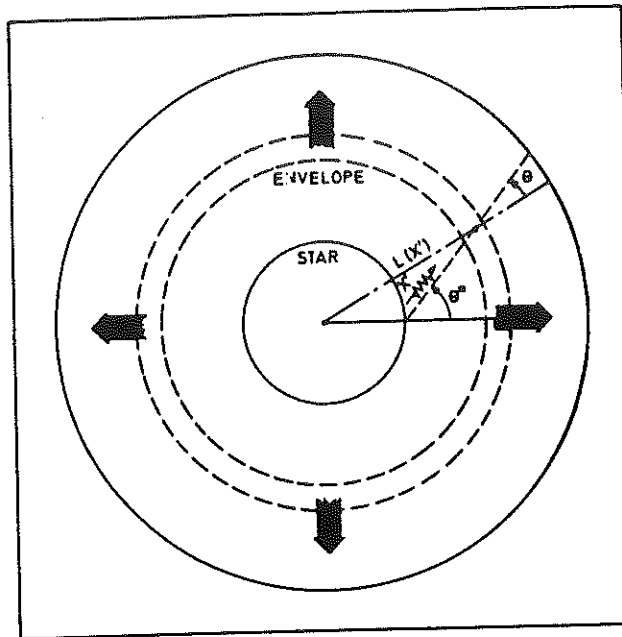


Fig. 2. Inclination of the stellar rays emitted with a limb darkening law  $\psi(\mu^*)$  along a direction  $\mu^* \in [0, 1]$  (see text). Not to scale.

$\mu^* \in [0, 1]$  (see Figure 2), the expression for  $\beta_{12}^3$  is easily found to be (see Equation (17) in Surdej, 1981; hereafter referred to as Paper III)

$$\beta_{12}^3 = \frac{1}{2} \int_{1-2W(L(X'))}^1 \psi(\mu^*) \left( \frac{1 - \exp(-\tau_{12}(X', \mu))}{\tau_{12}(X', \mu)} \right) d\mu, \quad (60)$$

with

$$\mu^* = \sqrt{1 - (1 - \mu^2)L^2(X')}. \quad (61)$$

If the central source is point-like, i.e.  $R^* \rightarrow 0$  and  $L(X') \rightarrow \infty$ , the asymptotic expression of  $\beta_{12}^3$  given by (60) is reduced to

$$\beta_{12}^3(\infty) = \frac{1}{4L^2(X')} \left( \frac{1 - \exp(-\tau_{12}^r(X'))}{\tau_{12}^r(X')} \right) \frac{\bar{I}_c}{I_c}, \quad (62)$$

where

$$\bar{I}_c = 2I_c \int_0^1 \psi(\mu^*) \mu^* d\mu^* \quad (63)$$

represents the mean specific intensity of the stellar continuum  $I_c(\mu^*)$  integrated over the disk of the central core. Combining Equations (3) and (58)–(63), we finally obtain

$$P^N(X') = \beta_{12}^3 \tau_{12}^r(X') \frac{I_c}{\bar{I}_c} 4L^2(X'). \quad (64)$$

Let us concentrate now on the fraction  $E_{\text{abs}}(X)/E_c$  of unscattered stellar photons contributing to the line profile in the frequency interval  $X \in [-1, 0[$ . As the amount  $E_{\text{abs}}(X)$  of unscattered stellar radiation reaching a fixed observer at a frequency  $X \in [-1, 0[$  is expressed by

$$E_{\text{abs}}(X) = \frac{1}{2} \int_0^1 I_c(\mu^*) \exp(-\tau_{12}(X', \mu)) \mu^* d\mu^*; \quad (65)$$

and since, in the absence of any scattering in the atmosphere, we have

$$E_c = \frac{1}{2} \int_0^1 I_c(\mu^*) \mu^* d\mu^*, \quad (66)$$

and directly find by means of relations (59), (63), (65), and (66) that the quantity



$\exp(-\tau'_{12}(X'))$  appearing in Equation (1) must be replaced by

$$\frac{E_{\text{abs}}(X)}{E_c} = \frac{2I_c}{I_c} \int_0^1 \psi(\mu^*) \exp(-\tau'_{12}(X', \mu)) \mu^* d\mu^*, \quad (67)$$

with the frequency  $X'$  satisfying the equation

$$X' = X/\sqrt{1 - (1 - \mu^{*2})/L^2(X')}, \quad (68)$$

and where  $\mu$  is derived from Equation (61).

### C. LINE PROFILE AND MOMENTS $W_n$

On account of both the occultation and inclination effects investigated here above, expression (1) of the line profile function transforms into

$$\frac{E(X)}{E_c} = \left\{ \begin{array}{l} \int_{\text{Max}(X', -X_{\text{min}})}^1 \frac{P^N(X')P(X', X)}{2X'} dX' + \frac{E_{\text{abs}}(X)}{E_c}, \\ \text{if } X \in [-1, 0], \\ \int_{\text{Max}(X^N, -X_{\text{min}})}^1 \frac{P^N(X')P(X', X)}{2X'} dX' + 1, \\ \text{if } X \in ]0, X^0], \\ 1, \text{ if } X \in ]X^0, 1], \end{array} \right. \quad (69)$$

with the new quantities  $X^N, X^0, P^N(X')$  and  $E_{\text{abs}}(X)/E_c$  being defined in (56), (57), (64), and (67), respectively.

Adopting a similar reasoning as in the Appendix and making use of relations (5), (20), and (61) in the variable transformations  $\mu^* = \mu^*(\mu, X)$  and  $X = X(X', \mu)$ , we obtain for the expression of the  $n$ th order moment (see Equations (8) and (69))

$$\begin{aligned} W_n &= (1 + (-1)^n) \int_{-X_{\text{min}}}^1 \frac{P^N(X')X'^n}{2} \int_0^1 \mu^n P(X', X', \mu) d\mu dX' - \\ &- \int_{-X_{\text{min}}}^1 \frac{P^N(X')X'^n}{2} \int_{1-2W(L(X'))}^1 \mu^n P(X', X', \mu) d\mu dX' - \\ &- (-1)^n \int_{-X_{\text{min}}}^1 \frac{P^N(X')}{2} \frac{\beta_{12}^1(X')}{\beta_{12}^3(X')} X'^n \times \end{aligned} \quad (70)$$

$$\times \int_{1-2W(L(X'))}^1 \mu^n \psi(\mu^*) P(X', X' \mu) d\mu dX'.$$

For  $n = 0$ , the last equation reduces to

$$W_0 = - \int_{-X_{\min}}^1 P^N(X') \beta_{12}^3(X') / \beta_{12}^1(X') dX', \quad (71)$$

where  $\beta_{12}^3(X')$  stands for the escape probability  $\beta_{12}^3(X')$  calculated without limb darkening of the stellar core: i.e.,  $\psi(\mu^*) = 1$ . As expected, the non-zero value of  $W_0$  directly accounts for the equivalent width of the truncated part of the line profile caused by the partial occultation of the rear part of the expanding atmosphere.

For  $n = 1$ , we derive from Equation (70)

$$W_1 = \int_{-X_{\min}}^1 \frac{P^N(X') X'}{\beta_{12}^3(X')} \left[ \gamma_{12}(X') - \frac{\beta_{12}^3(X')}{\beta_{12}^1(X')} \gamma'_{12}(X') \right] dX', \quad (72)$$

where the escape probability

$$\gamma_{12}(X') = \frac{1}{2} \int_{1-2W(L(X'))}^1 \psi(\mu^*) \left( \frac{1 - \exp(-\tau_{12}(X', \mu))}{\tau_{12}(X', \mu)} \right) \mu d\mu \quad (73)$$

is directly proportional to the stellar radiative force acting on an atom at a distance  $L(X')$  (see Surdej, 1978). As before, the quantity  $\gamma'_{12}(X')$  stands for  $\gamma_{12}(X')$  calculated with  $\psi(\mu^*) = 1$ .

Within the optically thin approximation, Equation (72) reduces to

$$W_1 = \int_{-X_{\min}}^1 X' \tau_{12}^r(X') \left( 1 - \beta_{12}^3(X') \frac{I_c}{I_c} \right) dX'; \quad (74)$$

and since it is well established that the quantity  $\beta_{12}^3 I_c / I_c$  is almost independent of the limb-darkening of the stellar core (see Section 5.1 in Paper III), we conclude that the moment  $W_1$  is itself also negligibly affected by any limb darkening effects. We shall subsequently illustrate this result with a numerical application for the case of a strong limb-darkening law.

Assuming that there is mass conservation of the species under study and that

$$\beta_{12}^3(X') \frac{I_c}{I_c} \sim W(L(X')), \quad (75)$$

we obtain by means of Equations (19) and (74) a new relation between  $W_1$  and  $Mn$  (level)

$$W_1 = \frac{\Pi e^2}{mc} f_{12} \lambda_{12} \frac{A(\text{element}) \dot{M}n(\text{level})}{4\Pi\bar{\mu}M_{\text{amu}}v_{\text{max}}^2 R^*} q^c, \quad (76)$$

where the quantity

$$q^c = -\left(\frac{1}{2} + \frac{\Pi}{8}\right) + \frac{1}{2L_{\text{max}}} + \frac{1}{4L_{\text{max}}} \sqrt{1 - \left(\frac{1}{L_{\text{max}}}\right)^2} + \frac{1}{4} \arcsin\left(\frac{1}{L_{\text{max}}}\right) \quad (77)$$

is a correcting factor essentially due to the finite size of the stellar core (see Equation (22) for comparison). Let us point out that under the same conditions, CLS have derived in another formalism a very similar relation between  $W_1$  and  $\dot{M}n(\text{level})$ . For their particular choice of the velocity field  $X' = (1 - 1/L)$  and opacity distribution  $\tau'_{12}(X') \sim (1 - X')$ , a correcting factor  $q^c = -0.60$  characterizes their results rather than we have  $q^c(L_{\text{max}} \rightarrow \infty) = -0.89$  under the only assumption that there is mass-conservation in the flow.

If we include the strong limb-darkening law  $\psi(\mu^*) = \mu^{*2}$  in Equation (74), we would easily find that result (76) is recovered with, however, the factor  $q^c$  replaced by

$$q^\psi = -\left(\frac{\Pi}{2} - \frac{2}{3}\right) - \frac{2}{3}L_{\text{max}} + \frac{2}{3}\left(L_{\text{max}} + \frac{1}{2L_{\text{max}}}\right) \sqrt{1 - \left(\frac{1}{L_{\text{max}}}\right)^2} + \arcsin\left(\frac{1}{L_{\text{max}}}\right). \quad (78)$$

With all previous relations, we are now able to calculate the relative error affecting the determinations of the mass-loss rate based on the expressions of the moment  $W_1$  when including or neglecting the finite size and/or a strong limb darkening law for the stellar core. By means of Equations (22), (76)–(78), we can directly state that the relative error, expressed in %, which results between the two determinations of  $\dot{M}n(\text{level})$  when

TABLE II

Relative error  $1 + q^c$  (resp.  $1 + q^\psi$ ) between the values of  $\dot{M}n(\text{level})$  derived by means of Equations (76), (77), (resp. (76), (78)), and (22) as a function of  $L_{\text{max}}$

$L_{\text{max}}$	$1 + q^c$ (in %)	$1 + q^\psi$ (in %)
2	59.6	58.5
3	43.7	42.6
4	35.6	34.5
5	30.7	29.5
10	20.7	19.6
50	12.7	11.6
100	11.7	10.6
$\infty$	10.7	9.6

taking or not taking into account the finite size (resp. the limb-darkening law  $\psi(\mu^*) = \mu^{*2}$ ) of the central source is equal to  $1 + q^c$  (resp.  $1 + q^\psi$ ). We have reported in Table II the values of these relative errors as a function of  $L_{\max}$ .

From the results in the first column of Table II, we conclude that neglecting the finite size of the stellar core leads to an underestimate, usually less than 50%, in the determination of the mass-loss rate. Furthermore, by comparing the values for  $1 + q^c$  and  $1 + q^\psi$  in that same table, we confirm the very negligible effect ( $\sim 1\%$ ) of a strong limb-darkening on the evaluation of the quantity  $\dot{M}n$  (level).

In practice, the relative size  $L_{\max}$  of the expanding atmosphere where is formed an observed line profile is unknown. As it is reasonable to assume that  $L_{\max} \gg 1$ , the final relation which should be adopted between  $\dot{M}n$  (level) and the observed value  $W_1$  of an unsaturated P Cygni profile is

$$\dot{M}n \text{ (level)} = \left( \frac{\Pi e^2}{mc} \frac{f_{12} \lambda_{12} A \text{ (element)}}{4 \Pi \bar{\mu} M_{\text{amu}} v_{\max}^2 R^*} \right)^{-1} W_1 / q^c(x), \quad (79)$$

where  $q^c(x) = -0.8927$ .

By using this formula, we can ascertain that due to the unknown value of  $L_{\max}$ , the relative error  $(1 - q^c/q(x))$  affecting the determination of  $\dot{M}n$  (level) on the basis of the observed moment  $W_1$  for an unsaturated P Cygni profile should be less than about 30% (see Table III).

TABLE III

Relative error  $1 - q^c/q(x)$  between the values of  $\dot{M}n$  (level) derived by means of Equations (76) and (79) as a function of  $L_{\max}$

$L_{\max}$	$1 - q^c/q(x)$ (in %)
2	54.8
3	37.0
4	27.9
5	22.3
10	11.2
50	2.2
100	1.1
$x$	0.0

## 7. Conclusions

In the framework of the Sobolev approximation for the transfer of line photons (two-level atom model), we have studied the relation between the first order moment  $W_1 \propto \int (E(\lambda)/E_c - 1)(\lambda - \lambda_0) d\lambda$  and the quantity  $\dot{M}n$  (level) under various physical and geometrical conditions.

Considering first an outward-accelerating envelope around a central point-like source, we have derived the general expression of the  $n$ th order moment  $W_n$  of a line

profile (conservative scattering) in terms of the usual parameters inherent to Sobolev-type theories. For the case of optically thin lines and under the reasonable assumption that there is mass-conservation of the species in the flow (see Section 2), we have stated that the relation between  $W_1$  and  $\dot{M}n$  (level), initially established by Castor *et al.* (1981), is in fact independent of any adopted velocity field  $v(r)$ , and a fortiori of any ad hoc distribution for the fictive radial opacity  $\tau_{12}(X')$ .

Investigating the effects due to collisions ( $\varepsilon \neq 0$ ) and/or the superposition of a rotational velocity field  $v^\perp(r)$  in the atmosphere, we have concluded that none of these effects alter the previous results. We have then shown that neglecting the presence of an underlying photospheric absorption line has the net result of underestimating the mass-loss rate by a factor of 20% at maximum.

Most of P Cygni profiles observed in the ultraviolet spectrum of early-type stars are associated with resonance doublets for which the separation  $\Delta v_{23}$  of the two upper atomic levels 2 and 3 is usually smaller than the maximum expansion velocity  $v_{\max}$  of the envelope where they are formed. For the case of such unresolved doublet profiles, we have derived identical results to those for a single line transition. Care should however be taken in adopting the wavelength  $\lambda_D$  and the total oscillator strength  $f_D$  of the resonance doublet when calculating  $W_1$  and  $\dot{M}n$  (level).

Since we do not really know what is the relative size  $L_{\max}$  of the expanding envelope with respect to the stellar core, we have investigated in the last section the core effects (occultation, inclination and limb darkening) onto the determination of the mass-loss rate. This study has led us to refine the value of the multiplicative constant fixing the ratio of  $W_1$  to  $\dot{M}n$  (level) (see formula (79)). From detailed calculations we can ascertain that the relative error affecting the determination of the mass-loss rate by means of this last formula should be less than 30%, whatever the unknown value of  $L_{\max}$  is. As to the limb-darkening, we have shown that its effects were always negligible.

Recalling that the error affecting the measurement of  $W_1$  due to uncertainties in the setting of the wavelength scale  $\lambda$  and/or of the continuum level  $E_c$  should not exceed 10% (see Castor *et al.*, 1981) and in view of all previous results concerning the various physical and geometrical effects investigated in the present paper, we can safely conclude that Equation (79) offers a very powerful method of deriving mass-loss rates from the first order moment of unsaturated P Cygni profiles. The total uncertainty possibly affecting this determination should be smaller than 60% (20% + 30% + 10%), or still more conservatively than a factor 2. The only problem which still defies us is how 'to guess' a precise estimate for the fractional abundance  $n$  (level) of the elements observed in the stellar winds.

#### Acknowledgment

My thanks are due to Jean-Pierre Swings for reading the manuscript.

## Appendix

Inserting expression (1) of the line profile function  $E(X)/E_c$  into Equation (8) for the moment  $W_n$  leads to the result

$$\begin{aligned}
 W_n = & \left[ \int_{-1}^{x_{\min}} dX \int_{-X}^1 dX' + \int_{x_{\min}}^{-x_{\min}} dX \int_{-x_{\min}}^1 dX' + \right. \\
 & \left. + \int_{-x_{\min}}^1 dX \int_X^1 dX' \left( \frac{X^n P(X') P(X', X)}{2X'} \right) \right] - \\
 & - \int_{-1}^{x_{\min}} X'^n (1 - \exp(-\tau'_{12}(X'))) dX'. \quad (A1)
 \end{aligned}$$

We have sketched in Figure A1 the domain of integration defined by the first set of

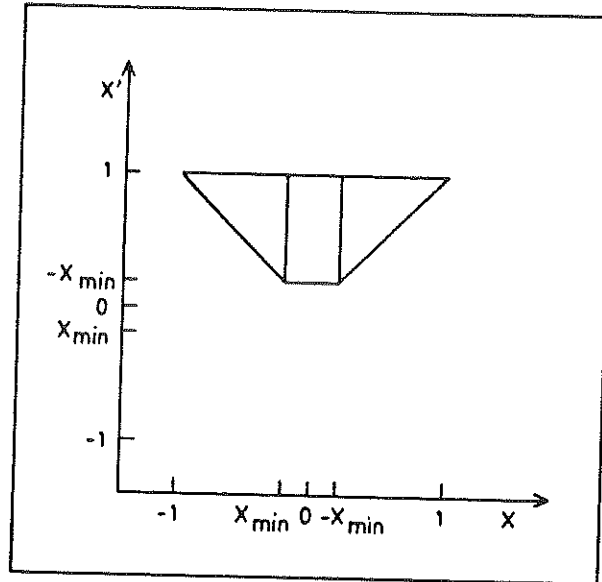


Fig. A1. Domain of integration in the plane  $(X, X')$  of the function  $X^n P(X') P(X', X)/2X'$  in Equation (A1).

integrals in the plane  $(X, X')$ . Interchanging the order of integration between  $X$  and  $X'$  in the last equation, and since

$$\left. \begin{aligned}
 & \text{and that} \quad \left. \begin{aligned}
 (-X)^n &= (-1)^n X^n, \\
 P(X', -X) &= P(X', X),
 \end{aligned} \right\} \quad (A2)
 \end{aligned}$$

we easily find that Equation (A1) reduces to

$$W_n = (1 + (-1)^n) \int_{-X_{\min}}^1 dX' \int_0^{X'} dX \left( \frac{X^n P(X') P(X', X)}{2X'} \right) - \int_{-1}^{X_{\min}} X'^n (1 - \exp(-\tau'_{12}(X'))) dX'. \quad (\text{A3})$$

Applying the variable transformations

$$\left. \begin{aligned} X &= X' \mu, \\ dX &= X' d\mu, \end{aligned} \right\} \quad (\text{A4})$$

and

$$\left. \begin{aligned} X' &= -X, \\ dX' &= -dX, \end{aligned} \right\} \quad (\text{A5})$$

to the first and second members of Equation (A3), respectively, and adopting the implicit convention that for  $X' \in [-X_{\min}, 1]$   $\tau'_{12}(X')$  is evaluated at  $-X'$ , we finally obtain the desired expression for  $W_n$  as

$$W_n = (1 + (-1)^n) \int_{-X_{\min}}^1 \frac{P(X') X'^n}{2\beta_{12}^1(X')} \int_0^1 \mu^n \left( \frac{1 - \exp(-\tau_{12}(X', \mu))}{\tau_{12}(X', \mu)} \right) d\mu dX' - (-1)^n \int_{-X_{\min}}^1 X'^n (1 - \exp(-\tau'_{12}(X'))) dX'. \quad (\text{A6})$$

**Note added in proof.** A recent work by Surdej (1982, submitted to *Astron. Astrophys.*) confirms the validity of the present results (cf. Equation (79)) irrespective of the Sobolev approximation used for the transfer of line rotation in outward-accelerating envelopes as well as of the assumption of mass-conservation for the species in the flow.

For practical use, Equation (79) may be rewritten as

$$\dot{M}(-M_{\odot}/\text{year}) \bar{n}(\text{level}) = -1.19 \times 10^{21} v_{\max}^2 (\text{km s}^{-1}) \times R^*(-R_{\odot}) W_1 / f_{12} \lambda_{12} (10^3 \text{ \AA}) A(\text{element}),$$

where

$$\bar{n}(\text{level}) = \int_1^{L_{\max}} (W(L) - 1) \frac{n(\text{level})}{L^2} dL \bigg/ \int_1^{L_{\max}} (W(L) - 1) \frac{dL}{L^2}$$

is a representative value for the fractional abundance of the relevant ion in the expanding atmosphere.

## References

- Castor, J. I.: 1970, *Monthly Notices Roy. Astron. Soc.* **149**, 111.  
Castor, J. I. and Lamers, H. J. G. L. M.: 1979, *Astrophys. J. Suppl.* **39**, 481.  
Castor, J. I., Abbott, D. C., and Klein, R. I.: 1975, *Astrophys. J.* **195**, 157.  
Castor, J. I., Lutz, J. H., and Seaton, M. J.: 1981, *Monthly Notices Roy. Astron. Soc.* **194**, 547.  
Lucy, L. B.: 1971, *Astrophys. J.* **163**, 95.  
Olson, G. L.: 1981, *Astrophys. J.* **245**, 1054.  
Olson, G. L. and Castor, J. I.: 1981, *Astrophys. J.* **244**, 179.  
Olson, G. L. and Ebbets, D.: 1981, *Astrophys. J.* **248**, 1021.  
Sobolev, V. V.: 1947, *Dnižuščiesja Oboločki Zvezd*, Leningrad (transl. *Moving Envelopes of Stars*; translated from Russian by S. Gaposchkin, Harvard University Press, Cambridge, Mass., 1960).  
Sobolev, V. V.: 1957, *Astron. Zh.* **34**, 694 (trans. *Soviet Astron.* **1**, 678).  
Sobolev, V. V.: 1958, in V. A. Ambartsumyan (ed.), *Theoretical Astrophysics*, Chapter 28, Pergamon Press Ltd, London.  
Surdej, J.: 1977, *Astron. Astrophys.* **60**, 303.  
Surdej, J.: 1978, *Astron. Astrophys.* **62**, 135.  
Surdej, J.: 1979, *Astron. Astrophys.* **73**, 1 (Paper I).  
Surdej, J.: 1980, *Astrophys. Space Sci.* **73**, 101 (Paper II).  
Surdej, J.: 1981, *Astrophys. Space Sci.* **79**, 213 (Paper III).



### Article 3

## A GENERALIZED METHOD FOR DERIVING MASS-LOSS RATES: THE FIRST ORDER MOMENT OF UNSATURATED P CYGNI LINE PROFILES

Surdej, J.: 1983, *Astrophys. Space Sci.* 90, 299-311.

Pour le cas des raies optiquement minces, nous montrons dans cet article que la relation  $W_1 - \dot{M}$ , établie dans l'article 1, reste applicable même en l'absence de validité de l'approximation de Sobolev utilisée pour le transfert de la radiation spectrale au sein d'atmosphères en expansion rapide. Par conséquent, tous les résultats établis dans le contexte des "enveloppes en expansion rapide", et se référant principalement à la non-dépendance de la relation  $W_1 - \dot{M}$  vis-à-vis de nombreux effets physiques (présence d'une raie photosphérique sous-jacente, assombrissement centre-bord, type de la loi d'opacité  $\tau_{12}^r(v)$ , etc.) et géométriques (choix du champ de vitesse radial  $v(r)$ , rotation de l'atmosphère, etc.), restent inchangés pour des champs de vitesse arbitraires (c'est-à-dire de type non-Sobolev) pouvant caractériser par exemple les mouvements d'enveloppes autour d'étoiles de type chaud ou froid, de quasars BAL et même de nuages de gaz interstellaire se trouvant dans une phase de contraction.

100 200 300

www.mca.gov.sg

**A GENERALIZED METHOD FOR DERIVING MASS-LOSS  
RATES:  
THE FIRST ORDER MOMENT OF UNSATURATED  
P CYGNI LINE PROFILES**

J. SURDEJ\*

*Institut d'Astrophysique, Université de Liège, Belgium*

(Received 3 September, 1982)

**Abstract.** For the case of optically thin lines, we show that the relation existing between the first order moment  $W_1 \propto \int (E(\lambda)/E_c - 1)(\lambda - \lambda_{1,2}) d\lambda$  of a P Cygni profile and the quantity  $\dot{M}n(\text{level})$ , where  $\dot{M}$  is the mass-loss rate of the central star and  $n(\text{level})$  the fractional abundance of the ion under study, is in fact independent of any Sobolev-type approximations used for the transfer of line radiation, contrary to what has been assumed in some previous works (Castor *et al.*, 1981; Surdej, 1982). Consequently, all results established in the context of 'very rapidly' expanding atmospheres and mainly referring to the non-dependence of  $W_1$  vs various physical (underlying photospheric absorption line, limb darkening, etc.) and geometrical (velocity field  $v(r)$ , etc.) effects remain unchanged for arbitrary (e.g. non-Sobolev type) outward-accelerating velocity laws.

Whenever applied with caution, Equation (50) thus provides a very powerful means of deriving mass-loss rates – with a total uncertainty less than 60 percent – from the measurement  $W_1$  of unsaturated P Cygni profiles observed in the spectrum of early – as well as late – type stars, quasars, etc.

### 1. Introduction

In the framework of the Sobolev approximation (Sobolev, 1947, 1957, 1958; Castor, 1970; Lucy, 1971), Castor *et al.* (1981, referred to below as CLS) have established for the case of optically thin lines that the first order moment  $W_1 \propto \int (E(\lambda)/E_c - 1)(\lambda - \lambda_{1,2}) d\lambda$  of a P Cygni line profile is proportional to the quantity  $\dot{M}n(\text{level})$ , where  $\dot{M}$  is the mass-loss rate of the central star and  $n(\text{level})$  the fractional abundance of an ion in the lower atomic level associated with the given line transition  $1 \rightleftharpoons 2$ . Whereas CLS have applied this relation for specific distributions of the velocity field ( $X' = 1 - 1/L$ ) and of the fictive radial opacity ( $\tau'_{12}(X') \propto (1 - X')$ ), Surdej (1982, hereafter referred to as Paper I) has shown that under the reasonable assumption of mass-conservation of the relevant species in the flow, the relation  $W_1 \propto \dot{M}n(\text{level})$  was in fact nearly independent on various physical and geometrical effects such as the type of 'supersonic' velocity law  $v(r)$ , collisions ( $\epsilon \neq 0$ ) and/or the superposition of a rotational velocity field  $v^\perp(r)$  in the atmosphere, the presence of an underlying photospheric absorption line, an unresolved resonance doublet profile, a (strong) limb darkening law  $\psi(\mu^*)$  for the central core, etc. For more details about these results and conclusions, we refer the reader to Paper I.

\* Chercheur Qualifié au Fonds National de la Recherche Scientifique, Belgium.

In the present work, we demonstrate that the relation existing between the first order moment  $W_1$  and  $\dot{M}n(\text{level})$  equally applies for arbitrary (e.g. non-Sobolev type) outward-accelerating envelopes from which P Cygni type profiles are observed. Therefore, it is concluded that the first order moment  $W_1$  of an unsaturated P Cygni line profile provides a powerful means of deriving mass-loss rates from early- as well as late-type stars, quasars, etc. whenever a good estimate for  $n(\text{level})$  is available.

## 2. General Hypotheses

In the following, we consider spherically symmetric envelopes in expansion with a radial velocity  $v(r)$  around a central stellar core with radius  $R^*$ . We assume that the flowing atoms are scattering radiation in a resonance line transition  $1 \rightleftharpoons 2$  and that, in the frame of the moving atoms, the emitted photons are completely redistributed in frequency and direction. At a distance

$$L = r/R^*, \quad (1)$$

let  $\Phi_L(v - v_{12})$  (see Figure 1) represent an arbitrary – but symmetric – function describing the interaction of the two levels (1 denoting the lower and 2 the upper one) with photons around the central frequency  $v_{12}$  of the transition. As usually, we suppose that  $\Phi_L(v - v_{12})$  is normalized to unity when integrated over frequency and equal to zero outside the interval  $[v_{12} - \Delta v/2, v_{12} + \Delta v/2]$ ,  $\Delta v(L)$  being the maximum width of the absorption profile due to turbulent, chaotic, etc. motions of the atoms.

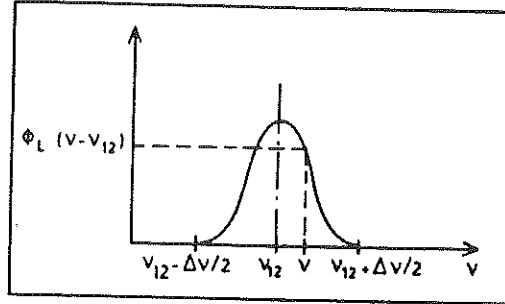


Fig. 1. Absorption profile function in the frame of the moving atoms (see text).

In terms of the dimensionless frequency

$$X = - \frac{(v - v_{12})}{(v_{\max} - v_{12})} \quad (2)$$

where, in accordance with the Doppler relation

$$\frac{v - v_{12}}{v_{12}} = \frac{v(L)}{c} \mu, \quad (3)$$

\* We stress that this situation could refer to a very slowly expanding atmosphere around a late-type star.

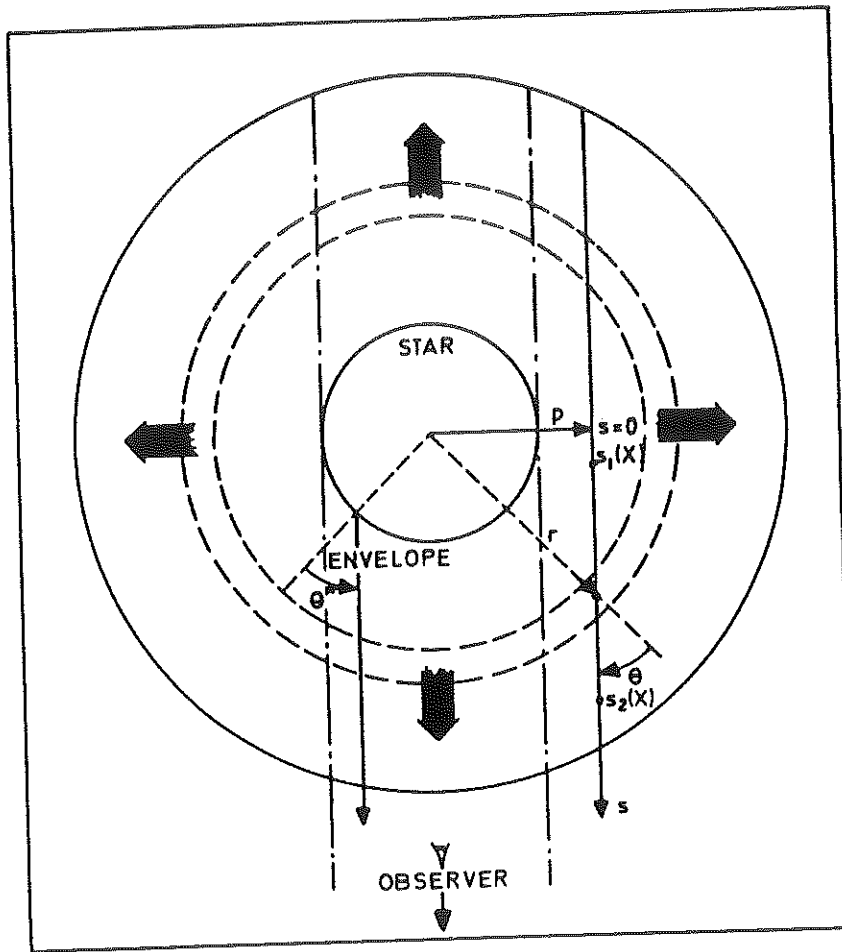


Fig. 2. Geometry in an expanding envelope around a stellar core (see text). No scale is respected.

in which  $\nu$  (resp.  $\nu_{\max}$ ) is the frequency at which a fixed observer receives radiation scattered in the envelope at a point  $L$  (resp.  $L_{\max}$ ) along a direction  $\mu = \cos(\theta)$  (resp.  $\mu = 1$ ; see Figure 2), the expression of the line opacity  $\tau_{12}^p(X)$  evaluated at a frequency  $X$  along a direction parallel to the line of sight with abscissae  $s$  and impact parameter  $p$  is given by

$$\tau_{12}^p(X) = \int_{s_1^p(X)}^{s_2^p(X)} n_1(L) k_{12} \Phi_L(\nu_L - \nu_{12}) ds. \quad (4)$$

In this equation, the local frequency  $\nu_L$  defined by

$$\nu_L = \nu - \nu_{12} \frac{v(L)\mu}{c} \quad (5)$$

refers to the frequency of a line photon that would be seen by an observer moving with the medium at  $L$  along the direction  $\mu$ .

With

$$X_L = \frac{-v(L)\mu}{v_{\max}} \quad (6)$$

representing the dimensionless local frequency at which a stellar photon would be scattered in the line center by atoms moving with a velocity  $v(L)\mu$ , we easily establish by means of Equations (2), (3), and (5) the useful relation

$$X_L = X + \frac{v_L - v_{12}}{v_{\max} - v_{12}} \quad (7)$$

For the case of outward-accelerating envelopes, the coordinates  $(L_1, \mu_1)$  (resp.  $(L_2, \mu_2)$ ) of the integration limit  $s_1^p(X)$  (resp.  $s_2^p(X)$ ) appearing in Equation (4) are directly obtained by posing  $v_L = v_{12} + \Delta v/2$  (resp.  $v_L = v_{12} - \Delta v/2$ ) in relation (7). Of course, this necessarily implies the dependence of  $\Delta v$  to be known as a function of  $L$ . Finally, let us mention that the quantity  $n_1(L)$  in Equation (4) represents the volume population of the ground level and that – neglecting stimulated emission – the absorption coefficient  $k_{12}$  is expressed by

$$k_{12} = \frac{\pi e^2}{mc} f_{12}, \quad (8)$$

where  $\pi e^2/mc$  is the classical cross-section and  $f_{12}$  the oscillator strength of the line transition.

### 3. Expression of an Unsaturated P Cygni Line Profile

Given the values  $X_L = \pm 1$  and  $v_L = v_{12} \mp \Delta v/2$  in relation (7), we directly find that in the rest frame of a fixed observer a P Cygni profile is formed within the frequency interval  $X \in [X_{\min}^{(1)}, X_{\max}^{(2)}]$ , where

$$\text{and } \left. \begin{aligned} X_{\min}^{(1)} &= -1 - \frac{\Delta v/2}{v_{\max} - v_{12}}, \\ X_{\max}^{(2)} &= 1 + \frac{\Delta v/2}{v_{\max} - v_{12}}, \end{aligned} \right\} \quad (9)$$

$\Delta v/2$  being evaluated at the maximum radius  $L_{\max}$  of the expanding envelope.

Let  $E(X)$  be the total amount of spectral energy, defined per frequency and solid angle units, radiated by the medium towards a fixed observer at a frequency  $X \in [X_{\min}^{(1)}, X_{\max}^{(2)}]$ . The quantity  $E(X)$  is then simply given by the integration of the monochromatic function  $I^p(X)$  over a plane perpendicular to the line of sight. In the frame of a fixed observer

$I^p(X)$  accounts for the intensity of line radiation emitted along a direction parallel to the line of sight for the given values of the frequency  $X$  and impact parameter  $p$ . Due to the symmetry of the envelope (see Figure 2), we have

$$E(X) = 2\pi \int_0^{r_{\max}} I^p(X) p \, dp. \tag{10}$$

Making the clear distinction between the contributions due to unscattered ( $I_u^p(X)$ ) and scattered ( $I_s^p(X)$ ) stellar radiation to the monochromatic intensity  $I^p(X)$ , we easily find that

$$I_u^p(X) = I_c \psi(\mu^*) \exp(-\tau_{12}^p(X)), \quad \text{if } p \in [0, R^*]; \tag{11}$$

in which we have assumed that the specific intensity radiated by the central source along a direction  $\mu^* \in [0, 1]$  is

$$I_c(\mu^*) = I_c \psi(\mu^*); \tag{12}$$

$\psi(\mu^*)$  being the limb darkening law along the direction  $\mu^* = \cos(\theta^*)$  (see Figure 2) and that

$$I_s^p(X) = \int_{s_1^p(X)}^{s_2^p(X)} \varepsilon_{12}(s) \Phi_L(v_L - v_{12}) \exp\left(-\int_s^{s_2^p(X)} n_1(L') k_{12} \Phi_L(v_L - v_{12}) \, ds'\right) \, ds$$

if  $p \in [0, r_{\max}]$ ; (13)

with  $\varepsilon_{12}(s)$  denoting the volume emission coefficient calculated in a frame moving with the fluid.

With the definition of the integrated stellar flux

$$E_c = 2\pi R^{*2} \int_0^1 I_c \psi(\mu^*) L_p \, dL_p, \tag{14}$$

where

$$L_p = p/R^* \tag{15}$$

and

$$\mu^* = \sqrt{1 - L_p^2}, \tag{16}$$

the expression of the line profile function  $E(X)/E_c$  may be written as

$$\frac{E(X)}{E_c} = \frac{2 \int_0^{L_{\max}} (I_u^p(X) + I_s^p(X)) L_p \, dL_p}{\bar{I}_c}, \tag{17}$$

where

$$\bar{I}_c = 2I_c \int_0^1 \psi(\mu^*) \mu^* d\mu^* \quad (18)$$

represents the mean specific intensity of the stellar continuum.

For the case of optically thin lines – i.e., assuming  $\exp(-\tau_{12}) \sim 1 - \tau_{12}$  – and taking into account the occultation effect for line radiation emitted with positive frequencies towards a fixed observer, the P Cygni line profile function reduces to

$$\frac{E(X)}{E_c} = \frac{E_u(X)}{E_c} + \frac{E_s(X)}{E_c},$$

with

$$\frac{E_s(X)}{E_c} = \frac{E_s^{(1)}(X)}{E_c} + \frac{E_s^{(2)}(X)}{E_c}, \quad (19)$$

where

$$\frac{E_u(X)}{E_c} = 1 - \frac{2I_c}{\bar{I}_c} \int_{\text{Max}(0, \mu \uparrow)}^{\text{Inf}(1, \mu \downarrow)} \psi(\mu^*) \tau_{12}^p(X) \mu^* d\mu^*,$$

and

$$\frac{E_s^{(1)}(X)}{E_c} = \frac{2}{\bar{I}_c} \int_{\text{Max}(0, \mu \uparrow)}^{\text{Inf}(1, \mu \downarrow)} \int_{s_f^*(X)}^{s_g^*(X)} \varepsilon_{12}(L) \Phi_L(v_L - v_{12}) \cdot$$

$$\left[ 1 - \int_s^{s_g^*(X)} n_1(L') k_{12} \Phi_{L'}(v_{L'} - v_{12}) ds' \right] ds \mu^* d\mu^*, \quad (20)$$

if

$$X \in [X_{\text{med}}^{(2)}, X_{\text{min}}^{(1)}],$$

and where

$$\frac{E_s^{(2)}(X)}{E_c} = \frac{2}{\bar{I}_c} \int_1^{L_{\text{sup}}(X)} \int_{s_f^*(X)}^{s_g^*(X)} \varepsilon_{12}(L) \Phi_L(v_L - v_{12}) \cdot$$

$$\left[ 1 - \int_s^{s_g^*(X)} n_1(L') k_{12} \Phi_{L'}(v_{L'} - v_{12}) ds' \right] ds L_p dL_p,$$

if

$$|X| \leq |X_{\text{min}}^{(2)}|.$$



The expressions for the frequencies  $X_{\min}^{(2)}, X_{\text{med}}^{(1)}$  (which will be later used),  $X_{\text{med}}^{(2)}$  and angle cosines  $\mu_1^*, \mu_2^*$  appearing in the last equation are easily derived on the basis of results (6), (7), and (16)

$$X_{\min}^{(2)} = -\sqrt{1 - 1/L_{\max}^2} - \frac{\Delta v(L_{\max})/2}{v_{\max} - v_{12}}, \tag{21}$$

$$X_{\text{med}}^{(1)} = \frac{-v_0}{v_{\max}} + \frac{\Delta v(L = 1)/2}{v_{\max} - v_{12}}, \tag{22}$$

$v_0$  being the radial velocity  $v(r)$  at the stellar surface,

$$X_{\text{med}}^{(2)} = \frac{\Delta v(L = 1)/2}{v_{\max} - v_{12}}, \tag{23}$$

$$\mu_1^* = \sqrt{1 + L_{\max}^2 \left\{ \left( X + \frac{\Delta v(L_{\max})/2}{v_{\max} - v_{12}} \right)^2 - 1 \right\}}, \tag{24}$$

and

$$\mu_2^* = \frac{v_{\max}}{v_0} \left( -X + \frac{\Delta v(L = 1)/2}{v_{\max} - v_{12}} \right). \tag{25}$$

Let us finally note that the upper limit  $L_{\text{sup}}(X)$  in Equation (20) depends on both  $\Delta v(L)$  and  $v(L)$ .

#### 4. First-Order Moment of an Unsaturated P Cygni Profile

Combining the results obtained in the previous sections with the definition of the first order moment  $W_1 \propto \int (E(\lambda)/E_c - 1)(\lambda - \lambda_{12}) d\lambda$  of a P Cygni line profile (see CLS and Paper I), we find that

$$W_1 = \int_{X_{\min}^{(1)}}^{X_{\max}^{(2)}} \left( \frac{E(X)}{E_c} - 1 \right) X dX. \tag{26}$$

Since, in the optically-thin approximation,

$$\int_{s > s_1^*(X)}^{s_2^*(X)} n_1(L) k_{12} \Phi_L(v_L - v_{12}) ds < \tau_{12}^*(X) < 1, \tag{27}$$

we may state that the contribution  $E_s^{(2)}(X)/E_c$  to the line profile is an even function of the frequency  $X$ . Consequently, expression (26) for the first order moment of an

unsaturated P Cygni profile can easily be reduced to

$$W_1 = \frac{2}{I_c} \int_{X_{\min}^{(1)}}^{X_{\max}^{(2)}} X dX \int_{\text{Max}(0, \mu_1^*)}^{\text{Inf}(1, \mu_2^*)} \mu^* d\mu^* \int_{sf(X)}^{sf_2(X)} (S_{12}(L) - I_c \psi(\mu^*)). \quad (28)$$

$$\alpha_{12}(L) \Phi_L(v_L - v_{12}) ds,$$

where

$$S_{12}(L) = \varepsilon_{12}(L)/\alpha_{12}(L) \quad (29)$$

represents the source function for the line transition  $1 \rightleftharpoons 2$ , and

$$\alpha_{12}(L) = n_1(L)k_{12}, \quad (30)$$

the volume absorption coefficient evaluated at a distance  $L$  in the rest frame of the fluid.

In a steady state, we find that for a two-level atom model

$$S_{12}(L) = J_{12}(L), \quad (31)$$

where, within the optically thin approximation, the mean intensity  $J_{12}(L)$  of the radiation field reduces to

$$J_{12}(L) = I_c W^\psi(L); \quad (32)$$

with

$$W^\psi(L) = \frac{1}{2} \int_0^1 \psi(\mu^*) \mu^*/L^2 \sqrt{1 - \frac{(1 - \mu^{*2})}{L^2}} d\mu^* \quad (33)$$

being a generalized geometrical dilution factor. Indeed, in the absence of any limb darkening, i.e. assuming  $\psi(\mu^*) = 1$ , we recover the expected result

$$W(L) = \frac{1}{2} \left( 1 - \sqrt{1 - \frac{1}{L^2}} \right). \quad (34)$$

In the remainder of this section, we shall reduce Equation (28) to its most simple form. If we visualize first in Figure 3 the domain of integration defined by the first set of integrals in the plane  $(X, \mu^*)$ , it is straightforward to interchange the order of integration between  $X$  and  $\mu^*$  in Equation (28). Taking into account results (31)–(33), we obtain

$$W_1 = \frac{2I_c}{I_c} \int_0^1 \mu^* d\mu^* \int_{X_{\min}^{(1)}(\mu^*)}^{X_{\max}^{(2)}(\mu^*)} X dX \int_{sf(X)}^{sf_2(X)} (W^\psi(L) - \psi(\mu^*)) \times \quad (35)$$

$$\times \alpha_{12}(L) \Phi_L(v_L - v_{12}) ds,$$

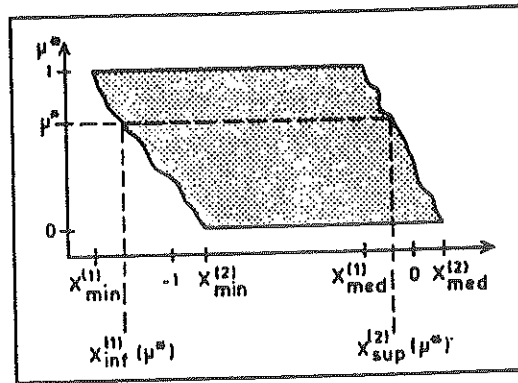


Fig. 3. Domain of integration in the plane  $(X, \mu^*)$  for the first pair of integrals in Equation (28). Not drawn to scale.

the expressions of the integration limits  $X_{inf}^{(1)}(\mu^*)$ ,  $X_{sup}^{(2)}(\mu^*)$  being derived by inverting relations (24) and (25), respectively,

$$\left. \begin{aligned}
 X_{inf}^{(1)}(\mu^*) &= - \sqrt{1 - \frac{(1 - \mu^{*2})}{L_{max}^2} - \frac{\Delta v(L_{max})/2}{v_{max} - v_{12}}}, \\
 \text{and} \\
 X_{sup}^{(2)}(\mu^*) &= \frac{-v_0}{v_{max}} \mu^* + \frac{\Delta v(L = 1)/2}{v_{max} - v_{12}}.
 \end{aligned} \right\} \quad (36)$$

Similarly, after performing in Equation (35) the variable transformation

$$L = S/\mu, \quad dL = \mu dS, \quad (37)$$

where (see Figure 2)

$$S = s/R^*, \quad (38)$$

and

$$\mu = \cos(\theta), \quad (39)$$

and defining the new profile function

$$\phi_L(X - X_L) = \Phi_L(v_L - v_{12}), \quad (40)$$

which is such that

$$\int_{X_L - [(\Delta v(L)/2)/(v_{max} - v_{12})]}^{X_L + [(\Delta v(L)/2)/(v_{max} - v_{12})]} \phi_L(X - X_L) dX = \frac{1}{v_{max} - v_{12}}, \quad (41)$$

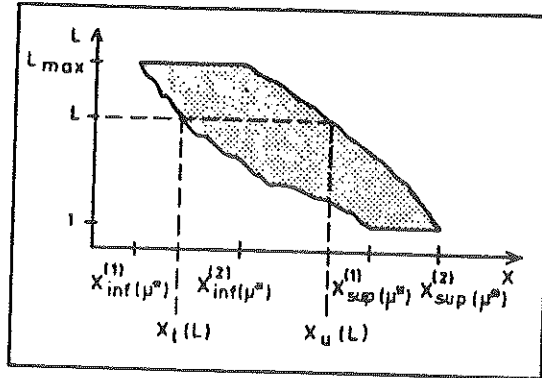


Fig. 4. Domain of integration in the plane  $(X, L)$  for the second pair of integrals in Equation (35). Not drawn to scale.

we can easily interchange the order of integration between  $X$  and  $L$  (see Figure 4) in expression (35) to obtain

$$\begin{aligned}
 W_1 = & \frac{2I_c R^*}{I_c} \int_0^1 \mu^* d\mu^* \int_1^{L_{\max}} (W^\psi(L) - \psi(\mu^*)) \frac{\alpha_{12}(L)}{\mu(\mu^*, L)} dL \times \\
 & \times \int_{X_1(L)}^{X_u(L)} X \phi_L(X - X_L) dX.
 \end{aligned}
 \tag{42}$$

The lower (1) and upper ( $u$ ) limits appearing in the last integral are easily derived by setting  $v_L = v_{12} \pm \Delta v/2$  in Equation (7)

$$X_1(L) = X_L - \frac{\Delta v(L)/2}{v_{\max} - v_{12}},$$

and

$$X_u(L) = X_L + \frac{\Delta v(L)/2}{v_{\max} - v_{12}}.
 \tag{43}$$

Since we have assumed  $\phi_L(X - X_L)$  to be a symmetric function and taking into account results (6) and (41), it is straightforward to perform the last integration in Equation (42). We readily obtain

$$\begin{aligned}
 W_1 = & -\frac{2I_c R^*}{I_c} \int_0^1 \mu^* d\mu^* \int_1^{L_{\max}} (W^\psi(L) - \psi(\mu^*)) \times \\
 & \times \alpha_{12}(L) \frac{v(L)}{v_{\max} (v_{\max} - v_{12})} dL.
 \end{aligned}
 \tag{44}$$

Making use of relations (3), (8), (18), (30) and expressing the ground level population  $n_1(L)$  in terms of the mass-loss rate  $\dot{M}$  of the central object (see CLS), Equation (44) may be rewritten in a more elegant form as

$$W_1 = \frac{\pi e^2}{mc} f_{12} \lambda_{12} \frac{A(\text{element}) \dot{M}}{4\pi \bar{\mu} M_{\text{amu}} v_{\text{max}}^2 R^*} \int_1^{L_{\text{max}}} \left( \frac{I_c}{\bar{I}_c} W^\psi(L) - 1 \right) \times \frac{n(\text{level})}{L^2} dL, \quad (45)$$

where  $n(\text{level})$  represents the fractional abundance of the relevant ion in the ground state,  $A(\text{element})$  the abundance of the element itself,  $\bar{\mu}$  the mean atomic weight of the nuclei in the flow,  $M_{\text{amu}}$  the unit of atomic mass and  $\lambda_{12}$  the wavelength of the line transition  $1 \rightleftharpoons 2$ .

Referring the reader to Equations (60) and (74)–(78) of Paper I, we can directly state that expression (45) derived here for the first order moment  $W_1$  of an unsaturated P Cygni line profile is identical to that obtained in the pure formalism of Sobolev-type approximations used for the transfer of line radiation. The meaning of this conclusion namely implies that all results derived in Paper I, and concerning mainly the non-dependence of  $W_1$  – and subsequently the derivation of  $\dot{M}$  – vs various physical and geometrical effects, equally apply for the case of an arbitrary (e.g. non-Sobolev type) outward-accelerating envelope. As an example, we have demonstrated in Paper I that in the context of ‘very rapidly’ expanding envelopes, neglecting a strong limb darkening effect for the central source in the expression of  $W_1$  would lead to an overestimate of the mass-loss rate  $\dot{M}$  by a factor as small as 1%. Consequently, within a very good approximation, we may replace Equation (45) by

$$W_1 = \frac{\pi e^2}{mc} f_{12} \lambda_{12} \frac{A(\text{element}) \dot{M}}{4\pi \bar{\mu} M_{\text{amu}} v_{\text{max}}^2 R^*} \int_1^{L_{\text{max}}} (W(L) - 1) \frac{n(\text{level})}{L^2} dL, \quad (46)$$

where the geometrical dilution factor  $W(L)$  has been defined in (34).

Assuming now that the fractional abundance  $n(\text{level})$  is a constant across the medium, i.e. there is mass conservation of the species under study, the expression of the first order moment  $W_1$  takes the final form

$$W_1 = \frac{\pi e^2}{mc} f_{12} \lambda_{12} \frac{A(\text{element}) \dot{M} n(\text{level})}{4\pi \bar{\mu} M_{\text{amu}} v_{\text{max}}^2 R^*} q^c(L_{\text{max}}), \quad (47)$$

with

$$q^c(L_{\text{max}}) = -\left(\frac{1}{2} + \frac{\pi}{8}\right) + \frac{1}{2L_{\text{max}}} + \frac{1}{4L_{\text{max}}} \sqrt{1 - \left(\frac{1}{L_{\text{max}}}\right)^2} + \frac{1}{4} \arcsin\left(\frac{1}{L_{\text{max}}}\right). \quad (48)$$

Although the approximation of mass conservation should be essentially good for resonance lines of dominant ions in the flow, it could be inappropriate for some other ions. If this is the case, we may overcome the difficulty by replacing  $n(\text{level})$  in Equation (47) by

$$\bar{n}(\text{level}) = \int_1^{L_{\max}} (W(L) - 1) \frac{n(\text{level})}{L^2} dL \bigg/ \int_1^{L_{\max}} (W(L) - 1) \frac{dL}{L^2}, \quad (49)$$

i.e. a representative value for the fractional abundance of the relevant ion in the flow.

Finally, regarding the dependence of  $W_1$  – or  $\dot{M}$  – onto the ‘a priori’ unknown value  $L_{\max}$  for the size of the expanding envelope, we have already established in Paper I that replacing  $q^c(L_{\max})$  by its asymptotic expression  $q^c(\infty) = -0.8927$  in Equation (47) will just result in underestimating the mass-loss rate  $\dot{M}$  by a factor never exceeding 30%.

## 5. Conclusions

Irrespective of any Sobolev-type approximations used for the transfer of line radiation in outward-accelerating envelopes, we have demonstrated in the present work that a unique relation does actually exist between the mass-loss rate  $\dot{M}$  of a central star and the first order moment  $W_1$  of an unsaturated P Cygni profile. On speculative physical grounds, this result is not so surprising since the optically thin approximation enables one to avoid, strictly speaking, the true problem of radiative transfer... it is as if at different frequencies, the observer were seeing at different depths the cross-section of each individual ion in front of the stellar disk, thus measuring  $W_1$ , or similarly  $\dot{M}$ .

Adopting cosmic abundances (Allen, 1976), we derive from Equation (47) the very useful relation

$$\dot{M}(-M_{\odot}/\text{year})n(\text{level}) = -1.1910^{-21} \frac{v_{\max}^2(-\text{km s}^{-1})R^*(-R_{\odot}-)W_1}{f_{12}\lambda_{12}(-10^3 \text{ \AA})A(\text{element})}, \quad (50)$$

where, as usually,  $M_{\odot}$  and  $R_{\odot}$  stand for the solar mass and radius units. Since this relation is identical to that derived in Paper I for the case of ‘very rapidly’ expanding atmospheres and that we have already investigated there its dependence vs various physical and geometrical effects, we summarize and generalize hereafter the main conclusions of that study:

– With  $n(\text{level})$  being a representative value (cf. Equation (49)) for the fractional abundance of the relevant ion in the flow, Equation (50) allows a direct determination of the mass-loss rate  $\dot{M}$ , irrespective of the type of radial velocity field  $v(r)$  characterizing the expansion of the envelope.

– Considering the effects due to collisions ( $\varepsilon \neq 0$ ) and/or the superposition of a rotational velocity field  $v^{\perp}(r)$  in the atmosphere, we can state that none of these effects modifies relation (50).

- Neglecting the presence of an underlying photospheric absorption line has the net result of underestimating the mass-loss rate by a factor of 20% at maximum.
- For the case of an unresolved resonance multiplet profile, care should be taken in adopting the wavelength  $\lambda_D$  and the total oscillator strength  $f_D$  of the multiplet when calculating  $W_1$  (see Equation (7) of Paper I) and  $\dot{M}$  from Equation (50).
- Due to the fact that we have implicitly used the asymptotic value  $q^*(\infty)$  instead of  $q^*(L_{\max})$  (see Equation (48)) when deriving relation (50), there results a possible underestimate of the mass-loss rate by a factor  $\leq 30\%$ .
- As to the limb darkening, its effects are always negligible.

Finally, referring the reader to the work by CLS for the possible error ( $\sim 10\%$ ) affecting the measurement of  $W_1$  from an observed line profile, we may safely conclude that, within a total uncertainty less than roughly 60% (20% + 30% + 10%), Equation (50) offers a powerful method for deriving mass-loss rates from the first order moment of unsaturated P Cygni profiles. Let us still stress that this method can be applied – indistinctly – to any of the early- as well as late-type stars, quasars, etc. known to be losing mass.

#### Acknowledgement

It is a pleasure to thank Jean-Pierre Swings for critical reading of the manuscript.

#### References

- Allen, C. W.: 1976, *Astrophysical Quantities*, 3rd edition, University of London, The Athlone Press.
- Castor, J. I.: 1970, *Monthly Notices Roy. Astron. Soc.* **149**, 111.
- Castor, J. I., Lutz, J. H., and Seaton, M. J.: 1981, *Monthly Notices Roy. Astron. Soc.* **194**, 547 (CLS).
- Lucy, L. B.: 1971, *Astrophys. J.* **163**, 95.
- Sobolev, V. V.: 1947, *Dnižuščiesja Oboločki Zvězd*, Leningrad (*Moving Envelopes of Stars*, translated from Russian by S. Gaposchkin, Harvard University Press, Cambridge, Mass., 1960).
- Sobolev, V. V.: 1957, *Astron. Z.* **34**, 694 (translated *Soviet Astron.* **1**, 678).
- Sobolev, V. V.: 1958, in V. A. Ambartsumyan (ed.), *Theoretical Astrophysics*, Chapter 28, Pergamon Press Ltd., London.
- Surdej, J.: 1982, *Astrophys. Space Sci.* **88**, 31.





#### Article 4

### DETERMINATION OF MASS-LOSS RATES FROM EARLY-TYPE STARS ON THE BASIS OF "LOG(W<sub>1</sub>)-LOG(W<sub>1</sub><sup>0</sup>)" DIAGRAMS

Surdej, J.: 1983, *Astron. Astrophys.* 127, 304-308.

En utilisant des expressions réalistes pour le champ de vitesse  $v(r)$  et la loi d'opacité  $\tau_{12}^r(v)$  caractérisant des atmosphères en expansion rapide, nous présentons dans cet article les résultats du calcul du moment d'ordre 1,  $W_1 \propto \int (E(\lambda)/E_c - 1) (\lambda - \lambda_{12}) d\lambda$ , de profils de raies de type P Cygni en fonction du paramètre  $W_1^0$ , proportionnel à la quantité  $\dot{M} \bar{n}(\text{level})$ . Nos résultats montrent très clairement que les courbes "log(W<sub>1</sub>)-log(W<sub>1</sub><sup>0</sup>)" résultantes ne dépendent pratiquement que de la loi d'opacité  $\tau_{12}^r(v)$  et que pour les faibles opacités, la relation  $W_1 \propto \dot{M} \bar{n}(\text{level})$  est bien vérifiée, indépendamment du choix de  $v(r)$  et  $\tau_{12}^r(v)$ . Pour des valeurs de  $W_1 \geq 0,24$ , les profils de raies deviennent saturés et le moment d'ordre 1 ne permet plus de déduire qu'une limite inférieure au taux de perte de masse  $\dot{M}$ . Une comparaison est faite entre cette technique de détermination du taux de perte de masse  $\dot{M}$  et celle qui consiste à reproduire au mieux les observations au moyen de profils de raies théoriques.



## Determination of mass-loss rates from early-type stars on the basis of “ $\log(W_1) - \log(W_1^0)$ ” diagrams

J. Surdej\*

Institut d'Astrophysique, Université de Liège, avenue de Cointe 5, B-4200 Cointe-Ougrée, Belgium

Received March 30, accepted July 8, 1983

**Summary.** Using realistic expressions for the velocity  $v(r)$  and opacity  $\tau'_{12}(X')$  distributions in rapidly expanding atmospheres, we present numerical results for the first order moment  $W_1 \propto \int (E(\lambda)/E_c - 1)(\lambda - \lambda_{12})d\lambda$  of a P Cygni line profile calculated as a function of the parameter  $W_1^0 \propto M\bar{n}(\text{level})$ , where  $M$  represents the mass-loss rate and  $\bar{n}(\text{level})$  the average fractional abundance of the relevant ion. Our calculations clearly show that the resulting “ $\log(W_1) - \log(W_1^0)$ ” curves depend almost essentially on  $\tau'_{12}(X')$  and that for unsaturated P Cygni line profiles the relation  $W_1 \propto M\bar{n}(\text{level})$  holds irrespective of  $v(r)$  and  $\tau'_{12}(X')$ . For  $W_1 \geq 0.24$ , the line profiles become saturated and the first order moment  $W_1$  does not provide anymore accurate information on the mass-loss rate. This technique of mass-loss determination and that which consists in fitting observed line profiles with theoretical ones are compared.

**Key words:** radiative transfer – Sobolev approximation – mass-loss – P Cygni profile – first order moment

### 1. Introduction

Castor et al. (1981, referred to below as CLS) have first established that, in the framework of the Sobolev approximation (Sobolev, 1947, 1957, 1958) and for the case of optically thin lines, the first order moment  $W_1 \propto \int (E(\lambda)/E_c - 1)(\lambda - \lambda_{12})d\lambda$  of a P Cygni profile provides a good mean for deriving the mass-loss rate  $M$  of a central object. Although CLS have applied this technique for specific distributions of the velocity and line opacity, Surdej (1982) has shown that a unique relation does actually exist between  $W_1$  and the quantity  $M\bar{n}(\text{level}) - \bar{n}(\text{level})$  representing the average fractional abundance of an ion in the lower atomic level associated with the given line transition – irrespective of various physical (collisions, limb darkening, etc.) and geometrical (velocity law  $v(r)$ , rotation, etc.) conditions prevailing in the expanding atmosphere. Furthermore, it was subsequently demonstrated (Surdej, 1983) that the relation  $W_1 \propto M\bar{n}(\text{level})$  is also independent of any Sobolev-type approximations used for the transfer of line radiation.

Adopting realistic expressions for the velocity and opacity distributions, we illustrate for the case of supersonic flows the

results of various numerical applications showing the dependence of  $W_1$  vs. the quantity  $W_1^0 \propto M\bar{n}(\text{level})$ . The goal of these calculations is at least three-fold:

- (i) to provide star observers the possibility of deriving the quantity  $M\bar{n}(\text{level})$  from a “ $\log(W_1) - \log(W_1^0)$ ” diagram on the basis of an observed value for the first order moment  $W_1$  of a P Cygni line profile. This method is much more flexible than the tedious comparison of an observed line profile with theoretical ones (Castor and Lamers, 1979);
- (ii) to assign an error estimate to the mass-loss rate determination;
- (iii) to determine the critical value  $W_1^*$  such that for  $W_1 > W_1^*$  the first order moment ceases to be a sensitive mass-loss indicator, i.e. the P Cygni line profile is saturated.

### 2. Models for the expanding atmosphere

Estimates of mass-loss rates for early-type stars are usually derived from a comparison between observed and theoretical P Cygni line profiles. The latter are calculated under the assumption of resonance scattering and make use of the Sobolev approximation for the transfer of line radiation (cf. “An atlas of theoretical P Cygni profiles” by Castor and Lamers, 1979). In this context, the model for the expanding envelope is essentially characterized by two functions: the velocity distribution  $v(r)$  and the radial optical depth  $\tau'_{12}(v)$ . Empirical models based on this formulation clearly indicate that preferential velocity and opacity distributions (see the compilation in Table 1) lead to the best model fittings of observed P Cygni profiles, specially those associated with resonance lines in the ultraviolet spectrum of early-type stars (Castor and Lamers, 1979; Olson and Castor, 1981; Garmany et al., 1981). Therefore, in the remainder of this paper we shall adopt these same velocity and opacity distributions in order to calculate realistic values for the first order moment  $W_1$  of P Cygni profiles.

As usually (see Table 1),  $R^*$  denotes the radius of the stellar core and  $v_0, v_\infty$  represent the initial and terminal velocities of the flow.  $k_1, \dots, k_n$  are constants related to atomic, physical and stellar parameters. Let us note that among the eighteen possible models inferred from Table 1, case (C- $\alpha$ ) refers to a radiation-driven atmosphere (cf. Castor et al., 1975) in which there is mass conservation of the relevant species.

In the calculation of  $W_1$ , we assume that the stellar core emits a continuum that is flat over the frequency range of the line profile, with no photospheric absorption line and no limb darkening. The effects of photospheric absorption and limb darkening have been discussed by Surdej (1982).

\* Chercheur qualifié au Fonds National de la Recherche Scientifique (Belgium)

**Table 1.** Velocity and opacity distributions adopted in the present work for calculating the first order moment  $W_1$  of P Cygni line profiles

(A)	$v(r) = v_0 + (v_\infty - v_0) (1 - \sqrt{R^*/r})$
(B)	$v(r) = v_0 + (v_\infty - v_0) (1 - R^*/r)$
(C)	$v(r) = v_\infty \sqrt{1 - (1 - (v_0/v_\infty)^2) R^*/r}$
( $\alpha$ )	$\tau_{12}^x(v) = k_\alpha / (x^2 v \frac{dv}{dx})$
( $\beta$ )	$\tau_{12}^x(v) = k_\beta (1 - v(r)/v_\infty)$
( $\gamma$ )	$\tau_{12}^x(v) = k_\gamma$
( $\delta$ )	$\tau_{12}^x(v) = k_\delta \sqrt{1 - v(r)/v_\infty}$
( $\epsilon$ )	$\tau_{12}^x(v) = k_\epsilon (1 - v(r)/v_\infty)^2$
( $\eta$ )	$\tau_{12}^x(v) = k_\eta / v(r)$

### 3. The first order moment $W_1$

Following CLS, the first order moment of a P Cygni line profile is defined as

$$W_1 = \int_{-1}^1 \left( \frac{E(X)}{E_c} - 1 \right) x dx, \quad (1)$$

where

$$X = X' \cos(\theta), \quad (2)$$

with

$$X' = -v(r)/v_\infty, \quad (3)$$

refers to the dimensionless frequency of a line photon, emitted at a radial distance  $r$  along a direction  $\mu = \cos(\theta)$ , with respect to a distant observer.  $E(X)/E_c$  represents the line profile function in the frequency interval  $X \in [-1, 1]$ .

Surdej (1982, hereafter Paper I) has shown that Eq. (1) can be conveniently reduced to the form

$$W_1 = \int_{-X_{\min}}^1 4L^2(X') \tau_{12}^x(X') \gamma_{12}(X') [1 - \beta_{12}^3(X')/\beta_{12}^1(X')] x' dx', \quad (4)$$

where  $L(X')$  expresses the radial distance  $r$  in stellar radii  $R^*$  units. For the velocity distributions in Table 1, we have

$$X_{\min} = -v_0/v_\infty \quad (5)$$

and let us recall [cf. Eqs. (1.11), (1.60), and (1.73)<sup>1</sup>] that the escape probabilities  $\beta_{12}^1$ ,  $\beta_{12}^3$  and  $\gamma_{12}$  are averages of quantities essentially depending on the fictive opacity

$$\tau_{12}(X', \mu) = \tau_{12}^x(X') / \left( \mu^2 \left( 1 - \frac{d \ln L(X')}{d \ln X'} \right) + \frac{d \ln L(X')}{d \ln X'} \right). \quad (6)$$

<sup>1</sup> I.e. Eqs. (11), (60), and (73) in Paper I

For the case of optically thin lines (see Surdej, 1983, hereafter Paper III), Eq. (4) reduces to

$$W_1^0 = \frac{\pi e^2}{mc} f_{12} \lambda_{12} \frac{A(\text{element}) \dot{M} \bar{n}(\text{level})}{4\pi \bar{\mu} M_{\text{amu}} v_\infty^2 R^*} q^c(L_{\max}), \quad (7)$$

with

$$q^c(L_{\max}) = \int_1^{L_{\max}} (W(L) - 1) \frac{dL}{L^2}, \quad (8)$$

and

$$\bar{n}(\text{level}) = \int_1^{L_{\max}} (W(L) - 1) \frac{n(\text{level})}{L^2} dL / q^c(L_{\max}), \quad (9)$$

where  $W(L)$  is the geometrical dilution factor,  $L_{\max}$  the maximum size of the expanding atmosphere and  $A(\text{element})$  the abundance of the relevant element. All other symbols in Eq. (7) have their usual meaning.

Noticing [see Eq. (I.19)] that in terms of atomic and stellar parameters we have

$$\tau_{12}^x(X') = \frac{\pi e^2}{mc} f_{12} \lambda_{12} \frac{A(\text{element}) \dot{M} n(\text{level})}{2\pi \bar{\mu} M_{\text{amu}} v_\infty^2 R^*} \frac{d(1/L)}{d(X'^2)}, \quad (10)$$

it is easy to rewrite the general expression of the fictive radial opacity as

$$\tau_{12}^x(X') = \frac{2W_1^0 n(\text{level})}{q^c(L_{\max}) \bar{n}(\text{level})} \frac{d(1/L)}{d(X'^2)}. \quad (11)$$

From this result and Eq. (4) we conclude that for a given model in Table 1, the first order moment  $W_1$  of a P Cygni line profile is a function of the unique parameter  $W_1^0$ , assuming of course that the values of  $X_{\min}$  and  $L_{\max}$  are known.

### 4. "Log( $W_1$ ) - log( $W_1^0$ )" diagrams

Since the best theoretical fittings of observed P Cygni line profiles suggest no truncation of the expanding atmosphere, i.e.  $L_{\max} \gg 1$ , and a ratio  $v_0/v_\infty \sim 0.01$  (Castor and Lamers, 1979; Garmany et al., 1981), we have performed extensive calculations of the first order moment  $W_1$  [see Eq. (4)] assuming that  $L_{\max} = 1000$  and  $X_{\min} = -0.01$ . Considering separately the opacity distributions ( $\alpha$ ), ( $\beta$ ), ..., ( $\eta$ ) in Table 1, we have illustrated in Figs. 1-6 the results of these numerical applications for each of the three velocity distributions. The resulting diagrams represent the quantity  $\log_{10}(W_1)$  as a function of  $\log_{10}(W_1^0)$ . 50 values of  $\log(W_1^0)$  equally spaced in the range  $[-3, 3]$  have been used for constructing a single curve in Figs. 1-6. In order to assess an error estimate to the quantity  $\dot{M} \bar{n}(\text{level})$  derived from a "log( $W_1$ ) - log( $W_1^0$ )" diagram, we have superposed in Fig. 7 the results of the 18 model calculations.

### 5. Discussion and conclusions

A look at Figs. 2-6 first suggests that the "log( $W_1$ ) - log( $W_1^0$ )" curves calculated for a same opacity distribution  $\tau_{12}^x(X')$  are very little dependent on the type used for the velocity field  $v(r)$ . Recalling (see Paper I) that the relative error, expressed in percent, which results between the two determinations of  $W_1$  when taking and not taking into account the finite size of the central source is

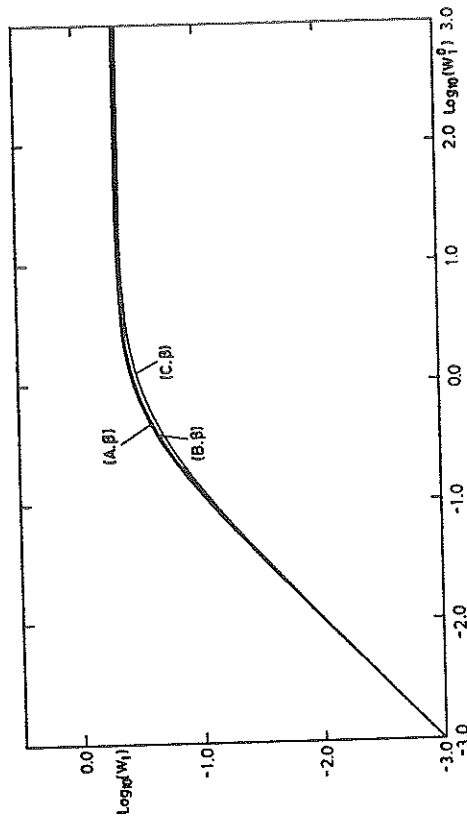


Fig. 2. "log(W<sub>1</sub>) - log(W<sub>1</sub><sup>0</sup>)" curves for the three models (A·β), (B·β), and (C·β) (see Table 1)

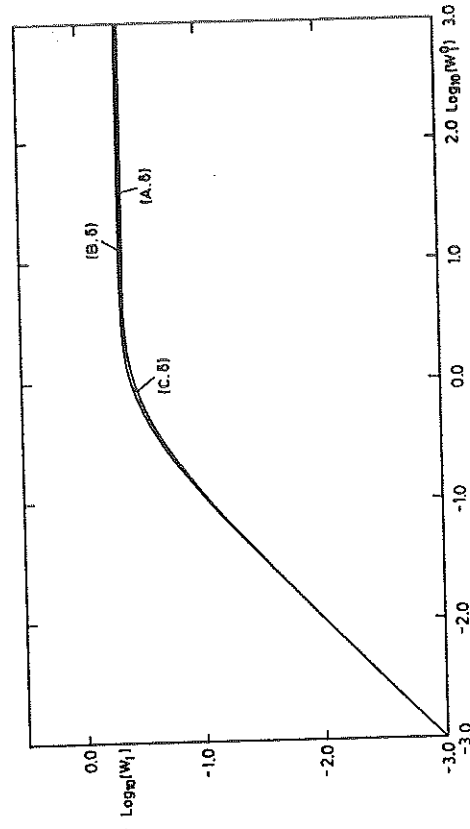


Fig. 4. "log(W<sub>1</sub>) - log(W<sub>1</sub><sup>0</sup>)" curves for the three models (A·δ), (B·δ), and (C·δ) (see Table 1)

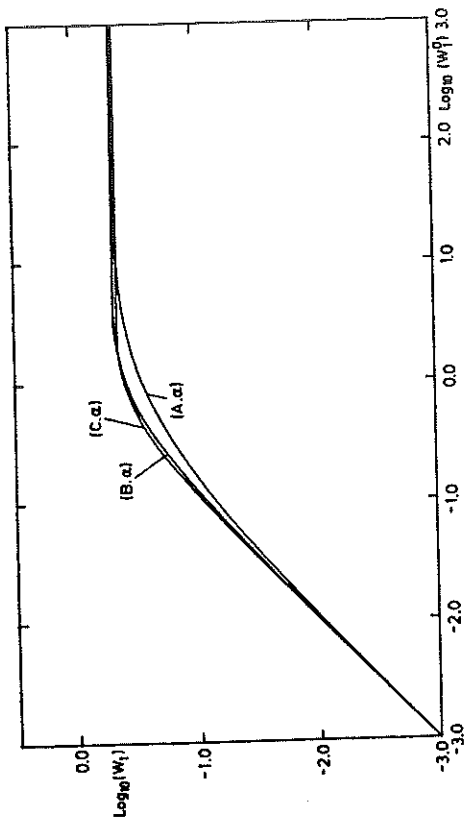


Fig. 1. "log(W<sub>1</sub>) - log(W<sub>1</sub><sup>0</sup>)" curves for the three models (A·α), (B·α), and (C·α) (see Table 1)

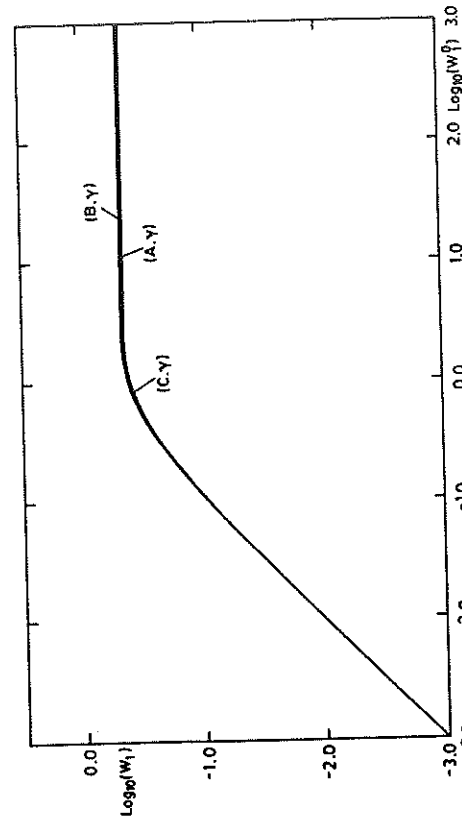


Fig. 3. "log(W<sub>1</sub>) - log(W<sub>1</sub><sup>0</sup>)" curves for the three models (A·γ), (B·γ), and (C·γ) (see Table 1)

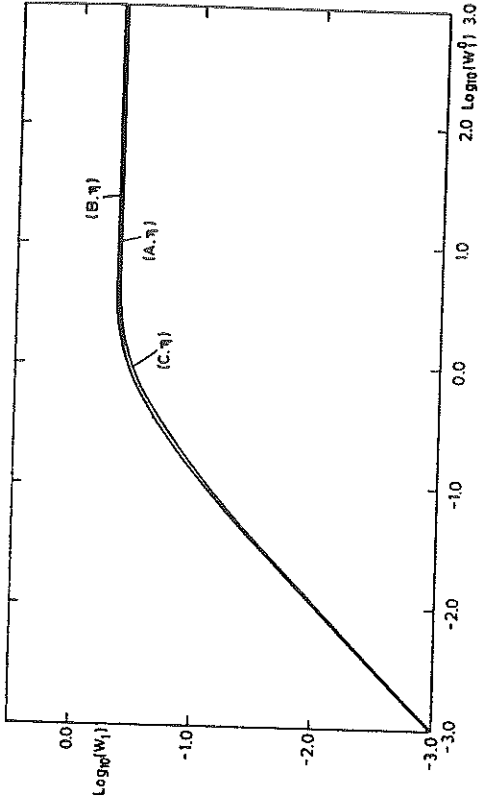


Fig. 6. “ $\log(W_1) - \log(W_1^0)$ ” curves for the three models (A ·  $\eta$ ), (B ·  $\eta$ ), and (C ·  $\eta$ ) (see Table 1)

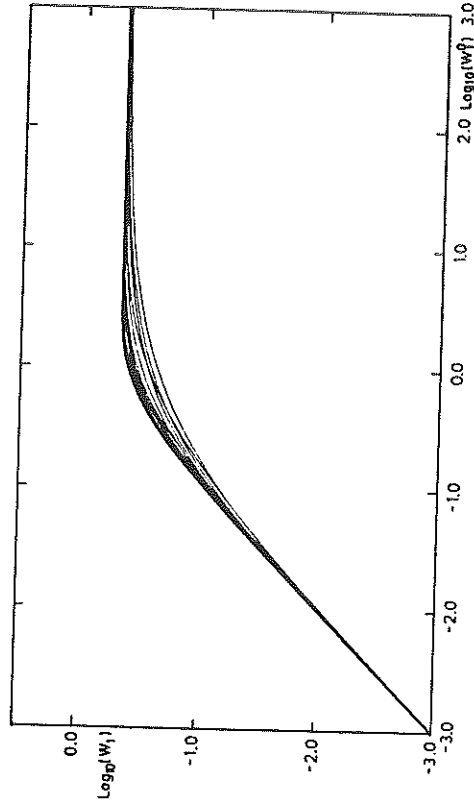


Fig. 7. Superposition of the eighteen “ $\log(W_1) - \log(W_1^0)$ ” curves shown in Figs. 1–6

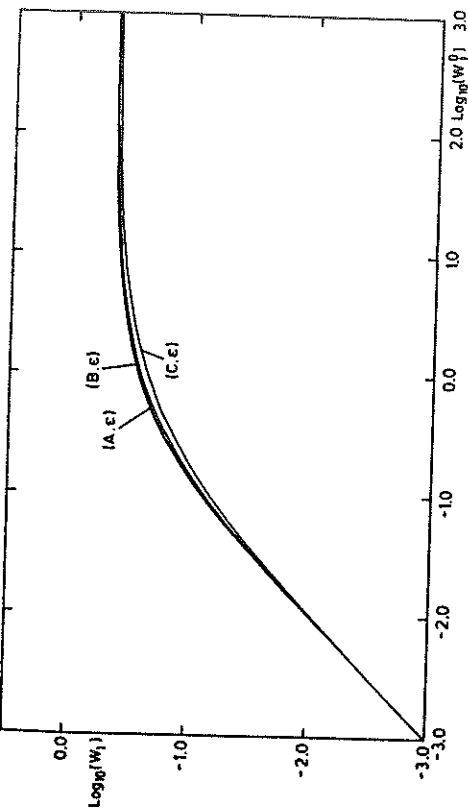


Fig. 5. “ $\log(W_1) - \log(W_1^0)$ ” curves for the three models (A ·  $\epsilon$ ), (B ·  $\epsilon$ ), and (C ·  $\epsilon$ ) (see Table 1)

of the order of 10% and that, within the “point-like star” approximation, we have

$$W_1 = \int_{-X_{\min}}^1 (1 - \exp(-\tau'_{12}(X'))) X' dX', \quad (12)$$

i.e., the first order moment  $W_1$  does only depend on the opacity distribution  $\tau'_{12}(X')$ , the very slight deviations observed in Figs. 2–6 between each of the three “ $\log(W_1) - \log(W_1^0)$ ” curves are directly interpreted. For the calculations presented in Fig. 1, the assumption of mass conservation in the flow implies distinct opacity distributions  $\tau'_{12}(X')$  for each of the velocity fields  $v(r)$ . It results that the “ $\log(W_1) - \log(W_1^0)$ ” curves differ appreciably between each other. Let us still insist that for a known or given opacity distribution  $\tau'_{12}(X')$ , Figs. 2–6 offer the possibility of deriving the quantity  $\dot{M}\bar{n}(\text{level})$ , almost irrespectively of the velocity distribution  $v(r)$ .

As expected, Fig. 7 clearly shows that all “ $\log(W_1) - \log(W_1^0)$ ” curves are characterized by a common linear branch – i.e.  $W_1 = W_1^0$  – for small values of  $\log(W_1^0)$ . It is this trend of variation that was predicted in Paper I. Furthermore, the possibility of deriving the quantity  $\dot{M}\bar{n}(\text{level})$  from the analysis of an unsaturated P Cygni line profile was generalized to the case of arbitrary (e.g. non-Sobolev type) velocity fields. Let us recall the useful relation

$$\dot{M}(M_{\odot}/\text{yr})\bar{n}(\text{level}) = -1.19 \cdot 10^{-21} \frac{v_{\infty}^2 (\text{km s}^{-1}) R^*(R_{\odot}) W_1^0}{f_{12} \lambda_{12} (10^3 \text{ \AA}) A(\text{element})}, \quad (13)$$

derived in Paper II.

For increasing values of  $\log(W_1^0)$ , the P Cygni profiles become saturated. Using " $\log(W_1) - \log(W_1^0)$ " curves, it is then only possible to infer a lower limit for the  $\dot{M}\bar{n}(\text{level})$  quantity. The first order moment  $W_1$  is anymore a sensitive mass-loss indicator. As  $\log(W_1^0) \rightarrow \infty$ , there results an asymptotic value  $\log(W_1) \sim -0.32$ .

Finally, assuming that the models compiled in Table 1 encompass most of realistic cases, we can estimate from the dispersion of the " $\log(W_1) - \log(W_1^0)$ " curves in Fig. 7 the lower value  $W_1^*$  such that, due to the uncertainty in the choice of a model, the relative error affecting a mass-loss rate determination is about equal to 100%. We easily find that  $W_1^* = 0.24$ .

## 6. Comparison between the "line profile fitting" and "first order moment" techniques for the determination of mass-loss rates

We think that it is very appropriate at this stage to compare the two principal techniques used for the determination of mass-loss rates on the basis of line profile analysis.

In the "line profile fitting" technique, the types of velocity and opacity distributions are obtained by matching observed profiles with theoretical ones, using for instance the atlas of Castor and Lamers (1979). By means of the following relation [cf. Eq. (10)]

$$\dot{M}n(\text{level}) = \frac{2\pi\bar{\mu}M_{\text{amu}}v_{\infty}^2R^*}{\frac{\pi e^2}{mc}f_{12}\lambda_{12}A(\text{element})} \left( \tau'_{12}(X') \frac{d(X'^2)}{d(1/L)} \right), \quad (14)$$

one can then calculate the quantity  $\dot{M}n(\text{level})$ . When evaluating the right hand side of Eq. (14), the value of  $L(X')$  corresponding to  $X' = -0.5$  is generally chosen such that the quantity in parentheses depends very little on the accurate type of velocity field  $v(r)$ . Contrary to our results [see Eq. (13)], this implies that the fractional abundance  $n(\text{level})$  in Eq. (14) does not represent an average value across the envelope but that calculated at  $L(X' = -0.5)$ . Consequently, in order to derive  $\dot{M}n(\text{level})$  should be evaluated at  $X = -0.5$ , a requirement that is never fulfilled.

Before concluding, let us point out some similarities between the two techniques. Indeed, Castor and Lamers (1979) have first reported that the absorption component of a P Cygni profile depends very strongly on the opacity distribution  $\tau'_{12}(X')$ , but only

very little on the velocity law  $v(r)$  and that in the limit of very thick lines, the profiles are independent of  $\tau'_{12}(X')$ . The reader will notice at once the striking analogy between these remarks and those discussed in the previous section for the case of the first order moment  $W_1$ .

In conclusion, it is clear that a compromise between the two mentioned techniques will lead to the best determination of a mass-loss rate. For the case of underresolved line profiles, the "first order moment" will be the only useful technique. For the case of unsaturated - but sufficiently resolved - P Cygni profiles, the "line profile fitting" technique will always provide a good estimate for the opacity and velocity distributions as well as for the mass-loss rate [ $n(\text{level})$  being evaluated at  $X = -0.5$ ] characterizing the flow. In addition, the measurement of  $W_1$  will then allow a straight determination of the quantity  $\dot{M}\bar{n}(\text{level})$  from the relevant " $\log(W_1) - \log(W_1^0)$ " curve in Figs. 2-6.

*Acknowledgements.* It is a pleasure for me to thank the referee, Dr. J. Castor, for his comments on the conclusions.

## References

- Castor, J.I., Abbott, D.C., Klein, R.I.: 1975, *Astrophys. J.* **195**, 157  
 Castor, J.I., Lamers, H.J.G.L.M.: 1979, *Astrophys. J. Suppl.* **39**, 481  
 Castor, J.I., Lutz, J.H., Seaton, M.J.: 1981, *Monthly Notices Roy. Astron. Soc.* **194**, 547 (CLS)  
 Garmany, C.D., Olson, G.L., Conti, P.S., Van Steenberg, M.E.: 1981, *Astrophys. J.* **250**, 660  
 Olson, G.L., Castor, J.I.: 1981, *Astrophys. J.* **244**, 179  
 Sobolev, V.V.: 1947, *Dnižuščiesja Oboločki Znezd*, Leningrad (transl. Moving Envelopes of Stars; translated from Russian by S. Gaposchkin, Harvard University Press, Cambridge, MA, 1960)  
 Sobolev, V.V.: 1957, *Astron. Zh.* **34**, 694 (*Trans. Soviet. Astron.* **1**, 678)  
 Sobolev, V.V.: 1958, in *Theoretical Astrophysics*, Chap. 28, ed V.A. Ambartsumyan, Pergamon Press, London  
 Surdej, J.: 1982, *Astrophys. Space Sci.* **88**, 31 (Paper I)  
 Surdej, J.: 1983, *Astrophys. Space Sci.* **90**, 299 (Paper II)

1000

1000



Articles 5 et 6

A POWERFUL METHOD FOR DERIVING MASS-LOSS RATES FROM PLANETARY NEBULAE AND OTHER OBJECTS: THE FIRST ORDER MOMENT  $W_1$  OF UNSATURATED P CYGNI LINE PROFILES

Surdej, J.: 1982, dans les compte-rendus du Symposium UAI N°103, Planetary Nebulae, Londres, p 337.

A NEW APPROACH FOR DERIVING THE MASS-LOSS RATES OF BAL QUASARS: - THE FIRST ORDER MOMENT  $W_1$  OF AN UNSATURATED P CYGNI ABSORPTION COMPONENT

Surdej, J.: 1983, dans "Quasars and Gravitational Lenses, 24<sup>th</sup> Liège Astrophysical Colloquium", Institut d'Astrophysique, Ulg, pp. 616-620.

Dans ces deux communications scientifiques présentées lors du Symposium de l'UAI N°103 (Planetary Nebulae) à Londres et du 24<sup>ème</sup> Colloque International d'Astrophysique de Liège (Quasars and Gravitational Lenses), nous avons décrit les avantages ainsi que les conditions d'applicabilité de la méthode du moment d'ordre 1 en vue de déduire les taux de perte de masse  $\dot{M}$  des noyaux de nébuleuses planétaires et des quasars de type BAL (Broad Absorption Line) à partir de l'analyse des profils de raies de type P Cygni non saturés observés dans leurs spectres.

100

A POWERFUL METHOD FOR DERIVING MASS-LOSS RATES FROM PLANETARY NEBULAE AND OTHER OBJECTS: THE FIRST ORDER MOMENT  $W_1$  OF UNSATURATED P CYGNI LINE PROFILES

Jean Surdej  
Institut d'Astrophysique, Universite de Liège, Belgium

For the case of optically thin lines, we show that the relation existing between the first order moment

$$W_1 \approx (E(\lambda)/E_c - 1) (\lambda - \lambda_{12}) d\lambda$$

of a P Cygni line profile and the quantity  $\dot{M} n$  (level) (cf. Castor, Lutz and Seaton, 1981), where  $\dot{M}$  is the mass-loss rate of the central star and  $n$  (level) the fractional abundance of the relevant ion, is in fact independent of any Sobolev-type approximations used for the transfer of line radiation. Consequently, all results established in the context of "very rapidly" expanding atmospheres (see Surdej, 1982) and mainly referring to the non-dependence of  $W_1$  on various physical (underlying photospheric absorption line, limb darkening, collisions, multiplet line transitions, etc.) and geometrical (radial and rotational velocity fields, size of the atmosphere, etc.) effects remain unchanged for arbitrary (e.g. non-Sobolev type) outward-accelerating velocity laws.

Whenever applied with caution, the following relation

$$\dot{M} (-M_{\odot}/\text{year}) n (\text{level}) = -1.19 \cdot 10^{-21} v_{\text{max}}^2 (-\text{km/sec}) R^* (-R_{\odot}) W_1 / (f_{12} \lambda_{12} (-10^3 \text{\AA}) A(\text{element})),$$

where the different symbols have their usual meaning, thus provides a very powerful means of deriving mass-loss rates - with a total uncertainty less than 60 per cent - from the measurement  $W_1$  of unsaturated P Cygni profiles observed in the spectrum of planetary nebulae, early as well as late-type stars, quasars, etc.

Castor, J.I., Lutz, J.H. and Seaton, M.J.: 1981, Monthly Notices Roy. Astron. Soc. 194, 547.

Surdej, J.: 1982, Astrophys. Space Sci. 88, 31.

PERINOTTO: Did you try to apply your method to any observed objects?  
SURDEJ: Only to NGC 6543, for which we derive the same mass loss rate (to within 50%) as Castor, Lutz and Seaton.



A New Approach For Deriving The Mass-loss Rates Of BAL Quasars :- The First Order Moment  $W_1$  Of An Unsaturated P Cygni Absorption Component

Jean Surdej (X)

Institut d'Astrophysique, Université de Liège, Belgium

Paper n° 88

Abstract : Under the reasonable assumption that the broad blue-shifted absorption line components observed in the spectra of broad absorption line (BAL) quasars arise from the scattering of line photons in a gas which is spherically-ejected from a central core, we show that the technique of the first order moment ( $W_1 \propto \int (E(\lambda)/E_c - 1)(\lambda - \lambda_{12})d\lambda$ ) of an unsaturated P Cygni profile can be conveniently applied to the observations in order to derive the mass-loss rates ( $\dot{M}$ ) of BAL quasars. For non-relativistic flows, the relation between  $\dot{M}$  and  $W_1$  is given by :

$$\dot{M}(-M_{\odot}/\text{year}) = -5.28 \cdot 10^{-14} v_{\text{max}}^2 (-\text{km/sec}) R_q (-\text{pc}) W_1 / (f_{12} \lambda_{12} (-10^3 \text{\AA}) A(\text{element}) \bar{n}(\text{level})),$$

where  $\bar{n}(\text{level})$  is the mean fractional abundance of the relevant ion and where the other symbols have their usual meaning.

1. Introduction

When visualizing P Cygni type profiles such those observed in the spectra of broad absorption line (BAL) quasars (see Weymann, 1983 and Turnshek, 1983, these proceedings), we are led to consider "at least" three different basic models in order to account for the observations :

- In the first model (model I, the "disconnected" model), the expanding absorbing gas is located far away from the emission line region (cf. Fig. 1.a). The resulting P Cygni line profile that would be observed by a distant observer is then simply given by the superposition of a broad blueshifted absorption component with a "classical" emission line (see Fig. 1.b).
- In the second model (model II, the "mixed" model), the absorbing gas is closely connected with the emission line region (cf. Fig. 2.a). The corresponding P Cygni line profile results from a complex radiative interaction between the line photons and both the emitting and absorbing gas (cf. Fig. 2.b).
- The third conceivable model (model III, the "ad-hoc" model) consists of an absorbing region which has a very adequate conical geometry (cf. Fig. 3.a, adapted from Fig. 4 of Junkkarinen, 1983, Ap. J. 265, 73). The resulting P Cygni line profile is also a "kind" of superposition between a blue-shifted broad absorption component and a "classical" emission (see Fig. 3.b).

Taking advantage of the general similarities existing be-

X Chercheur Qualifié au Fonds National de la Recherche Scientifique (Belgium)

tween the P Cygni line profiles observed in the spectra of early-type stars (cf. the UV resonance line transitions) and BAL quasars, and, since it seems to be well established that for the first class of objects, models I and/or II provide a reasonable description of the geometry -spherically symmetric- necessary to account for the observations (cf. Castor and Lamers, 1979, Ap. J. Suppl. 39, 481 and references therein), we show hereafter that the first order moment ( $W_1$ ) of an unsaturated P Cygni line profile can be conveniently applied in order to derive mass-loss rates ( $\dot{M}$ ) of BAL quasars. Let us point out that if model III would turn out to be the correct one, there would be consequently no hope to derive any meaningful mass-loss rate for BAL QSOs since the value of  $\dot{M}$  would depend on where the distant observer is actually located in space with respect to the observed quasar.

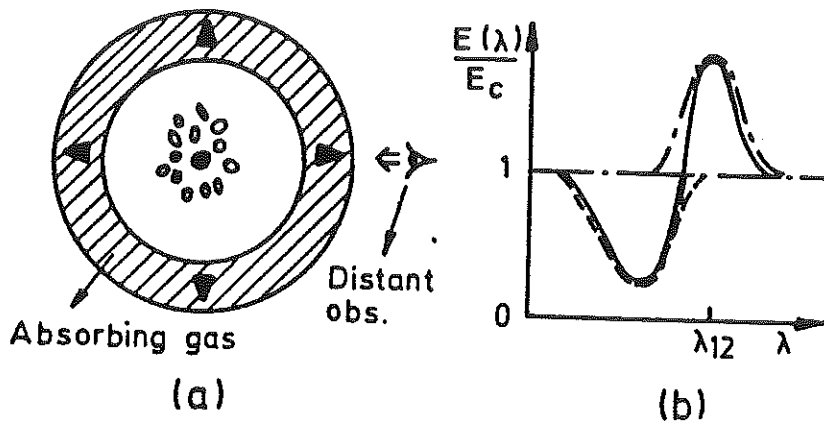


Figure 1 :  
Model I (see text)

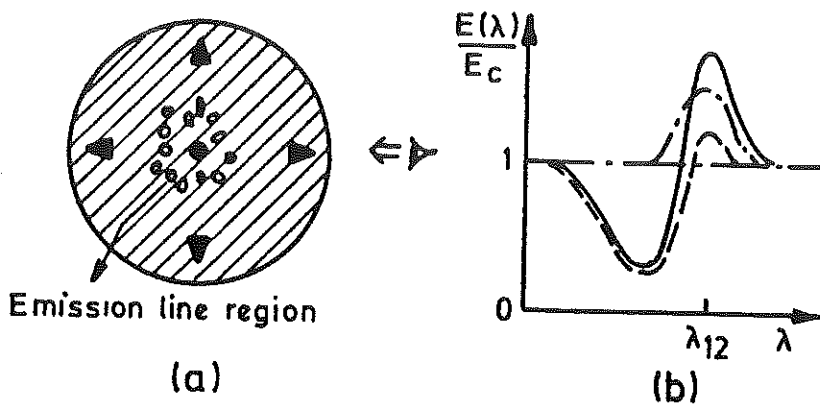


Figure 2 :  
Model II (see text)

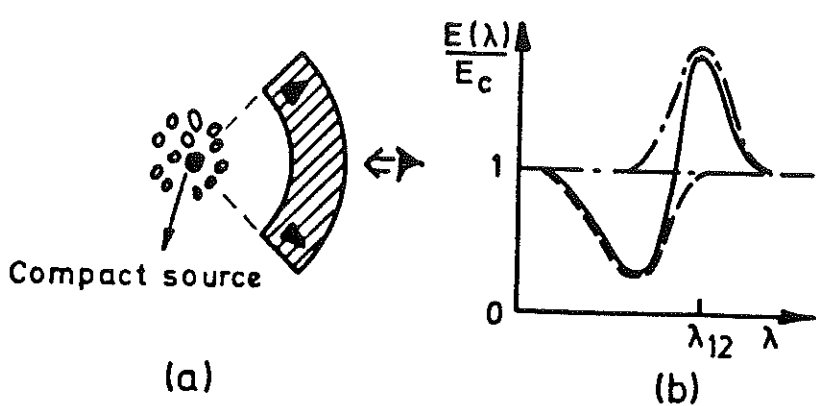


Figure 3 :  
Model III (see text)  
Note : In Figs. 1-3,  
part (b) illustrates the  
resulting P Cygni profile  
(full line) as formed by  
a mere superposition or  
a complex combination of  
the blueshifted absorption  
(dotted line) and the  
"classical" emission  
(dot-dashed line)

## 2. The first order moment $W_1$ for the case of optically thin lines

Castor, Lutz and Seaton (1981, MNRAS 194, 547) have first established that in the framework of the Sobolev approximation (cf. Sobolev, 1960, Moving Envelopes of Stars; transl. from Russian by S. Gaposchkin) and for the case of optically thin lines, the first order moment  $W_1$  of a P Cygni line profile, i.e. the quantity

$$W_1 = (c/(\lambda_{12} v_{\max}))^2 \int (E(\lambda)/E_c - 1) (\lambda - \lambda_{12}) d\lambda, \quad (1)$$

provides a good mean of deriving the mass-loss rate  $\dot{M}$  of a central object (star, QSO, etc.). Although Castor, Lutz and Seaton have applied this technique for specific distributions of the velocity and line opacity, it is straightforward to show (see below) that a unique relation between  $W_1$  and  $\dot{M}$  actually holds, irrespective of the types of velocity and opacity distributions.

Indeed, if the P Cygni line profile is not saturated (cf. Fig. 4.b) - i.e. the expanding envelope is optically thin to the line radiation-, one can easily state that (neglecting for the moment the occultation effect) the line radiation emitted from the approaching and receding lobes of the envelope (see Fig. 4.a) will equally contribute to the blue and red sides of the "emission" line profile seen by a distant observer; in other words, the "emission" line profile is a symmetric function with respect to  $\lambda - \lambda_{12}$ . Denoting by  $E_{\text{abs}}(\lambda)/E_c$  the profile of the absorption component which arises from the scattering of line photons in the gas just located between the central core and the observer, Equation (1) then reduces to

$$W_1 = (c/(\lambda_{12} v_{\max}))^2 \int (E_{\text{abs}}(\lambda)/E_c - 1) (\lambda - \lambda_{12}) d\lambda. \quad (2)$$

Since

$$E_{\text{abs}}(\lambda)/E_c = \exp(-\tau_{12}), \quad (3)$$

where  $\tau_{12}$  is the line opacity and that, in the optically thin approximation

$$\exp(-\tau_{12}) \sim 1 - \tau_{12}, \quad (4)$$

Equation (2) takes the convenient form

$$W_1 = (c/(\lambda_{12} v_{\max}))^2 \int \tau_{12}(\lambda) (\lambda - \lambda_{12}) d\lambda. \quad (5)$$

Adopting the Sobolev-type expression of  $\tau_{12}$  (see Castor, 1970, MNRAS, 149, 111)

$$\tau_{12} = n_1 (\pi e^2 / mc) f_{12} \lambda_{12}^2 \frac{dv}{dr}, \quad (6)$$

$n_1$  being the volume population of the lower atomic level of the line transition 1→2, and with the help of the classical Doppler relation

$$(\lambda - \lambda_{12}) / \lambda_{12} = v/c, \quad (7)$$

Expression (5) can be then reduced to

$$W_1 = (\pi e^2 / mc) f_{12} \lambda_{12}^2 / v_{\max}^2 \int_{R_q}^{r_{\max}} n_1 v dr. \quad (8)$$

Defining the fractional abundance  $n(\text{level})$  of an ion in the lower atomic level 1 by

$$n(\text{level}) = n_1/N(\text{element}), \quad (9)$$

where  $N(\text{element})$  is the total number density of the given element which has an abundance

$$A(\text{element}) = N(\text{element})/N_{\text{tot}}, \quad (10)$$

$N_{\text{tot}}$  representing the total nucleon density at a distance  $r$ , it is straightforward to combine Equation (8) with the expression of the mass-loss rate

$$\dot{M} = -4\pi r^2 v N_{\text{tot}} \bar{\mu} M_{\text{amu}}, \quad (11)$$

to finally obtain

$$W_1 = (\pi e^2/mc) f_{12} \lambda_{12} A(\text{element}) \dot{M} \bar{n}(\text{level}) (1/L_{\text{max}}^{-1}) / (4\pi \bar{\mu} M_{\text{amu}} v_{\text{max}}^2 R_q), \quad (12)$$

where  $\bar{\mu}$  is the mean atomic weight of the nuclei in the flow,  $M_{\text{amu}}$  the unit of atomic mass and

$$\bar{n}(\text{level}) = \int_1^{L_{\text{max}}} n(\text{level}) d(1/L) / \int_1^{L_{\text{max}}} d(1/L), \quad (13)$$

$L$  representing the dimensionless distance to the central core ( $R_q$ )

$$L = r/R_q. \quad (14)$$

This short demonstration has led to the expected result (see Equation (12)) : there exists a unique relation between  $\dot{M}$  and  $W_1$ , irrespective of any choice for the velocity and/or opacity distributions. Furthermore, if one takes into account the "occultation" effect, detailed calculations (see Surdej, 1982, *Astrophysics and Sp. Science* 88, 31 and Surdej, 1983, *Astrophysics and Sp. Science* 90, 299) show that the following relation

$$\dot{M} (-M_{\odot}/\text{year}) = -5.28 \cdot 10^{-14} v_{\text{max}}^2 (-\text{km/sec}) R_q (-\text{pc}) W_1 / (f_{12} \lambda_{12} (-10^3 \text{\AA}) A(\text{element}) \bar{n}(\text{level})), \quad (15)$$

where

$$\bar{n}(\text{level}) = \int_1^{L_{\text{max}}} (W(L)-1) n(\text{level}) d(1/L) / \int_1^{L_{\text{max}}} (W(L)-1) d(1/L), \quad (16)$$

with

$$W(L) = 0.5(1 - \sqrt{1 - (1/L^2)}), \quad (17)$$

being the geometrical dilution factor, applies very generally since it is independent of :

- the velocity field  $v(r)$
  - the opacity distribution  $\tau_{12}$
  - the collisional excitation parameter  $\epsilon$
  - a possible rotation of the expanding atmosphere
  - the presence of an underlying photospheric absorption line ( $\Delta\dot{M}/\dot{M} \lesssim 20\%$ ) and similarly of an underlying "emission" line
- } i.e. matter needs not being ejected in a continuous flow !



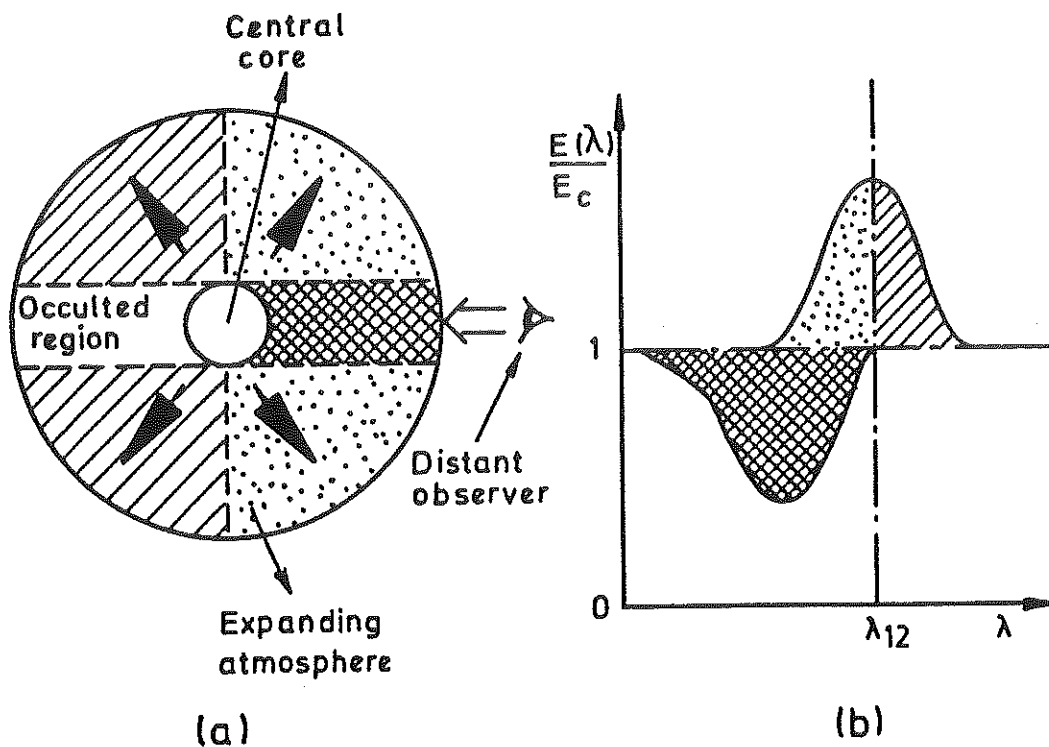


Figure 4 : The different geometrical regions of the expanding atmosphere from which (red- and blue- shifted) emission and absorption of line radiation contribute to the formation of a P Cygni line profile (see part (b)) are represented in part (a) of this illustration

(cf. model II)

- the multiplet structure of a resonance line transition
- the existence of a strong limb darkening law of the central core
- the Sobolev approximation used for handling the transfer of line radiation.

It is without saying that for the case of a BAL quasar, the first order moment  $W_1$  is to be calculated after reduction of the observations (P Cygni line profile) into the rest frame of the QSO.

We intend to investigate in the near future the correction(s) -if any- which should be applied to Equation (15) for the case of relativistic flows.



## Article 7

### ANALYSIS OF P CYGNI LINE PROFILES: GENERALIZATION OF THE $N^{\text{TH}}$ ORDER MOMENT $W_N$

Surdej, J.: 1985, *Astron. Astrophys.* 152, 361-370.

Pour le cas d'une raie de résonance simple, nous avons généralisé dans cet article l'expression du moment  $W_n$  en vue d'étudier la dépendance des profils de raies de type P Cygni observés en fonction du taux de perte de masse  $\dot{M}$ , du champ de vitesse  $v(r)$  et de la loi d'opacité  $\tau_{12}^r(v)$ . Adoptant des expressions réalistes pour  $v(r)$  et  $\tau_{12}^r(v)$ , nous avons construit des diagrammes de type " $\log(W_n) - \log(W_n^0)$ " qui permettent de déduire les valeurs des paramètres physiques  $W_n^0$  à partir de valeurs  $W_n$  mesurées. Pour  $n = 0, 1, 2$  et  $3$ , nous montrons que  $W_n^0$  est lié respectivement à la densité de colonne  $N_1$ , au taux de perte de masse  $\dot{M} \bar{n}(\text{level})$ , à la colonne d'impulsion et à (deux fois) la colonne d'énergie cinétique des ions emportés par le vent stellaire. Pour le cas des profils de raies non saturés, on a bien sûr la relation  $W_n = W_n^0$ . Nous suggérons aussi de reporter dans des diagrammes théoriques de type " $\log(W_n) - \log(W_0)$ " les valeurs mesurées de  $W_n$  afin de déduire le champ de vitesse  $v(r)$  et la loi d'opacité  $\tau_{12}^r(v)$  qui caractérisent au mieux les profils de raies observés.



## Analysis of P Cygni line profiles: generalization of the $n$ th order moment $W_n$

J. Surdej\*

European Southern Observatory, Karl-Schwarzschild-Str. 2, D-8046 Garching, Federal Republic of Germany

Received February 7, accepted May 24, 1985

**Summary.** The generalization of the  $n$ th order moment  $W_n$  of a P Cygni line profile leads to a new approach of deriving the various physical quantities which characterize the phenomenon of mass-loss around stars, quasars, etc.

Considering first the case of rapidly expanding atmospheres (Sobolev approximation), we present in two types of different diagrams the results of calculations of  $W_n$  ( $n = 0, 1, 2$ , and  $3$ ) for realistic velocity ( $v(r)$ ) and opacity ( $\tau'_{1,2}(X')$ ) distributions. In the first so-called “ $\log(W_n) - \log(W_n^0)$ ” diagrams, we show that for unsaturated P Cygni profiles there exists a linear relation, irrespective of the choice of  $v(r)$  and  $\tau'_{1,2}(X')$ , between the observed moment  $W_n$  and the physical parameter  $W_n^0$ . For  $n = 0, 1, 2$  and  $3$ , we establish that  $W_n^0$  is a quantity directly related to the column density  $N_1$ , to the mass-loss rate  $\dot{M}\bar{n}^{(1)}$  (level), to the column impulsion and to (twice) the column kinetic energy, respectively, of the relevant species in the flow. A consistent definition of the average fractional abundance  $\bar{n}^{(n)}$  (level) of an ion is given. The values of  $\bar{n}^{(n)}$  (level) are found to be little dependent on the value of the order  $n$ .

When the Sobolev-type approximations used for the transfer of line radiation are no longer fulfilled, we find that only the relation  $W_1 \propto \dot{M}\bar{n}^{(1)}$  (level) remains valid and that the relation  $W_0 \propto N_1$  still holds provided that the expanding envelope is much larger than the stellar core and that the macroscopic velocity  $v(r)$  of the flow is greater everywhere than the chaotic (thermal and turbulent) velocities  $u(r)$  of the ions.

For values of  $W_0 > 0.31$ ,  $W_1 > 0.24$ ,  $W_2 > 0.17$  or  $W_3 > 0.15$ , the corresponding moment  $W_n$  ceases to provide an accurate estimate of the physical parameter  $W_n^0$ . It is then only possible to assign a lower limit to the value of  $W_n^0$ . By just locating observed values of the moments  $W_n$  ( $n = 1, 2$  and  $3$ ) and of  $W_0$  in combined “ $\log(W_n) - \log(W_0)$ ” diagrams, we propose a new way of determining the types of opacity and velocity distributions characterizing the flow. Of course, this only applies to the non-saturated region of the “ $\log(W_n) - \log(W_0)$ ” diagrams. Our numerical applications do also clearly show that the moments  $W_n$  of an observed P Cygni line profile are very dependent on  $\tau'_{1,2}(X')$  and that they are definitely less sensitive to  $v(r)$ .

**Key words:** lines: formation – lines: profile – radiation transfer – stars: mass loss

---

\* *Chercheur Qualifié au Fonds National de la Recherche Scientifique, Belgium*

### 1. Introduction

The first concept of the  $n$ th order moments  $W_n$  of a P Cygni line profile has been given by Castor et al. (1981) who have developed a theory particularly well adapted to the interpretation of IUE and other low resolution spectra. In the framework of the Sobolev approximation (Sobolev, 1947, 1957, 1958; Castor, 1970) and for the case of optically thin lines, these authors have established a linear relation between the first order moment  $W_1$  and the quantity  $\dot{M}n$  (level), where  $n$  (level) is the fractional abundance of an ion in the lower atomic level associated with the given line transition and  $\dot{M}$  is the mass-loss rate of the central source. Whereas this relation has been set up by Castor et al. for particular opacity ( $\tau'_{1,2}(X') \propto (1 - X')$ ) and velocity ( $X' = 1 - 1/L$ ) distributions, Surdej (1982) has shown that this result was in fact independent of the choice taken for these distributions and that, furthermore, it was irrespective of the Sobolev-type approximations used for describing the transfer of line radiation (Surdej, 1983b).

We are then naturally led to wonder about the possibility of deriving the additional – all remaining? – physical parameters characterizing a P Cygni line profile on the basis of the other moments  $W_n$  ( $n \neq 1$ ). It is easy to establish that for even values of the order  $n$  ( $n = 0, 2$ , etc.), the expression of the moments  $W_n$  remains a complicated function of these physical parameters. A slightly modified definition of  $W_n$  allows one to overcome these difficulties (Sect. 2). In the context of rapidly expanding atmospheres (Sect. 3), we derive the general expression of  $W_n$  in terms of well known quantities such as  $\tau'_{1,2}(X')$ ,  $X'$  and  $W_1^0$ . For unsaturated P Cygni line profiles, we establish the linear relations existing between  $W_n$  and the physical parameter  $W_n^0$ .

Adopting realistic expressions for the velocity and opacity distributions (cf. Castor and Lamers, 1979; Garmany et al., 1981), we present (Sect. 4) and discuss (Sect. 5) the results of calculations of the moments  $W_n$  in two types of different diagrams: the “ $\log(W_n) - \log(W_n^0)$ ” and “ $\log(W_n) - \log(W_0)$ ” diagrams. The physical representation of the parameters  $W_n^0$  is then given in Sect. 6. In Sect. 7, we test and generalize the validity of some of the linear relations  $W_n \propto W_n^0$  for the case of slowly expanding (i.e. non-Sobolev type), optically thin atmospheres. Discussion and conclusions form the last Section.

### 2. Generalization of the $n$ th order moment $W_n$ of a P Cygni line profile

Considering a two-level atom model interacting with line photons (conservative scattering) in a spherical envelope that is

accelerated radially outward around a central source, let us generalize the expression of the  $n$ th order moment of a P Cygni line profile (see Castor et al., 1981) as follows:

$$W_n = \frac{\lambda_{12}}{\lambda_{\min}(\lambda_{12} - \lambda_{\min})} \int_{\lambda_{\min}}^{\infty} \left( \frac{E(\lambda)}{E_c} - 1 \right) \left| \frac{\lambda - \lambda_{12}}{\lambda_{12} - \lambda_{\min}} \right|^n \cdot \text{sign}(\lambda - \lambda_{12}) \left( \frac{\lambda_{\min}}{\lambda} \right)^{n+2} d\lambda, \quad (1)$$

with  $E(\lambda)/E_c$  being the normalized line profile function and where  $\lambda_{12}$  (resp.  $\lambda_{\min}$ ) denotes the rest (resp. most blueshifted) wavelength of the line profile in the frame of the observer. It is then convenient to make use of the dimensionless frequency

$$X = -(v - v_{12})/(v_{\max} - v_{12}), \quad (2)$$

such that the previous expression of  $W_n$  reduces to

$$W_n = \int_{-1}^1 \left( \frac{E(X)}{E_c} - 1 \right) \text{sign}(X) |X|^n dX. \quad (3)$$

Let us immediately note that the moments  $W_n$  are defined irrespective of the possible redshift – or blueshift – of the astronomical object under study (quasar, star, etc.).

### 3. Rapidly expanding atmospheres

Using at first Sobolev-type approximations for the transfer of line radiation in rapidly expanding atmospheres (cf. Surdej, 1979; referred to below as Paper I) and assuming – for the sake of simplicity – that the central core, having a radius  $R^*$ , emits a flat continuum with no photospheric absorption line and with no limb darkening ( $\Psi(\mu^*) = 1$ ), let us follow a similar reasoning as in Surdej (1982; Paper II) in order to transform Equation (3) into (compare Eqs. (1) and (4) with (II.7) and (II.70)<sup>1</sup>)

$$W_n = \int_{-\lambda_{\min}}^1 \tau'_{12}(X') 4L^2(X') X'^n \gamma_n (1 - 2W(L(X')), 1) \cdot (1 - \beta_{12}^3(X')/\beta_{12}^3(X')) dX', \quad (4)$$

where

$$\gamma_n(a, b) = \frac{1}{2} \int_a^b \mu^n \frac{(1 - \exp(-\tau_{12}(X', \mu)))}{\tau_{12}(X', \mu)} d\mu. \quad (5)$$

We briefly recall that:

–  $X' = v(r)/v_\infty$  denotes the frequency at which a stellar photon is likely to be scattered in the medium at a radial distance  $r$  where the macroscopic velocity is  $v(r)$ .  $v_\infty$  stands for the asymptotic velocity  $v(r)$  as  $r \rightarrow \infty$ .

–  $L(X') = r/R^*$ ,

–  $W(L(X'))$  is the geometrical dilution factor at a distance  $L(X')$  (cf. Eq. (II.53)).

– The frequency  $X_{\min}$  is such that  $L(-X_{\min}) = 1$ .

–  $\beta_{12}^3 (= \gamma_0(1 - 2W(L(X')), 1))$  and  $\beta_{12}^3 (= \gamma_0(-1, 1))$  are the well known escape probabilities of a line photon in an expanding atmosphere.

–  $\tau'_{12}(X')$  and  $\tau_{12}(X', \mu)$  are fictitious opacities evaluated at  $L(X')$  along a direction making an angle  $\theta = 0$  and  $\theta = \arccos(\mu)$  with respect to the radial direction (cf. Eqs. (II.19) and (II.20)).

A more complete description of the above quantities may be found in Paper II.

Because the “point-like” star approximation is essentially a good one, and is very useful in order to understand the asymptotic behaviours of more general solutions given by Eq. (4), we merely state the result when  $R^* \rightarrow 0$

$$W_n^* = \int_{-\lambda_{\min}}^1 X'^n (1 - \exp(-\tau'_{12}(X'))) dX'. \quad (6)$$

Let us mention that with the old definition of the moments  $W_n$  (cf. Castor et al., 1981 and Paper II), no such simple relations (Eqs. (4) and (6)) could be derived for even values of  $n$ . Within a good approximation, one can show that for even values of  $n$ ,  $W_n^{\text{old}} \sim (1/(n+1) - 1)W_n$  such that  $W_0^{\text{old}} \sim 0$  and  $|W_n^{\text{old}}| < |W_n|$  for  $n > 0$ .

#### 3.1. The optically thin case

For the case of optically thin lines (i.e.,  $\tau_{12}(X', \mu) < 1$ ) and recalling the expression of the fictitious radial opacity (cf. Eq. (II.19))

$$\tau'_{12}(X') = K \cdot \dot{M} n(\text{level}) \frac{A(ell)}{v_\infty^2} \frac{d(1/L)}{X' dX'}, \quad (7)$$

with the constant

$$K = \frac{\pi e^2}{mc} f_{12} \lambda_{12} / (4\pi \bar{\mu} M_{\text{amu}} R^*), \quad (8)$$

and where:

- $\dot{M}$  denotes the mass-loss rate of the central object,
- $n(\text{level})$  is the fractional abundance of the relevant ion in the lower atomic level  $l$  of the given line transition,
- $A(ell)$  is the abundance of the given element,
- $f_{12}$  is the oscillator strength of the line transition,
- $\bar{\mu}$  is the mean atomic weight of the nuclei and
- $M_{\text{amu}}$  is the unit of atomic mass.

Equation (4) now takes the form

$$W_n^0 = K \dot{M} X'^{n-1} \bar{n}^{(n)}(\text{level}) q_{(\infty)}^n \frac{A(ell)}{v_\infty^2}, \quad (9)$$

with the average quantities being defined as

$$X'^{n-1} = \frac{\int_1^\infty X'^{n-1} n(\text{level}) (1 - (1 - 1/L^2)^{(n+1)/2}) (1 + \sqrt{1 - 1/L^2}) dL}{\int_1^\infty n(\text{level}) (1 - (1 - 1/L^2)^{(n+1)/2}) (1 + \sqrt{1 - 1/L^2}) dL}, \quad (10)$$

$$\bar{n}^{(n)}(\text{level}) = \frac{\int_1^\infty n(\text{level}) (1 - (1 - 1/L^2)^{(n+1)/2}) (1 + \sqrt{1 - 1/L^2}) dL}{\int_1^\infty (1 - (1 - 1/L^2)^{(n+1)/2}) (1 + \sqrt{1 - 1/L^2}) dL} \quad (11)$$

and with the constant  $q_{(\infty)}^n$  given by

$$q_{(\infty)}^n = \frac{1}{(n+1)} \int_1^\infty (1 - (1 - 1/L^2)^{(n+1)/2}) (1 + \sqrt{1 - 1/L^2}) dL, \quad (12)$$

leading to the values:  $q_{(\infty)}^0 = -1.00000$ ,  $q_{(\infty)}^1 = -0.89271$ ,  $q_{(\infty)}^2 = -0.81737$  and  $q_{(\infty)}^3 = -0.76029$ .

<sup>1</sup> i.e. Eqs. (7) and (70) in Paper II

Considering the "point-like" star approximation, we easily find that Eq. (9) should be replaced by

$$W_n^{*0} = -KM \overline{X^{n-1}} \bar{n}(\text{level}) \frac{A(ell)}{v_\infty^2}, \quad (13)$$

with the average quantities now defined as

$$\overline{X^{n-1}} = \frac{\int_1^\infty X^{n-1} n(\text{level})/L^2 dL}{\int_1^\infty n(\text{level})/L^2 dL}, \quad (14)$$

$$\bar{n}(\text{level}) = \frac{\int_1^\infty n(\text{level})/L^2 dL}{\int_1^\infty 1/L^2 dL}. \quad (15)$$

Let us note here that the average fractional abundance  $\bar{n}(\text{level})$  is no longer dependent on the order  $n$  of the considered moment.

### 3.2. The optically thick case

If the expanding atmosphere gets optically thick ( $\tau_{12}(X', \mu) > 1$ ) to the spectral line radiation, Eq. (4) can be easily transformed into

$$W_n^i = \int_{-X_{\min}}^1 L^2(X') X'^n \left\{ \left( 1 - \frac{d \ln L}{d \ln X'} \right) \frac{1}{(n+3)} \left( 1 - \left( 1 - \frac{1}{L^2} \right)^{(n+3)/2} \right) + \frac{d \ln L}{d \ln X'} \frac{1}{(n+1)} \left( 1 - \left( 1 - \frac{1}{L^2} \right)^{(n+1)/2} \right) \right\} \left( 1 + \sqrt{1 - \frac{1}{L^2}} \right) dX', \quad (16)$$

assuming that  $\beta_{12}^3(X')/\beta_{12}^1(X') \sim W(L(X'))$ . We conclude that the asymptotic values  $W_n^i$  are only velocity field dependent.

If the dimensions of the central object are negligible with respect to that of the moving envelope, Eq. (16) should be replaced by

$$W_n^{*i} = \frac{1 - (-X_{\min})^{n+1}}{n+1}. \quad (17)$$

For  $X_{\min} = -0.01$ , we have  $\log_{10}(W_n^{*i}) = -0.00, -0.30, -0.48$  and  $-0.60$  for  $n = 0, 1, 2$  and  $3$ , respectively.

### 4. Numerical applications

Combining Eqs. (7) and (9) for  $n = 1$ , the expression of the fictitious radial opacity may be rewritten as

$$\tau_{12}^i(X') = \frac{W_1^0 n(\text{level}) d(1/L)}{q_{(\infty)}^1 \bar{n}^{(1)}(\text{level}) X' dX'}. \quad (18)$$

For any specified velocity and opacity distributions, it is then straightforward to compute the moments  $W_n$  (cf. Eq. (4)) as well as  $W_n^0$  (see Eq. (9)) as a function of the parameter  $W_1^0$ . Such calculations have already been performed and discussed for the case  $n = 1$  (see Surdej, 1983a; Paper III). Adopting the 3 velocity fields and 6 opacity distributions discussed in that paper (see Table 1), we have illustrated in Figs. 1-3 the 18 resulting " $\log_{10}(W_n) - \log_{10}(W_n^0)$ " model calculations for  $n = 0, 2$  and  $3$ . In Figs. 4-6 we show the 18 " $\log_{10}(W_n) - \log_{10}(W_0)$ " curves for

**Table 1.** Adopted velocity and opacity distributions for calculating the moments  $W_n$  of P Cygni line profiles. The value of the constants  $k_\alpha, \dots, k_\eta$  essentially depends on the choice of the value of the parameter  $W_1^0$  [see Eq. (18)]

(A)	$X' = -X_{\min} + (1 + X_{\min})(1 - 1/\sqrt{L})$
(B)	$X' = -X_{\min} + (1 + X_{\min})(1 - 1/L)$
(C)	$X' = \sqrt{1 - (1 - X_{\min}^2)/L}$
( $\alpha$ )	$\tau_{12}^i(X') = k_\alpha \left/ \left( \frac{X' dX'}{d(1/L)} \right) \right.$
( $\beta$ )	$\tau_{12}^i(X') = k_\beta (1 - X')$
( $\gamma$ )	$\tau_{12}^i(X') = k_\gamma$
( $\delta$ )	$\tau_{12}^i(X') = k_\delta \sqrt{1 - X'}$
( $\epsilon$ )	$\tau_{12}^i(X') = k_\epsilon (1 - X')^2$
( $\eta$ )	$\tau_{12}^i(X') = k_\eta / X'$

$n = 1, 2$  and  $3$ , respectively. In order to construct each single curve in Figs. 1-6, 50 equally spaced values of  $\log_{10}(W_1^0)$  have been chosen in the range  $[-3, 3]$ . As in Paper III, we have taken the values  $X_{\min} = -0.01$  and  $L_{\max} = 1000$  (i.e.,  $L_{\max} \gg 1$ ).

### 5. Discussion of the results illustrated in Figs. 1-6

On the basis of " $\log(W_1) - \log(W_1^0)$ " diagrams, we have shown in Paper III how it is possible to derive the value of the parameter  $W_1^0$  - a quantity that is proportional to  $M \bar{n}^{(1)}(\text{level})$  - from the measurement of the first order moment  $W_1$  of an observed P Cygni line profile. Similarly, using " $\log(W_n) - \log(W_n^0)$ " diagrams (see Figs. 1-3) it is possible to estimate the values of the parameters  $W_n^0$  ( $n = 0, 1, 2$ , etc.) from the measurement of the moments  $W_n$ . The physical representation of the parameters  $W_0^0, W_2^0$  and  $W_3^0$ , defined in Sect. 3.1, shall be discussed later (see Sect. 6).

Let us immediately point out that for the case of unsaturated profiles ( $\tau_{12}^i(X') < 1$ ), we have the linear relation (cf. Sect. 3.1)

$$W_n = W_n^0, \quad (19)$$

irrespective of the velocity and/or opacity distributions used for modelling the expanding envelope.

For large values of  $W_1^0$ , and correspondingly of  $W_n^0$ , the atmosphere gets optically thick and the P Cygni profiles become saturated. Using " $\log(W_n) - \log(W_n^0)$ " diagrams, it is then only possible to derive a lower limit for the value of the parameter  $W_n^0$ . As  $\log(W_n^0) \rightarrow \infty$ ,  $\log(W_n)$  tends towards the asymptotic value  $\log(W_n^i)$  (see Sect. 3.2). If we assume that the " $\log(W_n) - \log(W_n^0)$ " curves illustrated in Figs. 1-3 encompass most of the realistic solutions, we can then estimate from the observed dispersion of these curves the lowest value  $W_n^i$  such that, due to the uncertainty in the choice of a model, the relative error affecting the determination of  $W_n^0$  is roughly equal to 100%. We find that  $W_0^i = 0.31, W_1^i = 0.24$  (see Paper III),  $W_2^i = 0.17$  and  $W_3^i = 0.15$ .

We can still notice in Figs. 1-3 that the " $\log(W_n) - \log(W_n^0)$ " curves calculated for a same opacity distribution  $\tau_{12}^i(X')$  are very little dependent on the type used for the velocity field  $v(r)$  (e.g. models (A. $\gamma$ ), (B. $\gamma$ ) and (C. $\gamma$ )). The results are directly accounted for by the greater sensitivity of the line profile function  $E(X)/E_c$  - and of the resulting moments  $W_n, W_n^*$  - onto the choice of

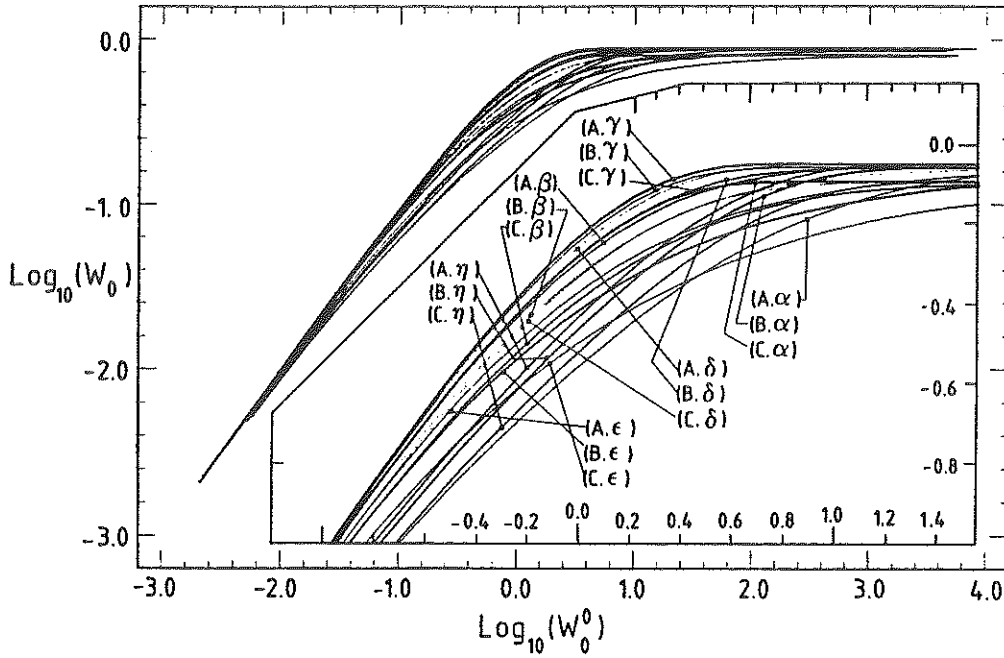


Fig. 1. " $\text{Log}_{10}(W_0) - \text{Log}_{10}(W_0^0)$ " curves for the eighteen possible models derived from Table 1

the opacity distribution rather than on the choice of the velocity field. Considering, for instance, the case of a "point-like" star, we directly see from Eq. (6) that the moment  $W_n^*$  essentially relies on the distribution  $\tau'_{12}(X)$ . The " $\log(W_n) - \log(W_n^0)$ " curves pertaining to the models labelled (A.  $\alpha$ ), (B.  $\alpha$ ) and (C.  $\alpha$ ) in Figs. 1-3 do appear to be very different from one another. Indeed, we recall that these model calculations are characterized by the assumption of mass conservation in the flow (see Table 1) and that

consequently there is a distinct opacity distribution which corresponds to each velocity field.

All these considerations do also apply to the " $\log(W_n) - \log(W_0)$ " curves displayed in Figs. 4-6. The very slight dependence of these curves versus the choice of the velocity field is particularly well seen here. In principle, these " $\log(W_n) - \log(W_0)$ " curves can be used in the following manner: measurement of the moments  $W_n$  ( $n = 1, 2, \text{etc.}$ ) and  $W_0$  from an observed line profile

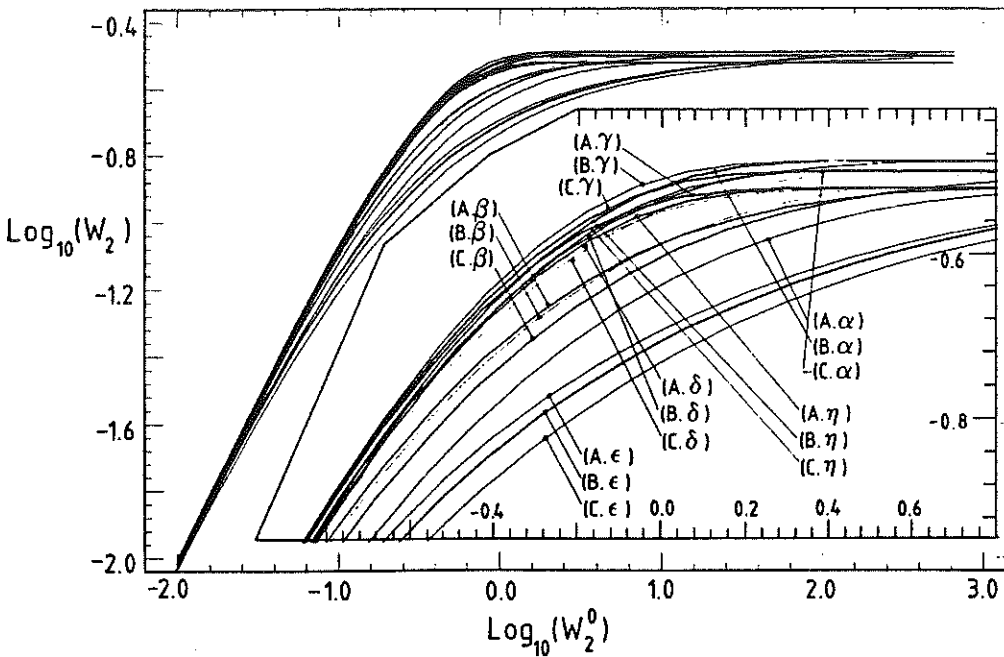


Fig. 2. " $\text{Log}_{10}(W_2) - \text{Log}_{10}(W_2^0)$ " curves for the eighteen possible models derived from Table 1



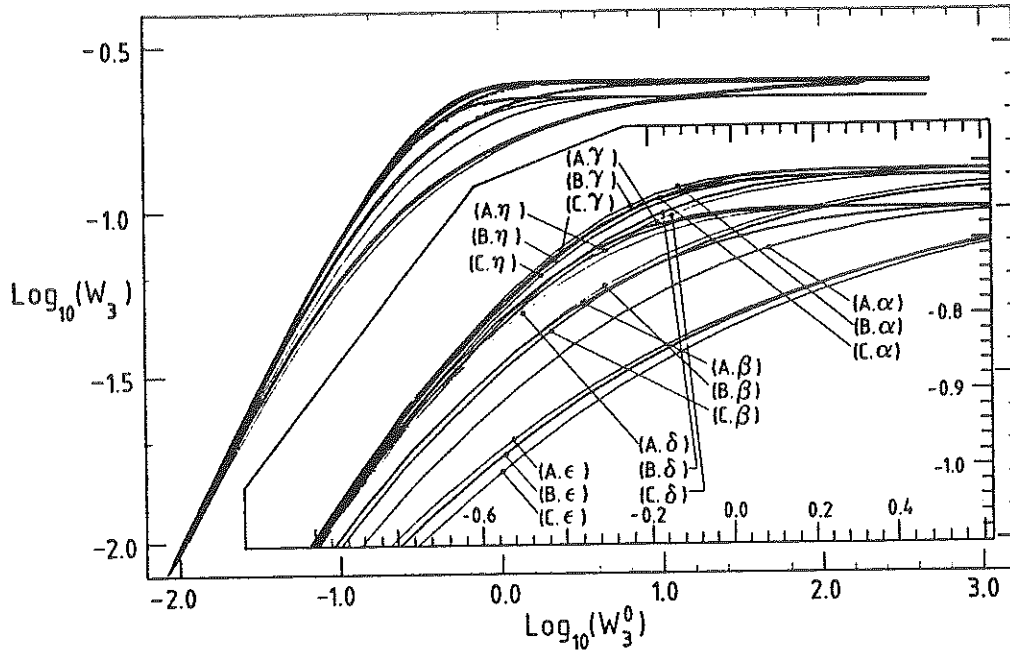


Fig. 3. " $\text{Log}_{10}(W_3) - \text{Log}_{10}(W_3^0)$ " curves for the eighteen possible models derived from Table 1

should allow one to determine the type of opacity and velocity distributions characterizing that particular P Cygni profile by just locating the measured " $\log(W_n) - \log(W_0)$ " points in Figs. 4-6. Let us remark that for unsaturated P Cygni profiles the relation between  $\log(W_n)$  and  $\log(W_0)$  is essentially linear (the corresponding  $W_n^0/W_1^0$  ratios for  $n = 0, 2$  and  $3$  are listed in Table 2). As the profiles get saturated, there results a crowding effect between all curves: in that region of the " $\log(W_n) - \log(W_0)$ "

diagrams, it is no longer possible to distinguish between the different models! As  $W_1^0 \rightarrow \infty$ , the different curves tend towards the asymptotic values " $\log(W_n^0) - \log(W_0^0)$ " which are only velocity field dependent (cf. Sect. 3.2).

We note in Figs. 4-6 that for opacity distributions of the type

$$\tau_{1,2}(X) \propto (1 - X)^p, \tag{20}$$

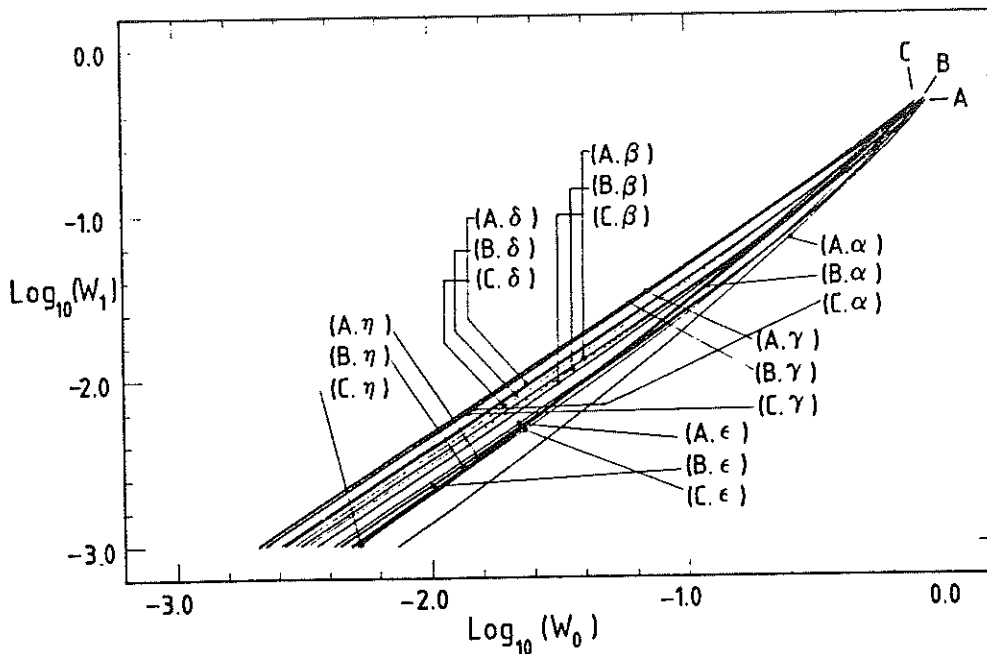


Fig. 4. " $\text{Log}_{10}(W_1) - \text{Log}_{10}(W_0)$ " curves for the eighteen possible models derived from Table 1

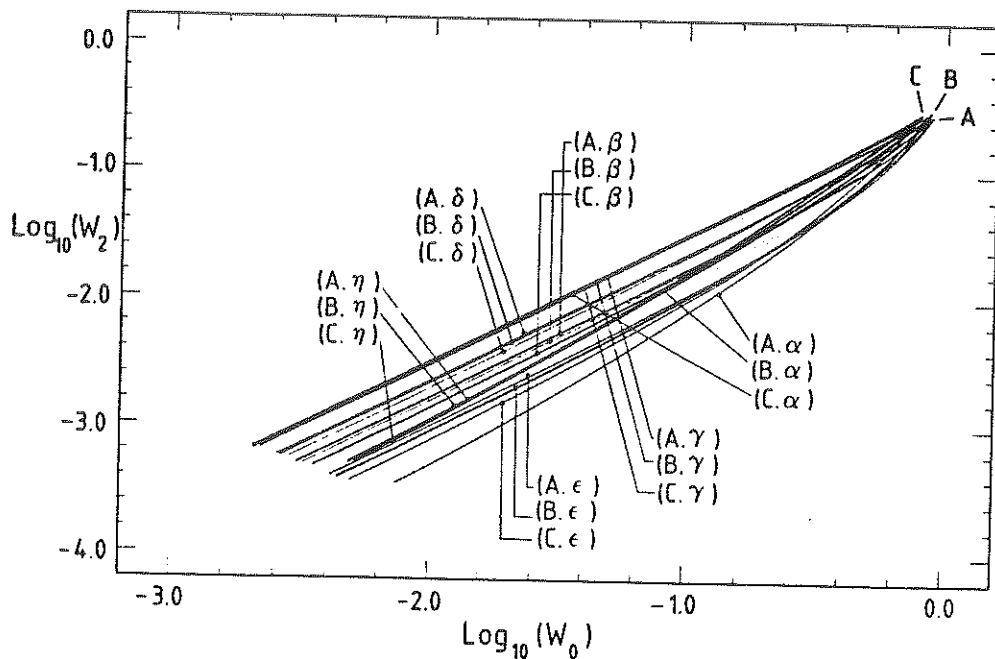


Fig. 5. "Log<sub>10</sub>(W<sub>2</sub>) - Log<sub>10</sub>(W<sub>0</sub>)" curves for the eighteen possible models derived from Table 1

there is an increasing shift between the nearly parallel "log(W<sub>n</sub>) - log(W<sub>0</sub>)" curves as the parameter  $y$  increases ( $y = 0, \frac{1}{2}, 1$  and 2 for the models labelled (\*,  $\gamma$ ), (\*,  $\delta$ ), (\*,  $\beta$ ) and (\*,  $\epsilon$ ), respectively, in Figs. 4-6).

Although it is unlikely that a single measured "log(W<sub>1</sub>) - log(W<sub>0</sub>)" point would suffice to derive both the unknown opacity and velocity distributions, we think that the simultaneous use of different "log(W<sub>n</sub>) - log(W<sub>0</sub>)" diagrams will enable one to derive these two important physical quantities characterizing an observed line profile.

6. Physical representation of the parameters  $W_n^0$  through the related quantities  $Q_n, R_n, S_n$  and  $T_n$

Adopting the following relation between  $Q_n$  and  $W_n^0$

$$Q_n = \frac{W_n^0 v_\alpha^{n+1}}{K q_{(\alpha)}^n}, \tag{21}$$

we find by means of Eq. (9) that

$$Q_n = M v^{n-1} \bar{n}^{(n)}(\text{level}) A(eI). \tag{22}$$

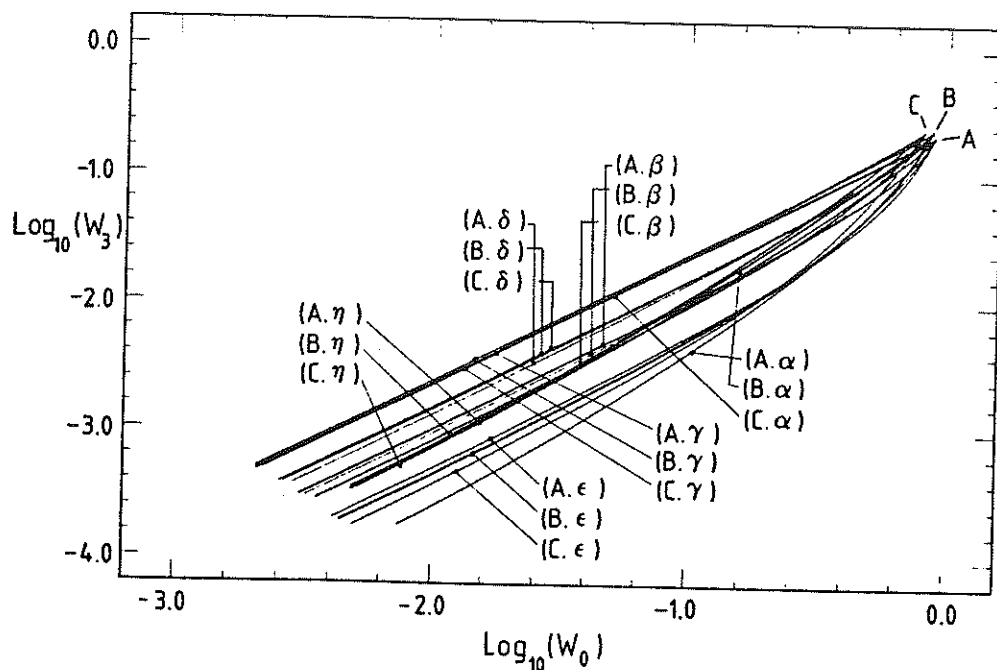


Fig. 6. "Log<sub>10</sub>(W<sub>3</sub>) - Log<sub>10</sub>(W<sub>0</sub>)" curves for the eighteen possible models derived from Table 1

Table 2. The ratios  $W_n^0/W_1^0$ ,  $\bar{n}^{(n)}(\text{level})/\bar{n}^{(1)}(\text{level})$  and the average quantity  $\bar{X}^{n-1}$  ( $n = 0, 2$  and  $3$ ) for the velocity laws (A)–(C) and the opacity distributions ( $\alpha$ )–( $\eta$ ) (see Table 1)

	$n$	(A)			(B)			(C)		
		$W_n^0/W_1^0$	$\bar{n}^{(n)}/\bar{n}^{(1)}$	$\bar{X}^{n-1}$	$W_n^0/W_1^0$	$\bar{n}^{(n)}/\bar{n}^{(1)}$	$\bar{X}^{n-1}$	$W_n^0/W_1^0$	$\bar{n}^{(n)}/\bar{n}^{(1)}$	$\bar{X}^{n-1}$
( $\alpha$ )	0	8.2720	1.0000	7.3845	5.2156	1.0000	4.6560	2.2196	1.0000	1.9815
	2	0.3505	1.0000	0.3828	0.5146	1.0000	0.5620	0.6554	1.0000	0.7158
	3	0.1792	1.0000	0.2104	0.3483	1.0000	0.4090	0.4917	1.0000	0.5773
( $\beta$ )	0	3.0787	0.9326	2.9470	3.2368	0.9823	2.9416	3.6072	1.0947	2.9416
	2	0.5010	1.0520	0.5201	0.4919	1.0063	0.5339	0.4752	0.9323	0.5567
	3	0.3019	1.0942	0.3240	0.2950	1.0069	0.3440	0.2816	0.8805	0.3755
( $\gamma$ )	0	2.0870	0.9116	2.0438	2.0847	0.9388	1.9824	2.2196	1.0000	1.9815
	2	0.6486	1.0726	0.6604	0.6635	1.0459	0.6929	0.6554	1.0000	0.7158
	3	0.4732	1.1348	0.4896	0.4985	1.0824	0.5408	0.4917	1.0000	0.5773
( $\delta$ )	0	2.5637	0.9216	2.4833	2.6525	0.9612	2.4635	2.8962	1.0496	2.4633
	2	0.5687	1.0626	0.5845	0.5661	1.0251	0.6031	0.5530	0.9631	0.6271
	3	0.3772	1.1150	0.3972	0.3780	1.0423	0.4258	0.3670	0.9339	0.4614
( $\epsilon$ )	0	4.1551	0.9549	3.8845	4.4391	1.0203	3.8840	5.1001	1.1722	3.8841
	2	0.4007	1.0310	0.4245	0.3874	0.9747	0.4341	0.3665	0.8853	0.4521
	3	0.2023	1.0537	0.2254	0.1923	0.9486	0.2380	0.1775	0.8022	0.2598
( $\eta$ )	0	5.1023	0.9547	4.7710	5.2156	1.0000	4.6560	5.7626	1.1053	4.6542
	2	0.5032	1.0372	0.5299	0.5146	1.0000	0.5620	0.5108	0.9406	0.5931
	3	0.3299	1.0691	0.3623	0.3483	1.0000	0.4090	0.3476	0.9013	0.4528

For the particular cases of  $n = 1, 2$  and  $3$ ,  $Q_n$  merely represents the mass-loss rate, an average impulsion rate and (twice) an average kinetic energy rate carried out by the relevant species in the envelope.

Let us point out that the dependence of the average fractional abundance  $\bar{n}^{(n)}(\text{level})$  versus the order  $n$  is only small. For the eighteen model calculations illustrated in Figs. 1–6 we have reported in Table 2 the ratios  $\bar{n}^{(n)}(\text{level})/\bar{n}^{(1)}(\text{level})$  for  $n = 0, 2$  and  $3$ . In no case does the relative error between  $\bar{n}^{(n)}(\text{level})$  and  $\bar{n}^{(1)}(\text{level})$  exceed 20%. We have also indicated in Table 2 the values of  $\bar{X}^{n-1}$  ( $n = 0, 2$  and  $3$ ) calculated for the eighteen models. As expected, the highest values of  $\bar{X}^{n-1}$  ( $n = 2, 3$ ) – and correspondingly, of  $Q_n$  – do occur for the steepest velocity field and the smoothest opacity distribution listed in Table 1 (i.e. model (C. $\alpha$ ) equivalent to (C. $\gamma$ )).

Another interpretation of the parameter  $W_n^0$  may also be obtained in a different way. Let us define the quantity  $R_n$  such as

$$R_n = \frac{W_n^0 v_\infty^{n+1} (n+1)}{\frac{\pi e^2}{mc} \int_{1,2} \lambda_{1,2}} \quad (23)$$

Combination of Eqs. (9)–(12) and (II.16)–(II.18) for the expression of the mass-loss rate  $\dot{M}$  leads to the interesting result

$$R_n = \int_{R^*}^{\infty} n_1(r) v(r)^n \left( 1 - \left( 1 - \left( \frac{R^*}{r} \right)^2 \right)^{(n+1)/2} \right) \times \left( 1 + \sqrt{1 - \left( \frac{R^*}{r} \right)^2} \right) \left( \frac{r}{R^*} \right)^2 dr, \quad (24)$$

with  $n_1$  being the volume density of the relevant ion in the lower atomic level. For  $n = 0, 1, 2$ , etc., the quantity  $R_n$  thus repre-

sents the column density, the column velocity, (twice) the column square velocity, etc., of the species under consideration. We have the obvious relation

$$Q_n/R_n = 4\pi \bar{\mu} M_{\text{amu}} R^* / (q_{(\infty)}^n (n+1)). \quad (25)$$

It is then natural to define the additional quantities

$$S_n = Q_n / (\bar{n}^{(n)}(\text{level}) A(eI)), \quad (26)$$

and

$$T_n = R_n \bar{\mu} M_{\text{amu}} / (\bar{n}^{(n)}(\text{level}) A(eI)), \quad (27)$$

such that for  $n = 1, 2, 3$ , etc.,  $S_n$  represents the mass-loss rate, an average impulsion rate, (twice) an average kinetic energy rate, etc., and  $T_n$  represents the column mass, the column impulsion, (twice) the column kinetic energy, etc., of all species that have been ejected by the star. We have also the relation

$$S_n/T_n = 4\pi R^* / (q_{(\infty)}^n (n+1)). \quad (28)$$

The estimate of  $\bar{n}^{(n)}(\text{level})$  remains the only true limitation to the precise determination of the quantities  $S_n$  and  $T_n$ .

Whereas the values of the moments  $W_n$  – and  $W_n^0$  – depend on the accurate determination of the maximum velocity  $v_\infty$  ( $W_n \propto v_\infty^{-(n+1)}$ ) on an observed line profile, it is interesting to note that none of the quantities  $Q_n$ ,  $R_n$ ,  $S_n$  or  $T_n$  are sensitive to this.

Let us finally recall that for saturated P Cygni line profiles, it is only possible to infer lower limits for the values of the physical quantities  $Q_n$ ,  $R_n$ ,  $S_n$  and  $T_n$ .

### 7. Slowly expanding atmospheres

For the case of optically thin lines ( $\tau'_{1,2}(X') < 1$ ), we have already established that the relation existing between the first order moment  $W_1$  and the quantity  $M\bar{n}^{(1)}$ (level) (cf. Eq. (9) and Sect. 6) holds irrespective of any Sobolev-type approximations used for the transfer of line radiation (Surdej, 1983b; Paper IV).

Considering such slowly expanding and optically thin atmospheres, we have investigated the possible generalization of the previous result to any order  $n = 0, 1, 2$ , etc. Our conclusions are summarized below.

For a star having finite dimensions, it can be shown (cf. Appendix A) that for even values of  $n$  ( $n = 0, 2, 4, \dots$ ) there is no simple relation between the  $n$ th order moment – denoted hereafter  $W_n^*$  – of a P Cygni line profile and the parameter  $W_n^0$  (see Eq. (9)). As expected, for  $n = 1$ , we have

$$W_1^* = \frac{W_1^0}{\left(1 + \frac{u(L_{\max})}{v_\infty}\right)^2}, \quad (29)$$

with  $u(L_{\max})$  being the maximum chaotic (thermal, turbulent, etc.) velocity of the ions at  $L_{\max}$ . For  $n = 3$ , we find that

$$W_3^* = \frac{W_3^0}{\left(1 + \frac{u(L_{\max})}{v_\infty}\right)^4} \left(1 + \left(\frac{\bar{u}(\bar{L})}{v_\infty}\right)^2 \frac{W_1^0}{W_3^0}\right), \quad (30)$$

where  $\bar{u}(\bar{L})$  represents a typical average thermal velocity in the wind.

Within the “point-like” star approximation, and assuming that the macroscopic velocity  $v(r)$  is everywhere greater than the local maximum chaotic velocity  $u(L)$  of the ions, we obtain for  $n = 0$  and  $n = 1$  the interesting results (cf. Appendix B)

$$W_0^{**} = \frac{W_0^0}{\left(1 + \frac{u(L_{\max})}{v_\infty}\right)}, \quad (31)$$

and

$$W_1^{**} = \frac{W_1^0}{\left(1 + \frac{u(L_{\max})}{v_\infty}\right)^2}, \quad (32)$$

where  $W_0^{*0}$  and  $W_1^{*0}$  are given by Eq. (13).

For  $n = 2$  and  $n = 3$ , we find that

$$W_2^{**} = \frac{W_2^0}{\left(1 + \frac{u(L_{\max})}{v_\infty}\right)^3} \left(1 + \frac{1}{3} \left(\frac{\bar{u}(\bar{L})}{v_\infty}\right)^2 \frac{W_0^0}{W_2^0}\right), \quad (33)$$

and

$$W_3^{**} = \frac{W_3^0}{\left(1 + \frac{u(L_{\max})}{v_\infty}\right)^4} \left(1 + \left(\frac{\bar{u}(\bar{L})}{v_\infty}\right)^2 \frac{W_1^0}{W_3^0}\right). \quad (34)$$

Since the ratios  $W_0^{*0}/W_2^{*0}$  and  $W_1^{*0}/W_3^{*0}$  are of the order  $(v_\infty/\bar{v})^2$ , Eqs. (33) and (34) reduce to those obtained in the context of rapidly expanding atmospheres whenever the typical average maximum chaotic velocity  $\bar{u}$  is negligible with respect to the average macroscopic velocity  $\bar{v}$ . Let us finally remark that the additional correcting factor  $1/(1 + u(L_{\max})/v_\infty)^{n+1}$  appearing in

Eqs. (29)–(34) just accounts for the fact that radiation contributing to the observed frequency  $\nu_{\max}$  (cf. Eq. (2)) is due to line photons emitted – or absorbed – radially at  $L_{\max}$  with a local frequency  $\nu_{1,2} + \Delta\nu(L_{\max})/2$ . Because in a rapidly expanding atmosphere, the width  $2u = (\Delta\nu/\nu_{1,2})c$  of the line transition is negligible when compared to the maximum velocity  $v_\infty$  (Sobolev approximation), the correcting factor is essentially equal to unity.

### 8. Discussion and conclusions

The main conclusions of the present work have already been summarized in the abstract. We shall not repeat them here. In the remainder, we just aim at discussing two different points: i) some remarks on the correct use of the average fractional abundance  $\bar{n}^{(n)}$ (level); ii) a comparison between the “line profile fitting” technique and the use of the moments  $W_n$  when analyzing P Cygni line profiles.

In view of the results obtained in Sect. 3, we wish to warn the reader against some possible misuse of the average fractional abundance  $\bar{n}^{(n)}$ (level) – also referred to in the literature as the mean ionization fraction  $\bar{q}_i$  – of an ion in the expanding atmosphere. Indeed, several authors make the implicit or explicit wrong assumption that the quantity  $\bar{X}'^{-1}\bar{n}$ (level) (see Eq. (13)) is equivalent to  $\bar{q}_i \int_0^1 1/(X'L^2) dL$ . From this, they infer an unjustified relation between the column density  $N_i$  of the relevant ion and the mass-loss rate  $\dot{M}$ , namely

$$\bar{q}_i \propto N_i/\dot{M}, \quad (35)$$

where the constant of proportionality only depends on the adopted velocity field  $v(r)$  (cf. Lamers et al., 1980; Garmany et al., 1981; Gathier et al., 1981). Using Eqs. (13) and (23), we rigorously find that

$$\bar{n}(\text{level}) \propto N_i/(\dot{M}\bar{X}'^{-1}), \quad (36)$$

where the average quantity  $\bar{X}'^{-1}$  is essentially dependent on the chosen opacity distribution. Considering for instance the model calculations performed in Sect. 4, a look at Table 2 clearly indicates that for a given velocity field, the quantity  $\bar{X}'^{-1}$  may vary by as much as  $\sim 260\%$ , thus invalidating relation (35).

Let us now compare the two major techniques used for the determination of the physical parameters characterizing a P Cygni line profile. In the first of these techniques, the types of velocity  $v(r)$  and opacity  $\tau'_{1,2}(X')$  distributions are obtained by matching observed profiles with theoretical ones, using for instance the atlas of Castor and Lamers (1979). When doing this, an additional parameter  $T$  (equivalent to  $W_0^0$ , see Eq. (9)) is scaled in order to achieve the best fitting. Alike this procedure, we have shown that it was possible to derive the same quantities by just locating the measured moments  $W_n$  of a P Cygni profile in “ $\log(W_n) - \log(W_n^0)$ ” and “ $\log(W_n) - \log(W_0)$ ” diagrams. In our case, the additional scaling factor that we have used is the parameter  $W_1^0$  (see Eq. (18)).

Whereas in the “line profile fitting” approach there is no direct way of testing the unicity of the solution (i.e. the unicity of  $\tau'_{1,2}(X')$ ,  $X'(L)$  and  $W_0^0$ ), we have seen that realistic error estimates of the derived parameters  $W_n^0$  could be assigned on the basis of “ $\log(W_n) - \log(W_n^0)$ ” diagrams. Furthermore, by locating the measured moments  $W_n$  in “ $\log(W_n) - \log(W_0)$ ” diagrams, it is possible to infer the most likely opacity distribution and – to a lesser extent – the velocity field which suit best the observations

Recalling that the theory of the moments  $W_n$  is particularly well suited to the analysis of underresolved line profiles (see Castor et al., 1981), there is no doubt that a realistic confrontation between the moments  $W_n$  of observed P Cygni profiles and the calculations presented here will shed more light on the correctness of all our assumptions.

For the sake of completeness, we rewrite hereafter in practical units the useful relations between the physical quantities  $Q_n$ ,  $R_n$  and the parameter  $W_n^0$  (see Eqs. (21) – (24)). Remembering that for  $n = 1, 2, 3$ , etc.,  $Q_n$  represents the mass-loss rate, an average impulsion rate and (twice) an average kinetic energy rate, etc., carried out by the relevant species, we have

$$Q_n (M_\odot \text{ yr}^{-1} (\text{km s}^{-1})^{n-1}) = 8.673 \cdot 10^{-22} v_\infty (\text{km s}^{-1})^{n+1} \frac{R^*(R_\odot) \bar{\mu} W_n^0}{f_{12} \lambda_{12} (10^3 \text{ \AA}) q_{(\infty)}^n}, \quad (37)$$

and

$$R_n (\text{cm}^{-2} (\text{km s}^{-1})^n) = 3.768 \cdot 10^{11} \frac{(n+1) v_\infty (\text{km s}^{-1})^{n+1} W_n^0}{f_{12} \lambda_{12} (10^3 \text{ \AA})} \quad (38)$$

such that for  $n = 0, 1$  and  $2$ ,  $R_n$  represents the column density, the column velocity and (twice) the column square velocity of the ion under consideration.

#### Appendix A

In order to establish the expression of the generalized moment  $W_n$  for the case of a slowly expanding and optically thin atmosphere around a stellar core having a radius  $R^*$ , let us follow the same reasoning as in Paper IV. Let us first replace Eqs. (IV.3) and (IV.5) by the more precise relation

$$v = v_L \left( 1 + \frac{v(L)}{c} \mu \right), \quad (A.1)$$

which is such that  $v_{\text{max}} = (v_{12} + \Delta v(L_{\text{max}})/2)(1 + v_\infty/c)$ . It naturally follows that Eqs. (IV.7), (IV.9), (IV.21) – (IV.25), (IV.36) and (IV.43) will undergo slight modifications due to the possible presence of the correcting factor  $1/(1 + u(L_{\text{max}})/v_\infty)$ . Replacing now  $W_1$  by  $W_n^{(2)}$  and the factor  $X$  by  $\text{sign}(X)|X|^n$  in Eqs. (IV.26), (IV.28), (IV.35) and (IV.42), we directly find that in the absence of limb darkening (i.e.  $\Psi(\mu^*) = 1$ )

$$W_n^s = 2R^* \int_0^1 \mu^* d\mu^* \int_1^{L_{\text{max}}} (W(L) - 1) \frac{n_1 \frac{\Pi e^2}{mc} f_{12}}{\mu(\mu^*, L)} I_n(L) dL, \quad (A.2)$$

with

$$I_n(L) = \int_{-\Delta v/2}^{\Delta v/2} \text{sign} \left( X_L - \frac{lc}{v_{12} v_\infty} \right) \left| X_L - \frac{lc}{v_{12} v_\infty} \right|^n \Phi_L(l) dl / \left( \left( 1 + \frac{u(L_{\text{max}})}{v_\infty} \right)^{n+1} v_{12} \frac{v_\infty}{c} \right). \quad (A.3)$$

The dimensionless frequency  $X_L$  is here defined by

$$X_L = -X' \mu, \quad (A.4)$$

<sup>2</sup> s referring to “slowly expanding and optically thin atmospheres”.

where  $\mu$  denotes the cosine of the angle between the line-of-sight and the radial direction.

Under the assumption that the redistribution function  $\Phi_L(l)$  is symmetric, we derive for  $n = 1$

$$I_1(L) = X_L / \left( \left( 1 + \frac{u(L_{\text{max}})}{v_\infty} \right)^2 v_{12} \frac{v_\infty}{c} \right). \quad (A.5)$$

With the help of Eqs. (II.16) – (II.18), we then straightforwardly find the result

$$W_1^s = K \dot{M} \bar{n}^{(1)}(\text{level}) q_{(\infty)}^{c_1} \frac{A(eI)}{v_\infty^2} \cdot \frac{1}{\left( 1 + \frac{u(L_{\text{max}})}{v_\infty} \right)^2}, \quad (A.6)$$

which for  $L_{\text{max}} \rightarrow \infty$  is equivalent to Eq. (29).

For  $n = 3$ , we similarly obtain

$$I_3(L) = \left( X_L^3 + X_L \left( \frac{\bar{u}(L)}{v_\infty} \right)^2 \right) / \left( \left( 1 + \frac{u(L_{\text{max}})}{v_\infty} \right)^4 v_{12} \frac{v_\infty}{c} \right), \quad (A.7)$$

where we have used the approximation

$$\bar{u}(L)^2 = 3 \int_{-\Delta v/2}^{\Delta v/2} l^2 \Phi_L(l) dl / (v_{12} v_\infty)^2. \quad (A.8)$$

Inserting (A.7) into (A.3), we find that

$$W_3^s = (K \dot{M} X'^2 \bar{n}^{(3)}(\text{level}) q_{(\infty)}^{c_3} \frac{A(eI)}{v_\infty^2} + W_1^0 \frac{\bar{u}(\bar{L})}{v_\infty}) / \left( 1 + \frac{u(L_{\text{max}})}{v_\infty} \right)^4, \quad (A.9)$$

which for  $L_{\text{max}} \rightarrow \infty$  is equivalent to Eq. (30).

For even values of  $n$  ( $n = 0, 2$ , etc.), Eq. (A.3) fails to reduce to any tractable result. This is because for some values of  $L$  and  $\mu$  (e.g.  $\mu = 0$ ), the quantity  $X_L - lc/(v_{12} v_\infty)$  may take positive values when  $l \in [-\Delta v/2, 0]$ . Since within the “point-like” star approximation we have  $\mu = 1$ , we do expect interesting results whenever  $v(L) > u(L)$  everywhere in the atmosphere (see Appendix B).

#### Appendix B

Within the “point-like” star approximation, let us evaluate the expression of the moments  $W_n^{*s}$  assuming that the optically thin atmosphere is slowly expanding. Using the results of Appendix A and imposing the condition  $R^* \rightarrow 0$ , it is straightforward to establish that Eqs. (A.2) and (A.3) transform into

$$W_n^{*s} = -R^* \int_1^{L_{\text{max}}} n_1 \frac{\Pi e^2}{mc} f_{12} I_n^*(L) dL, \quad (B.1)$$

and

$$I_n^*(L) = - \int_{-\Delta v/2}^{\Delta v/2} \left| \frac{lc}{v_{12} v_\infty} - X_L \right|^n \Phi_L(l) dl / \left( \left( 1 + \frac{u(L_{\text{max}})}{v_\infty} \right)^{n+1} v_{12} \frac{v_\infty}{c} \right), \quad (B.2)$$

respectively, provided that the condition  $v(L) > u(L)$  is fulfilled everywhere in the expanding envelope.

Particularizing first to the case  $n = 0$ , we find that

$$I_0^*(L) = -1 / \left( \left( 1 + \frac{u(L_{\text{max}})}{v_\infty} \right) v_{12} \frac{v_\infty}{c} \right), \quad (B.3)$$

and

$$W_0^{**} = -KM\overline{X}^{n-1}\overline{n}(\text{level})\frac{A(eI)}{v_\infty^2}\frac{1}{\left(1+\frac{u(L_{\max})}{v_\infty}\right)}. \quad (\text{B.4})$$

Letting  $L_{\max} \rightarrow \infty$ ; this latter result is equivalent to Eq. (31).

For  $n = 1$

$$I_1^*(L) = X_L \left/ \left( \left( 1 + \frac{u(L_{\max})}{v_\infty} \right)^2 v_{12} \frac{v_\infty}{c} \right), \quad (\text{B.5}) \right.$$

and from this, it is obvious to recover Eq. (32).

For  $n = 2$  and  $n = 3$ , we have successively

$$I_2^*(L) = -\left( X_L^2 + \frac{1}{3} \left( \frac{\overline{u}(L)}{v_\infty} \right)^2 \right) \left/ \left( \left( 1 + \frac{u(L_{\max})}{v_\infty} \right)^3 v_{12} \frac{v_\infty}{c} \right), \quad (\text{B.6}) \right.$$

and

$$I_3^*(L) = \left( X_L^3 + X_L \left( \frac{\overline{u}(L)}{v_\infty} \right)^2 \right) \left/ \left( \left( 1 + \frac{u(L_{\max})}{v_\infty} \right)^4 v_{12} \frac{v_\infty}{c} \right), \quad (\text{B.7}) \right.$$

where  $\overline{u}(L)^2$  has been defined in Eq. (A.8). Inserting Eqs. (B.6) and (B.7) into (B.1), it is straightforward to recover the results (33) and (34), when  $L \rightarrow \infty$ .

#### References

- Castor, J.I.: 1970, *Monthly Notices Roy. Astron. Soc.* **149**, 111  
 Castor, J.I., Lamers, H.J.G.L.M.: 1979, *Astrophys. J. Suppl.* **39**, 481  
 Castor, J.I., Lutz, J.H., Seaton, M.J.: 1981, *Monthly Notices Roy. Astron. Soc.* **194**, 547  
 Garmany, C.D., Olson, G.L., Conti, P.S., Van Steenberg, M.E.: 1981, *Astrophys. J.* **250**, 660  
 Gathier, R., Lamers, H.J.G.L.M., Snow, T.P.: 1981, *Astrophys. J.* **247**, 173  
 Lamers, H.J.G.L.M., Gathier, R., Snow, T.P.: 1980, *Astrophys. J. (Letters)* **242**, L33  
 Sobolev, V.V.: 1947, *Dnižuščiesja Oboločki Zvezd*, Leningrad (transl. *Moving Envelopes of Stars*; translated from Russian by S. Gaposchkin, Harvard University Press, Cambridge, Mass., 1960)  
 Sobolev, V.V.: 1957, *Astron. Zh.* **34**, 694 (trans. *Soviet Astron.* **1**, 678)  
 Sobolev, V.V.: 1958, in V.A. Ambartsumyan (ed.), *Theoretical Astrophysics*, Chapter 28, Pergamon Press Ltd., London  
 Surdej, J.: 1979, *Astron. Astrophys.* **73**, 1 (Paper I)  
 Surdej, J.: 1982, *Astrophys. Space Sci.* **88**, 31 (Paper II)  
 Surdej, J.: 1983a, *Astron. Astrophys.* **127**, 304 (Paper III)  
 Surdej, J.: 1983b, *Astrophys. Space Sci.* **90**, 299 (Paper IV)

## Article 8

### THE $N^{\text{TH}}$ ORDER MOMENT $W_N^{\text{D}}$ OF A RESONANCE DOUBLET P CYGNI LINE PROFILE

Surdej, J., Hutsemékers, D.: 1990, *Astron. Astrophys.*, sous presse.

Etant donné que la plupart des profils de raies de type P Cygni observés dans le spectre ultraviolet d'étoiles de type chaud, de noyaux de nébuleuses planétaires et dans le spectre visible de quasars BAL à grand redshift sont associés avec des doublets de résonance (cf. OVI, NV, SiIV, CIV, etc.), il était intéressant de développer la théorie des moments  $W_n^{\text{D}}$  pour le cas d'un doublet de résonance. Le présent article propose une telle étude ainsi que des diagrammes d'intérêt astrophysique en vue de déterminer le taux de perte de masse  $\dot{M}$  et les distributions  $v(r)$  et  $\tau_{12}^r(v)$  caractérisant les profils de raies observés à partir de la mesure de leurs moments  $W_n^{\text{D}}$  ( $n = 0-3$ ).





# The $n^{\text{th}}$ order moment $W_n^D$ of a resonance doublet P Cygni line profile

J. Surdej <sup>1</sup> and D. Hutsemékers <sup>2 3</sup>

Institut d'Astrophysique, Université de Liège  
Avenue de Cointe, 5, B-4200 Cointe-Ougrée, Belgium

Running title: The moment  $W_n^D$  of a resonance doublet P Cygni line profile

Proofs and offprint requests to be sent to:

J. Surdej  
Institut d'Astrophysique  
Université de Liège  
Avenue de Cointe, 5  
B-4200 Cointe-Ougrée  
Belgium

Thesaurus code numbers: 12.01.1, 12.03.1, 18.04.1, 19.48.1

Submitted to: Astronomy and Astrophysics (Main Journal)

Section: Stellar Atmospheres

---

<sup>1</sup>Chercheur qualifié au Fonds National de la Recherche Scientifique (Belgium)

<sup>2</sup>Aspirant au Fonds National de la Recherche Scientifique (Belgium)

<sup>3</sup>Present address: European Southern Observatory, La Silla, Casilla 19001, Santiago 19, Chile

## Summary

In the framework of the Sobolev approximation, we have developed in the present paper the theory of the  $n^{\text{th}}$  order moment  $W_n^D \propto \int (E(\lambda)/E_c - 1)(\lambda - \lambda_D)^n d\lambda$  of a P Cygni line profile  $E(\lambda)/E_c$  due to a resonance doublet line transition with an effective wavelength  $\lambda_D$ . We show that in the optically thick approximation, the asymptotic value  $W_n^{D,t}$  is entirely dependent on both the doublet separation  $\Delta$  and the type of the velocity field  $v(r)$  characterizing the expanding atmosphere. As expected, the most useful P Cygni profiles appear to be those which are unsaturated. From the observed moments  $W_n^D$  of such profiles, it is possible to derive the value of the parameters  $W_n^{D,0}$ , irrespective of the types of the velocity and opacity  $\tau_D^l(X')$  distributions and of the doublet separation  $\Delta$ . The parameters  $W_n^{D,0}$  ( $n = 1, 2$  and  $3$ ) are simply related to astrophysical quantities of general interest. For instance,  $W_1^{D,0}$  is directly proportional to  $\dot{M}\bar{n}^{(1)}(\text{level})$ , where  $\dot{M}$  is the mass-loss rate and  $\bar{n}^{(1)}(\text{level})$  the average fractional abundance of the relevant ion. Adopting eighteen possible combinations of realistic velocity and opacity distributions, we have carried out extensive numerical calculations of  $W_n^D$ . Although we intend to publish elsewhere the bulk of these data ( $\simeq 17280$  pairs of calculated moments), several diagrams of astrophysical interest are presented here. For instance, we explain how to use the very compact " $\log_{10}(W_n^D/W_n^{D,t}) - \log_{10}(W_n^{D,0}/W_n^{D,t})$ " diagrams in order to infer the value of  $W_n^{D,0}$  from the measurement of  $W_n^D$ . We also describe how to determine the types of the velocity and opacity distributions from the location of the observed moments  $W_n^D$  in theoretical " $\log_{10}(W_1^D) - \log_{10}(-W_0^D)$ " and " $\log_{10}(W_3) - \log_{10}(W_1^D)$ " diagrams. Finally, we discuss the limits and the possible applications of this theory to existing sets of observations.

**Key words:** radiative transfer – Sobolev approximation – mass-loss – P Cygni line profiles – moments  $W_n$

# 1 Introduction

A very convenient way to retrieve the physical information contained in an observed P Cygni line profile  $E(\lambda)/E_c$  due to a *single* resonance line transition  $1 \rightleftharpoons 2$  is to make use of its calculated moments  $W_n^s \propto \int (E(\lambda)/E_c - 1) |\lambda - \lambda_{12}|^n \text{sign}(\lambda - \lambda_{12}) d\lambda$  (see Surdej, 1985 and references therein). As a first application, we have suggested to represent in theoretical "log<sub>10</sub>( $W_n^s$ ) - log<sub>10</sub>( $W_{n'}^s$ )" diagrams ( $n \neq n'$ ) the measured values of the moments  $W_n^s$  ( $n = 0, 1, 2$  and  $3$ ) in order to infer the types of opacity ( $\tau_{12}^r(v)$ ) and velocity ( $v(r)$ ) distributions characterizing the rapidly expanding atmosphere in which the observed line profile is formed. We have also shown that the moments  $W_0^s$ ,  $W_1^s$ ,  $W_2^s$  and  $W_3^s$ , measured for an unsaturated P Cygni line profile, are directly related to the column density  $N_1$ , to the fractional mass-loss rate  $\dot{M} \bar{n}^{(1)}$  (level) -  $\bar{n}^{(1)}$  (level) representing the average fractional abundance of the considered ion - , to the column momentum and to (twice) the column kinetic energy, respectively, of the relevant species in the flow. The relation between  $W_1^s$  and  $\dot{M} \bar{n}^{(1)}$  (level) has been generalized to the cases of *resonance doublet* (Surdej, 1982) and *subordinate* (Hutsemékers and Surdej, 1987) line transitions. However, the other relations ( $n = 0, 2, 3$ , etc.) as well as the use of the "log<sub>10</sub>( $W_n^s$ ) - log<sub>10</sub>( $W_{n'}^s$ )" diagrams are not directly applicable to the analysis of resonance doublet profiles. There are at least two reasons for this: (i) the expression of the line profile function  $E(\lambda)/E_c$  characterizing a doublet line transition appears to be more complex than the one describing a single line transition, (ii) if  $\lambda_D$  denotes the central wavelength of a resonance doublet, the above expression of the moment has to be replaced by  $W_n^D \propto \int (E(\lambda)/E_c - 1) (\lambda - \lambda_D)^n d\lambda$  such that physically tractable relations may still be established in the optically thin approximation.

Because most of P Cygni profiles observed in the UV spectra of early-type stars, planetary nebula nuclei as well as in the optical spectra of high redshift BAL quasars are due to resonance doublet line transitions, there is an obvious interest to develop the theory of the  $n^{\text{th}}$  order moment  $W_n^D$ . The present paper constitutes a first step

in that direction.

In Section 2, we first establish the expression of  $W_n^D$  assuming that there is no radiative coupling between the two single resonance line transitions of the doublet. The complex radiative interactions between line photons emitted in the transitions  $1 \rightleftharpoons 2$  and  $1 \rightleftharpoons 3$  and atoms located throughout the expanding atmosphere are subsequently taken into account when deriving the general expression of  $W_n^D$  in Section 3. Asymptotic values of  $W_n^D$  in the optically thin and optically thick approximations are also derived there. Section 4 deals with numerical applications and a few diagrams of astrophysical interest are presented and described in Section 5. The physical representation of selected parameters derived from the observed moments of resonance doublet P Cygni profiles is given in Section 6 and general conclusions form the last Section.

## 2 Approximation of a resonance doublet by two independent line transitions

Adopting the following expression for the  $n^{\text{th}}$  order moment  $W_n^D$  of a resonance doublet P Cygni line profile (the subscript “D” standing for “doublet”)

$$W_n^D = \left( \frac{c}{\lambda_D v_\infty} \right)^{n+1} \int \left( \frac{E(\lambda)}{E_c} - 1 \right) (\lambda - \lambda_D)^n d\lambda, \quad (1)$$

where the effective wavelength of the doublet is

$$\lambda_D = (1 - \varepsilon) \lambda_{12} + \varepsilon \lambda_{13}, \quad (2)$$

with

$$\varepsilon = f_{13} / (f_{12} + f_{13}), \quad (3)$$

$\lambda_{12}$ ,  $f_{12}$  (resp.  $\lambda_{13}$ ,  $f_{13}$ ) denoting the central wavelength and oscillator strength of the line transition  $1 \rightleftharpoons 2$  (resp.  $1 \rightleftharpoons 3$ ) and  $v_\infty$  the maximal radial velocity  $v(r)$  of the flow, and making use of the dimensionless frequency

$$X_D = \left( \frac{\lambda - \lambda_D}{\lambda_D} \right) \frac{c}{v_\infty}, \quad (4)$$

it is straightforward to reduce Equation (1) to

$$W_n^D = \int_{-1-(1-\epsilon)\Delta}^{1+\epsilon\Delta} \left( \frac{E(X_D)}{E_c} - 1 \right) X_D^n dX_D. \quad (5)$$

It is also very convenient to define (cf. Eq.(4) and Fig.1) the dimensionless frequencies  $X$  and  $Y$  associated with  $\lambda_{12}$  and  $\lambda_{13}$ , such that

$$X = X_D - \epsilon\Delta \quad (6)$$

and

$$Y = X_D + (1 - \epsilon)\Delta, \quad (7)$$

with

$$\Delta = \Delta v_{23}/v_\infty, \quad (8)$$

$\Delta v_{23}$  being the Doppler velocity separation between the two line transitions of the resonance doublet (cf. Surdej, 1980, hereafter referred to as Paper I; see also Lamers et al., 1987). If one may assume that the composite line profile  $E(X_D)/E_c$  results from the mere superposition of the two line profile functions  $E_{12}(X)/E_c$  and  $E_{13}(Y)/E_c$ , each being independently formed from one another, we obtain the interesting relation

$$W_n^D = \int_{-1}^{+1} \left( \frac{E_{12}(X)}{E_c} - 1 \right) (X + \epsilon\Delta)^n dX + \int_{-1}^{+1} \left( \frac{E_{13}(Y)}{E_c} - 1 \right) (Y - (1 - \epsilon)\Delta)^n dY. \quad (9)$$

This result is rigorously exact in only two cases: (i) when the expanding atmosphere is optically thin to the spectral line radiation, and (ii) for values of the doublet separation  $\Delta \geq 2$ .

Defining the moments  $W_n^{12}$  and  $W_n^{13}$  (the subscripts "12" and "13" referring to the single line transitions  $1 \rightleftharpoons 2$  and  $1 \rightleftharpoons 3$ , respectively) by means of Eq.(5), where we have replaced  $X_D$  by  $X$  and  $Y$ , respectively, we can express Eq.(9) as follows:

$$W_0^D = W_0^{12} + W_0^{13},$$

$$\begin{aligned}
W_1^D &= W_1^{12} + W_1^{13} + \varepsilon \Delta W_0^{12} - (1 - \varepsilon) \Delta W_0^{13}, \\
W_2^D &= W_2^{12} + W_2^{13} + 2\varepsilon \Delta W_1^{12} - 2(1 - \varepsilon) \Delta W_1^{13} \\
&\quad + \varepsilon^2 \Delta^2 W_0^{12} + (1 - \varepsilon)^2 \Delta^2 W_0^{13}, \\
W_3^D &= W_3^{12} + W_3^{13} + 3\varepsilon \Delta W_2^{12} - 3(1 - \varepsilon) \Delta W_2^{13} + 3\varepsilon^2 \Delta^2 W_1^{12} \\
&\quad + 3(1 - \varepsilon)^2 \Delta^2 W_1^{13} + \varepsilon^3 \Delta^3 W_0^{12} - (1 - \varepsilon)^3 \Delta^3 W_0^{13},
\end{aligned} \tag{10}$$

i.e. the moments  $W_n^D$  ( $n = 0, 1, 2$  and  $3$ ) appear as straightforward linear combinations of the moments  $W_{n'}^{12}$  and  $W_{n'}^{13}$  ( $n' \leq n$ ) of each of the single line transitions forming the resonance doublet. It is interesting to consider now the two usual asymptotic regimes: the optically thin and optically thick approximations.

## 2.1 The optically thin approximation

For the case of optically thin lines, it is easy to show (see Appendix A ) that the moment  $W_n^{ij}$ , associated with a single resonance transition  $i \rightleftharpoons j$ , is directly proportional to the oscillator strength  $f_{ij}$ . We can therefore write the equality

$$\varepsilon W_n^{12} = (1 - \varepsilon) W_n^{13}, \tag{11}$$

such that relation (10) reduces now to (the subscript "0" referring to the optically thin case) :

$$\begin{aligned}
W_0^{D,0} &= (W_0^{12} + W_0^{13}), \\
W_1^{D,0} &= (W_1^{12} + W_1^{13}), \\
W_2^{D,0} &= (W_2^{12} + W_2^{13}) + \Delta^2 \varepsilon (1 - \varepsilon) (W_0^{12} + W_0^{13}), \\
W_3^{D,0} &= (W_3^{12} + W_3^{13}) + 3\Delta^2 \varepsilon (1 - \varepsilon) (W_1^{12} + W_1^{13}) \\
&\quad + \Delta^3 \varepsilon (1 - \varepsilon) (2\varepsilon - 1) (W_0^{12} + W_0^{13}).
\end{aligned} \tag{12}$$

Replacing the values of the moment  $W_n^{12} + W_n^{13}$  in Eq.(12) by those given for an optically thin, single resonance line having an equivalent oscillator strength  $f_D =$

$f_{12} + f_{13}$  and a central wavelength  $\lambda_D$  (see Surdej, 1982, hereafter referred to as Paper II), it will be easy and useful in Section 3.3 to compare the above results with those derived from the rigorous expression of  $W_n^D$ .

## 2.2 The optically thick approximation

Eq.(10) can also be conveniently used to calculate asymptotic values of  $W_n^D$  when the atmosphere gets optically thick and  $\Delta \rightarrow 2$ . Assuming that  $\tau_{12} \gg 1$ ,  $\tau_{13} \gg 1$  (see Paper II), we have

$$W_n^{12} = W_n^{13} = W_n^{thick} = W_n^t, \quad (13)$$

such that Eq.(10) now transforms into (the subscript "t" referring to the optically thick case)

$$\begin{aligned} W_0^{D,t} &= 2W_0^t, \\ W_1^{D,t} &= 2W_1^t + (2\varepsilon - 1)\Delta W_0^t, \\ W_2^{D,t} &= 2W_2^t + 2(2\varepsilon - 1)\Delta W_1^t + \Delta^2(2\varepsilon^2 - 2\varepsilon + 1)W_0^t, \\ W_3^{D,t} &= 2W_3^t + 3(2\varepsilon - 1)\Delta W_2^t + 3\Delta^2(2\varepsilon^2 - 2\varepsilon + 1)W_1^t \\ &\quad + (\varepsilon^3 - (1 - \varepsilon)^3)\Delta^3 W_0^t, \end{aligned} \quad (14)$$

i.e the moments  $W_n^{D,t}$  ( $n = 0, 1, 2$  and  $3$ ) are simple linear combinations of the moments  $W_{n'}^t$  ( $n' \leq n$ ) of an optically thick, single line transition which central wavelength and oscillator strength are not necessarily specified. Replacing in Eq.(14) the values of  $W_n^t$  by those calculated for the case of a single resonance line profile that is formed in an optically thick atmosphere (see Paper II), one easily derives the asymptotic values of  $W_n^D$ . Since the former ones essentially depend on the velocity distribution characterizing the outflow, we have reported in Table 2 values of  $W_n^t$  and  $W_n^{D,t}$  for the three velocity fields listed in Table 1. We have also adopted  $X_{min} = -0.01$ ,  $\varepsilon = 2/3$  and  $\Delta = 1.8$ . These results will be compared in Section 3.4 with self-consistent calculations of  $W_n^D$ .

### 3 The general case

Considering a three-level atom model, the transfer of spectral line radiation in a rapidly expanding envelope is complicated by the fact that photons emitted at a point R in the transition  $3 \rightarrow 1$  may interact with atoms at distant points R', via the line transition  $1 \rightleftharpoons 2$ . We refer the reader to Paper I for a comprehensive study of these distant interactions between atoms and line photons. In the framework of the Sobolev approximation, we establish hereafter the general expression of the resonance doublet profile formed in an atmosphere that is rapidly expanding around a central stellar core having a finite radius  $R_*$ .

#### 3.1 Expression of the resonance doublet profile $E(X_D)/E_c$

The general expression  $E(X_D)/E_c$  of a resonance doublet P Cygni profile formed in a spherically symmetric atmosphere may be written as (see Eq.(II.42) for the restricted case of a point-like star)

$$\frac{E(X_D)}{E_c} = \frac{E_{12}(X = X_D - \varepsilon\Delta)}{E_c} + \frac{E_{13}(Y = X_D + (1 - \varepsilon)\Delta)}{E_c} + \frac{E_{abs}(X_D)}{E_c}, \quad (15)$$

where the different contributions refer to the scattered line photons in the resonance transitions  $1 \rightleftharpoons 2$  and  $1 \rightleftharpoons 3$ , as well as to the stellar photons which did not suffer any scattering. In the absence of limb darkening and assuming that the central core radiates with an intensity  $I_c$  that is constant over the frequency range  $X_D \in [-1 - (1 - \varepsilon)\Delta, 1 + \varepsilon\Delta]$  (see Fig.1), one can easily derive, with the help of Eqs.(II.56), (II.67), and (II.69), the following expressions:

$$\begin{aligned} & \int_{\max(|X|, -X_{\min})}^1 P_{12}^N(X') P_{12}(X', X) \frac{dX'}{2X'}, \quad \text{if } X \in [-1, 0], \\ \frac{E_{12}(X)}{E_c} = & \int_{\max(|X^N|, -X_{\min})}^1 P_{12}^N(X') P_{12}(X', X) \frac{dX'}{2X'}, \quad \text{if } X \in ]0, X^0], \quad (16) \\ & 1, \quad \text{if } X \in ]X^0, 1], \end{aligned}$$



with

$$X_{min} = -v_0/v_\infty, \quad (17)$$

$v_0$  being the radial velocity at the stellar surface and where the frequency  $X^N$  fulfills the condition

$$X^N = -X/(1 - 2W(L(X^N))). \quad (18)$$

$W(L(X^N))$  stands for the geometrical dilution factor

$$W(L) = \frac{1}{2}(1 - \sqrt{1 - (1/L)^2}), \quad (19)$$

evaluated at the radial distance  $r(X^N) = L(X^N)R_*$ , where the reduced radial velocity

$$X' = v(\tau)/v_\infty \quad (20)$$

is equal to  $-X^N$ .

The frequency

$$X^0 = 1 - 2W(L_{max}) \quad (21)$$

is such that for  $X > X^0$ , there is total occultation of the rear part of the expanding envelope contributing to the line profile at the frequency  $X$ .  $L_{max}$  denotes the size of the atmosphere in stellar radii  $R_*$  units. Reminding results (I.24)-(I.26), (II.58) and (II.64), we easily obtain the expression of the integrands in Eq.(16):

$$P_{12}^N(X') = (\beta_{12}^5(X') + J_{12}^2(X')/I_c) \tau_{12}^r(X') 4L^2(X') \quad (22)$$

and

$$P_{12}(X', X) = \frac{(1 - \exp(-\tau_{12}(X', X)))}{\tau_{12}(X', X) \beta_{12}^1(X')}, \quad (23)$$

where  $\tau_{12}(X', X)$  (resp.  $\tau_{12}^r(X')$ ) represents the fictitious opacity in the transition  $1 \Rightarrow 2$  evaluated at the distance  $L(X')$  along directions making a cosine angle

$$\mu = -X/X', \quad (24)$$

(resp.  $\mu = 1$ ) with the radial direction.  $\beta_{12}^1(X')$  denotes the usual escape probability of a line photon (cf. Eq.(I.10)). We also have

$$\beta_{12}^5(X') = \int_{\Omega=4\pi W} \frac{1 - \exp(-\tau_{12}(X', \omega))}{\tau_{12}(X', \omega)} \exp(-\tau_{13}(X'', \omega'')) \frac{d\omega}{4\pi} \quad (25)$$

and

$$\frac{J_{12}^2(X')}{I_c} = \int_{\Omega(R, R'')} \frac{\beta_{13}^3(X'')}{\beta_{13}^1(X'')} (1 - \exp(-\tau_{13}(X'', \omega''))) \cdot \frac{(1 - \exp(-\tau_{12}(X', \omega)))}{\tau_{12}(X', \omega)} \frac{d\omega}{4\pi}, \quad (26)$$

such that  $I_c \beta_{12}^5$  and  $J_{12}^2$  account for the mean intensity of the radiation field in the transition  $1 \rightleftharpoons 2$  due to the diluted stellar continuum and to line photons emitted in the transition  $1 \rightleftharpoons 3$  by distant atoms located at points  $R''(L(X''))$  along directions  $\omega''$  (cf. Paper I). In a very similar way, we find that

$$\begin{aligned} & \int_{\max(|Y|, -X_{\min})}^1 P_{13}^N(X') P_{13}(X', Y) \exp(-\tau'_{12}) \frac{dX'}{2X'}, \quad \text{if } Y \in [-1, 0], \\ \frac{E_{13}(Y)}{E_c} = & \int_{\max(|Y^N|, -X_{\min})}^1 P_{13}^N(X') P_{13}(X', Y) \exp(-\tau'_{12}) \frac{dX'}{2X'}, \quad \text{if } Y \in ]0, X^0], \quad (27) \\ & 1, \quad \text{if } Y \in ]X^0, 1], \end{aligned}$$

where the factor  $\exp(-\tau'_{12})$  expresses the probability for a photon emitted in the line transition  $1 \rightleftharpoons 3$  to escape the expanding atmosphere without being scattered in the line transition  $1 \rightleftharpoons 2$  by atoms located at large distances from the point of emission. All quantities appearing in Eq.(27) can be defined by analogy with those in Eq.(16), with the exception of (cf. Eq.(II.64))

$$P_{13}^N(X') = \beta_{13}^3(X') \tau_{13}^r(X') 4L^2(X'), \quad (28)$$

where

$$\beta_{13}^3(X') = \int_{\Omega=4\pi W} \frac{(1 - \exp(-\tau_{13}(X', \omega)))}{\tau_{13}(X', \omega)} \frac{d\omega}{4\pi}. \quad (29)$$

Note here that if the central continuum source were point-like (i.e.  $L_{max} \gg 1$ ), the contribution  $P_{13}^N(X')$  would reduce to  $P_{13}(X') = (1 - \exp(-\tau_{13}^r(X')))$ . We remind that  $P_{13}(X')$  represents the probability for a stellar photon emitted with an initial frequency  $X'$  to be scattered at a distance  $L(X')$  and that  $P_{13}(X', Y)$  corresponds to the probability that this photon will finally escape the expanding atmosphere along a direction making a cosine angle  $\mu = -Y/X'$  with the radial direction. As far as the fraction  $E_{abs}(X_D)/E_c$  of unscattered stellar photons is concerned, its contribution to the resonance doublet P Cygni line profile in the frequency interval  $X_D \in [-1 - (1 - \varepsilon)\Delta, \varepsilon\Delta]$  is easily derived to be

$$\frac{E_{abs}(X_D)}{E_c} = 2 \int_0^1 \exp(-\tau_{12}(X', \mu_{12})) \exp(-\tau_{13}(Y', \mu_{13})) \mu_* d\mu_*, \quad (30)$$

where

$$X' = (\varepsilon\Delta - X_D)/\mu_{12}, \quad (31)$$

with  $\mu_{12} = \sqrt{1 - (1 - \mu_*^2)/L^2(X')}$ , if  $X_D \in [-1 + \varepsilon\Delta, \varepsilon\Delta]$ , and similarly

$$Y' = -(X_D + (1 - \varepsilon)\Delta)/\mu_{13}, \quad (32)$$

with  $\mu_{13} = \sqrt{1 - (1 - \mu_*^2)/L^2(Y')}$ , if  $X_D \in [-1 - (1 - \varepsilon)\Delta, -(1 - \varepsilon)\Delta]$ ,  $\tau_{12}$  (resp.  $\tau_{13}$ ) being set equal to zero in Eq.(30) if no solution  $(X', \mu_{12})$  (resp.  $(Y', \mu_{13})$ ) is found.

We can now make use of all previous results (Eqs.(15)-(32)) to derive the explicit form of Eq.(5).

### 3.2 Expression of the moment $W_n^D$

Inserting relations (15),(16),(27) and (30) in Eq.(5) and following a procedure similar to that described in Appendix B for the particular contribution of  $E_{12}(X)/E_c$ , we obtain the general result

$$W_n^D = \int_{-X_{min}}^1 \frac{\tau_{12}^r(X') (\beta_{12}^5(X') + J_{12}^2(X')/I_c) 4 L^2(X')}{\beta_{12}^1(X')} dX'$$

$$\begin{aligned}
& \cdot \frac{1}{2} \int_{-(1-2W(L(X')))}^1 (-X'\mu + \varepsilon\Delta)^n \frac{(1 - \exp(-\tau_{12}(X', \mu)))}{\tau_{12}(X', \mu)} d\mu dX' \\
+ & \int_{-X_{\min}}^1 \frac{\tau_{13}^r(X') \beta_{13}^3(X') 4L^2(X')}{\beta_{13}^1(X')} \frac{1}{2} \int_{-(1-2W(L(X')))}^1 (-X'\mu - (1-\varepsilon)\Delta)^n \\
& \cdot \frac{(1 - \exp(-\tau_{13}(X', \mu)))}{\tau_{13}(X', \mu)} \exp(-\tau'_{12}) d\mu dX' \\
+ & 2 \int_0^1 \mu_* d\mu_* \int_{-\sqrt{1-(1-\mu_*^2)/L_{\max}^2}}^{X_{\min} \mu_* + \varepsilon\Delta} X_D^n \\
& \cdot (\exp(-\tau_{12}(X', \mu_{12})) \exp(-\tau_{13}(Y', \mu_{13})) - 1) dX_D. \tag{33}
\end{aligned}$$

For values of  $L_{\max} \gg 1$ , the "point-like" star approximation is essentially a good one and it provides a very useful model to understand more easily the asymptotic behaviour of more general solutions given by Eq.(33). We merely state the result when  $R_* \rightarrow 0$  (the subscript "\*" stands here for the "point-like" star approximation)

$$\begin{aligned}
W_n^{D*} &= \int_{-X_{\min}}^1 \frac{(1 - \exp(-\tau_{12}^r(X'))) \exp(-\tau'_{13}) + \tau_{12}^r(X') (J_{12}^2(X')/I_c) 4L^2(X')}{\beta_{12}^1(X')} \\
& \cdot \frac{1}{2} \int_{-1}^{+1} (-X'\mu + \varepsilon\Delta)^n \frac{(1 - \exp(-\tau_{12}(X', \mu)))}{\tau_{12}(X', \mu)} d\mu dX' \\
+ & \int_{-X_{\min}}^1 \frac{(1 - \exp(-\tau_{13}^r(X'))) \beta_{13}^3(X') 4L^2(X')}{\beta_{13}^1(X')} \frac{1}{2} \int_{-1}^1 (-X'\mu - (1-\varepsilon)\Delta)^n \\
& \cdot \frac{(1 - \exp(-\tau_{13}(X', \mu)))}{\tau_{13}(X', \mu)} \exp(-\tau'_{12}) d\mu dX' \\
+ & \int_{-1-(1-\varepsilon)\Delta}^{X_{\min} + \varepsilon\Delta} X_D^n (\exp(-\tau_{12}^r(X')) \exp(-\tau'_{13}(Y')) - 1) dX_D. \tag{34}
\end{aligned}$$

### 3.3 The optically thin case

#### 3.3.1 Central core with finite dimensions

For unsaturated ( $\tau_{12} < 1, \tau_{13} < 1$ ) resonance doublet P Cygni profiles, Eq.(33) is easily transformed into (see Appendix C)

$$W_n^{D,0} = \int_{-X_{\min}}^1 \tau_{12}^r(X') W(L(X')) 4L^2(X')$$

$$\begin{aligned}
& \cdot \frac{1}{2} \int_{-(1-2W(L(X')))}^1 (-X'\mu + \varepsilon\Delta)^n d\mu dX' \\
+ & \int_{-X_{min}}^1 \tau_{13}^r(X') W(L(X')) 4L^2(X') \\
& \cdot \frac{1}{2} \int_{-(1-2W(L(X')))}^1 (-X'\mu - (1-\varepsilon)\Delta)^n d\mu dX' \quad (35) \\
- & \int_{-X_{min}}^1 \tau_{12}^r(X') 4L^2(X') \frac{1}{2} \int_{1-2W(L(X'))}^1 (-X'\mu + \varepsilon\Delta)^n d\mu dX' \\
- & \int_{-X_{min}}^1 \tau_{13}^r(X') 4L^2(X') \frac{1}{2} \int_{1-2W(L(X'))}^1 (-X'\mu - (1-\varepsilon)\Delta)^n d\mu dX'.
\end{aligned}$$

Considering the particular values of  $n = 0, 1, 2$  and  $3$ , Eq.(35) leads to the results

$$\begin{aligned}
W_0^{D,0} &= \int_{-X_{min}}^1 (\tau_{12}^r(X') + \tau_{13}^r(X')) (1 - 4L^2W) dX', \\
W_1^{D,0} &= \int_{-X_{min}}^1 X' (\tau_{12}^r(X') + \tau_{13}^r(X')) (1 - W) dX', \\
W_2^{D,0} &= \int_{-X_{min}}^1 X'^2 (\tau_{12}^r(X') + \tau_{13}^r(X')) \\
& \quad \cdot \frac{2}{3} (W(1 + (1-2W)^3) - 1 + (1-2W)^3) L^2 dX' \quad (36) \\
& + \varepsilon(1-\varepsilon)\Delta^2 \int_{-X_{min}}^1 (\tau_{12}^r(X') + \tau_{13}^r(X')) (1 - 4L^2W) dX', \\
W_3^{D,0} &= \int_{-X_{min}}^1 X'^3 (\tau_{12}^r(X') + \tau_{13}^r(X')) (1 - \frac{1}{2L^2})(1 - W) dX' \\
& + 3\varepsilon(1-\varepsilon)\Delta^2 \int_{-X_{min}}^1 X' (\tau_{12}^r(X') + \tau_{13}^r(X')) (1 - W) dX' \\
& + \varepsilon(2\varepsilon - 1)(1-\varepsilon)\Delta^3 \int_{-X_{min}}^1 (\tau_{12}^r(X') + \tau_{13}^r(X')) (1 - 4L^2W) dX'.
\end{aligned}$$

Referring to the asymptotic expressions established in Appendix A for the moment  $W_n^{ij}$  ( $n = 0, 1, 2$  and  $3$ ) of a single resonance line transition  $i \rightleftharpoons j$ , we conclude that result (36) is essentially equivalent to that given in Eq.(10) provided that all  $W_n^{ij}$  have been replaced by their corresponding expression from Eq.(A.1). This agreement partly testifies about the self-consistency of the results derived in this chapter.

### 3.3.2 The point-like stellar core

Following a similar reasoning as that in Appendix C, expression (34) of the moment  $W_n^{D*}$ , established for the case of a point-like star, simplifies in the optically thin approximation to

$$\begin{aligned}
 W_n^{D*,0} &= \int_{-X_{\min}}^1 \tau_{12}^r(X') \frac{1}{2} \int_{-1}^{+1} (-X'\mu + \varepsilon\Delta)^n d\mu dX' \\
 &+ \int_{-X_{\min}}^1 \tau_{13}^r(X') \frac{1}{2} \int_{-1}^{+1} (-X'\mu - (1-\varepsilon)\Delta)^n d\mu dX' \\
 &+ (-1)^{n+1} \left[ \int_{-X_{\min}}^1 \tau_{12}^r(X') (X' - \varepsilon\Delta)^n dX' \right. \\
 &\quad \left. + \int_{-X_{\min}}^1 \tau_{13}^r(X') (X' + (1-\varepsilon)\Delta)^n dX' \right]. \quad (37)
 \end{aligned}$$

For the particular values of  $n = 0, 1, 2$  and  $3$ , we obtain

$$\begin{aligned}
 W_0^{D*,0} &= 0, \\
 W_1^{D*,0} &= \int_{-X_{\min}}^1 X' (\tau_{12}^r(X') + \tau_{13}^r(X')) dX', \\
 W_2^{D*,0} &= -\frac{2}{3} \int_{-X_{\min}}^1 X'^2 (\tau_{12}^r(X') + \tau_{13}^r(X')) dX', \quad (38) \\
 W_3^{D*,0} &= \int_{-X_{\min}}^1 X'^3 (\tau_{12}^r(X') + \tau_{13}^r(X')) dX' \\
 &\quad + 3\varepsilon(1-\varepsilon)\Delta^2 \int_{-X_{\min}}^1 X' (\tau_{12}^r(X') + \tau_{13}^r(X')) dX'.
 \end{aligned}$$

### 3.4 The optically thick case

If the expanding medium is optically thick to the spectral line radiation in the transitions  $i \rightleftharpoons j$  ( $i=1, j=2$  and  $3$ ), we can make in Eq.(33) the approximation  $\exp(-\tau_{ij}) = 0$ , provided of course that the corresponding direction of light propagation crosses a surface of possible interaction. Furthermore, expressing in Eq.(33) the fictitious opacity  $\tau_{ij}(X', \mu)$  in terms of its radial component, i.e. in a spherical envelope

$$\tau_{ij}(X', \mu) = \tau_{ij}^r(X') / \left[ \mu^2 \left( 1 - \frac{d \ln L}{d \ln X'} \right) + \frac{d \ln L}{d \ln X'} \right], \quad (39)$$

we directly see that the optically thick expression of  $W_n^D$  does not depend anymore on the form of the opacity distribution  $\tau_{ij}^r(X')$  but that it essentially relies on the type of velocity field  $v(r)$  characterizing the expanding atmosphere. Although it is not possible to reduce Eq.(33) to a simple analytic expression when  $\tau_{ij} \gg 1$ , we can establish such expressions for  $\beta_{12}^1(X')$ ,  $\beta_{13}^1(X')$ ,  $\beta_{13}^3(X')$ , etc. and therefore suppress one level of integration in Eq.(33). Taking into account the exact form of the geometrical loci of distant interacting points  $(R, R')$  as a function of the relative doublet separation  $\Delta$  (cf. Eq.(I.14) and see Hutsemékers, 1988), we have illustrated in Figs.2-5 the results of numerical calculations of  $W_n^D$  versus  $\Delta = 0.0, 0.2, 0.5, 0.8, 1.0, 1.2, 1.5$  and  $1.8$  for  $n = 0, 1, 2$  and  $3$ , adopting the velocity fields A, B and C explicited in Table 1. Let us note the very good agreement between the results calculated here for  $\Delta = 1.8$  and those reported in Table 2.

## 4 Numerical applications

By means of Eqs.(2)-(3) and since

$$f_D = f_{12} + f_{13}, \quad (40)$$

the fictitious radial opacity of a resonance doublet line transition ( $\tau_D^r(X') = \tau_{12}^r(X') + \tau_{13}^r(X')$ ) may be expressed as (cf. Eq.(II.19))

$$\tau_D^r(X') = K M n(\text{level}) \frac{A(el)}{v_\infty^2} \frac{d(1/L)}{X' dX'}, \quad (41)$$

with the constant

$$K = \frac{\pi e^2}{m c} f_D \lambda_D / (4 \pi \bar{\mu} M_{amu} R_*), \quad (42)$$

where:

- $A(el)$  represents the abundance of the relevant element,
- $\bar{\mu}$  is the mean atomic weight of the nuclei and
- $M_{amu}$  is the unit of atomic mass: all the other symbols have their usual meaning.

Inserting Eq.(41) into expression (36) of  $W_1^{D,0}$ , we easily recover the linear relation existing between the first order moment of an unsaturated resonance doublet P Cygni profile and the mass-loss rate  $\dot{M}$  (cf. Paper II and Surdej, 1983 a,b)

$$W_1^{D,0} = K \dot{M} \bar{n}^{(1)}(\text{level}) q^{c1}(\infty) \frac{A(\text{el})}{v_\infty^2}, \quad (43)$$

where the average fractional abundance

$$\bar{n}^{(1)}(\text{level}) = \frac{\int_1^\infty n(\text{level})(1-W) dL/L^2}{\int_1^\infty (1-W) dL/L^2}, \quad (44)$$

and

$$q^{c1}(\infty) = - \int_1^\infty (1-W) dL/L^2 = -0.89271. \quad (45)$$

If one adopts now the form of the opacity distributions given in Table 1, namely

$$\tau_D^r(X') = C^{\text{te}} \tau^r(X'), \quad (46)$$

we find out by inserting the last relation into Eq.(36) that the fictitious radial opacity  $\tau_D^r(X')$  may be rewritten as

$$\tau_D^r(X') = \frac{W_1^{D,0} \tau^r(X')}{\int_{-X_{\min}}^1 \tau^r(X') X' (1-W) dX'}. \quad (47)$$

It therefore appears straightforward to compute the moments  $W_n^D$  (cf. Eq.(33)) and  $W_n^{D,0}$  (see Eq.(36)) as a function of the parameter  $W_1^{D,0}$  for various opacity and velocity distributions as well as for different values of the doublet separation  $\Delta$ . Because the moments  $W_2^{D,0}$  and  $W_3^{D,0}$  in Eq.(36) appear to be linear combinations (involving the doublet separation  $\Delta$ ) of more elementary moments alike those expressed in Eq.(A.1), it is also very convenient to define and use the following moments

$$\begin{aligned} W_2 &= W_2^D - \varepsilon(1-\varepsilon)\Delta^2 W_0^D, \\ W_3 &= W_3^D - 3\varepsilon(1-\varepsilon)\Delta^2 W_1^D - \varepsilon(2\varepsilon-1)(1-\varepsilon)\Delta^3 W_0^D. \end{aligned} \quad (48)$$

In the optically thin approximation, the latter ones reduce to

$$\begin{aligned} W_2^0 &= \int_{-X_{\min}}^1 X'^2 \tau_D^r(X') \frac{2}{3} (W(1+(1-2W)^3) - 1 + (1-2W)^3) L^2 dX', \\ W_3^0 &= \int_{-X_{\min}}^1 X'^3 \tau_D^r(X') \left(1 - \frac{1}{2L^2}\right) (1-W) dX', \end{aligned} \quad (49)$$



i.e. alike  $W_0^{D,0}$  and  $W_1^{D,0}$  in Eq.(36),  $W_2^0$  and  $W_3^0$  are not dependent on the doublet separation  $\Delta$ . Furthermore, we shall see in Section 6 that the latter moments are simply related to astrophysical quantities of general interest.

Considering the 3 velocity fields and 6 opacity distributions listed in Table 1, we have computed for the eight doublet separations  $\Delta = 0.0, 0.2, 0.5, 0.8, 1.0, 1.2, 1.5$  and  $1.8$  the pairs of moments  $(W_0^D, W_0^{D,0})$ ,  $(W_1^D, W_1^{D,0})$ ,  $(W_2^D, W_2^{D,0})$ ,  $(W_2, W_2^0)$ ,  $(W_3^D, W_3^{D,0})$  and  $(W_3, W_3^0)$  as a function of 20 values of  $\log_{10}(W_1^0)$  in the range  $[-3.5, 3.5]$ . We have also adopted the values  $\epsilon = 2/3$ ,  $X_{min} = -0.01$  and  $L_{max} = 1000$ . There results a total number of  $(3 \times 6 \times 8 \times 6 \times 20 =)$  17280 pairs of calculated moments which may be represented against each other in many various ways. These data as well as more details about their calculations, accuracies, etc. will be published in a separate paper (Hutsemékers and Surdej, 1989a). Some of the most representative diagrams constructed from these data are illustrated in the next Section. We also discuss there the potential use of such diagrams in the context of astrophysical applications.

## 5 A few diagrams of astrophysical interest

We have illustrated in Figs. 6 and 7 typical " $\log_{10}(W_n^D) - \log_{10}(W_n^{D,0})$ " curves for  $n = 0$  and  $n = 3$ , respectively, and for two different values of the doublet separation ( $\Delta = 0.2$  and  $1.0$ ). One notices immediately that apart from a mere translation (cf. the indicated arrow), there exists a great similarity between two curves pertaining to a same velocity and opacity model but different values of the doublet separation. With the exception of a few notable cases (cf.  $n = 2$  and  $\Delta \geq 0.6$ ;  $n = 3$  and  $\Delta \geq 1.2$  for the models A. $\alpha$ , A. $\eta$ , B. $\eta$  and C. $\eta$  further described in Hutsemékers and Surdej (1989a)), this trend appears to be very general and we can take advantage of this as follows. Let us construct from our data " $\log_{10}(W_n^D/W_n^{D,t}) - \log_{10}(W_n^{D,0}/W_n^{D,t})$ " diagrams (see Figs. 8-11). In agreement with our previous statement, we find that, within a very good approximation, these new diagrams are independent on the value of the doublet separation  $\Delta$ . It therefore becomes possible, on the basis of a sin-

gle " $\log_{10}(W_n^D/W_n^{D,t}) - \log_{10}(W_n^{D,0}/W_n^{D,t})$ " diagram to determine the value of the parameter  $W_n^{D,0}$  from the measurement of  $W_n^D$  and the knowledge of  $W_n^{D,t}$  versus  $\Delta$  (cf. Figs. 2-5). If the P Cygni line profile under study is sufficiently unsaturated, our measurements fall on the linear part of the curves and we recover the result  $W_n^{D,0} = W_n^D$ , irrespective of the velocity and opacity distributions. As the observed line profile gets more saturated, the derived value of  $W_n^{D,0}$  becomes more and more dependent on the choice of the velocity and opacity distributions. It is only then possible to derive a lower limit to the value of the parameter  $W_n^{D,0}$ . As  $\log_{10}(W_n^{D,0}) \rightarrow \infty$ ,  $\log_{10}(W_n^D)$  tends towards the asymptotic value  $\log_{10}(W_n^{D,t})$  (see Section 3.4). As already discussed for the case of a single resonance line transition (Surdej, 1985 – Paper III –), it should also be very useful to represent in theoretical " $\log_{10}(W_n^D) - \log_{10}(W_n^{D,t})$ " or " $\log_{10}(W_n) - \log_{10}(W_n^{D,t})$ " diagrams observed values of the corresponding moments in order to infer the type of the velocity and opacity distributions characterizing the line profiles under study. A general look at our data (cf. Figs. 8-11) indicates that for odd values ( $n = 1, 3, \dots$ ) of the order, the moments are mostly sensitive to the form of  $\tau_D^L(X')$  whereas for even values ( $n = 0, 2, \dots$ ) of  $n$ , the moments are opacity dependent at moderate optical depths but entirely velocity dependent as the line profile gets progressively saturated. Therefore, we suggest as a first possible application to use simultaneously " $\log_{10}(W_1^D) - \log_{10}(W_0^D)$ " and " $\log_{10}(W_3) - \log_{10}(W_1^D)$ " diagrams in order to characterize at best the velocity and opacity distributions from measurements of the relevant moments. Such diagrams are illustrated in Figs. 12 and 13 for  $\Delta = 0.5$ . Note that for optically thin lines, the linear part of the theoretical curves is irrespective of the doublet separation (their slopes may be found in Table 3). It is very likely that other combinations of the calculated moments will prove useful to the interpretation of observed line profiles. Any such diagrams may be constructed from the numerical data compiled in Hutsemékers and Surdej (1989a).

## 6 Physical representation of the parameters $W_n^{D,0}$ and $W_n^0$

Following a similar approach as in Paper III for the case of a single resonance line transition and adopting the definitions

$$\begin{aligned} V_n^0 &= W_n^{D,0} & \text{for } n &= 0, 1, \\ V_n^0 &= W_n^0 & \text{for } n &= 2, 3, \end{aligned} \quad (50)$$

we may combine Eqs.(36), (41), (42) and (49) to derive the interesting relation

$$V_n^0 = K \overline{M X^{m-1} \bar{n}^{(n)}(\text{level})} q^{cn}(\infty) \frac{A(el)}{v_\infty^2}. \quad (51)$$

The average quantities are defined as

$$\overline{X^{m-1}} = \frac{\int_1^\infty X^{m-1} n(\text{level}) F_n(L) dL}{\int_1^\infty n(\text{level}) F_n(L) dL} \quad (52)$$

and

$$\bar{n}^{(n)}(\text{level}) = \frac{\int_1^\infty n(\text{level}) F_n(L) dL}{\int_1^\infty F_n(L) dL}. \quad (53)$$

We also have

$$q^{cn}(\infty) = \int_1^\infty F_n(L) dL, \quad (54)$$

where the function  $F_n(L)$  is expressed by

$$\begin{aligned} F_0(L) &= \frac{4L^2 W - 1}{L^2}, \\ F_1(L) &= -\frac{(1-W)}{L^2}, \\ F_2(L) &= \frac{2}{3}(1-W(1+(1-2W)^3) - (1-2W)^3), \\ F_3(L) &= -\frac{1}{L^2}(1 - \frac{1}{2L^2})(1-W), \end{aligned} \quad (55)$$

leading to the values  $q^{c0}(\infty)=0.14159$ ,  $q^{c1}(\infty)=-0.89271$ ,  $q^{c2}(\infty)=0.60971$  and  $q^{c3}(\infty)=-0.76029$ .

Adopting the following relations

$$Q_n = \frac{V_n^0 v_\infty^{n+1}}{K q^{cn}(\infty)}, \quad (56)$$

and

$$R_n = -\frac{Q_n q^{cn}(\infty)}{4 \pi \bar{\mu} M_{amu} R_*}, \quad (57)$$

we easily find by means of Eqs.(42) and (51)-(54) that the above expressions reduce to

$$Q_n = \dot{M} \overline{v^{n-1}} \bar{n}^{(level)} A(el), \quad (58)$$

and

$$R_n = \int_{R_*}^{\infty} n_1(r) v(r)^n F_n(L) L^2 dr, \quad (59)$$

where  $n_1(r)$  represents the volume density of the relevant ion in the lower atomic level. As for the case of a single resonance line transition, the above results permit to conclude that for  $n = 1, 2$  and  $3$ ,  $Q_n$  represents the mass-loss rate, an average momentum rate and (twice) an average kinetic energy rate carried out by the relevant species in the flow. Except for  $n = 0$ , the dependence of the average fractional abundance  $\bar{n}^{(n)}(level)$  as a function of the order  $n$  is quite small (see Table 3). It is interesting to compare at this stage the values  $V_n^0/V_1^0$ ,  $\bar{n}^{(n)}/\bar{n}^{(1)}$  and  $\overline{X^{n-1}}$  reported in Table 3 with those derived for the case of a single resonance line transition (cf. Table 2 in Paper III). The similarities and differences existing between those quantities are easily understood on account of the basic definitions and properties of the respective moments. Another interpretation of the physical parameter  $V_n^0$  may be obtained from Eq.(59). Indeed, for  $n = 1, 2$ , etc. the quantity  $R_n$  provides a measure of the column velocity, (two third of) the column square velocity, etc., of the species under consideration. For  $n = 0$ , we obtain

$$R_0 = \int_{R_*}^{\infty} n_1(r) (4 L^2 V - 1) dr, \quad (60)$$

and since  $4L^2W \simeq 1$ , this quantity ceases to provide an estimate of the column density. This result constitutes a major difference with that obtained for the case of a single resonance line transition (cf. Paper III). The necessity to adopt different definitions for the moments  $W_n^D$  and  $W_n^s$  (see Introduction) is the main cause of this.

## 7 Conclusions

Because most of the P Cygni profiles observed in the ultraviolet spectra of early-type stars, planetary nebula nuclei and in the optical spectra of high redshift BAL quasars are due to lines such as C IV  $\lambda\lambda$  1548.2, 1550.8, Si IV  $\lambda\lambda$  1393.8, 1402.8, N V  $\lambda\lambda$  1238.8, 1242.8, O VI  $\lambda\lambda$  1031.9, 1037.6, etc., for which  $\Delta v_{23} = 498, 1939, 965, 1653$  km/s, respectively, there is a real need to develop the theory of the  $n^{\text{th}}$  order moment  $W_n^D$  for the particular case of a *resonance doublet transition*. The present work merely constitutes a first step in that direction and we therefore discuss at the end of this section the limits of the applicability of our method to real sets of observations.

But first of all, let us summarize the content of this contribution to the theory of the  $n^{\text{th}}$  order moment  $W_n^D$  : deriving a suitable expression for the resonance doublet profile  $E(X_D)/E_c$  (see Eq.(15)), we have established the general expression of the moment  $W_n^D$  in Eq.(33). We have demonstrated that, in the optically thin case, the latter equation reduces to the same expression as that directly obtained for a resonance doublet approximated by two independent line transitions. This same result applies in the optically thick approximation provided that the doublet separation  $\Delta \geq 2$ . For  $\Delta < 2$ , the asymptotic value  $W_n^{D,t}$  remains very dependent on  $\Delta$  as well as on the type of the velocity field  $v(r)$  (see Figs. 2-5).

Adopting realistic expressions for  $v(r)$  and for the opacity distribution  $\tau_D^r(X')$ , we have performed extensive calculations of  $W_n^D$  ( $n = 0, 1, 2$  and  $3$ ). A few diagrams of astrophysical interest have been presented. We have namely discussed the potential use of the normalized " $\log_{10}(W_n^D/W_n^{D,t}) - \log_{10}(W_n^{D,0}/W_n^{D,t})$ " diagrams in

order to infer the values of the parameters  $W_n^{D,0}$  (see Figs. 8–11). For unsaturated P Cygni line profiles, we recover (cf. Paper III) the very useful relation  $W_n^{D,0} = W_n^D$ , irrespective of the choice of  $v(r)$ ,  $\tau_D^r(X')$  and of the doublet separation  $\Delta$ . We have shown that the physical parameters  $W_n^{D,0}$  (and simple linear combinations of these) are simply related to quantities of astrophysical interest. For  $n = 1, 2$  and  $3$ , the above parameters are directly expressed in terms of the mass-loss rate, an average impulsion rate and (twice) an average kinetic energy rate, respectively, carried out by the relevant species in the expanding atmosphere. We have also suggested to use simultaneously the " $\log_{10}(W_1^D) - \log_{10}(-W_0^D)$ " and " $\log_{10}(W_3) - \log_{10}(W_1^D)$ " diagrams in order to determine the types of  $v(r)$  and  $\tau_D^r(X')$ .

As far as the applicability of the present method is concerned, let us stress here that we did not include yet in the theory the possible departures from the Sobolev approximation (cf. the "turbulence" effects discussed by Bertout, 1984 and Lamers et al., 1987), the effects of underlying photospheric absorption lines for the resonance doublet transitions (but see Surdej, 1982 for a discussion of this effect on the first order moment  $W_1^s$ ). Furthermore, if "shell components" are seen to perturb the observed absorption trough, they should be taken away before measuring the moments of the intrinsic P Cygni profiles. Potential users of the theory of the moments  $W_n^D$  should therefore be aware of the above limitations before applying it to real observations (cf. IUE spectra of O-type stars). We personally consider that the "moments" method should allow one to test efficiently the theory against observations, in a statistical sense. For instance, comparison between theoretical and observed " $\log_{10}(W_n^D) - \log_{10}(W_{n'}^D)$ " diagrams constructed from a large sample of P Cygni profiles should help in pointing out the existence of systematic departures and in identifying the physical cause(s). We are presently following such an approach in our analysis of the P Cygni profiles observed in the spectra of high redshift BAL QSOs as well as those displayed in the IUE Atlas of O-type spectra published by Walborn et al. (1985). From the analysis of the latter profiles, we have found out that in addition to the known photospheric and interstellar contamination due to the

resonance doublet line transitions, a photospheric pollution of the stellar continuum by several tens of other line transitions is severely affecting each of the different Si IV, C IV, He II and N IV P Cygni profiles (Nemry et al., 1989 ). As to the improvements to be brought to the model discussed in this paper, we are presently investigating the effects of turbulence (cf. Lamers et al., 1987) onto " $\log_{10} (W_n^D) - \log_{10} (W_n^{D,o})$ " and " $\log_{10} (W_n^D) - \log_{10} (W_{n'}^D)$ " diagrams similar to those illustrated in Figs. 5-13. Of course, no difference should be found for the most interesting case of unsaturated, resonance doublet, P Cygni profiles.

Let us still finally mention that since the theory of the moments  $W_n^D$  is particularly well suited to the interpretation of under-resolved line profiles (see Castor et al., 1981), P Cygni profiles observed with IUE in the low resolution mode provide us with a potential set of observations to be analysed in this way. As a first application of the present results, Hutsemékers and Surdej (1989b) have revisited the mass-loss rates of seventeen central stars of planetary nebulae observed with IUE.

## Appendix A

By means of Equation (II.70), i.e. Equation (70) in Paper II, we easily establish that the expression for the moment  $W_n^{ij}$  ( $n = 0, 1, 2$  and  $3$ ) of a single resonance line transition  $i \rightleftharpoons j$  reduces to

$$\begin{aligned}
 W_0^{ij} &= \int_{-X_{\min}}^1 \tau_{ij}^r(X') (1 - 4L^2W) dX', \\
 W_1^{ij} &= \int_{-X_{\min}}^1 X' \tau_{ij}^r(X') (1 - W) dX', \\
 W_2^{ij} &= \int_{-X_{\min}}^1 X'^2 \tau_{ij}^r(X') \frac{2}{3} (W(1 + (1 - 2W)^3) - 1 + (1 - 2W)^3) L^2 dX', \\
 W_3^{ij} &= \int_{-X_{\min}}^1 X'^3 \tau_{ij}^r(X') \left(1 - \frac{1}{2L^2}\right) (1 - W) dX'.
 \end{aligned} \tag{A.1}$$

Since the fictitious radial opacity  $\tau_{ij}^r$  is proportional to the oscillator strength  $f_{ij}$  (see Eq.(II.19)), we also have  $W_n^{ij} \propto f_{ij}$ .

## Appendix B

Inserting expression (16) for  $E_{12}(X)/E_c$  into Eq.(5) for the moment  $W_n^D$  leads to the result

$$\begin{aligned}
 W_n^{D,12} &= \int_{-1+\epsilon\Delta}^{\epsilon\Delta} X_D^n \int_{\max(|X_D-\epsilon\Delta|, -X_{\min})}^1 P_{12}^N(X') P_{12}(X', X_D - \epsilon\Delta) \frac{dX'}{2X'} dX_D \\
 &+ \int_{\epsilon\Delta}^{X_0+\epsilon\Delta} X_D^n \int_{\max(|X_D|, -X_{\min})}^1 P_{12}^N(X') P_{12}(X', X_D - \epsilon\Delta) \frac{dX'}{2X'} dX_D. \tag{B.1}
 \end{aligned}$$

We have sketched in Figure B1 the domain of integration defined by the above sets of integrals in the plane  $(X_D, X')$ . Interchanging the order of integration between  $X_D$  and  $X'$  in the last Equation, we find

$$W_n^{D,12} = \int_{-X_{\min}}^1 \frac{P_{12}^N(X') dX'}{2X'} \int_{\epsilon\Delta - X'}^{X'(1-2W(L(X')))+\epsilon\Delta} P_{12}(X', X_D - \epsilon\Delta) X_D^n dX_D. \tag{B.2}$$

Applying the variable transformation (cf. Eqs.(6) and (24))

$$\begin{aligned}
 X_D &= -X'\mu + \epsilon\Delta, \\
 dX_D &= -X'd\mu,
 \end{aligned} \tag{B.3}$$



and with the help of expressions (22) and (23), we obtain the desired expression for  $W_n^{D,12}$  (cf. Eq.(33))

$$W_n^{D,12} = \int_{-X_{\min}}^1 \frac{\tau_{12}^r(X')(\beta_{12}^5(X') + J_{12}^2(X')/I_c) 4 L^2(X')}{\beta_{12}^1(X')} \cdot \frac{1}{2} \int_{-(1-2W(L(X')))}^1 (-X'\mu + \epsilon\Delta)^n \frac{(1 - \exp(-\tau_{12}(X', \mu)))}{\tau_{12}(X', \mu)} d\mu dX'. \quad (\text{B.4})$$

## Appendix C

Under the assumption that the expanding atmosphere is optically thin to the spectral line radiation in the transitions  $1 \rightleftharpoons 2$  and  $1 \rightleftharpoons 3$ , the following approximations:

$$\begin{aligned} \beta_{12}^5(X') &\simeq W, \\ \beta_{12}^1(X') &\simeq 1, \\ J_{12}^2(X') &\simeq 0, \\ \frac{(1 - \exp(-\tau_{12}(X', \mu)))}{\tau_{12}(X', \mu)} &\simeq 1, \\ \frac{(1 - \exp(-\tau_{13}(X', \mu)))}{\tau_{13}(X', \mu)} &\simeq 1, \\ \beta_{13}^3(X') &\simeq W, \\ \beta_{13}^1(X') &\simeq 1, \\ \exp(-\tau'_{12}) &\simeq 1, \end{aligned} \quad (\text{C.1})$$

can be conveniently used in the two first sets of integrals of Eq.(33). By means of the variable transformations (6), (7) and (31), (32) and since for constant values of  $\mu_*$  we have the relations

$$\begin{aligned} dX &= -\frac{\tau_{12}^r(X')}{\tau_{12}(X', \mu_{12})} \frac{dX'}{\mu_{12}}, \\ dY &= -\frac{\tau_{13}^r(Y')}{\tau_{13}(X', \mu_{13})} \frac{dY'}{\mu_{13}}, \end{aligned} \quad (\text{C.2})$$

we obtain the third set of integrals in Eq.(33)

$$\begin{aligned}
& 2 \int_0^1 \mu_* d\mu_* \int_{-\sqrt{1-(1-\mu_*^2)/L^2} - (1-\epsilon)\Delta}^{X_{\min} \mu_* + \epsilon\Delta} X_D^n \\
& \quad \cdot (\exp(-\tau_{12}(X', \mu_{12})) \exp(-\tau_{13}(Y', \mu_{13})) - 1) dX_D \\
= & -2 \int_0^1 \mu_* d\mu_* \left[ \int_{-X_{\min}}^1 (-X'\mu + \epsilon\Delta)^n \tau_{12}^r(X') \frac{dX'}{\mu} \right. \\
& \quad \left. + \int_{-X_{\min}}^1 (-Y'\mu - (1-\epsilon)\Delta)^n \tau_{13}^r(Y') \frac{dY'}{\mu} \right]. \tag{C.3}
\end{aligned}$$

Interchanging the order of integration between  $\mu_*$  and  $X'$ ,  $X_*$  and  $Y'$  and using afterwards the variable transformation

$$\begin{aligned}
\mu &= \sqrt{1 - (1 - \mu_*^2) / L^2}, \\
\mu d\mu &= \mu_* d\mu_* / L^2, \tag{C.4}
\end{aligned}$$

the right member of Eq. (C.3) is easily reduced to the result given in Eq.(35).

## References

- Bertout, C.: 1984, *Astrophys. J.*, **285**, 269
- Castor, J.I., Lutz, J.H., Seaton, M.J.: 1981, *Monthly Notices Roy. Astron. Soc.* **194**, 547
- Hutsemékers, D., Surdej, J.: 1987, *Astron. Astrophys.* **173**, 101
- Hutsemékers, D.: 1988, Ph. D. Thesis, University of Liège (Belgium)
- Hutsemékers, D., Surdej, J.: 1989a, in preparation
- Hutsemékers, D., Surdej, J.: 1989b, *Astron. Astrophys.* , in press
- Lamers, H.J.G.L.M., Cerruti-Sola, M., Perinotto, M.: 1987, *Astrophys. J.* **314**, 726
- Nemry, F., Surdej, J., Hernaiz, H.: 1989 , in preparation
- Surdej, J.: 1980, *Astrophys. Space Sci.* **73**, 101 (Paper I)
- Surdej, J.: 1982, *Astrophys. Space Sci.* **88**, 31 (Paper II)
- Surdej, J.: 1983a, *Astrophys. Space Sci.* **90**, 299
- Surdej, J.: 1983b, *Astron. Astrophys.* **127**, 304
- Surdej, J.: 1985, *Astron. Astrophys.* **152**, 361 (Paper III)
- Walborn, N.R., Nichols-Bohlin, J.N., Panek, R.J.: 1985, Nasa Reference Publication 1155

## Acknowledgements

It is a great pleasure to thank Véronique Hutsemékers for her help in typing the manuscript and Armand Kransvelt for drawing the figures.

## Figure captions:

- **Figure 1:** Schematic example of a resonance doublet P Cygni line profile  $E(\lambda)/E_c$  plotted versus the observed wavelength  $\lambda$  and the dimensionless frequencies  $X_D$ ,  $X$  and  $Y$  (see text). We have here assumed that  $\Delta = 1/2$  and  $\varepsilon = 2/3$ .
- **Figure 2:**  $\log_{10}(-W_0^{D,t})$  values calculated from Eq.(33) as a function of the relative doublet separation  $\Delta = 0.0, 0.2, 0.5, 0.8, 1.0, 1.2, 1.5$  and  $1.8$  assuming that  $\tau_{12}, \tau_{13} \gg 1$ . The three curves refer to the velocity fields A, B and C given in Table 1.
- **Figure 3:** Same as in Fig.2 but for  $\log_{10}(W_1^{D,t})$ .
- **Figure 4:** Same as in Fig.2 but for  $\log_{10}(-W_2^{D,t})$ .
- **Figure 5:** Same as in Fig.2 but for  $\log_{10}(W_3^{D,t})$ .
- **Figure 6:** " $\log_{10}(-W_0^D) - \log_{10}(-W_0^{D,0})$ " curves calculated for the eighteen possible models from Table 1. The results are shown for two values of the doublet separation  $\Delta$ . A, B and C refer to the different velocity fields used for modeling the expanding atmosphere.
- **Figure 7:** " $\log_{10}(W_3^D) - \log_{10}(W_3^{D,0})$ " curves calculated for the eighteen possible models from Table 1 and two different doublet separations.
- **Figure 8:** " $\log_{10}(W_0^D/W_0^{D,t}) - \log_{10}(W_0^{D,0}/W_0^{D,t})$ " curves calculated for the eighteen possible models from Table 1 and  $\Delta=0.5$ . Note that within a very good approximation, these calculations are irrespective of the doublet separation  $\Delta$ .
- **Figure 9:** Same as in Fig.8 but for " $\log_{10}(W_1^D/W_1^{D,t}) - \log_{10}(W_1^{D,0}/W_1^{D,t})$ " curves.
- **Figure 10:** Same as in Fig.8 but for " $\log_{10}(W_2^D/W_2^{D,t}) - \log_{10}(W_2^{D,0}/W_2^{D,t})$ " curves.

- **Figure 11:** Same as in Fig.8 but for " $\log_{10}(W_3^D/W_3^{D,t}) - \log_{10}(W_3^{D,0}/W_3^{D,t})$ " curves.
- **Figure 12:** " $\log_{10}(W_1^D) - \log_{10}(-W_0^D)$ " curves calculated for the eighteen possible models from Table 1 and  $\Delta=0.5$ . Here, the linear part of the curves remains independent on the doublet separation. However, the saturated part (higher values of  $|W_0^D|$  and  $W_1^D$ ) is very much dependent on  $\Delta$ .
- **Figure 13:** Same as in Fig.12 but for " $\log_{10}(W_3) - \log_{10}(W_1^D)$ " curves.
- **Figure B1:** Domain of integration in the plane  $(X_D, X')$  of the integrand  $X_D^N P_{12}^N(X') P_{12}(X', X_D - \epsilon\Delta)/2X'$  appearing in Eq.(B.1).

Table 1: Adopted velocity and opacity distributions for calculating the moments  $W_n^D$  of resonance doublet P Cygni line profiles

(A)	$X'$	$= -X_{min} + (1 + X_{min})(1 - 1/\sqrt{L})$
(B)	$X'$	$= -X_{min} + (1 + X_{min})(1 - 1/L)$
(C)	$X'$	$= \sqrt{1 - (1 - X_{min}^2)/L}$
( $\alpha$ )	$\tau'(X')$	$= d(1/L) / X' dX'$
( $\beta$ )	$\tau'(X')$	$= 1 - X'$
( $\gamma$ )	$\tau'(X')$	$= 1$
( $\delta$ )	$\tau'(X')$	$= (1 - X')^{1/2}$
( $\epsilon$ )	$\tau'(X')$	$= (1 - X')^2$
( $\eta$ )	$\tau'(X')$	$= 1/X'$

Table 2: Asymptotic values of  $W_n^t$  and  $W_n^{D,t}$  according to Eqs. (13) and (14) for  $\varepsilon = 2/3$  and  $\Delta = 1.8$

velocity field	$\log(-W_0^t)$	$\log(W_1^t)$	$\log(-W_2^t)$	$\log(W_3^t)$
A	-1.143	-0.338	-0.636	-0.660
B	-0.914	-0.323	-0.607	-0.609
C	-0.724	-0.344	-0.609	-0.616
	$\log(-W_0^{D,t})$	$\log(W_1^{D,t})$	$\log(-W_2^{D,t})$	$\log(W_3^{D,t})$
A	-0.842	-0.058	-1.387	0.411
B	-0.613	-0.057	-0.842	0.419
C	-0.424	-0.101	-0.539	0.380

**Table 3:** The ratios  $V_n^0/V_1^0$ ,  $\bar{n}^{(n)}(level)/\bar{n}^{(1)}(level)$  and the average quantity  $\overline{X^{m-1}}$  (see Eqs.(50)-(53),  $n = 0, 2$  and  $3$ ) for the velocity laws (A)-(C) and the opacity distributions ( $\alpha$ )-( $\eta$ ) (see Table 1)

$n$		(A)			(B)			(C)		
		$V_n^0/V_1^0$	$\bar{n}^{(n)}/\bar{n}^{(1)}$	$\overline{X^{m-1}}$	$V_n^0/V_1^0$	$\bar{n}^{(n)}/\bar{n}^{(1)}$	$\overline{X^{m-1}}$	$V_n^0/V_1^0$	$\bar{n}^{(n)}/\bar{n}^{(1)}$	$\overline{X^{m-1}}$
( $\alpha$ )	0	3.2590	1.0000	20.523	2.1763	1.0000	13.705	0.6419	1.0000	4.0426
	2	0.2461	1.0000	0.3599	0.3641	1.0000	0.5325	0.4729	1.0000	0.6917
	3	0.1792	1.0000	0.2104	0.3483	1.0000	0.4090	0.4917	1.0000	0.5773
( $\beta$ )	0	0.4364	0.3291	8.3498	0.7361	0.7662	6.0501	1.5854	1.9861	5.0270
	2	0.3430	0.9890	0.5073	0.3531	1.0024	0.5151	0.3676	1.0117	0.5313
	3	0.3019	1.0942	0.3240	0.2950	1.0069	0.3440	0.2816	0.8805	0.3755
( $\gamma$ )	0	0.1754	0.1531	7.2116	0.2955	0.3814	4.8785	0.6419	1.0000	4.0426
	2	0.4375	0.9821	0.6514	0.4588	0.9909	0.6772	0.4729	1.0000	0.6917
	3	0.4732	1.1348	0.4896	0.4985	1.0824	0.5408	0.4917	1.0000	0.5773
( $\delta$ )	0	0.2926	0.2366	7.7860	0.5009	0.5766	5.4712	1.0840	1.5041	4.5388
	2	0.3862	0.9855	0.5731	0.3990	0.9972	0.5850	0.4140	1.0071	0.6011
	3	0.3772	1.1150	0.3972	0.3780	1.0423	0.4258	0.3670	0.9339	0.4614
( $\epsilon$ )	0	0.7847	0.5231	9.4474	1.2767	1.1214	7.1704	2.7207	2.8648	5.9807
	2	0.2793	0.9954	0.4103	0.2874	1.0101	0.4161	0.2992	1.0157	0.4308
	3	0.2023	1.0537	0.2254	0.1923	0.9486	0.2380	0.1775	0.8022	0.2598
( $\eta$ )	0	1.6787	0.5660	18.678	2.1763	1.0000	13.705	3.6976	2.2554	10.325
	2	0.3441	0.9908	0.5079	0.3641	1.0000	0.5325	0.3815	1.0042	0.5556
	3	0.3299	1.0691	0.3623	0.3483	1.0000	0.4090	0.3476	0.9013	0.4528

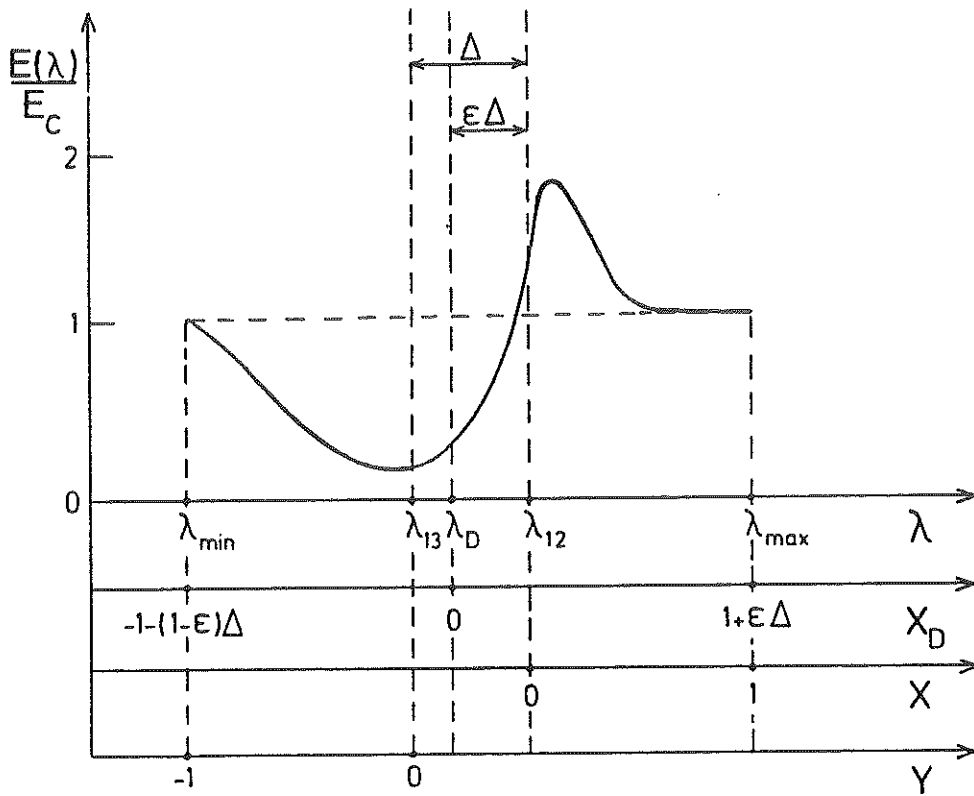


Fig. 1

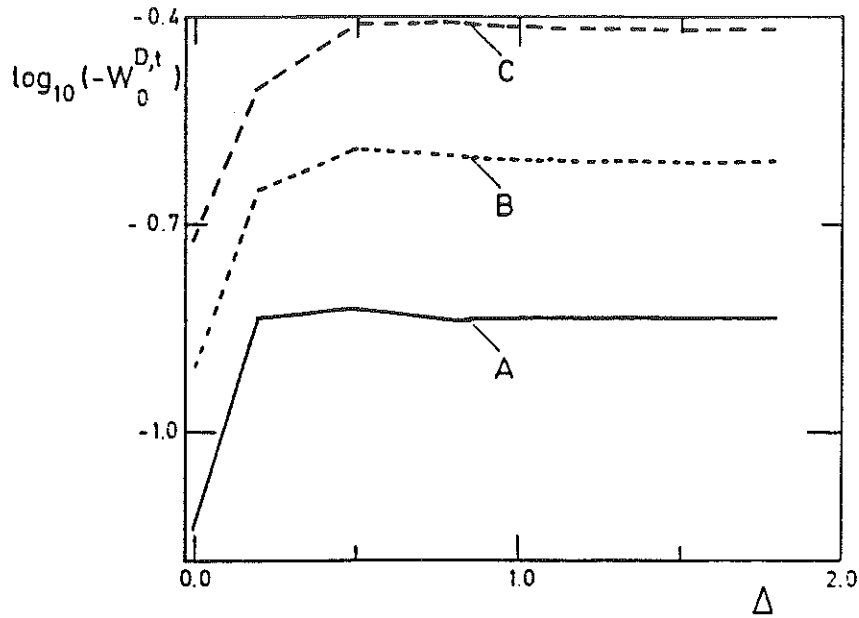


Fig. 2



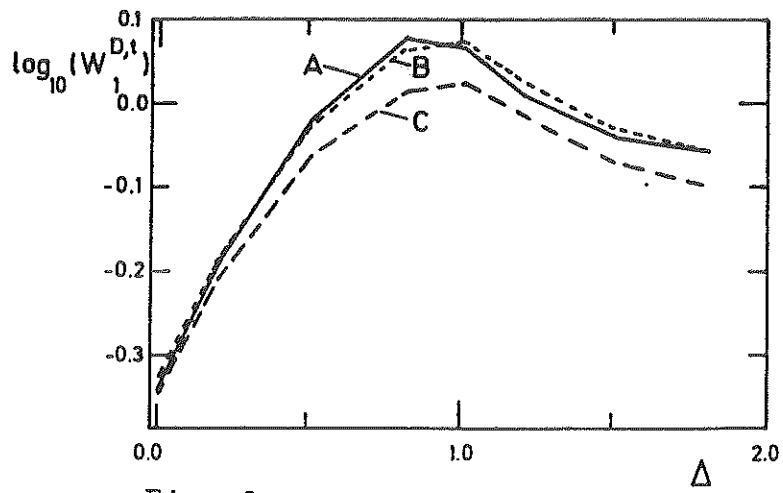


Fig. 3

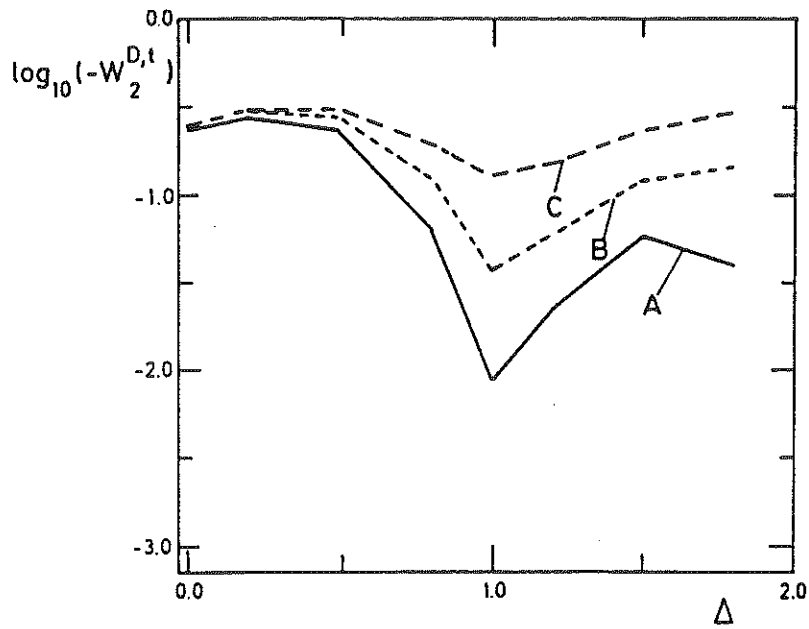


Fig. 4

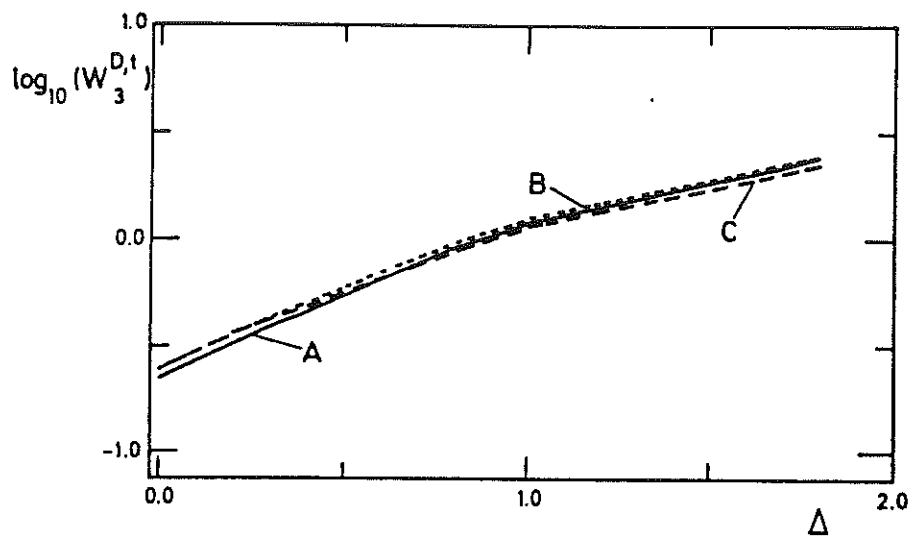


Fig. 5

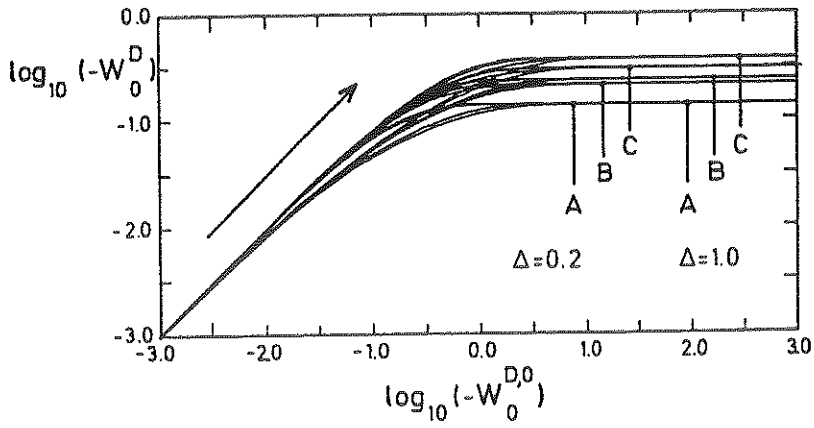


Fig. 6

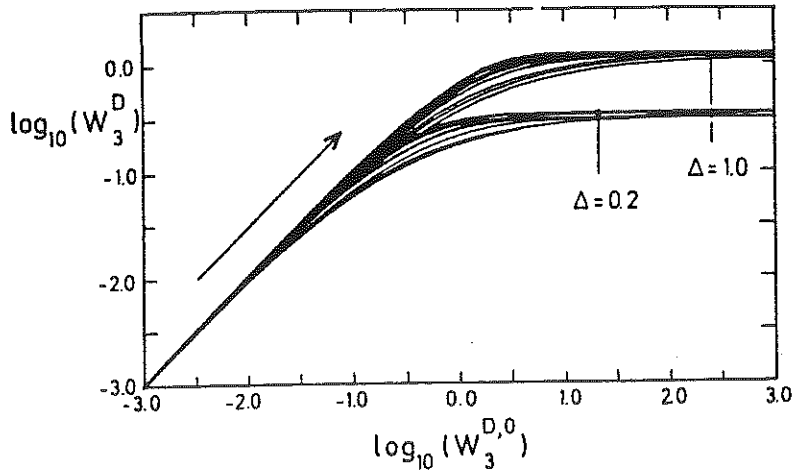


Fig. 7

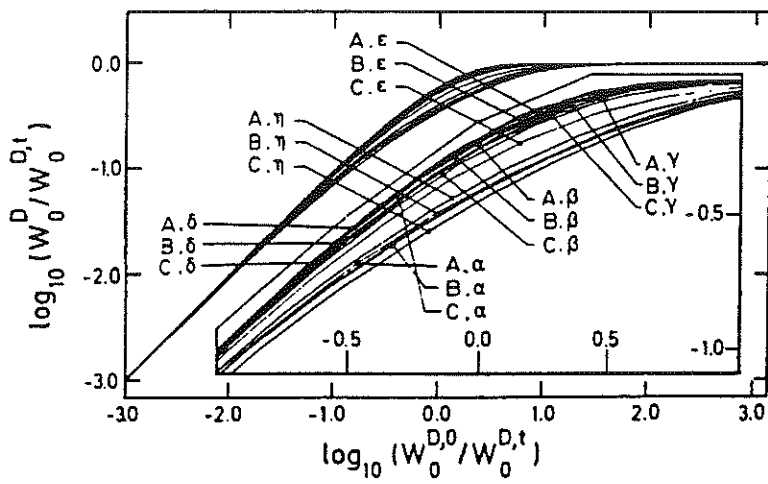


Fig. 8

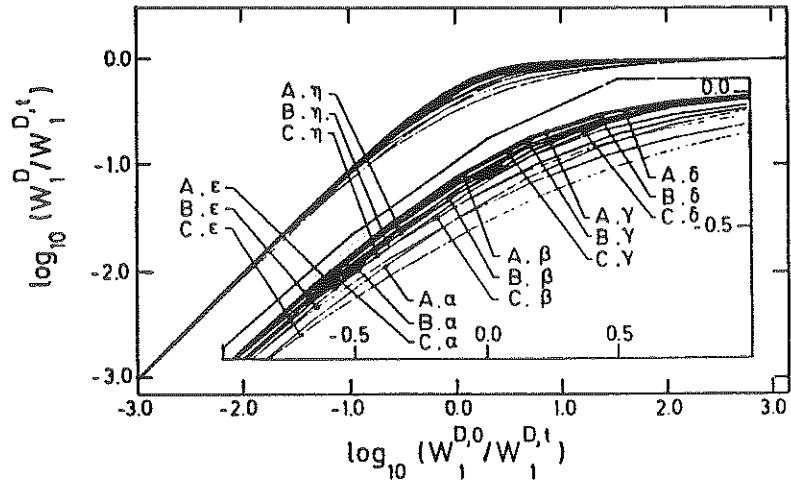


Fig. 9

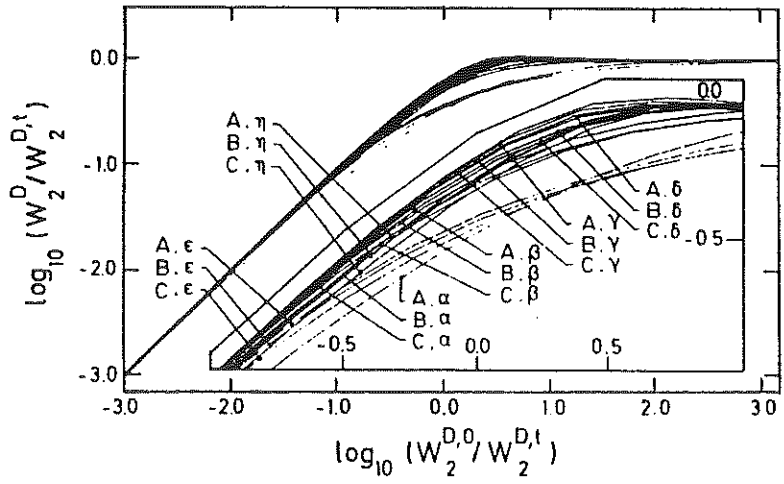


Fig. 10

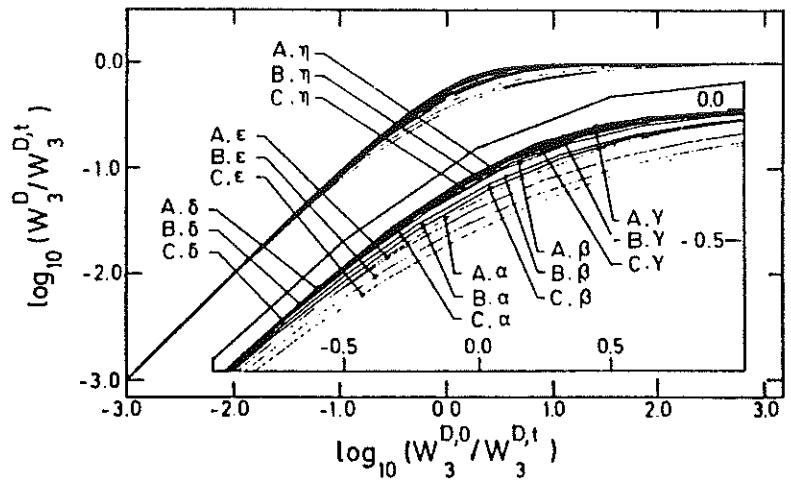


Fig. 11

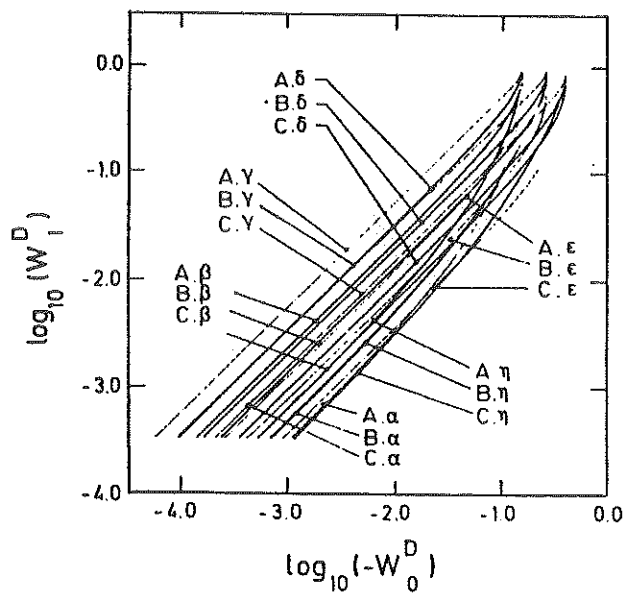


Fig. 12

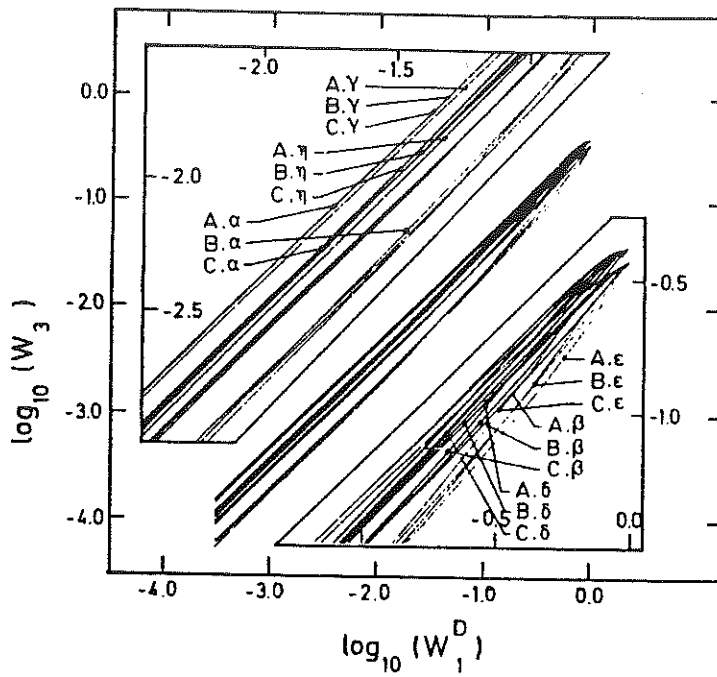


Fig. 13

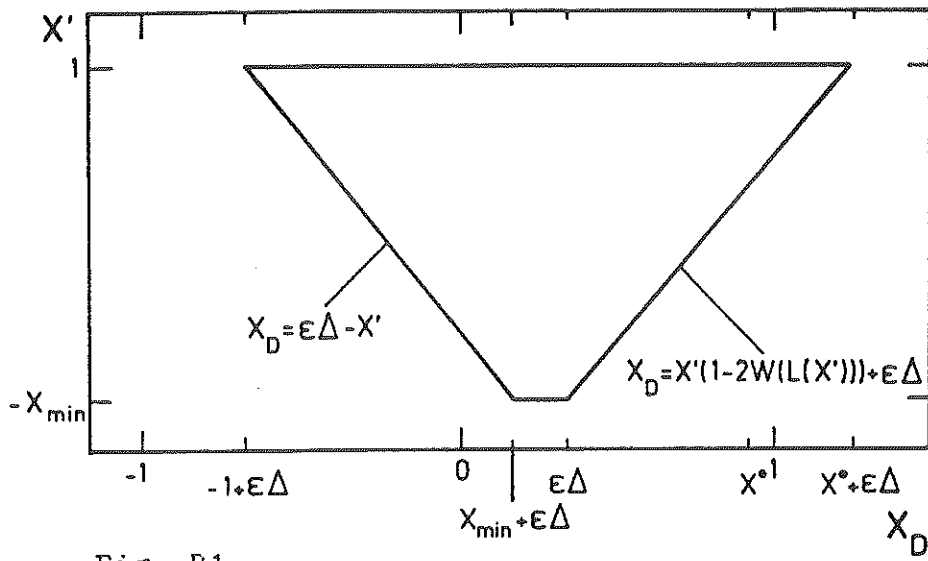


Fig. B1



## Article 9

### FORMATION OF P CYGNI LINE PROFILES IN RELATIVISTICALLY EXPANDING ATMOSPHERES

Hutsemékers, D., Surdej, J.: 1990, *Astrophys. J.*, sous presse.

Les profils de raies de type P Cygni observés dans les spectres de supernovae et de quasars BAL présentent très souvent des déplacements Doppler atteignant quelques dizaines de milliers de kilomètres par seconde. C'est pourquoi, dans le cadre de l'approximation de Sobolev, nous avons généralisé l'étude du transfert radiatif au cas des atmosphères en expansion relativiste. Dans l'article qui suit, nous présentons pour une transition de résonance simple les expressions relativistes de la fonction source  $S_{12}$ , du profil de raie  $E(X)/E_c$  et des moments  $W_n^R$ . De nombreuses applications numériques sont illustrées sous forme de diagrammes et nous soulignons les différences essentielles entre les comportements classiques et relativistes des surfaces d'égale fréquence  $X$ , de la fonction source, du profil de raie  $E(X)/E_c$  et des moments d'ordre  $n$ . Un des résultats les plus intéressants que nous avons obtenus est d'avoir démontré que le moment  $W_1^R$  reste un excellent indicateur du taux de perte de masse  $\dot{M}$  pour des enveloppes en expansion relativiste.





# Formation of P Cygni line profiles in relativistically expanding atmospheres

Damien Hutsemékers<sup>1</sup> and Jean Surdej<sup>2,3</sup>

1. European Southern Observatory, La Silla, Chile

2. Institut d'Astrophysique, Liège, Belgium

Submitted to: Astrophysical Journal

---

<sup>3</sup>Also, Chercheur Qualifié au Fonds National de la Recherche Scientifique (Belgium)

## Abstract

The P Cygni line profiles observed in the spectrum of broad absorption line quasars, supernovae, etc., are sometimes characterized by very large Doppler velocities. In order to interpret more accurately such profiles, we have generalized the Sobolev theory for the transfer of line radiation to the case of the special relativity.

Considering spherically symmetric expanding envelopes, we first discuss the deformations suffered by the surfaces of equal frequency when the velocities become comparable to that of light. For a single line formed in an atmosphere with a monotonic velocity field, we note the possible appearance of distant interactions at very large expansion velocities, a relativistic effect which may be of considerable importance when evaluating the amplitude of radiative forces.

Following a probabilistic formalism, we subsequently establish the expression of the source function and that of the line profile. We find that the relativistic P Cygni line profiles are significantly different from those computed in the framework of the classical theory: for increasing values of the terminal wind velocity, the red emission wing becomes definitely narrower than the blue one while the line center emission increases. These modifications are mainly due to the redistribution of the scattered line photons in a frequency interval which is no longer symmetrical, in accordance with the relativistic expression of the Doppler effect.

We finally study the first order moment of unsaturated P Cygni line profiles and show that, in the relativistic case, this moment is still directly proportional to the mass-loss rate. For the case of slightly and strongly saturated line profiles, we compute the first order moment curves of growth which, after normalization, are also found to be little dependent on the relativistic corrections and very useful for the determination of mass-loss rates.

**Subject headings:** line profiles – quasars – radiative transfer – relativity – stars: supernovae

# 1 Introduction

P Cygni line profiles characterized by relativistic Doppler velocities are currently observed in the spectrum of astronomical objects like, for instance, supernovae (Weiler and Sramek, 1988) and broad absorption line (BAL) quasars (Weymann and Foltz, 1983)

For extreme velocities ( $v \geq 0.2c$ ), we naturally expect that the classical theory will cease to provide an accurate description of the observed line profiles. This can be easily understood by considering the Doppler effect which is essential in the formation of P Cygni line profiles (Beals, 1929, 1931). Its relativistic expression is significantly more complex than in the low velocity regime (see next Section) and implies that the absolute frequency shift of photons scattered by material receding with a velocity  $v$  (redshift) is smaller than the shift produced by material moving towards the observer at  $-v$  (blueshift). The red emission wing of relativistic P Cygni line profiles will therefore be significantly narrower than the blue one, an asymmetry which is not present in the classical limit (see e.g. the atlas of profiles due to Castor and Lamers, 1979).

The aim of this paper is to derive the expression of line profiles formed in a relativistically expanding atmosphere assumed to be spherically symmetric and stationary. We restrict ourselves to the study of pure photon scattering by a two-level atom with complete redistribution in the fluid frame. In addition, we adopt the Sobolev approximation (Sobolev, 1947, 1958) for the treatment of the radiative transfer. If the very large velocities considered here are associated with similarly large velocity gradients throughout the envelope, this approximation is even more adequate than in cases describable in the classical limit. Our approach is quite different of that of Mihalas (1980) who uses the comoving-frame formalism to study the transfer of the continuum radiation in relativistic flows.

After briefly recalling the basic equations and notations (Section 2), we discuss in Section 3 the modifications undergone by the surfaces of equal frequency when the fluid velocity becomes comparable to that of light. These surfaces are especially useful in order to visualize the transfer of line photons through the envelope. Following a

probabilistic point-of-view, we derive in Section 4 the expression of transfer quantities such as the optical depth, the escape probabilities and the source function. This allows us to determine, in Section 5, the relativistic expression of a P Cygni line profile. In Section 6, we study the first order moment of relativistic line profiles, a quantity which is particularly useful for the determination of mass-loss rates. Numerical applications are presented in Section 7. Finally, conclusions form the last Section.

Different formalisms based on the Sobolev approximation have been used to derive the classical expression of P Cygni line profiles (Castor, 1970; Lucy, 1971; Surdej, 1979). In this paper, we follow the probabilistic approach developed by Surdej which, as we shall see, is quite easy to generalize to the relativistic case. We will frequently refer to Paper I (Surdej, 1977) in which the classical escape probabilities and source function are derived and to Papers II and III (Surdej, 1979, 1982) where line profiles are discussed.

## 2 Some basic equations

If we apply to the photon four-momentum the Lorentz transformation between a rest frame (observer's frame) and a frame moving at a constant velocity  $v$  (comoving or fluid frame), it is easy to derive the well-known relations

$$\nu_0 = \nu \gamma (1 - \mu\beta) \quad (1)$$

and

$$\mu_0 = \frac{\mu - \beta}{1 - \mu\beta}, \quad (2)$$

where

$$\gamma = \frac{1}{\sqrt{1 - \beta^2}} \quad (3)$$

and

$$\beta = \frac{v}{c}, \quad (4)$$

$\mu = \cos \theta$  being the angle-cosine describing the direction of the photon propagation and  $\nu$  the frequency (Mihalas, 1978). Both  $\mu$  and  $\nu$  are measured in the rest frame while quantities with the suffix zero are measured in the comoving frame. As usual,  $c$  represents the light velocity. We immediately see from Eq. (1) –the relativistic form of the Doppler effect– that the absolute frequency shift  $|\nu_0 - \nu|$  depends on the sign of  $\mu$  for velocities comparable to that of light. For  $\mu = 0$ , this shift is no longer equal to zero.

Let us now consider the transformations for the opacity ( $\alpha_\nu$ ), the emissivity ( $\epsilon_\nu$ ) and the specific intensity ( $I_\nu$ ). As shown by Thomas (1930) and Mihalas (1978, 1984), the requirement that independent observers in both rest and comoving frames measure the same number of photon events leads to the following relations:

$$\frac{I_\nu}{\nu^3} = \frac{I_{\nu_0}^0}{\nu_0^3}, \quad (5)$$

$$\nu \alpha_\nu = \nu_0 \alpha_{\nu_0}^0 \quad (6)$$

and

$$\frac{\epsilon_\nu}{\nu^2} = \frac{\epsilon_{\nu_0}^0}{\nu_0^2}, \quad (7)$$

where, again, all quantities with the suffix zero are measured in the comoving frame. We also have the useful relations

$$\nu^2 d\omega = \nu_0^2 d\omega_0 \quad (8)$$

and

$$\nu d\nu d\omega = \nu_0 d\nu_0 d\omega_0, \quad (9)$$

$d\omega$  representing a solid angle element measured in the rest frame.

### 3 The surfaces of equal frequency

Let us consider a spherically symmetric atmosphere expanding around a central core of radius  $r_c$ . The velocity of the flow  $v(r)$  – $r$  denoting the radial distance to the core–

is supposed to increase continuously from  $v_c$ , the velocity at the surface of the core, to  $v_\infty$ , the terminal velocity.

If we assume that the fluid is populated by two-level ( $1 \rightleftharpoons 2$ ) atoms emitting photons at the comoving line center frequency  $\nu_{12}^0$ , all photons seen by a rest-observer with a specified frequency  $\nu$  are emitted from surfaces satisfying the relation (see Eq. (1))

$$\nu_{12}^0 = \nu \gamma(r) (1 - \mu\beta(r)). \quad (10)$$

Solving this equation in  $r$  and  $\mu$  for different values of  $\nu$  provides us with the *surfaces of equal frequency*  $\nu$ . Strictly speaking, these surfaces should be considered as thin shells because the thermal velocities are not exactly equal to zero when compared to the macroscopic velocity field. Now, if we define the dimensionless frequency

$$X = -\frac{\nu - \nu_{12}^0}{\nu_{max} - \nu_{12}^0}, \quad (11)$$

$\nu_{max}$  representing the maximum frequency which corresponds to the terminal velocity  $+v_\infty$ , we easily find that

$$X = -\frac{\frac{\sqrt{1-\beta^2}}{1-\mu\beta} - 1}{\sqrt{\frac{1+\beta_\infty}{1-\beta_\infty}} - 1}, \quad (12)$$

where  $\beta_\infty$  is equal to  $v_\infty/c$ . So defined, the dimensionless frequency  $X$  always satisfies the relation

$$-1 \leq X \leq \sqrt{\frac{1-\beta_\infty}{1+\beta_\infty}} = X_\infty^R, \quad (13)$$

from which we immediately notice that no photons of frequencies  $X \geq X_\infty^R$  are emitted towards the observer.

Adopting the velocity law  $v(r) = v_c + (v_\infty - v_c)(1 - r_c/r)$ , representative of outward accelerating envelopes (see Section 7), we have computed surfaces of equal frequency  $X$  for different values of  $\beta_\infty$ . Examples are illustrated in Fig. 1 a-d. We immediately see that, unlike in the classical case, the surfaces strongly depend on the value of the terminal velocity and that very unsymmetric parts of the atmosphere may contribute to the frequencies  $X$  and  $-X$ .

It is also interesting to consider the surfaces of equal frequency obtained for velocity laws of the type  $v(r) \propto r^n$ . Such surfaces are illustrated in Fig. 2 a-d and show similar deformations for increasing values of  $\beta_\infty$ . But in addition, at very high velocities, we see that photons emitted towards the observer may intercept the same surface a second time and consequently be reabsorbed. This corresponds to the appearance of distant interactions in highly relativistic flows, a situation already known for the case of decelerated or nonmonotonic flows (see Rybicki and Hummer, 1978, and Paper II). It is clear that such interactions completely modify the transfer of line radiation and may be of fundamental importance when evaluating the amplitude of the radiative forces. We should nevertheless note that these interactions are only present for very high values of  $\beta$  and never for velocity distributions of the type considered in Section 7. We will therefore not discuss in more detail this effect in the remainder of this paper.

We emphasize that the strong and non-linear dependence of the surfaces of equal frequency upon  $\beta_\infty$  forces us to consider the terminal velocity as a totally independent parameter when computing line profiles.

## 4 Photon escape probability and source function

For the treatment of line transfer, we follow the probabilistic approach (cfr. Paper I). This approach is particularly interesting in the relativistic case because we can easily manipulate invariants; a probability being nothing else than a ratio of photon numbers that is identical in both the rest and the comoving frames.

Since photon number must be carefully distinguished from energy, we prefer to use hereafter quantities like  $I_\nu^N = I_\nu/h\nu$  and  $\epsilon_\nu^N = \epsilon_\nu/h\nu$ ,  $h$  denoting the Planck constant. The transformation laws of such quantities are immediately derived from Eqs. (5)-(7).

In order to *define* the useful transfer quantities (optical depth, absorption or escape probabilities, etc), we set ourselves in the rest frame where it is easier to follow the trajectories of atoms as well as photons. While most of these quantities are frame independent, it is often more convenient to *calculate* them in the comoving frame

where, for example, the opacity and the emissivity are isotropic. Because the flow is accelerated, we must consider transformations between the rest frame and a series of frames which move at constant velocity, coinciding instantaneously with the fluid at a selected point.

In addition to the Sobolev approximation which states that most of the physical characteristics of the fluid can be considered as constant at some –small– distance scale (see the next Subsection), we assume that the material advection is negligible. Because this latter approximation is certainly not valid for ultra-relativistic flows ( $\beta \simeq 1$ ) – due to the time dilatation the distance travelled by a fluid element during the lifetime of an excited atomic state may become comparable to the Sobolev distance scale – we restrict our discussion to reasonable relativistic velocities (typically  $\beta_\infty \leq 0.8$ ) which, in any case, encompass most of the existing observations.

#### 4.1 Relativistic expression of the photon escape probability

Let us follow a photon emitted at a point  $s_E$  in the moving fluid and seen, by a rest observer, at a frequency  $\nu$  and propagating along a direction with abscissae  $s$ . This situation is illustrated schematically in Fig. 3. This photon has a probability  $d\tau_\nu = \alpha_\nu(s)ds$  of being absorbed between  $s$  and  $s + ds$  and therefore a probability  $e^{-\tau_\nu}$  of leaving the envelope without any absorption, the optical depth  $\tau_\nu$  taking the form

$$\tau_\nu = \int_{s_E}^{\infty} \alpha_\nu ds . \quad (14)$$

In order to easily calculate  $\alpha_\nu$ , we consider comoving frames coinciding instantaneously with the fluid at each point  $s$  along the trajectory. In these frames, the opacity can be expressed by

$$\alpha_{\nu_0}^0(s) = \alpha_{12}^0(r) \Phi_0(\nu_0 - \nu_{12}^0) , \quad (15)$$

where  $\alpha_{12}^0(r)$  is the total opacity in the transition  $1 \rightleftharpoons 2$  and  $\Phi_0(\nu_0 - \nu_{12}^0)$  the atomic absorption profile. This absorption profile is assumed to be zero outside of the frequency interval  $[\nu_0 - \Delta\nu_0/2, \nu_0 + \Delta\nu_0/2]$ ; the width  $\Delta\nu_0$  includes the Doppler line broadening caused by thermal agitation, microturbulence, etc. As usual, this profile is



normalised by the relation

$$\int \Phi_0(\nu_0 - \nu_{12}^0) d\nu_0 = 1. \quad (16)$$

The rest observer can transform expression (15) with the help of relation (6) and write the optical depth

$$\tau_\nu = \int_{s_E}^{\infty} \frac{\nu_0(s)}{\nu} \alpha_{12}^0(s) \Phi_0(\nu_0 - \nu_{12}^0) ds. \quad (17)$$

Let us now estimate the probability that if a photon is emitted at the point  $s_E$  (see Fig. 3), it is emitted in the frequency interval  $[\nu, \nu + d\nu]$  and in the solid angle interval  $[\omega, \omega + d\omega]$ . This probability, while frame independent, is more conveniently calculated in the comoving frame where we have assumed complete redistribution in frequency and in direction. It takes the simple form

$$\Phi_0(\nu_0^E - \nu_{12}^0) d\nu_0^E \frac{d\omega_0}{4\pi} \quad (18)$$

where

$$\nu_0^E = \nu \gamma(s_E) (1 - \mu(s_E) \beta(s_E)), \quad (19)$$

$d\omega_0$  being the comoving solid angle corresponding to  $d\omega$ . The mean probability that a photon emitted at  $s_E$  directly escapes the atmosphere may therefore be written

$$\beta_{12}^1(\tau) = \int_{\Omega_0=4\pi} \int_{-\infty}^{+\infty} e^{-\tau\nu} \Phi_0(\nu_0^E - \nu_{12}^0) d\nu_0^E \frac{d\omega_0}{4\pi}. \quad (20)$$

In a very rapidly accelerating fluid, a photon of given frequency can only be absorbed within a small region of the envelope whose thickness  $\Delta S(\tau, \mu)$  is directly related to the absorption profile width  $\Delta\nu_0$  via the Doppler relation. The approximation introduced by Sobolev (1947, 1958) consists in assuming that both the physical and the kinematic fluid properties, except for the fluid velocity, are constant along spatial distances  $\Delta S$ . It is adequate whenever the thickness  $\Delta S$  is very small compared to the envelope dimensions, i.e. if the velocity gradient is high and if the absorption width  $\Delta\nu_0$  is small enough. Using this approximation after changing in Eq. (17) the variable of integration from  $s$  to  $\nu_0$ , the expression of the escape probability  $\beta_{12}^1$  reduces to

$$\beta_{12}^1 = \int_{\Omega_0=4\pi} \frac{1 - e^{-\tau_{12}}}{\tau_{12}} \frac{d\omega_0}{4\pi} \quad (21)$$

and finally, with Eq. (8), to

$$\beta_{12}^1 = \int_{-1}^{+1} \frac{1 - e^{-\tau_{12}}}{\tau_{12}} \frac{d\mu}{2\eta^2} \quad (22)$$

where

$$\tau_{12} = \frac{\alpha_{12}^0}{\nu_{12}^0} \eta^2 \left| \left( \frac{\partial \eta}{\partial s} \right)^{-1} \right| \quad (23)$$

and

$$\eta(r, \mu) = \gamma(1 - \mu\beta). \quad (24)$$

Differentiating Eq. (24), we easily obtain

$$\tau_{12}^r(r, \mu) = \tau_{12}^r \left| \frac{(1 - \mu\beta)^2}{(1 - \beta) [\mu(\mu - \beta) + (1 - \mu^2)(1 - \beta^2)(d \ln r / d \ln \beta)]} \right| \quad (25)$$

and

$$\tau_{12}^r(r) = \tau_{12}(\mu = +1) = \frac{\alpha_{12}^0}{\nu_{12}^0} \left( \frac{d\beta}{dr} \right)^{-1} \frac{(1 - \beta)}{\gamma}. \quad (26)$$

The  $\beta_{12}^1$  and  $\tau_{12}$  expressions are more complex than in the classical case (see Paper I). In particular, they are no longer symmetric in  $\mu$ . This is illustrated in Fig. 4 where we can note that for relativistic velocities, the photon escape probability  $(1 - e^{-\tau_{12}})/\tau_{12}$  is much greater in the direction of motion ( $\mu = +1$ ) than in the opposite one ( $\mu = -1$ ). Nevertheless, the Sobolev optical depth  $\tau_{12}$  can still be written with the general and meaningful expression

$$\tau_{12} = \frac{\alpha_{12}^0}{\Delta\nu} \Delta S, \quad (27)$$

$\Delta\nu$  being the rest frequency interval corresponding to  $\Delta\nu_0$ . It is important to recall that in the framework of the Sobolev approximation, a photon of given frequency can only be scattered within a very small region of the envelope before finally escaping it. The line transfer may therefore be considered as purely *local* and the Sobolev optical depth  $\tau_{12}$  is sufficient to characterize the radiation-matter interactions at each *point* in the envelope.

## 4.2 Relativistic expression of the source function

To derive the expression of the source function we first need to evaluate the mean intensity of the radiation field. This is more easily done in the comoving frame where the process of emission is isotropic. In this frame, we denote by  $J_{12}^{N,0}$  the mean specific intensity weighted on the line profile and divided by  $h\nu_{12}^0$ .

$J_{12}^{N,0}$  contains two major contributions: the first one is due to photons issued from the central core (the distant contribution) and the other one to photons locally scattered (the local contribution). Let us first estimate the distant contribution assuming that the core is emitting a continuum whose intensity  $I_c^N$ , measured by the rest observer, is constant over the line profile and does not show any limb darkening effect. For this observer, the intensity of the radiation emitted at a frequency  $\nu$  by a point of the core surface and reaching another point located in the envelope, is equal to  $I_c^N e^{-\tau_\nu}$ ,  $\tau_\nu$  representing the optical depth between the core surface and the considered point in the envelope. Measured in the comoving frame which coincides instantaneously with the fluid at this point, this intensity is equal to  $\eta^2 I_c^N e^{-\tau_\nu}$ , following Eq. (5) and remembering that  $I_c^N$  has also been divided by  $h\nu$ . Averaging this quantity in the comoving frame over both the line absorption profile and the directions, we obtain the distant contribution to the mean intensity whose expression

$$\int_{\Omega_0=4\pi} \int_{-\infty}^{+\infty} \eta^2 I_c^N e^{-\tau_\nu} \Phi_0(\nu_0 - \nu_{12}^0) d\nu_0 \frac{d\omega_0}{4\pi} \quad (28)$$

reduces, in the framework of the Sobolev approximation, to

$$I_c^N \int_{4\pi W} \frac{1 - e^{-\tau_{12}}}{\tau_{12}} \frac{d\omega}{4\pi}, \quad (29)$$

$W$  denoting the geometrical dilution factor  $(1 - \sqrt{1 - (r_c/r)^2})/2$ . The quantity

$$\beta_{12}^3(r) = \int_{4\pi W} \frac{1 - e^{-\tau_{12}}}{\tau_{12}} \frac{d\omega}{4\pi} = \int_{1-2W}^1 \frac{1 - e^{-\tau_{12}}}{\tau_{12}} \frac{d\mu}{2} \quad (30)$$

represents the mean penetration probability of photons emitted from the central core. It is important to note that in a relativistically expanding envelope,  $\beta_{12}^3$  is no longer equal to the mean probability that a photon escapes directly the envelope and intercepts

the central core. This latter probability is in fact equal to (see Eq. (22))

$$\int_{-1}^{-(1-2W)} \frac{1 - e^{-\tau_{12}}}{\tau_{12}} \frac{d\mu}{2\eta^2}. \quad (31)$$

The difference between escape and penetration mean probabilities is simply due to different assumptions about the directional variation of the radiation field: for  $\beta_{12}^1$ , we assume the isotropic emission in the local comoving frame and for  $\beta_{12}^3$ , the isotropic emission from the distant core in the rest frame. Besides from the factor that incorporates the direction behavior of the radiation field, the penetration and escape probabilities for one direction are the same:  $(1 - e^{-\tau_{12}})/\tau_{12}$ .

The local contribution to the mean intensity  $J_{12}^{N,0}$  can be evaluated following a similar reasoning (see also Paper I). However since the Sobolev line transfer is purely local, the photon input-output being controlled at each point in the envelope by the probabilities  $\beta_{12}^3$  and  $\beta_{12}^1$ , it is clear that in the comoving frame this local contribution takes the same form as in the classical approximation, i.e.  $S_{12}^{N,0}(1 - \beta_{12}^1)$  which simply represents the fraction of photons having not directly escaped the envelope,  $S_{12}^{N,0}(r) = \epsilon_{12}^{N,0}/\alpha_{12}^0$  denoting the source function measured in the comoving frame. Combining these two contributions, we may write

$$J_{12}^{N,0} = S_{12}^{N,0}(1 - \beta_{12}^1) + \beta_{12}^3 I_c^N. \quad (32)$$

Because we only consider the pure scattering of line photons, we have also

$$J_{12}^{N,0} = S_{12}^{N,0} \quad (33)$$

and consequently

$$S_{12}^{N,0} = \frac{\beta_{12}^3}{\beta_{12}^1} I_c^N. \quad (34)$$

As we shall see in Section 7, the numerical values of  $S_{12}^{N,0}$  only slightly depend  $v_\infty$ , even if  $v_\infty$  is relativistic. But, measured in the rest frame, the source function  $S_{12}^N(r, \mu) = S_{12}^{N,0}/\eta^2$  is clearly anisotropic for relativistic velocities, taking higher values along the direction of motion.

## 5 Relativistic expression of the line profile function

In deriving the expression of the line profile function  $E(X)/E_c$ , we first assume—as in Paper II—that the central core is point-like. This constitutes a reasonable approximation for the case of accelerated flows and it allows us to follow step by step a photon emitted from the core with a better understanding of the basic line formation mechanism as well as of the relativistic effects. The expression of the line profile is subsequently, and quite easily, generalized to the case of a central core with finite dimensions.

### 5.1 The point-like core approximation

Let us consider a photon emitted by a point-like core along a radial direction ( $\mu = +1$ ) and with a dimensionless frequency  $X'$ . In the framework of the Sobolev approximation, this photon can only interact with the material at a given point  $r(X')$  in the envelope, fixed by the Doppler relation and the velocity distribution  $\beta(r)$  characterizing the flow. We therefore only consider photons with frequencies  $X'$  in the interval  $[-1, X_{min}]$  corresponding to the distance interval  $[+\infty, r_c]$ , the value of  $X_{min}$  being found from Eq.(12) where we replace  $\beta$  by  $\beta_c = v_c/c$  and  $\mu$  by  $+1$ . If absorbed at  $r(X')$ , this photon of initial frequency  $X'$  can escape the envelope along any direction with  $\mu$  in the interval  $[-1, +1]$ , i.e. with a frequency  $X$  such that  $X(\mu = +1) \leq X \leq X(\mu = -1)$  or

$$X' \leq X \leq -\sqrt{\frac{1-\beta}{1+\beta}} X' = X^R. \quad (35)$$

This frequency interval  $[X', X^R]$  may be up to twice narrower than in the classical case where it is equal to  $[X', -X']$ . Let us note that the variable set  $(X', X)$  is completely equivalent to the set  $(r, \mu)$  and it will be advantageously used in the remainder of this paper.

The probability that this photon of frequency  $X'$  could be absorbed at the distance

$r(X')$  is simply equal to

$$P_a(X') = 1 - e^{-\tau_{12}^r}, \quad (36)$$

$\tau_{12}^r(X')$  denoting the radial optical depth defined by Eq.(26). If absorbed, the photon has a probability

$$P_n(X') = (1 - \beta_{12}^1)^n \quad (37)$$

of undergoing  $n$  other local scatterings. It will finally escape the envelope along directions towards the observer, i.e. within the interval  $[\mu, \mu + d\mu]$  or similarly in the frequency interval  $[X, X + dX]$ , with a probability  $P_e(X', X)dX$ . Because we have assumed complete redistribution in the comoving frame, this latter probability is simply expressed by

$$P_e(X', X)dX = \frac{1 - e^{\tau_{12}}}{\tau_{12}} \frac{dX}{X^R - X'}, \quad (38)$$

$\tau_{12}(X', X)$  denoting the Sobolev optical depth along the observer direction. The factor  $dX/(X^R - X')$ , equal to  $d\mu_0/2 = d\mu/2\eta^2$ , indicates that photons are uniformly reemitted in the frequency interval  $[X', X^R]$ . Because this interval is narrower than in the classical case, the probability  $dX/(X^R - X')$  that a photon scattered at  $r(X')$  is reemitted with a frequency between  $X$  and  $X + dX$  may be significantly increased. Combining these different probabilities, we derive the probability that a photon emitted by the core at a frequency  $X'$  escapes the envelope towards the observer with a frequency in the interval  $[X, X + dX]$  and after an arbitrary number of local scatterings:

$$P(X', X)dX = P_a(X') \left[ \left( 1 + \sum_{n=1}^{\infty} P_n(X') \right) P_e(X', X)dX \right] \quad (39)$$

which reduces to

$$P(X', X) = \frac{1 - e^{-\tau_{12}^r}}{X^R - X'} \frac{1 - e^{-\tau_{12}}}{\beta_{12}^1 \tau_{12}}. \quad (40)$$

Summing over all frequencies  $X'$  contributing to the observed frequency  $X$ , we immediately obtain the contribution to the line profile due to the scattered line photons,

$$\frac{E^S(X)}{E_c} = \int_{X'_{inf}}^{X'_{sup}} P(X', X)dX', \quad (41)$$

assuming that the central core emits photons in constant number over the frequency interval of interest. In absence of limb darkening,  $E_c$  is equal to  $\pi I_c^N$ . The frequency

interval  $[X'_{inf}, X'_{sup}]$  may be found from relations (12), (13) and (35): photons reaching the observer with a frequency  $X$  can only originate, if  $X \leq 0$ , from scattering of photons with an initial frequency  $X'$  in the interval  $[-1, \min(X, X_{min})]$  and, if  $X > 0$ , from the scattering of photons with a frequency  $X'$  in the interval  $[-1, \min(X'_c, X_{min})]$ , where  $X'_c$  is solution of  $\mu(X'_c, X) = -1$ , i.e.  $X'_c = -X/(1 + X - X/X_\infty^R)$ . Let us recall that for frequencies  $X > X_\infty^R$  there are no scattered photons ( $E^S(X)/E_c = 0$ ) so that the scattered contribution becomes very asymmetrical for increasing values of  $\beta_\infty$ .

Finally, the total line profile function  $E(X)/E_c$  is obtained by adding the contribution  $E^S(X)/E_c$  due to the scattered line photons and the contribution  $E^A(X)/E_c$  due to photons reaching directly the observer, this latter contribution being expressed by

$$\begin{aligned} \frac{E^A(X)}{E_c} &= 1 - P_a(X) \quad \text{if } X \leq X_{min} \\ \text{and} \quad \frac{E^A(X)}{E_c} &= 1 \quad \text{if } X > X_{min}. \end{aligned} \quad (42)$$

## 5.2 The central core with finite dimensions

For a central core having finite dimensions, one must consider that back-scattered photons may strike it and that these cannot reach the observer any longer. This is the well-known occultation effect. In addition, photons originating from the core are not only emitted along radial directions ( $\mu = +1$ ) but also along inclined ones. We call this the inclination effect (cfr. Paper III).

Considering first the contribution  $E^S(X)/E_c$  due to scattered photons, we take into account the occultation effect by replacing, for positive  $X$  values, the frequency limit  $X'_{sup}$  by  $X''_{sup} = \min(X''_c, X_{min})$  where  $X''_c$  is solution of  $\mu_c(X''_c, X) = -1 + 2W(r(X''_c))$ . It is also clear that in Eq.(39), the factor  $P_a(X')$  must be replaced by a new quantity  $P'_a(X')$  which accounts for the fraction of photons emitted by the core along non-radial directions. Recalling that  $P'_a(X')I_c^N$  and  $\beta_{12}^3 I_c^N$  are respectively proportional to the number of core photons absorbed at  $r(X')$  and to the number of core photons arriving at  $r(X')$ , we have the relation

$$\frac{P'_a(X')}{P_a(X')} = \frac{\beta_{12}^3(r(X'))}{\beta_{12}^3(r/r_c \rightarrow \infty)} \quad (43)$$

which reduces to

$$P'_a(X') = \beta_{12}^3(X') \tau_{12}^r(X') 4L^2(X') \quad (44)$$

where  $L = r/r_c$ . The contribution due to scattered photons can therefore be written

$$\frac{E^S(X)}{E_c} = \int_{X'_{inf}}^{X'_{sup}} \frac{\beta_{12}^3}{\beta_{12}^1} \frac{1 - e^{-\tau_{12}}}{\tau_{12}} \frac{4L^2 \tau_{12}^r}{X^R - X'} dX' . \quad (45)$$

By integrating over the core surface, we easily show (cfr. Paper III) that the contribution  $E^A(X)/E_c$  due to photons reaching the observer without having suffered any scattering may be generalized to

$$\begin{aligned} \frac{E^A(X)}{E_c} &= 2 \int_0^1 e^{-\tau_{12}(X', \mu)} \mu_* d\mu_* & \text{if } X < X_* \\ \text{and} \quad \frac{E^A(X)}{E_c} &= 1 & \text{if } X \geq X_* , \end{aligned} \quad (46)$$

where  $X'$  is solution of  $1 - (1 - \mu^2(X', X))L^2(X') = \mu_*^2$ . In this relation, the value of  $\tau_{12}$  must be set to zero if no solution of  $X' \leq X_{min}$  can be found. The frequency  $X_*$ , solution of  $\mu(X_{min}, X_*) = 0$ , is explicitly expressed by

$$X_* = \frac{B_\infty X_{min}^2}{[(1 - B_\infty X_{min})^2 + 1]} \geq 0 \quad (47)$$

where, for simplicity, we have introduced

$$B_\infty = \frac{\nu_{max} - \nu_{12}^0}{\nu_{12}^0} = \sqrt{\frac{1 + \beta_\infty}{1 - \beta_\infty}} - 1 . \quad (48)$$

It is interesting to note that photons with positive  $X$  frequencies can be absorbed in the envelope. This relativistic effect ( $X_* = 0$  in the classical limit) remains small and needs high  $|X_{min}|$  values in order to become significant. This effect is implicitly included in the expression of the emission profile (Eq.(45)).

## 6 The first order moment of unsaturated relativistic P Cygni line profiles

The first order moment of a P Cygni line profile has been introduced by Castor et al. (1981) as a powerful tool for deriving mass-loss rates. Subsequent work by Surdej



(1982, 1983b) has shown that a unique linearity relation does actually exist between the first order moment of an unsaturated line profile and the fractional mass-loss rate, irrespective of various physical (opacity distribution, collisions, limb darkening, etc.) and geometrical (velocity law, rotation, etc.) conditions prevailing in the expanding envelope as well as of any Sobolev-type approximations used for the transfer of line radiation. In this Section we investigate the behavior of the first order moment when the flow becomes relativistic.

The  $n^{\text{th}}$  order moment of a line profile can be defined as

$$W_n^R = \left( \frac{1}{\nu_{max} - \nu_{12}^0} \right)^{n+1} \int_{-\infty}^{+\infty} \left( \frac{E(\nu)}{E_c} - 1 \right) (\nu_{12}^0 - \nu)^n d\nu, \quad (49)$$

an expression which, in terms of the dimensionless frequency  $X$ , easily reduces to

$$W_n^R = \int_{-1}^{X^R} \left( \frac{E(X)}{E_c} - 1 \right) X^n dX. \quad (50)$$

In the low velocity regime, this definition of  $W_n^R$  is exactly equivalent to that of Castor et al. (1981).

Let us now evaluate the first order moment of *unsaturated* line profiles considering first the point-like core approximation. For such profiles, the first order moment will be denoted by  $W_1^{R,0}$ .

## 6.1 The point-like core approximation

The expression of the moment  $W_1^{R,0}$  can be easily obtained by combining Eqs. (41), (42) and (50). We nevertheless prefer to follow a rather different approach which provides us with a better understanding of the moment properties.

Up to now, we have evaluated the line profile expression by summing at each frequency  $X$  the different fractions of line photons reaching an observer after having undergone an arbitrary number of scatterings, i.e. we have considered the envelope as a juxtaposition of surfaces of equal frequency  $X$ . On the other hand, we can imagine the envelope as an assembly of shells of radius  $X'$  and thickness  $\Delta X'$ . Because the Sobolev transfer is purely local, the line profile formed in the whole envelope is nothing else than the sum of the profiles due to such shells. The same applies for the moment

$W_1^{R,0}$  and we can write

$$W_1^{R,0} = \int_{-1}^{X_{min}} W_1^{R,0}(X') dX', \quad (51)$$

$W_1^{R,0}(X') dX'$  representing the first order moment of the profile formed in the shell of radius  $X'$  and thickness  $dX'$ . If the envelope is optically thin, the profile due to a shell is very simple (see Fig. 5a) and the corresponding moment  $W_1^{R,0}(X') dX'$  can be evaluated by simply summing up elementary surfaces. From Fig. 5b, we obtain

$$W_1^{R,0}(X') \Delta X' = \tau_{12}^r |X'| \Delta X' - \frac{\tau_{12}^r \Delta X'}{X^R - X'} |X'| \frac{|X'|}{2} + \frac{\tau_{12}^r \Delta X'}{X^R - X'} X^R \frac{X^R}{2} \quad (52)$$

or

$$W_1^{R,0}(X') = \tau_{12}^r \frac{X^R - X'}{2}, \quad (53)$$

giving finally

$$W_1^{R,0} = \int_{-1}^{X_{min}} \tau_{12}^r(X') \frac{(X^R - X')}{2} dX'. \quad (54)$$

It is interesting to note that the detailed expression of the line profile (Eqs. (41), (42)) is not necessary in order to calculate the moment  $W_1^{R,0}$  in the optically thin approximation. We also clearly see that the difference between this expression and the classical one (see Paper III) arises from the asymmetry of the relativistic emission profile.

Let us now develop the expression of the optical depth  $\tau_{12}^r(X')$  given by Eq. (26). Neglecting the stimulated emission correction, the opacity  $\alpha_{12}^0$  may be written

$$\alpha_{12}^0 = N_1^0 \left( \frac{\pi e^2}{mc} \right)_0 f_{12}^0, \quad (55)$$

or

$$\alpha_{12}^0 = n_1 A(el) N_{tot}^0 \left( \frac{\pi e^2}{mc} \right)_0 f_{12}^0, \quad (56)$$

where  $N_1^0$  represents the number of atoms in the lower state 1 measured per unit of proper volume,  $f_{12}^0$  the oscillator strength,  $A(el)$  the abundance of the element,  $n_1$  the fractional abundance of the element's atoms which are in the lower state and  $N_{tot}^0$

the total number of nuclei measured per unit of proper volume. The other quantities have their usual meaning. The suffix zero reminds us that the relevant quantities are defined in the comoving frame. If there is conservation of the total nucleus number, the equation of continuity leads to the relation

$$4\pi r^2 v(r) (N_{tot}^0 \bar{\mu} M_{amu}^0) \gamma = \dot{M}, \quad (57)$$

where  $\dot{M}$  denotes the proper mass-loss rate,  $\bar{\mu}$  the mean atomic weight of the nuclei and  $M_{amu}^0$  the unit of atomic mass. The Lorentz factor  $\gamma$  appears in Eq. (57) because the volume of a fluid element ( $\propto 1/N_{tot}^0$ ) is lower when measured in the observer frame. Combining these relations with the definitions of  $X$ ,  $X'$  and  $L$ , we finally obtain

$$\tau_{12}^r = K_{12}^0 \dot{M} n_1 \left(\frac{1}{cB_\infty}\right)^2 \frac{2 dL}{L^2 (X' - X^R) dX'} \quad (58)$$

where

$$K_{12}^0 = \left(\frac{\pi e^2}{mc}\right)_0 f_{12}^0 \lambda_{12}^0 \frac{A(el)}{4\pi \bar{\mu} M_{amu}^0 r_c}. \quad (59)$$

The moment  $W_1^{R,0}$  can therefore be written

$$W_1^{R,0} = K_{12}^0 \frac{\dot{M}}{(cB_\infty)^2} \int_1^\infty n_1 \frac{dL}{L^2}, \quad (60)$$

showing us that the linear relation between the mass-loss rate and the first order moment of an unsaturated P Cygni line profile still holds in the relativistic case.

## 6.2 The central core with finite dimensions

If we consider the finite dimensions of the central core, we can write the first order moment as

$$W_1^{R,0} = \int_{-1}^{X_{min}} \tau_{12}^r \frac{(X^R - X')}{2} \Omega(X') dX', \quad (61)$$

where the factor  $\Omega(X')$  mainly accounts for the part of the scattered line photons which do not reach the observer due to occultation by the core. The expression of  $\Omega(X')$  is fairly complex. It can be derived by replacing in the moment definition (50) the line profile by its expression (45),(46) where we impose  $\tau_{12} \ll 1$ . We find

$$\Omega(X') = 4L^2 \left(\frac{1 - B_\infty X'}{2 - B_\infty X'}\right)^2 \left[W \frac{X_c^2}{X'^2} - W - 2 \frac{S_1(X')}{X'^2}\right] \quad (62)$$

where

$$S_1(X') = \frac{1}{B_\infty^2} \left[ \ln\left(\frac{1 - B_\infty X_{|c|}}{1 - B_\infty X'}\right) + \frac{1}{(1 - B_\infty X_{|c|})} - \frac{1}{(1 - B_\infty X')} \right], \quad (63)$$

with

$$X_c = \frac{1}{B_\infty} \left[ 1 - (1 - B_\infty X') \frac{1 - \beta}{1 + (1 - 2W)\beta} \right] \quad (64)$$

and

$$X_{|c|} = \frac{1}{B_\infty} \left[ 1 - (1 - B_\infty X') \frac{1 - \beta}{1 - (1 - 2W)\beta} \right]. \quad (65)$$

Let us recall that in the classical limit the factor  $\Omega(X')$  is simply equal to  $1 - W$  (see Paper III).

If we now replace  $\tau_{12}^r$  by its expression (58) and define

$$\langle n_1 \rangle = \frac{\int_1^\infty n_1 \frac{\Omega}{L^2} dL}{\int_1^\infty \frac{\Omega}{L^2} dL}, \quad (66)$$

$$q^c = \int_1^\infty \frac{\Omega}{L^2} dL, \quad (67)$$

we obtain the useful relation

$$\dot{M} \langle n_1 \rangle = W_1^{R,0} \frac{(B_\infty c)^2}{q^c K_{12}^0}. \quad (68)$$

This general relation allows the immediate determination of mass-loss rates from the measurement of the moment  $W_1^{R,0}$  of unsaturated line profiles, if the average ionization fraction  $\langle n_1 \rangle$  is known. In principle, the normalisation factor  $q^c$  depends on both  $\beta_\infty$  and the type of velocity law but, as we can see from Table 1, this dependence is negligible for the considered models. Thus, as in the classical limit, Eq. (68) holds within a good approximation irrespective of the kind of velocity law chosen to represent the expanding atmosphere. In addition, the relative constancy of  $q^c$  confirms the fact that the moment  $W_1^{R,0}$  constitutes a useful physical parameter.

If we now want to evaluate mass-loss rates from slightly or strongly saturated profiles we have to use  $W_1^R - W_1^{R,0}$  diagrams. Such diagrams are constructed numerically in the next Section.

## 7 Numerical applications

We present here a few examples of typical source functions, P Cygni line profiles and  $W_1^R - W_1^{R,0}$  diagrams computed when the velocities become comparable to that of light.

In all these applications, we use the first order moment  $W_1^{R,0}$  to parametrize the opacity. From Eqs. (58) and (68), the radial optical depth  $\tau_{12}^r$  can be written

$$\tau_{12}^r = W_1^{R,0} \frac{n_1}{q^c < n_1 >} \frac{2 dL}{L^2 (X' - X^R) dX'} \quad (69)$$

or

$$\tau_{12}^r = \frac{W_1^{R,0}}{q^c < n_1 >} \tau^r(v/v_\infty), \quad (70)$$

$\tau^r(v/v_\infty)$  representing the dependence of the opacity distribution as a function of  $v/v_\infty$ . The factor  $< n_1 >$  is evaluated by making Eqs. (61) and (70) consistent. In the remainder, we adopt the following opacity laws:

$$\begin{aligned} (\beta) \quad \tau^r(v/v_\infty) &= 1 - v/v_\infty & (71) \\ (\gamma) \quad \tau^r(v/v_\infty) &= 1 \\ (\delta) \quad \tau^r(v/v_\infty) &= (1 - v/v_\infty)^{1/2} \\ (\epsilon) \quad \tau^r(v/v_\infty) &= (1 - v/v_\infty)^2 \end{aligned}$$

which are of the form  $\tau^r(v/v_\infty) = (1 - v/v_\infty)^\gamma$ . It is generally considered that this type of opacity laws provides a good description of the expanding atmospheres around early-type stars (Castor and Lamers, 1979; Garmany et al., 1981). We also adopt the following velocity distributions:

$$\begin{aligned} (A) \quad v(L) &= v_c + (v_\infty - v_c)(1 - 1/\sqrt{L}) & (72) \\ (B) \quad v(L) &= v_c + (v_\infty - v_c)(1 - 1/L) \\ (C) \quad v(L) &= v_\infty \sqrt{1 - (1 - v_c^2/v_\infty^2)/L} \end{aligned}$$

which are also thought to encompass most of the observed velocity fields prevailing in expanding envelopes (Castor et al., 1975; Castor and Lamers, 1979; Olson, 1981; Olson and Ebbets, 1981). The various combinations of the different opacity and velocity laws

lead to twelve distinct models. In consistency with our previous papers, we shall label them in the form (A. $\beta$ ) for example, where A denotes the type of velocity law and  $\beta$  the type of opacity distribution. Finally, all our calculations have been done using four values of  $\beta_\infty$ : 0.01, 0.2, 0.5 and 0.8, the first one corresponding to the classical limit. In all cases (except for Figs. 7 g-h), we also take  $\beta_c/\beta_\infty = 0.01$ .

The source function  $S_{12}^{N,0}$  is illustrated in Figs. 6a,b for two different values of the parameter  $W_1^{R,0}$ . As we can see, the changes with  $\beta_\infty$  remain reasonably small.

Figs. 7a-h illustrate typical P Cygni line profiles computed from Eqs. (45) and (46). We immediately notice that the profiles now depend significantly on the value of the terminal velocity (while they do not in the classical theory) but that rather high values of  $\beta_\infty$  are nevertheless needed in order to cause severe modifications. These modifications —a shortening of the red emission wing accompanied by an increase of the emission line intensity— are mainly due to the variation of the radial opacity  $\tau_{12}^r$  with  $\beta_\infty$  (via the factor  $\langle n_1 \rangle$  in Eq.(70)) and to the redistribution of photons in a frequency interval which gets narrower and more asymmetrical as  $\beta_\infty$  is increased. This latter effect is definitely the dominant one, the opacity changes with  $\beta_\infty$  remaining small. In fact,  $\langle n_1 \rangle$  does not vary by more than a factor three in the considered  $\beta_\infty$  range (see Table 2). We should also like to point out that for high values of  $\beta_c$  the maximum of the emission peak may appear redshifted (Fig. 7h).

Let us now consider the  $W_1^R - W_1^{R,0}$  diagrams (see Fig. 8). By simply reporting in such diagrams the measured moment  $W_1^R$  of an observed P Cygni line profile, we can derive the parameter  $W_1^{R,0}$  and consequently, via Eq. (68), the fractional mass-loss rate (or a lower limit if the line profile is saturated). This method is especially useful for the analysis of unresolved line profiles. For more details, we refer the reader to our previous papers (Surdej, 1983a; Hutsemékers and Surdej, 1987; Surdej and Hutsemékers, 1989). In the present application, we have computed line profiles for different values of  $W_1^{R,0}$  and via Eq. (50), their moment  $W_1^R$ . The results are reported in Fig. 8a for two extreme models. The  $W_1^R - W_1^{R,0}$  curves show a clear dependence on  $\beta_\infty$ , especially for high values of  $W_1^{R,0}$ , so that we need in principle one diagram for each value of the terminal velocity. Again, this behavior is mainly caused by the emission profile

asymmetry. We can nevertheless minimize this dependence by normalizing the curves with respect to the asymptotic value  $W_1^{R,t}$  of the moment calculated in the optically thick approximation, i.e.  $W_1^{R,0} \rightarrow \infty$ . The values of the moment  $W_1^{R,t}$  are reported in Table 3 considering the different models. The normalized curves, illustrated in Fig. 8b, are definitely less affected by the value of  $\beta_\infty$  so that one diagram of this type may be sufficient to evaluate mass-loss rates with a reasonable degree of accuracy. Normalized diagrams computed for the twelve possible models are illustrated in Fig. 9a-d. As in the classical limit, the curves are mainly dependent on the opacity distribution.

## 8 Discussion and conclusions

We have learnt in the previous sections how it was important to include the relativistic corrections in the radiative transfer in order to calculate correctly the source and the line profile functions for large values of  $\beta_\infty$ .

One of the most unexpected effects is certainly the appearance of distant interactions in the envelope when the velocities approach that of light. As in the case of decelerated flows (cfr. Surdej, 1978), these interactions may be of great importance when evaluating the amplitude of the radiative forces. Even if they can be neglected most of the time for the type of velocity laws considered here, they can be of much greater importance for other velocity distributions, specially those characterized by very high velocity gradients.

As we have seen, the P Cygni line profiles formed in relativistically expanding envelopes also suffer important modifications mainly due to the redistribution of photons in a frequency interval whose asymmetry is directly related to the relativistic expression of the Doppler effect. Before comparing the relativistic profiles with the observed ones, it is necessary to rebin the latter ones in a dimensionless frequency scale ( $X$ ), the asymmetry of the profiles being different on a wavelength scale (i.e. the most extended wing becomes the red one <sup>4</sup>). Up to now, the highest expansion velocities (0.2c)

<sup>4</sup>More precisely, if we define the dimensionless wavelength  $Y = -(\lambda - \lambda_{12}^0)/(\lambda_{min} - \lambda_{12}^0)$ , equivalent to the dimensionless frequency  $X$  (Eq. (11)) in the classical limit, we easily see that the line profile

measured from the most extended part of a P Cygni line profile have been reported from the spectra of BAL quasars. For such velocities, the profile modifications remain small compared to the classical case especially if we remember that other effects, like turbulence, can alter the profiles to a larger extent (see the discussion by Surdej and Hutsemékers, 1987). Nevertheless, even for  $\beta_\infty = 0.2$ , the relativistic corrections do reveal noticeable effects (cf. Fig. (7)).

In spite of the large differences seen for  $\beta_\infty \geq 0.2$ , it is quite surprising that the linear relation between the mass-loss rate and the first order moment of unsaturated line profiles still holds in the relativistic case. This general relation is therefore independent of many physical and geometrical approximations. Also, the normalized  $W_1^R - W_1^{R,0}$  diagrams only slightly depend on the terminal velocity so that, if the adopted models actually represent realistic physical conditions prevailing in expanding atmospheres, they provide a powerful tool for deriving mass-loss rates. This is especially true from a statistical point-of-view as well as in the context of the analysis of unresolved line profiles.

Throughout this paper, we have introduced limiting approximations. One of the most restrictive is certainly the hypothesis that the opacity and velocity laws representing the expanding envelopes in the classical limit are still adequate in the relativistic case. Only a detailed dynamical analysis could check this hypothesis which is as important as the effects of distant interactions. Due to these approximations, this paper is nothing more than a first step towards a better understanding of the formation of P Cygni line profiles in relativistically expanding atmospheres.

## Acknowledgements

It is a pleasure to thank here the referee for his constructive comments. Part of this work was done while DH was a research assistant at the National Funds for Scientific Research (FNRS, Liège Institute of Astrophysics, Belgium).

---

is formed in the wavelength interval  $[-1, Y_\infty^R = 1/X_\infty^R]$  which is greater than the frequency interval given by Eq. (13).



## References

- Beals, C.: 1929, *Monthly Notices Roy. Astron. Soc.*, **90**, 202
- Beals, C.: 1931, *Monthly Notices Roy. Astron. Soc.*, **91**, 966
- Castor, J.I.: 1970, *Monthly Notices Roy. Astron. Soc.*, **149**, 111
- Castor, J.I., Abbott, D.C., Klein, R.I.: 1975, *Astrophys. J.*, **195**, 157
- Castor, J.I., Lamers, H.J.G.L.M.: 1979, *Astrophys. J. Suppl.*, **39**, 481
- Castor, J.I., Lutz, J.H., Seaton, M.J.: 1981, *Monthly Notices Roy. Astron. Soc.*, **194**, 547
- Garmany, C.D., Olson, G.L., Conti, P.S., van Steenberg, M.E.: 1981, *Astrophys. J.*, **250**, 660
- Hutsemékers, D., Surdej, J.: 1987, *Astron. Astrophys.*, **173**, 101
- Hutsemékers, D., Surdej, J.: 1989, *Astron. Astrophys.*, **219**, 237
- Lucy, L.: 1971, *Astrophys. J.*, **163**, 5
- Mihalas, D.: 1978, *Stellar Atmospheres*, Freeman.
- Mihalas, D.: 1980, *Astrophys. J.*, **237**, 574
- Mihalas, D., Mihalas, B.W.: 1984, *Foundations of Radiation Hydrodynamics*, Oxford.
- Olson G.L.: 1981, *Astrophys. J.*, **245**, 1054
- Olson G.L., Ebbets D.: 1981, *Astrophys. J.*, **248**, 1021
- Rybicki, G.B., Hummer, D.G.: 1978, *Astrophys. J.*, **219**, 654
- Sobolev, V.V.: 1947, *Dnižuščiesja Oboločki Zvezd*, Leningrad, transl. Moving envelopes of stars; translated from Russian by S. Gaposchkin, Harvard University Press, Cambridge, Mass., 1960

Sobolev, V.V.: 1958, in V.A. Ambartsumyan (ed.), *Theoretical Astrophysics*, Chapter 28, Pergamon Press Ltd., London

Surdej, J.: 1977, *Astron. Astrophys.*, **60**, 303 (Paper I)

Surdej, J.: 1978, *Astron. Astrophys.*, **62**, 135

Surdej, J.: 1979, *Astron. Astrophys.*, **73**, 1 (Paper II)

Surdej, J.: 1982, *Astrophys. Space Sci.*, **88**, 31 (Paper III)

Surdej, J.: 1983a, *Astron. Astrophys.*, **127**, 304

Surdej, J.: 1983b, *Astrophys. Space Sci.*, **90**, 299

Surdej, J., Hutsemékers, D.: 1987, *Astron. Astrophys.*, **177**, 42

Surdej, J., Hutsemékers, D.: 1989, *Astron. Astrophys.*, in press

Thomas, L.: 1930, *Quart. J. Math.*, **1**, 239

Weiler, K.W., Sramek, R.A.: 1988, *Ann. Rev. Astron. Astrophysics*, **26**, 295

Weymann, R., Foltz, C.: 1983, in the proceedings of the 24th Liège International Astrophysical Colloquium, "Quasars and Gravitational Lenses", p. 538

**Damien Hutsemékers:** European Southern Observatory, La Silla, Casilla 19001, Santiago 19, Chile

**Jean Surdej:** Institut d'Astrophysique, Université de Liège, 5 av. de Cointe, B-4200 Cointe-Ougrée, Belgium

Table 1: *The factor  $q^c$  as a function of  $\beta_\infty$  for the three velocity laws*

$\beta_\infty$	velocity law		
	A	B	C
0.01	0.89	0.89	0.89
0.20	0.89	0.89	0.89
0.50	0.89	0.88	0.86
0.80	0.88	0.86	0.81

Table 2: The ratio  $\langle n_1 \rangle / \langle n_1 \rangle_{\text{classical}}$  as a function of  $\beta_\infty$  for the different models

model	$\beta_\infty$		
	0.2	0.5	0.8
A. $\beta$	0.90	0.71	0.42
A. $\gamma$	0.94	0.85	0.74
A. $\delta$	0.92	0.77	0.54
A. $\epsilon$	0.88	0.64	0.32
B. $\beta$	0.90	0.71	0.43
B. $\gamma$	0.94	0.86	0.76
B. $\delta$	0.92	0.77	0.55
B. $\epsilon$	0.88	0.64	0.32
C. $\beta$	0.90	0.71	0.44
C. $\gamma$	0.95	0.87	0.80
C. $\delta$	0.92	0.78	0.57
C. $\epsilon$	0.87	0.64	0.32

Table 3:  $\log W_1^{R,t}$  as a function of  $\beta_\infty$  for the three velocity laws

$\beta_\infty$	velocity law		
	A	B	C
0.01	-0.31	-0.32	-0.35
0.20	-0.34	-0.36	-0.38
0.50	-0.40	-0.42	-0.44
0.80	-0.47	-0.49	-0.51

## Captions for figures

- **Figure 1 a-d:** Evolution of the surfaces of equal frequency  $X$  as a function of  $\beta_\infty = 0.01$ (a, cf. the classical case), 0.2(b), 0.5(c) and 0.8(d) for a typical velocity law (B of Eq. (72)). The surfaces actually extend to infinity although for presentation they have been limited by boxes of  $80 \times 80$  in units of  $r_c$ . Let us also recall that no photons are emitted at frequencies  $X > X_\infty^R$  where  $X_\infty^R = 1.0$ (a), 0.82(b), 0.58(c) and 0.33(d).
- **Figure 2 a-d:** Like in Fig. 1 a-d, we see the evolution of the surfaces of equal frequency  $X$  as a function of  $\beta_\infty = 0.01$ (a), 0.2(b), 0.8(c) and 0.98(d) but for the velocity law  $v(r)/v_\infty = r/r_{max}$  where  $r_{max}$ , the maximum radial dimension of the envelope, is taken equal to  $10 r_c$ . The values of  $X_\infty^R$  are respectively 1.0(a), 0.82(b), 0.58(c) and 0.10(d). The appearance of distant radiative interactions in the moving envelope are clearly visible on (d).
- **Figure 3:** For a rest observer, a photon emitted at the point  $s_E$  is seen to travel along a direction with abscissae  $s$ . At each point of the trajectory, we can associate a reference frame moving with a constant velocity  $v[r(s)]$  and coinciding instantaneously with the fluid at this point.
- **Figure 4:** The ratio  $\tau_{12}(r, \mu)/\tau_{12}^r(r)$  is represented here in a polar diagram for different values of  $\beta_\infty$  (0.01, 0.2, 0.5 and 0.8). It is calculated at the distance  $r = 5r_c$  from the central core for a typical velocity law (B of Eq. (72)). The direction of motion is indicated. For  $\mu = \cos \theta = 1$ , we have always  $\tau_{12}/\tau_{12}^r = 1$  while in the opposite direction ( $\mu = -1$ ), this ratio depends strongly on the value of  $\beta_\infty$ .
- **Figure 5:** The first figure (a) illustrates schematically the very simple line profile issued from an optically thin shell of radius  $X'$  and thickness  $\Delta X'$  ( $\Delta X'$  is in reality much smaller than represented). Part of the photons emitted by the point-like core are absorbed at the frequency  $X'$  and reemitted in the frequency interval  $[X', X^R]$  (cfr. Eq. (35)). The material being optically thin, the area of

the absorption part of the line profile is equal to  $\tau_{12}^r(X')\Delta X'$ . Because the photon number is conserved and because the core is assumed point-like,  $\tau_{12}^r(X')\Delta X'$  also represents the area of the emission line profile. Fig. (b) represents schematically the line profile multiplied by  $|X|$ , as in the first order moment definition (Eq. (50)). This moment can be calculated by simply summing up the elementary surfaces (see text).

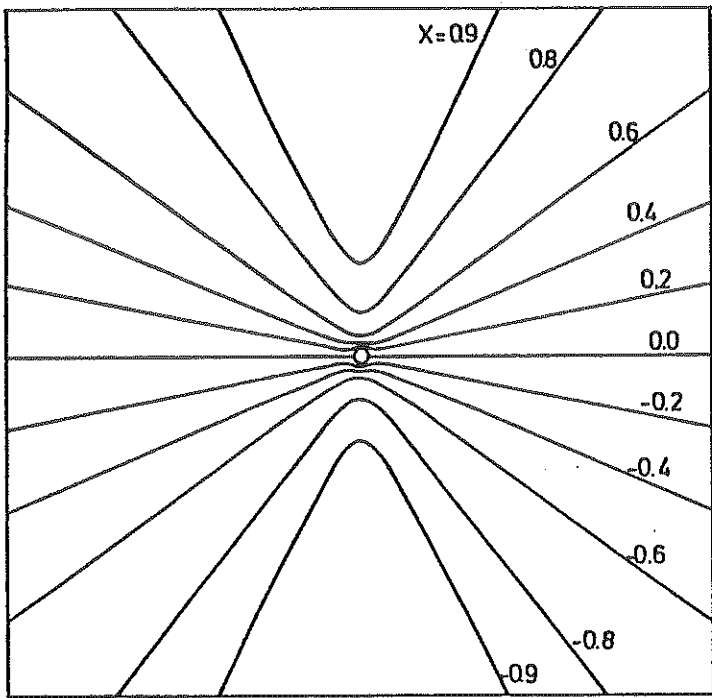
- **Figure 6 a,b:** Examples of source functions  $S_{12}^{N,0}$  multiplied by  $L^2$  to remove the main geometrical effect. They are computed for the  $\beta_\infty$  values 0.01, 0.2, 0.5 and 0.8 and for the typical model (B. $\beta$ ). The parameter  $W_1^{R,0}$  has been taken equal to 1.0 (a) and 0.1 (b).
- **Figure 7 a-h:** Examples of relativistic P Cygni line profiles computed for  $\beta_\infty$  values of 0.01, 0.2, 0.5 and 0.8. Their characteristics are given below. Figs. (b) and (d) illustrate the absorption and emission components of the profiles shown in Figs. (a) and (c).

figure	model	$W_1^{R,0}$	$\beta_c/\beta_\infty$
a	B. $\beta$	1.0	0.01
c	B. $\beta$	0.1	0.01
e	C. $\beta$	1.0	0.01
f	B. $\varepsilon$	1.0	0.01
g	B. $\beta$	1.0	0.20
h	B. $\beta$	1.0	0.90

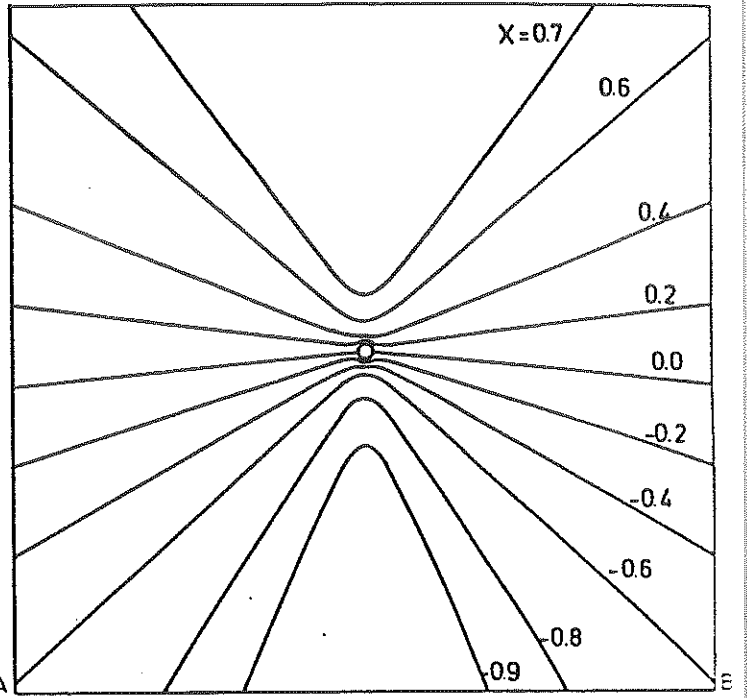
- **Figure 8 a,b:** The first figure illustrates the behavior of the  $W_1^R - W_1^{R,0}$  curves as a function of  $\beta_\infty$  for two extreme models. As  $\beta_\infty$  increases, the asymptotic limit  $W_1^{R,t}$  decreases. The same curves are illustrated in (b) but normalized by the moment  $W_1^{R,t}$  whose values are given in Table 3.
- **Figure 9 a-d:** Normalized  $W_1^R - W_1^{R,0}$  diagrams are represented here for values of  $\beta_\infty$  respectively equal to 0.01 (a), 0.2 (b), 0.5 (c) and 0.8 (d). They have been computed for the twelve considered models. Since the relative positions of the

different curves remain the same, we have only indicated their label in the last figure.

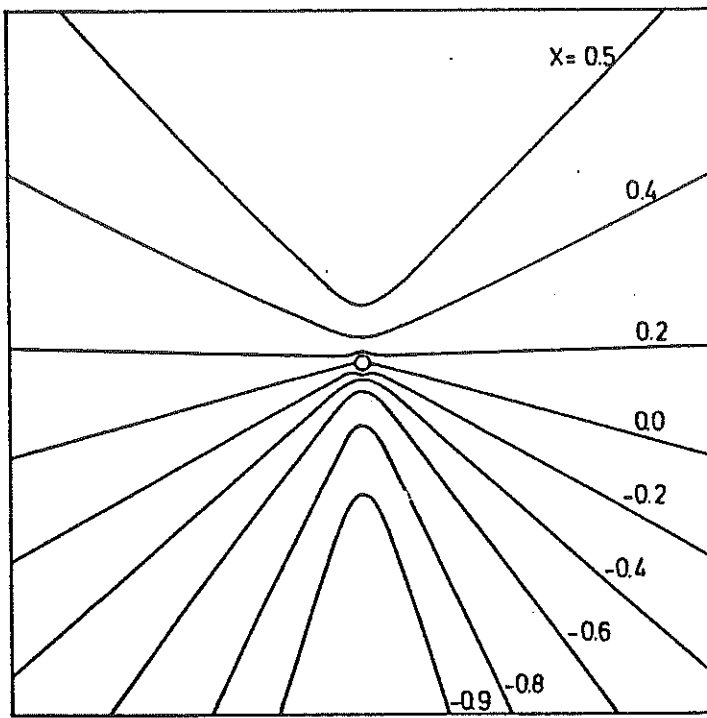




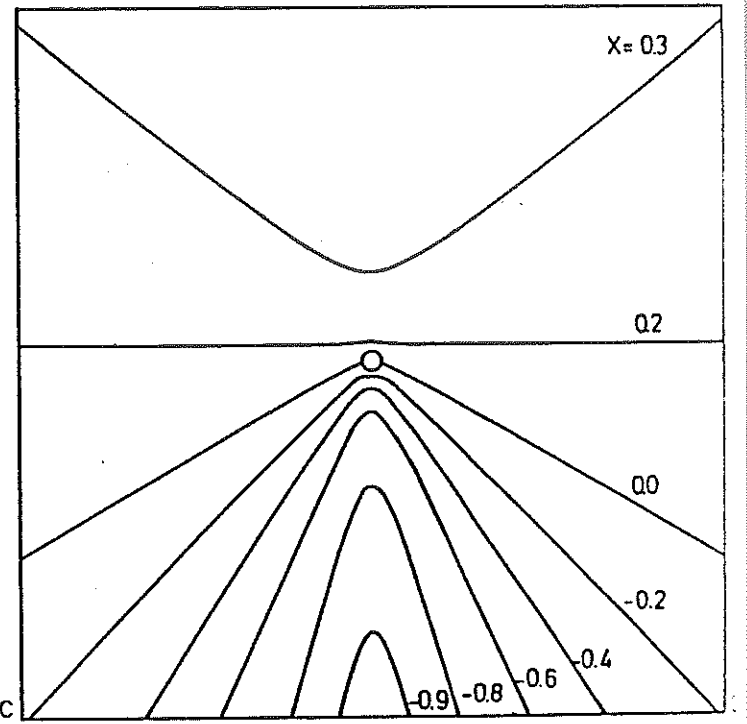
Observer



Observer



Observer



Observer

Fig. 1

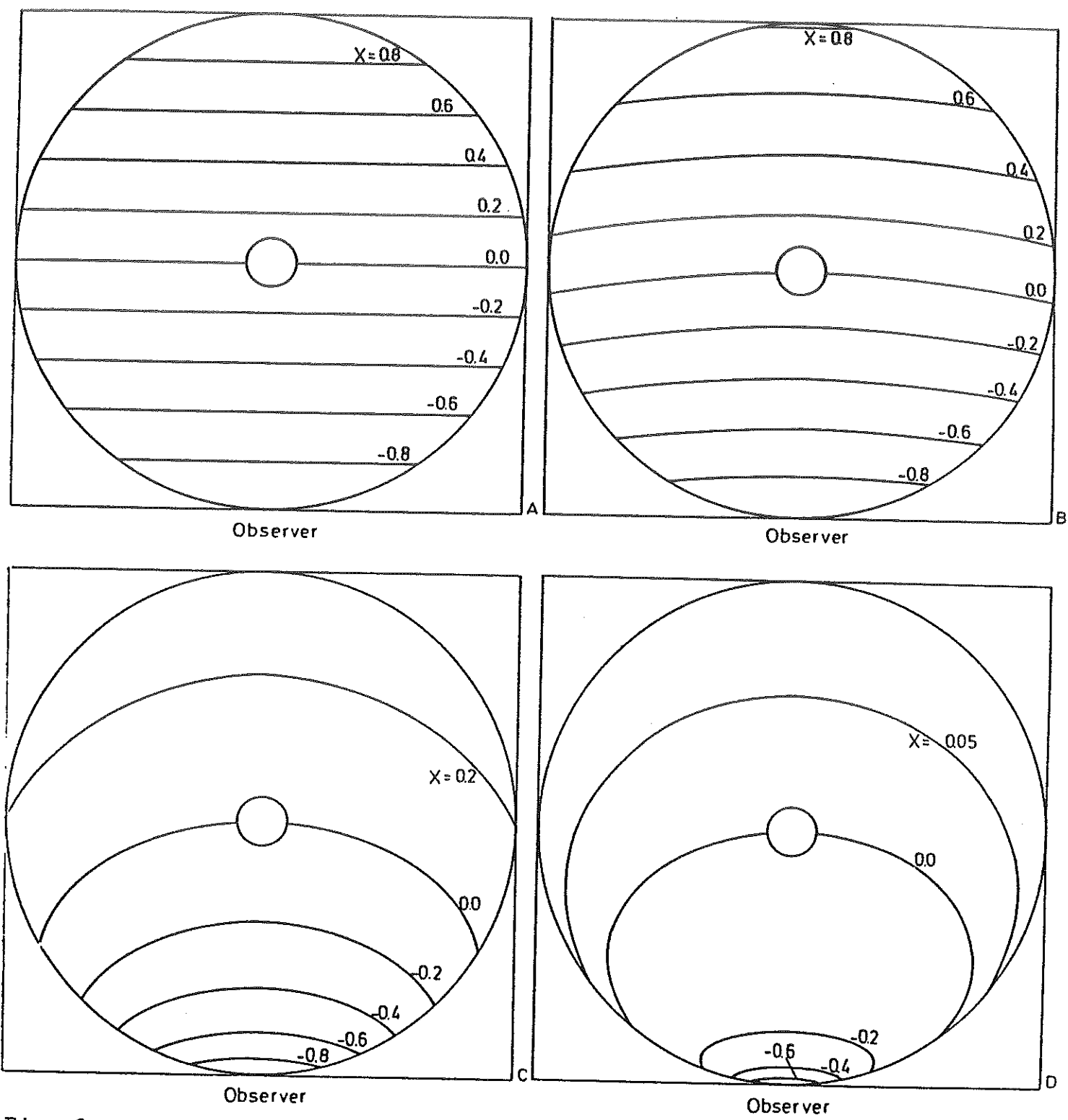


Fig. 2

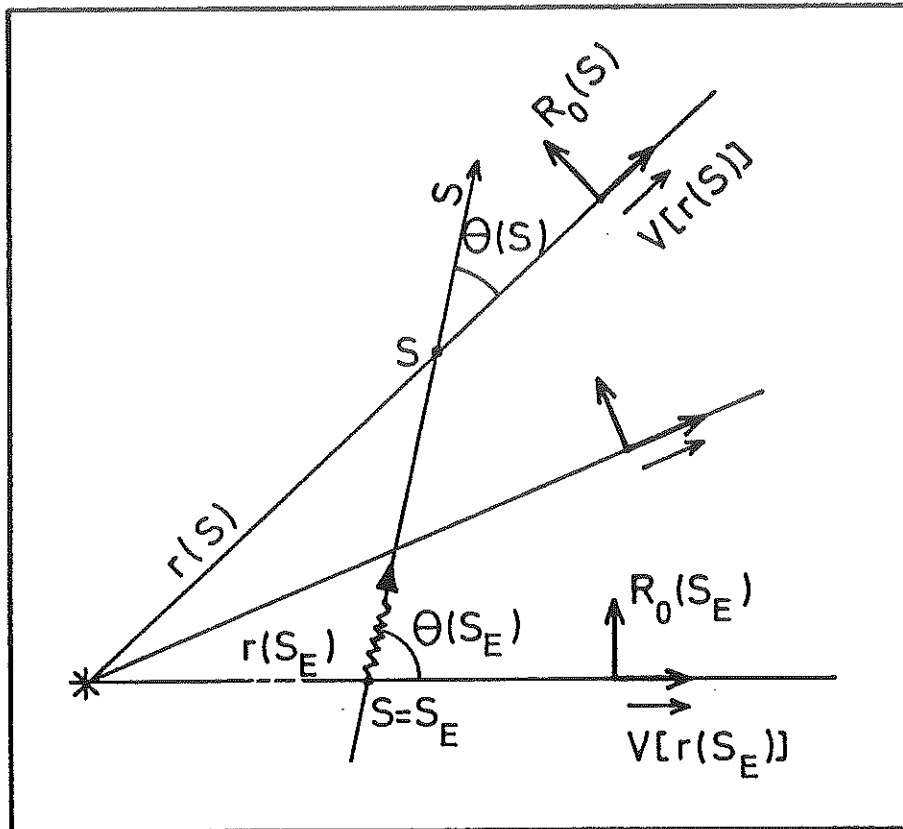


Fig. 3

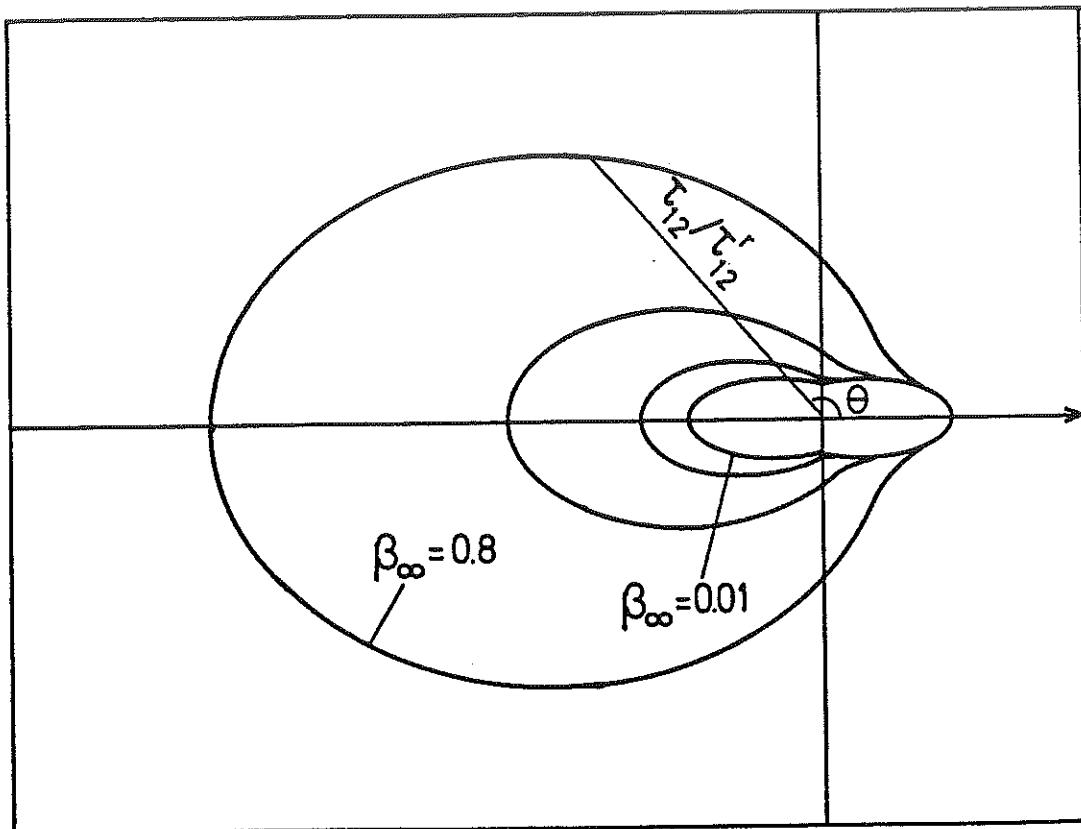


Fig. 4

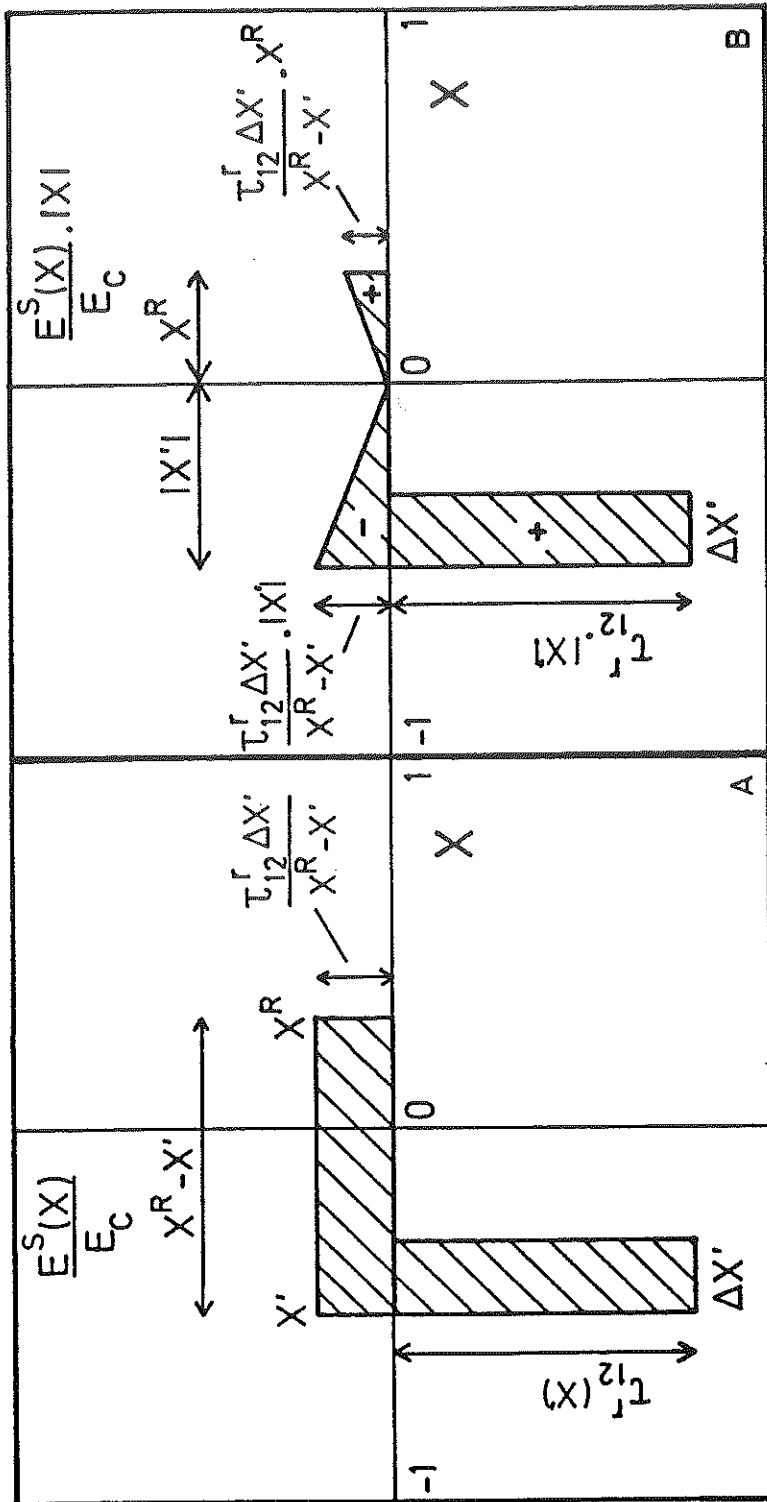


Fig. 5a

Fig. 5b

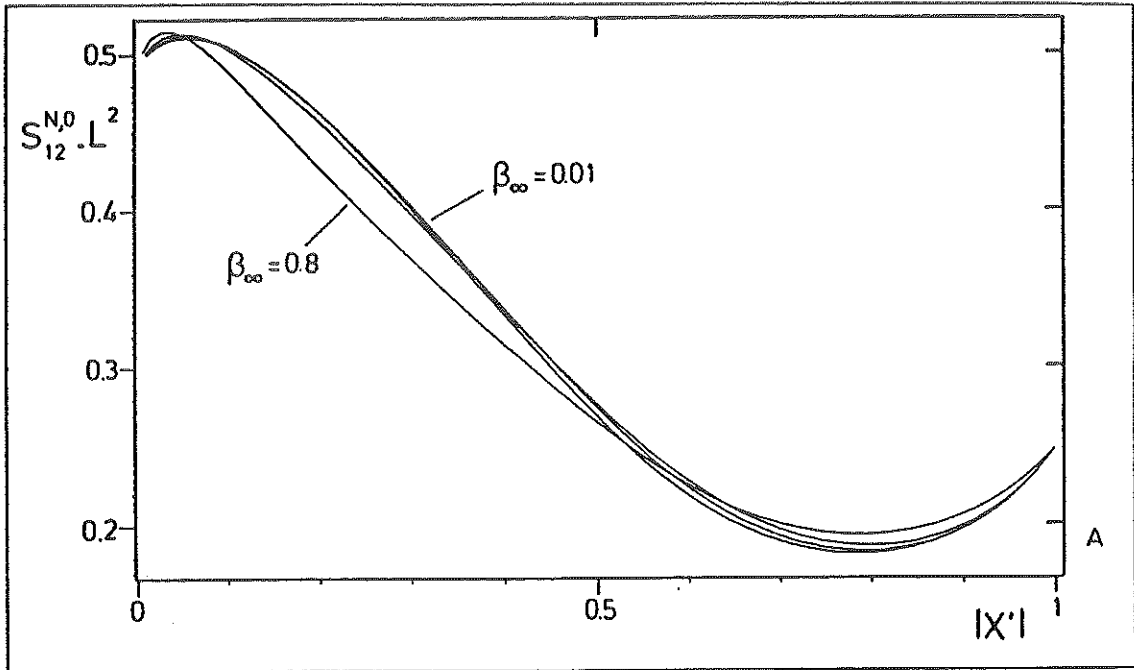


Fig. 6a .

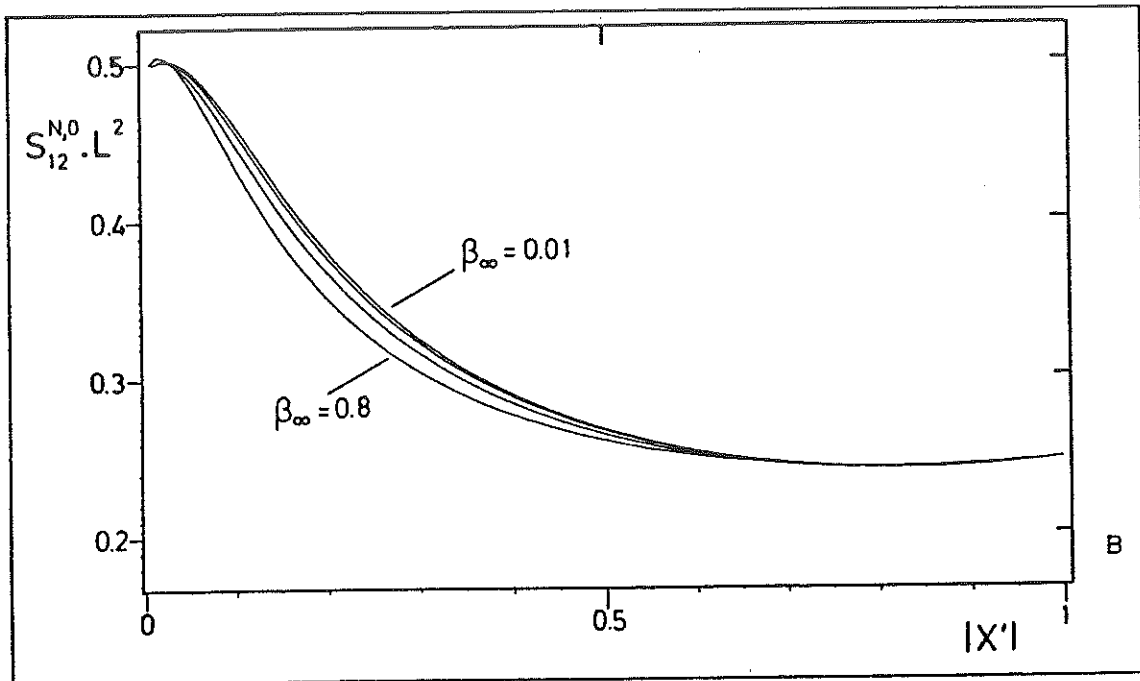


Fig. 6b

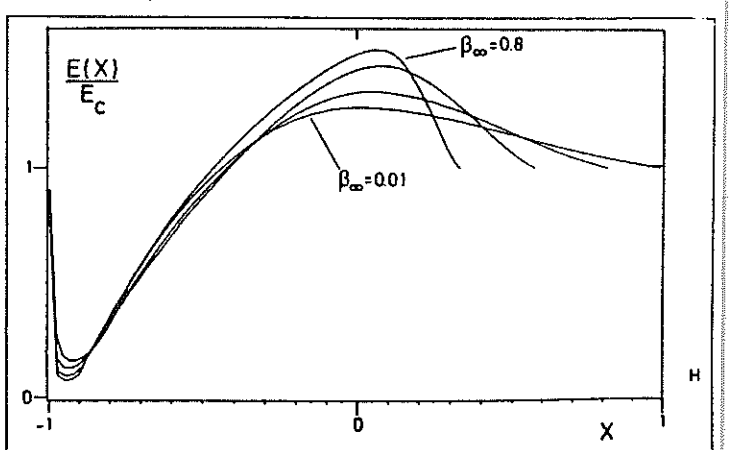
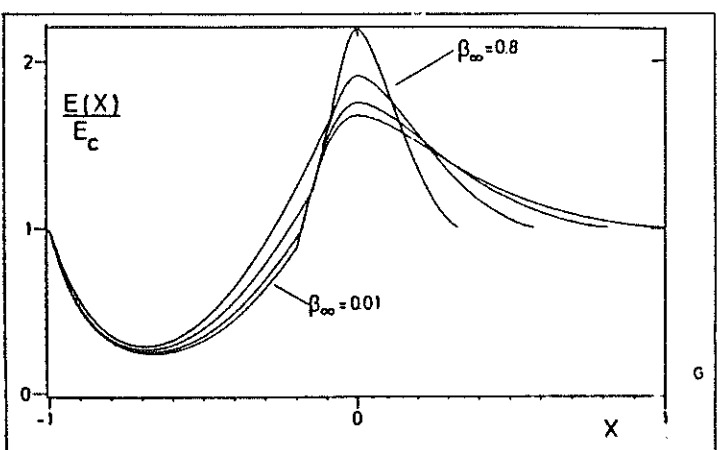
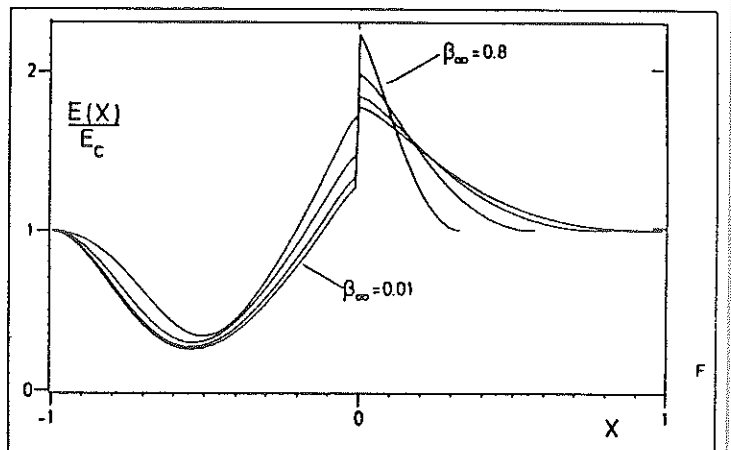
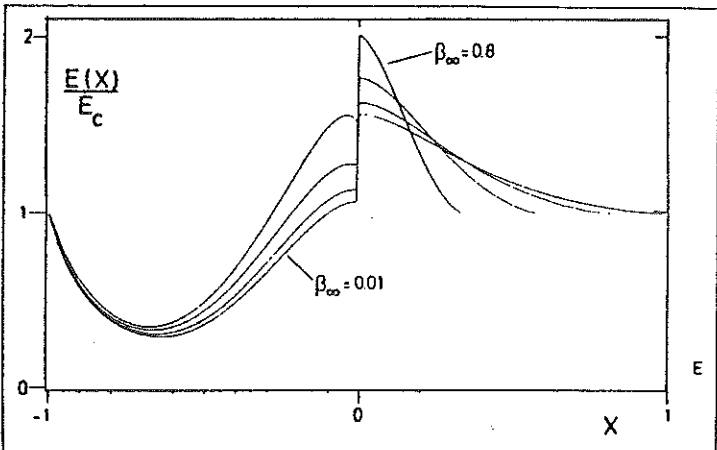
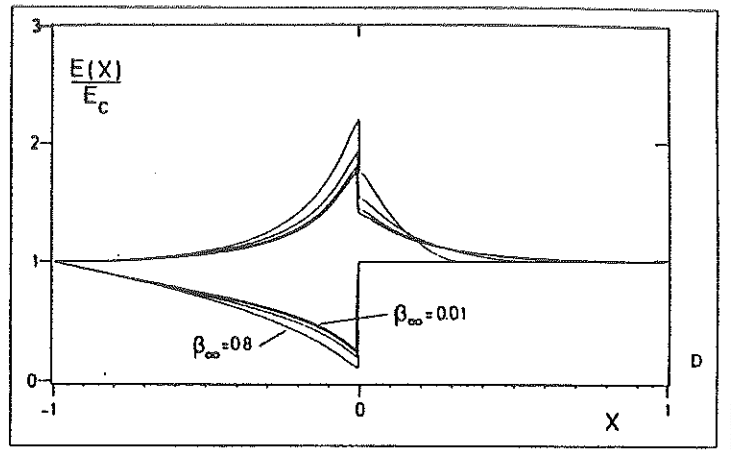
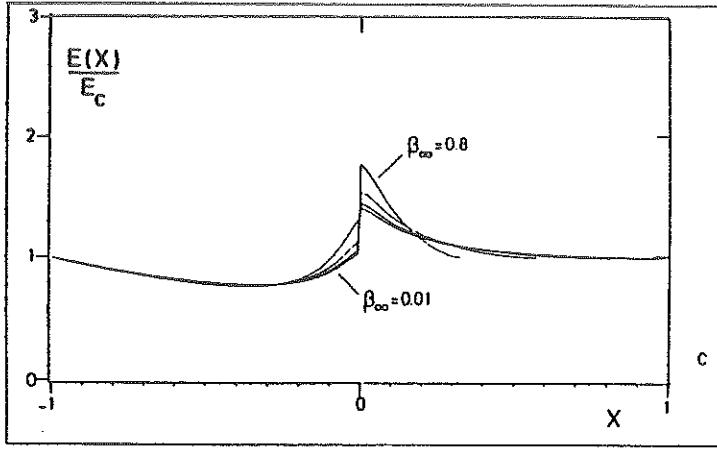
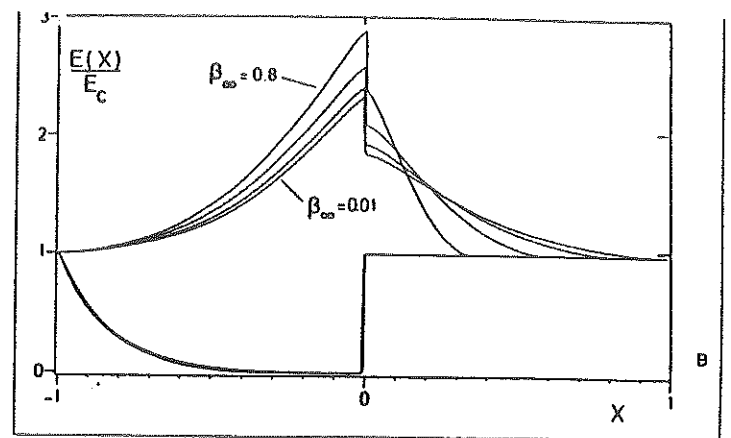
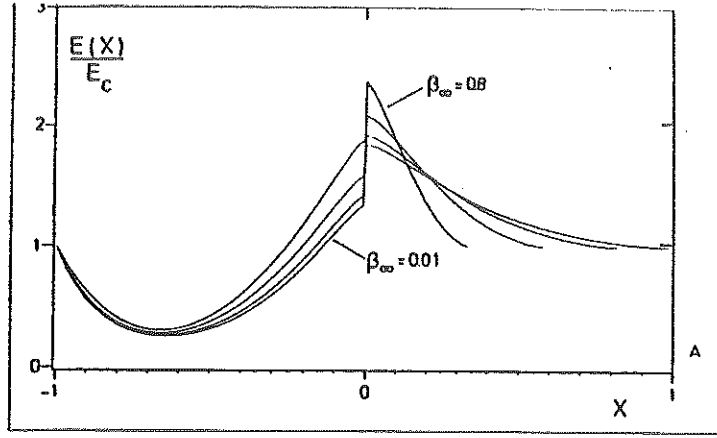


Fig. 7

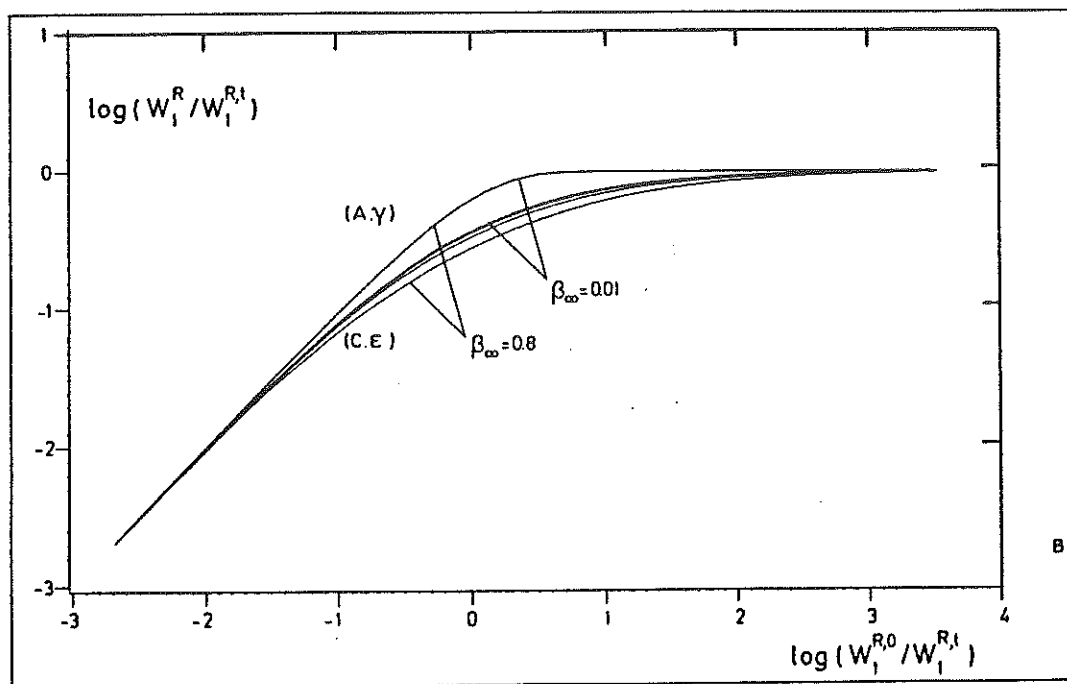
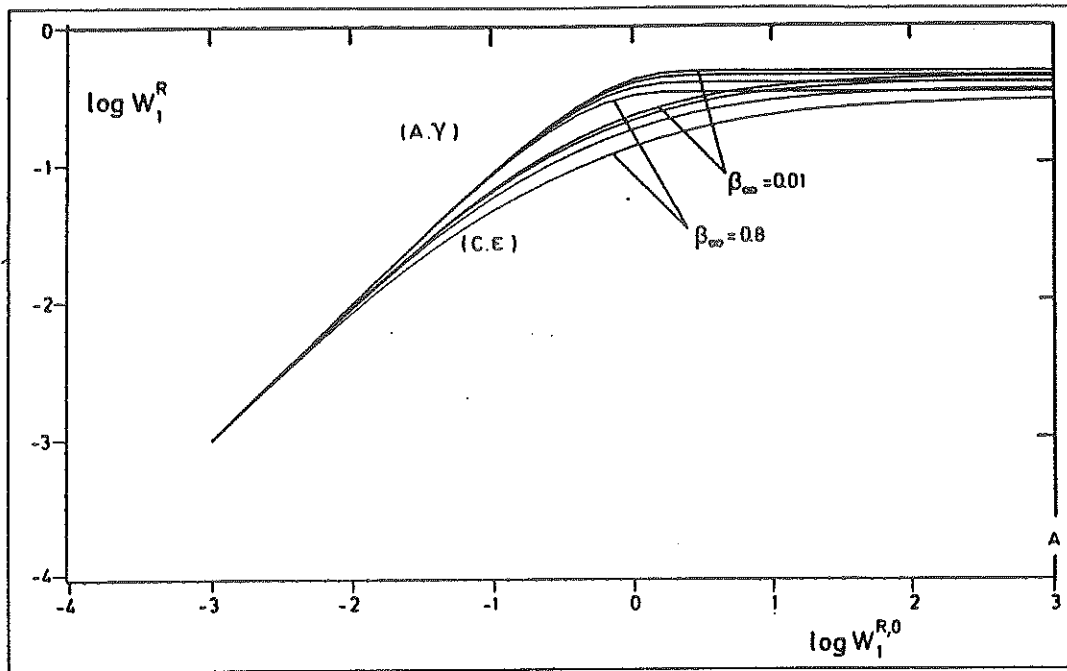


Fig. 8

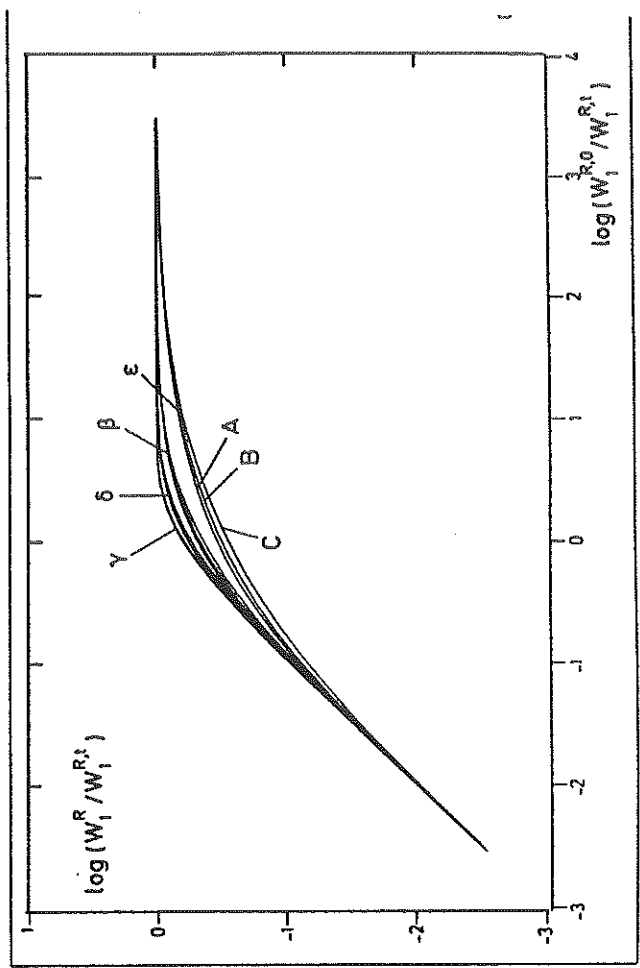
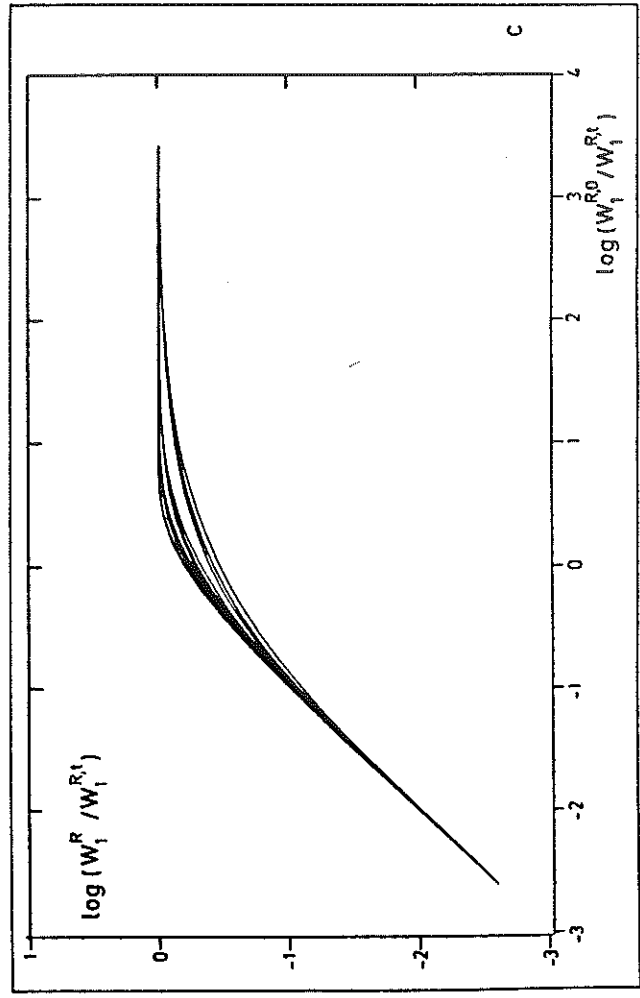
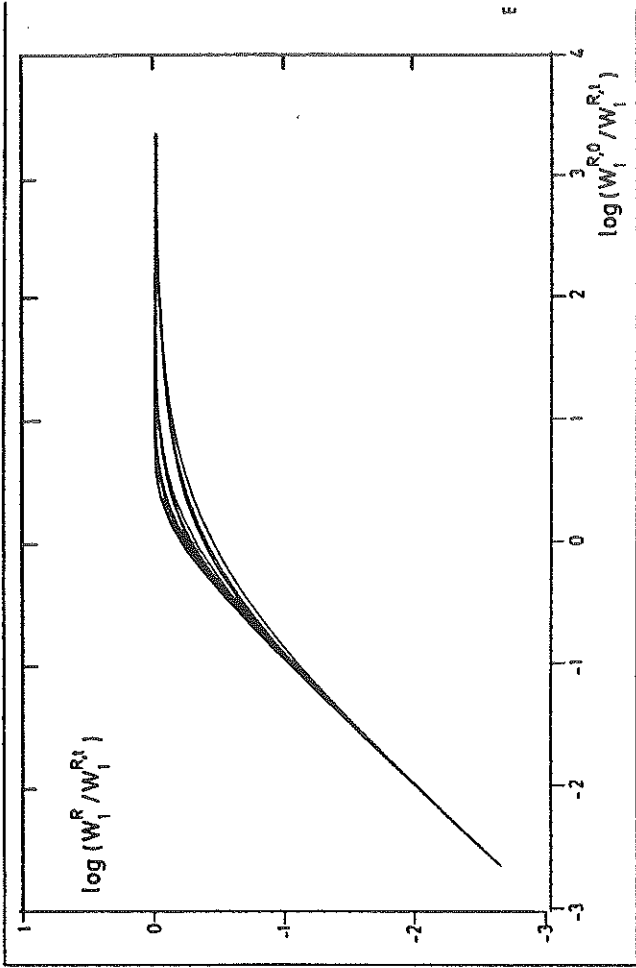
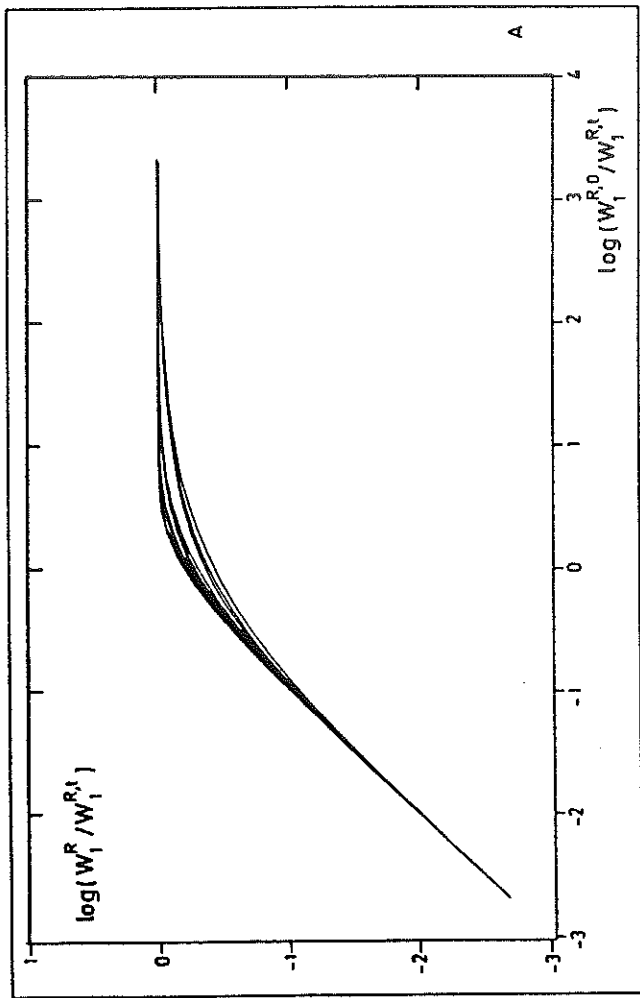


Fig. 9



## Article 10

### REVISITED MASS-LOSS RATES FOR THE NUCLEI OF THE PLANETARY NEBULAE NGC 6210, NGC 6826 AND NGC 6543: THE FIRST ORDER MOMENT $W_1$ OF SUBORDINATE LINE PROFILES

Hutsemékers, D., Surdej, J.: 1987, *Astron. Astrophys.* **173**, 101-107.

Nous présentons dans cet article des déterminations du taux de perte de masse  $\dot{M}$  obtenues pour les étoiles centrales des nébuleuses planétaires NGC 6210, NGC 6826 et NGC 6543. Ces déterminations ont été faites à partir de la mesure du moment d'ordre 1 des profils de type P Cygni observés pour les raies de OIV  $\lambda$  1342 et OV  $\lambda$  1371. Pour ce faire, nous avons tout d'abord établi la relation entre  $W_1$  et  $\dot{M}$  pour des raies optiquement minces issues de niveaux excités. Utilisant des expressions réalistes pour le champ de vitesse  $v(r)$  et la loi d'opacité  $\tau_{12}^r(v)$ , nous avons alors construit numériquement des diagrammes de type " $\log(W_1) - \log(W_1^0)$ " qui nous ont permis d'évaluer les écarts à la relation  $W_1 = W_1^0$ . Nous avons ainsi pu mettre en évidence une sous-estimation systématique, par un facteur variant entre 7 et 20, des taux de perte de masse  $\dot{M}$  publiés précédemment pour les trois noyaux de nébuleuses planétaires en question.



## Revisited mass-loss rates for the nuclei of the planetary nebulae NGC 6210, NGC 6826 and NGC 6543: the first order moment $W_1$ of subordinate line profiles

D. Hutsemékers\* and J. Surdej\*\*

Institut d'Astrophysique, Université de Liège, Avenue de Cointe, 5, B-4200 Liège, Belgium

Received March 28, accepted June 30, 1986

**Summary.** Using realistic expressions for the velocity and opacity distributions in rapidly expanding atmospheres, we present the results of numerical calculations for the first order moment  $W_1$  of subordinate P Cygni line profiles as a function of the parameter  $W_1^0 \alpha \dot{M} \langle n_g \rangle$ , where  $\dot{M}$  represents the mass-loss rate of the central star and  $\langle n_g \rangle$ , the average fractional abundance of the relevant ion across the region of the envelope where the subordinate line profile is formed.

Our calculations clearly show that for unsaturated P Cygni line profiles the relation  $W_1 \propto \dot{M} \langle n_g \rangle$ , holds irrespective of the type of the opacity and/or velocity distributions. For currently observed P Cygni line profiles, the misuse of this relation can lead to an underestimate of the mass-loss rates by more than one order of magnitude. This is illustrated for the case of 3 selected central stars of planetary nebulae (NGC 6210, NGC 6826 and NGC 6543) for which mass-loss rates have been revisited.

**Key words:** radiation transfer – mass-loss – moment  $W_1$  – P Cygni profiles – planetary nebulae

### 1. Introduction

Castor, Lutz and Seaton (1981, referred to below as CLS) have first established that, in the framework of the Sobolev approximation (Sobolev, 1947, 1957, 1958) and for the case of an optically thin line, the first order moment  $W_1$  of a P Cygni line profile provides a good mean of deriving the mass-loss rate  $\dot{M}$  of a star, and is particularly well adapted to the interpretation of IUE and other low resolution spectra.

Although CLS have applied this technique for specific distributions of the velocity and line opacity, Surdej (1982, 1983b) has shown that if the line profile is unsaturated, a unique relation does actually exist between  $W_1$  and the quantity  $W_1^0 \alpha \dot{M} \bar{n}$  (level) where  $\bar{n}$  (level) is the average fractional abundance of an ion in the lower atomic level associated with the given line transition, irrespective of various physical (opacity distribution,

collisions, limb darkening, . . .) and geometrical (velocity law, rotation, . . .) conditions prevailing in the expanding envelope as well as of any Sobolev-type approximations used for the transfer of line radiation.

Adopting realistic expressions for the velocity and opacity distributions, Surdej (1983a, referred to below as Paper I) has constructed “ $\log W_1 - \log W_1^0$ ” diagrams for resonance line transitions which allow star observers to derive directly the quantity  $\dot{M} \bar{n}$  (level) and to assign an error estimate to the mass-loss rate determinations. However, if the excitation potential of the lower level of a subordinate line transition is large enough, the population of this level is essentially accounted for by photoexcitations from the ground level and therefore shows a strong dependence upon the radial distance such that the quantity  $\bar{n}$  (level) is then not defined anymore. Furthermore, subordinate lines such as O IV  $\lambda$  1341 and O V  $\lambda$  1371, whenever observed in the ultraviolet spectra obtained with the Copernicus and International Ultraviolet Explorer (IUE) satellites, have intensively been used for the determination of mass-loss rates because they are often unsaturated and because the interesting approximation  $\bar{n}(\text{O IV}) + \bar{n}(\text{O V}) = 1$  can reasonably be made, independently of any adopted ionization model.

Therefore, in order to give a direct way of deriving mass-loss rates from the spectra of early-type stars, PN nuclei, quasars, etc., we have computed “ $\log W_1 - \log W_1^0$ ” diagrams for the case of subordinate line transitions. On the basis of these diagrams, we have derived the mass-loss rate  $\dot{M}$  of three selected central stars of planetary nebulae for which sufficient observational data are available.

### 2. The first order moment $W_1$ of subordinate line profiles

The present calculations of the first order moment of a subordinate P Cygni line profile are performed within the framework of the spherical geometry and Sobolev approximations. These assumptions are reasonably correct for the case of the winds surrounding early-type stars and have been recently discussed by various authors (see e.g. Schönberg, 1985 and references therein).

The expression of the first order moment of a line profile due to a transition between a lower level  $l$  and an upper level  $u$  has been first written by CLS as:

$$W_1 = \left( \frac{c}{\lambda_{lu} v_\infty} \right)^2 \int_{-\infty}^{+\infty} \left( \frac{F_\lambda - F_c}{F_c} \right) (\lambda - \lambda_{lu}) d\lambda, \quad (1)$$

Send offprint requests to: D. Hutsemékers

\* Aspirant au Fonds National de la Recherche Scientifique (Belgium)

\*\* Also, Chercheur qualifié au Fonds National de la Recherche Scientifique (Belgium)

where  $v_\infty$  is the terminal velocity of the wind, directly measurable from the extent of the violet wing of saturated resonance line profiles.  $F_\lambda$  and  $F_c$  denote the flux in the line and in the continuum, respectively. This equation can be conveniently reduced to the form (cf. Paper I):

$$W_1 = \int_{-X_{\min}}^1 4L^2(X') \tau'_{lu}(X') \gamma_{lu}(X') \left(1 - \frac{\beta_{lu}^3(X')}{\beta_{lu}^1(X')}\right) X' dX', \quad (2)$$

taking into account the effects of the finite dimensions of the stellar core. In this relation,

$-X' = -v(r)/v_\infty$  is the dimensionless frequency of a stellar photon scattered in the expanding atmosphere at a radial distance  $r$ ,

$-X_{\min} = -v_0/v_\infty$ ,  $v_0$  being the velocity of the wind at the stellar surface,

$-L(X') = r/R^*$  represents the radial distance expressed in stellar radii  $R^*$  units,

$\tau'_{lu}$  refers to the radial optical depth of the transition  $l - u$  while  $\gamma_{lu}$ ,  $\beta_{lu}^3$ ,  $\beta_{lu}^1$  are escape probabilities which depend on both the velocity and opacity distributions (these have been defined in Surdej (1982)). This expression of  $W_1$  implicitly assumes the two-level atom model approximation for the line transition  $l - u$ . CLS have shown this approximation to be essentially good for the most interesting subordinate lines observed in the ultraviolet spectrum of early-type stars, i.e. O IV  $\lambda$  1341, O V  $\lambda$  1371 and N IV  $\lambda$  1718. In terms of stellar and atomic parameters, the expression of the opacity takes the form

$$\tau'_{lu}(X') = \frac{\pi e^2}{mc} f_{lu} \lambda_{lu} \frac{A(\text{el}) \dot{M}}{2\pi \bar{\mu} M_{\text{amu}} v_\infty^2 R^*} n_l \frac{d(1/L)}{d(X'^2)}. \quad (3)$$

Within the optically thin approximation ( $\tau_{lu} \ll 1$ ), it is easy to derive the value of the first order moment (cf. Paper I):

$$W_1^0 = \frac{\pi e^2}{mc} f_{lu} \lambda_{lu} \frac{A(\text{el}) \dot{M}}{4\pi \bar{\mu} M_{\text{amu}} v_\infty^2 R^*} \int_1^\infty n_l \frac{(W(L) - 1)}{L^2} dL, \quad (4)$$

where  $W(L)$  is the geometrical dilution factor,  $A(\text{el})$  the abundance of the relevant element and  $n_l$  the fractional abundance of the ion in the lower atomic level  $l$ ; the remaining symbols have their usual meaning.

If the excitation potential of the lower level  $l$  of the line transition is high enough such that photoexcitations dominate collisional excitations when populating the level  $l$  from the ground level  $g$ , we find that the ionization fractions  $n_l$  and  $n_g$  can be related as follows:

$$\frac{n_l}{n_g} = \frac{g_l \lambda_{gl}^3}{g_g 2hc} I_{\nu_{gl}}^c \frac{\beta_{gl}^3}{\beta_{gl}^1}, \quad (5)$$

where  $\beta_{gl}^1$  (resp.  $\beta_{gl}^3$ ) represents the probability that a photon scattered in the line transition  $g - l$  will escape locally the expanding atmosphere along any direction (resp. along those directions striking the stellar core);  $I_{\nu_{gl}}^c$  is the monochromatic intensity of the stellar continuum at the frequency  $\nu_{gl}$ ;  $g_l$  and  $g_g$  being the statistical weights of the excited and ground levels. Using Eq. (5), we can rewrite Eq. (4) in the form

$$W_1^0 = \frac{\pi e^2}{mc} f_{lu} \lambda_{lu} \frac{A(\text{el}) \dot{M}}{4\pi \bar{\mu} M_{\text{amu}} v_\infty^2 R^*} \frac{g_l \lambda_{gl}^3}{g_g 2hc} I_{\nu_{gl}}^c \langle n_g \rangle_s \langle \beta_{gl}^3 / \beta_{gl}^1 \rangle q^c(\infty) \quad (6)$$

where

$$\langle \beta_{gl}^3 / \beta_{gl}^1 \rangle = \frac{\int_1^\infty \frac{\beta_{gl}^3 (W(L) - 1)}{\beta_{gl}^1 L^2} dL}{\int_1^\infty \frac{(W(L) - 1)}{L^2} dL} \quad (7)$$

is an average equivalent dilution factor,

$$\langle n_g \rangle_s = \frac{\int_1^\infty n_g \frac{\beta_{gl}^3 (W(L) - 1)}{\beta_{gl}^1 L^2} dL}{\int_1^\infty \frac{\beta_{gl}^3 (W(L) - 1)}{\beta_{gl}^1 L^2} dL}, \quad (8)$$

and

$$q^c(\infty) = \int_1^\infty \frac{(W(L) - 1)}{L^2} dL \quad (9)$$

is equal to  $-0.8927$ . In Eqs. (6) and (8),  $\langle n_g \rangle_s$  represents the fraction of the ion in the ground level averaged over the region where the subordinate line is formed, i.e. in a region which extends from the stellar surface to a few ( $\sim 3$ ) stellar radii. At such a distance, the photoexciting radiation becomes so diluted that it does not affect anymore the formation of the subordinate line profile: for  $L > 3$ , its contribution to the quantity  $\langle n_g \rangle_s$  is found to be of the order of 1%.

### 3. Determination of the fractional mass-loss rate $\dot{M} \langle n_g \rangle_s$

From Eq. (6) we directly see that a simple linear relation exists between the first order moment  $W_1^0$  of an optically thin subordinate line profile and the quantity  $\dot{M} \langle n_g \rangle_s$ .

For the case of resonance lines, this relation is irrespective of the velocity and opacity distributions (Surdej, 1982), but for the excited lines, the quantity  $\langle \beta_{gl}^3 / \beta_{gl}^1 \rangle$  does depend on both these distributions. In order to estimate the dependence of this relation on  $v(r)$  and  $\tau'_{gl}(v)$ , we have calculated  $\langle \beta_{gl}^3 / \beta_{gl}^1 \rangle$  for 3 typical velocity laws (see Table 1 and next section), assuming both that the photoexciting line is optically thin or optically thick. If the photoexciting line is optically thick, the ratio of the escape probabilities reduces to

$$\frac{\beta_{gl}^3}{\beta_{gl}^1} = W(L) \frac{\alpha + (1 - \alpha)(1 + z + z^2)/3}{\alpha + (1 - \alpha)/3}, \quad (10)$$

**Table 1.** Adopted velocity and opacity distributions for calculating the moment  $W_1$  of P Cygni subordinate line profiles

(A)  $X' = -X_{\min} + (1 + X_{\min})(1 - 1/\sqrt{L})$

(B)  $X' = -X_{\min} + (1 + X_{\min})(1 - 1/L)$

(C)  $X' = \sqrt{1 - (1 - X_{\min}^2)/L}$

( $\alpha$ )  $\tau'_{gl}(X') \propto 1 \left/ \left( \frac{X' dX'}{d(1/L)} \right) \right.$

( $\beta$ )  $\tau'_{gl}(X') \propto (1 - X')$

( $\gamma$ )  $\tau'_{gl}(X') \propto 1$

( $\delta$ )  $\tau'_{gl}(X') \propto \sqrt{1 - X'}$

( $\epsilon$ )  $\tau'_{gl}(X') \propto (1 - X')^2$

( $\eta$ )  $\tau'_{gl}(X') \propto 1/X'$

**Table 2.** Computed values of  $\langle \beta_{g1}^3/\beta_{g1}^1 \rangle$  for the three different velocity laws assuming that the photoexciting line is optically thick or thin

	Velocity law	$\langle \beta_{g1}^3/\beta_{g1}^1 \rangle$
Optically thick case	A	0.1209
	B	0.1182
	C	0.1003
Optically thin case	A, B, C	0.0933

where

$$\alpha = \frac{d \ln L}{d \ln X'}, \quad (11)$$

and

$$z = \sqrt{1 - \left(\frac{1}{L}\right)^2}. \quad (12)$$

In the optically thin case, this ratio is independent of the velocity law and is simply given by

$$\frac{\beta_{g1}^3}{\beta_{g1}^1} = W(L). \quad (13)$$

The computed values of  $\langle \beta_{g1}^3/\beta_{g1}^1 \rangle$  are listed in Table 2. We see that  $\langle \beta_{g1}^3/\beta_{g1}^1 \rangle$  is very slightly dependent on the velocity law as well as on the opacity of the photoexciting line. If we choose for  $\langle \beta_{g1}^3/\beta_{g1}^1 \rangle$  a mean value of  $0.103 \pm 0.013$ , and taking  $\bar{\mu} = 1.26$  (Allen, 1973), we can easily calculate the quantity  $\dot{M}\langle n_g \rangle_s$  from the first order moment  $W_1^0$  of an optically thin subordinate line by means of the relation:

$$\dot{M}\langle n_g \rangle_s = -4.71 \cdot 10^{-21} \frac{g_g}{g_l} \frac{v_\infty^2 R^*}{\lambda_{g1}^3 J_{v_{g1}}^c \int_{\lambda_{lu}} A(\text{el})} W_1^0, \quad (14)$$

which, within a good approximation ( $\pm 13\%$ ), is independent of both the velocity and opacity distributions. In this relation  $\dot{M}$

is given in  $M_\odot/\text{yr}$ ,  $v_\infty$  in  $\text{km s}^{-1}$ ,  $\lambda_{g1}$  and  $\lambda_{lu}$  in  $10^3 \text{ \AA}$ ,  $R^*$  in  $R_\odot$  and  $J_{v_{g1}}^c$  in  $\text{erg cm}^{-2} \text{ s}^{-1} \text{ Hz}^{-1}$ . Unlike the case of resonance line transitions (Surdej, 1985), we immediately see from Eq. (1) that the quantity  $\dot{M}\langle n_g \rangle_s$  is also irrespective of  $v_\infty$ . This is particularly interesting for the analysis of subordinate lines which are formed near the stellar core ( $L \lesssim 3$ ) and which therefore cannot provide a correct determination of  $v_\infty$ .

#### 4. "log $W_1 - \log W_1^0$ " diagrams

##### 4.1. Numerical applications

Combining Eqs. (3) and (6) and with the help of the opacity distribution of the photoexciting line transition (cf. Paper I)

$$\tau_{g1}^r \propto n_g \frac{d(1/L)}{X' dX'}, \quad (15)$$

we can write the expression of the opacity  $\tau_{lu}^r$  as

$$\tau_{lu}^r = W_1^0 \frac{n_g}{\langle n_g \rangle_s} \frac{\beta_{g1}^3/\beta_{g1}^1}{\langle \beta_{g1}^3/\beta_{g1}^1 \rangle} \frac{d(1/L)}{q^c(\infty) X' dX'}, \quad (16)$$

and, finally

$$\tau_{lu}^r = W_1^0 \frac{\tau_{g1}^r(\beta_{g1}^3/\beta_{g1}^1)}{\int_{-X_{\text{min}}}^1 \tau_{g1}^r(\beta_{g1}^3/\beta_{g1}^1)(1 - W(L)) X' dX'}. \quad (17)$$

$\tau_{lu}^r$  depends on the opacity of the transition  $g-l$  and on the ratio of the escape probabilities  $\beta_{g1}^3$  and  $\beta_{g1}^1$ . In order to avoid the introduction of an additional parameter, we shall consider the two extreme distinct cases: the photoexciting line is optically thick or optically thin such that the ratio  $\beta_{g1}^3/\beta_{g1}^1$  reduces to Eqs. (10) or (13), respectively. For such cases,  $\tau_{lu}^r$  is only dependent on the distribution of the opacity of the photoexciting line as well as on the type of the velocity law. Therefore, for a given set of opacity and velocity laws, the first order moment  $W_1$  (see Eq. (2)) can readily be computed against values of the parameter  $W_1^0$ .

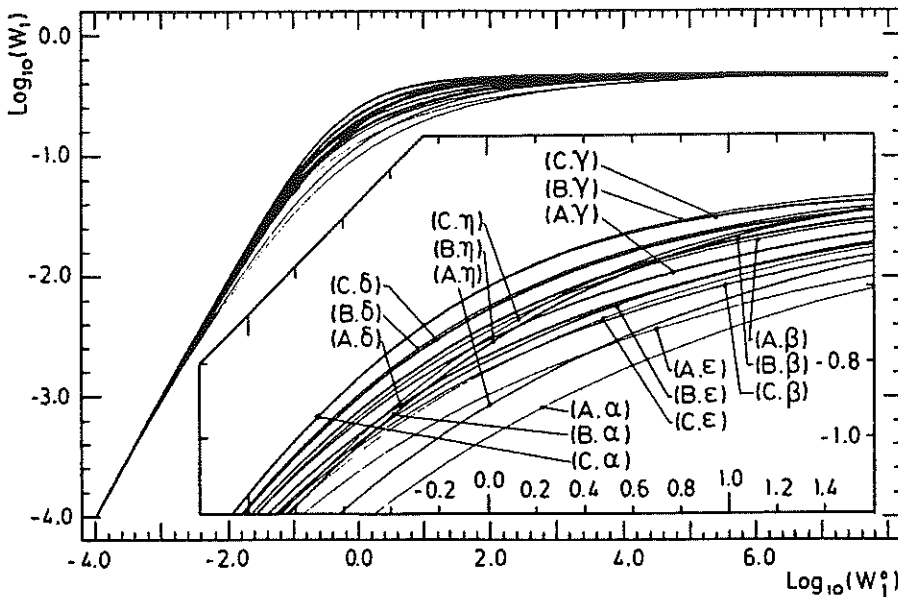


**Fig. 1.** "log<sub>10</sub>  $W_1 - \log_{10} W_1^0$ " curves computed for the eighteen possible models derived from Table 1 assuming that the  $g-l$  photoexciting line transition is optically thin

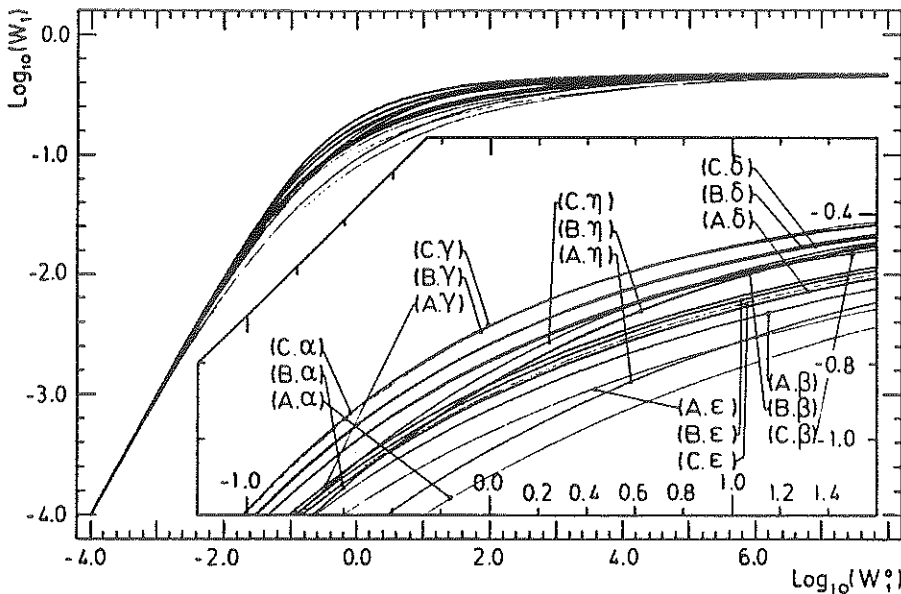


Fig. 2. " $\log_{10} W_1 - \log_{10} W_1^0$ " curves computed for the eighteen possible models derived from Table 1 assuming that the  $g - i$  photoexciting line transition is optically thick

In Paper I, a series of resonance line opacity and velocity distributions which seem to well represent those characterizing winds of early-type stars have been compiled and are given with suitable notations in Table 1. Let us recall that case (C. $\alpha$ ) refers to a radiation-driven wind (Castor et al., 1975) in which there is mass conservation of the relevant species.

The diagrams representing  $\log_{10} W_1$  versus  $\log_{10} W_1^0$  have been computed for the eighteen possible models assuming alternatively that the photoexciting line is optically thin or thick. These are illustrated in Figs. 1–2. Numerical values are also given in the Appendix. As in Paper I,  $X_{\min} = -0.01$  has been adopted, a value currently quoted for the wind of early-type stars.

#### 4.2. Discussion of the results

As expected, Figs. 1 and 2 clearly show that all " $\log W_1 - \log W_1^0$ " curves are characterized by a common linear branch – i.e.  $W_1 = W_1^0 -$  for small values of  $\log W_1^0$ . As  $\log W_1^0 \rightarrow \infty$ , there results an asymptotic value  $\log W_1 \rightarrow -0.32$ , irrespective of any model and equal to the asymptotic value of  $\log W_1$  computed for the case of a resonance line (see Paper I). For intermediate opacities, an observed value of  $W_1$  leads to a precise value of  $W_1^0$  – and consequently of  $\dot{M} \langle n_g \rangle$ , if, and only if, the opacity and velocity distributions are known. Whenever they are not, we can estimate the error affecting the derived value of  $W_1^0$  from the observed dispersion of the curves in Figs. 1 and 2. In doing this, we implicitly assume that the models compiled in Table 1 encompass most of realistic cases.

Comparison between two curves taken from Figs. 1 and 2, computed for the same opacity and velocity distributions, shows that these are not too much dependent on the choice (assumed to be alternatively optically thin or optically thick) of the opacity of the photoexciting line even for intermediate values of  $W_1^0$ . For reasonably saturated lines ( $W_1 \lesssim 0.20$ ) the uncertainty affecting  $\dot{M}$  never exceeds 50%. We also see that, for each of these eighteen models, the curve computed under the optically thin approximation ( $\tau_{g1} \ll 1$ ) always provides a lower limit for the mass-loss rate.

It is also interesting to note that the curves computed for the subordinate lines (see Figs. 1–2) are more dispersed than those

calculated for typical resonance lines (cf. Fig. 7 of Paper I). This is mainly due to the fact that the radial opacity  $\tau'_{lu}$  of a subordinate line depends on the velocity distribution (see Eq. (17)) while the opacity  $\tau'_{g1}$  of a resonance line does not – except if the opacity distribution  $\alpha$  is considered. We also see in Figs. 1–2 that, for a given opacity law, the curves obtained for the velocity laws B and C appear very similar while that calculated for the velocity law A is always shifted towards higher values of  $\log W_1^0$  such that the use of this less steep velocity law always provides higher mass-loss rate estimates when determined from the same measured value of  $W_1$ .

Therefore, the present " $\log W_1 - \log W_1^0$ " curves are model dependent within a larger interval of  $\log W_1^0$  values than for the case of a resonance line transition. This implies that a lower value of  $W_1$  must be measured in order to be located on the linear branch. This constitutes a fortunate situation since, whenever a resonance line profile is saturated, weaker features are generally observed for excited lines thus still providing an interesting possibility of deriving an accurate mass-loss rate.

Comparison between the quantity  $\langle n_g \rangle_s$ , derived from the analysis of subordinate line profiles and  $\langle n_g \rangle$  for the case of resonance line profiles of the same ion (cf. Paper I) can give information on the distribution of the ionization fraction across the envelope. The ratio  $\langle n_g \rangle_s / \langle n_g \rangle$ , is reported in Table 3 for the eighteen models. We see that this ratio is not too much dependent on the opacity approximation ( $\tau_{g1} > 1$  or  $\tau_{g1} < 1$ ) made for the photoexciting line. However, larger differences are noticed between the ratios obtained for different model calculations. A ratio  $\langle n_g \rangle_s / \langle n_g \rangle$ , greater than unity refers to a distribution of the ionization fraction increasing outwards while a ratio smaller than one refers to a decreasing one.

## 5. Examples of mass-loss rate determinations

### 5.1. Determination of $\dot{M}$ for three selected central stars of planetary nebulae

In order to apply our method, we have selected in the literature some objects for which measurements of the first order moment

Table 3. The ratio  $\langle n_b \rangle / \langle n_g \rangle$ , computed for the eighteen models listed in Table 1

Model	Optically thin case	Optically thick case
A. $\alpha$	1.0000	1.0000
B. $\alpha$	1.0000	1.0000
C. $\alpha$	1.0000	1.0000
A. $\beta$	2.4031	2.6670
B. $\beta$	1.1105	1.1443
C. $\beta$	0.5615	0.5179
A. $\gamma$	4.9557	5.8583
B. $\gamma$	2.0870	2.3528
C. $\gamma$	1.0000	1.0000
A. $\delta$	3.2754	3.7414
B. $\delta$	1.4297	1.5309
C. $\delta$	0.7046	0.6716
A. $\epsilon$	1.5695	1.6647
B. $\epsilon$	0.8020	0.7847
C. $\epsilon$	0.4240	0.3764
A. $\eta$	1.6922	1.7391
B. $\eta$	1.0000	1.0000
C. $\eta$	0.5707	0.5328

of UV subordinate line profiles were available. The recent paper by Cerruti-Sola and Perinotto (1985, hereafter CP) provides such a list of  $W_1$  values derived from lines observed in low-resolution IUE spectra of central stars of planetary nebulae. NGC 6543 observed by CLS, can also be added to this list.

These UV subordinate lines are probably contaminated by the presence of a nebular emission line and/or an underlying photospheric absorption one. Since the former one arises in a huge nebula located well beyond the expanding atmosphere, its contribution to the first order moment is negligible for reasons of symmetry. The error made by neglecting the presence of a possible strong photospheric absorption line has the effect of underestimating, by less than 20%, the derived mass-loss rate (Surdej, 1982).

The most uncertain parameter in using the UV subordinate lines for mass-loss rate determinations is the intensity  $I_{\nu_1}$ , which must be evaluated in the unobservable region of the far UV spectrum. CP, as well as CLS, have computed this intensity assuming that the star radiates as a black-body at an effective temperature  $T_{\text{eff}}$ . Unfortunately, this constitutes a very rough approximation whenever extrapolated beyond the Lyman limit. Furthermore, the model calculations, independently of the determination of a reliable  $T_{\text{eff}}$ , remain uncertain because they are quite dependent on an unknown chemical composition (see the discussion by Pottasch, 1984). Therefore, we prefer to use the far UV flux determinations by Natta et al. (1980), based on the analysis of the successive stages of ionization of a given element in the nebula, a method which does not require the knowledge of the effective temperature of the star. As pointed out by these authors, a black-body flux distribution does not match their flux determinations and therefore remains a bad approximation for the prediction of the far UV spectrum.

Finally, we have found in the literature three planetary nebulae which do have a central star analysed by Natta et al. (1980)

and for which  $W_1$  measurements have been published. These are NGC 6210, NGC 6826 and NGC 6543.

It should be noticed that, except for CIV in NGC 6210, the resonance lines of CIV and NV are completely saturated in the spectra of these central stars. Some values of their moment  $W_1$  do even exceed the theoretical asymptotic value given in Paper I, showing that for large opacities the doublet structure of these lines must absolutely be taken into consideration. This also clearly demonstrates that any determination of mass-loss rates using the first order moment of these resonance lines based on the approximation  $W_1 = W_1^0$  will result in meaningless estimates.

In order to avoid the problem of deriving the ionization fractions, we have only considered the oxygen subordinate lines O IV  $\lambda$  1341 and O V  $\lambda$  1371, assuming that  $\langle n_b \rangle_s(\text{O IV}) + \langle n_g \rangle_s(\text{O V}) = 1$ , such that our mass-loss rates will only provide lower limit estimates. We have also assumed that the abundance of oxygen in the stellar wind is the same as in the nebula (the values are taken from Natta et al., 1980).

Our mass-loss rate determinations are reported in Table 4 altogether with the following quantities:

- column 3: the first order moment as found in the literature for O IV  $\lambda$  1341 and O V  $\lambda$  1371,
- column 4: the value of  $\log W_1^0$  obtained from the diagrams illustrated in Figs. 1 and 2. A mean value is reported here with an error estimate derived from the dispersion of the curves,
- column 5: the calculated value of  $\dot{M} \langle n_b \rangle_s$  using Eq. (14) and the data of Natta et al. (1980). The terminal velocity is taken from the same source as the  $W_1$  values,
- column 6: the value of  $\dot{M}$  obtained assuming that  $\langle n_b \rangle_s(\text{O IV}) + \langle n_g \rangle_s(\text{O V}) = 1$ .

As we can immediately see from Table 4, our mass-loss rates are greater by more than one order of magnitude than those obtained by CLS and CP.

Before discussing the origin of these discrepancies, we want to point out that we have considered O IV  $\lambda$  1341 as forming a single line, despite its multiplet structure. Indeed, if the line is not saturated, this approximation is essentially correct (see CLS and Surdej, 1982) and we can therefore assume that the error possibly induced by this approximation is not too large, at least for NGC 6210 and NGC 6826.

## 5.2. Discussion of our results

The large discrepancy existing between the results of CLS, CP and ours is mainly due to the misuse by these authors of the approximation  $W_1 = W_1^0$  for non unsaturated lines. It can be readily seen in Figs. 1-2 that for measured values of  $\log W_1$  between -1.4 and -0.7 (see Table 4), the use of this linear relation results in a systematic underestimate of the mean value of  $W_1^0$  - and consequently of  $\dot{M}$  - by a factor varying between 3 and 20. All the  $W_1$  values measured for the O IV and O V lines observed with IUE in the low resolution mode and reported by CP are too great to justify the use of the linear relation between  $W_1$  and  $\dot{M}$ . Therefore we conclude that all their mass-loss rates have probably been underestimated. An independent mass-loss rate determination was performed by Adam and Köppen (1985) for the nucleus of NGC 1535 on the basis of the fitting of line profiles observed in IUE high-resolution spectra. Their value of  $\dot{M}$  is 2 orders of magnitude greater than that given by CP for

Table 4.  $\dot{M}$  for selected central stars of planetary nebulae

PN	Line	$W_1$	$\log W_1^0$	$\dot{M}\langle n_g \rangle_s$ ( $M_\odot/\text{yr}$ )	$\dot{M}$ ( $M_\odot/\text{yr}$ )	Previous estimates of $\dot{M}$ s
NGC 6210	O IV	0.06 <sup>a,c</sup>	-0.74 ± 0.39	6.7 10 <sup>-9</sup>	1.2 10 <sup>-8</sup>	6 10 <sup>-10</sup> <sup>a</sup>
	O V	0.12 <sup>a</sup>	-0.03 0.62	5.3 10 <sup>-9</sup>		
NGC 6826	O IV	0.04 <sup>a,c</sup>	-1.02 0.30	1.1 10 <sup>-7</sup>	1.5 10 <sup>-7</sup>	2 10 <sup>-8</sup> <sup>a</sup>
	O V	0.07 <sup>a</sup>	-0.58 0.45	3.7 10 <sup>-8</sup>		
NGC 6543	O IV	0.19 <sup>b</sup>	0.60 0.88	1.6 10 <sup>-6</sup>	1.7 10 <sup>-6</sup>	1 10 <sup>-7</sup> <sup>b</sup>
	O V	0.13 <sup>b</sup>	0.03 0.64	5.3 10 <sup>-8</sup>		

## Notes

<sup>a</sup> Value from Cerruti-Sola and Perinotto (1985)

<sup>b</sup> Value from Castor, Lutz and Seaton (1981)

<sup>c</sup> As suggested by Cerruti-Sola and Perinotto (1985), the value of  $W_1$  has already been divided by three in order to take into account the contamination by the Cu  $\lambda$  1335 interstellar line

the same object but similar to the value that we have obtained on the basis of "log  $W_1 - \log W_1^0$ " diagrams (we also obtained  $\dot{M} = 10^{-7} M_\odot/\text{yr}$  for NGC 1535 using the same data and approximations as Adam and Köppen, 1985. The  $W_1$  measurements are from CP). It is interesting to note that an increase of the majority of the mass-loss rates derived by CP will reinforce their suggestion that there might exist a difference between the winds of planetary nebulae nuclei and Population I OB stars since the same order of mass-loss rates are observed in stars having very different luminosities. But it could also be due to an abundance problem in the wind of PN nuclei.

Another source of discrepancy is the assumption by CP that the central star radiates as a black-body at the He II Zanstra temperature when they derive the intensity  $I_{\nu_1}^*$  of the far UV stellar continuum. Indeed, first, the slope of the flux distribution cannot be adequately fitted by a black-body distribution (Natta et al., 1980) and, secondly, the Zanstra temperature  $T_2(\text{He II})$  does probably overestimate the effective temperature of the star when a stellar wind is present (Adam and Köppen, 1983, 1985). If we accept the fact that the three planetary nebulae nuclei are surrounded by a wind as that modeled by Adam and Köppen (1985) for the case of NGC 1535, the energy distribution – only increased below  $\lambda$  228 Å – will slightly affect the fluxes determined by Natta et al. (1980) near  $\lambda$  600 Å which enter Eq. (14). Therefore, the use of the black-body approximation with  $T = T_2(\text{He II})$  for the three investigated central stars of PN, rather than the UV flux determinations of Natta et al. (1980), results in underestimates of  $\dot{M}$  by a factor of about 3.

It should also be pointed out that in the method first developed by CLS, the quantity  $n(\text{level})$  does not represent an average value across the envelope as in our calculations but is evaluated at a distance  $L = 2$ . At such a distance, the photoexcited levels are unfortunately largely depopulated such that the mass-loss rates they derive are systematically overestimated by a factor 2.3.

We can finally give an estimate of the total uncertainty which affects our mass-loss rates. The error on  $\log W_1^0$  due to the dispersion of the curves is on the average 0.5 dex (see Table 4). Natta et al. (1980) have reported an uncertainty of about 0.3 dex on their flux values. For planetary nebulae in general, the quantities  $R^*$  and  $A(\text{el})$  are both only known within a factor 2 (0.3 dex).

Therefore, taking into account the error due to the possible presence of an underlying photospheric absorption line (20%), the total uncertainty affecting  $\log \dot{M}$  is approximately 0.7 dex. Whereas the uncertainties due to departures from the classical radiative transfer model used here are thought to be small when compared to the others, it should be kept in mind that large systematic errors may be introduced in assuming that the oxygen abundance in the wind is the same as in the nebula and that only two ionization stages are present.

## 6. Discussion and conclusions

The first order moment method, applied to P Cygni line profiles of resonance lines, has been shown to be a very powerful method for deriving mass-loss rates (CLS, Surdej 1982, 1983a,b). Since the resonance lines are often saturated while unsaturated P Cygni profiles are available from subordinate lines, we have generalized this method to lines originating from excited levels.

In the framework of the Sobolev approximation, we have shown that for unsaturated subordinate lines, there exists a unique relation between the first order moment  $W_1$  and the quantity  $\dot{M}\langle n_g \rangle_s$  independently of any velocity and/or opacity distributions. If the line is not sufficiently unsaturated, the use of "log  $W_1 - \log W_1^0$ " diagrams still allows one to determine mass-loss rates of early-type stars, PNN, BAL quasars, etc. as well as an estimate of the error. This method is the only useful one for the analysis of unresolved P Cygni profiles (CLS) and is complementary to the "line profile fitting" technique (Olson, 1981) used when analyzing unsaturated and sufficiently well resolved P Cygni profiles, as already pointed out in Paper I.

From the comparison of mass-loss rates obtained with similar methods, we wish to warn the reader against some possible misuse of the relation  $W_1 = W_1^0$  whenever the line is not sufficiently unsaturated. We conclude that the mass-loss rates previously derived for the central nuclei of the planetaries NGC 6210 (CP), NGC 6826 (CP), NCG 6543 (CLS) and NGC 1535 (CP) have been systematically underestimated by more than one order of magnitude when compared to those determined in the present work.

We also conclude that high signal to noise spectroscopic data of faint, i.e. unsaturated, P Cygni profiles are very necessary in



order to provide accurate but still inexistent mass-loss rate estimates for a wide variety of celestial objects (early-type stars, PN nuclei, BAL quasars, etc.).

bei München). JS wishes to thank again Prof. L. Woltjer and Prof. G. Setti for making his stay possible. We also thank Mrs. M. Houssolange-Macours and J. Bosseloirs for typing the manuscript and drawing the figures.

*Acknowledgments.* Part of this work was made while JS was a paid associate at the European Southern Observatory (Garching

#### Appendix

**Table A1.** For selected values of  $\log_{10}(W_1)$ , we have listed hereafter the smallest and greatest values of  $\log_{10}(W_1^0)$  as obtained from the eighteen model calculations illustrated in Figs. 1 and 2

Results referring to Fig. 1			Results referring to Fig. 2		
$\log_{10}(W_1)$	$\log_{10}(W_1^0)_s - \log_{10}(W_1^0)_g$	$\log_{10}(W_1^0)_g$	$\log_{10}(W_1)$	$\log_{10}(W_1^0)_s - \log_{10}(W_1^0)_g$	$\log_{10}(W_1^0)_g$
-3.091	-3.096	-3.049	-3.089	-3.090	-3.049
-3.002	-3.004	-2.954	-2.999	-3.004	-2.948
-2.894	-2.901	-2.831	-2.889	-2.889	-2.825
-2.800	-2.806	-2.725	-2.798	-2.795	-2.725
-2.694	-2.691	-2.600	-2.695	-2.691	-2.599
-2.602	-2.599	-2.499	-2.600	-2.596	-2.493
-2.498	-2.496	-2.382	-2.493	-2.487	-2.362
-2.400	-2.396	-2.265	-2.398	-2.398	-2.245
-2.299	-2.292	-2.148	-2.292	-2.281	-2.111
-2.205	-2.200	-2.025	-2.202	-2.192	-1.994
-2.104	-2.089	-1.891	-2.106	-2.085	-1.871
-2.001	-1.983	-1.757	-2.003	-1.979	-1.726
-1.905	-1.879	-1.629	-1.901	-1.865	-1.578
-1.803	-1.771	-1.487	-1.804	-1.762	-1.425
-1.700	-1.662	-1.333	-1.694	-1.644	-1.255
-1.600	-1.550	-1.183	-1.602	-1.530	-1.099
-1.500	-1.436	-1.016	-1.500	-1.404	-0.909
-1.404	-1.321	-0.857	-1.401	-1.287	-0.709
-1.303	-1.207	-0.673	-1.302	-1.159	-0.500
-1.201	-1.068	-0.458	-1.200	-1.022	-0.266
-1.098	-0.937	-0.232	-1.094	-0.858	0.024
-1.003	-0.800	0.002	-1.004	-0.702	0.308
-0.901	-0.633	0.303	-0.903	-0.507	0.664
-0.799	-0.460	0.640	-0.800	-0.284	1.077
-0.695	-0.256	1.099	-0.700	-0.008	1.608
-0.600	-0.000	1.625	-0.599	0.365	2.312
-0.493	0.393	2.444	-0.493	0.986	3.206
-0.400	1.078	-	-0.399	1.938	-

#### References

- Adam, J., Köppen, J.: 1983, *Planetary nebulae*, IAU Symp. Nr 103, p. 338
- Adam, J., Köppen, J.: 1985, *Astron. Astrophys.* **142**, 461
- Allen, C.W.: 1973, *Astrophysical Quantities*, Athlone Press, Univ. of London
- Castor, J.I., Abott, D.C., Klein, R.I.: 1975, *Astrophys. J.* **195**, 157
- Castor, J.I., Lutz, J.H., Seaton, M.J.: 1981, *Monthly Notices Roy. Astron. Soc.* **194**, 547 (CLS)
- Cerruti-Sola, M., Perinotto, M.: 1985, *Astrophys. J.* **291**, 237 (CP)
- Natta, A., Pottasch, S.R., Preite-Martinez, A.: 1980, *Astron. Astrophys.* **84**, 284
- Pottasch, S.R.: 1984, *Planetary Nebulae*, Reidel, Dordrecht
- Olson, G.L.: 1981, *Astrophys. J.* **248**, 1021
- Schönberg, K.: 1985, *Astron. Astrophys.* **148**, 405
- Sobolev, V.V.: 1947, *Dnižuščiesja Oboločki Zvezd*, Leningrad, transl. Moving Envelopes of Stars; translated from Russian by S. Gaposchkin, Harvard University Press, Cambridge, Mass., 1960
- Sobolev, V.V.: 1957, *Astron. Zh.* **34**, 694 (trans. Soviet Astron. *J.*, 678)
- Sobolev, V.V.: 1958, in V.A. Ambartsumyan (ed.), *Theoretical Astrophysics*, Chapter 28, Pergamon Press Ltd., London
- Surdej, J.: 1982, *Astrophys. Space Sci.* **88**, 31
- Surdej, J.: 1983a, *Astron. Astrophys.* **127**, 304 (Paper I)
- Surdej, J.: 1983b, *Astrophys. Space Sci.* **90**, 299
- Surdej, J.: 1985, *Astron. Astrophys.* **152**, 361



Article 11

REVISITED MASS-LOSS RATES FOR A SAMPLE OF CENTRAL STARS OF  
PLANETARY NEBULAE

Hutsemékers, D., Surdej, J.: 1989, *Astron. Astrophys.* 219, 237-238.

Au moyen de diagrammes de type " $\log(W_1) - \log(W_1^0)$ " calculés pour des raies issues de niveaux excités, nous avons re-déterminé les taux de perte de masse  $\dot{M}$  de dix-sept noyaux de nébuleuses planétaires observés à faible résolution spectroscopique au moyen du satellite IUE. La valeur moyenne des taux de perte de masse que nous avons déduits se situe entre  $10^{-7}$  et  $10^{-8} M_{\odot}/\text{an}$ . Nous confirmons qu'il n'est pas possible d'extrapoler la relation luminosité-taux de perte de masse ( $L - \dot{M}$ ), établie pour les étoiles jeunes de type OB, en vue de déduire le taux de perte de masse  $\dot{M}$  des étoiles centrales des nébuleuses planétaires à partir de leur luminosité  $L$ .



## Revisited mass-loss rates for a sample of central stars of planetary nebulae

D. Hutsemékers\*<sup>\*\*\*</sup> and J. Surdej<sup>\*\*\*</sup>

Institut d'Astrophysique, Université de Liège, Avenue de Cointe, 5, B-4200 Cointe-Ougrée, Belgium

Received November 16, 1988; accepted January 18, 1989

**Summary.** Using improved relations for the first order moment of a P Cygni line profile, we have re-derived mass-loss rates for a sample of seventeen central stars of planetary nebulae observed with IUE in the low resolution mode. The average value of our mass-loss rates lies between  $10^{-7}$  and  $10^{-8} M_{\odot}/\text{yr}$ . We confirm the fact that the mass-loss rates of central stars of planetary nebulae cannot be simply extrapolated from the "mass-loss rate-luminosity" relation existing for Population I OB stars.

**Key words:** stars; mass-loss – planetary nebulae

### 1. Introduction

A significant number of central stars of planetary nebulae (CSPNs) are known to display in their ultraviolet spectra well developed P Cygni line profiles associated with fast ejected winds. The analysis of such profiles should therefore provide us with a better understanding of the possible effects of the wind on the structure of the nebula as well as on the evolution of the central star. On the basis of low resolution spectra obtained with the International Ultraviolet Explorer satellite (IUE), Cerruti-Sola and Perinotto (1985, hereafter CP) have studied the most representative sample of CSPN winds. These authors have namely derived the mass-loss rates ( $\dot{M}$ s) of seventeen CSPNs using the first order moment ( $W_1$ ) of selected P Cygni profiles. We recall that this method is well adapted to the analysis of low resolution IUE spectra since it is the only one which allows a quantitative interpretation of unresolved line profiles (Castor et al., 1981; Surdej, 1982, 1983a, b).

Because CP have applied a  $\dot{M} - W_1$  relation derived in the optically thin approximation to observed P Cygni profiles that were not unsaturated, Hutsemékers and Surdej (1987, 1988; hereafter Papers I and II) have pointed out that their mass-loss rates were systematically underestimated by more than one order of magnitude. Therefore, we re-derive in the present paper mass-loss rates of the CSPNs belonging to the CP sample with the help of improved first order moment calculations.

\* Aspirant au Fonds National de la Recherche Scientifique (Belgium)

\*\* Present address: European Southern Observatory, La Silla, Casilla 19001, Santiago 19, Chile

\*\*\* Chercheur Qualifié au Fonds National de la Recherche Scientifique (Belgium)

### 2. Mass-loss rate determination

Our mass-loss rates are essentially computed following a similar procedure as that described in Paper I. The measured moment  $W_1$  of a P Cygni line profile is first reported in a " $\log W_1 - \log W_1^0$ " diagram in order to infer the value of  $W_1^0$ . This latter parameter is directly proportional to the fractional mass-loss rate  $\dot{M} \bar{n}_g$ ,  $\bar{n}_g$  representing the average ionization fraction of the considered element. The theoretical " $\log W_1 - \log W_1^0$ " diagrams as well as the exact relation between  $W_1^0$  and  $\dot{M} \bar{n}_g$  (which involves atomic and stellar quantities) are given in Paper I for the case of subordinate line profiles and in Surdej and Hutsemékers (1989, hereafter Paper III) for the case of resonance doublet line transitions. Let us recall that the " $\log W_1 - \log W_1^0$ " curves depend on the opacity and velocity distributions characterizing the expanding envelope, except in a linear branch – corresponding to unsaturated line profiles – where  $W_1 = W_1^0$  independently of both types of these distributions. Theoretical " $\log W_1 - \log W_1^0$ " diagrams have been computed for eighteen combinations of realistic opacity and velocity distributions. But, since these distributions are a priori unknown, we adopt here as the most representative model the average " $\log W_1 - \log W_1^0$ " curve of the eighteen possible models.

Useful P Cygni line profiles are observed for the O IV  $\lambda 1341$ , O V  $\lambda 1371$ , N IV  $\lambda 1718$  subordinate lines and for the C IV  $\lambda 1549$  resonance doublet. The ionization fraction  $\bar{n}_g$  is evaluated following Cerruti-Sola and Perinotto (1985). If both the O IV and O V lines are present in the spectrum, we compute the mass-loss rate using the reasonable approximation  $\bar{n}_g(\text{O IV}) + \bar{n}_g(\text{O V}) = 1$ . These mass-loss rates constitute our best determinations. In the other cases, we adopt, for each ion, an average value of the ionization fraction calculated from the CSPNs where  $\dot{M}$  has been estimated assuming that  $\bar{n}_g(\text{O IV}) + \bar{n}_g(\text{O V}) = 1$ .

Because the aim of this paper is to investigate the effects of the line profile saturation on the mass-loss rate estimates, we adopt the measured  $W_1$  values and stellar parameters given by CP.

Our results are summarized in Table 1. For the sake of completeness, the mass-loss rates of previously investigated objects (NGC 6210, NGC 6826 and NGC 6543; cf. Paper I) are also reported in that Table. Let us note that we have not considered NGC 40 because the C IV line observed in the spectrum of this object is completely saturated and cannot provide any useful estimate of the mass-loss rate.

**Table 1.** Estimates of mass-loss rates for a sample of central stars of planetary nebulae

Nebula	Line	$W_1$	$W_1^0$	$\bar{n}_g$	$\dot{M} \bar{n}_g$	$\dot{M}$
NGC 6210	O IV	0.060	0.20	0.56	6.7-09	1.2-08
	O V	0.120	0.91	0.44	5.3-09	
NGC 6826	O IV	0.040	0.10	0.73	1.1-07	1.5-07
	O V	0.070	0.27	0.27	3.7-08	
NGC 6543	O IV	0.063	0.22	0.62	8.7-08	1.4-07
	O V	0.130	1.14	0.38	5.3-08	
NGC 1535	O IV	0.037	0.09	0.35	1.4-09	4.0-09
	O V	0.120	0.91	0.65	2.6-09	
IC 2149	O IV	0.087	0.42	0.97	1.7-06	1.8-06
	O V	0.050	0.14	0.03	4.9-08	
IC 3568	O IV	0.043	0.11	0.62	9.4-09	1.5-08
	O V	0.090	0.46	0.38	5.8-09	
IC 4593	O IV	0.020	0.04	0.54	1.4-08	2.6-08
	O V	0.070	0.27	0.46	1.2-08	
SwSt 1	O IV	0.050	0.14	0.87	1.7-07	2.0-07
	O V	0.060	0.20	0.13	2.6-08	
NGC 5189	N IV	0.290	36.10	0.50	1.6-07	3.2-07
NGC 6572	O IV	0.037	0.09	0.50	1.5-09	6.3-09
	N IV	0.160	2.11	0.50	4.8-09	
NGC 6891	O V	0.070	0.27	0.50	3.0-10	1.3-09
	N IV	0.070	0.27	0.50	9.9-10	
NGC 7009	O V	0.180	3.25	0.50	1.0-09	2.1-09
A 30	O V	0.120	0.91	0.50	1.2-10	2.5-10
A 78	O V	0.210	6.06	0.50	3.0-09	6.0-09
NGC 2371	C IV	0.380	1.74	2.0-04	7.6-11	3.8-07
IC 418	C IV	0.320	1.77	2.0-04	3.5-12	1.8-08
Hu 2-1	C IV	0.270	0.64	2.0-04	2.4-11	1.2-07

*Remarks:* As suggested by Cerruti-Sola and Perinotto (1985), we have divided the measured moment  $W_1$  (O IV) by three in order to take into account the blend with the interstellar line C II  $\lambda$  1335. Looking at high-resolution spectra of the central star of NGC 6543 (Bianchi et al., 1986), we can note that, also for this object, O IV  $\lambda$  1341 seems to be contaminated by C II  $\lambda$  1335. Therefore, we have divided by three the  $W_1$  (O IV) value measured by Castor et al. (1981) and obtained for the central star of NGC 6543 a lower  $\dot{M}$  estimate than that given in Paper I. Our mass-loss rates are expressed in  $M_\odot/\text{yr}$ .

### 3. Discussion and conclusions

We immediately see from Table 1 that in all cases the parameter  $W_1^0$  is significantly greater than the measured moment  $W_1$  and that, consequently, assuming the P Cygni line profiles to be unsaturated – i.e.  $W_1^0 = W_1$  – would lead to systematic errors on the mass-loss rate estimates ( $\dot{M} \propto W_1^0$ ). It is important to note here that P Cygni line profiles which do not reach the zero-intensity level (or even 50% of the continuum level) cannot be consequently classified as unsaturated ones. This is easy to understand if we remember that P Cygni line profiles result from the mere superposition of an emission and an absorption line profile.

We should keep in mind that even our most reliable  $\dot{M}$  estimates – obtained from both O IV and O V lines – are affected by uncertainties as large as one order of magnitude (cf. Paper I) and that the other  $\dot{M}$  values – obtained in adopting an average ionization fraction – are only useful from a statistical point of

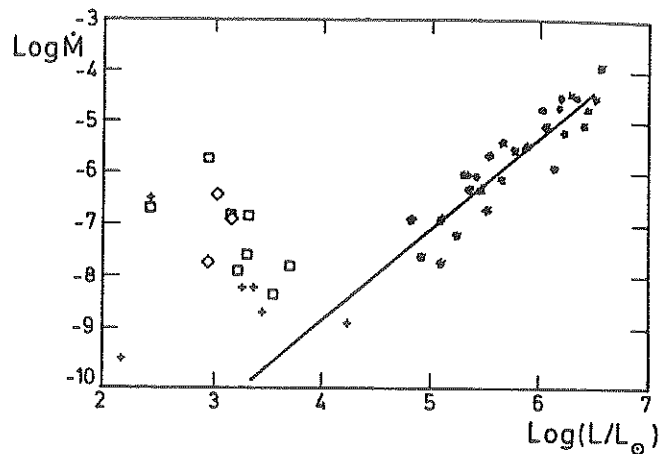


**Fig. 1.** Mass-loss rates (in  $M_\odot/\text{yr}$ ) evaluated for the CP sample of central stars of planetary nebulae are reported here as a function of the stellar luminosity;  $\square$  represent our best  $\dot{M}$  estimates, i.e. those obtained from the O IV  $\lambda$  1341 and O V  $\lambda$  1371 lines when they are both detected, + represent the  $\dot{M}$  values obtained from subordinate lines adopting an average ionization fraction,  $\diamond$  represent the  $\dot{M}$  values obtained from the C IV  $\lambda$  1549 resonance doublet and \* refer to the data of Abbott (1982) characterizing Population I OB stars

view. On the mean, these latter values do not show any systematic difference when compared to our best  $\dot{M}$  estimates. Let us remark that within these uncertainties, our  $\dot{M}$  values are in agreement with those obtained for objects observed in the IUE high resolution mode (Bianchi et al., 1986; Bombeck et al., 1986). This is especially true if we adopt the same stellar parameters as these authors.

Looking at Fig. 1, where we have reported our  $\dot{M}$  estimates against the stellar luminosity, we find, as CP, that mass-loss rates of CSPNs cannot be simply extrapolated from the mass-loss rates of young OB stars, especially if we remember that our best  $\dot{M}$  estimates still consist of lower limits.

The average mass-loss rate of the investigated CSPNs lies between  $10^{-7}$  and  $10^{-8} M_\odot/\text{yr}$ . Following Schönberner (1983), mass-loss is thought to possibly affect the evolution of the central star only if  $\dot{M} > 10^{-7} M_\odot/\text{yr}$ . It is therefore not yet clear whether mass-loss plays an important role on the evolution of a typical CSPN.

### References

- Abbott, D.C.: 1982, *Astrophys. J.* **259**, 282  
 Bianchi, L., Cerrato, S., Grewing, M.: 1986, *Astron. Astrophys.* **169**, 227  
 Bombeck, G., Köppen, J., Bastian, U.: 1986, ESA SP-263, p. 287  
 Castor, J.I., Lutz, J.H., Seaton, M.J.: 1981, *Monthly Notices Roy. Astron. Soc.* **194**, 547  
 Cerruti-Sola, M., Perinotto, M.: 1985, *Astrophys. J.* **291**, 237  
 Hutsemékers, D., Surdej, J.: 1987, *Astron. Astrophys.* **173**, 101 (Paper I)  
 Hutsemékers, D., Surdej, J.: 1988, in *Mass Outflows from Stars and Galactic Nuclei*, eds. L. Bianchi, R. Gilmozzi, Reidel, Dordrecht, p. 253 (Paper II)  
 Schönberner, D.: 1983, *Astrophys. J.* **272**, 708  
 Surdej, J.: 1982, *Astrophys. Space Sci.* **88**, 31  
 Surdej, J.: 1983a, *Astron. Astrophys.* **127**, 304  
 Surdej, J.: 1983b, *Astrophys. Space Sci.* **90**, 299  
 Surdej, J., Hutsemékers, D.: 1989, *Astron. Astrophys.* (submitted) (Paper III)

### Chapitre 3

#### CONTAMINATION PHOTOSPHERIQUE DES PROFILS DE RAIES DE TYPE P CYGNI OBSERVES DANS LE SPECTRE ULTRAVIOLET DES ETOILES DE TYPE O

La publication par Walborn, Nichols-Bohlin et Panek (1985) d'un atlas de spectres IUE pour des étoiles de type O dans le domaine spectral  $\lambda\lambda$  1200-1900 Å nous a incité à mesurer les moments  $W_n$  ( $n = 0-3$ ) des profils observés pour les raies de SiIV, CIV, HeII  $\lambda$  1640 et NIV  $\lambda$  1718. Lors de ces mesures, nous avons expérimenté de sérieuses difficultés en essayant de fixer le niveau du spectre continu local  $E_c$  qui apparaît dans la définition des moments d'ordre  $n$  (cf. Equation 2.1). Il est très vite apparu qu'une absorption de ce continu par de très nombreuses raies interstellaires et photosphériques, pour la plupart inconnues jusqu'ici, était la cause principale de ces problèmes. La construction de différents spectres moyens à partir des 101 spectres publiés pour 98 étoiles distinctes dans l'atlas IUE montre bien cet effet. Ainsi, nous avons illustré dans les figures 3.1 et 3.2 la région spectrale voisine de CIV résultant respectivement de la moyenne des 50 premiers et 51 derniers spectres de l'atlas. La similarité frappante entre les très nombreux détails spectraux visibles dans ces différents spectres atteste qu'il ne s'agit pas de bruit mais bien d'une véritable pollution du spectre continu et des profils de raies de type P Cygni observés par des raies en absorption. Une étude détaillée de ces spectres a été réalisée tout récemment par Nemry, Surdej et

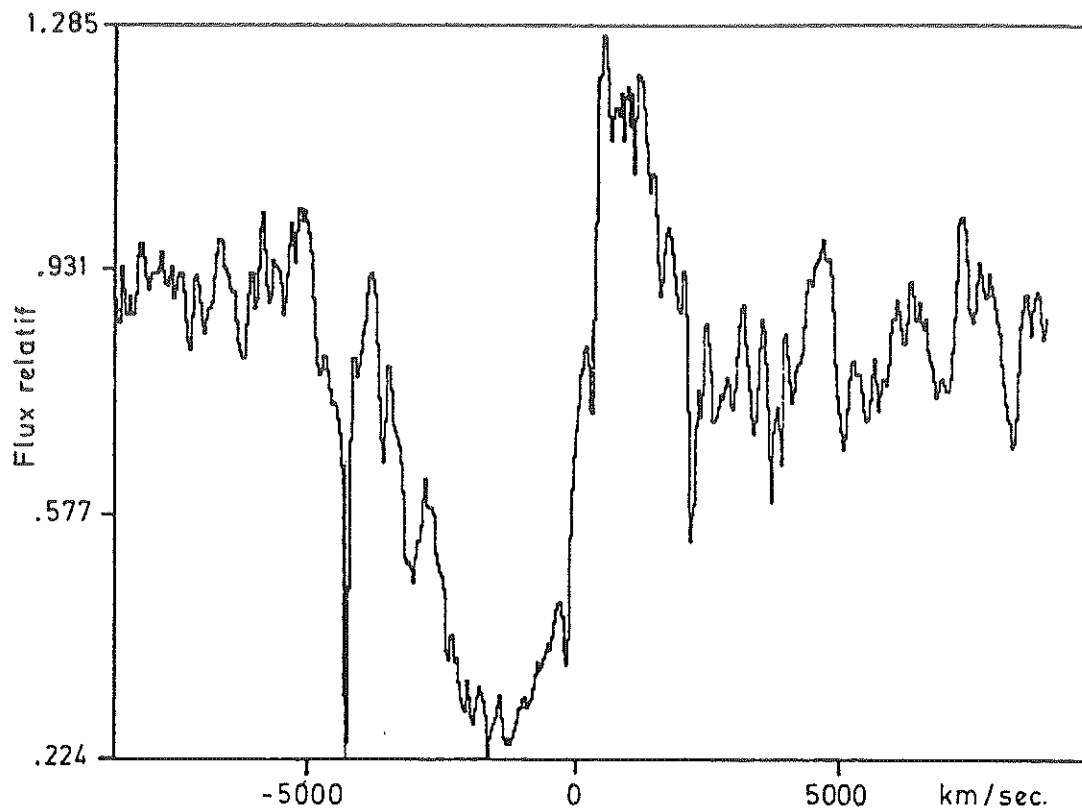


Figure 3.1: Moyenne du profil de raie de CIV pour les 50 premiers spectres IUE publiés par Walborn, Nichols-Bohlin et Panek (1985).

Hernaiz (1990, article 12) et a conduit à plusieurs conclusions intéressantes. Au moyen de tables d'identification de raies spectrales publiées par Ekberg (1975), Ekberg et Edlen (1978), Bruhweiler, Kondo et McCluskey (1981) et Dean et Bruhweiler (1985), nous avons tout d'abord trouvé que la pollution photosphérique du spectre continu stellaire des étoiles de type O dans les domaines  $\lambda\lambda$  1270-1500 (SiIV) et  $\lambda\lambda$  1500-1860 Å (CIV, HeII et NIV) est principalement causée par des raies de FeV et FeIV. Par ailleurs, nous avons montré que la non prise en compte de cet effet de contamination photosphérique des profils de raies de type P Cygni conduit à des mesures erronées du moment  $W_1$ , résultant en des incertitudes sur la détermination du taux de perte de masse  $\dot{M}$



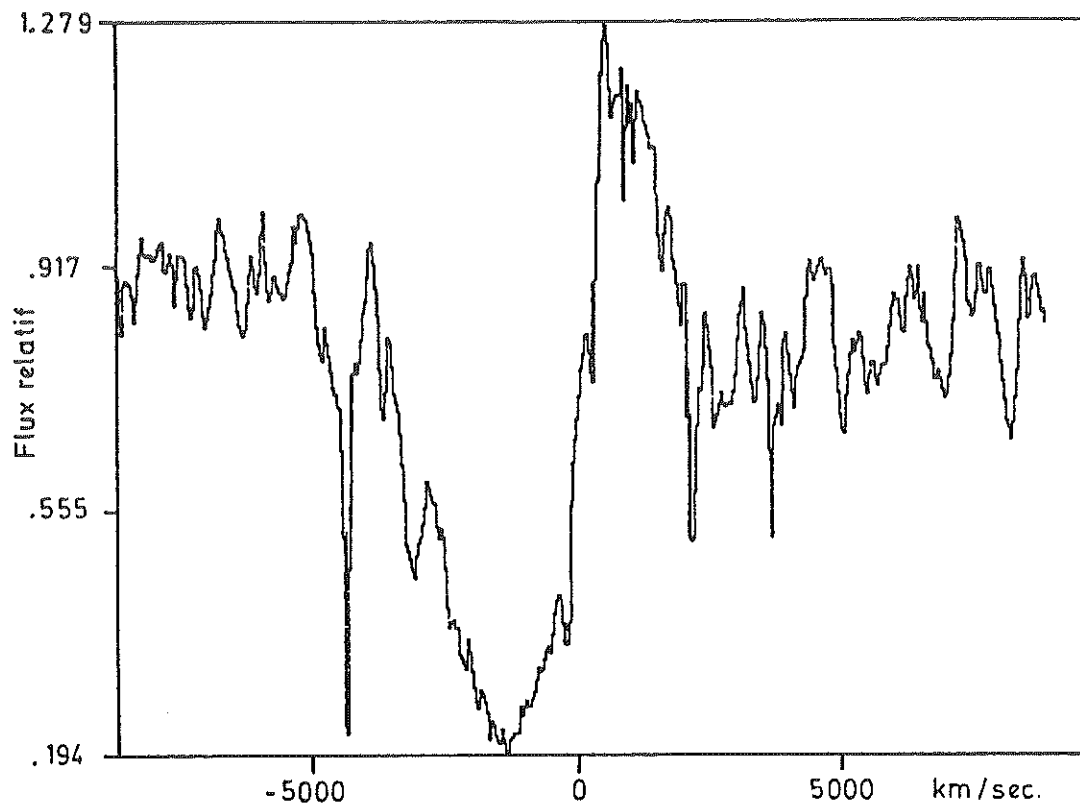


Figure 3.2: Moyenne du profil de raie de CIV pour les 51 derniers spectres IUE publiés par Walborn, Nichols-Bohlin et Panek (1985).

pouvant atteindre 50% et plus. En ce qui concerne le profil de raie de CIV, la présence de raies multiples de FeIV en absorption au voisinage de  $\lambda\lambda$  1527 et 1533 Å affecte même une détermination correcte de la vitesse terminale du vent stellaire à partir de la mesure de la position de l'aile bleue de la composante en absorption du profil P Cygni (cf. Figs. 3.1, 3.2 et les Figs. 3b-e dans Blomme, 1990). Les composantes étroites en émission apparaissant près de l'émission centrale de CIV sont aussi le résultat de la pollution photosphérique par des raies de FeIV (cf. Figs. 3.1, 3.2 et la Fig. 1 dans Bernabeu, Magazzù et Stalio, 1989). Nous avons suggéré une méthode de correction des profils de raies observés et celle-ci devrait conduire à une révision systématique des taux de perte de masse  $\dot{M}$  publiés pour les étoiles

de type O. En toute rigueur, les calculs théoriques de profils de raies de type P Cygni visant à reproduire les spectres d'étoiles de type O devront dorénavant prendre en compte comme condition initiale le spectre continu stellaire pollué par les très nombreuses raies photosphériques en absorption dues aux ions  $\text{Fe}^{3+}$  et  $\text{Fe}^{4+}$ . En collaboration avec Françoise Nemry et Damien Hutsemékers, nous effectuons en ce moment de tels calculs qui incluent aussi des effets de turbulence dans l'atmosphère en expansion. Notre approche est semblable à celle suivie par Lamers, Cerruti-Sola et Perinotto (1987) et Perinotto, Cerruti-Sola et Lamers (1989), à la différence près que nos calculs de la fonction source  $S_{12}$  sont aussi effectués d'une façon cohérente, c'est-à-dire en tenant compte des effets de turbulence.

## Article 12

### POLLUTION OF P CYGNI LINE PROFILES BY FEIV AND FEV PHOTOSPHERIC ABSORPTION IN THE ULTRAVIOLET SPECTRUM OF O-TYPE STARS

Nemry, F., Surdej, J., Hernaiz, A.: 1990, soumis à Astron. Astrophys. Letters.

Lors de l'analyse des spectres IUE ( $\lambda\lambda$  1200-1900 Å) des étoiles de type O publiés dans l'atlas de Walborn, Nichols-Bohlin et Panek (1985), nous avons mis en évidence un effet de pollution majeur des profils de raies de type P Cygni dus à SiIV, CIV, HeII et NIV par de nombreuses raies interstellaires et photosphériques présentes en absorption. Nous avons trouvé que des raies photosphériques de FeV et FeIV étaient responsables de cette contamination, respectivement dans les domaines spectraux  $\lambda\lambda$  1270-1500 (SiIV) et  $\lambda\lambda$  1500-1860 Å (CIV, HeII, NIV). Au moyen de la méthode du moment d'ordre 1, nous avons montré que les effets de cette pollution photosphérique peuvent conduire à des erreurs systématiques de l'ordre de 50% et plus lors de la détermination du taux de perte de masse  $\dot{M}$  des étoiles de type O. Nous soulignons l'importance de corriger les profils de raies observés de cette pollution photosphérique avant de déduire les valeurs des paramètres physiques ( $\dot{M}$ ,  $v_{\max}$ ,  $v(r)$ ,  $\tau_{12}^r(v)$ , etc.) caractérisant les atmosphères en expansion autour des étoiles de type O.



Pollution of P Cygni line profiles by FeIV and FeV photospheric absorption in the ultraviolet spectrum of O-type stars

F. Nemry <sup>1,\*</sup>, J. Surdej <sup>1,\*\*</sup> and A. Hernaiz <sup>2</sup>

<sup>1</sup> Institut d'Astrophysique, Université de Liège,  
Avenue de Cointe 5, B-4200 Liège, Belgium

<sup>2</sup> I.A.F.E.  
CC67 - SUC28  
1428 Buenos Aires, Argentina

\* also, Aspirant au Fonds National de la Recherche Scientifique (Belgium)

\*\* also, Chercheur Qualifié au Fonds National de la Recherche Scientifique (Belgium)

Proofs to be sent to: Dr. J. Surdej  
Institut d'Astrophysique,  
Université de Liège,  
Avenue de Cointe 5,  
B-4200 Liège, Belgium

Send offprint requests to: see above address

Thesaurus code numbers: 12.01.1, 12.02.1, 12.03.1, 19.09.1,  
19.48.1

Section: Letters

Submitted to: Main Journal of Astronomy and Astrophysics

Abstract: When visualizing the IUE Atlas of O-Type Spectra from 1200 to 1900 Å (Walborn et al. 1985), one notices immediately that underlying interstellar and photospheric absorption lines do affect significantly both the star continuum and the P Cygni profiles due to resonance line transitions of SiIV, CIV, etc. We report here that the main pollution in the spectral ranges 1270-1500 and 1500-1860 Å is caused by photospheric absorption lines of FeV and FeIV, respectively. Making use of the first order moment  $W_1$  of a P Cygni line profile, we show that the effect of this photospheric pollution may lead to systematic errors, exceeding typically 50 %, in the determination of mass loss rates. We also emphasize the importance to correct the observed P Cygni line profiles for this pollution when studying the dependence of the physical parameters, terminal velocity, etc. of the stellar winds upon the various classes and types of O stars.

Key-words: Lines: formation, Lines: identification, Lines: profile, Spectroscopy, Stars: mass loss.

## 1. Introduction:

The publication by Walborn, Nichols-Bohlin and Panek (1985, referred hereafter as WNP) of an atlas of IUE O-type spectra has provided astrophysicists with a unique tool to study the mass loss phenomena taking place in the atmospheres of early-type stars. Among the various methods proposed for analyzing the P Cygni profiles due to resonance line transitions, the  $n^{\text{th}}$  order moment technique has proven to be well adapted for a statistical investigation of the properties of stellar winds (Surdej, 1983b, 1985; Surdej and Hutsemékers, 1990). The moment  $W_n$  of a P Cygni line profile appears to be the generalization of the equivalent width of an absorption line and gives rise, in the case of expanding atmospheres, to useful astrophysical diagrams similar to the well known curve of growth for the case of static atmospheres. We recall here that, in the optically thin approximation, the moments  $W_1$ ,  $W_2$  and  $W_3$  are directly related to the mass loss, to the momentum and to the kinetic energy rates of the expanding envelope, respectively (Castor et al. 1981; Surdej, 1982, 1983a, Surdej, 1985). In the process of constructing  $W_n - W_{n'}$  diagrams ( $n \neq n'$ ) from measurements of the  $n^{\text{th}}$  order moments of the P Cygni profiles compiled in WNP, we have experienced serious difficulties in setting unambiguously the level of the local stellar continua. Therefore, in order to identify all interstellar and photospheric absorption lines affecting the continuum spectrum of those early-type stars, we have summed up and averaged the 101 spectra of 98 stars listed in the atlas. It has then become clear that the P Cygni profiles themselves were severely polluted not only by known interstellar lines but also by unidentified photospheric absorption lines. We report here on the identification of these "polluting" lines and also about their effects on the determination of mass loss rates, terminal velocities, etc. as derived from the analysis of observed P Cygni line profiles.

## 2. Identification of the polluting absorption lines:

In order to identify all interstellar lines present in the IUE spectra of O-type stars (see WNP for a detailed description of the spectrograms in their atlas), we decided first to construct different sets of averaged spectra: we chose 10 sets of 10 averaged spectra, 4 sets of 25 averaged spectra, etc. The comparison of the resulting mean spectra led us to the conclusion that, alike the case of well known interstellar lines (cf. compilation in WNP, Table 3),

most of the other features seen in the individual spectra were also due to physical lines and not to noise, as it is sometimes believed. In a second step, we made use of the compilation of atomic wavelengths data by Kelly and Palumbo (1973), by Striganov and Sventitskii (1968) and by Moore (1962, 1967, 1970, 1971, 1975), and could identify some of the lines as being of interstellar or photospheric origin but the results were not very satisfactory because most of the absorption features remained unidentified. We could solve this puzzle thanks to line identifications reported by Bruhweiler et al. (1981) and Dean and Bruhweiler (1985) for the spectra of the subdwarfs BD+75°325, HD49798 and BD+28°4211 and of the main-sequence star HD46202. We could finally complete all our identifications using the lists of experimental wavelengths and predicted relative intensities of FeV by Ekberg (1975) and of FeIV by Ekberg and Edlen (1978). A detailed list of line identifications in the whole average spectrum will be published elsewhere (Nemry et al. 1990a). To summarize, we can say that the FeV lines dominate in the spectral range 1270-1500 Å, while the FeIV lines are more prominent between 1500 and 1860 Å. In this Letter, we concentrate on the identification of the polluting lines located within the P Cygni line profiles due to SiIV, CIV, HeII and NIV, which are of general interest for the study of mass loss from O-type stars.

### 2.1 SiIV $\lambda\lambda$ 1393, 1402 Å :

A forest of FeV lines affects considerably the whole SiIV P Cygni line profile. FeIV does only contribute marginally to this line pollution. These effects are well illustrated in Figs. 1a and 1b where the vertical lines indicate the positions and strengths of the FeV (upper part) and FeIV (lower part) lines. Known interstellar and photospheric absorption lines are also marked in these figures. Fig. 1a represents the average SiIV P Cygni line profile for 28 supergiant O-type stars selected from the atlas of WNP. Figure 1b refers to a subsample of 20 main-sequence and dwarf O-type stars, characterized by fainter luminosities and revealing no wind effects. We shall take advantage in Section 3 of this well known SiIV stellar wind - luminosity effect (Walborn and Panek, 1984, compare Figs. 1a and 1b) to evaluate the influence of line pollution on the determination of mass loss parameters. Let us note the general very good agreement between the positions and strengths of the FeV lines and the absorption features polluting both the local stellar



continuum (cf. the series of lines near  $\lambda\lambda$  1374, 1376, 1378, 1415 and 1420 Å) and the SiIV P Cygni profile (cf. the strong lines near  $\lambda\lambda$  1388, 1398, 1401, 1402, 1407 and 1409 Å) .

## 2.2 CIV $\lambda\lambda$ 1548, 1550 Å :

With the exception of five objects in the WNP atlas, all stars display in their spectra a P Cygni profile for the CIV resonance line transitions. We have therefore illustrated in Figure 2 the average CIV line profile as obtained from all 98 stars. We notice that unlike for SiIV, a main pollution caused by FeIV lines occurs in this spectral range. The most noticeable feature is the strong depression of the star continuum on the red side of the CIV P Cygni profile due to the increasing density of FeIV lines with wavelength. Also striking are the blends of FeIV absorption lines near  $\lambda\lambda$  1527 and 1533 Å which affect a proper determination of the terminal velocity from the measurement of the blue edge of the CIV line profile (cf. Figs. 3b-e in Blomme, 1990). The narrow emission peak components which are often seen near the center of the CIV emission line profile (cf. Fig. 2 and Fig. 1 in Bernabeu et al. 1989) are also artefacts of the FeIV line pollution.

## 2.3 HeII $\lambda$ 1640 Å :

Figure 3 represents a plot of the average spectral region near HeII as obtained also from the spectra of all 98 stars. The presence of strong FeIV lines near the rest position of HeII makes questionable the real presence of this line.

## 2.4 NIV $\lambda$ 1718 Å :

In the spectral region near NIV  $\lambda$  1718 Å , as in the previous one, the density of FeIV lines is quite high. In particular, there are blends of strong FeIV lines near  $\lambda\lambda$  1718 and 1724 Å which perturb significantly the NIV absorption trough and the red wing of the emission component.

## 2.5 conclusions:

We have seen that in each of the SiIV, CIV, HeII and NIV spectral regions, there is an essentially good correlation between the expected strengths of FeIV and/or FeV lines and the observed intensities of the polluting photospheric absorption lines. We may naturally wonder now: i) whether there is any influence of the

stellar parameters on the intensities of those FeIV and FeV lines? and ii) what are the effects of the Fe lines on the determination of the physical parameters characterizing the observed P Cygni profiles?

### 3. Influence of the stellar parameters on the observed intensities of the polluting iron lines:

In order to test the possible effects of the effective temperature  $T_{\text{eff}}$  and of the stellar luminosity  $L_*$  on the observed intensities of FeIV and FeV lines in the spectra of the 98 stars compiled in WNP, we have constructed several (6) distinct groups of stars characterized by different average values of  $T_{\text{eff}}$  and  $L_*$ . The stellar parameters of these stars were taken from Howarth and Prinja (1989) and Groenewegen and Lamers (1989). We compared then the intensity of the FeIV and FeV lines in the average spectra of the six different groups of stars and report here the following points i) the intensity of the FeV lines increases with  $\log(T_{\text{eff}}) \in [4.46, 4.70]$  while the FeIV lines present the opposite trend, ii) the strength of the FeIV lines is quite insensitive to the stellar luminosity  $\log(L_*) \in [4.50, 6.20]$ , iii) while the same is true for the FeV lines at temperatures in the range  $\log(T_{\text{eff}}) \geq 4.58$ , the strength of the FeV lines does also increase with  $\log(L_*) \in [4.50, 6.20]$  for  $\log(T_{\text{eff}}) \leq 4.58$ , and finally, iv) the absorption feature present at  $\lambda 1640 \text{ \AA}$ , and usually attributed to HeII, shows the same behaviour with  $T_{\text{eff}}$  as the FeIV lines. This supports again our previous claim that HeII is probably not present in the atmospheres of most O-type stars.

### 4. Influence of the FeIV and FeV lines on the determination of the physical parameters characterizing the observed P Cygni profiles:

As already noticed in Section 2.2, the presence of FeIV lines in the CIV P Cygni line profile affects a proper determination of the edge velocity. In order to evaluate the additional effects of the polluting lines on the estimate of mass loss rates, we have performed measurements of the first order moment  $W_1$  for the SiIV and CIV profiles in different ways. For the SiIV line profiles, we made use of the average spectrum of the stars showing no wind effects (see Fig. 1b) to correct for the FeV pollution in the average spectrum of the supergiant stars displaying well developed SiIV

P Cygni profiles (see Fig. 1a). A first order correction was applied as follows: we divided the spectrum "1a" by "1b" outside the region occupied by the SiIV emission line component, whereas we subtracted spectrum "1b" - 1 from spectrum "1a" in the spectral region occupied by the SiIV emission line component. The result is shown in Fig. 4 where the solid line represents the original spectrum (cf. Fig. 1a) and where the dashed line corresponds to the corrected spectrum. This figure provides a good illustration of the FeV lines blanketing effect. Three different local continua, labelled A, B and C, have also been represented in this figure. The two first ones correspond to the uncorrected line profile. Continuum A was estimated assuming that one ignores totally the presence of the FeV lines. Continuum B is represented by taking into account the presence of these lines. The latter was drawn just below the level of the highest points in the observed spectral continuum. Using these different continua, we assigned an edge velocity (cf. the positions of the crosses in Fig. 4). Then, we measured the first order moment  $W_1$  (A & B) in both cases. Continuum C was drawn with respect to the corrected line profile and was used to measure the first order moment  $W_1$  (C) considered as being the most accurate one. It was easy to determine in this way the error affecting the mass loss rate estimates based upon the previous measurements. A similar treatment was applied to the CIV line profile illustrated in Fig. 2, using the average spectrum of the five stars showing no wind effect as the correcting spectrum. The results are shown in Fig. 5. Again, we can visualize the spectacular blanketing effect due to the FeIV lines, increasing towards longer wavelengths. We then made use of the " $\log(W_1) - \log(W_1^0)$ " diagrams calculated for resonance doublet P Cygni line profiles in the context of the Sobolev approximation (Surdej and Hutsemékers, 1990). Recalling that the quantity  $W_1^0$  is proportional to the product of the mass loss rate  $\dot{M}$  and the fractional abundance  $n(\text{level})$  of the ion under study, we have reported in Table 1 the relative uncertainties affecting the mass loss rate estimates for the SiIV, CIV line profiles illustrated in Figs. 4 and 5 as well as average values derived for a dozen of other representative cases in the WNP atlas. Since the relative uncertainties due to the FeIV and FeV line pollution in the mass loss rate estimates are typically of the order of 50%, but also possibly larger, it is imperative to take the polluted continuum stellar spectrum as a boundary condition when calculating

theoretical P Cygni line profiles representative of O-type stars. Results summarized in Table 1 clearly show that it is not just sufficient to set a pseudo continuum below the level of the highest points in the observed spectral continuum to correct for the effects of underlying photospheric and interstellar absorption lines. Finally, with the exception of optically thin P Cygni line profiles (Surdej, 1983a, 1985), it is also very important to include in the radiative transfer the effects of turbulence present in the atmospheres of O-type stars (Hamann, 1981, Lamers et al., 1987, Groenewegen et al., 1989, Groenewegen and Lamers, 1989, Nemry et al. 1990b).

#### References:

- Bernabeu, G., Magazzù, A., Stalio, R.: 1989, *Astron. Astrophys.* 226, 215
- Blomme, R.: 1990, *Astron. Astrophys.* 229, 513
- Bruhweiler, F.C., Kondo, Y., McCluskey, G.E.: 1981, *Astrophys. J. Suppl.* 46, 255
- Castor, J.I., Lutz, J.H., Seaton, M.J.: 1981, *Monthly Notices Roy. Astron. Soc.* 194, 547
- Dean, C.A., Bruhweiler, F.C.: 1985, *Astrophys. J. Suppl.* 57, 133
- Ekberg, J.O.: 1975, *Phys. Scripta* 12, 42
- Ekberg, J.O., Edlen, B.: 1978, *Phys. Scripta* 18, 107
- Groenewegen, M.A.T., Lamers, H.J.G.L.M.: 1989, *Astron. Astrophys. Suppl. Ser.* 79, 359
- Groenewegen, M.A.T., Lamers, H.J.G.L.M., Pauldrach, A.W.A.: 1989, *Astron. Astrophys.* 221, 78
- Hamann, W.-R.: 1981, *Astron. Astrophys.* 93, 353
- Howarth, I.D., Prinja, R.K.: 1989, *Astrophys. J. Suppl.* 69, 527
- Kelly, R.L., Palumbo, L.J.: 1973, "Atomic and ionic emission lines below 2000 angstroms", *N&L Rept.* N°7599.
- Lamers, H.J.G.L.M., Cerruti-Sola, M., Perinotto, M.: 1987, *Astrophys. J.* 314, 726
- Moore, C.E.: 1962, *NBS Circ.* 488, §4
- Moore, C.E.: 1967, *NSRDS-NBS3*, §2
- Moore, C.E.: 1970, *NSRDS-NBS3*, §3
- Moore, C.E.: 1971, *NSRDS-NBS3*, §4
- Moore, C.E.: 1975, *NSRDS-NBS3*, §5
- Nemry, F., Surdej, J., Hernaiz, A.: 1990a, in preparation
- Nemry, F., Hutsemékers, D., Surdej, J.: 1990b, in preparation

Striganov, Sventitskii: 1968, "Tables of spectral lines of neutral and ionized atoms", Plenum Publishing Corporation

Surdej, J.: 1982, *Astrophys. Space Sci.* 88, 31

Surdej, J.: 1983a, *Astrophys. Space Sci.* 90, 299

Surdej, J.: 1983b, *Astron. Astrophys.* 127, 304

Surdej, J.: 1985, *Astron. Astrophys.* 152, 361

Surdej and Hutsemékers: 1990, *Astron. Astrophys.*, in press

Walborn, N.R., Panek, R.J.: 1984, *Astrophys. J. Letters* 280, L27

Walborn, N.R., Nichols-Bohlin, J., Panek, R.J.: 1985, *International Ultraviolet Explorer Atlas of O-type Spectra from 1200 to 1900 Å*, NASA RP-1155 (WNP)

Table 1: Relative uncertainties affecting the estimate of mass loss rates  $\dot{M}$  when no corrections for the pollution of FeIV and FeV lines are brought to the observed P Cygni profiles. The labels A, B and C refer to the different settings of the local stellar continuum (see Text).

P Cygni line profile	$\frac{ \dot{M}(A) - \dot{M}(C) }{\dot{M}(C)}$	$\frac{ \dot{M}(B) - \dot{M}(C) }{\dot{M}(C)}$
SiIV as illustrated in Fig.4	32%	33%
CIV as illustrated in Fig.5	65%	36%
Other representative line profiles in the WNP atlas	54%	45%

Figure captions:

- Figure 1: (a) Representative SiIV P Cygni line profile for supergiant O-type stars as constructed from the average spectrum of 28 objects selected in the WNP atlas. The vertical lines at the top and at the bottom of this figure represent the expected positions and strengths of FeV and FeIV lines, respectively (see Text) (b) Same as (a) but for a sub-sample of 20 main-sequence and dwarf O-type stars.
- Figure 2: Same as Fig. 1 but for the CIV P Cygni line profile and the complete sample of 98 O-type stars from the WNP atlas.
- Figure 3: Same as Fig. 2 but for the spectral region near the HeII line transition.
- Figure 4: The solid line in this figure represents the original SiIV P Cygni line profile of supergiant O-type stars as illustrated in Fig. 1a. The dashed line corresponds to the former line profile corrected for the pollution of photospheric absorption lines by means of the stellar spectrum in Fig. 1b, unaffected by stellar wind effects (see Text). The horizontal lines labelled A, B and C represent different settings of the local stellar continuum used when measuring the first order moment  $W_1$ .
- Figure 5: As Fig. 4 but for the representative CIV P Cygni line profile of a sample of 20 main-sequence and dwarf O-type stars.

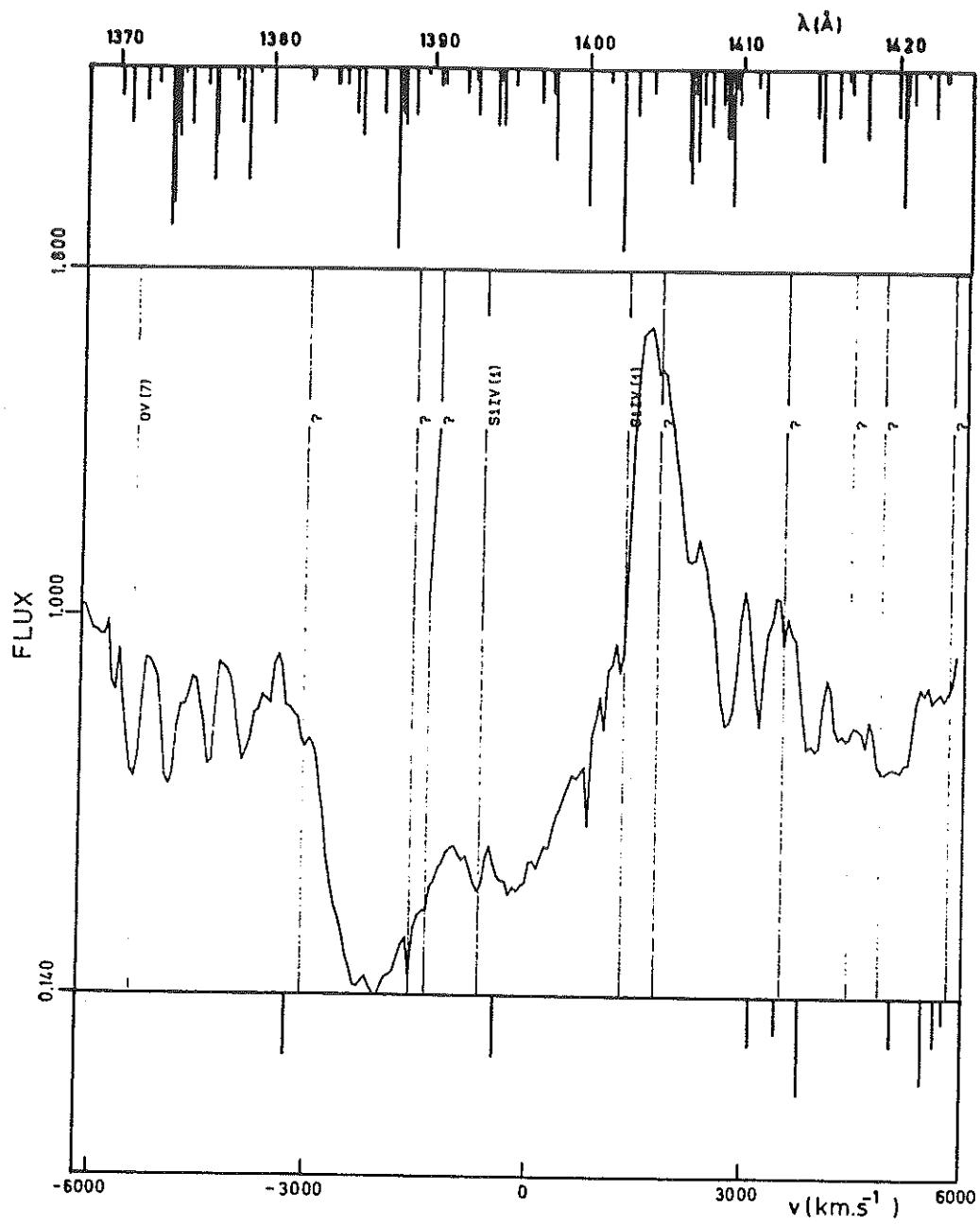


Fig. 1a



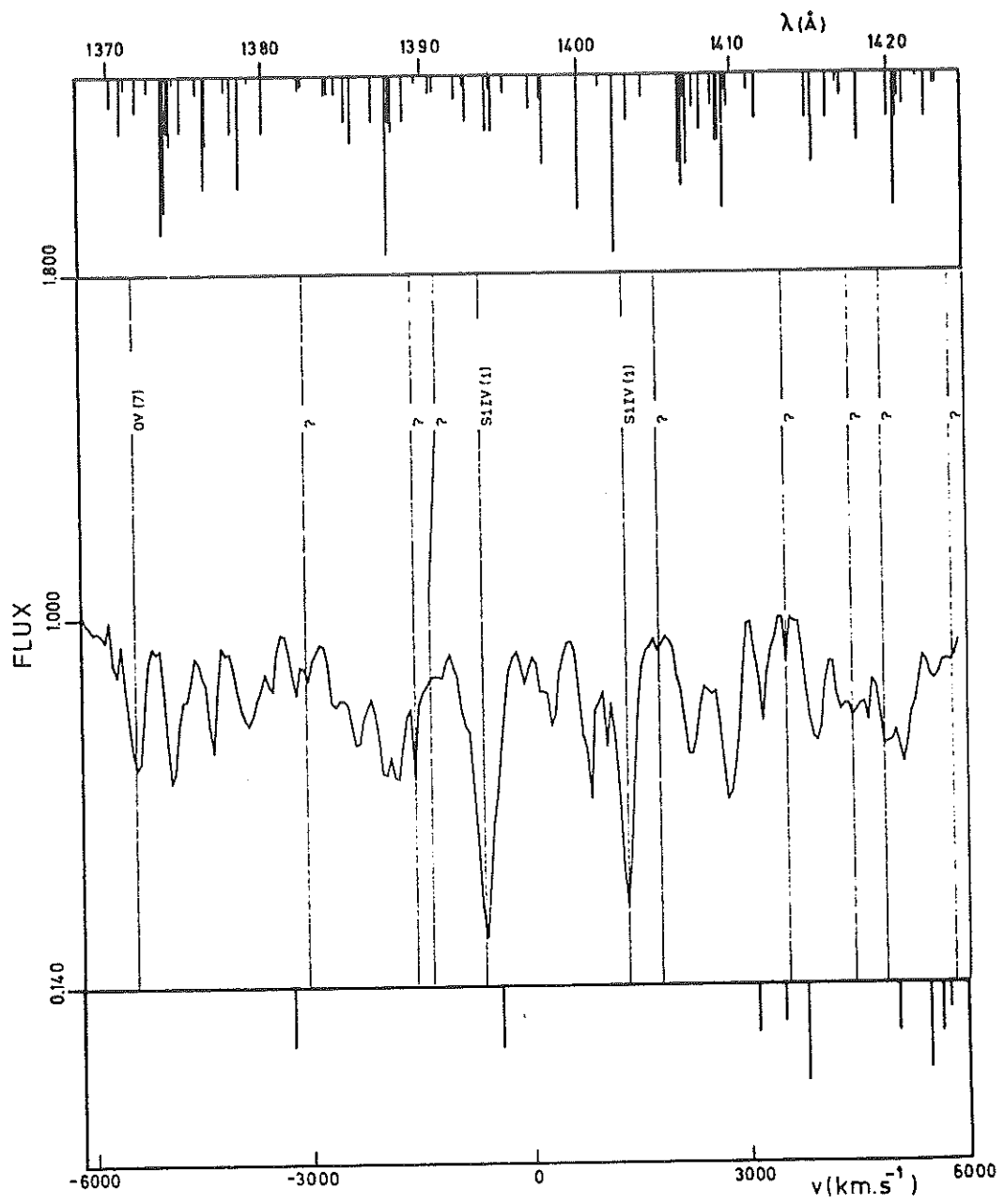


Fig. 1b

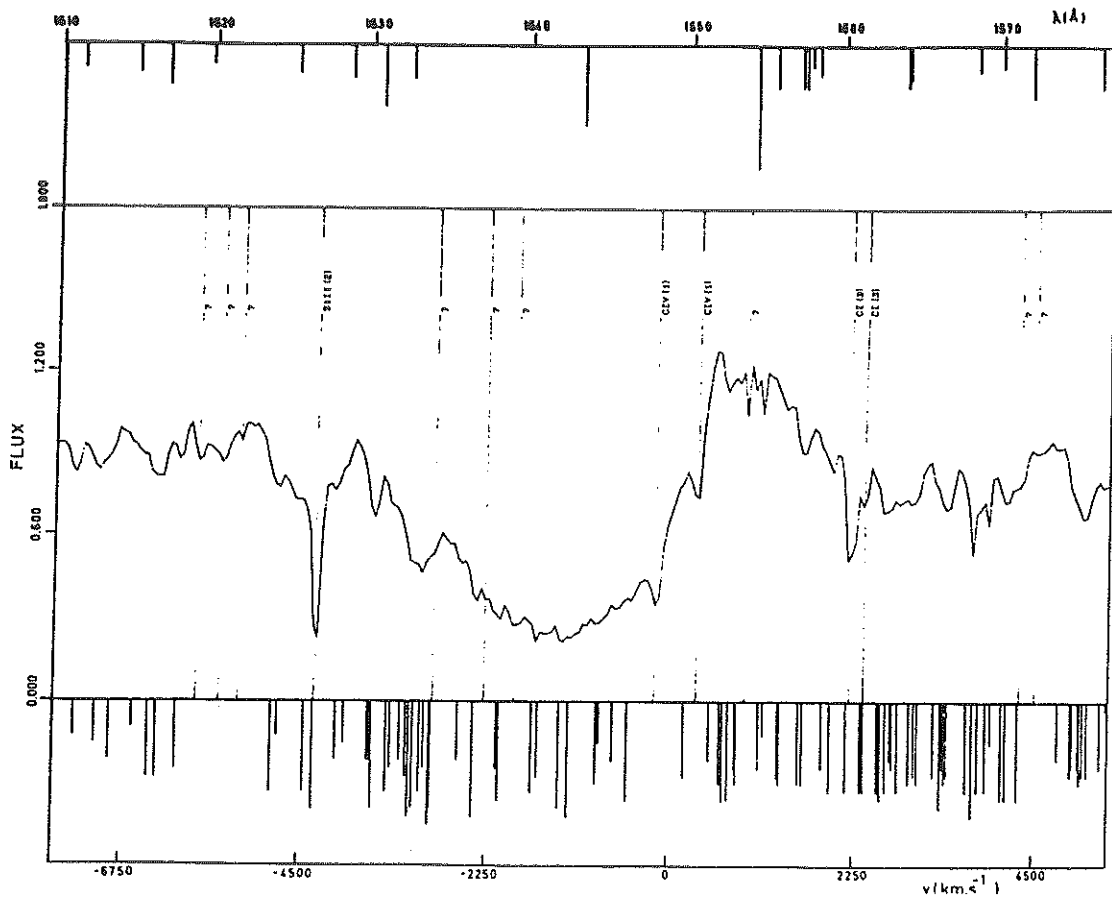


Fig. 2

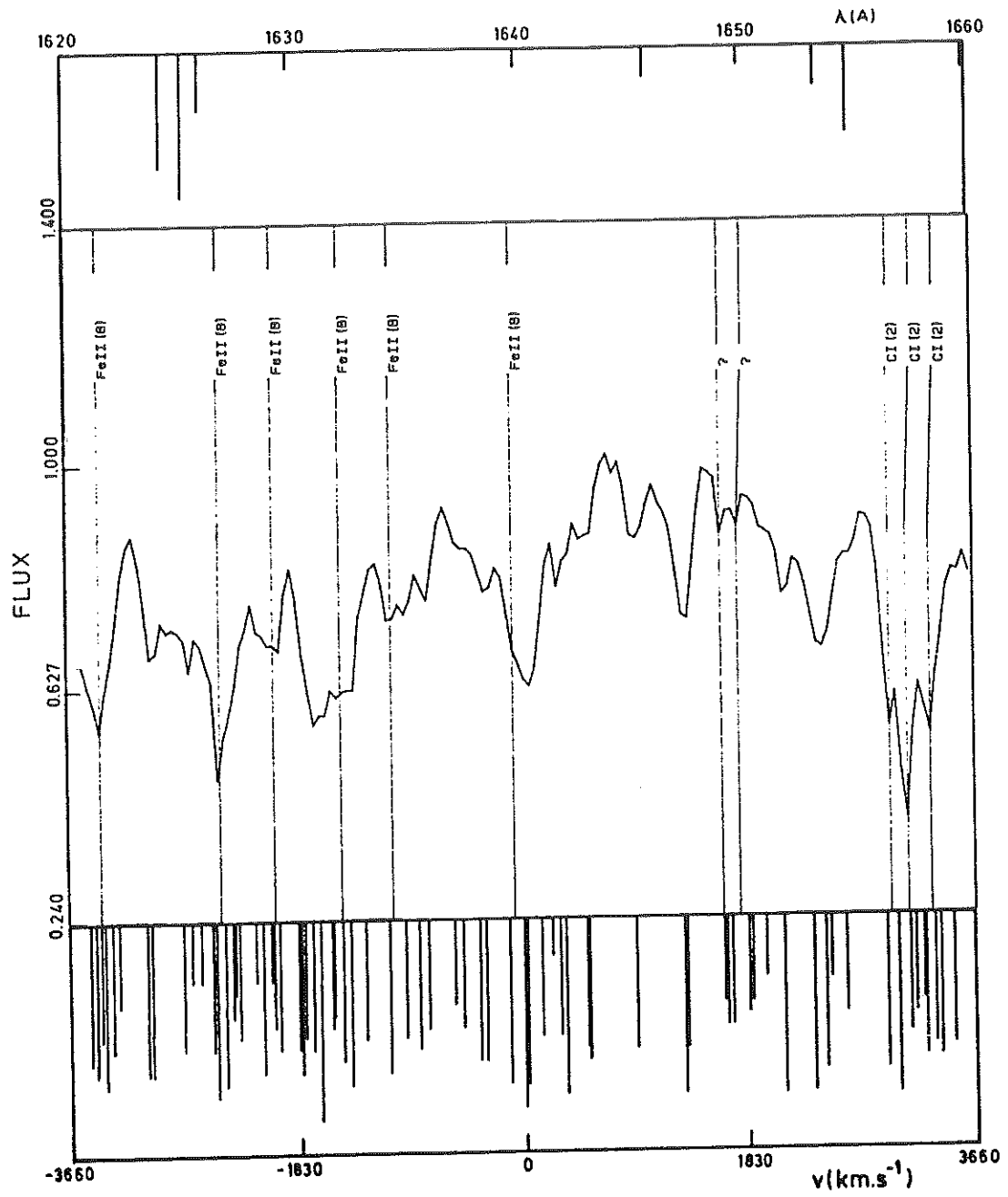


Fig. 3

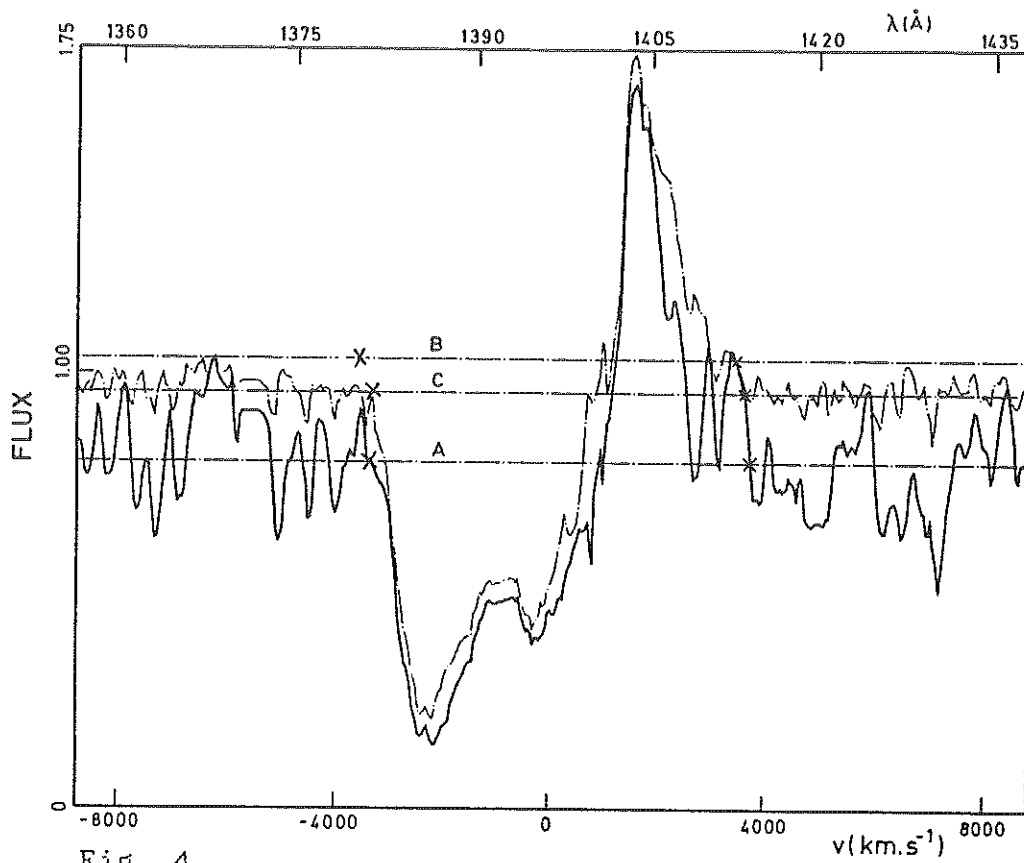


Fig. 4

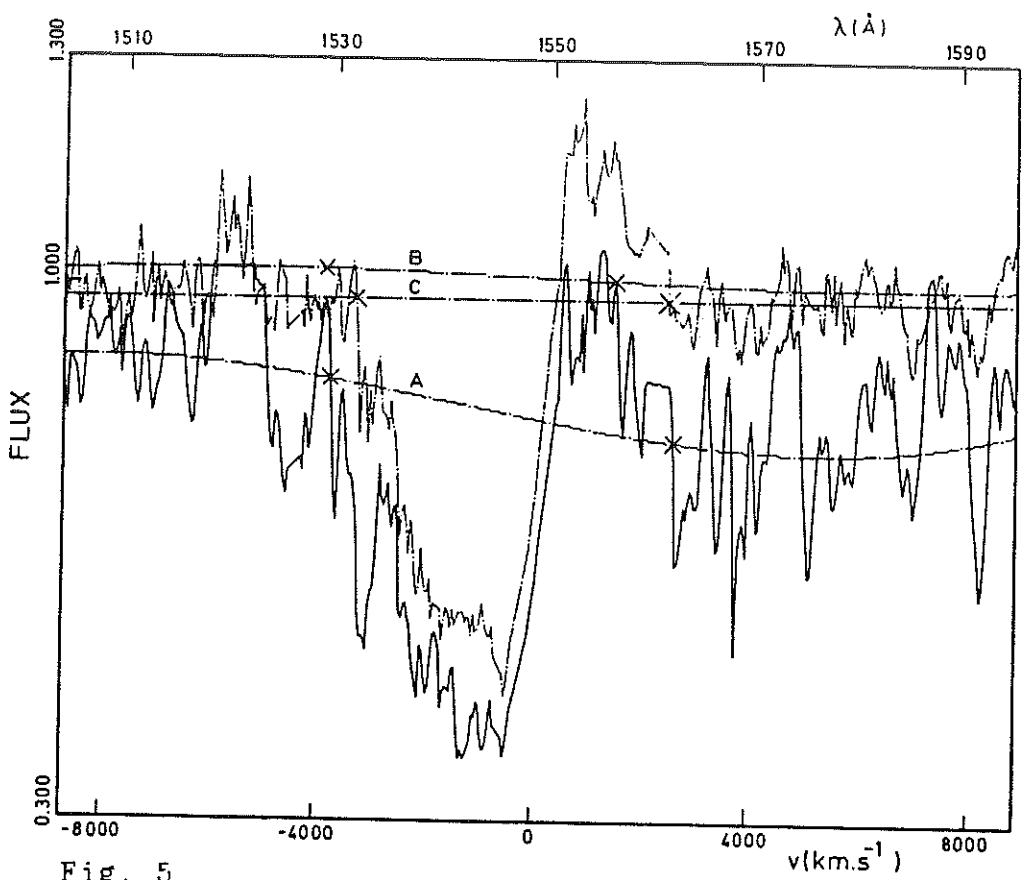


Fig. 5

## Chapitre 4

### QUASARS DE TYPE BAL ET EFFETS DE MICRO-LENTILLE GRAVITATIONNELLE

Les quasars de type BAL (Broad Absorption Line), abrégés dans la suite par quasars BAL, représentent une petite fraction (3-10%) des noyaux actifs de galaxies à grand redshift qui montrent dans leur spectre des profils de raies de type P Cygni pour la plupart des doublets de résonance d'atomes fortement ionisés ( $\text{Si}^{3+}$ ,  $\text{C}^{3+}$ ,  $\text{N}^{4+}$  et  $\text{O}^{5+}$ ). Ces quasars sont aussi connus pour être des sources radio faibles (Weymann, Carswell et Smith, 1981) et, dans le domaine spectral visible, pour être photométriquement variables (Netzer et Sheffer, 1983) et polarisés (Moore et Stockman, 1984). Malgré de nombreux efforts observationnels et théoriques (Turnshek, 1988), aucun modèle satisfaisant n'a encore permis d'expliquer d'une façon simple et convaincante l'origine et la signification physique du phénomène BAL (voir les arguments présentés par Surdej et Hutsemékers, 1987, article 13 et Hutsemékers et Surdej, 1988b en faveur de l'existence de deux populations distinctes de quasars BAL et non-BAL). Nous inspirant de la suggestion d'Ostriker et Vietri (1985, 1990) suivant laquelle certaines des propriétés d'objets de type BL Lac pourraient résulter d'artefacts observationnels causés par des effets de micro-lentille gravitationnelle, nous proposons dans ce qui suit que l'amplification chromatique sélective d'un quasar ordinaire par des micro-lentilles situées entre celui-ci et l'observateur est capable d'induire des effets de type BAL dans le

spectre de quasars distants. Nous démontrons ci-après qu'un tel scénario est plausible pour autant que le rayon d'action caractéristique des lentilles gravitationnelles (rayon d'Einstein de l'ordre de  $10^{-3}$ - $10^{-2}$  pc pour une étoile de masse solaire et des distances cosmologiques) est comparable, ou légèrement supérieur, à la dimension de la source quasi-stellaire émettant le spectre continu.

Suite à la découverte du premier exemple de mirage gravitationnel pour le quasar Q0957+561 (Walsh, Carswell et Weymann, 1979), Chang et Refsdal (1979, 1984) et Young (1981) ont suggéré que des étoiles individuelles situées dans la galaxie défectrice étaient capables de modifier les propriétés observationnelles (luminosité, polarisation et spectre) de chacune des images individuelles de la source. Ainsi, une source de radiation quasi-stellaire, ayant un redshift  $z_s$  et située le long de la ligne de visée juste derrière une étoile défectrice de masse  $M$  à un redshift  $z_d$ , subira des effets observables de lentille gravitationnelle (déformation et multiplication d'images avec des séparations angulaires  $\Delta\theta \approx 10^{-6}$  secondes d'arc, amplification de luminosité, etc.) si sa dimension est comparable, ou inférieure, au rayon d'Einstein généralisé  $\zeta_0$  (Grieger, Kayser et Refsdal, 1988)

$$\zeta_0 = ((1 - \sigma_c) (4G/c^2) M D_{ds} D_s/D_d)^{1/2}, \quad (4.1)$$

où  $D_s$ ,  $D_d$  et  $D_{ds}$  sont respectivement les distances métriques angulaires mesurées entre l'observateur et la source, l'observateur et le défecteur et le défecteur et la source. La quantité  $\sigma_c$  représente la densité de masse par unité de surface de la matière distribuée de façon homogène au voisinage de la micro-lentille, en unités de la densité critique

$$\sigma_c = (1/\pi) (c^2/4G) (D_s/D_{ds} D_d). \quad (4.2)$$

Pour des valeurs standard des paramètres cosmologiques ( $H_0 = 75$  km/sec/Mpc,  $q_0 = 0,5$  et  $\Lambda = 0$ ) et considérant le cas d'une étoile de masse solaire et d'un quasar à un redshift  $z_s = 2$ , nous trouvons que le rayon critique  $\zeta_0$  est compris entre  $2,5 \cdot 10^{-2}$

et  $2,2 \cdot 10^{-3}$  pc lorsque le redshift  $z_d$  du déflecteur varie de 0,1 à 1,9 (voir Table 1). Etant donné qu'on admet que la dimension de la source quasi-stellaire ( $R_c \approx 10^{-4}-10^{-2}$  pc) émettant le spectre continu est beaucoup plus petite que celle de la région émettant les larges raies en émission ( $R_{BLR} \approx 10^{-1}-10^1$  pc), la première sera beaucoup plus affectée par des effets de micro-lentille que la seconde et ceci conduira à de fortes variations de la luminosité du quasar, accompagnée par des changements appréciables de la largeur équivalente des larges raies en émission (cf. Kayser, Refsdal et Stabell, 1986).

Table 1: Rayon  $\zeta_0$  et échelle de temps  $\tau_0$  caractéristiques en fonction du redshift  $z_d$  de la micro-lentille. Ces résultats ont été obtenus au moyen de l'équation 4.1 pour les valeurs des paramètres suivants:  $M = 1M_\odot$ ,  $\sigma_c = 0$ ,  $z_s = 2$ ,  $H_0 = 75$  km/sec/Mpc,  $q_0 = 0,5$ ,  $\Lambda = 0$ ,  $v_{obs} = 400$  km/sec,  $v_d = 600$  km/sec et  $v_s = 500$  km/sec.

$z_d$	$\zeta_0$ (0,001 pc)	$\tau_0$ (ans)	$z_d$	$\zeta_0$ (0,001 pc)	$\tau_0$ (ans)
0,01	78,1	3,7	1,2	6,9	21,6
0,05	35,3	8,3	1,4	5,8	19,3
0,1	25,3	11,7	1,8	3,2	11,6
0,2	18,2	16,0	1,9	2,2	8,3
0,4	13,2	20,9	1,95	1,6	5,9
0,8	9,2	23,7	1,99	0,7	2,6

La grande variabilité photométrique et spectro-polarimétrique des objets éruptifs de type BL Lac 0846+51W1 (Ostriker et Vietri 1985; Nottale, 1986; Stickel, Fried et Kühr, 1989), 0235+164 (Stickel, Fried et Kühr, 1988a) et 0537-441 (Stickel, Fried et Kühr, 1988b) a été interprétée avec succès comme résultant d'effets d'amplification gravitationnelle sélective d'une source d'arrière-plan par un objet compact ( $\zeta_0/R \gg 1$ ) situé dans une galaxie à faible redshift  $z_d$ . Le déplacement de la micro-lentille par rapport à la source serait directement responsable de la variabilité photométrique observée au cours du temps (cf. Fig. 73

dans Surdej, 1987a pour une illustration de ce phénomène). Une discussion plus générale relative à l'interprétation de la grande variabilité photométrique de certaines classes d'objets extragalactiques (OVVs, BL Lacs, etc.) en termes d'effets de micro-lentille est donnée à la section 4.2 de l'article 14 (Surdej, 1990). Des simulations numériques élaborées confirment les prédictions précédentes. Ainsi, Kayser, Refsdal et Stabell (1986) et Kayser et al. (1989) trouvent que pour de faibles valeurs de la profondeur optique des micro-lentilles ( $\tau_{\text{lens}} \leq 0,4$ ), une source distante reste pour la plupart du temps très peu amplifiée mais que, occasionnellement, on peut assister à de grands sursauts de sa luminosité ( $\Delta m \geq 2-3$  mag.). Pour des valeurs plus réalistes de la profondeur optique  $\tau_{\text{lens}} \geq 0,4$ , Schneider et Weiss (1987) et Wambsganss, Paczyński et Katz (1990) trouvent que le domaine dans lequel les effets dus à une micro-lentille isolée dominant, reste toutefois très limité. À de telles profondeurs optiques, les quelques résultats fragmentaires publiés montrent que suite à une haute densité des anti-caustiques dans le plan de la source, de grands facteurs d'amplification de la luminosité du quasar ( $\approx 2-3$  mag.) peuvent être atteints sans que pour cela ce dernier varie de façon importante au cours du temps ( $\Delta m \leq 0,5$  mag.). Nous proposons donc que pour des valeurs de  $\tau_{\text{lens}} \gg 1$  et  $\zeta_0$  comparable, ou légèrement supérieure, à la dimension de la source émettant le spectre continu (c'est-à-dire pour des valeurs de  $z_d$  proches de  $z_s$ ), les micro-lentilles non seulement amplifient mais aussi résolvent spatialement le disque de la source quasi-stellaire, révélant de cette façon les processus radiatifs prenant place juste devant, et dans le voisinage proche, du quasar. Supposant pour l'instant que tous les quasars possèdent un vent quasi-stellaire responsable de la formation des larges raies en émission, on s'attendrait naturellement à voir dans le spectre de tels objets soumis à des effets de micro-lentille, des composantes en absorption décalées vers le bleu conduisant à l'apparence de profils de raies de type P Cygni pour des transitions de résonance d'atomes fortement ionisés. D'autres prédictions fort intéressantes de ce modèle peuvent encore être faites. En effet, suite aux mouvements relatifs de la source, du déflecteur et de l'observateur, des



variations temporelles devraient être observées dans la structure de la composante P Cygni en absorption et pour la largeur équivalente de la raie en émission. On peut prévoir que de telles variations spectroscopiques devraient être observables au cours d'intervalles de temps  $\tau_0 \approx \zeta_0 / V$ , où  $V$  représente la vitesse relative de la source par rapport à l'anti-caustique (Kayser et Refsdal, 1989). Pour des valeurs réalistes de la vitesse transversale de l'observateur ( $v_{\text{obs}} \approx 400$  km/sec), de la micro-lentille ( $v_d \approx 600$  km/sec) et de la source ( $v_s \approx 500$  km/sec), nous trouvons que  $\tau_0$  est de l'ordre de quelques années à quelques dizaines d'années (cf. Table 1), tout à fait en accord avec les échelles de temps de 2, 4, 7 et 10 ans observées respectivement pour les quasars BAL Q1303+308 (Foltz et al., 1987), H1413+117 (Turnshek et al., 1988), Q1246-057 (Smith et Penston, 1988) et UM232 (Barlow, Junkkarinen et Burbidge, 1989). De plus, nous pouvons prédire que si la galaxie hôte des micro-lentilles est suffisamment massive et bien alignée par rapport à la ligne de visée, des images multiples du quasar pourraient être parfois détectées et celles-ci constitueraient d'excellents candidats pour la recherche des effets micro-lentille discutés ci-avant.

C'est au cours d'une recherche observationnelle de mirages gravitationnels au sein d'un échantillon de quasars très lumineux (Surdej et al., 1987, article 15) que le quasar BAL H1413+117 a été identifié par notre équipe de recherche en astrophysique extragalactique avec un mirage gravitationnel formé de quatre images quasi-stellaires illusoire (Magain et al. 1988, article 16). Ce mirage est connu depuis lors sous le nom du *Trèfle à quatre feuilles*. Pour une description plus détaillée de notre projet de recherche de mirages gravitationnels à l'Observatoire Européen Austral (ESO, Chili), à l'Observatoire NRAO (VLA, Nouveau-Mexique) et au moyen du Télescope Spatial de Hubble (projet NASA/ESA), nous référons le lecteur à toute une série d'autres articles plus spécialisés (Surdej et al. 1988a-c, 1989; Swings et al. 1990; Magain et al. 1990 et article 14).

La modélisation des observations optiques ainsi que des observations radio obtenues pour le mirage gravitationnel H1413+117 avec le Very Large Array font l'objet de l'article 17

(Kayser et al. 1990). On présente dans ce travail les premiers arguments théoriques et observationnels (imagerie directe) indiquant que l'image la plus faible (image D) du Trèfle à quatre feuilles est sujette à des effets de micro-lentille. La probabilité que de tels effets affectent les trois autres images s'avère aussi ne pas être négligeable. Par ailleurs, au moyen d'observations spectroscopiques à haute résolution angulaire obtenues avec SILFID (Spectrographe Intégral à Linéarisation par Fibres de l'Image Directe; Vanderriest et Lemonnier, 1988) au foyer Cassegrain du télescope CFH (Hawaii), nous avons pu montrer que les très légères différences spectroscopiques détectées dans la structure des profils de raies de type P Cygni pour les doublets de résonance de SiIV, CIV et AlIII entre l'image D et les autres images (A+B+C) peuvent aussi être tout simplement interprétées en termes d'effets de micro-lentille (voir Figure 4.1; Angonin, Vanderriest et Surdej, 1990 et Angonin et al. 1990, article 18).

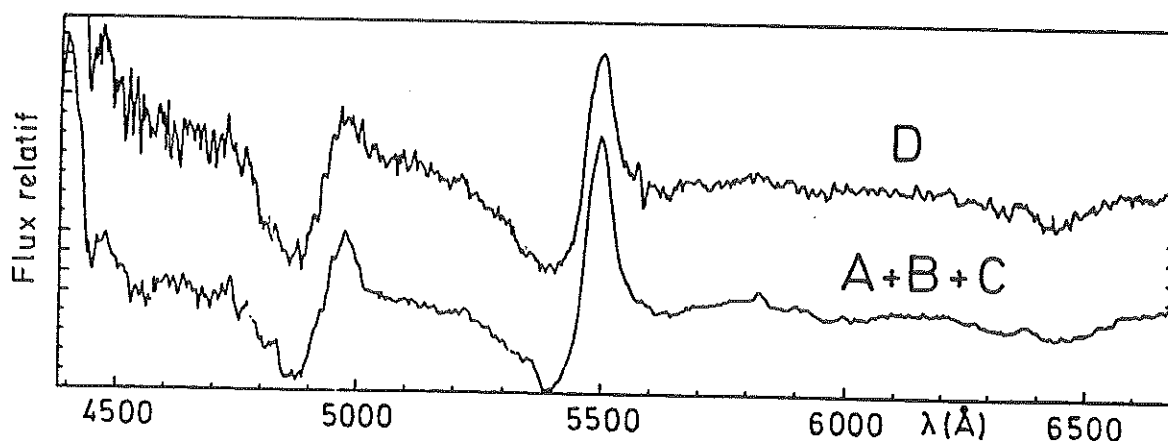


Figure 4.1: Spectres des différentes images du mirage gravitationnel H1413+117: Cette figure illustre le spectre moyen des images A, B, C et le spectre individuel de l'image D du mirage gravitationnel H1413+117. Ces données ont été obtenues lors de conditions d'agitation atmosphérique exceptionnellement favorables (FWHM  $\approx 0,5''$ ) au moyen du spectrographe SILFID installé au foyer Cassegrain du télescope CFH de 3,6m (Hawaii). De légères différences dans les profils d'absorption et d'émission de type P Cygni sont visibles entre ces deux spectres. Ces différences sont interprétées comme étant dues à un effet différentiel de micro-lentille agissant sur les faisceaux lumineux des images A, B, C et D.

Etant donné que pour  $\zeta_0 / R \approx 1$ , les effets induits par des micro-lentilles consistent en une amplification sélective de la brillance du quasar et des processus radiatifs prenant place au voisinage de la source émettant le spectre continu, la plupart des autres caractéristiques observationnelles des quasars BAL peuvent aussi être expliquées directement. Par exemple, les propriétés générales des quasars BAL i) d'être des sources radio faibles (Weymann, Carswell et Smith, 1981), ii) d'être modérément variables aux longueurs d'onde visibles (Netzer et Sheffer, 1983), iii) d'être anormalement polarisés (Moore et Stockman, 1984), iv) de présenter des raies en émission aux caractéristiques tout à fait différentes de celles observées dans les spectres des quasars non-BAL, comme par exemple l'absence de raies de [OIII] dans le spectre des quasars BAL à faible redshift (Hartig et Baldwin, 1986, Turnshek, 1988 et article 13), v) de révéler des profils de raies de type P Cygni variables (Foltz et al. 1987; Turnshek et al. 1988; Smith et Penston, 1988; Barlow, Junkkarinen et Burbidge, 1989), etc. apparaissent (au moins qualitativement) comme les symptômes observationnels naturels auxquels on peut s'attendre pour une source lointaine soumise à des effets de micro-lentille gravitationnelle.

Nous proposons ci-après quelques tests observationnels en vue de vérifier la thèse qu'au moins certains quasars BAL résultent d'effets d'amplification sélective par des micro-lentilles gravitationnelles. En effet, des systèmes de raies métalliques étroites en absorption associées avec la galaxie déflectrice et situées à des redshifts semblables, ou légèrement inférieurs, à celui de la source devraient être identifiables dans le spectre des quasars BAL. Pour les objets les plus proches, l'imagerie directe à haute résolution angulaire (cf. la caméra FOC à bord du Télescope Spatial de Hubble) devrait même permettre la détection de la galaxie déflectrice. Des quasars BAL tels que 1E 0104+315 (Stoche et al. 1984, 1987), H0903+175 (Hazard et al. 1986), Q0413-116 (Le Borgne et al. 1990), et bien d'autres situés à proximité de galaxies brillantes d'avant-plan, devraient faire l'objet d'une surveillance systématique (spectro-photopolarimétrie dans le domaine visible, monitoring dans le domaine des rayons X, etc.). Sur le plan théorique, des simulations

spectroscopiques de quasars soumis à des effets de micro-lentille (avec  $\zeta_0 / R \approx 1$ ) mériteraient d'être réalisées mais celles-ci seront bien sûr limitées par les lacunes de nos connaissances sur la structure et la physique des quasars en leur centre même. Nous avons toutefois illustré à la figure 4.2 le genre d'effets attendus, pour une micro-lentille isolée (cf. un trou noir) située le long de la ligne de visée, et agissant sur le spectre d'un quasar aux raies en émission pure. Comme on pouvait s'y attendre, le spectre initial se trouve littéralement métamorphosé en un spectre aux profils de raies de type P Cygni.

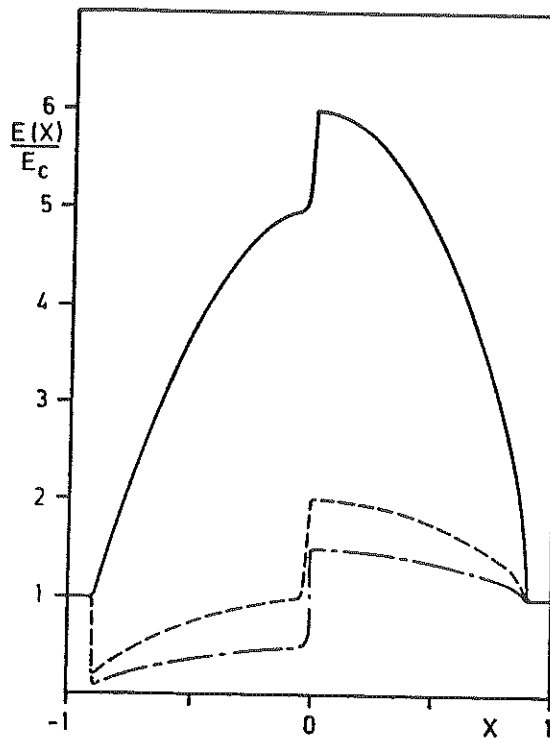


Figure 4.2: Exemples d'effets de micro-lentille sur le spectre d'un quasar ordinaire: Nous avons calculé les effets d'une micro-lentille (cf. un trou noir) passant juste devant un quasar émettant une raie spectrale en émission pure (trait continu). Les profils de raies  $E(X)/E_c$  résultants sont illustrés respectivement en traits interrompus et en traits mixtes pour les valeurs de  $\zeta_0/R = 5$  et 10. Nous avons supposé que l'enveloppe en expansion autour du quasar est très étendue ( $r_{\max}/R \gg 1$ ) et que les collisions des particules sont principalement responsables de l'émissivité de l'atmosphère.

## Article 13

### GEOMETRY OF THE MASS-OUTFLOWS AROUND BROAD ABSORPTION LINE QSOs AND FORMATION OF THE COMPLEX LY-ALPHA + NV LINE PROFILE

Surdej, J., Hutsemékers, D.:1987, *Astron. Astrophys.* **177**, 42-50.

Nous présentons tout d'abord dans cet article les arguments observationnels supportant la thèse que les quasars de type BAL et non-BAL forment deux classes d'objets distincts. Les principaux arguments sont: i) la largeur équivalente de la composante en émission de CIV est plus faible dans le spectre des quasars BAL, ii) la présence de raies de FeII et FeIII en émission y est aussi plus caractéristique, iii) la quasi-absence de la raie Ly $\alpha$  en émission et en absorption est remarquable dans le spectre de certains de ces quasars BAL, iv) par contre, l'intensité de la composante de la raie NV en émission y est en moyenne plus élevée. Nous utilisons enfin un modèle simple d'enveloppe en expansion rapide à symétrie sphérique pour simuler des profils de raies de type P Cygni fort semblables à ceux qui sont observés dans le spectre des quasars BAL (en particulier le profil de raie complexe dû à Ly $\alpha$  + NV).



## Geometry of the mass-outflows around broad absorption line QSOs and formation of the complex Ly $\alpha$ + N v Line profile

J. Surdej\* and D. Hutsemékers\*\*

Institut d'Astrophysique, Université de Liège, Avenue de Cointe, 5, B-4200 Cointe-Ougrée, Belgium

Received September 30, accepted November 26, 1986

**Summary.** In order to further elucidate the question whether all quasars are affected by the broad absorption line (BAL) phenomenon, we investigate in the present work the possibility that observed BAL profiles are formed in spherically symmetric expanding atmospheres. We first show that the small residual intensity and/or large equivalent width reported for some absorption troughs (C IV, Si IV, etc.) may very well be reproduced by the resonance scattering of line photons across spherically symmetric BAL regions, taking into account the possible effects due to turbulence, occultation and/or electron collisions. Reanalyzing the distributions of the N v emission peak ratio, i.e.  $N v/I_c$ , observed in representative samples of BAL and non-BAL QSOs, we confirm that the N v emission strength appears to be generally higher in the spectrum of BAL quasars. Furthermore, using Sobolev-type approximations for the transfer of line radiation in spherically expanding envelopes, we find that an overall good agreement can be achieved between the theory and the observed attenuation of the Ly $\alpha$  emission-line, the observed enhancement of the N v emission strength and the possible presence of a shoulder-like feature in the red wing of the N v emission profile. All these results are certainly consistent with the view that BAL and non-BAL QSOs form two distinct classes of quasars.

**Key words:** lines: profile – quasars: mass loss

### 1. Introduction

Blueshifted broad absorption lines (BALs) are seen in the spectrum of as much as 3 to 10 percent of the total number of moderate-to-high redshift quasars discovered on objective prism plates (Hazard et al., 1984). Nevertheless, it is still unclear how much observational biases affect the true distribution of BAL QSOs in space and time (Turnshek, 1986). The level of ionization observed for the BALs is appreciably high (cf. C IV, N v and O VI resonance lines) and the Doppler velocity shifts involved are of the order of  $0.1c$ , up to  $0.2c$ . We refer the reader to the review papers by Weymann et al. (1981), Weymann and Foltz (1983) and Turnshek (1984b) for a more detailed description of the BAL characteristics.

Send offprint requests to: J. Surdej

\* Also, Chercheur qualifié au Fonds National de la Recherche Scientifique (Belgium)

\*\* Also, Aspirant au Fonds National de la Recherche Scientifique (Belgium)

Whereas there is little doubt that the BALs are intrinsic to the quasars, there is not yet a general agreement on which mechanism(s) are responsible for the ejection and observed ionization of the outflowing gas (cf. Weymann et al., 1985). The same indetermination applies to the type of geometry characterizing the BAL region (BALR) giving rise to the observed P Cygni-like profiles. The first models accounting for these were based on the scattering of line photons in spherically symmetric expanding envelopes (Scargle et al., 1970, 1972; Grachev and Grinin, 1975; Surdej and Swings, 1981). In the remainder, we shall refer to these as to the "standard" models. However, several discrepancies between the theory and observations were invoked by various authors and resulted in crediting jet-, fan- and/or disk-like geometries at the prejudice of the previous models (cf. Junkkarinen et al., 1983; Junkkarinen, 1983; Turnshek, 1984b; etc.). In Sect. 2, we present arguments which lend support to the view that the claimed discrepancies are only apparent and that somewhat improved "standard" models remain physically viable.

Except for the case of the N v emission (see the different conclusions reached by Turnshek, 1984b and Hartig and Baldwin, 1986), it is well established that the emission-line properties of BAL QSOs are different from those of non-BAL QSOs (see e.g. Ly $\alpha$ , C IV, C III], Fe II, etc.). In Sect. 3, we have reanalyzed the distributions of the N v peak intensity-normalized to the nearby continuum-for two samples of BAL and non-BAL QSOs. In agreement with Turnshek (1984b, 1986), we find that the N v emission strength is generally higher in the spectrum of BAL QSOs.

These observational results are certainly consistent – although not necessarily demonstrative – with the view that BAL and non-BAL QSOs form two distinct classes of quasars.

Furthermore, using Sobolev-type approximations for the transfer of line radiation in spherically symmetric envelopes, we show in Sect. 4 that an overall good agreement can be achieved between the theory and the main characteristics of the complex Ly $\alpha$  + N v line profile observed in the spectrum of BAL quasars. The resonance line scattering of Ly $\alpha$  photons by  $N^{4+}$  ions provides one more independent argument in favour of the BALRs being intrinsic to the BAL QSOs.

General conclusions and a discussion form the last section.

### 2. Geometry of the BALRs

Scargle et al. (1970, 1972) were the first to interpret the formation of BAL profiles as due to the resonance scattering of line photons in spherically symmetric expanding envelopes. Particularizing

this "standard" model to the case of an outward-decelerating atmosphere, Grachev and Grinin (1975) and Surdej and Swings (1981) have shown that a fairly good agreement could be achieved between the theory and the C IV and Si IV P Cygni-like profiles observed in the spectrum of PHL 5200.

However, as more BAL QSOs were discovered and spectroscopically investigated, various authors claimed that the basic predictions of "standard" models were incompatible with the observations (cf. Junkkarinen, 1980, 1983; Turnshek, 1981, 1984b, etc.). The most often quoted discrepancies were that:

i) on the average, the equivalent width  $EW_{abs}$  of the blue-shifted absorption component of a BAL profile is substantially larger than the equivalent width  $EW_{em}$  of the scattered emission-line; and that

ii) the residual intensity observed in some highly saturated absorption troughs can be unusually small (i.e.  $E(X)/E_c \approx 0$ , where  $E(X)$  denotes the flux emitted by the expanding atmosphere at a given frequency  $X$ ;  $E_c$  being the flux radiated by the central source).

As a consequence, alternative models involving jet-, fan- and/or disk-like geometries were proposed. According to such models, the intrinsic fraction of QSOs which are undergoing the BAL phenomenon is equal to the observed fraction divided by the covering factor of the BALR (Weymann et al., 1985). This implies that BAL gas could be present around most, if not all QSOs.

In the remainder of this section, we show that both observational constraints (i) and (ii) might be accounted for after several improvements of the "standard" model have been made. Indeed:

a) Until recently, most of line profile calculations were entirely based on the Sobolev escape probability method (cf. Castor and Lamers, 1979). Under the assumption of pure resonance scattering of line photons, this class of models essentially produces profiles such that  $EW_{em}/EW_{abs} \sim 1$  and  $E(X)/E_c \neq 0$  over the whole frequency interval. The importance of *turbulence* in expanding atmospheres has led various authors to abandon Sobolev-type theories and to work out solutions of the transfer equation in the comoving frame of the fluid (Mihalas et al., 1975; Bastian et al., 1980; Hamann, 1981a; Schönberg, 1985a; Hempe and Schönberg, 1986). As the ratio between the stochastic and macroscopic velocities of the flow gets higher, the resulting P Cygni profiles are characterized by smaller values of  $EW_{em}/EW_{abs}$  as well as a larger frequency interval over which  $E(X)/E_c \approx 0$  (see Hamann, 1980, 1981b; Bertout, 1985; Schönberg, 1985b; Lamers et al., 1986).

Let us further note that:

b) The ratio  $EW_{abs}/EW_{em}$  also scales up with the importance of the *occultation* of the expanding atmosphere by the central core (cf. Drew and Giddings, 1982). This effect is particularly important for the case of outward-decelerating envelopes (see Surdej and Swings, 1981).

c) If the escape probability ( $\beta_{12}^1$ ) of a line photon is sufficiently small compared to its destruction probability ( $\epsilon_{12}$ ) by a *collisional de-excitation* and if the electron temperature of the expanding atmosphere is lower than the diluted radiation temperature, the resulting BAL profile will just appear to be made of a dark trough (Surdej, 1979a).

Because the "standard" model with the above improvement(s) (a) and/or possibly (b) and (c) allows one to account for the main observed characteristics of BAL profiles and since it is really the most simple model that physical self-consistency permits, we be-

lieve that spherically symmetric BALRs still constitute attractive and physically viable models. As we point out in the next sections, such models also provide a good explanation for the complex Ly $\alpha$  + N v line profile observed in the spectrum of BAL QSOs.

### 3. Emission-line properties of BAL QSOs

With the aim of further exploring the question of whether all quasars might be expelling matter at very high velocities, Turnshek (1984b) and Hartig and Baldwin (1986) have sought to compare the emission-line (EL) properties of BAL QSOs to those of non-BAL, i.e. "normal", QSOs. If the distribution of the EL properties were the same in the two groups of quasars, it would give further support to the view that all quasars undergo the BAL phenomenon. However, it is well established that the EL properties of BAL QSOs are different from those of non-BAL QSOs. Indeed:

i) On the average, the strength of the C IV emission-line is weaker for BAL QSOs (Turnshek, 1984b; Hartig and Baldwin, 1986).

ii) Both Fe II and Al III emissions appear to be stronger in the spectra of BAL QSOs (Wampler, 1986), specially in those which display well detached absorption troughs (Hartig and Baldwin, 1986).

iii) It is also very likely that the larger width reported by Turnshek (1984b) for the C III]  $\lambda$  1909 emission-line in the spectra of BAL QSOs is at least partially caused by unusually strong Al III  $\lambda$  1857 emission and by blends of Fe II and Fe III lines near  $\lambda \sim 1900 \text{ \AA}$  (Hartig and Baldwin, 1986).

iv) Of particular interest is the weakness or absence of both Ly $\alpha$  emission and blue-shifted absorption in most BAL QSOs (Hazard et al., 1984).

As far as estimates of the N v emission strength are concerned, Turnshek (1984b, 1986) and Hartig and Baldwin (1986) reach different conclusions. Turnshek finds that the N v emission is stronger for BAL QSOs rather than Hartig and Baldwin report a similar strength for both classes of QSOs. The latter authors have used approximately 15 quasars in each class; the non-BAL ones being taken from a single source. In order to further elucidate this discrepancy, we have extended the comparison of the N v emission strength to larger samples of quasars. We have selected four samples of non-BAL quasars (Osmer and Smith, 1976; Baldwin and Netzer, 1978; Smith et al., 1981 and Young et al., 1982) resulting in a total number of 52 objects for which reasonably good spectra have been published. We have similarly searched the literature for all BAL QSOs having a Ly $\alpha$  + N v line profile that was recorded with a sufficiently good signal to noise ratio. Table 1 lists 26 such members for which an estimate of the N v peak intensity, normalized to the nearby continuum (i.e.  $N v/I_c$ ), has been made. For both classes of quasars, the peak intensity of N v was simply measured above a hand-drawn continuum. However, because the ratio of the Ly $\alpha$  to N v strength (i.e. Ly $\alpha$ /N v) is much higher in the spectra of non-BAL QSOs than in those of BAL QSOs, the red wing of Ly $\alpha$  may seriously contaminate the  $N v/I_c$  measurements of the former QSOs. It is clear that there will result a systematic overestimate of the  $N v/I_c$  ratio measured for the non-BAL QSOs.

We have illustrated in Fig. 1a the normalized distributions of the  $N v/I_c$  measurements obtained for the 52 non-BAL and 26 BAL QSOs (cf. Table 1). Let us first point out that with the possible exception of the data by Smith et al. (1981), the individual



**Table 1.** List of the 26 BAL QSOs for which an estimate of the  $Nv/I_c$  ratio has been made. The BAL QSOs in italics refer to those which show the presence of a shoulder-like effect in the red wing of their  $Nv$  emission-line profile

BAL QSO	$Nv/I_c$	References
0104 + 315	2.6	12
<i>0128 - 367</i>	2:	17
0134 - 376	3.8	17
0324 - 407	2.2	11, 13
0333 - 380	1.6	5
0335 - 336	2:	5
0856 + 172	1.5:	1, 5
0903 + 173	1.8	1, 5
1011 + 091	2:	5, 15
1232 + 134	2.6	16
1246 - 057	2.3	6
1303 + 308	1.5	10
1309 + 056	3.2	10, 14
<i>1336 + 135</i>	2.8	5
<i>1413 + 117</i>	4.2	15
1414 + 089	2.4	5, 8
<i>1504 + 106</i>	2.1	5
2239 - 411	3.7	2
2241 - 370	2.9	2
UM 139	2.9:	3
MCS 141	2.9	7
MCS 232	1.5	7
MCS 253	2.9	9
<i>MCS 275</i>	1.7	7
<i>PHL 5200</i>	3.3	4, 21
RS 23	3.6	3

*Notes to Table 1:* (:) Uncertain measurement, (1) Turnshek, 1981, (2) Clowes et al., 1979, (3) Junkkarinen, 1980, (4) Junkkarinen et al., 1983, (5) Hazard et al., 1984, (6) Boksenberg et al., 1978, (7) Turnshek et al., 1980, (8) Foltz et al., 1983, (9) Shaver et al., 1982, (10) Turnshek et al., 1984, (11) Whelan et al., 1979, (12) Stocke et al., 1984, (13) Baldwin and Smith, 1983, (14) Young et al., 1982, (15) Drew and Boksenberg, 1984, (16) He et al., 1984, (17) Arp, 1984

distributions of  $Nv/I_c$  were found to be essentially the same for the four selected samples of non-BAL QSOs. Within the measurement uncertainties, Smith et al. (1981) also found that their estimates of the  $Nv$  strength were somewhat different from those previously determined by Osmer and Smith (1976) for the same objects. *It is clear from Fig. 1a that the distribution of  $Nv/I_c$  is markedly different between BAL and non-BAL QSOs.* We see that the  $Nv/I_c$  ratio is generally higher for BAL QSOs than the overestimated value measured for the other quasars. In order to roughly estimate how much our measurements of  $Nv/I_c$  are overestimated for the non-BAL QSOs, we have made new measurements of the  $Nv$  intensity peak from just above the extrapolated red wing of the  $Ly\alpha$  emission-line. Due to the better resolution as well as signal to noise ratio of the spectra published by Young et al. (1982), we have only performed these new measurements for this sample. Both the distributions of the corrected and uncorrected  $Nv/I_c$  measurements are reproduced in Fig. 1b. We clearly see from this figure that all values of  $Nv/I_c$

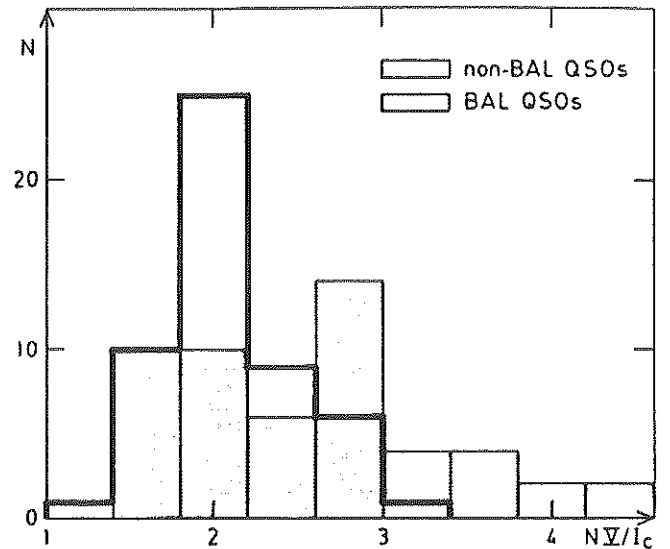


**Fig. 1a.** Normalized distributions of the  $Nv/I_c$  measurements determined for the 52 non-BAL and 26 BAL QSOs (see text)

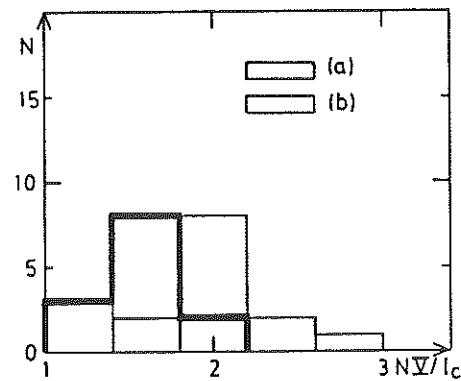


**Fig. 1b.** Referring to the sample of non-BAL quasars published by Young et al. (1982), this figure represents the  $Nv/I_c$  distributions derived from the  $Nv$  emission peak being measured from just above the continuum (a) as well as from the extrapolated red wing of the  $Ly\alpha$  emission-line (b)

referring to non-BAL QSOs might have been overestimated in Fig. 1a by as much as a factor 2. This is in agreement with independent estimations made by Osmer and Smith (1977). Therefore, we safely concur with Turnshek (1984b) that the observed  $Nv$  peak intensity is appreciably higher in the spectrum of BAL than in that of non-BAL QSOs.

#### 4. Formation of the complex $Ly\alpha + Nv$ line profile

One of the most outstanding features observed in the spectrum of high redshift BAL QSOs is the complex  $Ly\alpha + Nv$  line profile: the  $Ly\alpha$  emission and blueshifted absorption are unusually weak and/or absent (Hazard et al., 1984) whereas the  $Nv$  emission-line plus associated P Cygni-type absorption are generally well developed (cf. Sect. 3). Furthermore, because the velocity width of the  $Nv$  BAL trough is usually larger than the velocity separation between  $Ly\alpha$  and  $Nv$ , it was soon suggested that the BALR must

be located beyond the Ly $\alpha$  EL region (cf. Lynds, 1966). Further arguments supporting this view have been given by Weymann and Foltz (1983). One then naturally expects that the resonance line scattering (RLS) of Ly $\alpha$  photons by the receding N $^{4+}$  ions in a spherically symmetric envelope can account for both the attenuation of Ly $\alpha$  and the enhancement of the N v emission lines.

We have performed profile calculations along these lines, making use of the Sobolev approximation (Sobolev, 1947; Castor, 1970) for treating the radiative interactions between the N $^{4+}$  ions and the underlying continuum plus Ly $\alpha$  photons. Since the resulting Ly $\alpha$  + N v line profiles depend to some extent on both the adopted geometry and line formation mechanism, it is very likely that they should provide a useful diagnostic tool. At the end of this section, we compare the main characteristics of the theoretical line profiles with those observed in representative spectra of BAL QSOs.

#### 4.1. Expression of the complex Ly $\alpha$ + N v line profile

Because we do not intend to perform here accurate fittings of individual Ly $\alpha$  + N v line profiles but rather to delineate their main characteristics, we shall adopt in the following a model that is as simple as possible. We first consider that the resonance line transitions of N v at  $\lambda\lambda$  1238.8, 1242.8 Å can be modeled by a two-level atom that scatters photons in accordance with a complete redistribution in frequency and direction. We also assume that the central source which emits the continuum and Ly $\alpha$  photons is point-like with respect to the size of the outflowing BALR. Under such approximations and following Surdej (1979b), it is straightforward to establish that the expression  $E(X)/E_c$  of the complex Ly $\alpha$  + N v line profile as a function of the dimensionless frequency  $X$  takes the form

$$\frac{E(X)}{E_c} = \int_{-1}^{\min(-|X|, X_{\min})} (1 + \xi(X')) \frac{(1 - \exp(-\tau'_{12}(X'))) P(X', X) dX'}{|2X'|} + \begin{cases} (1 + \xi(X)) \cdot \exp(-\tau'_{12}(X)) & \text{if } X \in [-1, X_{\min}], \\ (1 + \xi(X)) & \text{if } X \in [X_{\min}, 1], \end{cases} \quad (1)$$

$\xi(X)$  representing the Ly $\alpha$  emission profile normalized to the continuum at the frequency  $X$  and where

$$X' = -v(L)/v_\infty, \quad (2)$$

$$X = X' \cdot \cos(\theta), \quad (3)$$

$$X_{\min} = -v_0/v_\infty, \quad (4)$$

and

$$P(X', X) = \frac{1 - \exp(-\tau_{12}(X', X))}{\tau_{12}(X', X)} \cdot \frac{1}{\beta_{12}^1(X')}. \quad (5)$$

We briefly recall hereafter the physical meaning of the different quantities appearing in the previous relations.  $v_0$  (resp.  $v_\infty$ ) denotes the initial (resp. terminal) radial velocity  $v(L)$  of the flow,  $L$  being the radial distance expressed in source radii units.  $\tau_{12}(X', X)$  (resp.  $\tau'_{12}(X')$ ) represents the fictive line opacity evaluated at a distance  $L(X')$  along a direction making an angle  $\theta$  (resp.  $\theta = 0$ ) with respect to the radial direction. These quantities are related as follows:

$$\tau_{12}(X', X) = \tau'_{12}(X') \left( \mu^2 \left( 1 - \frac{d \ln L}{d \ln |X'|} \right) + \frac{d \ln L}{d \ln |X'|} \right), \quad (6)$$

with

$$\mu = \cos(\theta). \quad (7)$$

$\beta_{12}^1(X')$  stands for the usual escape probability of a line photon emitted along any direction in the expanding medium

$$\beta_{12}^1(X') = \int_0^1 \frac{1 - \exp(-\tau_{12}(X', X'\mu))}{\tau_{12}(X', X'\mu)} d\mu. \quad (8)$$

#### 4.2. Numerical applications

By means of Eq. (1), it is straightforward to compute Ly $\alpha$  + N v line profiles under various physical conditions. For convenience, we adopt the velocity law

$$X' = X_{\min} + (1 + X_{\min})(1/L - 1) \quad (9)$$

and the opacity distribution

$$\tau'_{12}(X') = \tau_0(1 + X')^\gamma, \quad (10)$$

with  $X_{\min} = -0.01$ ,  $\tau_0$  and  $\gamma$  being free parameters. We further assume that the unabsorbed Ly $\alpha$  emission-line is adequately fitted by a gaussian profile

$$\xi(X') = A \cdot \exp\left(-\left(\frac{X' - X_L}{\sigma_X}\right)^2\right), \quad (11)$$

where  $A$  represents the Ly $\alpha$  emission peak intensity,  $X_L < 0$  corresponds to the ratio of the velocity separation between Ly $\alpha$  and N v ( $\sim -6000 \text{ km s}^{-1}$ ) to  $v_\infty$  and  $\sigma_X$  is related to the FWHM of the gaussian profile via the relation

$$\text{FWHM} \simeq 1.665 \sigma_X \cdot v_\infty. \quad (12)$$

Values of  $A \sim 3$  and  $\text{FWHM} \sim 4000 \text{ km s}^{-1}$  are typical for Ly $\alpha$  emission-lines observed in the spectrum of non-BAL QSOs. Therefore, we have adopted similar values for the computed Ly $\alpha$  + N v line profiles illustrated in Fig. 2. In this figure, the full line represents the Ly $\alpha$  + N v line profile  $E(X)/E_c$  according to Eq. (1), the dotted line corresponds to the underlying emission function  $1 + \xi(X)$ , the dashed line depicts the N v line profile that would be observed in the absence of Ly $\alpha$  - N $^{4+}$  interactions (set  $\xi(X) = 0$  in Eq. (1)) and, finally, the dotted-dashed line illustrates the contribution of Ly $\alpha$  photons to the N v emission profile (see next section).

#### 4.3. Discussion

First of all, we wish to point out that the calculations illustrated in Fig. 2 consist of representative Ly $\alpha$  + N v line profiles, whose main characteristics-discussed hereafter-are not significantly altered for other choices of the physical parameters.

As expected, the most important consequences of the interactions between the Ly $\alpha$  photons and the N $^{4+}$  ions are:

i) An attenuation of the Ly $\alpha$  emission-line. The absorption of Ly $\alpha$  may be partial (Fig. 2a) or complete (Fig. 2b) depending on the strength of the N v line opacity,

ii) An appreciable enhancement of the N v emission strength. We recall that both these spectral features are commonly observed in the spectrum of BAL QSOs (cf. Sect. 3). Furthermore,

iii) A shoulder-like feature is usually apparent on the red wing of the N v emission profile (cf. Figs. 2a and b).

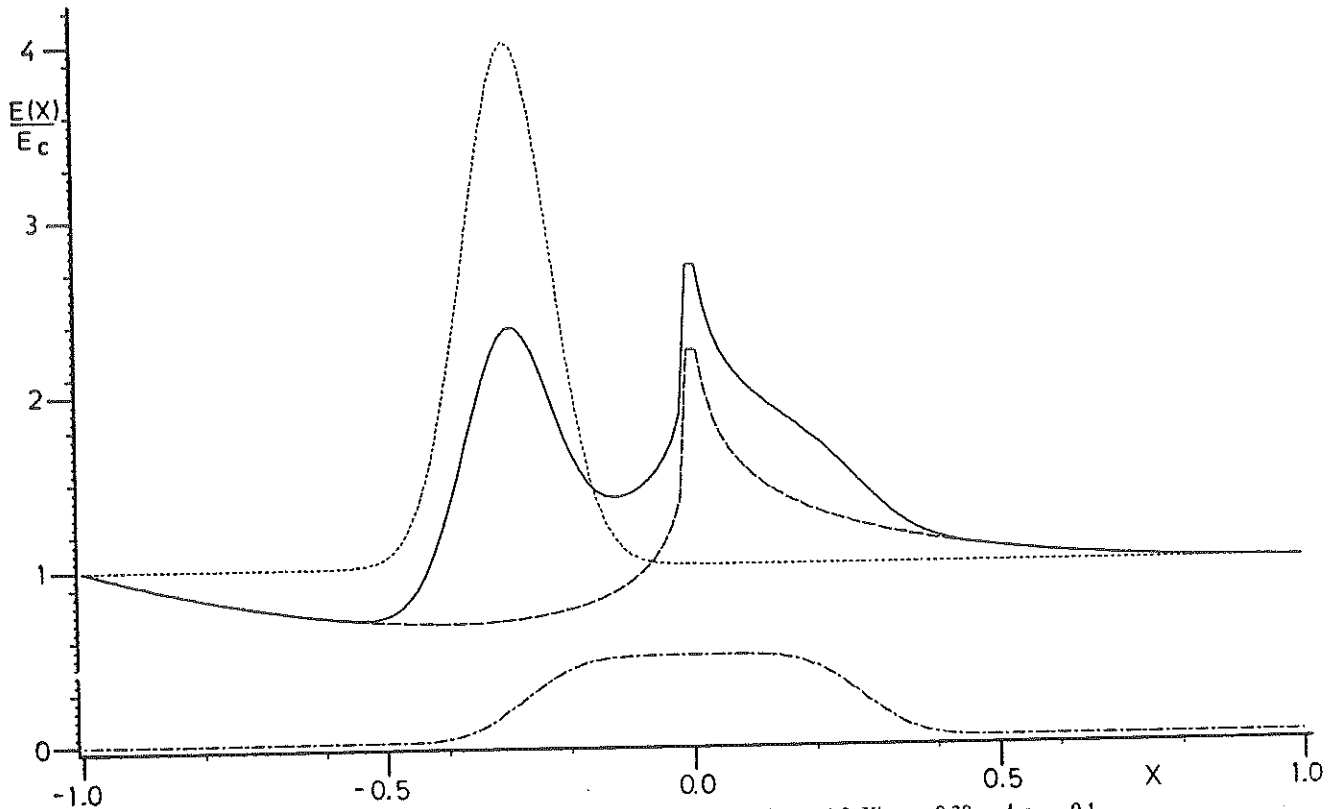


Fig. 2a. Computed Ly $\alpha$  + N v line profile for the choice of the parameters  $\tau_0 = 1.0$ ,  $\gamma = 1.0$ ,  $X'_L = -0.30$  and  $\sigma_x = 0.1$ . In this and the next figures, the full line represents  $E(X)/E_c$  versus  $X$  according to Eq. (1), the dotted line corresponds to the underlying emission function  $1 + \zeta(X)$ , the dashed line depicts the N v line profile that would be observed if there were no Ly $\alpha$  - N $^{4+}$  interactions and the dotted-dashed line illustrates the contribution of Ly $\alpha$  photons to the N v emission profile (cf. Eqs. (13) and (14))

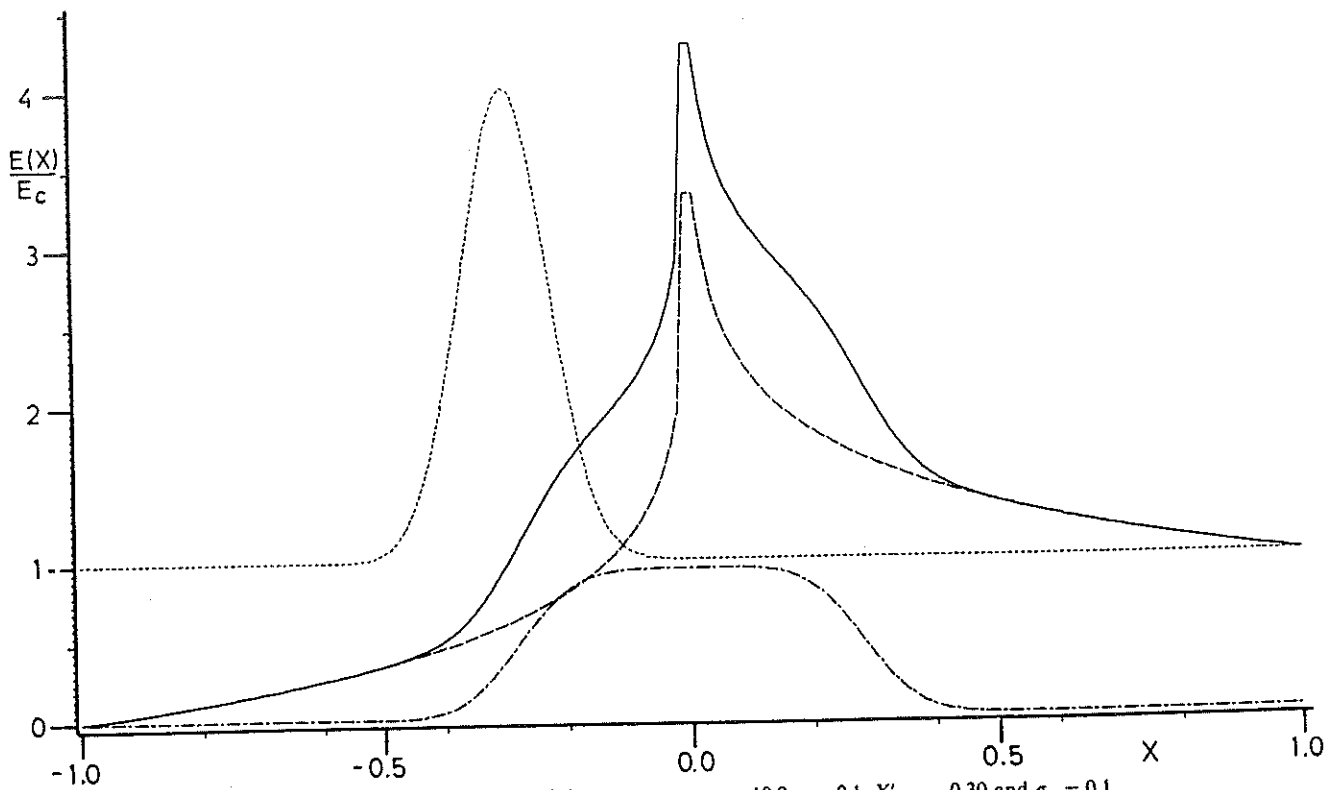


Fig. 2b. Computed Ly $\alpha$  + N v line profile for the choice of the parameters  $\tau_0 = 10.0$ ,  $\gamma = 0.1$ ,  $X'_L = -0.30$  and  $\sigma_x = 0.1$

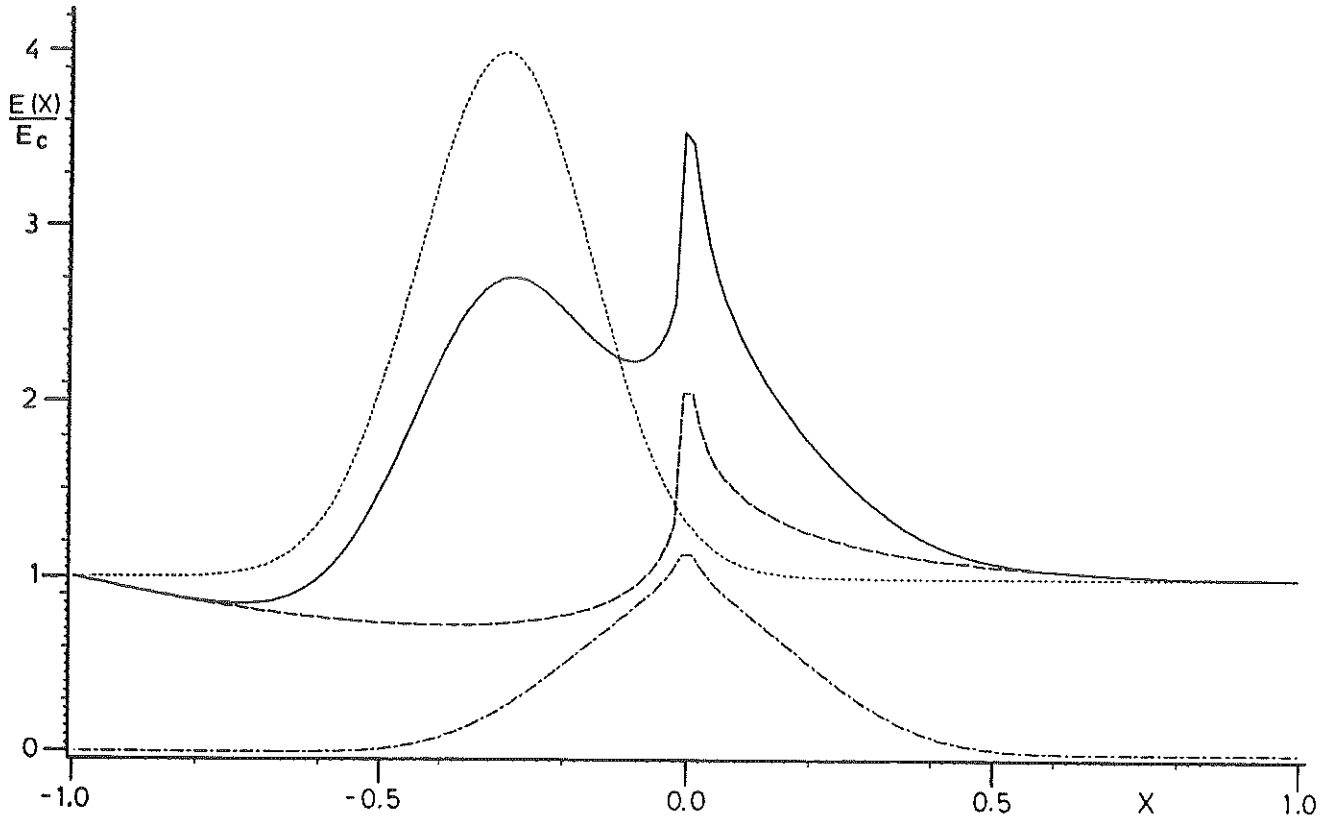


Fig. 2c. Computed Ly $\alpha$  + N v line profile for the choice of the parameters  $\tau_0 = 0.8$ ,  $\gamma = 1.0$ ,  $X'_L = -0.30$  and  $\sigma_X = 0.2$

There is some good evidence that such an asymmetry is detected in an appreciable number ( $\geq 25\%$ ) of BAL QSO spectra (see the BAL QSOs in italics in Table 1). We believe, for instance, that the tentatively identified Si II  $\lambda$  1263 emission-line in the spectrum of PHL 5200 (Junkkarinen et al., 1983), Q 2240.9-3702 (Clowes et al., 1979), Q 1413 + 117 (Drew and Boksenberg, 1984), etc. could be due to this shoulder-like effect. We shall discuss this point in Sect. 5.

Now, we should like to give further physical insight on the effects responsible for the main characteristics i), ii) and iii) of theoretical Ly $\alpha$  + N v line profiles described above. Considering that the intensity of the Ly $\alpha$  emission-line centered at  $X_L$  drops to negligible values at frequencies  $X_L - 2\sigma_X \lesssim X \lesssim X_L + 2\sigma_X$ , it is clear that most of Ly $\alpha$  photons will be scattered by the  $N^{4+}$  ions within a shell bounded by the radii  $L(X'_{inner} = X_L + 2\sigma_X)$  and  $L(X'_{outer} = X_L - 2\sigma_X)$ . This directly accounts for the attenuation of the Ly $\alpha$  emission-line observed in BAL QSO spectra (cf. the feature i) above). Furthermore, it is straightforward to establish that, within the frequency interval  $X \in [X'_{inner}, -X'_{inner}]$ , the contribution  $E(X)_{Ly\alpha}/E_c$  of Ly $\alpha$  photons scattered from the shell  $[L(X'_{inner}), L(X'_{outer})]$  to the emission-line profile  $E(X)/E_c$  is expressed by

$$E(X)_{Ly\alpha}/E_c = \int_{X'_{outer}}^{X'_{inner}} \xi(X') \frac{(1 - \exp(-\tau'_{12}(X'))) }{|2X'|} P(X', X) dX'. \quad (13)$$

Because for  $|X| < -X'_{inner}$  the redistribution function  $P(X', X)$  is only very slightly dependent on the frequency  $X$ , the contribution  $E(X)_{Ly\alpha}/E_c$  appears to be nearly constant in the frequency interval

$X \in [X'_{inner}, -X'_{inner}]$ . Outside this range, we find that

$$E(X)_{Ly\alpha}/E_c = \int_{X'_{outer}}^{\text{Max}(-|X|, X'_{outer})} \xi(X') \frac{(1 - \exp(-\tau'_{12}(X'))) }{|2X'|} P(X', X) dX' \quad (14)$$

is a function which rapidly decreases to zero as  $|X| \rightarrow -X'_{outer}$  (see the dotted-dashed lines in Fig. 2). The superposition of the rectangular emission profile  $E(X)_{Ly\alpha}/E_c$  to the contribution

$$E_c(X)/E_c = \int_{-1}^{\text{Min}(-|X|, X_{min})} \frac{(1 - \exp(-\tau'_{12}(X'))) }{|2X'|} P(X', X) dX' \quad (15)$$

due to the continuum source photons scattered across the whole expanding envelope provides a very good account for both the enhancement of the N v emission strength (cf. ii) above) and the shoulder-like feature located near the frequency  $-X'_{inner}$  in the red wing of the N v emission profile (cf. iii) above). As it might be expected, a symmetric shoulder-like feature is also apparent at the frequency  $X'_{inner}$  whenever the Ly $\alpha$  emission-line is strongly absorbed (cf. Fig. 2b).

The simple quantitative interpretation of the above spectral characteristics i), ii) and iii) clearly demonstrates that these are general properties of the spherically symmetric model plus resonance line scattering (RLS) and not artefacts caused by the particular choice of a velocity and/or opacity distribution(s), of the point-like source approximation, of the two-level atom model,

etc. However, we can easily foresee that these spectral characteristics will vanish whenever the N v optical depth gets too small in the frequency interval  $X' \in [X'_{outer}, X'_{inner}]$ . One also expects that for appreciably large widths of the Ly $\alpha$  emission-line, the scattering of Ly $\alpha$  photons will take place across the whole expanding envelope resulting in a contribution  $E(X)_{Ly\alpha}/E_c$  that is more sharply peaked near  $X = 0$ . While the N v emission peak will be strengthened, the shoulder-like feature will almost completely disappear (see Fig. 2c).

## 5. Conclusions

We have pointed out in the present work that a spherically symmetric expanding BALR in which the resonance scattering of line photons is consistently treated with the possible effects due to turbulence, occultation, collisions, etc. may very well account for the observed characteristics of P Cygni-like profiles in the spectra of BAL QSOs. If, on the contrary, one assumes that all quasars do have BALRs covering only a small fraction of the continuum source, "ad-hoc" geometries as well as physical mechanisms must be introduced in order to explain the observed BAL profiles as well as the different emission-line properties existing between BAL and "apparently" non-BAL QSOs.

In this context, we have established that alike the cases for the C IV, Ly $\alpha$ , C III], Al III, Fe II, Fe III, etc. emission-lines (Turnshek, 1984b; Hartig and Baldwin, 1986) the distribution of the N v emission peak, i.e.  $N v/I_c$ , is markedly different between BAL and non-BAL QSOs. In the framework of the Sobolev approximation, we have applied the "standard" model in order to simulate complex Ly $\alpha$  + N v line profiles. This simple model has allowed us to directly interpret the observed enhancement of the N v emission strength as well as the attenuation of the Ly $\alpha$  emission-line in the spectra of BAL QSOs. Furthermore, the prediction that a shoulder-like feature should be present in the red wing of the N v emission and its possible detection in the spectrum of at least 7 BAL QSOs<sup>1</sup> seem to indicate that the tentative identification of Si II  $\lambda$  1263 emission in those spectra is very doubtful. Indeed, any other low ionization broad emission-line (cf. Si II  $\lambda$  1556, etc.) has ever been reported with the presence of Si II  $\lambda$  1263 in BAL QSO spectra (Junkkarinen et al., 1983; Clowes et al., 1979; Drew and Bokseberg, 1984). In addition, Si II  $\lambda$  1263 has never been detected as a very conspicuous emission-line in the spectrum of non-BAL QSOs (see e.g. Baldwin, 1977). We believe that improved Ly $\alpha$  + N v theoretical line profiles including the finite structure of the N v resonance doublet as well as the possible effects due to turbulence, etc. should be compared with observations before more definite statements can be made. We actually develop such an improved "standard" model at the Liège Institute of Astrophysics (Surdej and Hutsemékers, 1987).

Recalling that the velocity structure of BALs ranges from smooth (P Cygni-type) to complex absorptions and that, for some BAL QSOs, the absorption troughs appear to be well detached

<sup>1</sup> It is likely that the shoulder-like feature is present in more BAL QSO spectra. However, the poor quality of some published spectra (bad S/N, insufficient spectral resolution) as well as the existence of physical complications (overlapping between the N v emission profile and the Si IV BAL, etc.) often prevent one from detecting it.

from the central emission-lines, it is interesting to mention that Turnshek (1984a) and Hartig and Baldwin (1986) report a possible correlation between BAL and EL properties: BAL QSOs exhibiting detached troughs with observable velocity structure often have weaker and/or broader high excitation emission-lines (e.g. C IV, Si IV). Since detached absorption troughs may directly be simulated, as a first approximation, by setting  $\xi(X') = 0$  and  $-1 < X_{min} < -0.01$  in Eq. (1), we find that the "standard" model also predicts weaker and broader emission-lines for such profiles (cf. Fig. 3). The net effect of adding some turbulence then results in better separating the blueshifted BAL from the broader and weaker emission-line (Surdej and Hutsemékers, 1986).

Considering:

i) that the improved "standard" model provides a good description of the observed high ionization C IV, Si IV, etc. line profiles (see Sect. 2);

ii) the whole set of differences existing between the EL properties of BAL and non-BAL QSOs (Turnshek, 1984b; Hazard et al., 1984; Hartig and Baldwin, 1986; see Sect. 3);

iii) that the "standard" model accounts very well for the main observed characteristics of the complex Ly $\alpha$  + N v line profile (see Sect. 4); and

iv) the fact that there seems to exist a correlation between the width, the strength of emission-line profiles and the velocity structure of the absorption troughs (see above), we conclude that it is highly plausible and natural to assume that BAL and non-BAL QSOs form two distinct classes of quasars. Furthermore, the possibility that the formation of a BALR results from the progressive destruction of a "normal" broad emission-line region (BELR) deserves some special attention. Indeed, Blumenthal and Mathews (1979) have proposed that the optically thick emission-line clouds giving rise to a "normal" emission line spectrum could, under certain circumstances, be radiatively expelled from the central non thermal source. As they accelerate away, these clouds expand and become optically thin in the Lyman continuum, producing broad absorption features in the high excitation lines due to resonance scattering. No Mg II absorption can however be formed. In such a scenario, BAL QSOs with smooth absorption troughs adjacent to the emission (cf. the spectra of RS 23, H 1413 + 113, PHL 5200, etc.) would represent objects in the early phase of the BAL phenomenon, the BALR and BELR being partially coexistent. BAL QSOs exhibiting detached troughs with observable velocity structure and weak, broad high excitation emission-lines (cf. the spectra of Q 0932 + 501, Q 1308 + 308, H 1414 + 090, etc.) would correspond to a more advanced stage of the BALR. It is also likely that if turbulence results from thermal instabilities occurring in an initially smooth flow, the relevant line profiles will show a more complex absorption structure and a weaker emission component, just as it is observed. If the general trend of the proposed scenario is correct, one would expect to observe marked differences between the properties of the narrow emission line region (NELR) pertaining to these two extreme classes of BAL QSOs and, more generally, to BAL and non-BAL QSOs. The lack of observable [O III] emission in the spectrum of several low redshift BAL QSOs (Turnshek, 1986) could, for instance, be an observational proof of the non-existence of a NELR whenever a BALR is present.

*Acknowledgements.* We thank both Mrs M. Macours-Houssonlogé and Mrs J. Bosseloirs for typing the manuscript and drawing the figures.

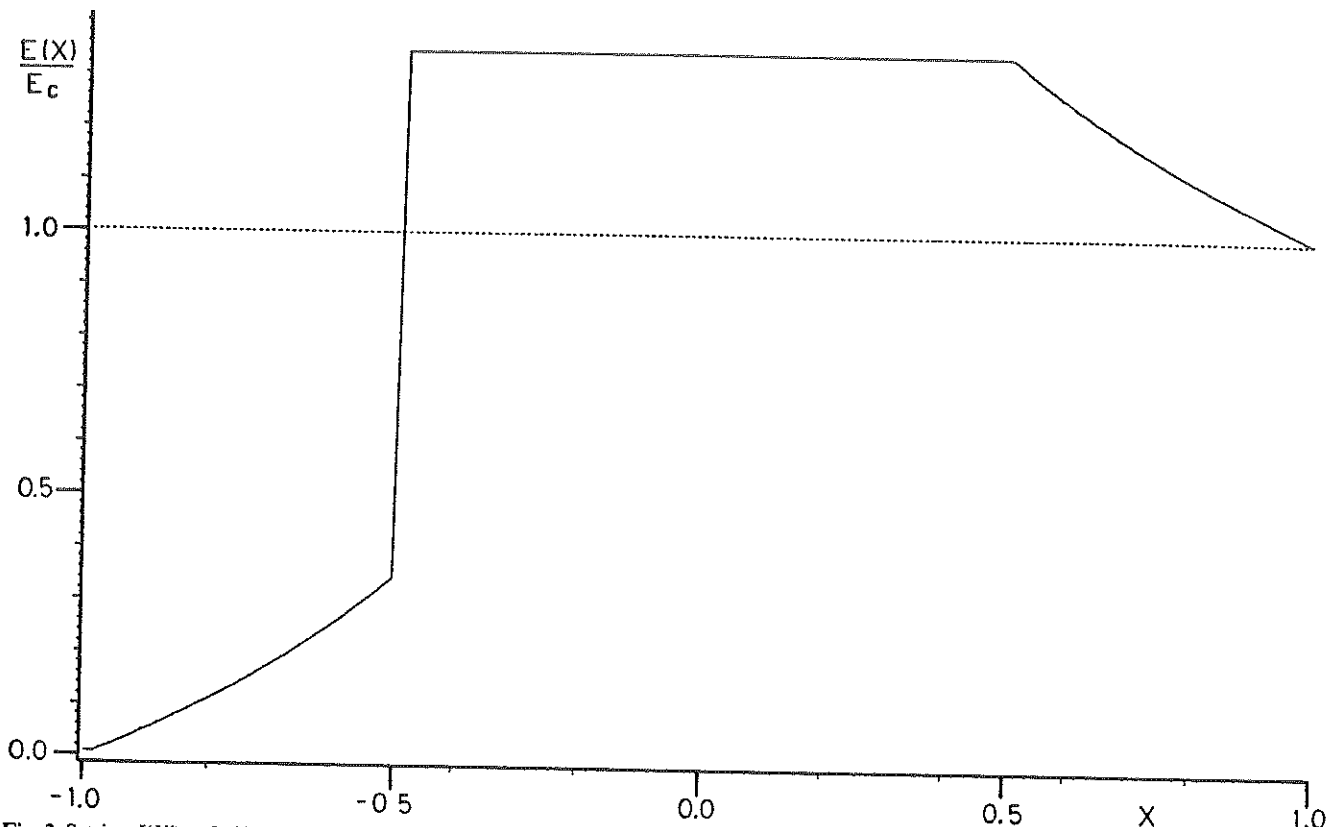


Fig. 3. Setting  $\zeta(X') = 0$ ,  $X_{\min} = -0.50$ ,  $\tau_0 = 10.0$  and  $\gamma = 0.1$  in Eq. (1), the resulting profile consists of a well detached absorption through cutting the blue wing of a broad and weak emission-line (compare with the N v profile given in Fig. 2b)

#### References

- Arp, H.: 1984, *Astrophys. J.* **285**, 547  
 Baldwin, J.A.: 1977, in the proceedings of a NATO Advanced Study Institute (University of Cambridge), "Active galactic nuclei", p. 51  
 Baldwin, J.A., Netzer, H.: 1978, *Astrophys. J.* **226**, 1  
 Baldwin, J.A., Smith, M.G.: 1983, *Monthly Notices Roy Astron. Soc.* **204**, 331  
 Bastian, U., Bertout, C., Stenholm, L., Wehrse, R.: 1980, *Astron. Astrophys.* **86**, 105  
 Bertout, C.: 1985, *Astron. Astrophys.* **144**, 87  
 Blumenthal, G.R., Mathews, W.G.: 1979, *Bull. Am. Astron. Soc.* **11**, 778  
 Boksenberg, A., Carswell, R.F., Smith, M.G., Whelan, J.A.J.: 1978, *Monthly Notices Roy Astron. Soc.* **184**, 773  
 Castor, J.I.: 1970, *Monthly Notices Roy Astron. Soc.* **149**, 111  
 Castor, J.I., Lamers, H.J.G.L.M.: 1979, *Astrophys. J. Suppl.* **39**, 481  
 Clowes, R.G., Smith, M.G., Savage, A., Cannon, R.D., Boksenberg, A., Wall, J.V.: 1979, *Monthly Notices Roy Astron. Soc.* **189**, 175  
 Drew, J., Giddings, J.: 1982, *Monthly Notices Roy Astron. Soc.* **201**, 27  
 Drew, J.E., Boksenberg, A.: 1984, *Monthly Notices Roy Astron. Soc.* **211**, 813  
 Foltz, C., Wilkes, B., Weymann, R., Turnshek, D.: 1983, *Publ. Astron. Soc. Pacific* **95**, 341  
 Grachev, S.I., Grinin, V.P.: 1975, *Astrofizika* **11**, 20  
 Hamann, W.-R.: 1980, *Astron. Astrophys.* **84**, 342  
 Hamann, W.-R.: 1981a, *Astron. Astrophys.* **100**, 169  
 Hamann, W.-R.: 1981b, *Astron. Astrophys.* **93**, 353  
 Hartig, G.F., Baldwin, J.A.: 1986, *Astrophys. J.* **302**, 64  
 Hazard, C., Morton, D.C., Terlevich, R., McMahon, R.: 1984, *Astrophys. J.* **282**, 33  
 He, X.-T., Cannon, R.D., Peacock, J.A., Smith, M.G., Oke, J.B.: 1984, *Monthly Notices Roy Astron. Soc.* **211**, 443  
 Hempe, K., Schönberg, K.: 1986, *Astron. Astrophys.* **160**, 141  
 Junkkarinen, V.T.: 1980, Ph.D. Thesis, University of California (San Diego)  
 Junkkarinen, V.T., Burbidge, E.M., Smith, H.E.: 1983, *Astrophys. J.* **265**, 51  
 Junkkarinen, V.T.: 1983, *Astrophys. J.* **265**, 73  
 Lamers, H.J.G.L.M., Cerruti-Sola, M., Perinotto, M.: 1986, preprint  
 Lynds, C.R.: 1966, *Astrophys. J.* **147**, 396  
 Mihalas, D., Kunasz, P.B., Hummer, D.G.: 1975, *Astrophys. J.* **202**, 465  
 Osmer, P.S., Smith, M.G.: 1976, *Astrophys. J.* **210**, 267  
 Osmer, P.S., Smith, M.G.: 1977, *Astrophys. J.* **213**, 607  
 Scargle, J.D., Caroff, L.J., Noerdlinger, P.D.: 1970, *Astrophys. J.* **161**, L115  
 Scargle, J.D., Caroff, L.J., Noerdlinger, P.D.: 1972, in "External Galaxies and Quasi Stellar Objects", D.S. Evans (ed.), p. 151  
 Schönberg, K.: 1985a, *Astron. Astrophys.* **148**, 405  
 Schönberg, K.: 1985b, *Astron. Astrophys. Suppl. Series* **62**, 339  
 Shaver, P.A., Boksenberg, A., Robertson, J.G.: 1982, *Astrophys. J.* **261**, L7

- Smith, M.G., Carswell, R.F., Whelan, J.A.J., Wilkes, B.J., Boksenberg, A., Clowes, R.G., Savage, A., Cannon, R.D., Wall, J.V.: 1981, *Monthly Notices Roy Astron. Soc.* **195**, 437
- Sobolev, V.V.: 1947, *Dnizuščiešja Oboložki Zvezd*, Leningrad (transl. Moving envelopes of stars; translated from Russian by S. Gaposchkin, Harvard University Press, Cambridge, Mass., 1960)
- Stocke, J.T., Liebert, J., Schild, R., Gioia, I.M., Maccacaro, T.: 1984, *Astrophys. J.* **277**, 43
- Surdej, J.: 1979a, Ph.D. Thesis, University of Liège (Belgium)
- Surdej, J.: 1979b, *Astron. Astrophys.* **73**, 1
- Surdej, J., Swings, J.P.: 1981, *Astron. Astrophys.* **96**, 242
- Surdej, J., Hutsemékers, D.: 1987, in preparation
- Turnshek, D.A., Weymann, R.J., Liebert, J.W., Williams, R.E., Strittmatter, P.A.: 1980, *Astrophys. J.* **238**, 488
- Turnshek, D.A.: 1981, Ph.D. Thesis, University of Arizona
- Turnshek, D.A.: 1984a, *Astrophys. J. Letters* **278**, L87
- Turnshek, D.A.: 1984b, *Astrophys. J.* **280**, 51
- Turnshek, D.A., Weymann, R.J., Carswell, R.F., Smith, M.G.: 1984, *Astrophys. J.* **277**, 51
- Turnshek, D.A.: 1986, to appear in the proceedings of the IAU Symposium 119, "Quasars", Bangalore (India)
- Wampler, E.J.: 1986, ESO preprint N° 421
- Weymann, R.J., Carswell, R.F., Smith, M.G.: 1981, *Ann. Rev. Astron. Astrophys.* **19**, 41
- Weymann, R., Foltz, C.: 1983, in the proceedings of the 24th Liège International Astrophysical Colloquium, "Quasars and Gravitational Lenses", Institut d'Astrophysique, ULg (Belgium), p. 538
- Weymann, R.J., Turnshek, D.A., Christiansen, W.A.: 1985, in the proceedings of the Santa Cruz Summer Workshop in Astrophysics, "Quasars and Active Galactic Nuclei"
- Whelan, J.A.J., Smith, M.G., Carswell, R.F.: 1979, *Monthly Notices Roy Astron. Soc.* **189**, 363
- Young, P., Sargent, W.L.W., Boksenberg, A.: 1982, *Astrophys. J. Suppl. Series* **48**, 455

**Note added in proof:** Optical imaging of the low redshift BAL QSO 1411 + 442 has led Hutchings (1986, preprint presented at the IAU Symposium No. 121) to conclude that "the BAL phenomenon is not connected with a highly inclined disk system, or with nuclear extinction".





## Article 14

### OBSERVATIONAL ASPECTS OF GRAVITATIONAL LENSING

Surdej, J.: 1990, rapport introductif présenté au "Toulouse Workshop on Gravitational Lenses (september 1989)", article de revue dans "Lecture notes in Physics, Gravitational Lensing", Y. Mellier, B. Fort, G. Soucail (eds.), Springer-Verlag, 360, 57.

Dans cet article de synthèse, nous discutons les différents aspects observationnels des lentilles gravitationnelles. Nous décrivons tout d'abord les multiples "surveys" de mirages gravitationnels qui sont actuellement en cours dans différents grands observatoires astronomiques. Nous passons en revue chaque cas connu de mirage gravitationnel et suggérons pour certains d'entre eux des observations complémentaires qui serviront à améliorer les modèles existants. Nous résumons enfin toutes les évidences observationnelles supplémentaires suggérant que des effets de lentille gravitationnelle affectent de façon significative notre vue de l'Univers lointain ainsi que notre compréhension de différentes classes d'objets extragalactiques (cf. objets de type BL Lac, OVVs, quasars BAL, etc.).



# Observational aspects of gravitational lensing

Jean Surdej

Institut d'Astrophysique, Université de Liège

Chercheur Qualifié au FNRS (Belgique)

## Abstract

In this review on the recent observational aspects of gravitational lensing, I first present the various systematic optical surveys for multiply lensed extragalactic objects that are being carried out at several observatories enjoying good seeing conditions. I then summarize the updated observational status of all proposed gravitational lens candidates, concentrating mainly on multiply lensed QSOs (the cases of giant luminous arcs, radio rings and distant 3C radio galaxies are described elsewhere in this volume). Finally, I give a general outline of all the additional pieces of observational evidence suggesting that gravitational lensing may (i) perturb significantly our view of the distant Universe and (ii) affect our physical understanding of various classes of extragalactic objects.

## 1. Introduction

The possible perturbations of our view of the distant Universe by gravitational lensing effects are strongly linked to the detailed distribution of matter at various scales. A theoreticians' approach usually consists in making use of all our present (but of course, limited) knowledge on the distribution of matter to predict the importance of such perturbations. Given all the modelling complications, limitations, as well as all yet unknown biases in our observations of distant objects, it is not surprising that the conclusions of such studies do oscillate between various degrees of pessimism or of optimism. There is a citation by Peebles, quoted in Blandford and Kochanek (1987), saying that: "Gravitational lenses provide a theorists' heaven and an observers' hell". I rather believe that the contrary is true and that the path through the examples will always remain shorter and more secure than that through the theories. This is also probably why, at least recently, observers have been more optimistic about the possible importance of gravitational lensing than theoreticians. Of course, there are exceptions and in this context, it is only fair to consider Sjur Refsdal as the leader of the optimistic supporters of gravitational lensing. The situation about "gravitational lensing" is a bit reminiscent of that associated with "atmospheric mirages". What does the average man think about the importance of atmospheric lensing effects on our view of distant earth-sources? (cf. the distant car lights seen along a straight road in Figure 1).

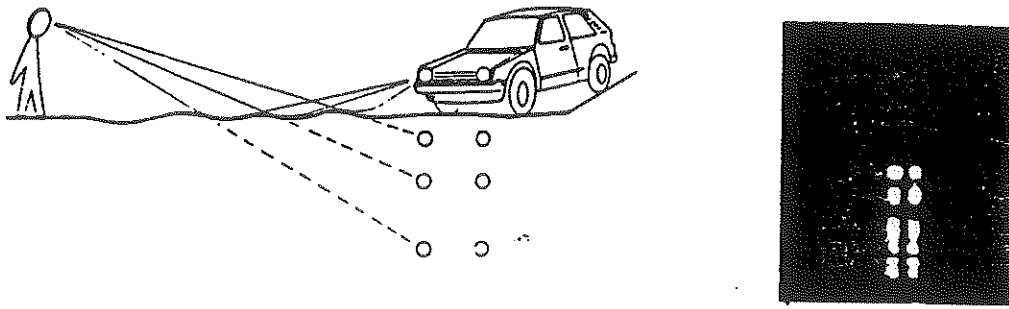


**Figure 1:** The figure at left gives a schematic representation of the light ray paths from a distant car when the ground turns out to be somewhat hotter than the ambient air. Because air refraction always leads to a bending of light rays towards regions of colder air, several lower and somewhat deformed images of a distant source (the car lights in this example) may result. The figure at right represents the multiple images due to the lights from a distant car, as photographed by J. Lehar and the author, along the US 60 road, between Magdalena and Datil near the VLA (New Mexico) on the night of 19 January 1989. The distance between the car and the observers was estimated to be about 10 miles. Such terrestrial mirages, usually made of two single images, can actually be seen everyday, almost from anywhere. In addition to significantly affect our view (image deformation, multiplication, etc.) of distant resolved earth-sources, atmospheric lensing is also often responsible for the light magnification of distant unresolved objects located along straight and long roads or across flat countrysides. Other examples of terrestrial mirages are illustrated in Surdej et al. (1989).

The answer to the analogous question for "gravitational lensing" is of course not so trivial. Ten years after the serendipitous discovery of the double quasar Q0957+561 A and B by Walsh, Carswell and Weymann (1979), both theoretical and observational researches on gravitational lensing have led to a formidable burst of published work. Partly guided by this monument of information but also trying not to cover topics already addressed in recent reviews on the subject of gravitational lensing (e.g. Canizares (1987), Blandford and Kochanek (1987), Nottale (1988), Turner (1989a, b), Barnothy (1989) and references therein), I have decided to focus the present paper on a general discussion of the various known (or only hypothesized) pieces of observational evidence which suggest that gravitational lensing may affect significantly our view and physical understanding of the distant Universe, and of its major constituents.

In section 2, I present an overview of the various systematic optical surveys that are presently being carried out all over the world in order to search for multiply lensed distant objects. In section 3, I have listed the updated observational status of the best recognized cases of multiply lensed objects. I also discuss individually the objects for which recent and outstanding observations have led to a better understanding of the gravitational lenses. Suggestions are also given as to which complementary observations should be carried out in order to still improve some of the lens models. Section 4 summarizes all the additional observational evidence on statistical effects due to gravitational lensing and I also discuss there the various classes of extragalactic objects which may actually consist of lensed sources. The last section deals with general conclusions.

Before closing this introduction, let me recall the challenging goals of studying known gravitational lens systems as well as of discovering new ones. First of all, it is known that a statistical evaluation of the occurrence of gravitational lensing within well defined samples of extragalactic objects is of prime importance in order to improve our knowledge on quasars and

distant radio galaxies (luminosity function, source counts, true part of their cosmic evolution). Detailed studies of identified gravitational lens systems are also important to test cosmological models (Refsdal 1964, 1966), to set constraints on the size and structure of the lensed source (Grieger et al. 1986, 1988) and to probe the luminous and dark matter distributions on various scales in the Universe (Refsdal 1964, 1966). In particular, gravitational lens studies can be used to set limits on populations of dark massive objects (Press and Gunn, 1973; Hewitt et al. 1987a; Webster et al., 1988a). Finally, analysis of narrow absorption lines observed in the spectrum of multiply lensed QSO images are of considerable interest for studies of the spatial structure of the inter-galactic medium. (cf. Foltz et al. 1984 and the paper by Smette et al. in these proceedings).

## 2. Optical surveys for multiply lensed extragalactic objects

Whereas the first gravitational lens systems have been discovered by chance, systematic searches for lenses have proved to be very successful in identifying new systems. I shall describe hereafter several of the on-going optical surveys for multiply lensed extragalactic objects (I refer to the article by B. Burke in this volume for a description of the radio surveys).

### 2.1 Highly Luminous Quasars as gravitationally lensed objects

Considering the canonical  $\log(N)$ - $B$  relation for the count number of quasars per unit area brighter than a given magnitude  $B$  (cf. Boyle et al. 1988), it is easy to calculate the number density enhancement  $q(M, B_0)$  of quasars in a flux limited sample ( $B_0$ ) subject to a magnification  $M$ . Following Narayan (1989), one finds that  $q(M, B_0) = (N(< B_0 + 2.5 \log M) / N(< B_0)) / M$ . Referring to Figure 1 in Narayan (1989) where the author has illustrated the dependence of  $q$  versus both  $M$  and  $B_0$ , one immediately sees that the magnification bias works preferentially well for a bright flux limited sample of QSOs. There are at least three optical surveys for multiply lensed QSO images which benefit from this magnification bias:

1. The Liège/ESO/Hamburg survey, initiated in November 1986 and terminated in November 1988. A description may be found in Surdej et al. (1988a-c) and an update is presented in these proceedings by Swings et al. and Magain et al. I briefly recall that it has consisted in a high resolution imaging of apparently ( $m_v < 18.5$ ) and intrinsically ( $M < -29$ ) bright quasars observable from ESO (Chile). Out of 111 quasars observed under an average seeing FWHM = 1.2", 25 turned out to be interesting candidates (i.e. 23% of HLQs showing elongated, multiple, or fuzzy images), 5 of which constitute very good lens candidates. The cases of UM673 and H1413+117 are described in Surdej et al. (1987) and Magain et al. (1988), respectively.

2. The Djorgovski and Meylan (1989a, b) optical survey for bright distant quasars that has been carried out during the past few years. It also consists in an optical (CCD) imaging search for gravitational lenses among a sample of ( $\approx 300$ ) high redshift QSOs having an apparently large absolute luminosity. So far, they found one new gravitational lens candidate UM425 (Meylan and Djorgovski, 1989), two probable binary quasars PKS1145-071 (Djorgovski et al., 1987) and PHL1222 (Meylan and Djorgovski, these proceedings), and several other promising candidates. As in the Liège/ESO/Hamburg survey, they also identified several cases of QSOs with foreground galaxies within a few arcsec. I refer to the paper by Meylan and Djorgovski in this volume for more detailed information on their survey.

3. The Crampton et al. (1989) optical survey. Using a new-image stabilizing camera at the CFHT, these authors have also made a direct imaging search for closely spaced gravitationally lensed QSO components. Out of 32 quasars with  $z > 1.6$ ,  $m_V < 19$  (i.e.  $M < -27.8$ ), seven were found to be good gravitational lens candidates, two of these having sub-arcsec. angular separations. This fraction (22%) of interesting HLQs is essentially the same as the one (23%) reported by Surdej et al. (1988c).

### *2.2 Quasars as gravitationally lensed objects*

Whereas it is expected that for a fainter limiting magnitude survey the quasar number-density enhancement  $q(M, B_0)$  will get smaller, such surveys have the advantage of dealing with a much larger number of objects. One such sample of fainter quasars ( $m_b < 19$ ) has been used as a basis for the automated survey for gravitational lenses described by Webster et al. (1988a). With the help of the Automated Plate Measuring (APM) facility at Cambridge, these authors have scanned both broadband direct and objective-prism Schmidt plates resulting in a survey of 2500 quasars, covering 130 sq. deg. of sky. Whereas this technique is only effective for separations greater than 2 - 3", it enables one to quantify different parameters (separation, magnitude difference, lens brightness, etc.) in the lens survey. Since the frequency of lensing for a given separation of lensed QSO images may be predicted, it allows one to set interesting constraints on the mass distribution in the Universe. The new wide separation gravitational lens candidate Q1429-008 recently reported by Hewett et al. (1989) has been found via this survey. The detection of statistical gravitational lensing by foreground mass distributions described in Webster et al. (1988b) is also based upon this survey. It is discussed at length by R. Webster in this volume.

### *2.3 Distant 3C radio sources as gravitationally lensed objects*

The magnification bias has also motivated Hammer, Nottale and Le Fèvre (1986) to assume that the distant ( $z > 1$ ) and powerful ( $P(178\text{MHz}) > 10^{28}$  W/Hz) radio sources (hereafter DPRSs) constitute some of the best extragalactic candidates to search for the presence of gravitationally lensed images at arcsec./sub-arcsec. angular scale resolutions and/or for an excess of foreground objects (galaxies, clusters) in the vicinity of the relevant targets. Approximately 75% of the high redshift 3C sources observed by Hammer and Le Fèvre (1989) in optimal seeing conditions with the CFHT at Mauna Kea have been resolved into multiple (2 to 6) components. Strong arguments supporting the mirage hypothesis have been obtained for 3C324, by high resolution imagery through narrow band filters (Le Fèvre et al. 1987; Hammer and Le Fèvre 1989). High spatial resolution imaging and spectroscopy obtained for 3C208.1 definitely prove that the optical appearance of this source is due to the close projection (3.9") of the optical counterpart of a radio loud quasar at  $z = 1.01$  and a foreground AGN at  $z = 0.159$  which gravitationally magnifies, by more than 0.5 mag., the background object (Le Fèvre and Hammer, 1989). Of special interest is that a detailed comparison between CCD frames obtained from a sample of 27 3C distant radio sources with  $z > 1$  and selected blank fields indicates a significant excess of foreground bright galaxies (up to  $m_R \approx 21$ ) and Abell/Zwicky clusters near the 3C sources (Hammer and Le Fèvre, 1989). It therefore seems that gravitational magnification by foreground galaxies and rich clusters is at least partly responsible for the observed radio and optical luminosities of the bright 3C sources. In particular, the following DPRSs: 3C194 and 3C225A (Le Fèvre and Hammer, 1988), 3C238, 3C241, 3C266 and 3C305.1 (Le Fèvre et al. 1988b), 3C13 and 3C256 (Le Fèvre et al. 1988a), 3C239, 3C252, 3C267, 3C322, 3C230, 3C297 and 3C469.1 (Hammer and Le Fèvre, 1989) have been

proposed to be either gravitationally magnified and/or multiply imaged. High spatial resolution narrow band imaging and/or deep 2D spectroscopy of most of these candidates are badly needed in order to further test the lensing hypothesis.

In closing I wish to mention here that the surveys described in 2.1.1, 2.1.2 and 2.3 constitute parts of an ESO key-programme that is being presently conducted at ESO-La Silla (see the description of the programme as well as the names of all participants in Surdej et al. 1989).

### 3. Gravitational lens candidates

Table I (see the appendix at the end of these proceedings) presents an updated list of the accepted and proposed candidates of multiply lensed extragalactic objects. Separate comments on individual gravitational lens systems follow:

*1. 0957+561:* The most extensive photometric monitoring of a gravitationally lensed quasar has of course been carried out for this famous double quasar. Tentative time delays of  $1.55 \pm 0.1$  years by Florentin-Nielsen (1984), 1.2 years by Schild and his collaborators and, very recently,  $1.14 \pm 0.06$  years by Vanderriest et al. (1989) have been reported. The radio time delay of  $< 500$  days derived by Lehár et al. (1989) essentially corroborates the optical value. Both the groups of Vanderriest and of Schild find however that the observed lightcurves of 0957+561 A and B cannot be fully interpreted in terms of intrinsic brightness variations of the quasar alone. Micro-lensing seems to contribute to the variations of the B component. Note however that Falco et al. (cf. these proceedings) cast some doubt on this whole interpretation. A spectrophotometric monitoring of the two image components of 0957+561 would certainly help in disentangling the effects due to intrinsic and/or extrinsic variability. Whereas the estimate of the mass of the lensing galaxy is fairly secure (cf. Borgeest, 1986; see Table I), a more precise modelling of the mass distribution in the lensing galaxy and its attendant cluster is necessary to derive a safe estimate for the Hubble parameter. A deep mapping in luminosity and velocity (velocity dispersion + redshift) of most of the foreground galaxies is necessary in order to better constrain the free parameters of the mass distribution. Very high angular resolution radio observations of images A and B at several epochs would also be extremely valuable.

*2. 1115+080:* Following the photometric variability study reported by Vanderriest et al. (1986), it is likely that micro-lensing effects are responsible for the brightness variations observed between the A1 and A2 image components. Spectrophotometry of the whole system at various epochs should provide us with a definite answer as to the reality of these effects. Note that in addition to the lensing galaxy detected by Shaklan and Hege (1987) between the A and B images, Henry and Heasley (1986) found that there was also a galaxy centred approximately midway between the two A components. These authors find that the properties of this galaxy (G4,  $M_V \approx -23.3$ ) are consistent with it being the brightest member of a small group at  $z = 0.305$  (cf. galaxies G1 and G2 in Young et al. 1981). If real, this would lend support to the micro-lensing induced variability suspected for the A twin components. By means of the pupil segmentation technique used with the CFHT (see Lelièvre et al. 1988), high angular resolution observations supporting this picture for PG1115+080 have been obtained by Arnaud et al. (1989). However, using speckle interferometric observations, Foy et al. (1985) have detected an elongation of image A2 and they suggested that it was caused by a fifth lensed QSO image, located at  $0.04''$  from A2. It is therefore clear that image A is made of more than simply two lensed QSO images and it is likely that further high angular

resolution imaging will be necessary in order to definitely settle this point. Although the redshift of the galaxy detected between the A and B images has not yet been directly measured, it is quite possible that for  $z = 0.305$ , the observed reddening of the B component relative to A, as seen in the spectra published by Young et al. (1981), is actually due to the contamination by the foreground galaxy. In any case, any serious modelling of this lens should take into account the several (5?) galaxies detected in the nearby field.

3. 2345+007: Nieto et al. (1988) have obtained very high angular resolution images of this system using a photon counting detector in its resolved imaging mode. By using recentring and selection algorithms plus image restoration techniques, they have achieved good S/N images with resolution of  $FWHM \approx 0.25''$ . These observations lend a good support to the gravitational lensing hypothesis of 2345+007 A and B because they reveal that the fainter (B) component actually consists of a double image (B1, B2 with roughly equal brightnesses), separated by  $0.36''$  and roughly aligned along the same direction as the A and B images, and that there is also good evidence for the outer of these two sub-images to be resolved along a direction perpendicular to the line between B1 and B2. Furthermore, comparison of the ratio A/B at the time of their observations with previously reported values suggests some variability in this system. A spectrophotometric monitoring of the A and B components would also be of great scientific interest to search for micro-lensing effects and/or for a measurable time delay between the two brighter image components.

4. 2016+112: This gravitational lens system appears to be very complex because it consists of at least three detected lensed images A-C', two foreground galaxies C and D, including one with a measured redshift  $z = 1.01$  and two diffuse narrow line emission regions, that appear to be physically distinct, and located near images A and B (see Figure 1 in Schneider et al. 1986). Observational evidence for the possible occurrence of micro-lensing effects has also been reported for this system and a spectrophotometric follow-up of the lensed QSO images would be of great value. See the contribution in this volume by Heflin et al. related to the interesting constraints that their VLBI observations impose on the proposed gravitational lens models (cf. those by Narasimha et al. 1987).

5. 1635+267: The detailed spectroscopic study of 1635+267 A and B by Turner et al. (1988) has led to the good conviction that this double quasar constitutes a good case of gravitational lensing. Indeed, not only were they able to show that the wavelengths, strengths, widths and profiles of different lines were the same, after a proper scaling and to within measuring errors, in the two image spectra but they also found that the excess of red light in the bright component resembles the continuum emission of a  $z \approx 0.57$  galaxy. Independently, the modelling of this system by Narasimha and Chitre (1988) also led to the prediction that a lensing galaxy should be located at  $0.75''$  from component A. One should of course try to image this system in red light and under very good seeing conditions in order to confirm the presence of the lensing galaxy ... nearly on top of the A (multiple?) image(s).

6. 2237+0305: First of all, superb high angular resolution imagery (Yee, 1988 and Schneider et al. 1988) and spectroscopy (De Robertis and Yee, 1988 and Adam et al. 1989) have convincingly demonstrated that the Einstein cross consists of four lensed images plus a central galaxy nucleus. Kayser and Refsdal (1989) have pointed out the uniqueness of this gravitational lens system to display micro-lensing effects. Indeed, i) because the expected time delays are so short, intrinsic



variability should show up almost simultaneously in the four images so that any difference may be attributed to micro-lensing, ii) due to the large distance ratio between the lens and the source, micro-lensing should lead to more frequent and rapid high amplification events (HAEs) and iii) the expected number of HAEs should be large (about 0.3 events per year and per image). It was therefore not a surprise when Irwin et al. (1989) announced the brightening by 0.5 mag. of component A on CCD frames obtained during the 1988 summer. CCD frames taken at La Silla by Remy et al. (1989) in april 1989 in the framework of the "Gravitational Lensing" ESO key-programme indicate that the relative brightening of image A was still about 0.3 mag. in blue light. Integral field spectrophotometric monitoring of this system, similar to the *one epoch* observations reported by Adam et al. (1989) with the TIGER spectrograph (Courtès et al. 1987), would also be extremely valuable. Such observations would present the additional potential of measuring simultaneously the rotational velocity field of the deflecting spiral galaxy. Note that simulations of micro-lensing effects for 2237+0305 by Wambsganss et al. (1989) predict unfortunately that the time scale and the amplitude of HAEs should not only depend on the source size and the relative transverse velocity between the source, the lens and the observer but that, due to the very strong effect of the shear by the galaxy, it should also depend on the direction of this velocity.

7. 0142-100: Since the lens of this system appears to be made of a single isolated galaxy at a redshift  $z = 0.49$  (the redshift of the galaxy D in Surdej et al. 1987 has been measured to be  $z = 0.17$ ), it constitutes a very good candidate to attempt an independent measurement of  $H_0$ . A photometric monitoring of 0142-100 A and B has been initiated two years ago at ESO. It should nevertheless be mentioned that we have failed to detect the A and B images with the VLA at 6cm in the A configuration (0.3 mJy r.m.s. noise).

8. 3C324: Spectroscopic confirmation of this first galaxy-galaxy gravitational lens system is strongly awaited. This optical source should also be monitored photometrically for the possible detection of a SN event in the different images.

9. 1413+117: This gravitational lens system has been resolved at 3.6 cm with the VLA in the A configuration. A detailed modelling of these observations has been made by Kayser et al. (1989) and supports very nicely the optical observations. High angular resolution integral spectroscopy of this system with the integral field spectrograph SILPHID (Vanderriest and Lemonnier, 1987) has enabled us to resolve the spectra of the four individual images (Angonin et al., these proceedings). Spectroscopic and photometric indications of micro-lensing effects in the D component have possibly been found.

10. 1120+019: Except for images A and B, no spectra have yet been obtained for the many other objects in the field of this gravitational lens candidate (see Meylan and Djorgovski, 1989).

11. 0414+0534: It would be very important to make a new attempt to determine the redshift of the optically detected object (source?). All four components of this system have been detected with VLBI to show compact flux at 18cm (Hewitt, 1989). There is no doubt that this gravitational lens system turns out to be a very interesting one.

12. 1429-008: Because of the slight, although probably real, spectroscopic differences seen between the two image components, better S/N spectra are mandatory in order to confirm or reject the lensing hypothesis for this system.

13. *M82 quasars*: This is just one example of QSO images with large separations and all general remarks which follow could apply equally well to many other cases of quasars having very similar redshifts and spectra but large angular separations. Paczynski and Gorski (1981) did actually first suggest that the unusual grouping of quasars near M82 (Burbidge et al. 1980) may consist of another case of gravitational lensing. In the lensing scenario, one or several of the observed QSO images could actually be multiple (due to macro-lensing by a galaxy located in one of the two hypothetical clusters) and one could try to detect i) the presence of a cluster by direct imaging (direct detection or search for distorted background galaxies), ii) the possible multiplicity of the QSO images, iii) the presence of additional magnified QSOs, iv) the similarity or, on the contrary, noticeable differences between the redshifts of the three identified quasars.

#### 4. Further observational evidence for gravitational lensing

##### 4.1 Statistical gravitational lensing

4.1.1 *Galaxies near flat radio spectrum quasars*: using an automatic search and classification technique for counting galaxies on CCD frames, Fugmann (1988, 1989) has reported, at typically a 97.5% significance level, an increase in the number density of relatively bright ( $r < 21.5$ ) galaxies towards distant ( $z > 1.7$ ) quasars. The increased number of galaxies seems to pertain mainly to fields of (12) flat-spectrum quasars with a much smaller increase near steep-spectrum and radio-quiet quasars. Fugmann invokes gravitational lensing effects, specially micro-lensing to account for these observations and he concludes that gravitational lensing contributes strongly to observed counts of distant sources, particularly to the statistics of flat-spectrum quasars. Whereas Tyson (1986) had also reported a QSO-galaxy correlation for moderately distant quasars ( $1 < z < 1.5$ ), Yee and Green (1984) did not. It is most likely that these different results arise because of the different fractions of radio quiet, steep and flat spectrum quasars constituting those different samples. Fugmann further postulates that gravitational lensing may be responsible for the appearance of different sub-classes of quasars (e.g. the optically quiet compact radio sources (OQCRSs) including objects such as AO0235 + 164, 0406 + 121, 0500 + 01, 1413 + 135, etc.). Since X-rays detected from selected quasars are supposedly emitted from a very compact core, one may naturally wonder whether X-ray selected quasars could also reveal observational evidence for statistical gravitational lensing.

4.1.2 *Galaxies near X-ray selected quasars*: during the course of an extensive program of spectroscopic identification of faint X-ray sources discovered serendipitously with the Einstein satellite, 10 X-ray selected AGNs have been discovered by Stocke et al. (1987) to lie within three optical diameters of bright ( $m_v < 18$ ) foreground galaxies. These authors report that, at a confidence level  $> 97.5\%$ , these AGNs have significantly higher redshifts than X-ray selected ones in general. Stocke and his collaborators have interpreted their findings in terms of micro-lensing in which stars in the foreground galaxy significantly brighten the X-ray emission from these higher redshift AGNs, allowing them to be detected. However, Rix and Hogan (1989) have recently re-investigated this problem by taking deeper CCD frames of the complete sample of the 56 X-ray flux limited AGN fields (MSS initial sample) in order to enlarge the subsample of AGNs with foreground galaxies ( $R < 20.5$ ) from 3 to a total of 8. On the basis of these new data, Rix and Hogan conclude that there is no longer any evidence for lensing effect by the galaxies. The presence of an excess of high redshift X-ray selected quasars near bright foreground galaxies remains still a subject of debate.

*4.1.3 Galaxies near APM quasars:* at a significance level greater than 99.99%, Webster et al. (1988b) have presented evidence for the detection of an excess of distant quasars ( $z > 0.5$ ,  $B_r < 18.7$ ) associated with foreground galaxies ( $r < 6''$ ,  $B_r < 21$ ) and they invoke gravitational lensing effects in order to account for such a large number of associations. However, they report that the mass of the foreground galaxies must be substantially greater than is conventionally attributed to a luminous galaxy and its halo. I believe that this apparent problem could be easily overcome if one could prove that the principal deflector lies much closer to the line-of-sight (e.g.  $r < 1.5''$ ) than it has been claimed. Several such tight associations have been identified in the HLQ samples described above (see Magain et al. in these proceedings and also section 4.1.12). Given the excess of 4.4 times more APM quasars near galaxies, which corresponds to an average magnification of 2.7, Narayan (1989) has shown that, if this effect is really caused by gravitational lensing, then the quasar-galaxy correlation found by Webster et al. must be smaller than the reported one by a factor of about 2 and/or the magnitude limit of their survey should be brighter by a few tenths of magnitude than the one reported ( $B_r = 18.7$ ). Narayan also demonstrates that the observed effect does not require halos of foreground galaxies to be composed of micro-lenses (stars, black holes, etc.); the quasar-galaxy correlation works equally well with smooth halos. All these conclusions directly follow from the quasar luminosity function and are independent of the lens structure. This result shows how important it is to know accurately what the unlensed luminosity function of quasars is (see the contribution in this volume by R. Webster for an update of their findings on the APM QSO-galaxy associations).

*4.1.4 The giant luminous arcs:* see the updated report by B. Fort in these proceedings.

*4.1.5 Distorted background galaxies:* using a similar technique to that of Tyson and his collaborators, Elston et al. (1989) have carried out searches for statistical gravitational lensing effects using background galaxies projected on selected rich, massive clusters. They found that the background galaxies are preferentially aligned at  $90^\circ$  to a radial vector from the cluster center. Some good agreement is reached between the observed distributions of position angles and those of lensing models. They consider this finding as evidence that the background galaxies are being lensed by the foreground clusters (see also the contributions by Tyson and Grossman in these proceedings).

*4.1.6 Anomalous quintets of galaxies:* Hammer and Nottale (1986a) have shown that the well known quintets of galaxies such as VV172, VV115, etc. which contain a discrepant redshift member may be fully understood in terms of the effects of gravitational magnification by the halo of the foreground quartet on the more distant galaxy.

*4.1.7 Gravitational lensing magnification of the bright cluster galaxies (BCGs):* Hammer and Nottale (1986b) have presented good evidence that the BCGs of the Kristian et al. (1978) sample lie in regions of the sky containing about two times more foreground Zwicky clusters, the latter clusters being approximately 5 times richer than the mean value for the whole sky. The authors suggest that the gravitational lens magnification of the BCGs by the foreground clusters has induced a strong selection effect in defining the Kristian et al. sample, artificially increasing the deceleration parameter  $q_0$  from 0.2 to about 1.7, as measured from the Hubble diagram of these objects.

*4.1.8 The Arp QSO-galaxy associations:* Nottale (1988) also presents good evidence that the Arp QSO-galaxy associations may be the result of the combined lensing effects of several superposed galaxies, groups and clusters near their lines-of-sight.

*4.1.9 Quasars with  $2.45 < z < 3.8$ :* speculations have been made by Ph. Véron that the second observed rise in the space comoving density of quasars from  $z = 2.45$  up to at least  $z = 3.8$  (Véron, 1986) could be due to statistical gravitational lensing effects by foreground objects located along their lines-of-sight.

*4.1.10 Gravitationally magnified narrow absorption line quasars:* to my knowledge, Nottale (1987) has reported the first observational evidence for gravitational lensing magnification within a sample of absorption line quasars. His conclusions are based upon a comparison between observational data on absorption line quasars with  $1.6 < z < 2.2$  from the catalogue of Barbieri et al. (1982) with predictions from the theory of multiple gravitational lensing (Nottale and Chauvineau, 1986). Nottale finds that the luminosity of a large fraction of known quasars with a redshift  $z > 1.6$  is enhanced by a factor up to about 10 because of the action of intervening matter (clusters of galaxies, superclusters) along their lines-of-sight. More recently, Thomas and Webster (1989, see also their contribution in these proceedings) have presented tests of both evolution and bias due to gravitational lensing in the number density of QSO metal absorption line systems. Their study is mainly based on sets of CIV and MgII absorption line systems observed and compiled by Sargent et al. (1988a-c). They do not find any evidence for evolution except perhaps in the high equivalent width systems, where gravitational lensing may affect the statistics. They rather propose a model in which the distribution of high equivalent width systems reflects clustering of an unevolving low equivalent width population. Note however that, unlike Nottale (1987), Thomas and Webster assume that gravitational lensing resulting from two or more independent systems is unlikely.

*4.1.11 Gravitationally magnified quasars with damped Ly $\alpha$  absorption line(s):* in studies of the formation of disk galaxies at high redshift, various authors have carried out a search for damped Ly $\alpha$  absorption in the spectra of high redshift QSOs. Smith et al. (1987) report that the observed number of those absorption lines is at least a factor five in excess of the number of galaxy disks expected to be intercepted by lines-of-sight to this sample of QSOs (cf. their Fig. 3). The derived column densities of those damped Ly $\alpha$  lines are found to be well in excess of  $10^{21} \text{cm}^{-2}$  (cf. their Fig. 4). Although these authors suggested that gaseous disks may form relatively early in galaxies and that they may be considerably larger at early epochs, I naturally suggest that gravitational lensing magnification could as well account for these observations in terms of induced observational biases, i.e. the quasars from this sample have been observed because they are preferentially magnified due to galaxy disks intercepting their lines-of-sight.

*4.1.12 Quasar-galaxy superpositions:* among the 23% of interesting HLQs found in the above surveys for gravitational lenses, quite a few of these objects turned out to show that a bright galaxy is superimposed on the central image of the QSO (see also the contribution by Magain et al. in these proceedings). We believe that this form of gravitational lensing magnification of background quasars (HLQs, etc.) could actually be more common than the formation of multiple images. One should note that a lensing galaxy has been identified on top, or very near to one of the lensed images in the cases of 0957+561, PG1115+080, 2016+112, and UM673. Recently, Arnaud et al. (1988) have published another nice case of a galaxy superimposed on an HLQ image. These au-

thors report the detection of a galaxy ( $z = 0.63$ ,  $M_r = -21.7$ ) at  $1.3''$  from the line-of-sight to the QSO 1209+107 ( $z = 2.19$ ). Another galaxy ( $z = 0.39$ ), lying at  $7''$  from the QSO had previously been identified by Cristiani (1987). Arnaud et al. conclude that the QSO is certainly gravitationally magnified by the first and second galaxy. One should also note that the distant flat-spectrum (Fugmann, 1988) and APM (Webster et al., 1988b) quasars are also good candidates to this form of lensing. In any case, one should derive the redshifts of the galaxies found in the vicinity of those distant quasars in order to have a definite proof that they constitute foreground objects. Indeed, at low redshifts (up to about  $z = 0.7$ ), most of us would tend to agree that a galaxy superimposed on a QSO image does actually consist of its host galaxy or a galaxy in interaction whereas for higher redshifts, we would be tempted to call it a foreground (lensing) object. Could it be for instance that some of the reported low redshift host galaxies are in fact foreground objects, and vice-versa at high redshifts?

#### 4.2 Gravitational lensing and AGN segregation

*4.2.1 Gravitationally lensed high luminosity AGNs:* in a spectrophotometric monitoring of high luminosity AGNs, Pérez et al. (1989) report that significant emission line variations take place in high luminosity, high redshift objects (cf. 3C 446, PKS 2134+004, etc.). These variations are found to occur on timescales much shorter than those expected from ionization models and therefore the authors invoke beaming of the optical and ultraviolet continuum towards the observer, leading to an anisotropic broad line emission region and a selection effect in favour of cases in which the axis of this anisotropy is close to the line-of-sight (cf. their Fig. 7). Since the phenomenological effects of gravitational lensing are very similar to those expected from beaming, it is equally plausible that the spectroscopic variations observed in high luminosity AGNs are caused by (micro-?) lensing effects. Let us mention that metal absorption line systems, at optimal redshifts for a lens, have been detected in the spectrum of most these objects.

*4.2.2 Rapid variability of extragalactic sources due to lensing effects:* Quirrenbach et al. (1989) have reported radio variability of several flat-spectrum compact sources with amplitudes in the range 10-20% and timescales of hours (cf. their Fig. 1). Although they discuss intrinsic effects and scattering in the interstellar medium as possible explanations for the observed rapid variability, they also mention that it could be due to micro-lensing effects in a foreground object. They searched for the presence of a lensing galaxy in the fields of 0716+71 and 0917+62 but did not find any object on the POSS plates. They conclude on this basis that the other interpretations are more likely to be the right ones. Besides taking deeper CCD frames of the above fields ... one should certainly postpone any sound and firm conclusion.

*4.2.3 OVV's as micro-lensed objects:* Chang and Refsdal (1979, 1984) have first proposed that the main observable effect of lensing by stars or compact objects in galaxies and their halos will be a noticeable photometric variability of the distant source, due to the passage of the micro-lens in front of its line-of-sight. Ostriker and Vietri (1985), Nottale (1986) and Schneider and Weiss (1987) have independently proposed that micro-lensed objects were to be searched among the Optically Violently Variable (OVV) extragalactic objects, particularly those behaving like BL Lac objects at maximum brightness and like quasars when fainter. In the case of 0846+51w1, Nottale (1986) has shown that all its observed properties (sudden brightening by 4 mag. in less than one month, changes of its spectrum between that of a BL Lac object and that of a QSO, etc.) could be explained by the effects of gravitational lensing due to a compact -Jupiter like- object ( $10^{-2} M_{\odot}$ ), lo-

cated within a galaxy at  $z = 0.072$  near the line-of-sight and that the core size of the central region emitting the QSO continuum is about  $2.10^{-4}$  pc. Stickel et al. (1989) recently reported that this BL Lac object displays a noticeable elongated appearance due to an intervening galaxy at  $z = 0.235$  located nearly exactly on the line-of-sight. This observation therefore strengthens the hypothesis by Nottale (1986) that the observed properties of 0846+51wl are markedly influenced by gravitational micro-lensing.

Stickel et al. (1988a) have also suggested that the correlated dramatic flux variability in the optical and radio wavebands of the BL Lac object AO0235+164 ( $z = 0.94$ ) are most likely the result of gravitational lensing of the compact non thermal BL Lac core in the intervening galaxies at  $z = 0.524$ , seen at  $2''$  to the south and at  $0.5''$  to the east from the background source. Note that Yanni et al. (1989) locate this second newly detected foreground object at  $1.3''$  east of AO0235+164. Surdej and his collaborators found recently good evidence that these two claimed galaxies are actually forming a single object. Kayser (1988) has analysed the plausibility of a micro-lensing model to explain the observed characteristics of AO0235+164. Although he finds that several observational data are in apparent contradiction with the micro-lensing hypothesis, he does not totally exclude that micro-lensing may contribute in part to the observed variability of AO0235+164. More investigations on this particular object are badly needed.

Stickel et al. (1988b) have presented convincing arguments that the southern blazar PKS0537-441 could be another example of a gravitationally lensed object. This blazar has been found by these authors to have an extended, spatially resolved appearance, despite its high redshift of  $z = 0.894$ . Using image decomposition techniques, Stickel and his collaborators have shown that a foreground disk galaxy ( $z = 0.186?$ ), seen nearly face on, lies very near the line-of-sight to the blazar (cf. their Figure 2). Stickel et al. derive  $M \approx -22.7$  and an exponential disk scale length of 4.3 kpc for the foreground galaxy. These authors propose that micro-lensing effects are responsible for the rapid and large optical variations (up to 5 mag.) previously observed for this object and that macro-lensing magnification by the foreground galaxy could account for the large luminosity radiated by this blazar. During an active state of the object in february 1985, Tanzi et al. (1986) found that PKS 0537-441 brightened by a similar factor ( $\approx 2$ ) in the IR, optical, UV and X-ray frequencies, suggesting that a same spatial region may be responsible for the emission in the whole spectral range observed. It is of course not difficult to account for these observational trends with a micro-lensing model that magnifies a very compact and distant source.

3C279, as one of the most variable ( $\delta B > 6.7$ ) and possibly most luminous QSO yet observed ( $M = -31.4$ ), constitutes another excellent candidate for micro- and/or macro- lensing effects (see the historical lightcurve of 3C279 in Figs. 1 and 2 of Eachus and Liller, 1975). Additional good micro-lensed candidates may be found among the following OVV: PKS0215+015, 0420-014, 0454-234, 0511-220, 0735+178, PKS0823-23, 1308+326, 1638+398, 3C345 (1641+399) and 3C446 (2223-052). Some of these candidates are known during different brightness phases to have a spectrum turning from that of a QSO to that of a BL Lac object. Others undergo sudden light brightening reminiscent of magnification by micro-lensing effects, and some are located very near a diffuse object and/or show narrow metallic absorption lines at an optimal redshift for a lens.

*4.2.4 Variability of some BAL profiles induced by micro-lensing effects:* variability of some broad absorption line (BAL) profiles have been reported for several objects: UM232 (Barlow et al., 1989), Q1246-057 (Smith and Penston, 1988), Q1303+308 (Foltz et al., 1987) and the well known clover-

leaf H1413 + 117 (Turnshek et al., 1988). In the latter case, it has been recently possible to obtain with the CFHT + SILFID spectrograph very high angular resolution spectra of each of the four QSO lensed images (cf. Angonin et al. in this volume). The spectrum of component D turns out to be markedly different from the other ones and I suggest that micro-lensing might be responsible for this. Other evidence for this effect comes from the photometric variability observed for that same image (see Kayser et al. 1989). The possible implication of this is that if an observer takes an integrated spectrum of H1413 + 117 under average seeing conditions ( $\text{FWHM} > 1''$ ), he may detect variability in the trough or emission line component(s) of the SiIV, CIV, etc. BAL profiles not only depending on when (time dependence of micro-lensing) he took the spectrum but also on how he set the instrument (width, orientation and exact location of the slit with respect to each of the four image components). It could therefore very well be that some of the variability of BAL profiles reported for other BAL QSOs is induced by micro-lensing effects ... and that, maybe, the BAL phenomenon itself could be closely related to gravitational lensing effects.

## 5. Conclusions

From an observational point of view, it has been shown in the previous sections that the challenge of further studying "gravitational lenses" is great, essential and manifold. Indeed, observations taken with the best performing instruments, and under the best seeing conditions, will certainly contribute: (i) to a better understanding of the already known examples of gravitational lensed objects (cf. section 3), (ii) to the discovery of new interesting cases (cf. section 2), (iii) to test the various proposed suggestions that gravitational lensing may significantly perturb our view of the distant Universe (cf. section 4.1) as well as to check how much gravitational lensing has induced an apparent segregation among the various specific classes of extragalactic objects (cf. section 4.2). In summary, there is no doubt that future observations of very remote objects will help us in assessing the real importance of the various known, recently hypothesized or yet unknown gravitational lens effects which seem to condition our view of the distant Universe (see Figure 2).

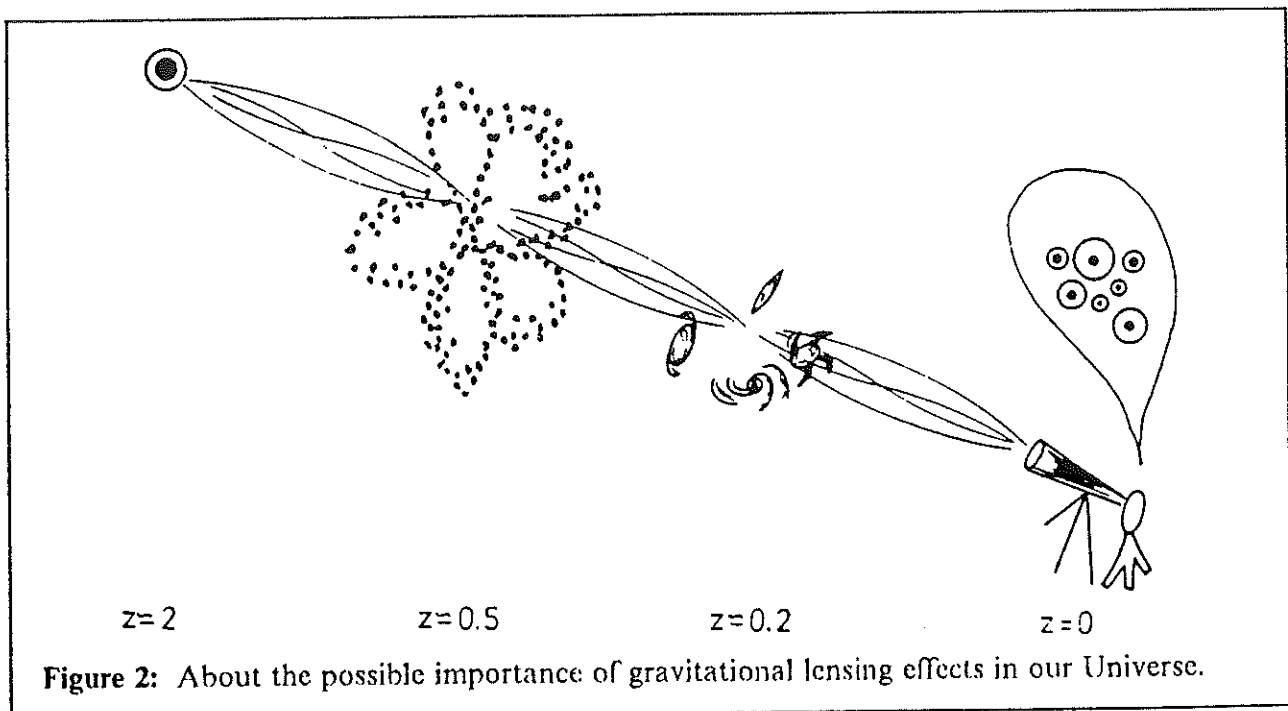


Figure 2: About the possible importance of gravitational lensing effects in our Universe.

**Acknowledgements:** It is a pleasure to thank my friends and colleagues Pierre Magain, Alain Smette and Jean-Pierre Swings for their careful reading of the manuscript. I also wish to thank them as well as George Djorgovski, François Hammer, Géo Meylan, Laurent Nottale, Olivier Le Fèvre, Sjur Refsdal and Peter Schneider for interesting discussions. Finally, my thanks also go to Armand Kransvelt for drawing the figures.

#### References:

- Adam, G., Bacon, R., Courtès, G. et al.: 1989, *Astron. Astrophys.* 208, L15.
- Arnaud, J., Hammer, F., Jones, J., Le Fèvre, O.: 1988, *Astron. Astrophys.* 206, L5.
- Arnaud et al.: 1989, private communication.
- Barbieri, C., Capaccioli, M., Cristiani, S. et al.: 1982, *Mem. S. A. It.* 53, 511.
- Barlow, T.A., Junkkarinen, V.T., Burbidge, E.M.: 1989, preprint.
- Barnothy, J.M.: 1989, in "Gravitational Lenses", eds. J.M. Moran et al., (New York: Springer-Verlag), p. 23.
- Blandford, R.D., Kochanek, C.S.: 1987, in "Jerusalem Winter School for Theoretical Physics": Vol. 4, "Dark Matter in the Universe", (World Scientific), Singapore, eds. J. Bahcall et al., p. 133.
- Borgeest, U.: 1986, *Astrophys. J.* 309, 467.
- Boyle, B.J., Shanks, T., Peterson, B.A.: 1988, *Mon. Not. Roy. Astr. Soc.* 235, 935.
- Burbidge, E.M., Junkkarinen, V.T., Koski, A.T. et al.: 1980, *Astrophys. J.* 242, L55.
- Canizares, C.R.: 1987, in "Observational Cosmology": Proceedings of IAU Symp. N° 124, eds. A. Hewitt et al. (Reidel: Dordrecht), p. 729.
- Chang, K., Refsdal, S.: 1979, *Nature* 282, 561.
- Chang, K., Refsdal, S.: 1984, *Astron. Astrophys.* 132, 168.
- Courtès, G., Georgelin, Y., Bacon, R. et al.: 1987, in "Instrumentation in Astronomy": Proceedings of the 1987 Santa Cruz Workshop, p. 266.
- Cowie, L.L., Hu, E.M.: 1987, *Astrophys. J.* 318, L33.
- Crampton, D., McClure, R.D., Fletcher, J.M. et al.: 1989, DAO preprint.
- Cristiani, S.: 1987, *Astron. Astrophys.* 175, L1.
- De Robertis, M.M., Yee, H.K.C.: 1988, *Astrophys. J.* 332, L49.
- Djorgovski, S., Spinrad, H.: 1984, *Astrophys. J.* 282, L1.
- Djorgovski, S., Perley, R., Meylan, G. et al.: 1987, *Astrophys. J.* 321, L17.
- Djorgovski, S., Meylan, G.: 1989a, in "Active Galactic Nuclei": Proceedings of the IAU Symp. N° 134, eds. D. Osterbrock and J. Miller, (Dordrecht: Kluwer), p. 269.
- Djorgovski, S., Meylan, G.: 1989b, in "Gravitational Lenses", eds. J.M. Moran et al., (New York: Springer-Verlag), p. 173.
- Eachus, L.J., Liller, W.: 1975, *Astrophys. J.* 200, L61.
- Elston, R., Grossman, S., Zaritsky, D.: 1989, preprint.
- Florentin-Nielsen, R.: 1984, *Astron. Astrophys.* 138, L19.
- Foltz, C.B., Weymann, R.J., Röser, H.-J. et al.: 1984, *Astrophys. J.* 281, L1.
- Foltz, C.B., Weymann, R.J., Simon, L.M. et al.: 1987, *Astrophys. J.* 317, 450.
- Foy, R., Bonneau, D., Blazit, A.: 1985, *Astron. Astrophys.* 149, L13.
- Fugmann, W.: 1988, *Astron. Astrophys.* 204, 73.
- Fugmann, W.: 1989, preprint.
- Grieger, B., Kayser, R., Refsdal, S.: 1986, *Nature* 324, 126.
- Grieger, B., Kayser, R., Refsdal, S.: 1988, *Astron. Astrophys.* 194, 54.
- Hammer, F., Nottale, L.: 1986a, *Astron. Astrophys.* 155, 420.
- Hammer, F., Nottale, L.: 1986b, *Astron. Astrophys.* 167, 1.
- Hammer, F., Nottale, L., Le Fèvre, O.: 1986, *Astron. Astrophys.* 169, L1.
- Hammer, F., Le Fèvre, O.: 1989, CFH preprint.
- Henry, J.P., Heasley, J.N.: 1986, *Nature* 321, 139.
- Hewett, P.C., Webster, R.L., Harding, M.E. et al.: 1989, preprint.
- Hewitt, J.N., Turner, E.L., Burke, B.F. et al.: 1987a, in "Observational Cosmology": Proceedings of IAU Symp. N° 124, eds. A. Hewitt et al. (Dordrecht: D. Reidel), p. 751.
- Hewitt, J.N., Turner, E.L., Lawrence, C.R. et al.: 1987b, *Astrophys. J.* 321, 706.
- Hewitt, J.N., Turner, E.L., Schneider, D.P. et al.: 1988, *Nature* 333, 537.



- Hewitt, J.N., Burke, B.F., Turner, E.L. et al.: 1989, in "Gravitational Lenses", Eds. J.M. Moran et al. (New York: Springer-Verlag), p. 147.
- Hewitt, J.N.: 1989, private communication.
- Huchra, J.P., Gorenstein, M., Kent, S. et al.: 1985, *Astron. J.* 90, 691.
- Irwin, M.J., Webster, R.L., Hewitt, P.C. et al.: 1989, CITA preprint.
- Kayser, R.: 1988, *Astron. Astrophys.* 206, L8.
- Kayser, R., Surdej, J., Condon, J.J. et al.: 1989, preprint.
- Kayser, R., Refsdal, S.: 1989, *Nature* 338, 745.
- Kristian, J., Sandage, A., Westphal, J.A.: 1978, *Astrophys. J.* 221, 383.
- Langston, G.I., Schneider, D.P., Conner, S.: 1989, preprint N° 346 from the MPI für Radioastronomie.
- Lawrence, C.R., Schneider, D.P., Schmidt, M. et al.: 1984, *Science* 223, 46.
- Le Fèvre, O., Hammer, F., Nottale, L. et al.: 1987, *Nature* 326, 268.
- Le Fèvre, O., Hammer, F., Nottale, L. et al.: 1988a, *Astrophys. J.* 324, L1.
- Le Fèvre, O., Hammer, F., Jones, J.: 1988b, *Astrophys. J.* 331, L73.
- Le Fèvre, O., Hammer, F.: 1988, *Astrophys. J.* 333, L37.
- Le Fèvre, O., Hammer, F.: 1989, CFH preprint.
- Lehár, J., Hewitt, J.N., Roberts, D.H.: 1989, in "Gravitational Lenses", eds. J.M. Moran et al. (New York: Springer-Verlag), p. 84.
- Lelièvre, G., Nieto, J.L., Salmon, D. et al.: 1988, *Astron. Astrophys.* 200, 301.
- Magain, P., Surdej, J., Swings, J.-P. et al.: 1988, *Nature* 334, 325.
- Meylan, G., Djorgovski, S.: 1989, *Astrophys. J.* 338, L1.
- Narasimha, D., Subramanian, K., Chitre, S.M.: 1987, *Astrophys. J.* 315, 434.
- Narasimha, D., Chitre, S.M.: 1988, preprint.
- Narayan, R.: 1989, *Astrophys. J.* 339, L53.
- Nieto, J.-L., Roques, S., Llebaria, A. et al.: 1988, *Astrophys. J.* 325, 644.
- Nottale, L., Chauvincau, B.: 1986, *Astron. Astrophys.* 162, 1.
- Nottale, L.: 1986, *Astron. Astrophys.* 157, 383.
- Nottale, L.: 1987, *Ann. Phys. Fr.* 12, 241.
- Nottale, L.: 1988, *Ann. Phys. Fr.* 13, 223.
- Ostriker, J.P., Vietri, M.: 1985, *Nature* 318, 446.
- Paczynski, B., Gorski, K.: 1981, *Astrophys. J.* 248, L101.
- Paczynski, B.: 1986, *Astrophys. J.* 308, L43.
- Pérez, E., Penston, M.V., Moles, M.: 1989, preprint.
- Press, W.H., Gunn, J.E.: 1973, *Astrophys. J.* 185, 397.
- Quirrenbach, A., Witzel, A., Krichbaum, T. et al.: 1989, *Nature* 337, 442.
- Refsdal, S.: 1964, *Mon. Not. Roy. Astr. Soc.* 128, 295 and 307.
- Refsdal, S.: 1966, *Mon. Not. Roy. Astr. Soc.* 132, 101.
- Remy et al.: 1989, private communication.
- Rix, H.-W., Hogan, C.J.: 1989, preprint N° 883 of the Steward Observatory.
- Sargent, W.L.W., Boksenberg, A., Steidel, C.C.: 1988a, *Astrophys. J. Suppl.* 68, 539.
- Sargent, W.L.W., Steidel, C.C., Boksenberg, A.: 1988b, *Astrophys. J.* 334, 22.
- Sargent, W.L.W., Steidel, C.C., Boksenberg, A.: 1988c, RGO preprint.
- Schneider, D.P., Gunn, J.E., Turner, E.L. et al.: 1986, *Astron. J.* 91, 991.
- Schneider, D.P., Turner, E.L., Gunn, J.E. et al.: 1988, *Astron. J.* 95, 1619; plus erratum in *Astron. J.* 96, 1755.
- Schneider, P., Weiss, A.: 1987, *Astron. Astrophys.* 171, 49.
- Shaklan, S.B., Hege, E.K.: 1987, preprint N° 609 of the Steward Observatory.
- Smith, H.E., Cohen, R.D., Bradley, S.L.: 1987, preprint.
- Smith, L.J., Penston, M.V.: 1988, *Mon. Not. Roy. Astr. Soc.* 235, 551.
- Stickel, M., Fried, J.W., Kühr, H.: 1988a, *Astron. Astrophys.* 198, L13.
- Stickel, M., Fried, J.W., Kühr, H.: 1988b, *Astron. Astrophys.* 206, L30.
- Stickel, M., Fried, J.W., Kühr, H.: 1989, preprint
- Stocke, J.T., Schneider, P., Morris, S.L. et al.: 1987, *Astrophys. J.* 315, L11.
- Surdej, J., Magain, P., Swings, J.-P. et al.: 1987, *Nature* 329, 695.
- Surdej, J., Magain, P., Swings, J.-P. et al.: 1988a, *Astron. Astrophys.* 198, 49.
- Surdej, J., Magain, P., Swings, J.-P. et al.: 1988b, in "Large Scale Structures: Observations and Instrumentation": Proceedings of the First DAEC Workshop (Paris-Meudon), eds. C. Balkowski and S. Gordon, p. 95.
- Surdej, J., Swings, J.-P., Magain, P. et al.: 1988c, *Astr. Soc. Pac. Conf. Ser.* 2, 183.

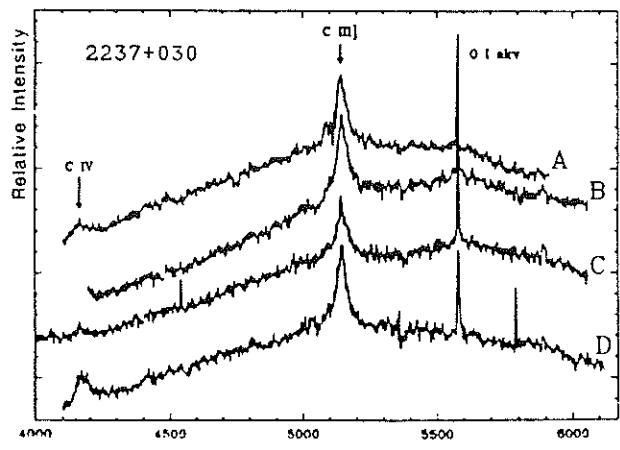
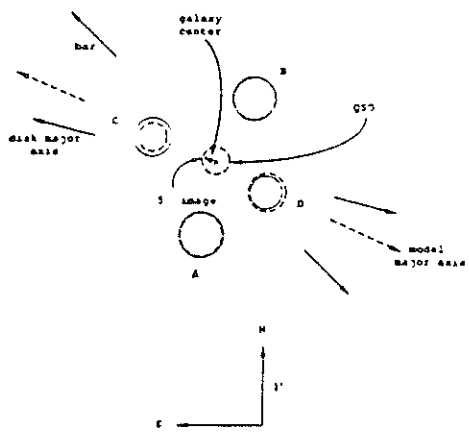
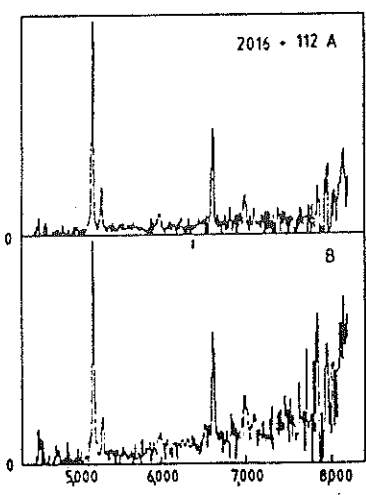
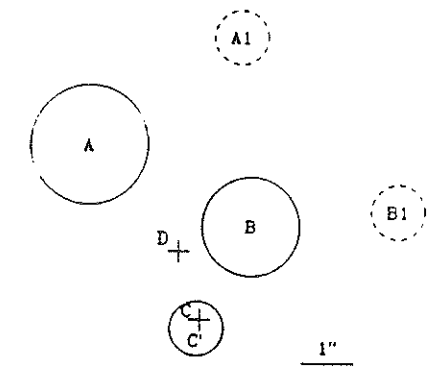
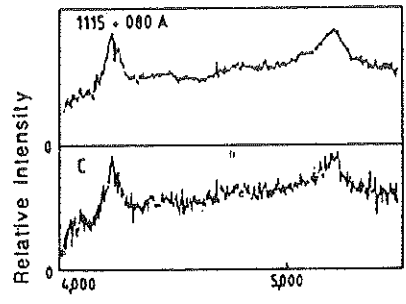
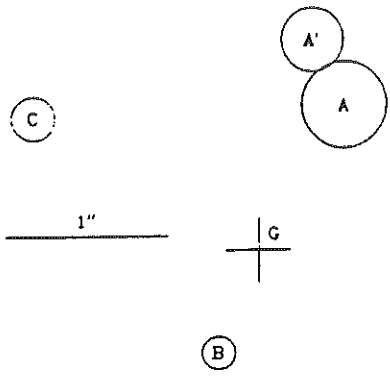
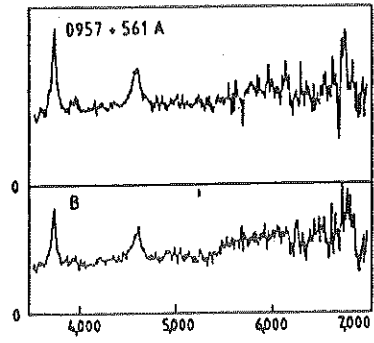
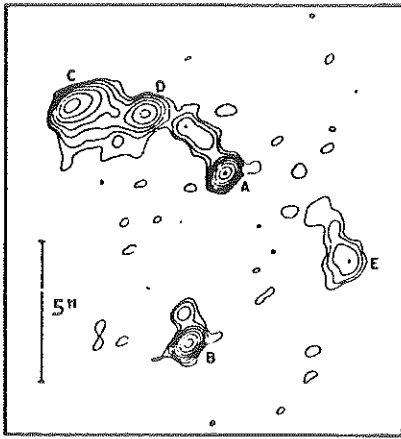
- Surdej, J., Arnaud, J., Borgceest, U. et al.: 1989, *The Messenger* 55, 8.
- Tanzi, E.G., Barr, P., Bouchet, P. et al.: 1986, *Astrophys. J.* 311, L13.
- Thomas, P.A., Webster, R.L.: 1989, CITA preprint.
- Turner, E.L., Hillenbrand, L.A., Schneider, D.P. et al.: 1988, *Astron.J.* 96,1682.
- Turner, E.L.: 1989a, in "Gravitational Lenscs", eds. J.M. Moran et al. (New York: Springer-Verlag), p. 69.
- Turner, E.L.: 1989b, in "The 14th Texas Symp. on Relativistic Astrophysics", preprint.
- Turnshek, D.A., Foltz, C.B., Grillmair, C.J. et al.: 1988, *Astrophys. J.* 325, 651.
- Tyson, J.A.: 1986, in "Quasars", Proceedings of the IAU Symp. N° 119, eds. G. Swarup and V.K. Kapahi (Dordrecht: Reidel), p. 551.
- Vanderriest, C., Wlérick, G., Lelièvre, G. et al.: 1986, *Astron. Astrophys.* 158, L5.
- Vanderriest, C., Lemonnier, J.P.: 1987, in "Instrumentation in Astronomy": Proceedings of the 1987 Santa Cruz Workshop, p. 304.
- Vanderriest, C., Schneider, J., Herpe, G. et al.: 1989, *Astron. Astrophys.* 215, 1.
- Véron, P.: 1986, *Astron. Astrophys.* 170, 37.
- Walsh, D., Carswell, R.F., Weymann, R.J.: 1979, *Nature* 279, 381.
- Wambsganss, J., Paczynski, B., Katz, N.: 1989, Preprint POP-315.
- Webster, R.L., Hewett, P.C., Irwin, M.J.: 1988a, *Astron. J.* 95, 19.
- Webster, R.L., Hewett, P.C., Harding, M.E. et al.: 1988b, *Nature* 336, 358.
- Weedman, D.W., Weymann, R.J., Green, R. et al.: 1982, *Astrophys. J.* 255, L5.
- Weymann, R.J., Latham, D., Angel, J.R.P. et al.: 1980, *Nature* 285, 641.
- Yanny, B., York, D.G., Gallagher, J.S.: 1989, *Astrophys. J.* 338, 735.
- Yee, H.K.C.: 1988, *Astron. J.* 95, 1331.
- Yee, H.K.C., Green, R.F.: 1984, *Astrophys. J.* 280, 79.
- Young, P., Deverill, R.S., Gunn, J.E. et al.: 1981, *Astrophys. J.* 244, 723.

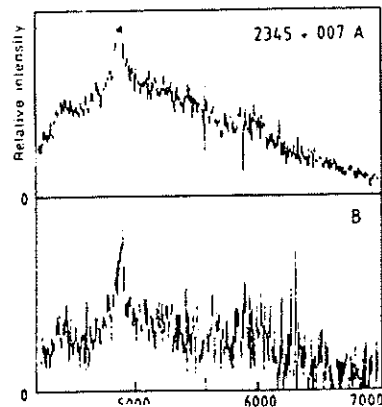
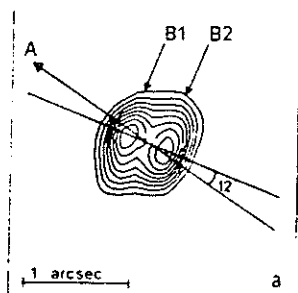
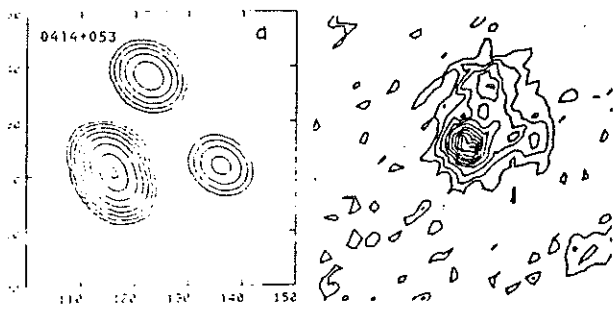
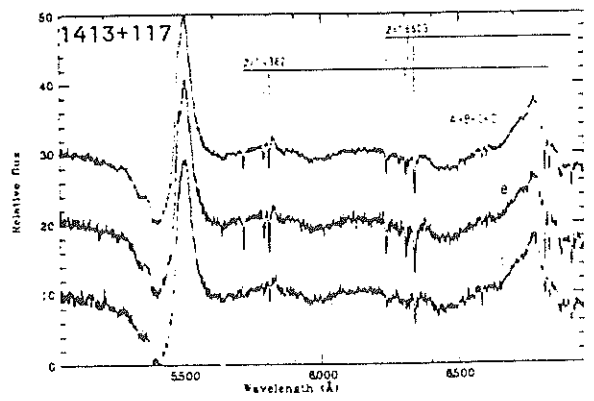
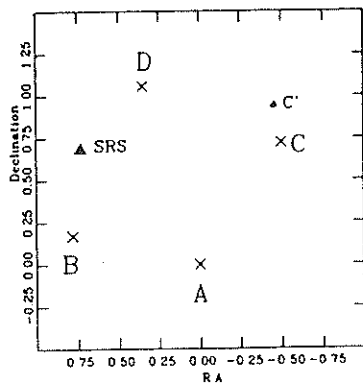
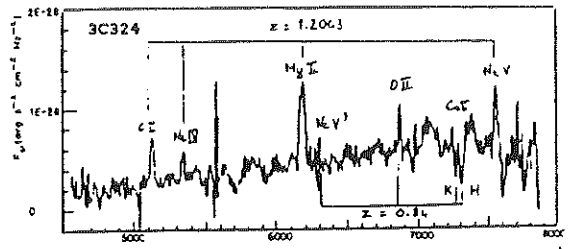
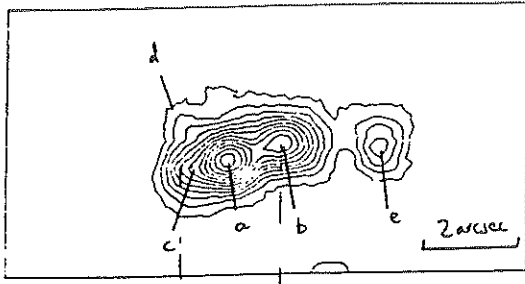
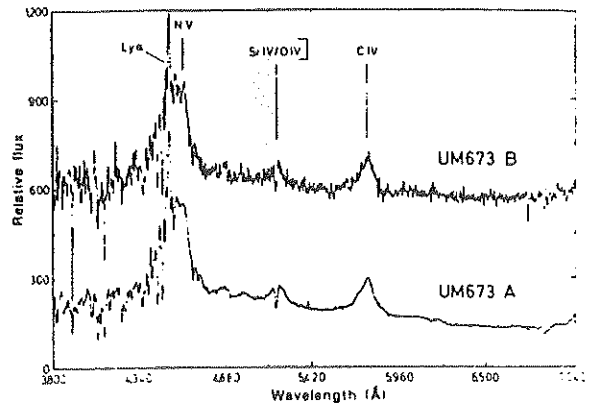
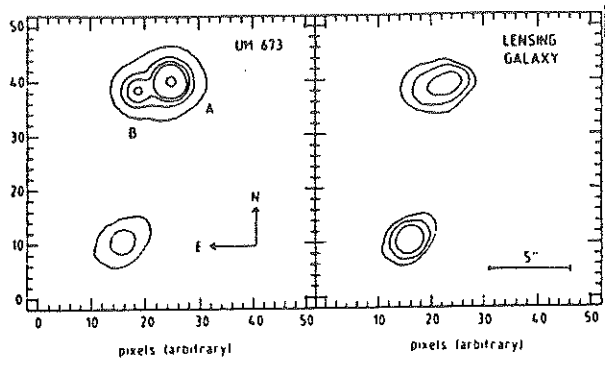
Gravitational lens candidates

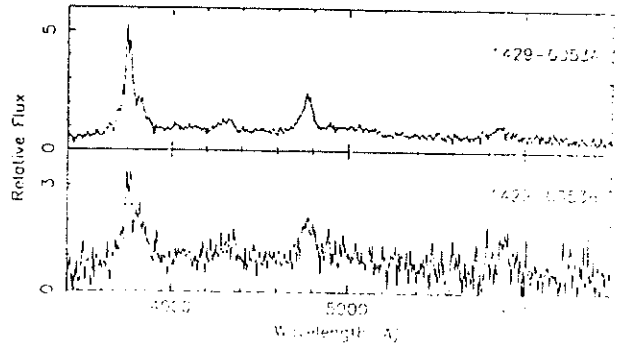
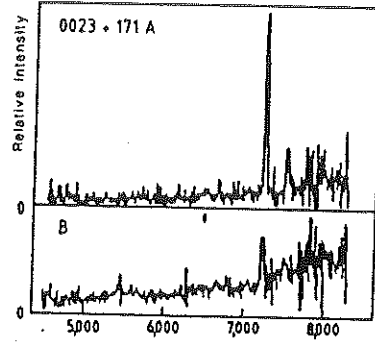
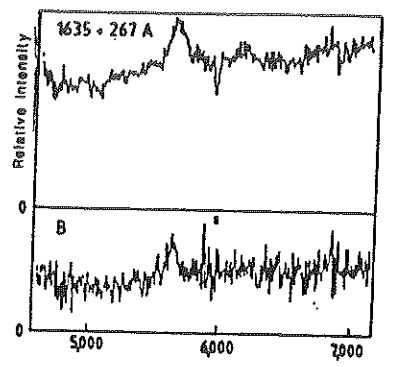
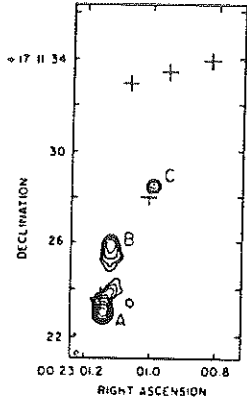
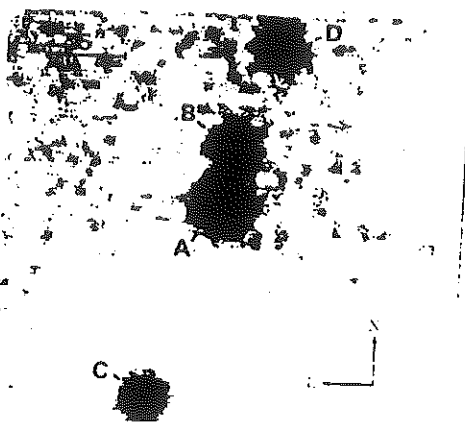
Source name (QSO/AGN)	Number of images	Image brightnesses/ Abs. Mag.	separation/ time delay	zs	Lens	Lens brightness	z1	M1(M0)/ (rad.)/ Mic.Lens	Detection (O/R)	Reference
<b>1. Presently accepted cases of multiply lensed source images</b>										
0957+561 A-B (QSO)	2	B=17.5 (A) 17.7 (B) M=-29.2	6.1" (A-B) (1.14 yrs)	1.41	G/C	R=18.5	0.36	8.7(11) (3.1") ML	O/R	Walsh et al., 1979
1115+080 A1/2-C (QSO)	4 (5?)	B=17.2 (A1) 17.2 (A2) 18.7 (B) 18.2 (C) M=-30.1	0.5" (A1-2) 1.8" (A-B) 2.3" (A-C) (dys, mnths)	1.72	G	R=19.8	?	? ML	0	Weymann et al., 1980
2016+112 A-C' (QSO)	3	i=22.9 (A) 23.2 (B) 24 (C') M=-25.6	3.4" (A-B) 3.8" (A-C') (0.5-1 yrs)	3.27	2Ga	i=21.9	1.01 ?	ML?	R/O	Lawrence et al., 1984
2237+030 A-D (QSO)	4	r=17.6 (A) 17.8 (B) 18.1 (C) 18.4 (D) M=-29.2	1.8" (A/B) 1.4" (A/C) 1.7" (A/D) (dys)	1.69	G	x=14.5	0.04	1.0(10) (0.9") ML	0	Huchra et al., 1985
0142-100 A-B (QSO)	2	B=17.0 (A) 19.1 (B) M=-30.2	2.2" (A-B) (7 weeks)	2.72	G	R=19	0.49	2.4(11) (2.2")	0	Surdej et al., 1987
3C324 A-B (AGN)	>2	R=22.7 (A) 23.3 (B)	2" (A-B)	1.206	G		0.84	1.0(12)	R/O	Le Fèvre et al., 1987
1413+117 A-D (QSO)	4	18.3 (A) 18.5 (B) 18.6 (C) 18.7 (D) M=-29.8	0.8" (A/B) 0.9" (A/C) 1.1" (A/D) (1 mnth)	2.55	G?	?	1.4? 1.7?	5.0(11) ML?	O/R	Hagain et al., 1988
0414+053 A-D (AGN?)	4	R=23 (A/D)	3" (A/D)	1.2?				1.0?	R/O	Hewitt et al., 1989
<b>2. Additional suspected cases of multiply lensed source images</b>										
2345+007 A-B1/2 (QSO)	3	B=19.5 (A) 22.0 (B1) 22.0 (B2) M=-27.3	7.3" (A-B) 0.4" (B1-2)	2.15	?	J>25.5		ML?	0	Weedman et al., 1982
1635+267 A-B (QSO)	2	19.2 (A) 20.8 (B) M=-28.1	3.8" (A-B)	1.96	G?	R=20	0.57?	1.0(12)?	0	Djorgovski and Spinrad, 1984
0023+171 AB-C (AGN)	2	r=22.8 (AB) 23.4 (C)	4.8" (AB-C)	0.95					R/O	Hewitt et al., 1987b
1429-008 A-B (QSO)	2	R=17.7 (A) 20.8 (B)	5.1" (A-B)	2.08	?		1.6?		0	Hewitt et al., 1989
1042+178 A-D (AGN)	4	21 (A/D)	1.6" (A-B)	0.92	?		0.5?		R/O	Hewitt et al., 1987a
1120+019 A-B (QSO)	2	V=16.2 (A) 20.8 (B) M=-29.1	6.5" (A-B)	1.46	G?/C?	R=22.5	0.6?		0	Heylan and Djorgovski, 1989
<b>3. Radio rings</b>										
1131+045 A-B	2+ ring	radio lobe	2.1" (ring diam.)	?	?	R=22			R/O?	Hewitt et al., 1988
1654+134	ring	radio lobe	2.1" (ring diam.)	1.74	G	r=18.7	0.25	9.5(10) (2.1")	R/O?	Langston et al., 1989
<b>4. Other proposed cases of multiply lensed and/or magnified source images</b>										
3C194, 3C225A										Le Fèvre and Hammer 1983
3C238, 3C241, 3C305.1										Le Fèvre, Hammer and Jones, 1988b
3C13, 3C256										Le Fèvre et al., 1988a
3C208.1										Le Fèvre and Hammer, 1989
<b>5. Multiply lensed QSO images with large separations (?)</b>										
M82 A-C (QSO)	3	V=20.5 (A) 20 (B) 20.5 (C)	216" (A/C)	2.04				?		Burbidge et al., 1980
<b>6. Twin galaxies imaged by string loops (?)</b>										
0249-186 A-D (AGN)	4X2		2.5" (A-A') 2.6" (B-B') 2.0" (C-C') 2.6" (D-D')	0.43 0.43 0.20 0.4	string?				0	Cowie and Hu, 1987
<b>7. Lensed gamma-ray bursters (?)</b>										
B1900+14 A-C (AGN?)	3		?	?	G?			1.0(10)		Paczynski, 1986

Explanations: G, Galaxy ML, Micro-lensing O, optical detection  
 C, Cluster rad., observed angular radius for R, radio detection  
 the estimated mass of the lens  
 See Surdej (1989, these proceedings) for the exact references.

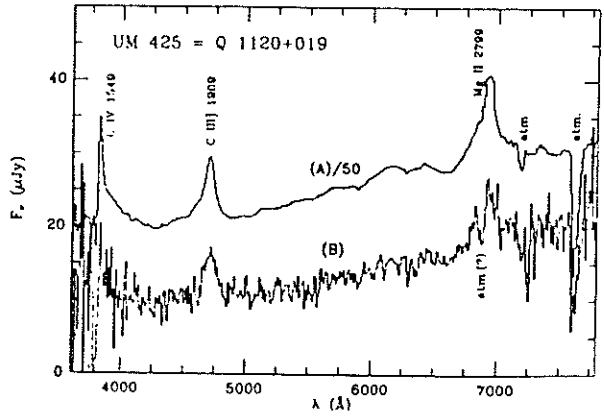
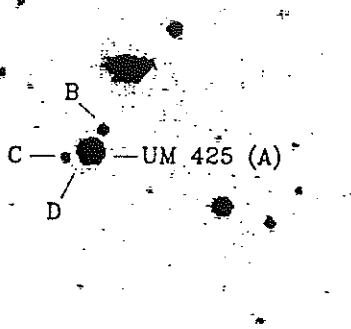
Figure 1: Identification fields and optical spectra of gravitational lens candidates







1042+178



6

## Article 15

### A NEW CASE OF GRAVITATIONAL LENSING

Surdej, J., Magain, P., Swings, J.-P., Borgeest, U., Courvoisier, T.J.-L., Kayser, R., Kellermann, K.I., Kühr, H., Refsdal, S.: Nature 329, 695-696.

Nous décrivons dans cet article la stratégie observationnelle systématique que nous avons utilisée à l'Observatoire Européen Austral (ESO, Chili) pour rechercher des mirages gravitationnels au sein d'un échantillon de quasars très lumineux ( $M_V \approx -29$ ). Nous présentons les premières observations résultant de la découverte d'un nouveau mirage gravitationnel pour le quasar UM673 ( $z = 2,719$ ). Ce mirage est formé de deux images quasi-stellaires A ( $m_R \approx 16,9$ ) et B ( $m_R \approx 19,1$ ), séparées par une distance angulaire de  $2,2''$ . Nous démontrons que la formation de ces deux images illusoires résulte de l'action d'une lentille gravitationnelle située entre la source et l'observateur, à un redshift  $z = 0,49$ . La modélisation de ce système conduit à la détermination d'une masse de  $2,4 \cdot 10^{11} M_\odot$  pour la galaxie défectrice et à l'estimation d'un décalage temporel  $\Delta t \approx 7$  semaines entre les moments de réception d'un même signal lumineux issu de la source suivant les deux trajectoires associées aux images A et B ( $H_0 = 75 \text{ km/sec/Mpc}$ ,  $q_0 = 0$ ).





## A new case of gravitational lensing

J. Surdej\*, P. Magain†, J.-P. Swings\*, U. Borgeest‡,  
 T. J.-L. Courvoisier§, R. Kayser‡, K. I. Kellermann||,  
 H. Kühr¶ & S. Refsdal‡

\* Institut d'Astrophysique, Université de Liège, Avenue de Cointe 5,  
 B-4200 Cointe-Ougrée, Belgium  
 † European Southern Observatory, Casilla 19001 Santiago 19, Chile  
 ‡ Hamburger Sternwarte, Gojenbergsweg 112,  
 D-2050 Hamburg 80, FRG  
 § ST-ECF, European Southern Observatory,  
 Karl-Schwarzschild Strasse 2, D-8046 Garching bei München, FRG  
 || National Radio Astronomy Observatory, Edgemont Road,  
 Charlottesville, Virginia 22903-2475, USA  
 ¶ Max-Planck-Institut für Astronomie, Königstuhl,  
 D-6900 Heidelberg 1, FRG

Even before the discovery of the first gravitational lens system<sup>1</sup> in 1979 (see ref. 2 for a recent review of the other published candidates), it was recognized that a statistical evaluation of the occurrence of gravitational lensing within a well-defined sample of quasars is important to understand better the quasar luminosity function and possibly the QSO phenomenon itself<sup>3</sup>, to test cosmological models<sup>4,5</sup> and to probe the luminous and dark matter distribution on various scales in the Universe<sup>4,6</sup>. A year ago, we began a systematic search from the European Southern Observatory (ESO) at La Silla, Chile, for gravitational lens systems in a selected sample of highly luminous quasars;  $M_V < -29.0$ . These objects are promising candidates for gravitationally lensed QSO images with arc-second and sub-arc-second separations (J.S. *et al.*, manuscript in preparation and refs 7 and 8). Since December 1986, we have identified four possible cases. Here we give a brief description of our first identified gravitational lens system UM673 = Q0142-100 = PHL3703<sup>9-11</sup>. It consists of two images, A ( $m_R = 16.9$ ) and B ( $m_R = 19.1$ ), separated by 2.2 arc s at a redshift  $z_q = 2.719$ . The lensing galaxy ( $m_R \approx 19$ ,  $Z_L \approx 0.49$ ) has also been found. It lies very near the line connecting the two QSO images,  $\sim 0.8$  arc s from the fainter one. Application of gravitational optometry to this system leads to a value  $M_0 \approx 2.4 \times 10^{11} M_\odot$  for the mass of the lensing galaxy and to  $\Delta t \approx 7$  weeks for the most likely travel-time difference between the two light paths to the QSO (assuming  $H_0 = 75 \text{ km s}^{-1} \text{ Mpc}^{-1}$ ,  $q_0 = 0$ ).

Our optical search for gravitationally lensed highly luminous quasars (HLQs) is being performed with a charge-coupled device (CCD) camera at the Cassegrain focus of the ESO/MPI (Max-Planck Institut) 2.2-m telescope. The selected HLQs are first observed through narrow-band filters chosen to isolate bright redshifted emission lines (Ly $\alpha$  or occasionally C III) as well as nearby continua in order to search for lensed QSO image candidates at moderate angular separations ( $\geq 1$  arc s). Taking advantage of the large dynamic range of the CCD detectors and of the excellent resolution of the 2.2-m telescope under optimal seeing conditions, we are able to resolve secondary images up to 4 magnitudes fainter than the primary one at angular separations near 1.1-1.3 arc s. We show in Fig. 1a the central part of a direct CCD frame obtained for UM673 on 6 December 1986 with the ESO faint object spectrograph and camera (EFOSC)<sup>12</sup> at the  $f/8$  Cassegrain focus of the ESO 3.6-m telescope. The CCD image was taken during a 2-min exposure through a Bessel R filter, and it clearly shows that UM673 is spatially resolved into two star-like images A ( $m_R = 16.9$ ) and B ( $m_R = 19.1$ ), separated by 2.2 arc s. The diffuse object labelled D in Fig. 1a is a galaxy in the field of the CCD.

Low dispersion spectra of UM673 A and B covering several spectral ranges from 3,660 to 10,000 Å were also taken with EFOSC at the beginning of December 1986. The B300 spectra recorded in the 3,800-7,040 Å wavelength interval at a resolution (FWHM) of  $\sim 13$  Å are reproduced in Fig. 2. Further description

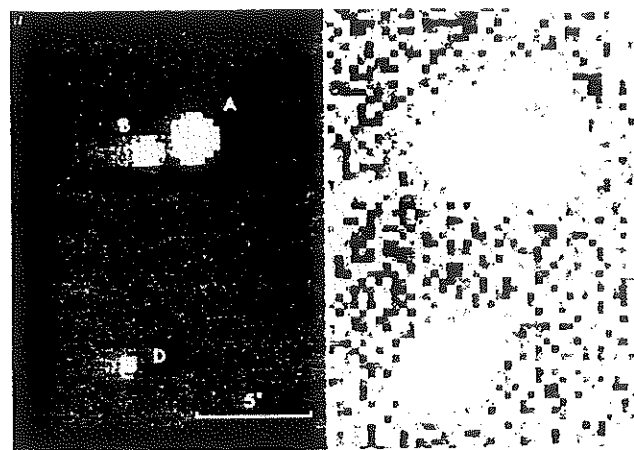


Fig. 1 a, The central part of a CCD frame of UM673 obtained with EFOSC in a 2 min exposure through a Bessel R filter on 6 December 1986. The highly luminous quasar is resolved into two quasi-stellar images A ( $m_R = 16.9$ ) and B ( $m_R = 19.1$ ) separated by 2.2 arc s. b, The result of subtracting the images of UM673 A and B from the original frame (a) after modelling their shapes with a double gaussian profile. The residual image is that of the lensing galaxy ( $m_R \approx 19$ ) at a redshift  $z_L \approx 0.49$ . Object D may be a member of an associated cluster of galaxies. On both these figures, the size of a single pixel is  $0.338''$ . North is up and East to the left. Courtesy of ESO.

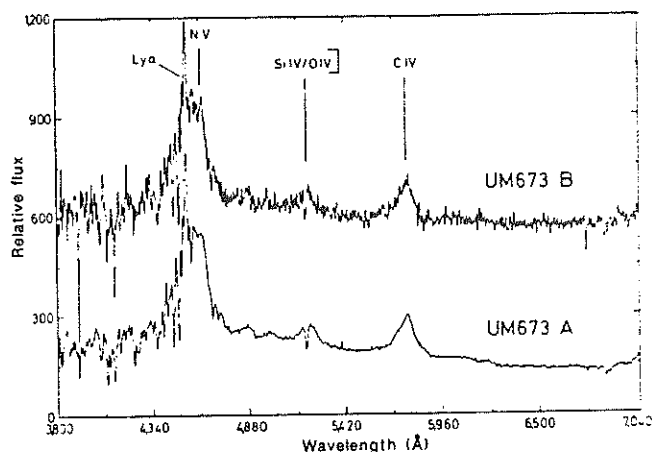


Fig. 2 The B300 low-dispersion spectra of UM673 A and B observed in December 1986 with EFOSC at the  $f/8$  Cassegrain focus of the ESO 3.6-m telescope. The spectrum of UM673 B has been multiplied by a factor 8.8 and offset by 400 units in ordinate. In this and the next figure, the ordinates refer to a relative flux scale and the abscissae correspond to wavelengths in angstroms.

of the instrumental setting and reduction and analysis of these and additional spectroscopic data will be published elsewhere. A careful comparison of the redshifts ( $z_q(A) = z_q(B) = 2.719 \pm 0.001$ ), derived from the Ly $\alpha$  + N V, Si IV/O IV] and C IV emission lines, as well as the perfect superposition achieved between the broad emission line (see the peculiar Ly $\alpha$  + N V blend) and narrow absorption line profiles in the spectra of UM673 A and B clearly establish an exceptional physical similarity between the two QSO images. It is therefore suggested that UM673 A and B are the gravitationally lensed images of a single distant quasar. This assertion is further supported by the result of a cross-correlation between the B300 spectra which leads to a velocity difference  $\Delta v = -24 \pm 109 \text{ km s}^{-1}$  between the QSO images A and B.

Furthermore, the spectrum of UM673 B presents a small but clear excess of continuum radiation at wavelengths  $\geq 5800$  Å.

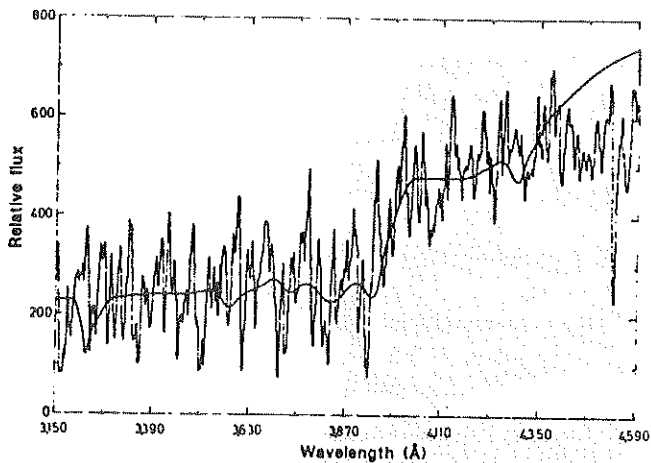


Fig. 3 The mean spectrum of brightest galaxies observed in distant galaxy clusters<sup>13</sup> is represented in this figure by the smooth line. It is a weighted superposition of 48 reasonably well-exposed spectra that have been cleaned and shifted to zero velocity. Note the prominent 4,000 Å break in this mean spectrum. The noisy spectrum is the subtraction of the B300(A) from the B300(B) spectrum after a flux normalization in the spectral range 3,800–5,700 Å and correction to zero redshift, assuming that this residual spectrum is that of the lensing galaxy at  $z_L = 0.49$ .

Assuming that the apparent reddening of UM673 B is caused by light contamination from an additional object, we extracted this excess of radiation as follows. We first multiplied the B300(B) spectrum by a constant factor so that the B300(B) and B300(A) spectra perfectly match each other in the wavelength range 3,800–5,700 Å. We then subtracted these two normalized spectra to obtain a residual spectrum that is well matched by the mean spectrum of brightest galaxies in distant clusters<sup>13</sup> at a redshift  $z = 0.49 \pm 0.01$  (see Fig. 3). We identify this residual spectrum as that of the gravitational lens producing the two observed QSO images.

A careful processing of the R CCD frame shown in Fig. 1a allowed us to detect the image of the suspected lensing galaxy. We show in Fig. 1b the result of subtracting the two QSO images from the original CCD frame (Fig. 1a) after modelling their shapes with a double gaussian profile. The heights of these profiles have been adequately scaled according to the QSO image brightnesses. We find that the centroid of the lensing galaxy is

located very close to the line joining the two QSO images, 0.8 arc s from the position of UM673 B. The integrated magnitude of this galaxy is measured to be approximately  $m_R = 19$ , a value comparable to what is predicted for an elliptical galaxy at a redshift  $z_g = 0.5$  (ref. 14).

Because we do not have yet any definite information on the exact orientation of the lensing galaxy, or on its immediate surroundings (whether there is an associated galaxy cluster, for example), we have used a simple model to estimate the mass  $M_0$  of the lensing galaxy (within the projected images) and the expected delay  $\Delta t$  between the travel times of the two lensed QSO images. Our calculations are based on a lens model made of a single galaxy that is axially symmetric with respect to the line of sight<sup>15</sup> and use the observed redshifts and positions of UM673 A and B, and of the deflector. For deceleration parameter  $q_0 = 0$ ,  $H_0 = 75 \text{ km s}^{-1} \text{ Mpc}^{-1}$ , and adopting a smooth mass distribution in the lensing galaxy, we find  $M_0 \approx 2.4 \times 10^{11} M_\odot$  and  $\Delta t \approx 7$  weeks. From an observational point of view, this predicted time delay appears ideal as it should be possible to measure it accurately within a single observing season. The challenge is great because it should allow, in principle, a determination of the galaxy mass  $M_0$  to be made independently of the value of Hubble's constant  $H_0$ <sup>16</sup>. UM673 also provides an excellent case of a gravitational lens for which it should be possible to model the lensing mass distribution in detail. This may then allow an independent determination of certain cosmological parameters.

We thank Marc Azzopardi, Valentina Zitelli and Hugo Schwarz for making available some of their observing time. J.S. is a Chercheur Qualifié au Fonds National de la Recherche Scientifique (Belgium), and T.J.-L.C. is affiliated to the Astrophysics Division of the Space Science Department of ESA.

Received 20 July; accepted 12 August 1987.

1. Walsh, D., Carswell, R. F. & Weymann, R. J. *Nature* 279, 381–384 (1979).
2. Canizares, C. R. in *IAU Symp. 124: Observational Cosmology* (eds Hewitt, A., Burbidge, G. & Fong, L. Z.) 729–744 (Reidel, Amsterdam, 1987).
3. Barnothy, J. M. & Barnothy, M. F. *Science* 162, 348–352 (1968).
4. Refsdal, S. *Mon. Not. R. astr. Soc.* 128, 307–310 (1964).
5. Refsdal, S. *Mon. Not. R. astr. Soc.* 132, 101–111 (1966).
6. Canizares, C. R. *Nature* 291, 620–624 (1981); erratum *Nature* 293, 490 (1981).
7. Turner, E. L., Ostriker, J. P. & Gott, J. R. III *Astrophys. J.* 284, 1–22 (1984).
8. Ostriker, J. P. & Vietri, M. *Astrophys. J.* 300, 68–76 (1986).
9. MacAlpine, G. M. & Feldman, F. R. *Astrophys. J.* 261, 412–421 (1982).
10. Berger, J. & Fringant, A.-M. *Astr. Astrophys. Suppl.* 61, 191–202 (1985).
11. Véron-Cetty, M.-P. & Véron, P. *European Southern Observatory Scient. Rep.* no. 5 (1987).
12. Dekker, H. & D'Odorico, S. *European Southern Observatory Operating Manual* no. 4 (1985).
13. West, R. M. & Kruszewski, A. *Irish astr. J.* 15, 25–35 (1981).
14. Coleman, G. D., Wu, C.-C. & Weedman, D. W. *Astrophys. J. Suppl. Ser.* 43, 393–416 (1980).
15. Borgeest, U. & Refsdal, S. *Astr. Astrophys.* 141, 318–322 (1984).
16. Borgeest, U. *Astrophys. J.* 309, 467–471 (1986).

## Article 16

### DISCOVERY OF A QUADRUPLY LENSED QUASAR: THE 'CLOVER LEAF' H1413+117

Magain, P., Surdej, J., Swings, J.-P., Borgeest, U., Kayser, R., Kühr, H., Refsdal, S., Remy, M.: Nature 334, 325-327.

Nous présentons dans cet article la découverte d'un second mirage gravitationnel au sein d'un échantillon de quasars très lumineux ( $M_V \leq -29$ ). Le nouveau mirage identifié pour le quasar H1413+117 est formé de quatre images quasi-stellaires, suggérant l'apparence d'un trèfle cosmique à quatre feuilles. H1413+117, avec un redshift  $z = 2,55$  et une magnitude apparente  $m_V \approx 17$ , constitue un des représentants les plus brillants de la classe des quasars de type BAL (Broad Absorption Line). Les quatre images illusoires de ce quasar sont séparées par des distances angulaires de l'ordre d'une seconde d'arc. Les spectres observés pour deux de ces quatre composantes révèlent des profils de raies de type P Cygni fort semblables pour les doublets de résonance de NV, SiIV, CIV et AlIII. Des raies étroites en absorption ( $z_a = 1,44$  et  $1,66$ ) sont détectées dans le spectre d'une seule de ces deux images. Ces raies sont très probablement formées dans des nuages de gaz associés avec la galaxie défectrice. Cette seconde découverte d'un mirage gravitationnel au sein d'un échantillon de quasars très lumineux atteste de l'efficacité de la méthode proposée pour identifier des systèmes d'images multiples ayant de faibles séparations angulaires.



## Discovery of a quadruply lensed quasar: the 'clover leaf' H1413+117

P. Magain\*, J. Surdej†, J.-P. Swings†, U. Borgeest‡, R. Kayser‡, H. Kühr§, S. Refsdal‡ & M. Remy||

\* European Southern Observatory, Karl-Schwarzschild Strasse 2, D-8046 Garching bei München, FRG  
 † Institut d'Astrophysique, Université de Liège, Avenue de Coïnte 5, B-4200 Coïnte-Ougrée, Belgium  
 ‡ Hamburger Sternwarte, Gojenbergsweg 112, D-2050 Hamburg 80, FRG  
 § Max-Planck-Institut für Astronomie, Königstuhl, D-6900 Heidelberg 1, FRG  
 || European Southern Observatory, Casilla 19001, Santiago 19, Chile

In November 1986 we began an optical search for examples of gravitational lensing in a sample of highly luminous quasars (HLQs,  $M_v < -29$ ), with the aims of improving our knowledge of the quasar luminosity function, studying the dark matter content of the Universe, and redetermining some important cosmological parameters. This survey has found one new case of lensing<sup>1,2</sup> and the general implications of the search have been summarized<sup>3</sup>. Here we report the discovery of a second gravitational lens system in the broad absorption line quasar H1413+117 (refs 4-6). Four images of comparable brightness are seen, separated by  $\sim 1$  arcsec. Spectra obtained of two of the images are identical apart from the presence of sharp absorption lines in one component, which are presumably due to gas clouds along the line of sight. The unique configuration of the images, together with the fairly rare occurrence of this type of quasar, makes it incontrovertible that this is a lensed system, not a cluster of quasars, and this second discovery made by imaging bright quasars establishes the power of the method for finding systems with small separations.

H1413+117, with a redshift of 2.55 and an apparent visual magnitude of 17, is one of the brightest members of the class of broad absorption line (BAL) quasars. The latter represent a few percent of the total number of quasars and display broad and deep absorptions on the short wavelength side of some of their emission lines<sup>7,8</sup>. The spectrum of H1413+117, which has already been studied in detail<sup>4-6</sup>, shows particularly smooth and deep lines of the P Cygni type. In addition, two narrow absorption line systems have been identified, at redshifts 1.66 and 2.07. These are attributed to intervening gas clouds, possibly associated with the lens(es).

Our images of H1413+117 were obtained with a charge-coupled device (CCD) camera at the Cassegrain focus of the ESO (European Southern Observatory)/MPI (Max Planck Institut) 2.2 m telescope at La Silla. A double density RCA CCD was used, each  $15 \mu\text{m}$  pixel corresponding to  $0.176$  arcsec on the sky. Good seeing conditions ( $0.8$  arcsec FWHM) allowed us to resolve the quasar image into four components (Fig. 1a). The positions and magnitudes of these four images were determined by simultaneously fitting double gaussian profiles, whose parameters had been determined from neighbouring stellar images. These are listed in Table 1, and Fig. 1b sketches the geometry of the system. Four CCD frames have been obtained and analysed in this way and give the same results within 2%, which is thus an estimate of the accuracy of our measurements. The mean separation between the images amounts to one arcsec, making this system the most compact case of gravitational lensing known so far.

Very good evidence that H1413+117 is gravitationally lensed comes from the peculiarity of its spectrum<sup>4-6</sup>, with broad absorptions reaching nearly zero residual intensity. If any of the four images were to correspond to another object, it is highly improbable that this object would have deep and broad absorption lines at exactly the same wavelengths. Thus, the light from such an object would fill in the absorptions, in contradiction with the observations.

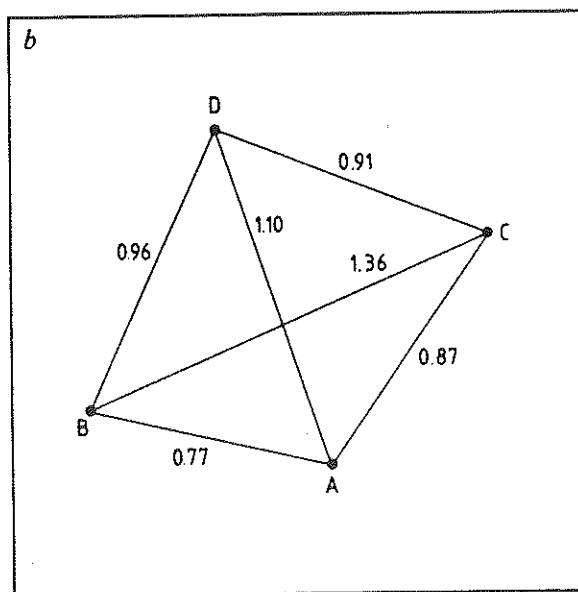
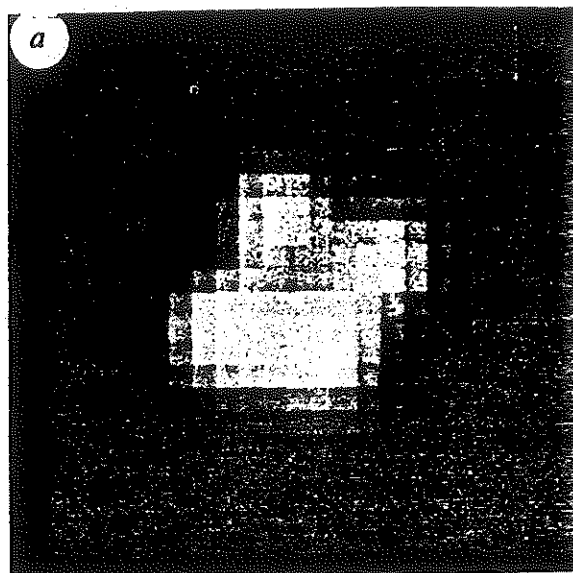


Fig. 1 a, The central part of a CCD frame of H1413+117 obtained with the ESO/MPI 2.2 m telescope through a Bessel R filter on 8 March 1988. b, Geometry of the system. Distances between components are indicated in seconds of arc. North is at the top and East to the left. Courtesy of ESO.

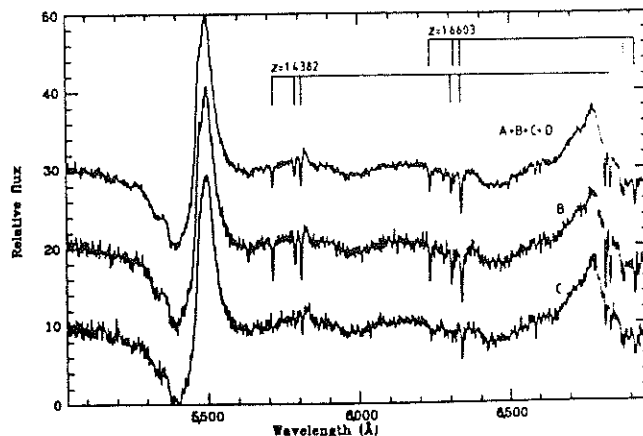


Fig. 2 Low dispersion spectra of components B and C, and of the whole system. The ordinate scale refers to the lower spectrum; the others are displaced vertically by 10 and 20 units. The two identified narrow absorption line systems are indicated.

Table 1 Geometry of the system

Component	$\Delta\alpha$	$\Delta\delta$	$\Delta m_R$
A	0.00	0.00	0.00
B	0.75	0.17	0.15
C	-0.50	0.71	0.30
D	0.35	1.04	0.40

— $\Delta\alpha, \Delta\delta$  = coordinates measured with respect to image A, in seconds of arc.  $\Delta m_R$  = magnitude difference with respect to image A, in filter R.

Further evidence for gravitational lensing is provided by our own spectra. These were obtained with the ESO faint object spectrograph and camera (EFOSC) (ref. 9) at the Cassegrain focus of the ESO 3.6-m telescope at La Silla. The instrument was rotated to roughly align the slit along the line joining the B and C images (position angle  $120^\circ$ ). The O150 grism<sup>9</sup> was used, giving a spectral resolution of  $\approx 7 \text{ \AA}$  in the range 5,000 to 7,000  $\text{\AA}$ . Three 30 min spectra were obtained and co-added. The mean seeing of 0.9 arcsec valued us to separate the spectra of the B and C components, although some contamination from A and D could not be avoided. These spectra are reproduced in Fig. 2 with the integrated spectrum (all four components). Within the limits of the accuracy of our data, the spectra of B and C are identical as far as the quasar features are concerned (continuum, emission and broad absorption lines), supporting the interpretation in terms of a gravitational lens. They are also identical to the whole integrated spectrum, indicating that components A and D probably also have the same spectrum. The emission line redshifts of B and C are identical at  $z = 2.551$ .

The only difference between the spectra of B and C lies in the narrow absorption lines, which are much stronger in the spectrum of B. The weak lines in the C spectrum may result from some contamination by the light of the other images. These absorption lines belong to two systems, at redshifts  $1.4382 \pm 0.0002$  (new) and  $1.6603 \pm 0.0003$ . The rather large redshift difference between these systems implies that the corresponding clouds are probably not associated.

Although the high degree of symmetry of this system would be easier to explain if the lensing object is located in between the four images, the presence of narrow absorption lines in the spectrum of the B image rather suggests that it lies in front of this component. But in the absence of any more detailed information on the lens, we have applied a simple model consisting

Table 2 Estimates of deflector mass and upper limit on time delay

Lens redshift	$M/10^{11} M_\odot$	$\Delta t_{\text{max}}$ (days)
0.50	1.0	15
1.00	2.5	50
1.44	4.8	120
1.66	6.8	170
2.07	15.3	350

of an axially symmetric galaxy lying on the optical axis, to which a very small asymmetric disturbance is added<sup>10,11</sup>. (Note that with such a transparent and non-singular lens, there should be a central fifth image, but it would be much too faint to be seen). The estimated mass  $M$  of the lensing galaxy is given in Table 2 as a function of the adopted redshift, including the redshifts of the known narrow absorption line systems. All data in this Table are computed assuming a value of  $75 \text{ km s}^{-1} \text{ Mpc}^{-1}$  for the Hubble constant  $H_0$  and a deceleration parameter  $q_0 = 0$ . The calculated masses are consistent with common estimates of galaxy masses. Rough upper limits  $\Delta t_{\text{max}}$  on the delay between the travel times of two opposite images are also listed in Table 2. More probable values are at least a factor of two smaller.

The expected time delays are short enough to be measured in one observing season. But, particularly for small lens redshifts, they may be even shorter than the variability timescale of the quasar itself, in which case they would be difficult to determine at all. On the other hand, such short time delays present the advantage that micro-lensing variability would be easier to distinguish from intrinsic variability. As there are four images close to the centre of the (hypothetical) lens galaxy, we expect the total probability for micro-lensing to be higher in this system than in any of the other known cases of gravitational lensing.

Received 25 April; accepted 10 June 1988.

1. Surdej, J. *et al. Nature* **329**, 695-696 (1987).
2. Surdej, J. *et al. Astr. Astrophys.* **198**, 49-60 (1988).
3. Surdej, J. *et al. Publ. Astron. Soc. Pac. Suppl., ESO Preprint no. 571* (Proc. NOAO Workshop on Optical Surveys for Quasars, in the press).
4. Hazard, C., Morton, D. C., Terlevich, R. & McMahon, R. *Astrophys. J.* **282**, 33-52 (1984).
5. Drew, J. E. & Boksenberg, A. *Mon. Not. R. astr. Soc.* **211**, 813-831 (1984).
6. Turnshek, D. A., Foltz, C. B., Grillmair, C. J. & Weymann, R. J. *Astrophys. J.* **325**, 651-670 (1988).
7. Weymann, R. J., Carswell, R. F. & Smith, G. A. *Rev. Astr. Astrophys.* **19**, 41-76 (1981).
8. Surdej, J. & Hutsemékers, D. *Astr. Astrophys.* **177**, 42-50 (1987).
9. Dekker, H. & D'Odorico, S. *European Southern Observatory Operating Manual no. 4* (1985).
10. Refsdal, S. *Mon. Not. R. astr. Soc.* **132**, 101-111 (1966).
11. Borgeest, U. & Refsdal, S. *Astr. Astrophys.* **141**, 318-332 (1984).

Article 17

NEW OBSERVATIONS AND GRAVITATIONAL LENS MODELS OF THE CLOVER LEAF  
QUASAR H1413+117

Kayser, R., Surdej, J., Condon, J.J., Kellermann, K.I., Magain, P.,  
Remy, M., Smette, A.: 1990, *Astrophys. J.*, sous presse.

Fort heureusement, le mirage gravitationnel identifié pour le quasar de type BAL H1413+117 est apparu suffisamment brillant dans le domaine radio pour pouvoir être détecté à 3,6cm et même être résolu en de multiples composantes au moyen du réseau géant de radiotélescopes (VLA) de l'Observatoire du NRAO (Nouveau-Mexique). Nous décrivons dans le présent article ces données radio ainsi que de nouveaux clichés électroniques obtenus dans le domaine visible pour le *Trèfle à quatre feuilles*. Ces dernières données ont été enregistrées au moyen d'une caméra CCD installée au foyer Cassegrain du télescope danois de 1,54m à l'Observatoire Européen Austral (ESO, Chili). Nous présentons un modèle simple de lentille gravitationnelle qui rend parfaitement compte des positions radio et optiques observées pour les quatre images illusoire de H1413+117. Ce modèle prédit des délais temporels extrêmement courts entre les moments d'arrivée d'un même signal lumineux pour les différentes images. Des arguments théoriques et observationnels (variabilité photométrique) suggèrent que l'image la plus faible (image D) de ce mirage gravitationnel est sujette à des effets de micro-lentille.





---

NEW OBSERVATIONS<sup>6</sup>  
AND GRAVITATIONAL LENS MODELS  
OF THE *CLOVER LEAF* QUASAR H1413+117

R.Kayser<sup>1</sup>, J.Surdej<sup>2,7</sup>, J.J.Condon<sup>3</sup>,  
K.I.Kellermann<sup>3</sup>, P.Magain<sup>2</sup>, M.Remy<sup>4</sup> and A.Smette<sup>5</sup>

<sup>1</sup> CITA, Toronto, Ontario, Canada

<sup>2</sup> Institut d'Astrophysique, Cointe-Ougrée, Belgium

<sup>3</sup> NRAO, Charlottesville, Virginia, U.S.A.

<sup>4</sup> ESO, La Silla, Chile

<sup>5</sup> ESO, Garching, F.R. Germany

<sup>6</sup> collected at the European Southern Observatory, LaSilla, Chile  
and at the National Radio Astronomy Observatory, Socorro, New Mexico

<sup>7</sup> also, Chercheur Qualifié au Fonds  
National de la Recherche Scientifique (Belgium)

1990

*Astrophysical Journal*

original version submitted August 8, 1989, received August 14, 1989

revised version submitted March 27, 1990

---

## Abstract

New optical and radio observations of the quadruple quasar H1413+117, the *Clover Leaf*, carried out with the 1.54m Danish telescope at ESO and with the VLA at NRAO are presented. The VLA data, obtained in the A configuration at 3.6cm, show radio counterparts at the positions of the four optical images and an additional strong radio source between images B and D. Gravitational lens models of H1413+117 using a) a single elliptical galaxy and b) two spherical galaxies are presented, which fit the positions of the four images of the quasar remarkably well. The models suggest that the strong radio source is a feature of the quasar, e.g. an ejected blob, which lies right on the caustic of the lens and is thereby strongly amplified. The time delays predicted by our models are sufficiently short to allow for their determination within one observational season, making H1413+117 an exceptionally well suited object for gravitational lens research.

Keywords: gravitational lenses — quasars: highly luminous — quasars: H1413+117

## 1 Introduction

The discovery of the first gravitationally lensed quasar 0957+561 (Walsh, Carswell and Weymann 1979), more than forty years after Zwicky's (1937 a,b) proposal that multiple images of distant objects lensed by foreground galaxies should be detectable, led to an outburst of theoretical as well as observational work on gravitational lensing (for recent reviews see, e.g., Blandford and Kochanek (1987); Nottale (1988); Refsdal and Kayser (1988); Turner (1989); Hewitt (1989)). Lensed quasars and galaxies (giant arcs) obviously probe the distribution of luminous and dark matter in the Universe and can be used to determine independently the masses of galaxies and clusters of

galaxies (Refsdal 1964; Borgeest 1986). The time delay between the images of a lensed quasar (or between the images of a supernova in lensed galaxies) may be used to determine the Hubble parameter without climbing up the cosmological distance ladder (Refsdal 1964; Kayser and Refsdal 1983; Kayser 1986; Gorenstein, Falco and Shapiro 1988). Gravitational micro-lensing may offer a possibility to learn about the size and the structure of the energy source of active galactic nuclei, as well as about the mass spectrum of compact objects in the lensing galaxy (Gott 1981; Canizares 1981, 1982; Grieger, Kayser and Refsdal 1988).

Another very important aspect of gravitational lensing is the *amplification bias*: lensing may influence the quasar luminosity function (see, e.g., Turner (1988) for a review) a) globally, thereby mimicking evolution, and b) locally near foreground galaxies, thereby producing apparent quasar-galaxy-associations (Webster *et al.* 1988; Schneider 1988; and references therein).

To better understand the quasar luminosity function (and thereby we hope the quasar phenomenon itself), we obviously need to understand the influence of lensing on it, thus the statistical evaluation of gravitational lensing within well-defined samples of quasars is of great importance. Several surveys for lensed objects are under way (Hewitt *et al.* 1989; Surdej *et al.* 1988b; Webster, Hewett and Irwin 1988; Crampton *et al.* 1989), using different selection criteria and methods, in order to perform this ambitious task.

In November 1986, we began an optical survey for lensed objects among the apparently ( $m_v < 17.5$ ) and intrinsically ( $M_v < -29.0$ ) highly luminous quasars (hereafter HLQs). These objects form a particularly promising sample since a) the probability of lensing is higher in a flux-limited sample than in a volume-limited one (Turner *et al.* 1984), b) the HLQs are the most likely objects for which the "intrinsic" brightness may in part be due to lensing, and c) the large cosmological distances of the HLQs imply a higher probability for galaxies to be located along their line-of-sights.

Our project has led to the discovery of two new lens systems, UM673 = Q0142-100 (Surdej *et al.* 1987; Surdej *et al.* 1988a) and H1413+117 (Magain *et al.* 1988) as well as several promising candidates (Surdej *et al.* 1988b).

H1413+117 ( $z_q = 2.55$ ,  $m_v = 17$ ) is one of the brightest members of the class of broad absorption line (BAL) quasars. The spectrum of H1413+117 shows two narrow absorption systems at redshifts 1.66 and 2.07 (Hazard *et al.* 1984; Drew and Boksenberg 1984; Turnshek *et al.* 1988). Under good seeing conditions (0.8 arcsec FWHM), we have been able to resolve H1413+117 into a *Clover Leaf* with four components having comparable brightness, separated by  $\approx 1$  arcsec (Magain *et al.* 1988). We have shown that the spectra of two of the images are identical (apart from sharp absorption line systems at  $z = 1.44$  and  $z = 1.66$ , which are much stronger in component B (Magain *et al.* 1988)), thereby supporting the hypothesis that H1413+117 is one quasar

quadruply imaged by a foreground gravitational lens.

In this paper, we present new optical and radio observations of the *Clover Leaf* H1413+117, as well as gravitational lens models accounting for the new observed properties of this exceptional object.

## 2 New Observations

### 2.1 Optical

New images of H1413+117 were obtained (by P.M. and M.R.) on April 27, 1988 with the Danish 1.54m telescope at ESO, LaSilla. In particular, B and I images were obtained under a seeing of 1.0 arcsec and 0.8 arcsec, respectively. The positions and brightness ratios, relative to image A are listed in table 1. Contamination of the red images by a foreground galaxy may introduce errors in the derived positions and brightness ratios.

In the case of image D, the R magnitude obtained on April 27 is found to be significantly fainter than the one which was obtained on April 8 (published in Magain *et al.* (1988)). Image D has clearly faded between the two observations.

We have also made use of an average seeing (FWHM=1.7"), 20 min R CCD exposure of H1413+117 obtained (by P.M.) with the ESO/MPI 2.2m telescope (pixel size = 0.35") on April 29, 1987 in order to detect and catalogue all objects located in the vicinity of the *Clover Leaf*. Taking as a

reference the brightest lensed image A, the relative positions, type (star or galaxy) and integrated R magnitude of the 59 detected objects are listed in Table 2. The R brightness of image A has been assumed to equal 18.30 . Without taking into account the error on  $m_R(A)$  , the  $m_R$  are precise at about  $\pm 0.15$  magnitudes. Figure 1 illustrates the location of the objects on the CCD frame. The objects have been selected using the following criteria: 1) they are at most 5.75 mag fainter than image A, i.e. 3 sigma above the background, 2) the FWHM of a fitted gaussian profile is at least 1.4 arcsec in order to discriminate real objects from cosmic rays and small scale spatial variations of the sky background. Objects with FWHM greater than 2.1 arcsec or at most 5 mag fainter than image A have been listed as galaxies.

## 2.2 Radio

Radio observations of the *Clover Leaf* have been obtained with the Very Large Array (VLA) of the National Radio Astronomy Observatory (NRAO, Socorro, New Mexico) on both January 13 (J.S. and K.I.K.) and February 4 (J.J.C.), 1989 ,using the A-array configuration. During these two independent runs, we observed for 90 min at 8.415 GHz (3.6cm) with a bandwidth of 100 MHz in each of the two circular polarizations. The source 1413+135 at B1950 position  $\alpha = 14\text{h } 13\text{m } 33.91\text{s}$ ,  $\delta = 13^\circ 34' 17.4''$  was observed as a phase calibrator. The two sets were edited and calibrated, and the visibility data were combined, Fourier transformed with natural weighting, CLEANed, and

restored with an 0.3 arcsec FWHM Gaussian beam using the AIPS reduction package. The r.m.s. noise on the natural weighted image made from combined data is 0.012 mJy. This image is shown in Fig. 2. As can be seen, H1413+117 appears to be fully resolved at radio wavelengths. The shape of the radio structure is quite similar to that of the optical *Clover Leaf* pattern, except for the presence of a relatively bright radio component (peak flux density of 0.195 mJy/beam) centered near  $\alpha = 14^{\text{h}} 13^{\text{m}} 20.1^{\text{s}}$ ,  $\delta = 11^{\circ} 43' 38''$ . This mysterious strong radio source will be referred hereafter as to the SRS component. The peak flux densities of the radio components A, B, and C' are 0.088, 0.171, and 0.081 mJy/beam, respectively.

### 2.3 Comparison of optical and radio data

In order to best adjust the overlap between the optical and radio images of the *Clover Leaf* (see Figure 3), we have first made an attempt to identify the possible radio counterparts of the 59 optically selected objects listed in Table 2. Unfortunately, apart from H1413+117 itself, none of these objects were detected on the VLA image. Since the VLA radio position of the *Clover Leaf* is accurate to better than 0.1", the best we could do to match the radio and optical positions consisted in performing accurate astrometric measurements of the integrated image of H1413+117 on the basis of an ESO Schmidt plate kindly taken for us by O. Pizarro. After various careful measurements by one of us (A.S.), the optical centroid of H1413+117 was derived to be  $\alpha$

$= 14^{\text{h}}13^{\text{m}}20.11^{\text{s}} \pm 0.04^{\text{s}}$ ,  $\delta = 11^{\circ}43'37.8'' \pm 0.4''$  for the 1950.0 equinox, which is in good agreement with the position given by Hazard *et al.* (1984). This measured position actually coincides with the southern-most part of the SRS feature seen on the VLA map (cf. the large triangle marked in Fig. 3). However, the best visual overlap that we could achieve between the radio and optical images of H1413+117 leads to a very slightly different position for the optical centroid (see Fig. 3). The difference between this and the previous optical position amounts to approximately  $0.6''$ , i.e. only 1.5 times the formal uncertainties of our astrometric measurements. Of course, this match between the optical and radio images of H1413+117 needs to be further checked on the basis of a higher sensitivity map to be obtained with the VLA. Further comparison between the optical and radio data of H1413+117 (cf. Figs. 2 and 3) indicates that images A, B and D coincide quite nicely between each other but that the optical image C is not very well matched in position by its relatively stronger radio counterpart C' (cf. the small triangle in Fig. 3) In addition, it seems that a weak extended radio source (WERS) connects the two radio images A and B. In the remainder, we show how a qualitative modeling of the *Clover Leaf* images may account for most of the above described features.



## 3 Gravitational Lens Models

### 3.1 Method

An advanced software package, named *GRAL*, for the modeling of gravitational lenses has been developed (by R.K.) over the past few years.

Within the usual limits (weak gravitational fields, small deflection angles), gravitational lensing can be described as a mapping from the image plane  $(\theta_x, \theta_y)$  to the source plane  $(\theta'_x, \theta'_y)$  or, alternatively, from the deflector plane  $(x, y)$  to the source plane  $(\xi, \eta)$  by the lens equation

$$\vec{\theta}' = \vec{\theta} + \frac{D_{ds}}{D_s} \vec{\alpha}(\vec{\theta}) \quad (1)$$

$$\vec{\zeta} = \frac{D_s}{D_d} \vec{z} + D_{ds} \vec{\alpha} \quad (2)$$

where  $\vec{\theta}' = (\theta'_x, \theta'_y)$ ,  $\vec{\theta} = (\theta_x, \theta_y)$ ,  $\vec{\zeta} = (\xi, \eta)$ ,  $\vec{z} = (x, y)$ ,  $\vec{\alpha} = (\alpha_x, \alpha_y)$  is the (two-dimensional) deflection angle and  $D_d$ ,  $D_s$  and  $D_{ds}$  are apparent size distances.

Usually the modeling of gravitational lenses is done by constructing a deflector model, searching for the images produced by this model and comparing the positions of these images to the observed ones. The model parameters are then changed in order to minimize the difference between observed and constructed image positions. This method, however, is pretty costly, since the images have to be found for each set of model parameters, which is very CPU-time consuming, even if the SDF-method (Schramm and Kayser 1987)

is used. *GRAL* therefore uses a different approach (Kayser 1990).

Obviously for each image  $i$ , found at  $\vec{\theta}_i$ , of one and the same source  $s$  the lens equation must lead to the same result:

$$\vec{\theta}_s = \vec{\theta}^i(\vec{\theta}_i) = \vec{\theta}^j(\vec{\theta}_j) \quad \forall i, j \quad . \quad (3)$$

Thus we simply trace *one* light ray back at each image position and compare the resulting source positions by computing the squared deviation

$$\Delta^2 = \sum_{i \neq j} |\vec{\theta}^i(\vec{\theta}_i) - \vec{\theta}^j(\vec{\theta}_j)|^2 \quad . \quad (4)$$

We then vary the model parameters (using a numerical evolution process) in order to minimize  $\Delta$ .

Some care has to be taken to choose appropriate initial values for the procedure, since the model parameter space may well have more than one local minimum of  $\Delta$ . By applying additional conditions, like limitations on the lens position(s) or the exclusion of the creation of additional bright images, certain parts of the parameter space can be excluded.

In contrast to other authors we make no attempt to fit the brightness ratios of the images. The brightness of the images is subject to changes due to intrinsic and microlensing-induced variability, thus values obtained at one epoch are useless for modelling. If eventually the time delay between the images is determined, and micro-lensing can be separated from intrinsic variability, the true brightness ratios may enter model calculations as parameters.

If a sufficient model has been found, the image configuration is constructed by means of the SDF-method (Schramm and Kayser 1987, see also Kayser and Schramm 1988). We then calculate the time delays and the local lensing parameters (convergence, shear, amplification) for the images.

For our models we have used the positions listed in Table 3, which are mainly based on our B observations in order to keep as small as possible errors due to reddening caused by an intervening galaxy. We have used a redshift of 1.44 for the deflector, which is a somewhat arbitrary choice given the set of observed absorption systems. However, our aim is mainly to show that the Clover Leaf *can* be produced by simple gravitational lenses, and this conclusion does not depend on the adopted redshift.

We have used  $H_0 = 75 \frac{\text{km/s}}{\text{Mpc}}$  throughout this paper, as well as a standard Friedmann cosmology with  $\Lambda = 0$  and  $q_0 = 1/2$ .

### 3.2 Models for the optical *Clover Leaf*

Two different models have been used to fit the positions of the four optical images, a) a single elliptical singular isothermal galaxy and b) two spherical singular isothermal galaxies with equal masses. The projected surface density  $\Sigma$  for singular isothermal galaxies is

$$\Sigma = \Sigma_0 x^{-1} \quad , \quad (5)$$

where  $x$  is either the radius  $r$  (for spherical galaxies) or the major half axis  $a$  (for elliptical galaxies).

The one-dimensional central velocity dispersion  $\sigma_v$  is then given by

$$\sigma_v^2 = 2 G \Sigma_0 \quad , \quad (6)$$

where  $G$  is the gravitational constant. As discussed by Kent and Falco (1988), flattening reduces  $\sigma_v^2$  by a factor of  $(\sqrt{1 - e_0^2} \arcsin e_0)/e_0$ , where  $e_0$  is the true (edge-on) eccentricity. Since only the eccentricity of the projected surface density is used in the lens models, we can only set an upper limit on  $\sigma_v$ .

The elliptical galaxies have been computed using the algorithm of Schramm (1988,1990), which is much easier to use than the somewhat cumbersome algorithm of Bourassa and Kantowski (1975).

We have six observables to fit (i.e. three independent relative image positions), and in both models five free parameters to adjust. Thus the models are *over-constrained*: We find no exact solutions (with zero residual) but one pronounced minimum of the residual with acceptable errors in the image positions.

The results of the simulations are presented in Tables 4 and 5 (model parameters for the best fits, note that *all* parameters have been adjusted simultaneously, none has been fixed during the modeling process), and in Figures 4 and 5 (image and source plane plots, including critical curves and caustics). As can be seen from the figures, both models fit equally well the

optical *Clover Leaf* observations. Model #2, however, produces an additional weak image between the centres of the two galaxies.

These models are best fits for the observed image positions as given in Tab.3. Errors in the resulting model parameters due to errors in these image positions have been estimated by varying the image positions. An error in the image positions of 0.01" (0.1") leads to errors of the order of 0.004" (0.08") in the x-position and 0.01" (0.1") in the y-position of the deflector galaxy,  $4 \times 10^5$  ( $3 \times 10^4$ )  $M_{\odot}/\text{pc}$  in the density parameter  $\Sigma_0$ , 0.004 (0.4) in the eccentricity and  $1^{\circ}$  ( $20^{\circ}$ ) in the position angle. This results should, however, not be over-interpreted: Our models are just examples to demonstrate that plausible models are possible for this object.

In Table 6, we present the expected time delays between the images in our models. Due to the symmetry of the configuration, the time delays are fairly small, it thus should be possible to measure them within one observing season (if H1413+117 shows sufficient intrinsic variability). As can be seen, the time delays are strongly model dependent, thus the time delays, if eventually determined, can be used to rule out certain models.

From the macro-models we can calculate the *local* lensing parameters (compare Kayser 1990) at each image, i.e. the convergence  $\kappa$  and the shear  $\gamma'$ , as well as the amplification

$$A_G = |(1 - \kappa - \gamma')(1 - \kappa + \gamma')|^{-1} \quad (7)$$

for the smooth deflector (Table 7). The parameters  $\kappa$  and  $\gamma'$  are important for the prediction of micro-lensing effects. Note that  $\kappa$  equals the total surface mass density  $\sigma_t$  in units of the critical density

$$\sigma_{crit} = \frac{1}{\pi} \frac{c^2}{4G} \frac{D_s}{D_{d_s} D_d} \quad , \quad (8)$$

which would lead to a complete focusing of a bundle of light rays (in the absence of shear). For H1413+117 the critical density is  $\sigma_{crit} = 6050 M_{\odot}/\text{pc}^2$ .

In both models, the brightness ratios of the images turn out to be quite different from the observed ones. This may, however, be explained by intrinsic variability and/or micro-lensing.

If we assume that H1413+117 shows *no* intrinsic variability, we can compare the observed brightness ratios with the ones predicted by our models under the assumption that the differences are due to micro-lensing. In Table 8, we list the predicted micro-lensing amplifications computed under these assumptions. We have here used the B magnitudes, since they are less subject to reddening than the I or R magnitudes. Note that the micro-lensing amplifications can only be predicted up to a constant factor, since the true source luminosity is not known. We have normalized the amplification such that the minimum amplification is 1.

Interestingly, in model #1 two of the four images, B and C, do not need any micro-lensing influence. In this model, image D is expected to show the largest micro-lensing amplification. The observed fading of image D within

the 19 days between our observations, may thus correspond to the second part of a high amplification event due to the crossing of a micro-caustic (Kayser, Refsdal and Stabell 1986; Grieger, Kayser and Refsdal 1988).

For each macro-image, the possible micro-lensing parameters  $\sigma$  (normalized number densities of micro-lenses) and  $\gamma$  (normalized shear), as introduced by Paczynski (1986) and Kayser, Refsdal and Stabell (1986), lie on the straight line

$$\sigma = 1 + \frac{\sigma_t - 1}{\gamma'} \gamma \quad (9)$$

in the  $\sigma$ - $\gamma$ -plane, compare Kayser and Refsdal (1989) and Kayser (1990), where  $\sigma_t$  is the total (projected) surface density, in units of the critical density  $\sigma_{crit}$ , see Eq.(8). Since the sign of  $\gamma'$  and  $\gamma$ , respectively, depends on the chosen coordinate system, we can restrict ourselves to  $\gamma \geq 0$  without loss of generality. Note that  $\text{sign}(\gamma) = \text{sign}(\gamma')$  for  $\sigma_c < 1$ , and  $\text{sign}(\gamma) = -\text{sign}(\gamma')$  for  $\sigma_c > 1$  ("over-focusing"), where  $\sigma_c$  is the surface density of the homogeneously distributed matter in units of  $\sigma_{crit}$ .

Since the fraction  $\epsilon$  of matter contained in stars is obviously limited by  $0 \leq \epsilon \leq 1$ , we find that a) for  $\sigma_t < 1$ , only scenarios with  $0 < \sigma < \sigma_t$  are allowed, and b) for  $\sigma_t > 1$ , only scenarios with either  $\sigma > \sigma_t$  or  $\sigma < 0$  (over-focusing) are allowed. In Fig. 6, we show the allowed parameter combinations  $(\sigma, \gamma)$  for the images of H1413+117 in our models. Again, image D in model #1 is expected to show the strongest influence due to micro-lensing.

### 3.3 The strong radio source

From our models we see that SRS lies right on the critical curve of the deflector. This is a very generic feature, since every possible lens model for H1413+117 *must* lead to a critical curve between each two of the images. Thus, SRS can be explained by an additional radio feature, e.g. an ejected blob, of the quasar, located on the lens caustic and thereby being strongly amplified. We have tried to reproduce the radio contour map by adding a second circular source to the quasar core. The location of this source is found by tracing SRS back to the source plane in the used model. The linear separation between the QSO and SRS is 1085 pc (corresponding to 0.21") in model #1 and 780 pc (0.15") in model #2, respectively.

Figures 7 and 8 show the results of these simulations. In both models, SRS can be reproduced nicely. Additional images are created near A and C in both models. The additional radio image near C may possibly explain the observed misplacement of C' relative to C.

In model #1, the second additional radio image lays right between A and B, thereby offering an explanation for WERS. Since WERS, like SRS, lays near or on the critical curve, another possibility to explain WERS is a jet crossing the caustic of the lens, thereby becoming strongly amplified only in a small region. The quality of our present data is, however, not sufficient to allow for a more detailed modelling of the extended structure of the radio



source.

## 4 Discussion and Outlook

Both of our adopted models fit remarkably well the optical *Clover Leaf* observations, as well as the radio structure of H1413+117 including SRS, thereby supporting the hypothesis that H1413+117 is indeed a gravitationally lensed quasar.

However, since both models are quite different, our simulations show also that at this stage, we are far from obtaining one unique model for the object. More and better observational data are needed in order to produce a larger set of parameters to be fitted, thereby reducing the allowed range of parameter space.

Especially a better VLA-map would be very useful, since this would offer the possibility of a more accurate modelling of the extended radio source by means of the combined DiSI/DiSoR-method proposed by Kayser and Schramm (1988). Note that a very similar method has later been used by Kochanek *et al.* (1989) for the successful modelling of the *Einstein Ring* MG1131+0456.

Monitoring of the *Clover Leaf* should also have high priority, since the time delays are very sensitive to the model. Besides, the measurement of the time delays is the only *real* proof of the lens scenario (see Narasimha and

Narlikar (1989) for an alternative explanation of multiple quasars).

The time delays predicted from our models are sufficiently short to allow a determination within one observational season, making H1413+117 an exceptionally well suited object for gravitational lens research. Micro-lensing may, however, make it difficult to separate the intrinsic variability from the observed light curves. On the other hand, since the expected time delays are short, it should be easy to proof whether observed variability is due to micro-lensing or not.

**Acknowledgements.** It is a pleasure to thank Thomas Schramm (Hamburg) for the implementation of the elliptical deflector code into the *GRAL* package. R.K. acknowledges support by a NATO research scholarship, granted by the German Academic Exchange Service (DAAD). J.S. acknowledges partial support during this research from NATO grant No. 0161/87. A.S. thanks Eric Gosset and the  $\Phi.V.$  for a lot of support. The National Radio Astronomy Observatory is operated by Associated Universities, Inc., under a cooperative agreement with the U.S. National Science Foundation.

## References

- Blandford, R. and Kochanek, C. 1987, in: *Dark Matter in the Universe*,  
Eds. J. Bahcall *et al.*, Singapore: World Scientific, p.133
- Borgeest, U. 1986, *Ap.J.* 309, 467
- Bourassa, R.R., Kantowski, R. 1975 *Ap.J.* 195, 13
- Canizares, C.R. 1981, *Nature* 291, 620
- Canizares, C.R. 1982, *Ap.J.* 263, 508
- Crampton, D., McClure, R.D., Fletcher, J.M., Hutchings, J.B. 1989,  
*Astron.J.* 98, 1188
- Drew, J.E. and Boksenberg, A. 1984, *M.N.R.A.S.* 211, 813
- Gorenstein, M.V., Falco, E.E., Shapiro, I.I. 1988, *Ap.J.* 327, 693
- Gott III, J.R. 1981, *Ap.J.* 243, 140
- Grieger, B., Kayser, R., Refsdal, S. 1988, *Astr.Ap* 194, 54
- Hazard, C., Morton, D.C., Terlevich, R., McMahon, R. 1984,  
*Ap.J.* 282, 33
- Hewitt, J.N. 1989, *NROC-Haystack preprint*, to appear in:  
*Cosmic Strings: the Current Status*, Eds. L.Kraus and F.S.Accetta
- Hewitt, J.N., Burke, B.F., Turner, E.L., Schneider, D.P., Lawrence, C.R.,  
Langston, G.I., Brody, J.P. 1989, to appear in:  
*Gravitational Lenses*, Eds. J.M.Moran *et al.*
- Kayser, R. 1986, *Astr.Ap.* 157, 204

- Kayser, R. 1990, *Ap.J.* in press
- Kayser, R. and Refsdal, S. 1983, *Astr.Ap.* 128, 156
- Kayser, R. and Refsdal, S. 1989, *Nature* 338, 745
- Kayser, R., Refsdal, S., Stabell, R. 1986, *Astr.Ap.* 166, 36
- Kayser, R. and Schramm, T. 1988, *Astr.Ap.* 191, 39
- Kent, S.M. and Falco, E.E. 1988, *A.J.* 96, 1570
- Kochanek, C.S., Blandford, R.D., Lawrence, C.R., Narayan, R. 1989,  
*M.N.R.A.S.* 238, 43
- Magain, P., Surdej, J., Swings, J.-P., Borgeest, U., Kayser, R., K"uhr, H.,  
Refsdal, S., Remy, M. 1988, *Nature* 334, 325
- Narasimha, D, Narlikar, J.V. 1989, *Ap.J.* 338, 44
- Nottale, L. 1988, *Ann. Phys. Fr.* 13, 223
- Paczynski, B. 1986 *Ap.J.* 301, 503
- Refsdal, S. 1964, *M.N.R.A.S.* 128, 307
- Refsdal, S. and Kayser, R. 1989, in: *The Post-Recombination Universe*  
NATO-ASI Series C 240, 297
- Schneider, P. 1988, *MPA 400*, submitted to *Astr.Ap.*
- Schramm, T. 1988, *Ph.D. Thesis*, University of Hamburg
- Schramm, T. 1990, *Astr.Ap.* in press
- Schramm, T. and Kayser, R. 1987, *Astr.Ap.* 174, 361
- Surdej, J., Magain, P., Swings, J.-P., Borgeest, U., Courvoisier, T.J.-L.,

- Kayser, R., Kellermann, K.I., K"uhr, H., Refsdal, S. 1987,  
*Nature* 329, 695
- Surdej, J., Magain, P., Swings, J.-P., Borgeest, U., Courvoisier, T.J.-L.,  
Kayser, R., Kellermann, K.I., K"uhr, H., Refsdal, S. 1988a,  
*Astr.Ap.* 198, 49
- Surdej, J., Swings, J.-P., Magain, P., Borgeest, U., Kayser, R., Refsdal, S.,  
Courvoisier, T.J.-L., Kellermann, K.I., K"uhr, H. 1988b,  
*Astr.Soc.Pac.Conf.Ser.* 2, 183
- Turner, E.L. 1988, in: *Dark Matter*, Eds. J.Audouze and Tran Thanh Van
- Turner, E.L. 1989, *POP-302b*, to appear in:  
*Proc. 14<sup>th</sup> Texas Symp. Rel. Astroph.*
- Turner, E.L., Ostriker, J.P., Gott III, J.R. 1984, *Ap.J.* 284, 1
- Turnshek, D.A., Foltz, C.B., Grillmair, C.J., Weymann, R.J. 1988,  
*Ap.J.* 325, 651
- Walsh, D., Carswell, R.F., Weymann, R.J. 1979, *Nature*, 279, 381
- Webster, R.L., Hewett, P.C., Irwin, M.J. 1988, *A.J.* 95, 19
- Webster, R.L., Hewett, P.C., Harding, M.E., Wegner, G.A. 1988,  
*Nature* 336, 358
- Zwicky, F. 1937a, *Phys.Rev.* 51, 290
- Zwicky, F. 1937b, *Phys.Rev.* 51, 679

JAMES J. CONDON : National Radio Astronomy Observatory,  
Edgemont Road, Charlottesville, VA 22903, U.S.A.  
E-mail: jcondon@nrao.edu

RAINER KAYSER : Canadian Institute for Theoretical Astrophysics,  
60 St. George Street, Toronto, Ontario M5S 1A1, Canada  
present address:  
Hamburger Sternwarte  
Gojenbergsweg 112, D-2050 Hamburg 80, F.R. Germany  
E-mail: st40010@dhhuni4.bitnet

KENNETH I. KELLERMANN : National Radio Astronomy Observatory,  
Edgemont Road, Charlottesville, VA 22903, U.S.A.  
E-mail: kkellerm@nrao.edu

PIERRE MAGAIN : Institut d'Astrophysique, Université de Liege,  
Avenue de Cointe 5, B-4200 Cointe-Ougrée, Belgium  
E-mail: u2182pm@bliulg11.bitnet

MARC REMY : European Southern Observatory,  
La Silla, Casilla 19001, Santiago 19, Chile  
E-mail: remy@dgaeso51.bitnet

ALAIN SMETTE : European Southern Observatory,  
Karl-Schwarzschild-Str. 2, D-8046 Garching bei München, F.R. Germany

E-mail: smette@dgaeso51.bitnet

JEAN SURDEJ :

Institut d'Astrophysique, Université de Liege,  
Avenue de Cointe 5, B-4200 Cointe-Ougrée, Belgium

E-mail: u2141js@bliulg11.bitnet

Table 1: Relative optical positions (in arcsec) and brightness ratios of images B, C and D with respect to A.

image	$\Delta\alpha(R)$	$\Delta\alpha(I)$	$\Delta\alpha(B)$	$\Delta\delta(R)$	$\Delta\delta(I)$	$\Delta\delta(B)$	$r(R)$	$r(I)$	$r(B)$
B	0.76	0.75	0.78	0.17	0.17	0.16	0.85	0.90	0.84
C	-0.51	-0.51	-0.50	0.72	0.73	0.72	0.74	0.76	0.83
D	0.38	0.35	0.36	1.07	1.07	1.06	0.61	0.59	0.61



Table 2: Objects in the vicinity of the Clover Leaf, see text. Relative positions are in arcsec.

No.	$\Delta\alpha$	$\Delta\delta$	$m_R$	type	No.	$\Delta\alpha$	$\Delta\delta$	$m_R$	type
1	16.71	-105.95	22.71	star	31	45.46	-16.52	22.71	star
2	3.24	-106.22	20.68	star	32	-32.38	-24.24	23.30	star
3	46.07	-99.80	23.35	star	33	-16.47	-15.11	20.47	galaxy
4	6.46	-100.13	23.37	star	34	-56.66	-12.84	22.22	galaxy
5	-29.31	-97.88	22.11	star	35	7.40	-3.87	23.69	star
6	-40.16	-102.34	21.89	star	36	-4.82	-5.82	23.72	star
7	-52.90	-97.52	21.57	star	37	-45.16	-0.62	23.05	star
8	19.48	-86.28	18.91	star	38	43.21	10.46	23.33	star
9	9.00	-81.76	23.18	star	39	31.80	10.46	19.90	galaxy
10	-57.84	-88.98	21.36	galaxy	40	17.38	7.66	18.39	star
11	30.21	-77.09	22.99	star	41	-28.55	6.60	23.73	star
12	31.88	-72.89	23.63	star	42	-22.70	14.90	22.53	galaxy
13	27.54	-72.61	21.76	star	43	-50.48	16.11	23.31	star
14	47.57	-68.10	23.16	star	44	-59.85	21.55	22.40	star
15	-9.63	-69.97	22.33	galaxy	45	47.27	32.45	16.91	star
16	-1.93	-64.07	21.18	star	46	38.18	35.62	22.71	star
17	-7.20	-63.90	23.57	star	47	-7.99	35.68	20.13	star
18	-9.41	-62.08	21.84	star	48	-27.28	30.12	20.97	galaxy
19	-17.59	-67.11	17.89	star	49	-58.22	31.79	23.34	star
20	-41.14	-71.54	22.36	galaxy	50	46.56	39.16	23.31	star
21	-43.49	-70.16	22.23	star	51	-56.96	43.68	22.97	star
22	-47.24	-71.41	22.75	star	52	4.90	47.73	23.87	star
23	-47.74	-65.74	23.49	star	53	2.54	52.03	21.35	galaxy
24	28.03	-53.62	21.65	galaxy	54	-15.17	54.16	23.51	star
25	22.45	-51.97	21.48	galaxy	55	-42.56	54.76	23.43	star
26	-6.27	-54.15	23.63	star	56	-53.36	57.96	21.97	star
27	-26.30	-56.26	22.55	star	57	38.61	60.54	23.37	star
28	-36.80	-48.81	22.98	star	58	5.76	62.73	22.06	galaxy
29	-13.45	-40.48	23.42	star	59	-37.33	64.44	23.26	star
30	40.69	-32.04	22.00	galaxy					

Table 3: Relative image positions (in arcsec) used for the models

image	$\Delta\alpha$	$\Delta\delta$
A	0.00	0.00
B	0.78	0.17
C	-0.50	0.72
D	0.35	1.06
SRS	0.73	0.68

Table 4: Parameters of Model #1

galaxy type	elliptical singular isothermal
surface density	$\Sigma(a) = \Sigma_0 a^{-1}$
position	$(-0.19'', 0.58'')$
eccentricity	0.903
position angle	$70^\circ$
density parameter $\Sigma_0$	$1.77 \cdot 10^7 M_\odot/\text{pc}$
velocity dispersion $\sigma_v$	$< 285 \text{ km/s}$

Table 5: Parameters of Model #2

galaxy type	spherical singular isothermal
surface density	$\Sigma(r) = \Sigma_0 r^{-1}$
galaxy 1 position	$(-0.53'', 0.34'')$
galaxy 2 position	$(0.21'', 0.65'')$
density parameter $\Sigma_0$	$6.05 \cdot 10^6 M_\odot/\text{pc}$
velocity dispersion $\sigma_v$	$228 \text{ km/s}$

Table 6: Time delays (in days)

images	model #1	model #2
A-B	-24.9	19.2
B-C	3.0	1.8
C-D	42.6	-30.7
D-A	-20.6	9.6

Table 7: Local lensing parameters

image	$\kappa$		$ \gamma' $		Ampl.	
	#1	#2	#1	#2	#1	#2
A	0.83	0.52	0.83	0.14	1.5	4.9
B	0.31	0.73	0.30	0.72	2.6	2.3
C	0.31	0.79	0.30	0.78	2.6	1.8
D	1.05	0.49	1.04	0.18	0.9	4.3
E		0.87		0.86		1.4

Table 8: Predicted micro-lensing amplifications

image	#1	#2
A	2.08	1.44
B	1.01	2.57
C	1.00	3.23
D	2.11	1.00

Figure 1: Reproduction of the 20 min. R CCD frame with each of the 59 objects detected near H1413+117 (see text and Table 2). North is up and East is to the left, the field size is  $2' \times 3'$ . Note that due to less than optimal seeing conditions, the Clover Leaf is not resolved on this frame.

Figure 2: 8.4 GHz VLA map of the field near H1413+117. The beams size is about  $0.3''$  FWHM. The contour levels are at -0.02, 0.02, 0.03, 0.04, 0.05, 0.06, 0.07, 0.08, 0.09, 0.10, 0.15 and 0.20 mJy/beam. Note that the closed contour centered about 0.5 arcsec south and 0.5 arcsec east of C corresponds to a local minimum.

Figure 3: Positions of the optical and the radio sources. The positions of the optical and radio images are marked with crosses, the positions of the additional radio sources are marked with triangles (see text)

Figure 4: Model #1 a) images and critical curves, b) source and caustics. The source radii are 125, 250, 500, 1000, and 2000pc, respectively. The galaxy centres are marked with crosses, the black triangles correspond to the observed image positions. The dotted lines are the critical curves and caustics, respectively.

Figure 5: Model #2 a) images and critical curves, b) source and caustics

Figure 6: Allowed micro-lensing parameters for the images in a) model #1 and b) model #2

Figure 7: Model #1: Quasar and SRS. Images produced by two circular sources of equal brightness: a) the quasar (position defined by back-tracing the quasars images) and b) a radio blob (position defined by back-tracing SRS)

Figure 8: Model #2: Quasar and SRS

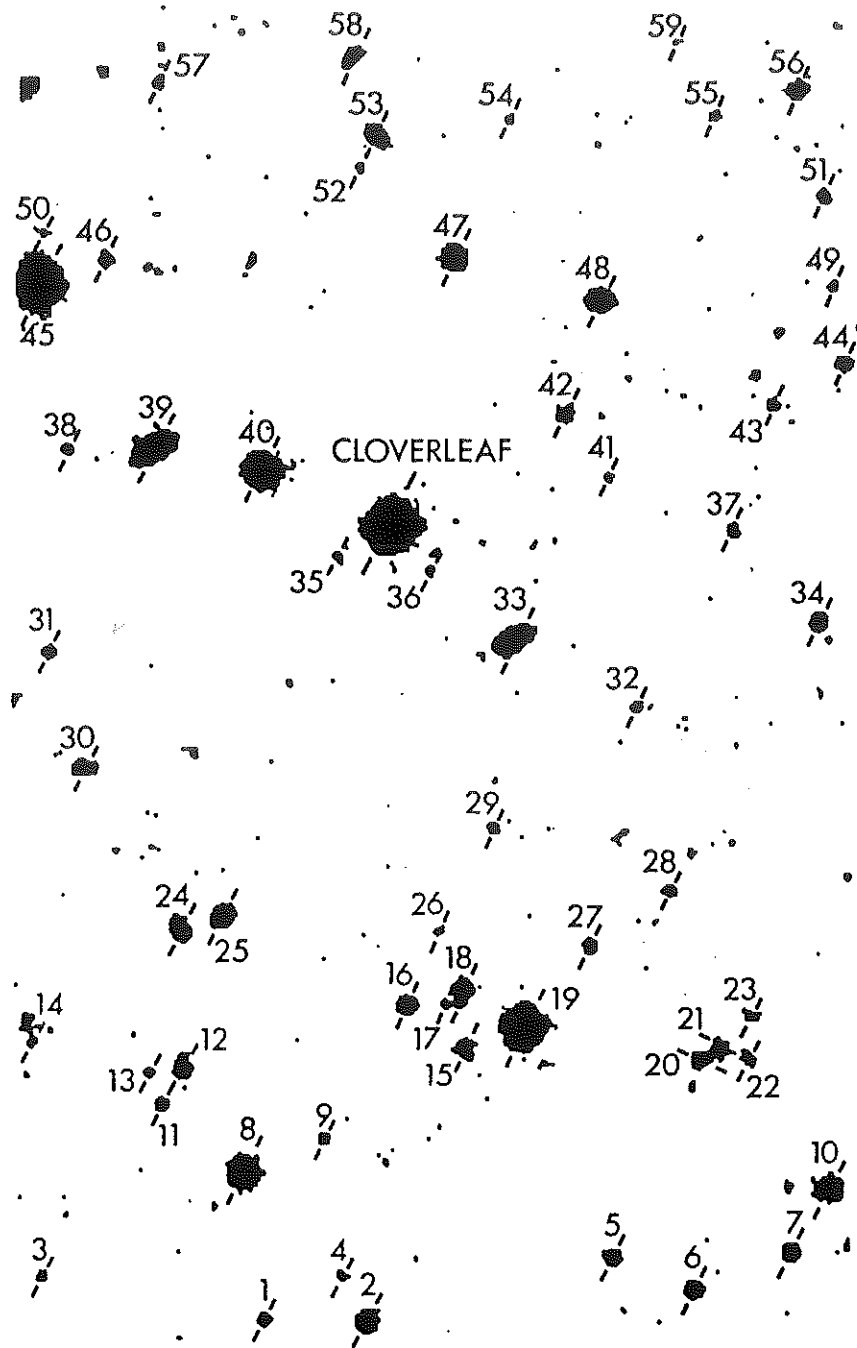


Fig. 1

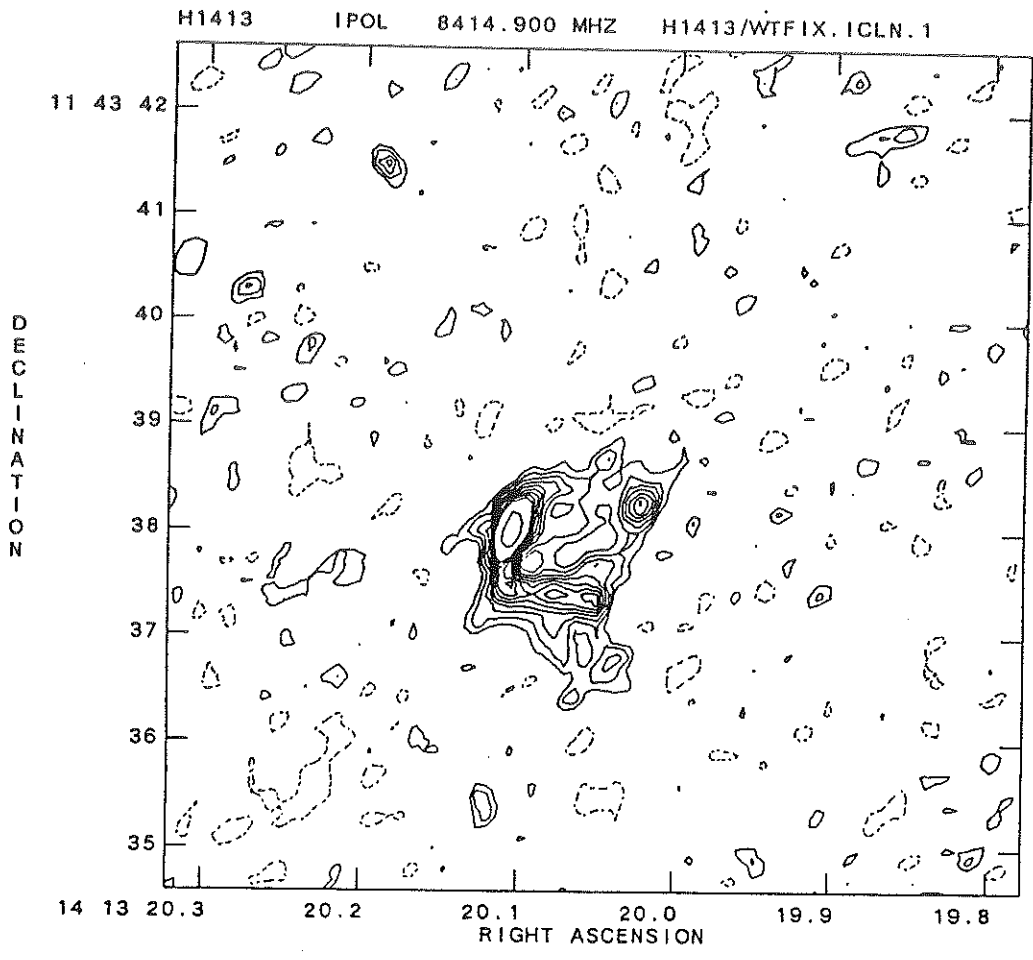


Fig. 2

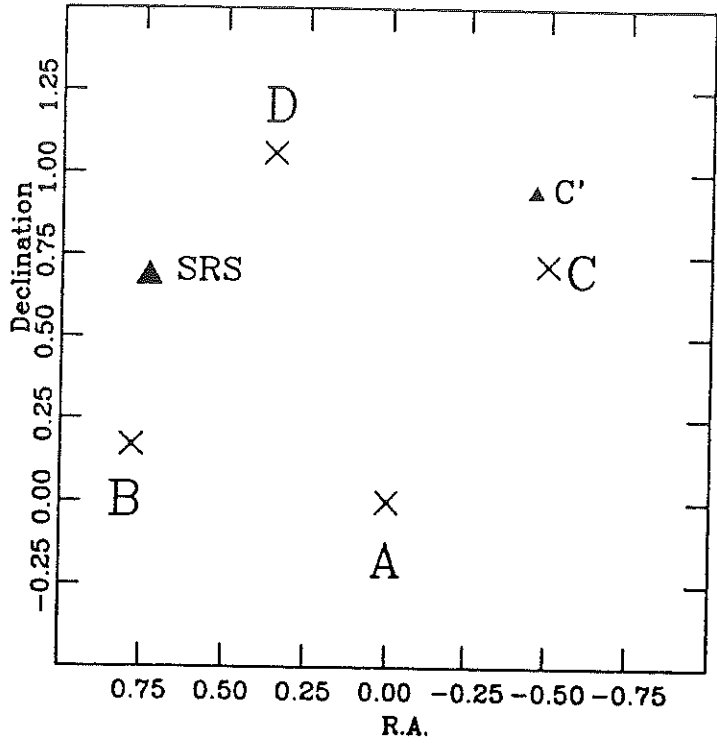


Fig. 3

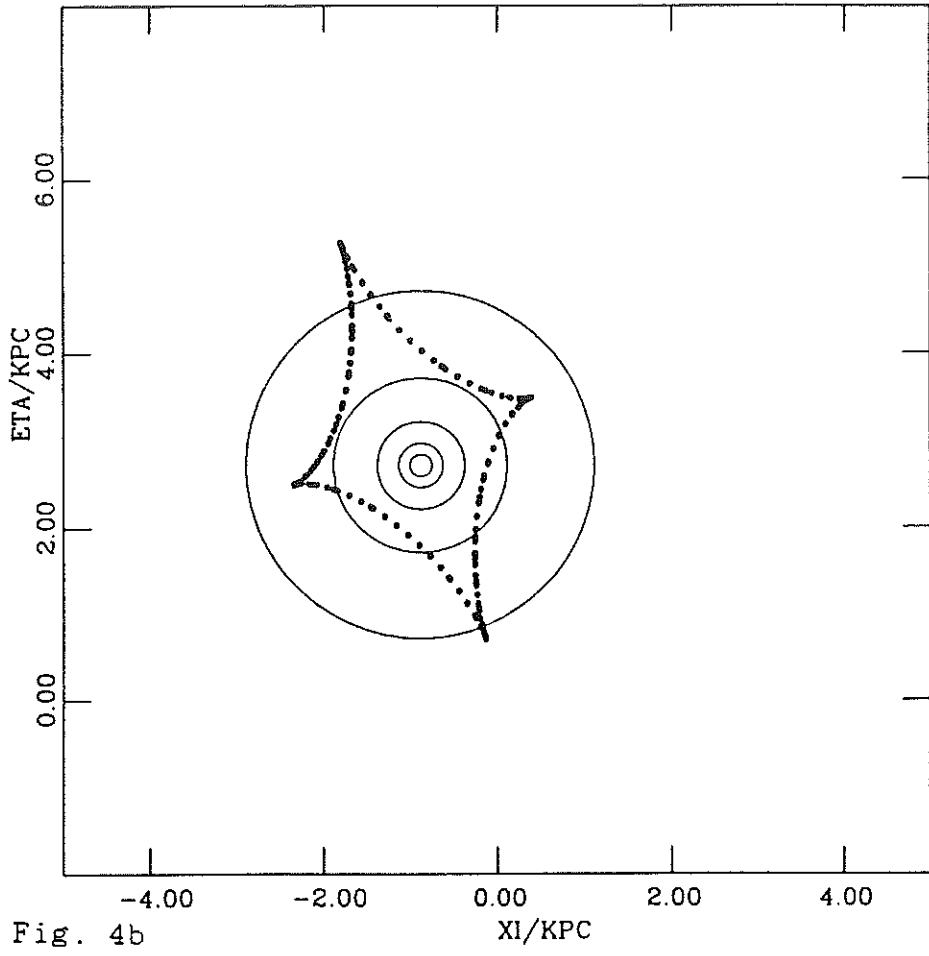
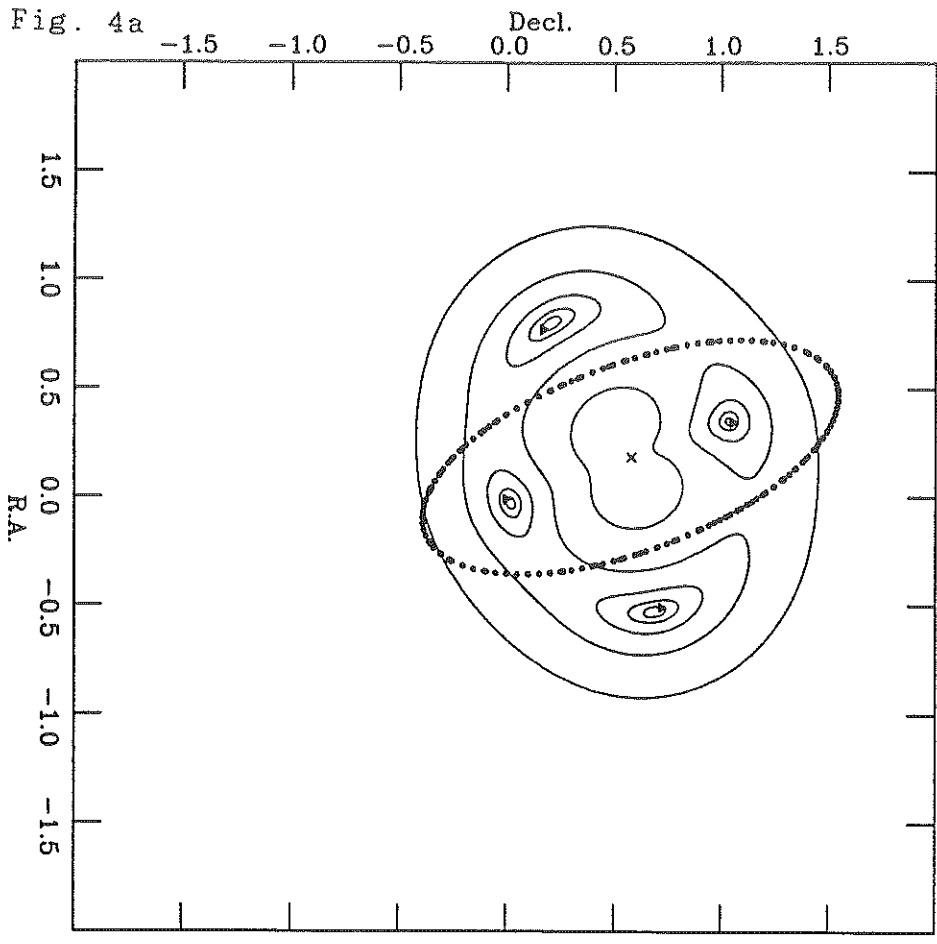


Fig. 4b

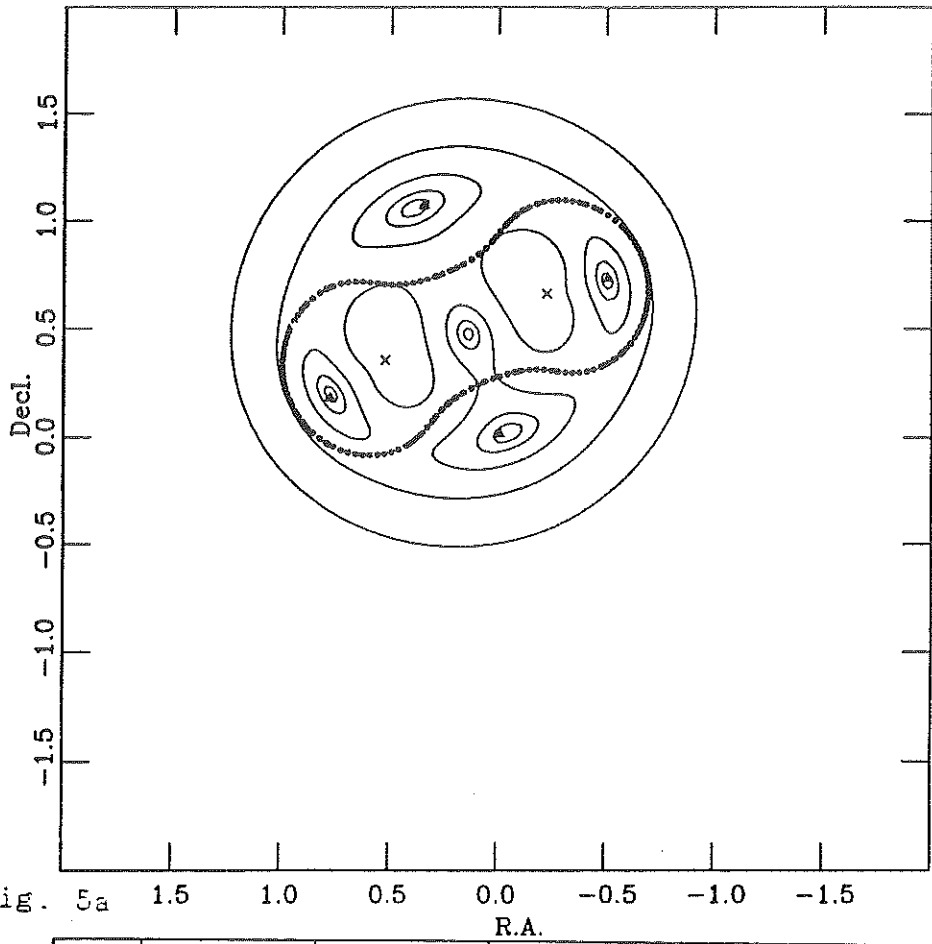


Fig. 5a

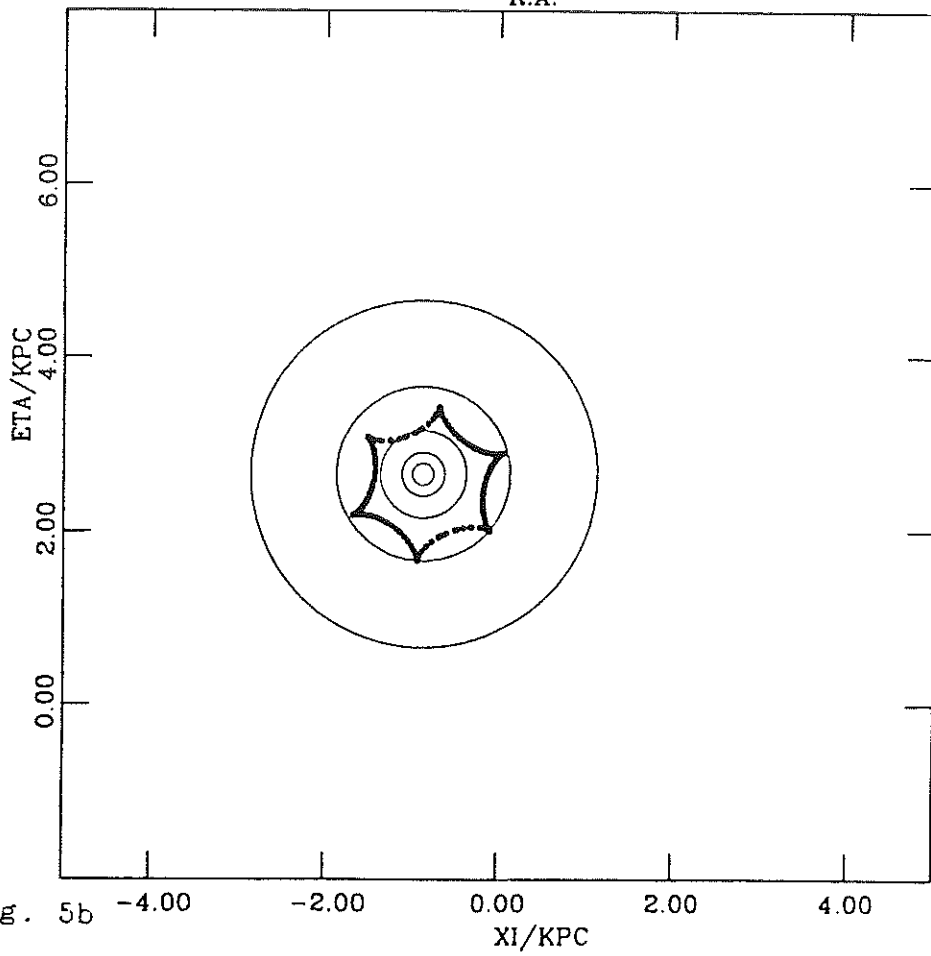


Fig. 5b



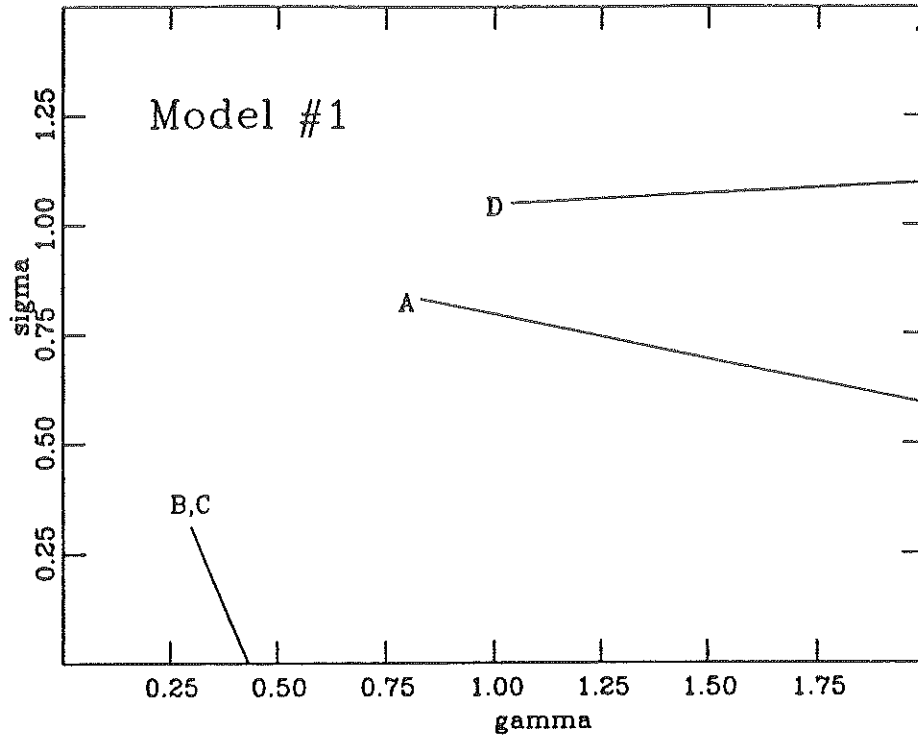


Fig. 6a

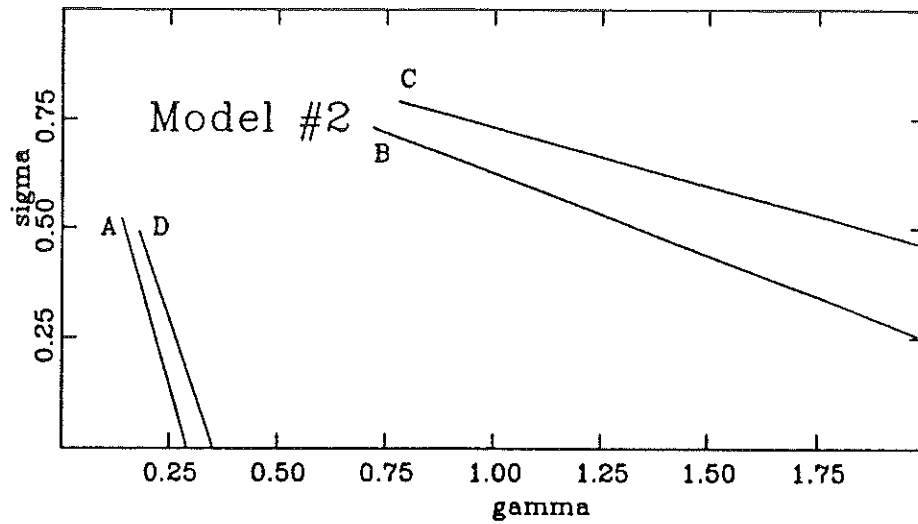


Fig. 6b

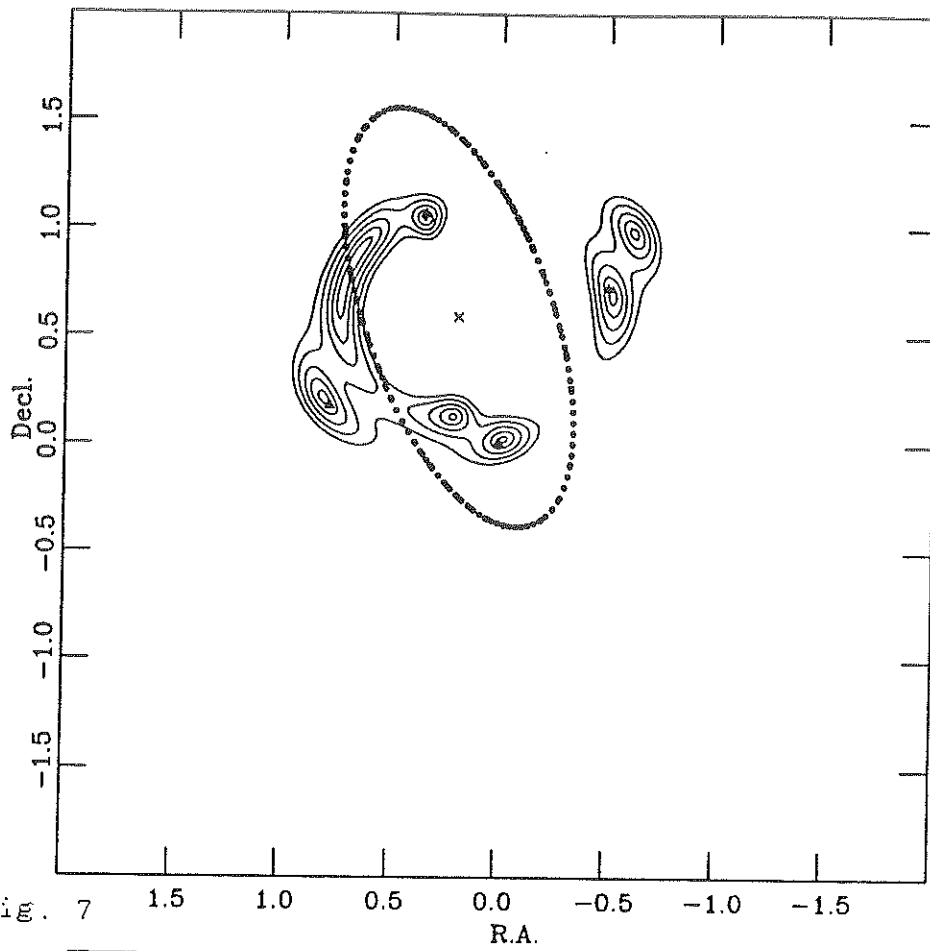


Fig. 7

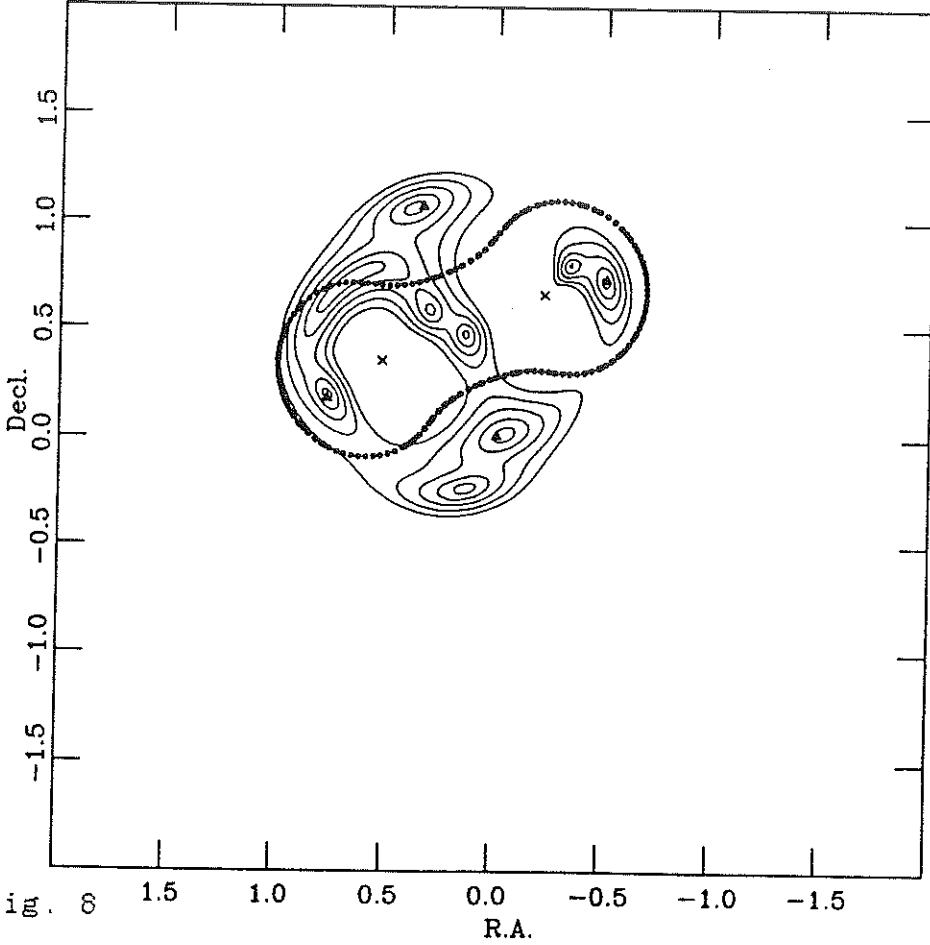


Fig. 8

Article 18

FIRST SPECTROSCOPIC EVIDENCE OF MICRO-LENSING ON A BAL QUASAR?:  
THE CASE OF H1413+117

Angonin, M.C., Remy, M., Surdej, J., Vanderriest, C.: 1990, *Astron. Astrophys. (Lettres)*, sous presse.

Sous des conditions d'agitation atmosphérique exceptionnellement favorables ( $\text{FWHM} \approx 0,5''$ ), il a été possible d'effectuer la spectroscopie bi-dimensionnelle du mirage gravitationnel H1413+117 au moyen du spectrographe SILFID attaché au foyer Cassegrain du télescope CFH de 3,6m (Hawaii). Nous décrivons dans cet article les résultats de ces observations. Après réduction des données, d'excellents spectres à moyenne résolution ont pu être extraits pour chacune des composantes individuelles du *Trèfle à quatre feuilles*. La comparaison de ces spectres révèle des différences très légères, mais réelles, entre les profils de raies de type P Cygni (SiIV, CIV et AlIII) observés pour les différentes images. Les différences détectées dans la structure des composantes en absorption, dans la largeur équivalente des raies en émission et dans la pente du spectre continu sont interprétées en termes d'effets de micro-lentille affectant préférentiellement certaines images (cf. l'image D) du *Trèfle à quatre feuilles*.



FIRST SPECTROSCOPIC EVIDENCE OF MICRO-LENSING  
ON A B.A.L. QUASAR ? : THE CASE OF H 1413 + 117.

M.C. Angonin<sup>(1)</sup>, M. Remy<sup>(2,3)</sup>, J. Surdej<sup>(2,4)</sup>, C. Vanderriest<sup>(1)</sup>.

(1) Observatoire de Paris-Meudon (DAEC) et U.R.A. 173 du CNRS  
5 place Janssen, F-92195 Meudon cedex (FRANCE).

(2) Institut d'Astrophysique, Université de Liège  
Avenue de Cointe, 5 B-4200 Ougrée-Liège (BELGIQUE).

(3) Aspirant au Fonds National de la Recherche Scientifique (BELGIQUE)

(4) Chercheur Qualifié au Fonds National de la Recherche Scientifique (BELGIQUE)

running title: Micro-lensing event in *H* 1413 + 117 ?

proofs and offprint requests should be sent to M.C. Angonin

Thesaurus code numbers:

17.02.1 (*H*1413 + 117)      07.37.1      15.01.1      19.09.1

section: Galaxies, cosmology

Submitted for publication in:

**Astronomy and Astrophysics (Letters)**

(\*) Based on observations made at the Canada-France-Hawaii telescope (Hawaii).

### Summary:

We have obtained, under optimal seeing conditions ( $\simeq 0.6''$  FWHM), new data for the quadruply lensed quasar  $H 1413 + 117$  using the bidimensional spectrograph SILFID at the C.F.H. telescope. The spectra recorded for each of the four individual images turn out to be quite similar, except for the narrow absorption line systems (probably related to the lenses) seen in images A and B and for marked differences in the spectrum of image D. When compared to the 3 other images, the spectrum of D shows smaller values for the emission lines/continuum ratio and a larger equivalent width for absorption features located in the blueshifted P Cygni profile.

We discuss briefly the possible explanations of these observations in terms of microlensing and/or intrinsic variability of the source.

## I) Introduction:

The BAL quasar  $H 1413 + 117$  has been resolved at optical wavelengths in 4 images having comparable brightness and forming a tight, nearly square, configuration (hence the nickname "clover leaf"). The great similarity existing between the spectra of the 2 most separated images (B, C) and the global spectrum strongly suggested that it is a new case of gravitational lensing (Magain et al., 1988). However, the compactness of the "clover leaf" has precluded to obtain until now uncontaminated spectra of the 4 images.

We tried to resolve this problem with the help of the bidimensional spectrograph SILFID (Vanderriest et al., 1987; Vanderriest and Lemonnier, 1988) at the Cassegrain focus of the Canada-France-Hawaii telescope. The aim of this letter is to present and discuss the data obtained under optimal seeing conditions with this instrumentation.

## II) Observations:

With SILFID, transforming the 2 spatial dimensions of the focal image of the telescope into a single one (the slit of the spectrograph) is achieved by means of a short fibre optics device: in the focal plane, about 400 fibres are closely packed into an hexagonal array and, at the other end of the device, they are just set in line to form a pseudo "slit". Following the dispersion, we may apply the exactly inverse geometrical transformation in order to reconstruct crude pictures of the object at any chosen wavelength.

Our spectra were obtained on 7 March 1989 during a period of strong wind, but very good seeing. Just in front of the fibre device, a small lens extended the focal length of the telescope so that each  $100\mu\text{m}$  diameter fibre subtended  $0.33$  arcsec on the sky. The scale is  $60\mu\text{m}$  per fibre on the detector (a Ford CCD with  $(512)^2$  pixels of  $20\mu\text{m}$ ). Fig. 1a displays a reconstructed picture in the wavelength range  $\simeq 4800 - 6600 \text{ \AA}$  and shows how the fibres were lightened by the object in the focal plane of the telescope. As the size of the CCD did not allow to cover the whole slit length, only about  $1/3$  of the initial hexagonal field could be reconstructed (160 useful fibres). We see that, even at  $0.33''$  per fibre, the spatial sampling is still too coarse. On the smoothed picture (fig. 1b), the average size of the images is about  $0.6''$  (FWHM), corresponding to an initial seeing of the order of  $0.5''$ .

Analysing the reconstructed picture, we could select those fibres whose data can be safely added for obtaining the spectra of each of the 4 images A, B, C and D with a minimum of contamination ( $<10\%$ ). This led to disregard many fibres fed with "mixed" light from 2 or more images. The possibility of such an *a posteriori* choice provides the best S/N ratio for a given seeing. Fig. 2 displays the spectra obtained in this way from the sum of two 30 min. exposures at  $235 \text{ \AA/mm}$ . The spectrophotometric standard Feige

67 (Massey et al., 1988), observed in the same conditions with SILFID, provided the flux calibration. Multiplying by a V filter response, one find a global magnitude for the system of 4 images:  $V = 17.10 \pm 0.05$ .

### III) Results:

First of all, we see that the overall shapes of the spectra extracted for each single image are very similar to each other, strengthening the gravitational lensing interpretation for the clover-leaf. The narrow absorption lines, already recognized by Magain et al. (1988) as belonging to two systems at redshifts 1.438 and 1.661, are seen with different intensities in the 4 spectra. Within the limit of accuracy fixed by the data noise, they are absent in image C and hardly significant in D. If we interpret these absorptions as arising in two lensing galaxies, our present data may help in locating these with respect to the 4 images. But direct imaging of the lenses would certainly be more secure.

In hope of detecting the deflectors, we tried to take advantage of the deep C IV absorption trough that reduces the intensity of the quasar almost to zero near 5400 Å. We have thus reconstructed an image within a 32 Å bandwidth around this wavelength but could set only an upper limit to the flux of the deflector corresponding to  $V \geq 23.5$ . This is not a very stringent constraint since at  $z \simeq 1.5$ , the deflectors could be 1 or 2 magnitudes fainter than this limit, their masses being of the order of  $10^{11} M_{\odot}$  (Magain et al., 1988; Kayser et al., 1989).

Another major spectral difference between the four images may be noticed after inspection of Fig. 2. Indeed, with respect to images A, B and C, the continuum of D is found to be marginally bluer and its ratio to the emission line fluxes is greater. Moreover, specific absorption features in the BAL line profiles appear to be significantly stronger in image D than in the three other images (see the arrows in Fig. 2). One of these features corresponds certainly to the C IV absorption component located at about -8500 km/s from the center of the emission line and reported to be possibly variable, in the integrated spectrum of H 1413+117 over a 4-year period, by Turnshek et al. (1988). This absorption feature is also seen at the same relative velocity in the Si IV and Al III 1857 Å P Cygni profiles.

### IV) Discussion:

There are at least two obvious ways to account for these observed spectral differences.

-a) If real, the difference in the slope of the continuum of D suggests a possible intrinsic variation of the source. The spectral difference observed in the BAL trough between images D and A, B, C could also be explained this way. The equivalent widths



of similar features ( Al III 1857 Å and high velocity components due to Si IV and C IV) have also been found to be variable in another BAL quasar, UM 232 (Barlow et al., 1989), in apparent correlation with the ionizing flux of the central source. In such a scenario, the characteristics observed for D should be exactly reproduced in the spectra of the other images, with shifts in time characterizing the geometry and mass distribution of the lensing system. For H 1413+117, these time delays are expected to be of the order of a few days or weeks, but their exact values and even their signs are very much model dependent (see Kayser et al., 1989).

The flux of image D seems to be indeed variable. Kayser et al. (1990) have reported a fading of D, with respect to the other images, of  $\simeq 0.15$  mag between their observations and those of Magain et al. (1988), recorded 6 weeks earlier. Prior to the bidimensional spectroscopy described above, we also took a 5 min. direct R CCD frame of H 1413+117 on the night of 7 march 1989. This CCD frame is essentially of good quality and it was straightforward to fit, in the least squares sense, the observed images of the clover leaf system using a four-component Moffat star profile. Fortunately, we could make use of a nearby and well exposed star image in order to determine the three unknown parameters of the single Moffat PSF. Furthermore, the finite size of the pixels was taken into account in the present fitting procedure (Remy and Magain, in preparation). The derived flux ratios for images B, C and D with respect to A are reported in Table 1 and may be compared with previous determinations. The flux level observed for D on 7 march 1989 appears to lie between the two previous measurements by Magain et al. (1988) and Kayser et al. (1990).

In any case, these observed variations seem to be too small for inducing appreciable changes in the ionization level of the BAL clouds.

-b) As already suggested by Kayser et al. (1990) on the sole basis of photometric variations, it is more likely that micro-lensing effects do exist in image D. We suggest that they could be responsible for the observed departures from the spectra of the other images. Knowing that micro-lensing effects are highly dependent on the source's size (see e.g. Kayser et al., 1986), we understand easily that if a star or group of stars, located in one of the lensing galaxies, come in front of the QSO's nucleus, it will lead to a significant magnification of the quasi-stellar continuum without (almost) affecting the broad spectral emission lines formed in the much larger BEL region. This now "classical" effect (see e.g. Rees, 1981) is suspected to be at work in several gravitational lenses and provides a straightforward explanation for the different equivalent widths of similar BELs observed in the spectra of the four lensed images of H 1413+117 (cf. Fig. 2). The same explanation

holds for the BALs: if the continuum source is being "resolved" by the microlens and if the BAL region is highly inhomogeneous on such scales, the star will then preferentially magnify one of the BAL components that happens to occult only a part of the continuum core.

Let  $R_c$  be the angular critical radius of the microlens. This represents also the typical length of the microlensing magnification gradient. An observable differential effect will take place if two conditions are fulfilled:

- (1)  $d_{cont} \ll R_c$
- (2)  $d_{abs} < d_{cont}$

where  $d_{cont}$  is the diameter of the continuum source and  $d_{abs}$  the equivalent diameter of the part heavily absorbed by the BAL clouds at the considered wavelength.

For a star of  $1 M_\odot$  in the lensing galaxy (supposed to be at  $z \simeq 1.5$ ),  $R_c$  is found to be about  $3 \cdot 10^{-2}$  pc at the distance of the source. In the standard model of the BALR with discrete clouds,  $d_{cont}$  is of the order of 1 pc so that inequality (1) is easily fulfilled, and the diameter of the absorbing clouds is not believed to be much larger than  $d_{cont}$ , making easy to also fulfill (2), in a random projection of such clouds over the continuum core (see for instance Drew and Giddings, 1982).

A good way of testing the likelihood of the differential absorption mechanism due to microlensing is to investigate whether the spectrum of image D may be reproduced by a straightforward combination of both a macro-lensing and micro-lensing contributions. In order to check this, we built a "synthetic" spectrum  $F_S(\lambda)$  (with S equal to the sum A+B+C cleared of the narrow absorption lines) and, neglecting completely microlensing for the emission lines, we can represent the spectrum  $F_D(\lambda)$  of D by:

$$F_D(\lambda) = k F_S(\lambda) + k' I_c(\lambda) R(\lambda) e^{-\tau'(\lambda)} \quad (3)$$

where  $k$  (resp.  $k'$ ) is a constant representing an effective amplification of image D due to macro-lensing (resp. micro-lensing),  $I_c(\lambda)$  is the underlying QSO continuum observed in spectrum S,  $R(\lambda)$  is a wavelength dependent factor correcting for the possibly different shape of the continuum spectrum emitted by the region of the QSO which is magnified by the micro-lens and  $\tau'(\lambda)$  is the opacity of this particular region as a function of wavelength. Similarly, we assume that the spectrum of S may be described by the following expression:

$$F_S(\lambda) = I_c(\lambda) e^{-\tau(\lambda)} + E(\lambda) \quad (4)$$

where  $\tau(\lambda)$  stands for the opacity, at wavelength  $\lambda$ , of the expanding envelope projected against the whole QSO core along the line-of-sight and where  $E(\lambda)$  is the profile of the emission line component. Fitting the spectra of D and S by means of Eqs. (3) and (4) leads to the following best parameter estimates:  $k = 0.15$ ,  $k' = 0.07$  and  $R(\lambda)$  is found

to be an almost linear function of  $\lambda$  such that  $R(5500) = 1$  and  $R(4500) = 2.1$ . Such values correspond to a moderate differential magnification: with respect to the macro-lensing contribution, it is as if micro-lensing brightens the QSO continuum of D by  $\simeq 0.4$  mag. The resulting attenuation factor  $e^{-\tau'(\lambda)}$  derived from this spectral decomposition is illustrated in Fig. 3. For comparison, we have also plotted in this figure the profile  $F_S(\lambda)/I_c(\lambda)$ . Referring to the absorption line profiles in Fig. 3, we see that at least three discrete absorption components located at about  $-3870$  (C IV and Si IV),  $-7750$  (C IV, Si IV and Al III) and  $-12330$  km/s (just C IV) from the center of their corresponding emission line have been enhanced by micro-lensing effects in the spectrum of image D. More details about these observations and the spectral decomposition will be published elsewhere.

So, the hypothesis of differential microlensing is a viable interpretation of the observed spectral differences between the faintest and the three other lensed images of H 1413+117. However, a definite proof is yet to be found. In broad band photometry, image D should display a light curve characteristic of micro-lensing events. We may also predict that the continuum of image D should be differently (probably more) polarized than that of the other three images. An even better proof would be to detect spectral variability in the BAL troughs, reflecting the star(s) motion in front of the BAL clouds. It is quite possible that Turnshek et al. (1988) have witnessed such an event between 1981 and 1985, even if centering of the 4 images (not yet resolved at that time) in the spectrograph slit can also be partly incriminated. We may of course predict that the enhancement of the blue component(s) should not last during the whole transit of the lensing star(s); at some phase, it should be replaced by a weakening.

## V) Conclusions:

Our bidimensional spectroscopic data strengthen the interpretation of H 1413+117 as a gravitational mirage. The differences observed in the spectrum of image D are either due to intrinsic variations of the source, or to a differential microlensing effect operating on the BAL clouds. We personally favour this second interpretation. In this context, it is therefore quite possible that the spectroscopic variations reported in the integrated image of H 1413+117 by Turnshek et al. (1988) are not intrinsic to the BAL quasar but caused by a mirage effect. Spectroscopic monitoring of the 4 images will help in discriminating between these various possible scenarios.

Detailed modeling of this gravitational lens system was of course beyond the scope of the present letter; it would even be premature to do so considering the paucity of the relevant data (cf. the still unknown precise location(s) and type of the lenses, etc.).

We just wished to present here new high angular resolution spectroscopic observations of the clover leaf and to attract the attention of potential observers on the interest and importance of getting further bidimensional spectroscopy of this object, with comparable or better spectral and spatial resolutions.

H 1413+117 has an unprecedented status, being at the same time a BAL quasar and a gravitational mirage. While it is believed that gravitational mirages of "normal" QSOs could help to improve our knowledge on their structure, we bet that the clover leaf will turn out to be a unique tool in order to better understand the BAL phenomenon itself.

#### References:

- Barlow T., Junkkarinen V., Burbidge M., 1989, *Astrophys. J.*, **347**, 674.
- Drew J., Giddings J., 1982, *Mon. Not. Roy. Astron. Soc.*, **201**, 27.
- Kayser R., Refsdal S., Stabell R., 1986, *Astron. Astrophys.*, **166**, 36.
- Kayser R., Surdej J., Condon J.J., Hazard C., Kellermann K.I., Magain P., Remy M., Smette A., 1990, *Astrophys. J.*, in press.
- Magain P., Surdej J., Swings J.P., Borgeest U., Kayser R., Kühr H., Refsdal S. & Remy M., 1988, *Nature*, **334**, 325.
- Massey P., Strobel K., Barnes J., Anderson E., 1988, *Astrophys. J.*, **328**, 315.
- Rees M., 1981, ESO conf. *"Scientific importance of high angular resolution at Infrared and Optical wavelengths"*, M.H. Ulrich, K. Kjær eds., p.423.
- Turnshek D., Foltz C., Grillmair C., Weymann R., 1988, *Astrophys. J.*, **325**, 651.
- Vanderriest C., Haddad B., Lemonnier J.P., 1987, *Annales Phys. Fr.*, Suppl. **5**, vol. 12, 207.
- Vanderriest C., Lemonnier J.P., 1988, "Instrumentation in Astronomy", *proc. IX<sup>th</sup> Santa Cruz workshop*, 304.

image :	08/03/1988 ( <i>Magain et al.</i> )	27/04/1988 ( <i>Kayser et al.</i> )	07/03/1989 ( <i>this work</i> )
<i>B</i>	0.87	0.87	$0.88 \pm 0.02$
<i>C</i>	0.76	0.77	$0.78 \pm 0.02$
<i>D</i>	0.69	0.60	$0.66 \pm 0.02$

Table 1: Photometric data:

Intensity ratios of the B, C and D images relative to A. The 08/03/1988 and 07/03/1989 data have been obtained in the R band; the values taken on 27/04/1988 refer to the average of 3 colours B, R and I.

**Figure captions:**

Figure 1:

The field of H 1413+117 reconstructed from bidimensional spectroscopic data (30 min. exposure at 235 Å/mm).

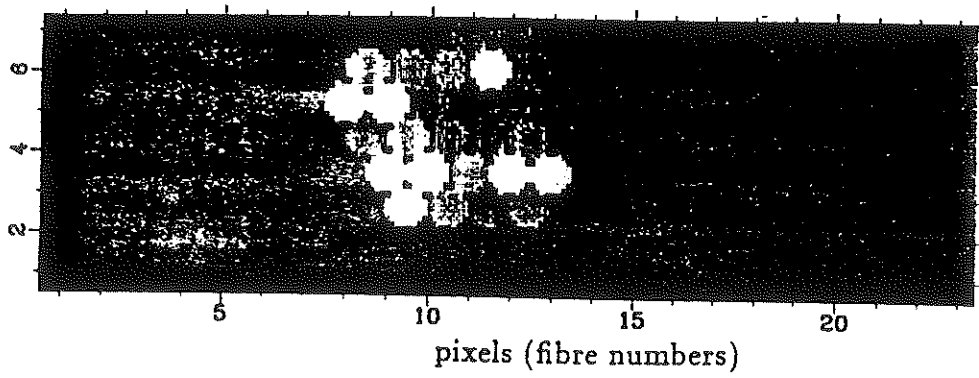
- a) Direct reconstruction in the wavelength range 4800 - 6600 Å showing the fibre array.
- b) The same picture smoothed with a gaussian filter (FWHM  $\simeq 0.15''$ ).

Figure 2:

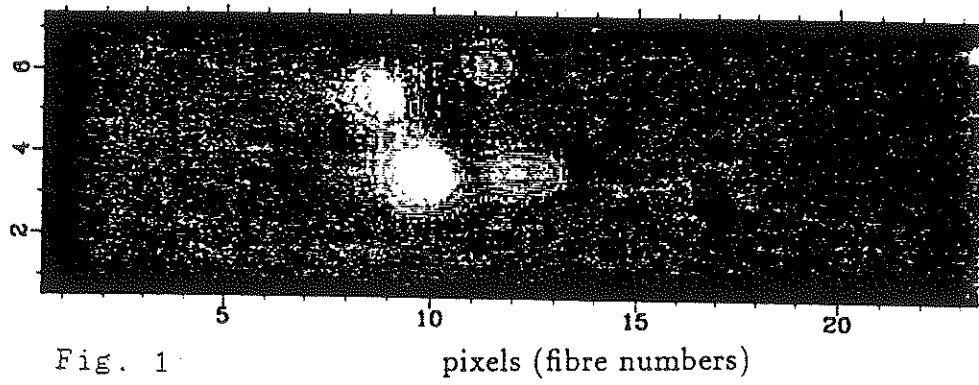
Spectra of the 4 images extracted from the low dispersion data (sum of two 30 min. exposures, 235 Å/mm, resolution  $\simeq 12$  Å). The vertical scale has been shifted for clarity between each spectrum. N.S. stands for poor Night Sky line subtraction. Note the differences in the structure of the BAL troughs for image D (arrows).

Figure 3:

Because of micro-lensing effects, the attenuation factor  $e^{-\tau(\lambda)}$ , calculated by means of Eqs. (3) and (4), accounts for the additional absorption components seen in the P Cygni profiles of image D. It is represented here as a function of  $\lambda$ . We have also illustrated in this figure the profile  $F_S(\lambda)/I_c$  whose blue wing gives a good representation of the attenuation factor  $e^{-\tau(\lambda)}$  (cf. Eq(4)).



a)



b)

Fig. 1

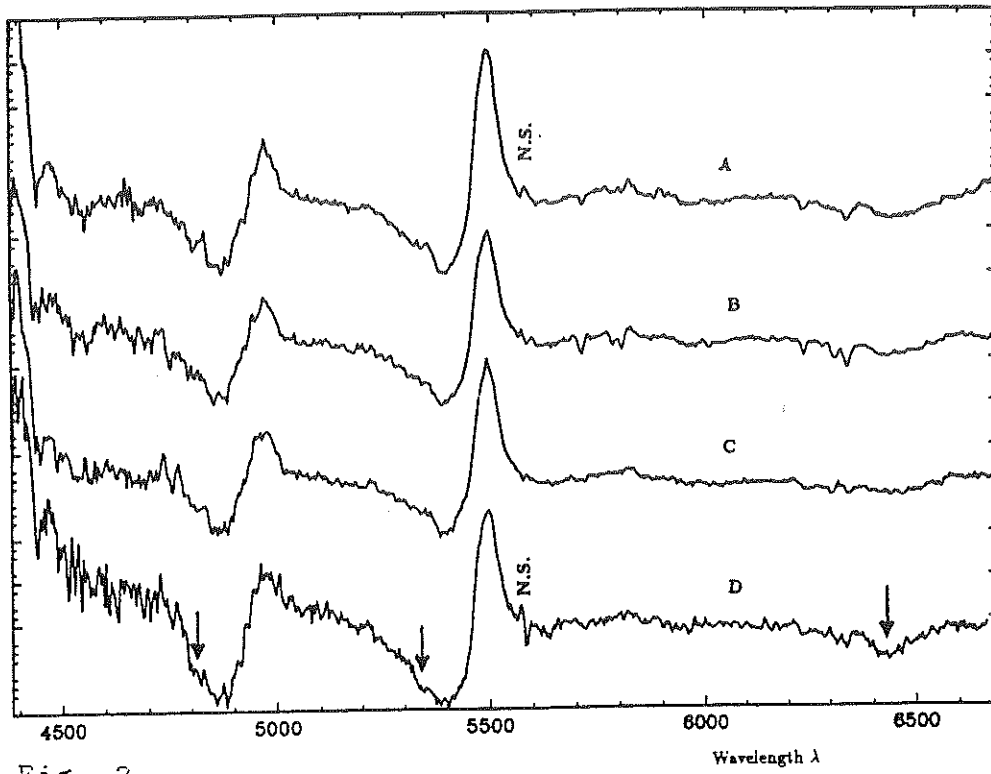


Fig. 2

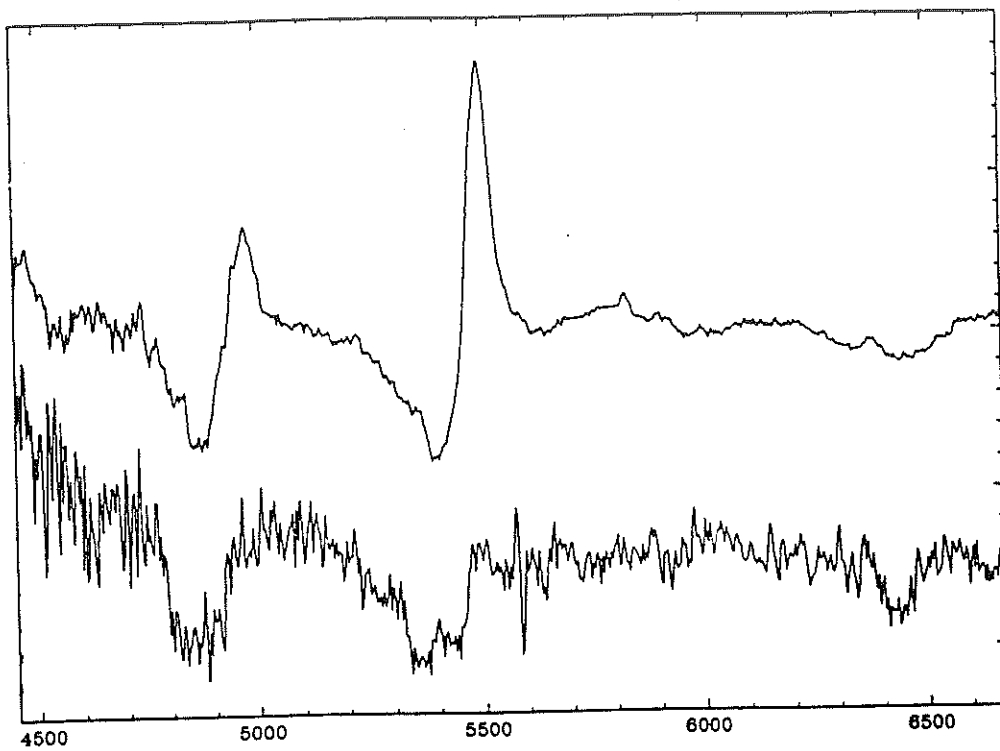


Fig. 3





## Chapitre 5

### CONCLUSIONS GENERALES ET PERSPECTIVES

Notre intérêt pour l'étude du transfert de la radiation spectrale au sein d'enveloppes en expansion rapide tient au moins à deux raisons principales: d'une part, mieux comprendre la formation des profils de raies de type P Cygni observés dans les spectres d'une grande variété d'objets galactiques (noyaux de nébuleuses planétaires, étoiles de type O, etc.) et extragalactiques (supernovae, quasars de type BAL, etc.) et, d'autre part, tester l'interprétation de ces profils en termes de paramètres astrophysiques simples. Ainsi, une des questions fondamentales que nous nous sommes posées au début des années 80 est celle de l'unicité de l'inversion d'un profil de raie observé en fonction du type du champ de vitesse  $v(r)$ , de la loi d'opacité  $\tau_{12}^r(v)$  et du taux de perte de masse  $\dot{M}$  caractérisant l'enveloppe éjectée par l'objet central étudié. Est-il par exemple possible que deux solutions très différentes pour le paramètre  $\dot{M}$  et les distributions  $v(r)$  et  $\tau_{12}^r(v)$  conduisent toutes deux à des ajustements acceptables d'un profil de raie observé? Nous nous sommes aussi interrogés sur la façon d'évaluer les incertitudes affectant la détermination de  $\dot{M}$  à partir de l'analyse de profils de raies observés. Que se passe-t-il lorsque la résolution spectrale des observations est dégradée? Enfin, existe-t-il des types privilégiés de profils de raies en vue de déterminer des taux de perte masse  $\dot{M}$  aussi précis que possible? La théorie des

moments  $W_n$  des profils de raies de type P Cygni, développée dans la présente dissertation, nous a permis de trouver des éléments de réponse à ces différentes questions.

Ainsi, nous montrons au chapitre 2 que le moment d'ordre 1 d'un profil de raie de type P Cygni non saturé permet de déduire de façon univoque la valeur du taux de perte de masse  $\dot{M}$ , indépendamment du choix adopté pour les distributions  $v(r)$  et  $\tau_{12}^r(v)$ , des effets d'assombrissement centre-bord de la source centrale, de la structure des multiplets de résonance considérés, de l'approximation de Sobolev utilisée pour traiter le transfert de la radiation, des effets relativistes induits par l'expansion très rapide de certaines atmosphères, etc. En d'autres termes, si deux solutions très distinctes pour les distributions  $v(r)$  et  $\tau_{12}^r(v)$  permettent un ajustement acceptable d'un profil de raie observé non saturé, on est assuré que les valeurs du paramètre  $\dot{M}$  déduites dans les deux cas seront quasiment identiques. Alors que les profils de raies de type P Cygni saturés, révélant des composantes en absorption et en émission très développées (cf. Fig. 2.1), constituent sans aucun doute les exemples les plus caractéristiques et remarquables des phénomènes de perte de masse, ces profils sont pratiquement inutilisables en vue de déduire les paramètres physiques des atmosphères en expansion. Il faut donc rechercher dans les spectres ultraviolets des étoiles de type O, des noyaux de nébuleuses planétaires, des quasars BAL, etc. des profils de raies de type P Cygni qui sont à peine détectables et observer ces derniers avec un rapport signal sur bruit aussi élevé que possible. C'est à ce seul prix qu'on peut espérer améliorer de façon significative nos futures estimations des taux de perte de masse  $\dot{M}$ .

En généralisant la méthode de la courbe de croissance - applicable aux atmosphères statiques - au cas des enveloppes en expansion rapide, nous avons montré au chapitre 2 comment il était possible d'utiliser des diagrammes de type " $\log(W_n) - \log(W_n^0)$ " et " $\log(W_n) - \log(W_{n'})$ " ( $n, n' = 0-3$ ) en vue de caractériser les distributions  $v(r)$ ,  $\tau_{12}^r(v)$  et les paramètres  $W_n^0$ ; ces derniers étant liés à la densité de colonne ( $n = 0$ ), au taux de perte de masse  $\dot{M}$  ( $n = 1$ ), à la colonne d'impulsion ( $n = 2$ ) et à (deux fois) la colonne d'énergie cinétique ( $n = 3$ ) de l'ion détecté dans le

vent stellaire. La théorie du moment d'ordre 1 nous a finalement permis de re-déterminer les taux de perte de masse  $\dot{M}$  d'un échantillon de dix-sept noyaux de nébuleuses planétaires observés avec le satellite IUE. Nous expliquons pourquoi les anciennes déterminations de  $\dot{M}$  avaient été systématiquement sous-estimées d'un facteur allant de 7 à 20.

Lors de l'analyse des spectres ultraviolets d'étoiles de type O publiés par Walborn, Nichols-Bohlin et Panek (1985), nous avons trouvé que les profils de type P Cygni observés pour les raies de résonance de SiIV, CIV, HeII et NIV étaient sévèrement contaminés par des raies photosphériques sous-jacentes dues aux ions  $\text{Fe}^{3+}$  et  $\text{Fe}^{4+}$ , conduisant à des incertitudes de l'ordre de 50% et plus lors de la détermination des taux de perte de masse  $\dot{M}$  (chapitre 3). Nous avons suggéré une méthode pour corriger ces effets de pollution et ceci devrait conduire à une révision systématique des taux de perte de masse  $\dot{M}$  publiés pour les étoiles de type O. Un autre aspect crucial de l'interprétation des profils de raies de type P Cygni concerne la vérification de l'hypothèse de symétrie sphérique des atmosphères en expansion rapide, sous-jacente à la plupart des modèles existants. Grâce à la mise en service récente de détecteurs électroniques linéaires et très sensibles (cf. les CCDs) dans les grands observatoires astronomiques, nous proposons de tester observationnellement cette hypothèse en effectuant la spectroscopie bi-dimensionnelle des nébuleuses à réflexion et/ou des échos de lumière situés autour d'astres remarquables qui sont sujets à des phénomènes de perte de masse (cf. Surdej et al. 1981 et Surdej et Swings, 1983 pour la nébuleuse à réflexion autour de l'étoile HD87643 et Surdej, 1988 et Detal et al. 1990 pour les échos de lumière autour de la supernova 1987a).

Enfin, nous avons décrit au chapitre 4 les observations spectroscopiques obtenues pour chacune des images individuelles du mirage gravitationnel H1413+117 au moyen d'un spectrographe bi-dimensionnel (SILFID) installé au foyer Cassegrain du télescope CFH (Hawaii). Nous rappelons que ce mirage cosmique est le deuxième à avoir été identifié par notre groupe de recherche en astrophysique extragalactique au sein d'un échantillon de quasars très lumineux ( $M_V < -29$ ). L'étude de ces données a révélé que des effets de micro-lentille gravitationnelle étaient responsables des

différences spectroscopiques observées entre les profils de raies de type P Cygni (SiIV, CIV et AlIII) des quatre images illusoire de ce quasar de type BAL. Tirant parti d'autres arguments théoriques et observationnels, nous avons suggéré que la plupart des caractéristiques observées pour les quasars BAL en général peuvent aussi être interprétées simplement en termes d'effets de micro-lentille gravitationnelle. Nous avons proposé que les quasars Q1303+308, Q1246-057 et UM232, pour lesquels des variations spectroscopiques significatives des profils de raies de type P Cygni ont déjà été annoncées constituent d'excellents candidats pour la recherche d'effets de micro-lentille gravitationnelle. Il en est de même pour les quasars BAL 1E 0104+315, H0903+175, Q0413-116 et d'autres situés à proximité de galaxies brillantes d'avant-plan.

## BIBLIOGRAPHIE

- Abbott, D.C.: 1982, *Astrophys. J.* 259, 282.
- Angonin, M.C., Vanderriest, C., Surdej, J.: 1990, dans "Lecture Notes in Physics, Gravitational Lensing", Y. Mellier, B. Fort, G. Soucail (eds.), Springer-Verlag, vol. 360, 124.
- Angonin, M.C., Remy, M., Surdej, J., Vanderriest, C.: 1990, *Astron. Astrophys. Letters*, sous presse (article 18).
- Barlow, T.A., Junkkarinen, V.T., Burbidge, E.M.: 1989, *Astrophys. J.* 347, 674.
- Beals, C.S.: 1929, *Monthly Notices Roy. Astron. Soc.* 90, 202.
- Beals, C.S.: 1931, *Monthly Notices Roy. Astron. Soc.* 91, 966.
- Bernabeu, G., Magazzù, A., Stalio, R.: 1989, *Astron. Astrophys.* 226, 215.
- Blomme, R.: 1990, *Astron. Astrophys.* 229, 513.
- Boggess, A., et al.: 1978, *Nature* 275, 372.
- Bruhweiler, F.C., Kondo, Y., McCluskey, G.E.: 1981, *Astrophys. J. Suppl.* 46, 255.
- Castor, J.I.: 1970, *Monthly Notices Roy. Astron. Soc.* 149, 111.
- Castor, J.I., Lamers, H.J.G.L.M.: 1979, *Astrophys. J. Suppl.* 39, 481.
- Castor, J.I., Lutz, J.H., Seaton, M.J.: 1981, *Monthly Notices Roy. Astron. Soc.* 194, 547.
- Cerruti-Sola, M., Perinotto, M.: 1985, *Astrophys. J.* 291, 237.
- Cerruti-Sola, M., Perinotto, M.: 1989, *Astrophys. J.* 345, 339.

- Chang, K., Refsdal, S.: 1979, *Nature* 282, 561.
- Chang, K., Refsdal, S.: 1984, *Astron. Astrophys.* 132, 168.
- Danziger, I.J., Fosbury, R.A.E., Alloin, D., Cristiani, S., Dachs, J., Gouiffes, C., Jarvis, B., Sahu, K.C.: 1987, *Astron. Astrophys.* 177, L13.
- Dean, C.A., Bruhweiler, F.C.: 1985, *Astrophys. J. Suppl.* 57, 133.
- Detal, A., Hutsemékers, D., Remy, M., Surdej, J., Van Drom, E.: 1990, *Astron. Astrophys.* 229, 427.
- Ekberg, J.O.: 1975, *Phys. Scripta* 18, 107.
- Ekberg, J.O., Edlen, B.: 1978, *Phys. Scripta* 18, 107.
- Foltz, C.B., Weymann, R.J., Morris, S.L., Turnshek, D.A.: 1987, *Astrophys. J.* 317, 450.
- Garmany, C.D., Olson, G.L., Conti, P.S., van Steenberg, M.E.: 1981, *Astrophys. J.* 250, 660.
- Grieger, B., Kayser, R., Refsdal, S.: 1988, *Astron. Astrophys.* 194, 54.
- Hartig, G.F., Baldwin, J.A.: 1986, *Astrophys. J.* 302, 64.
- Hazard, C., Morton, D.C., McMahon, R.G., Sargent, W.L.W., Terlevich, R.: 1986, *Monthly Notices Roy. Astron. Soc.* 223, 487.
- Hutsemékers, D., Surdej, J.: 1986, *Comptes rendus sur les Journées de Strasbourg, 8ème réunion*, p. 81.
- Hutsemékers, D., Surdej, J.: 1987, *Astron. Astrophys.* 173, 101 (article 10).
- Hutsemékers, D., Surdej, J.: 1988a, dans "Mass Outflows from Stars and Galactic Nuclei", L. Bianchi and P. Gilmozzi (eds.), Kluwer Academic Publishers, p. 253.
- Hutsemékers, D., Surdej, J.: 1988b, dans "Mass Outflows from Stars and Galactic Nuclei", L. Bianchi and R. Gilmozzi (eds.), Kluwer Academic Publishers, p. 405.
- Hutsemékers, D., Surdej, J.: 1989a, *Astron. Astrophys.* 219, 237 (article 11).
- Hutsemékers, D., Surdej, J.: 1989b, dans "Proceedings of the IAU Symposium n° 131, Planetary Nebulae", S. Torres-Peimbert (ed.), p. 317.
- Hutsemékers, D., Surdej, J.: 1990, *Astrophys. J.*, sous presse (article 9).

- Kayser, R., Refsdal, S., Stabell, R.: 1986, *Astron. Astrophys.* 166, 36.
- Kayser, R., Refsdal, S.: 1989, *Nature* 338, 745.
- Kayser, R., Weiss, A., Refsdal, S., Schneider, P.: 1989, *Astron. Astrophys.* 214, 4.
- Kayser, R., Surdej, J., Condon, J.J., Kellermann, K.I., Magain, P., Remy, M., Smette, A.: 1990, *Astrophys. J.*, sous presse (article 17).
- Lamers, H.J.G.L.M., Cerruti-Sola, M., Perinotto, M.: 1987, *Astrophys. J.* 314, 726.
- Le Borgne, J.F., Pelló, R., Sanahuja, B., Soucail, G., Mellier, Y., Breare, M.: *Astron. Astrophys.* 229, L13.
- Lucy, L.B.: 1971, *Astrophys. J.* 163, 95.
- Magain, P., Surdej, J., Swings, J.P., Borgeest, U., Kayser, R., Kühr, H., Refsdal, S., Remy, M.: 1988, *Nature* 334, 325 (article 16).
- Magain, P., Remy, M., Surdej, J., Swings, J.P., Smette, A.: 1990, dans "Lecture Notes in Physics, Gravitational Lensing", Y. Mellier, B. Fort, G. Soucail (eds.), Springer-Verlag, vol. 360, 88.
- Moore, R.L., Stockman, H.S.: 1984, *Astrophys. J.* 279, 465.
- Nemry, F., Surdej, J., Hernaiz, A.: 1990, *Astron. Astrophys. Letters*, soumis (article 12).
- Netzer, H., Sheffer, Y.: 1983, *Monthly Notices Roy. Astron. Soc.* 203, 935.
- Nottale, L.: 1986, *Astron. Astrophys.* 157, 383.
- Ostriker, J.P., Vietri, M.: 1985, *Nature* 318, 446.
- Ostriker, J.P., Vietri, M.: 1990, *Nature* 344, 45.
- Perinotto, M., Cerruti-Sola, M., Lamers, H.J.G.L.M.: 1989, *Astrophys. J.* 337, 382.
- Rybicki, G.B., Hummer, D.G.: 1978, *Astrophys. J.* 219, 654.
- Schneider, P., Weiss, A.: 1987, *Astron. Astrophys.* 171, 49.
- Smith, L.J., Penston, M.V.: 1988, *Monthly Notices Roy. Astron. Soc.* 235, 551.
- Sobolev, V.V.: 1947, *Dnizusciesja Obolocki Zvezd*, Leningrad (trad. *Moving Envelopes of stars*; traduit du Russe par S. Gaposchkin, Harvard University Press, Cambridge, Mass. 1960).

- Sobolev, V.V.: 1957, *Astron. Zh.* 34, 694 (trad. *Soviet Astron.* 1, 678).
- Sobolev, V.V.: 1958, dans "Theoretical Astrophysics", V.A. Ambartsumyan (ed.), Chapitre 28, Pergamon Press Ltd, London.
- Stickel, M., Fried, J.W., Kühr, H.: 1988a, *Astron. Astrophys.* 198, L13.
- Stickel, M., Fried, J.W., Kühr, H.: 1988b, *Astron. Astrophys.* 206, L30.
- Stickel, M., Fried, J.W., Kühr, H.: 1989, *Astron. Astrophys.* 224, L27.
- Stoche, J.T., Liebert, J., Schild, R., Gioia, I.M., Maccacaro, T.: 1984, *Astrophys. J.* 277, 43.
- Stoche, J.T., Schneider, P., Morris, S.L. et al.: 1987, *Astrophys. J.* 315, L11.
- Surdej, J.: 1977, *Astron. Astrophys.* 60, 303.
- Surdej, J.: 1978a, *Astron. Astrophys.* 62, 135.
- Surdej, J.: 1978b, *Astron. Astrophys.* 66, 45.
- Surdej, J.: 1979a, *Astron. Astrophys.* 73, 1.
- Surdej, J.: 1979b, *Dissertation de Doctorat, Université de Liège.*
- Surdej, J.: 1980, *Astrophys. Space Sci.* 73, 101.
- Surdej, A., Surdej, J., Swings, J.P., Wamsteker, W.: 1981, *Astron. Astrophys.* 93, 285.
- Surdej, J., Swings, J.P.: 1981, *Astron. Astrophys.* 96, 242.
- Surdej, J.: 1981, *Astrophys. Space Sci.* 79, 213.
- Surdej, A., Surdej, J., Swings, J.P.: 1982, *Astron. Astrophys.* 105, 242.
- Surdej, J., Heck, A.: 1982, *Astron. Astrophys.* 116, 80 (article 1).
- Surdej, J.: 1982a, dans "Proceedings of the IAU Symposium N° 103, Planetary Nebulae", London, p. 337 (article 5).
- Surdej, J.: 1982b, *Astrophys. Space Sci.* 88, 31 (article 2).
- Surdej, J., Swings, J.P.: 1983, *Astron. Astrophys.* 117, 359.
- Surdej, J.: 1983a, *Astrophys. Space Sci.* 90, 299 (article 3).
- Surdej, J.: 1983b, *Astron. Astrophys.* 127, 304 (article 4).



- Surdej, J.: 1983c, dans "Proceedings of the 24th Liège International Astrophysical Colloquium, Quasars and Gravitational Lenses", p. 616 (article 6).
- Surdej, J.: 1985, *Astron. Astrophys.* 152, 361 (article 7).
- Surdej, J., Hutsmékers, D.: 1987, *Astron. Astrophys.* 177, 42 (article 13).
- Surdej, J.: 1987a, dans "Exercises in Astronomy", J. Kleczek (ed.), D. Reidel Publishing Company, p. 247.
- Surdej, J.: 1987b, *Physicalia Mag.* 9, 175.
- Surdej, J., Magain, P., Swings, J.P., Borgeest, U., Courvoisier, T.J.-L., Kayser, R., Kellermann, K.I., Kühr, H., Refsdal, S.: 1987, *Nature* 329, 695 (article 15).
- Surdej, J., Magain, P., Swings, J.P., Borgeest, U., Courvoisier, T.J.-L., Kayser, R., Kellermann, K.I., Kühr, H., Refsdal, S.: 1988a, *Astron. Astrophys.* 198, 49.
- Surdej, J.: 1988, *Eur. J. Phys.* 9, 168.
- Surdej, J., Swings, J.P., Magain, P., Borgeest, U., Kayser, R., Refsdal, S., Courvoisier, T.J.-L., Kellermann, K.I., Kühr, H.: 1988b, dans "Proceedings of a workshop on optical surveys for quasars", *Astron. Soc. of the Pac. Conf. Series* 2, 183.
- Surdej, J., Magain, P., Swings, J.P., Remy, M., Borgeest, U., Kayser, R., Refsdal, S., Kühr, H.: 1988c, article de revue dans "The First D.A.E.C. Workshop on Large Scale Structures", compte-rendus édités par C. Balkowski et S. Gordon, p. 95.
- Surdej, J., Arnaud, J., Borgeest, U., Djorgovski, S., Fleischmann, F., Hammer, F., Hutsemékers, D., Kayser, R., Le Fèvre, O., Nottale, L., Magain, P., Meylan, G., Refsdal, S., Remy, M., Shaver, P., Smette, A., Swings, J.P., Vanderriest, C., Van Drom, E., Véron-Cetty, M., Véron, P., Weigelt, G.: 1989, *The Messenger* 55, 8.
- Surdej, J.: 1990, article de revue dans "Lecture Notes in Physics, Gravitational Lensing", Y. Mellier, B. Fort, G. Soucail (eds.), Springer-Verlag, vol. 360, 57 (article 14).
- Surdej, J., Hutsemékers, D.: 1990, *Astron. Astrophys.*, sous presse (article 8).
- Swings, J.P., Magain, P., Remy, M., Surdej, J., Smette, A., Hutsemékers, D., Van Drom, E.: 1990, dans "Lecture Notes in Physics, Gravitational Lensing", Y. Mellier, B. Fort, G. Soucail (eds.), Springer-Verlag, vol. 360, 83.
- Turnshek, D.A.: 1988, dans "QSO Absorption Lines: Probing the Universe", J. Blades, D. Turnshek, C. Norman (eds.), Cambridge University Press, p. 17.

- Turnshek, D.A., Foltz, C.B., Grillmair, C.J., Weymann, R.J.: 1988, *Astrophys. J.* 325, 651.
- Vanderriest, C., Lemonnier, J.P.: 1988, dans "Proceedings of the 1987 Santa Cruz Workshop, Instrumentation in Astronomy", p. 304.
- Walborn, N.R., Nichols-Bohlin, J.N., Panek, R.J.: 1985, "International Ultraviolet Explorer Atlas of O-type Spectra from 1200 to 1900 Å", NASA Reference Publication 1155.
- Walsh, D., Carswell, R.F., Weymann, R.J.: 1979, *Nature* 279, 381.
- Wambsganss, J., Paczyński, B., Katz, N.: 1990, *Astrophys. J.* 352, 407.
- Weiler, K.W., Sramek, R.A.: 1988, *Ann. Rev. Astron. Astrophys.* 26, 295.
- Weymann, R.J., Carswell, R.F., Smith, M.G.: 1981, *Ann. Rev. Astron. Astrophys.* 19, 41.
- Weymann, R., Foltz, C.: 1983, dans "Proceedings of the 24th Liège International Astrophysical Colloquium, Quasars and Gravitational Lenses", p. 538.
- Young, P.: 1981, *Astrophys. J.* 244, 756.